TECHNISCHE UNIVERSITÄT MÜNCHEN
Fakultät für Chemie
Lehrstuhl I für Technische Chemie

Microkinetic Modeling of Processes over Acid Zeolites: Olefin Cracking and Methanol-to-Olefins (MTO)

Sebastian Matthias Standl

Vollständiger Abdruck der von der Fakultät für Chemie der Technischen Universität München zur Erlangung des akademischen Grades eines

Doktor-Ingenieurs (Dr.-Ing.)

genehmigten Dissertation.

Vorsitzender: Prof. Dr. Johannes A. Lercher

Prüfer der Dissertation:
1. Prof. Dr.-Ing. Kai-Olaf Hinrichsen
2. Prof. Dr.-Ing. Harald Klein
3. Prof. Dr. Joris Thybaut (schriftliche Beurteilung)
   Hon.-Prof. Dr. Richard W. Fischer (mündliche Prüfung)

Die Dissertation wurde am 09.01.2020 bei der Technischen Universität München eingereicht und durch die Fakultät für Chemie am 07.07.2020 angenommen.

For Nadine and Olivia

Huc properate viri
salebrosum scandite
montem
pulchra laboris erunt
premia palma quies.

Allegoria del colle della Sapienza, Pinturicchio

Acknowledgments

First of all, I would like to express my sincere gratitude to my supervisor Prof. Dr.-Ing. Kai-Olaf Hinrichsen. Thank you for all your support over the years, especially during my time at the chair (but also before and afterwards). It was a pleasure to be part of the Lehrstuhl I für Technische Chemie (TCI), so thanks for the possibility to join as well as for this multifaceted and challenging topic. I really appreciate the trust you have placed in me and your continuous interest in my progress. I am thankful for helpful scientific discussions, new ideas and for the many opportunities to share our results on international conferences. Thank you for four awesome years at your chair.

Many thanks to Prof. Dr.-Ing. Harald Klein for being part of the examination commission as my second examiner. In addition, thank you for the very smooth and professional collaboration on our common publication - I highly appreciate your support on this.

I would like to say thank you to Prof. Dr. Johannes Lercher for being the chair of the examination commission - and, more importantly, for a pleasant collaboration within the lower olefins cluster (LOC). Thanks for providing both experimental data and inspirational thoughts.

Speaking of the LOC, I thank Prof. Dr. Richard Fischer for the support within the framework of MuniCat, for pointing out different perspectives during our monthly meetings and for being part of the commission during the oral exam.

Special thanks go to Prof. Dr. Joris Thybaut. I really appreciate your contribution as external reviewer for my examination. Moreover, I would like to thank you for the inspiring discussions we had at several occasions (conferences, summer schools, EUROKIN meeting). Thanks for sharing your knowledge and for always having a sympathetic ear.

It is not surprising that within four years, also many organizational and non-scientific problems evolve. As it would have been hard to solve these alone, I thank Heidi for her everlasting support. Thank you for always having an open door and for many lively conversations. A warm thank you goes to Thomas - not only for helping out with administrational problems, but also for

having a good time. I will keep in mind our common coffee breaks, vivid discussions during (and sometimes even subsequent to) the TCI seminars and your 60th birthday.

I would like to highlight the "CH 36304 group" (that still exists) with its incredible sense for good humor: Philipp, Chris and Thomas. Philipp, thank you for so many scientific conversations, but also for an awesome time when the background was not work-related. Thomas and Chris, thank you for a unique office atmosphere where we could discuss both science and also everything else. I really miss our CH 36304 background noise. Thanks a million to all PhD student colleagues who made life at TCI as unforgettable as it was. I cannot enumerate all the great memories I have, but let me mention at least the coffee breaks, TCI seminars, conferences, Aldersbach, TCI barbecues, darts... Thank you for the familiar atmosphere, the cooperativeness and the unique team spirit. Thanks to Daniel, David, Flo, Franz, Franz, Jennie, Johanna, Julia, Moe, My, Matthias, Matthias, Stefan and Tabea.

The creation of a microkinetic model would be impossible without proper experimental data. Felix, many thanks for the high number of measurements you performed - your persistence is highly appreciated. Also, thank you for having a good time within (and beyond) the LOC. In that context, I would like to thank also you, Daniel, for being such a nice LOC colleague. Maricruz and Yue, thanks for your support and your ideas that you brought up in our discussions. Many thanks to you, Tassilo, for a very pleasant and fruitful collaboration during my first months at the chair. I was lucky that I could build my house on a solid foundation in the form of your work as my predecessor - thank you. I am grateful to our partner from industry, the Clariant Produkte (Deutschland) GmbH. Markus, special thanks to you for such a pleasant collaboration over the years. Thank you for your input during the monthly meetings and for approving manuscripts and presentations always that fast.

I would like to say thank you to all students I supervised during my four years at the chair. All of you contributed to the final outcome of my dissertation. Many thanks for your work, the friendly and trustful atmosphere as well as for the many nice conversations, be it of scientific nature or not. Thank you Andreas, Daniel, Hannah, Johanna, Jonas, Karsten, Laura, Lei, Maximilian, Rosa, Seri, Tobias (twice!) and Yu.

This whole work would have been impossible without the support from my family and my good friends. Especially, I would like to thank my parents and my sister for giving me the possibility to pursue my goals and for such a pleasant common time over more than 30 years now. It is not surprising that over the years, some setbacks and devastating moments came up. Nadine, I cannot thank you enough for helping me out in those times and, of course, also for all the great memories we share. Thanks for all your support, for your patience, for not complaining when I locked myself in the study to finish my dissertation, for your valuable feedback in many different situations and for being such a wonderful wife and mother.

Abstract

In times of scarce oil reserves, stricter governmental regulations as well as rising environmental concerns within the society, alternative synthesis routes gain in importance. Olefin cracking and methanol-to-olefins (MTO) are two possible solutions to supply the polymer industry with their massive demand of lower olefins. Both are performed over acid zeolites like ZSM-5 and thus enable tailored product distributions and less energy consumption.

In this work, these processes are analyzed using microkinetic modeling studies, which means that each elementary reaction taking place on the catalytic surface is explicitly considered. The single-event methodology is used to reduce the number of unknown parameters while still depicting the complete reactivity. At first, a variety of different modeling approaches is discussed, ranging from simple to microkinetic examples. In addition, a complete picture of such deterministic literature models for both processes is given.

A single-event kinetic model for cracking of 1-pentene over ZSM-5 is introduced. This comprises the model itself as well as two reactor solutions for maximum propene production, a two-zone and a recycle reactor. The latter setup is further investigated in a detailed process optimization study where the operating conditions of highest economic benefit are evaluated as function of varying propene prices.

Moreover, it can be shown that the 1-pentene model is valid for $C_3^=$ to $C_7^=$ olefins as feed and even their arbitrary mixtures. A rigorous distinction is made between kinetic and catalyst descriptors, thereby allowing for a model transfer to different ZSM-5 catalysts. In another study, the microkinetic model is used to optimize the description of olefin adsorption on ZSM-5. Here, the most important pathways comprise π-complex formation first, followed by a protonation to intermediates of comparably low stability, but of ionic character at least for branched species.

Finally, this knowledge is used to develop a model for MTO over ZSM-5 that describes the fundamental kinetics when co-feeding olefins. The inclusion of several olefin methylation pathways resembles the fast carbon transfer from the oxygenates to the olefin hydrocarbon pool. The resulting model is evaluated to find conditions where propene formation is enhanced.

Kurzzusammenfassung

Im Hinblick auf die begrenzten Ölvorkommen, die strengeren gesetzlichen Anforderungen sowie das wachsende Bedürfnis nach mehr Klimaschutz innerhalb der Gesellschaft gewinnen alternative Syntheserouten an Bedeutung. Zwei solcher Konzepte, um die Polymerindustrie mit niederen Olefinen zu versorgen, sind Olefin-Cracking und Methanol-zu-Olefinen (MTO). Bei beiden Prozessen werden saure Zeolith-Katalysatoren wie ZSM-5 verwendet, was bedarfsgerechte Produktzusammensetzungen und einen geringeren Energieverbrauch ermöglicht.

In dieser Arbeit werden beide Prozesse anhand mikrokinetischer Modellierungen, sprich unter Berücksichtigung jeder möglichen Elementarreaktion, untersucht. Die Single-Event-Methodik erlaubt hierbei eine Reduktion der unbekannten Parameter ohne Genauigkeitsverlust. Eingangs wird zunächst die Bandbreite an Modellierungsansätzen detailliert beschrieben. Zudem erfolgt ein kompletter Überblick der deterministischen Literatur-Modelle für beide Prozesse.

Ein Single-Event-Modell zur Beschreibung vom 1-Penten-Cracking auf ZSM-5 wird vorgestellt. Dies beinhaltet zwei Reaktorkonzepte für maximale Propen-Produktion: ein Zweizonen- und ein Recycle-Reaktor. Letzterer wird in einer detaillierten Prozessoptimierung hinsichtlich gewinnmaximierender Betriebsbedingungen bei variierenden Propen-Preisen ausgewertet.

Darüber hinaus wird der universale Charakter des 1-Penten-Modells gezeigt, welches $C_3^=$ bis $C_7^=$ Olefine als auch deren beliebige Mischungen als Feed beschreiben kann. Durch strikte Trennung von kinetischen Größen und Katalysatoreigenschaften ist ein Transfer auf andere ZSM-5-Katalysatoren möglich. In einer weiteren Studie wird das Modell zur Optimierung der Beschreibung der Olefin-Adsorption auf ZSM-5 genutzt. Die wichtigsten Pfade sind zunächst die Bildung eines π-Komplexes sowie die Protonierung zu einem Intermediat von vergleichsweise geringer Stabilität, welches für verzweigte Spezies einen ionischen Charakter aufweist.

Abschließend werden diese Einblicke zur Modellerstellung für MTO auf ZSM-5 verwendet, um die Kinetik mit Olefin-Cofeed fundamental zu beschreiben. Die Notwendigkeit der Einbindung mehrerer Olefin-Methylierungsrouten unterstreicht den schnellen Kohlenstoff-Transfer von den Oxygenaten zum olefinischen Hydrocarbon-Pool. Das resultierende Modell wird hinsichtlich Bedingungen ausgewertet, die die Propen-Bildung fördern.

Contents

List of Figures

List of Schemes

List of Tables

Nomenclature

Latin Symbols

A	Pre-exponential factor	variable
$\tilde{A}$	Single-event pre-exponential factor	variable
A_{ac}	Active area of one tray	m^2
A_{ht}	Area required for heat transfer	m^2
A_{t}	Total area of one tray	m^2
a	Catalytic activity	-
C_{t}	Concentration of total acid sites	$\mathrm{mol\,kg_{cat}^{-1}}$
C_{t^*}	Concentration of free acid sites	$\mathrm{mol\,kg_{cat}^{-1}}$
CN_i	Carbon number	-
$C(i)$	Concentration	variable
c_i	Price	variable
$c_{p,i}$	Heat capacity at constant pressure	$\mathrm{J\,mol^{-1}\,K^{-1}}$
D_{B}	Bottom section diameter	m
D_{Col}	Column diameter	m
D_{O}	Outer tube diameter	m
D_{R}	Tube bundle diameter	m
D_{T}	Top section diameter	m
d_{P}	Particle diameter	m
dof	Degree of freedom	-
E_{a}	Activation energy	$\mathrm{J\,mol^{-1}}$
F	F-factor	$\mathrm{Pa^{0.5}}$
$F(i)$	Molar flow rate	$\mathrm{mol\,s^{-1}}$
f_i	Fugacity	Pa
G_i	Gibb's free energy	$\mathrm{J\,mol^{-1}}$
G_{t}	Total Gibb's free energy	J
H_i	Enthalpy	$\mathrm{J\,mol^{-1}}$
h	Planck constant	J s
$K_l(i)$	Equilibrium constant	variable
k_{B}	Boltzmann constant	$\mathrm{J\,K^{-1}}$
k_l	Rate constant	variable

$\tilde{k}_l$	Single-event rate constant	variable
L	Tube length	m
$M(i)$	Molecular mass	kg
$\dot{M}(i)$	Mass flow rate	$\mathrm{kg\,s^{-1}}$
$M_\mathrm{m}(i)$	Molar mass	$\mathrm{kg\,mol^{-1}}$
m	Type of reactant intermediate	-
N_A	Avogadro constant	$\mathrm{mol^{-1}}$
N_Exp	Number of experiments	-
$N_{el,i}$	Number of atoms of element *el*	-
N_Par	Number of parameters	-
N_Res	Number of fitting responses	-
N_T	Number of tubes	-
n	Type of product intermediate	-
n^ch	Number of chiral centers	-
n^d	Deactivation order	-
$n^\mathrm{d}_{\mathrm{H_2O}}$	Deactivation order of water adsorption	-
n^trans	Number of translational degrees of freedom	-
n_e	Number of single events	-
$n_{\mathrm{H_2O}}$	Reaction order of water adsorption	-
n_i	Number of moles	mol
OF	Objective function	variable
P_el	Electrical power	W
P_mech	Mechanical power	W
p	Pressure	Pa
$p(i)$	Partial pressure	Pa
Q_cool	Removed heat	J
$\dot{Q}_\mathrm{r}$	Heat flow due to reaction	W
R	Gas constant	$\mathrm{J\,mol^{-1}\,K^{-1}}$
$R(i)$	Net rate of production	$\mathrm{mol\,kg_{cat}^{-1}\,s^{-1}}$
r_l	Reaction rate	variable
S_i	Entropy	$\mathrm{J\,mol^{-1}\,K^{-1}}$
$\tilde{S}_i$	Single-event entropy	$\mathrm{J\,mol^{-1}\,K^{-1}}$
SSQ	Sum of squared residuals	variable
T	Temperature	K
U	Overall heat transfer coefficient	$\mathrm{W\,m^{-2}\,K^{-1}}$
t	Time	s
V	Volume	$\mathrm{m^3}$
$\dot{V}$	Volumetric flow rate	$\mathrm{m^3\,s^{-1}}$
$V_\mathrm{m}(i)$	Molar volume	$\mathrm{m^3\,mol^{-1}}$
v	Superficial velocity	$\mathrm{m\,s^{-1}}$

v^{po}	Specific pore volume	$\mathrm{m^3\,kg_{cat}^{-1}}$
W	Catalyst mass	$\mathrm{kg_{cat}}$
$w(i)$	Mass fraction	-
$X(i)$	Conversion	-
$Y(i)$	Weight-based yield	-
$y(i)$	Mole fraction	-
$\hat{y}(i)$	Modeled mole fraction	-

Greek Symbols

α	Parameter for carbon number dependence	$\mathrm{J\,mol^{-1}}$
α^l	Composed pre-exponential factor	variable
α_{i}	Inner heat transfer coefficient	$\mathrm{W\,m^{-2}\,K^{-1}}$
α_l	Deactivation parameter	-
α_{o}	Outer heat transfer coefficient	$\mathrm{W\,m^{-2}\,K^{-1}}$
β	Parameter for carbon number dependence	$\mathrm{J\,mol^{-1}}$
β^l	Linearization parameter	-
γ	Parameter for carbon number dependence	$\mathrm{J\,mol^{-1}\,K^{-1}}$
γ^l	Parameter for carbon number dependence	-
Δ	Difference	variable
ΔL	Characteristic length	m
Δp	Pressure drop	Pa
ΔT_{m}	Logarithmic mean temperature difference	K
δ	Parameter for carbon number dependence	$\mathrm{J\,mol^{-1}\,K^{-1}}$
δ^l	Linearization parameter	-
ε	Void fraction	-
η	Dynamic viscosity	Pa s
η_{C}	Isentropic efficiency	-
θ^*	Relative amount of free acid sites	-
$\theta(i)$	Coverage	-
κ	Reaction order	-
μ_i	Chemical potential	$\mathrm{J\,mol^{-1}}$
ν_{g}	Number of moles in gas phase	-
$\nu_l(i)$	Stoichiometric coefficient	-
ρ	Density	$\mathrm{kg\,m^{-3}}$
σ_{gl}	Global symmetry number	-
ϕ^l	Parameter for carbon number dependence	-
φ^l	Parameter for carbon number dependence	-
φ_l	Deactivation parameter	-
ω_i	Weighting factor	-

Superscript

ads	Adsorption
ao	Alkoxide
ar	Aromatization
CN	Carbon number
c	Consumption
chem	Chemisorption
ci	Carbenium ion
co	Composite value
coads	Co-adsorption
cr	Cracking
d	Deactivation
dim	Dimerization
f	Formation
g	Gas phase
H	Henry
in	Inlet value
Le	Lewis acid sites
l	Liquid phase
MF	Metal fiber
max	Maximum value
me	Methylation
meD	Double methylation
meht	Methanol-induced hydrogen transfer
out	Outlet value
PO	Powder
phys	Physisorption
prot	Protonation
reac	Reactant state
ref	Reference
SBAS	Strong Brønsted acid sites
sat	Saturation
TD	Thermodynamic
trans	Translational
zeo	Zeolite
π	π-Complex
0	Initial value
$\circ$	Standard condition ($p^\circ = 10^5$ Pa)
‡	Transition state

’	Reduced reaction rate: without C_{t*}^{SBAS}
”	Reduced reaction rate: without $C\left(R_{Me}^{+}\right)$

Subscript

ads	Adsorption
C	Carbon
cat	Catalyst
chem	Chemisorption
co	Consumption
coads	Co-adsorption
el	Electrical power
el	Running index for element
ext	External
Feed	Feed
f	Formation
fl	Fluid (in reactor)
g	Gas (in main column)
h	Running index for acid sites
i	Arbitrary species
int	Internal
j	Running index for arbitrary species
k	Running index for experiments
L	Value used in Langmuir approach
l	Arbitrary reaction step
max	Maximum value
NG	Natural gas
phys	Physisorption
pr	Production
prot	Protonation
q	Running index for reaction rate
r	Reaction
t	Total
v	Arbitrary species involved in reaction
w	Arbitrary species involved in reaction
zeo	Zeolite
π	π-Complex
0	Pre-exponential factor
‡	Transition state

Abbreviations

A_i	Aromatic compound
Ads.	Adsorption
AEI	Framework code of SAPO-18
BET	Brunauer-Emmett-Teller
C_i^{al}	Aliphatic compound with carbon number *i*
C_i^{ar}	Aromatic compound with carbon number *i*
C_i^{HC}	Hydrocarbon with carbon number *i*
C_i^{SP}	Side products with carbon number *i*
$C_i^{=}$	Olefin with carbon number *i*
C_x^{+}	Protonated intermediate
C_i	Paraffin with carbon number *i*
C_{ni}	*n*-Paraffin with carbon number *i*
CHA	Framework code of chabazite
Cond	Condenser
DFT	Density functional theory
DME	Dimethyl ether
DSC	Differential scanning calorimetry
EC#	Equality constraint number #
ER	Eley-Rideal
FCC	Fluid catalytic cracking
FER	Framework code of ferrierite
FID	Flame ionization detector
GA	Genetic algorithm
GC	Gas chromatograph
GC-FTIR	Gas chromatograph with Fourier transform infrared
GC-MS	Gas chromatograph with mass spectrometer
GHSV	Gas hourly space velocity
HBT	Hankinson-Brobst-Thomson
Hex#	Heat exchanger number #
HF	Hartree-Fock
HP	High pressure
HW	Hougen-Watson
IC#	Inequality constraint number #
Int	Intermediates
IR	Infrared
L	Langmuir
LH	Langmuir-Hinshelwood
LP	Low pressure
Mech.	Mechanistic scheme

MFI	Framework code of ZSM-5
MOR	Framework code of mordenite
MP	Medium pressure
MTG	Methanol-to-gasoline
MTH	Methanol-to-hydrocarbons
MTO	Methanol-to-olefins
MTP	Methanol-to-propylene
MTT	Framework code of ZSM-23
MW	Methanol and water
O_i	Olefin
O_v	Second olefin in dimerization
OM	Oxonium methylide
OV#	Optimization variable number #
Ox	Oxygenates (methanol and DME)
P_i	Paraffin
PCP	Protonated cyclopropane
PSSA	*Pseudo*-steady-state approximation
P#	Pump number #
P/E	Propene to ethene
p	Primary intermediate
QM-Pot	Quantum mechanics and interatomic potential functions
R^+_{DME}	Protonated DME
R^+_i	Protonated intermediate
R^+_{Me}	Surface methyl group
Reb	Reboiler
RN##	Reaction network number ##
SBU	Secondary building unit
Side prod.	Side products
s	Secondary intermediate
TCD	Thermal conductivity detector
TG	Thermogravimetry
TOS	Time-on-stream
t	Tertiary intermediate

1 Introduction

Parts of this chapter were published and are reprinted with permission from:

S. Standl, O. Hinrichsen
Kinetic Modeling of Catalytic Olefin Cracking and Methanol-to-Olefins (MTO) over Zeolites: A Review
Catalysts 8 (2018), 626, DOI 10.3390/catal8120626.

1.1 Motivation

Propene is one of the crucial building blocks originating from the petrochemical industry [1]. Around 90% of the worldwide supply is produced via fluid catalytic cracking (FCC) or steam cracking [2], the latter being the process with the highest energy demand in the chemical industry [3]. Besides the economic disadvantages, the enormous CO_2 emissions represent another problem [4, 5]. Moreover, the high-temperature process allows almost no product adjustment and the shift from higher feedstocks to ethane as feed further reduces $C_3^=$ yields [6]. In FCC, propene is a byproduct because this process is aimed at gasoline production [7].

An increase in propene demand is predicted [8, 9]; see, for example, a recent review by Blay *et al.* [2]. Thus, alternative catalytic processes are necessary. Cracking of higher olefins [2], methanol-to-hydrocarbons (MTH) [10], olefin metathesis [11, 12], propane dehydrogenation [13, 14], oxidative dehydrogenation of propane [15] or ethene-to-propene [2, 16] are amongst the most prominent alternative approaches.

Kinetic modeling is an indispensable tool for assessing reaction kinetics, heat management, product distribution and reactor performance [17, 18]. The application range of kinetic models depends on their complexity: many different strategies exist between the simplest approach, a power-law model and the highest level of detail, a microkinetic model. Models with less complexity are created relatively quickly and do not require much computational power, but they are restricted in terms of their possible applications. On the other hand, the preparation of

a microkinetic model is time-consuming and complicated, but it can be used to gain insight into intermediates and preferred reaction pathways, for extrapolation, transfer to other systems and optimization of both catalysts and the process [17, 19, 20].

When dealing with hydrocarbon conversion over zeolites as catalytic materials, reaction networks are extremely large because of the many different isomers. This is why kinetic modeling of these processes is challenging; without suitable assumptions, derivations and simplifications, no reasonable solutions can be achieved. Nevertheless, the importance of such models is especially high because propene, which is the desired compound in many processes, is an intermediate and not a final product. Insight into the most important pathways that produce propene is needed in order to maximize its output. Thus, innovative modeling approaches are required that depict the whole reactivity without being too demanding in calculation times.

1.2 Scope

In this work, microkinetic modeling studies are developed for olefin cracking and for methanol-to-olefins (MTO) as two alternative approaches for lower olefins production. During model development, the single-event methodology is used [19–21]. This concept allows for an effective reduction in the number of unknown kinetic parameters while each elementary reaction is still considered. In literature, several examples exist where this methodology is applied to hydrocracking over bifunctional catalysts, i.e., zeolites enriched with mostly Pt as metal phase [21–24]. Due to the varied catalyst properties, some steps of the underlying chemistry are different to pure olefin cracking.

In previous work [25], the single-event methodology could be transferred to isothermal data of 1-hexene cracking over ZSM-5. Kinetic parameters are then estimated using the same methodology and non-isothermal data of 1-pentene cracking, again over ZSM-5 [26]. As olefin cracking is part of the MTO reactivity, this model is to be extended with the methanol-related reactions to end up with a single-event kinetic model for MTO. However, a proof of concept has to be performed first, showing that the cracking model is valid for a bandwidth of carbon numbers and their mixtures as feed although it was developed with only 1-pentene as feed. Furthermore, more understanding of the adsorption steps during cracking is required before an application to MTO is possible. Because each reaction is depicted, the final models allow for a contribution analysis of the different pathways. With this additional information, optimal conditions and reactor concepts for maximum propene production should be developed, both for olefin cracking and for MTO.

In summary, scope of this work is not only the development of microkinetic models, but also their application with respect to optimization of the product spectrum. Another aim is to gain more insight into best practice in deterministic modeling. The single-event methodology should be further refined for olefin cracking and MTO. Moreover, the comparison with literature models should lead to an assessment of the most suitable methodology for a certain purpose when dealing with hydrocarbon reaction networks. Thus, it should help in finding suitable approaches for the particular requirements of future studies.

The different topics mentioned above are presented in the following chapters:

- **Chapter 2** discusses zeolites, thermodynamics as well as reactivity of olefin cracking and MTO. In addition, it explains different strategies for deterministic kinetic modeling of these systems. This is completed by a comprehensive summary of literature models. This chapter was published in similar form in:

  S. Standl, O. Hinrichsen
  Kinetic Modeling of Catalytic Olefin Cracking and Methanol-to-Olefins (MTO) over Zeolites: A Review
  Catalysts 8 (2018), 626.

- **Chapter 3** introduces the single-event kinetic model for 1-pentene cracking over ZSM-5. Its application in reactor design with the aim of maximum propene production is also shown, leading to two different concepts: the two-zone and the recycle reactor. Parts of this chapter were published in:

  T. von Aretin, S. Standl, M. Tonigold, O. Hinrichsen
  Optimization of the Product Spectrum for 1-Pentene Cracking on ZSM-5 Using Single-Event Methodology. Part 1: Two-Zone Reactor
  Chemical Engineering Journal 309 (2017), 886–897.

  T. von Aretin, S. Standl, M. Tonigold, O. Hinrichsen
  Optimization of the Product Spectrum for 1-Pentene Cracking on ZSM-5 Using Single-Event Methodology. Part 2: Recycle Reactor
  Chemical Engineering Journal 309 (2017), 873–885.

  S. Standl, O. Hinrichsen
  Kinetic Modeling of Catalytic Olefin Cracking and Methanol-to-Olefins (MTO) over Zeolites: A Review
  Catalysts 8 (2018), 626.

T. von Aretin, S. Schallmoser, S. Standl, M. Tonigold, J. A. Lercher, O. Hinrichsen
Single-Event Kinetic Model for 1-Pentene Cracking on ZSM-5
Industrial & Engineering Chemistry Research 54 (2015), 11792–11803.

Parts were also published as Supporting Information to:

S. Standl, T. Kühlewind, M. Tonigold, O. Hinrichsen
On Reaction Pathways and Intermediates During Catalytic Olefin Cracking over ZSM-5
Industrial & Engineering Chemistry Research 58 (2019), 18107–18124.

J. Sundberg, S. Standl, T. von Aretin, M. Tonigold, S. Rehfeldt, O. Hinrichsen, H. Klein
Optimal Process for Catalytic Cracking of Higher Olefins on ZSM-5
Chemical Engineering Journal 348 (2018), 84–94.

- **Chapter 4** is a proof of concept concerning the single-event methodology. The 1-pentene model is used to describe experimental data of two different literature studies where olefins of varying carbon numbers are used as feed. This chapter was published in similar form in:

  S. Standl, M. Tonigold, O. Hinrichsen
  Single-Event Kinetic Modeling of Olefin Cracking on ZSM-5: Proof of Feed Independence
  Industrial & Engineering Chemistry Research 56 (2017), 13096–13108.

- **Chapter 5** extends the recycle reactor from Chapter 3 with a complete process model. Here, a detailed optimization routine is performed, including not only the reactor and the respective conditions, but also the whole separation unit. This chapter was published in similar form in:

  J. Sundberg, S. Standl, T. von Aretin, M. Tonigold, S. Rehfeldt, O. Hinrichsen, H. Klein
  Optimal Process for Catalytic Cracking of Higher Olefins on ZSM-5
  Chemical Engineering Journal 348 (2018), 84–94.

- **Chapter 6** contains an analysis of adsorption steps of olefins on ZSM-5. The microkinetic character of the model is used to obtain insight into intermediates and to optimize the implementation of adsorption. This chapter was published in:

  S. Standl, T. Kühlewind, M. Tonigold, O. Hinrichsen
  On Reaction Pathways and Intermediates During Catalytic Olefin Cracking over ZSM-5
  Industrial & Engineering Chemistry Research 58 (2019), 18107–18124.

- **Chapter 7** discusses the single-event kinetic model for MTO over ZSM-5. Using the insight from the previous chapters, the cracking model can be extended with the methanol-related reactions. This chapter was published in:

  S. Standl, F. M. Kirchberger, T. Kühlewind, M. Tonigold, M. Sanchez-Sanchez, J. A. Lercher, O. Hinrichsen
  Single-Event Kinetic Model for Methanol-to-Olefins (MTO) over ZSM-5: Fundamental Kinetics for the Olefin Co-Feed Reactivity
  Chemical Engineering Journal 402 (2020), 126023.

- **Chapter 8** is a summary of the main findings of this work; it comprises recommendations and an outlook for further studies. Parts of this chapter were published in:

  S. Standl, O. Hinrichsen
  Kinetic Modeling of Catalytic Olefin Cracking and Methanol-to-Olefins (MTO) over Zeolites: A Review
  Catalysts 8 (2018), 626.

2 Theoretical Background

This chapter was published in similar form and is reprinted with permission from:

S. Standl, O. Hinrichsen
Kinetic Modeling of Catalytic Olefin Cracking and Methanol-to-Olefins (MTO) over Zeolites: A Review
Catalysts 8 (2018), 626, DOI 10.3390/catal8120626.

2.1 Zeolites

Originally, the term zeolite referred solely to aluminosilicates consisting of SiO_4 and AlO_4^- units. In the meantime, other materials with similar structural features have been included in the definition. All have a common crystalline and tetrahedral structure [27]. Two of their properties are especially important in the context of catalysis. Firstly, they have well-defined channels and intersections whose cross sections are often within the range of molecular size. Through this, a shape selectivity during reactions is achieved: the small openings can prevent certain molecules from entering or leaving the channels while the pore structure also influences the reaction transition states [28]. Secondly, zeolites contain acid sites which is why they are also called solid acids. Brønsted acidity arises when aliovalent cations such as Al^{3+} and Si^{4+} are connected via oxygen [27]. The resulting negativity of the framework is balanced by additional cations. The incorporation of H^+ creates a Brønsted acid hydroxyl group situated between aluminum and silicon. The oxygen itself acts as a Lewis base by providing electrons for the non-fully coordinated metal cations. The latter are typical Lewis acid sites, either within the framework or as extra-framework cations [29]. For industrial use, zeolites are often mixed with binders which provide a mesoporous surrounding of the crystals. This can also affect the catalytic performance [30, 31]. The resulting extrudates are then formed to the desired pellet shape.

Within a zeolite crystal, the tetrahedral units represent the primary building units. Their systematic arrangement leads to a block consisting of several tetrahedra which is referred to as a secondary building unit (SBU) [27]. The SBU is characteristic of a certain zeolite because

it is found periodically within the framework. A three-letter code is used to differentiate the various frameworks [32]. An important property is the channel opening which is defined by the number of cations: a ten-membered ring means that the opening is formed by ten cations connected via ten oxygen atoms. Eight-, ten- and twelve-membered rings are classified into small-, medium- and large-pore zeolites, respectively [27]. The Structure Commission of the International Zeolite Association presents an overview of the different zeolites online [33]. Details about morphology, synthesis and characterization can be found elsewhere [27–29, 32, 34]. Here, four important examples should be introduced.

ZSM-5 [35] is the second most applied zeolite in industry [34]. The framework code is MFI and the SBU consists of a pentasil unit, which itself is composed of eight rings with five cations each. It is a medium-pore zeolite where two types of pores can be found: straight channels along the (010) direction and zigzag channels along the (100) direction [34, 36]. These cross each other at intersections; a three-dimensional pore network is obtained with the openings $5.1 \times 5.5\,\text{Å}$ (straight channel) and $5.3 \times 5.6\,\text{Å}$ (zigzag channel) [27]. In general, ZSM-5 shows strong acidity, high activity and stability and a pronounced shape selectivity during hydrocarbons conversion [27].

ZSM-23 [37] with framework code MTT is another example of a medium-pore zeolite [27]. Its channels are one-dimensional with an opening of $5.2 \times 4.5\,\text{Å}$ [33]. This accelerates deactivation, but also yields more higher and branched olefins, which are suitable for gasoline production [38, 39].

The aluminophosphates consist of tetrahedral AlO_4^- and PO_4^+ units. Consequently, this framework is neutral [29]. When P is replaced by Si, a negative charge is introduced which creates acid sites. This leads to the silicoaluminophosphates with SAPO-34 and SAPO-18 as examples. Their strict framework ordering allows only even-numbered rings as pore openings [34]. While the Si/Al ratio must be greater than one for the aluminosilicates [29], it is usually less than one for SAPO. The structure of SAPO-34 [40] is similar to chabazite (framework code CHA) meaning it is a small-pore zeolite with an opening of 3.8 Å [41] and a three-dimensional cage structure. On the one hand, its moderate acidity in combination with the shape selectivity leads to high yields of lower olefins. On the other hand, SAPO catalysts are prone to rapid deactivation effects [42].

SAPO-18 [43] is isomorphic to SAPO-34, while the framework is of AEI type [41]. It belongs to the small-pore zeolites with openings similar to SAPO-34 [33]. Although these two SAPO examples also have the same Si/(Si+Al+P) ratio, the amount of Brønsted acid sites is significantly lower for SAPO-18. Hence, it has a longer lifetime [43, 44]. Moreover, synthesis of SAPO-18 is simpler and cheaper than for SAPO-34 [43].

2.2 Olefin Cracking

Several studies analyze the mechanism and product distribution of olefin cracking over zeolites [45–52]. A helpful overview can be found [2]. For the conversion of higher olefins to mainly propene, no commercial process has been achieved thus far.

Two main pathways must be differentiated: monomolecular cracking and dimerization with subsequent cracking. The former is only possible for olefins having carbon numbers greater than or equal to five. Ethene, propene and butenes must undergo a dimerization step first. The resulting higher olefin can either crack in a second step or it can react in another dimerization. This leads to a complex interconversion scheme [50]. Thermodynamics favor lower olefins at high temperatures. One reason is that dimerization is exothermic, while the cracking reaction is endothermic. In addition, adsorption effects might be important for this observation because adsorption is less favored at higher temperatures [53].

The different reaction steps and intermediates are shown in Scheme 2.1, using the monomolecular cracking of 2-methyl-2-hexene as example. Here, the adsorption step must be considered first: it is described as a two-step chemisorption at a Brønsted acid site, which can be divided into π-complex formation (1) and protonation (2) [54]. The resulting intermediate is depicted as a carbenium ion here, however, it should be noted that alkoxides are also proposed as stable intermediates [54–56]. In the initial form, monomolecular cracking would be energetically less desired because of the formation of a primary intermediate. By contrast, the molecule preferably undergoes two isomerization reactions: an additional side group is formed by branching via a protonated cyclopropane (PCP) transition state (3), whereas a subsequent methyl shift (4) changes the position of this side group. Cracking to a secondary propyl intermediate is now possible (5). The other product, 2-butene, is released directly to the gas phase. Finally, the deprotonation (6) and desorption (7) to propene take place. As illustrated in Scheme 2.1, all steps are reversible and only the cracking or dimerization as a backward reaction are of kinetic relevance. By contrast, the adsorption as well as isomerization reactions are often assumed to be *quasi*-equilibrated [21]. In addition to PCP branching and methyl shift, hydride shifts also exist as isomerization steps. The catalytic cycle illustrated in Scheme 2.1 gives already a first impression why microkinetic modeling of this reactivity is both challenging and important: the structure of each isomer is crucial for kinetics.

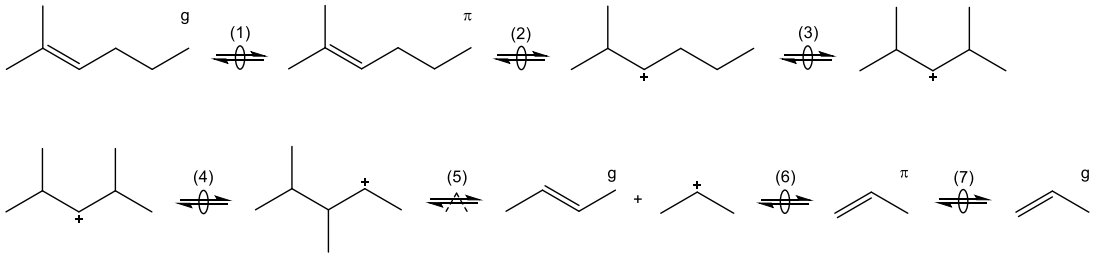

Scheme 2.1: Elementary reactions occurring during cracking of olefins connected to a complete catalytic cycle; the superscripts g and π represent olefins in the gas phase and bound in a π-complex, respectively; see main text for an explanation of the numbers.

Apart from these olefin interconverting steps, side reactions also exist [57, 58]. The most important pathway produces both paraffins and aromatics. It starts with a hydride transfer from an olefin to a protonated intermediate. The latter is converted to a paraffin, whereas the former leads to a protonated olefin. Provided the chain is long enough, a cyclization reaction takes place, yielding a cyclic olefin subsequent to a deprotonation [57]. Through two additional hydride transfers and deprotonations, an aromatic structure is obtained. This mechanism results in a ratio of 3:1 of paraffins to aromatics. However, the latter can form polymerized species, leading to coke, which also allows different ratios. The formation of methane is attributed to thermal cracking effects. Further elementary steps occurring during olefin interconversion, especially when many cyclic compounds are involved, are beyond the focus of this work and can be found, for example, in other publications [19, 59–62].

2.3 MTO

Since the conversion of methanol to hydrocarbons was discovered accidentally by two independent research teams at Mobil [63], many scientists have tried to determine the exact mechanism. At first, the focus of this process was on the production of high-octane compounds (methanol-to-gasoline, MTG), but the product spectrum always contained high quantities of olefins, which is why MTO was introduced [64]. A commercial solution for increasing propene yields by recycling the higher olefins is called methanol-to-propylene (MTP) [65]. The product composition depends heavily on the conditions, setup and catalyst [10]. Some general features of methanol conversion over zeolites are shown here.

When pure methanol is led over an acid zeolite, the reaction to form dimethyl ether (DME) and water proceeds quickly; the thermodynamic equilibrium is rapidly achieved. Several studies exist that consider the exact mechanism of this reaction [66–72]. The dissociative mechanism suggests that after methanol is chemisorbed, its dehydration leads to a surface methyl group. In a subsequent step, the latter reacts with a second methanol molecule to a protonated DME

which finally desorbs. In the associative route, DME is produced directly without forming the surface methyl group as an intermediate.

Mechanistically, the formation of the first C-C bond, i.e., the conversion of methanol and DME (oxygenates) to higher hydrocarbons, has been under debate for decades. It is still not fully understood, although some recent contributions underline the importance of formaldehyde in this context [73]. Previously, other mechanisms were proposed: the oxonium ylide mechanism, the carbene mechanism, the carbocationic mechanism, the free radical mechanism and the consecutive type mechanism. These are summarized and discussed in the review by Stöcker [64] and also elsewhere [9]. Despite the unresolved mechanism, the autocatalytic nature of MTO with a pure methanol feed is well-known [74, 75]. During the initiation phase, the conversion of oxygenates is almost zero because the formation of the first C-C bond is slow. After a certain contact time, the conversion increases: the first hydrocarbons are formed, this accelerates the conversion of oxygenates which again produces more hydrocarbons. Figure 2.1 clearly shows the resulting S-shape of the curve which only slows down when the concentration of oxygenates becomes too low. This is typically observed towards the end of the catalyst bed and thus for high values of the contact time. In Figure 2.1, the latter is defined as ratio of catalyst mass W and inlet molar flow rate $F_{\mathrm{C}}^{\mathrm{in}}$ of all carbon containing species.

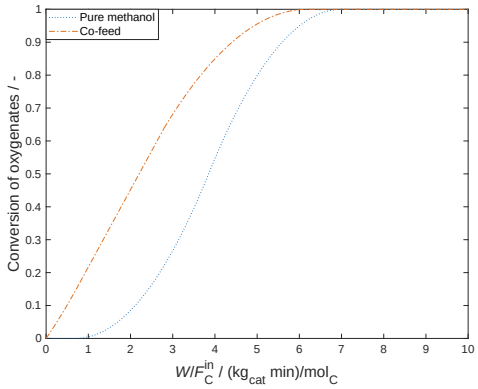

Figure 2.1: Typical case of oxygenates conversion as a function of contact time for a pure methanol feed and for a feed comprising olefins co-fed with methanol.

An important concept for MTO chemistry is the hydrocarbon pool proposed by Dahl and Kolboe [76–78]. According to this theory, adsorbed or trapped hydrocarbon species which are not further defined act as a co-catalyst through ongoing methylation and dealkylation reactions, the latter releasing mainly ethene and propene. It was suggested that the pool species are somehow similar to coke, i.e., polymethylated aromatic compounds formed during the early reaction stage [76]. Much research has gone into determining the exact structure of the aromatic compounds [10, 79–83]. Furthermore, two mechanistic pathways for methanol consumption and subsequent olefin dealkylation were suggested [81]. In the side-chain mechanism [84–88], one of the side chains of the aromatic compound is continuously growing until it is dealkylated

as olefin. By contrast, in the paring mechanism [89], the growth of the aromatic compound causes complex structural rearrangements which also lead to lower olefin release.

The trapped aromatics are especially important for small pore catalysts like SAPO-18 or SAPO-34. However, different characteristics were determined over ZSM-5. Here, olefins are the main species leading to methanol consumption by continuous methylation and cracking [45, 90]. This observation led to the proposal of the dual-cycle theory [91, 92]: it was found that yields of ethene correlate with those of aromatics in contrast to propene. Consequently, their formation routes must be mechanistically separated. Whereas the aromatic hydrocarbon pool is similar to the one described above, an olefin hydrocarbon pool also plays an important role. Here, olefins grow through methylation reactions and crack down to lower olefins again. Over ZSM-5, this is the main route towards propene, especially at high temperatures. Again, whether the olefins are methylated in a stepwise mechanism via a surface methyl group [66, 75] or in a concerted step [93] remains the subject of much debate. Furthermore, it has been observed that DME can also perform methylation reactions, a step which exhibits lower barriers than methanol [94, 95].

The formation of side products is not restricted to the evolution of polymethylated aromatics. The mechanism described in Section 2.2 for olefin cracking is also valid for MTO. However, it was observed that, when methanol is present, the side product formation is significantly higher than for the pure cracking case [58]; in addition, methane formation is pronounced [96]. This led to the proposal of a methanol-induced hydrogen transfer [97, 98] where again formaldehyde plays an important role. Scheme 2.2 shows the MTO reaction network over a ZSM-5 catalyst in a simplified way. This illustration emphasizes the dual-cycle mechanism, with the olefin-based cycle on the left side and the aromatic-based cycle on the right side. The latter is not further specified, i.e., it characterizes both the less methylated aromatics which are found in the product spectrum as well as the heavier compounds trapped in the pores.

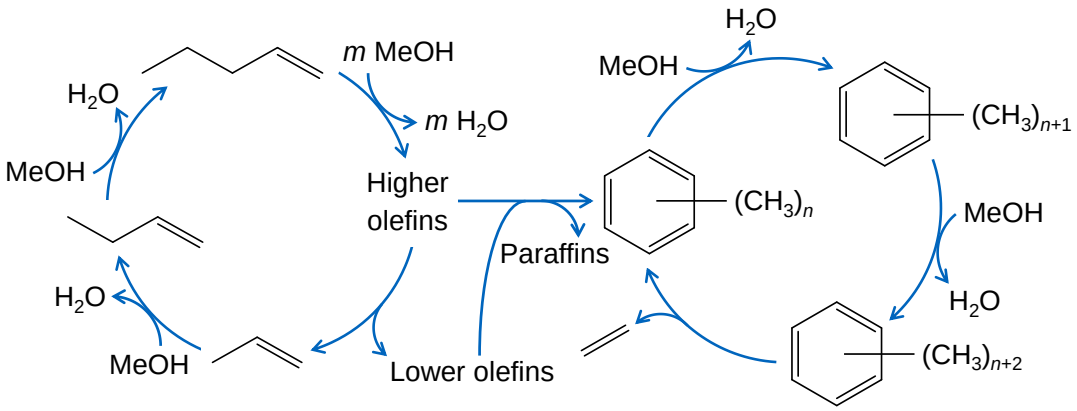

Scheme 2.2: Simplified reaction network for MTO over ZSM-5 with the olefin-based cycle on the left and the aromatic-based cycle on the right side; the latter produces mainly ethene, whereas aromatics and paraffins are formed through both olefin interconversion reactions and a methanol-induced pathway; adapted from literature [10].

As mentioned above, the undesired higher olefins are recycled and co-fed in the commercial MTP process [65, 99]. This changes the underlying chemistry drastically [100–105]: the slow formation of the first C-C bond is obsolete because higher hydrocarbons are available straightaway. Consequently, no initiation phase is observed; the oxygenates conversion increases immediately from the beginning as depicted in Figure 2.1.

Several reviews [10, 36, 64, 82, 106–111] and overviews [112] provide more details. Current research is focused on a wide range of issues, i.e., the exact mechanism of methylation [93, 94, 113–123], catalyst properties [120, 124–128], reaction conditions [102, 103, 129] and deactivation [95, 130–134]. Finally, an overview of the current state of MTO commercialization is given [83].

2.4 Thermodynamics

Many kinetic models require thermodynamic data, e.g., for the calculation of *quasi*-equilibrated or backward reactions. A correct implementation of equilibrium constants is crucial for the model performance; thus, the underlying theory and calculation procedures should be shown here. The results are compared with literature correlations. Thermodynamic equilibrium distributions are evaluated for olefin cracking as well as MTO. This is helpful as first step in order to find intermediate and stable products. Finally, insight into the influence of typical reaction conditions on equilibrium distributions might help in understanding overall reactivity. Thermodynamic equilibria are obtained by minimization of the total Gibb's free energy $G_\mathrm{t}(T)$ (see Equation (2.1)) [135–137]:

$$G_\mathrm{t}(T) = \sum_j \mu_j(T)\, n_j, \tag{2.1}$$

$$\mu_j(T) = \mu_j^\circ(T) + RT \ln\left(\frac{f_j}{f_j^\circ}\right). \tag{2.2}$$

Equation (2.1) yields an absolute value in joules, equal to the sum of all considered species j with their chemical potential $\mu_j(T)$ given as a molar value multiplied by the number of moles n_j of compound j when equilibrium is reached. In this state, the total number of moles n_t may differ from the initial value, thus n_t is not constant. For an ideal gas, the fugacity f_j equals the partial pressure $p(j)$, whereas f_j° is equivalent to a well-defined standard pressure p°. According to IUPAC [138], p° is set equal to 10^5 Pa. Although a standard temperature T° is defined as

273.15 K, the superscript $^\circ$ for thermo-physical properties only relates to the standard pressure [138]. The standard chemical potential $\mu_j^\circ(T)$ in Equation (2.2) is equal to the standard Gibb's energy of formation $\Delta_f G^\circ(T)$. Thus, the relation in Equation (2.3) is obtained,

$$\mu_j(T) = \Delta_f G_j^\circ(T) + RT \ln\left(\frac{p_t}{p^\circ}\right) + RT \ln\left(\frac{n_j}{n_t}\right). \tag{2.3}$$

When the total pressure p_t equals the standard pressure p°, the term in the middle of Equation (2.3) can be omitted. Values of $\Delta_f G_j^\circ(T)$ are tabulated in standard references [139], in several collections published by Alberty [140–154] or they can be calculated using group additivity methods [155–162]. According to the Gibbs-Helmholtz equation [135], $\Delta_f G_j^\circ(T)$ remains a function of temperature. When no suitable values are found in literature, $\Delta_f G_j^\circ(T)$ can be calculated via Equation (2.4),

$$\Delta_f G_j^\circ(T) = \Delta_f H_j^\circ(T) - T\left(S_j^\circ(T) - \sum_{el} N_{el,j} S_{el}^\circ(T)\right), \tag{2.4}$$

$$\Delta_f H_j^\circ(T) = \Delta_f H_j^\circ(298\,\mathrm{K}) + \int_{298\,\mathrm{K}}^{T} c_{p,j}(T)\,\mathrm{d}T, \tag{2.5}$$

$$S_j^\circ(T) = S_j^\circ(298\,\mathrm{K}) + \int_{298\,\mathrm{K}}^{T} \frac{c_{p,j}(T)}{T}\,\mathrm{d}T. \tag{2.6}$$

Since no standard entropy of formation exists, the sum over all elements *el* must be subtracted from $S_j^\circ(T)$; the former value is obtained by multiplying the standard entropy of the respective element $S_{el}^\circ(T)$ by the number of atoms $N_{el,j}$ which are part of compound *j*. The temperature dependence of the heat capacity can be described via polynomial approximations [163, 164].

For this work, $\Delta_f G_j^\circ(T)$ values as a function of temperature are extracted from literature for ethene ($C_2^=$) to octenes ($C_8^=$) [147], for methanol [150] and for water [139]. These are fitted to a second degree polynomial using *polyfit* within MATLAB. With the resulting coefficients, $\Delta_f G_j^\circ(T)$ can be evaluated for each desired temperature. For DME, heat capacity values [165] are fitted with the same routine. In combination with $\Delta_f H_j^\circ(298\,\mathrm{K})$ [166] and $S_j^\circ(298\,\mathrm{K})$ [167] as well as heat capacity and $S_j^\circ(298\,\mathrm{K})$ values for carbon, hydrogen and oxygen [139], $\Delta_f G_j^\circ(T)$ is calculated with the help of Equations (2.5) and (2.6). Two cases are analyzed here: a mixture of ethene to octenes and the system methanol/DME/water. These should represent the olefin cracking case and the MTO feed, respectively. The resulting equilibria as a function of temperature can be seen in Figure 2.2. They are obtained by minimizing Equation (2.1) using *fmincon* in MATLAB. Here, the *sqp* algorithm is applied which yields stable solutions independent of the starting values for the molar composition.

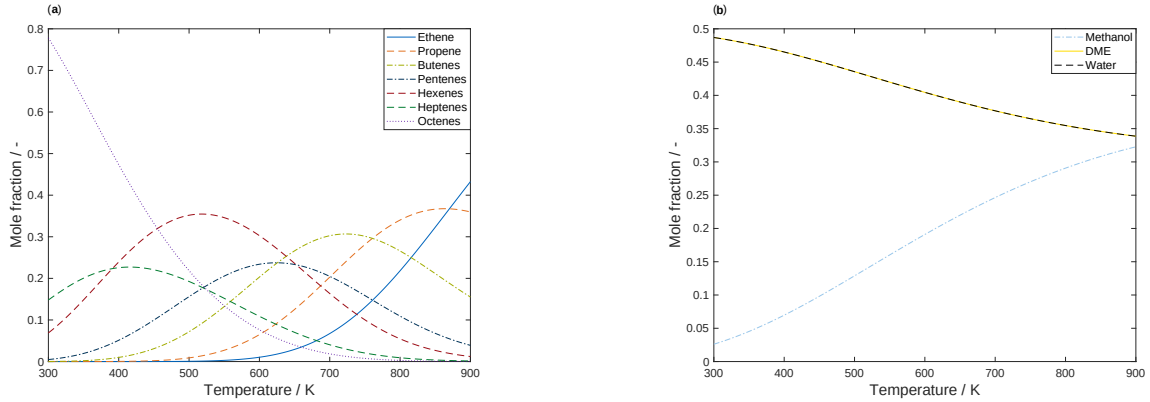

Figure 2.2: Composition of an equilibrated mixture as a function of temperature at standard pressure $p_t = p^\circ$ for $C_2^=$ to $C_8^=$ olefins, (a), and for the system methanol/DME/water, (b).

Figure 2.2 (a) shows a clear trend towards lower olefins at high temperatures. For an MTO feed, the equimolar fraction of DME and water decreases when the temperature is raised, see Figure 2.2 (b). During the conversion of methanol to DME and water, the number of moles remains constant, which is why a change in pressure does not affect the equilibrium. The influence of pressure on the olefin distribution is depicted in Figure 2.3 (a) for a characteristic cracking temperature of 650 K.

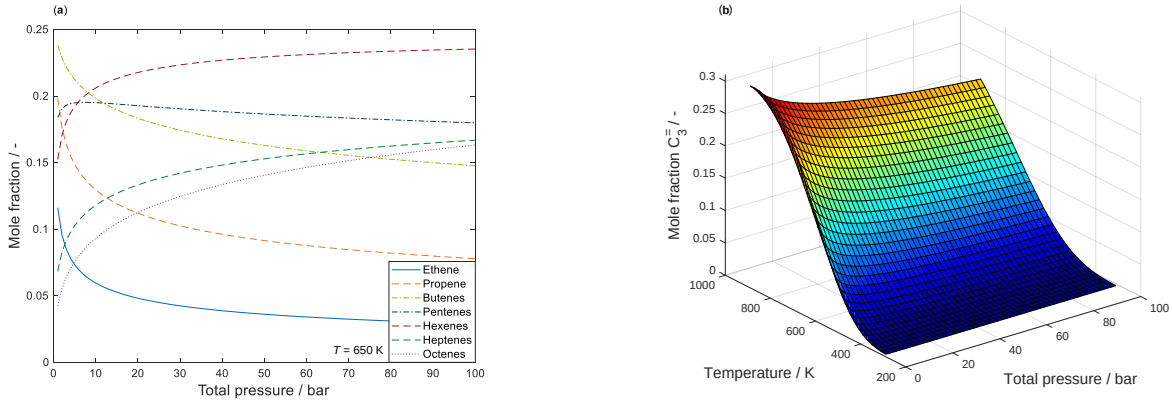

Figure 2.3: Composition of an equilibrated mixture for $C_2^=$ to $C_8^=$ olefins as function of total pressure at 650 K, (a), and evaluated as mole fraction of propene as function of both temperature and total pressure, (b).

It is obvious that thermodynamics favor the generation of higher olefins when the total pressure is increased. Figure 2.3 (b) summarizes the results for the desired product propene: for maximum yields, the pressure should be as low and the temperature as high as possible. However, the optimum conditions taken from Figure 2.3 deviate from an applicable industrial case. Usually, the equilibrated olefin distribution does not depict the process, because propene is an intermediate product here. This makes a proper description of reaction kinetics inevitable.

In this context, the thermodynamic equilibrium constant K^{TD} of the system methanol/DME/water is especially important because it can be incorporated into a model, e.g., to describe the equilibrated feed. In general, this value is accessible via the Gibb's free energy of reaction $\Delta_{\mathrm{r}}G^{\circ}(T)$ [135]. This relation is shown in Equation (2.7) using the exothermic reaction $2\mathrm{MeOH} \rightleftharpoons \mathrm{DME} + \mathrm{H_2O}$ as an example,

$$K^{\mathrm{TD}} = \exp\left(-\frac{\Delta_{\mathrm{r}}G^{\circ}(T)}{RT}\right) = \frac{p(\mathrm{DME})\,p\left(\mathrm{H_2O}\right)}{p(\mathrm{MeOH})^2}. \tag{2.7}$$

In the following, some literature correlations for this constant are shown. Figure 2.4 compares these approaches with the own solution from Figure 2.2.

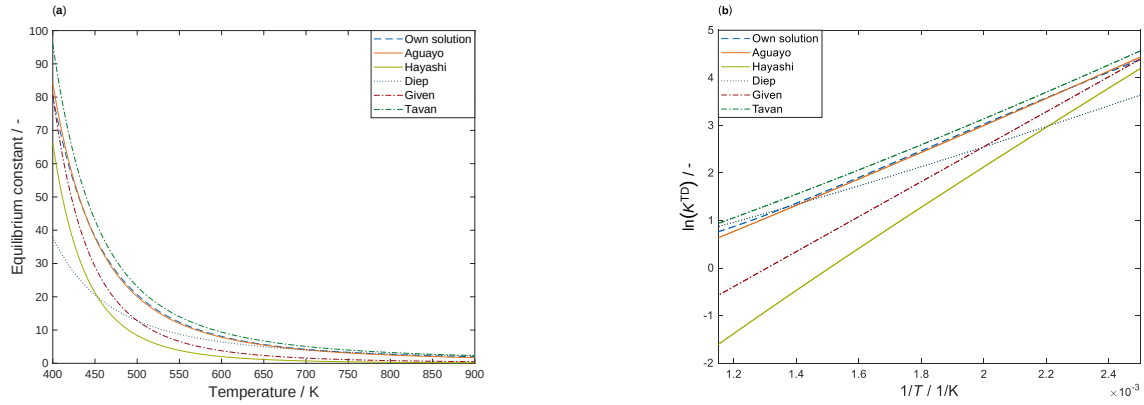

Figure 2.4: Equilibrium constants for the system methanol/DME/water, taken from different references [168–172] and compared with the own solution according to Figure 2.2, as a function of temperature with a regular scale, (a), and with a logarithmic scale, (b).

Figure 2.4 shows that only the correlation published by Aguayo *et al.* [168] closely matches the solution derived from thermodynamics. This correlation is represented by Equation (2.8),

$$K^{\mathrm{TD}} = \exp\left(-9.76 + \frac{3200\,\mathrm{K}}{T} + 1.07\ln\left(\frac{T}{\mathrm{K}}\right) - 6.57\times10^{-4}\frac{T}{\mathrm{K}} + 4.90\times10^{-8}\frac{T^2}{\mathrm{K}^2} + \frac{6050\,\mathrm{K}^2}{T^2}\right). \tag{2.8}$$

In the high temperature range, i.e., above 600 K, the correlations by Tavan and Hasanvandian [172] and Diep and Wainwright [170] also yield satisfying results, see Equations (2.9) and (2.10), respectively,

$$K^{\mathrm{TD}} = \exp\left(\frac{4019\,\mathrm{K}}{T} + 3.707\,\ln\left(\frac{T}{\mathrm{K}}\right) - 2.783\times10^{-3}\,\frac{T}{\mathrm{K}} + 3.8\times10^{-7}\,\frac{T^2}{\mathrm{K}^2} - \frac{65\,610\,\mathrm{K}^3}{T^3} - 26.64\right), \tag{2.9}$$

$$K^{\mathrm{TD}} = \exp\left(\frac{2835.2\,\mathrm{K}}{T} + 1.675\,\ln\left(\frac{T}{\mathrm{K}}\right) - 2.39\times10^{-4}\,\frac{T}{\mathrm{K}} - 0.21\times10^{-6}\,\frac{T^2}{\mathrm{K}^2} - 13.360\right). \tag{2.10}$$

By contrast, use of the correlations by Given [171] and Hayashi and Moffat [169] shown in Equations (2.11) and (2.12), respectively, is recommended only for temperatures not significantly greater than 400 K,

$$K^{\mathrm{TD}} = \exp\left(\frac{30\,564\,\mathrm{J\,mol^{-1}}}{RT} - 4.8\right), \tag{2.11}$$

$$K^{\mathrm{TD}} = \exp\left(\left(\frac{-6836\,\mathrm{K}}{T} + 3.32\,\ln\left(\frac{T}{\mathrm{K}}\right) - 4.75\times10^{-4}\,\frac{T}{\mathrm{K}} - 1.1\times10^{-7}\,\frac{T^2}{\mathrm{K}^2} - 10.92\right) \times \frac{4.1868\,\mathrm{J\,mol^{-1}\,K^{-1}}}{-R}\right). \tag{2.12}$$

The correlations by Gayubo *et al.* [173], Schiffino and Merrill [174] and Khademi *et al.* [175] are not shown here because their application leads to high deviation from the results in Figure 2.4. The equations by Gayubo *et al.* [173] and Hayashi and Moffat [169] are of the same form, but different values are used by the former group [173]. The authors refer to the review by Spivey [176] who used the equation by Hayashi and Moffat [169] with the original values.

2.5 Kinetic Modeling

2.5.1 General

A kinetic model describes the relation between rate r_l of a certain reaction l and the concentration of one or several reactants i [17, 177–180]. The latter can be expressed as partial pressure $p(i)$, as mole concentration per volume $C(i)$, as mole fraction $y(i)$ or as mass fraction $w(i)$. In the following, a subscript C in $p_{\mathrm{C}}(i)$, $y_{\mathrm{C}}(i)$ and $w_{\mathrm{C}}(i)$ means that only carbon containing

species are considered. The value $y_C(i)$ of a certain compound is determined by multiplying its number of carbon atoms by the number of molecules of this type and comparing this value with the total number of carbon atoms.

All literature examples and own models discussed here are deterministic kinetic models and involve three essential features: gathering of experimental data, creation of a reaction network that leads to the model equations and fitting of the kinetic parameters by comparing the modeled results with the obtained data.

According to the seven steps of heterogeneous catalysis [181], the description is simplified to adsorption, surface reaction and desorption provided that the influence of transport phenomena can be neglected. Adsorption is an exothermic step, in which the reactant interacts with the catalyst. It is divided into physisorption and chemisorption [182]. The former describes an undirected, unselective and comparably weak interaction, often with the catalyst surface, which is mainly caused by van der Waals forces. The chemisorption is highly selective and is formed, for example, through a chemical bond between reactant and active center. Here, the adsorption enthalpy is significantly higher compared to physisorption [182]. The reverse process to adsorption is desorption. From thermodynamics, it follows that high pressures and low temperatures favor adsorption. There are different strategies for describing these effects mathematically. A common approach is the Langmuir (L) isotherm in Equation (2.13), which depends on temperature [177, 183],

$$\theta(i) = \frac{K^{\mathrm{ads}}(i)\, p(i)}{1 + K^{\mathrm{ads}}(i)\, p(i)}, \tag{2.13}$$

with the relative coverage $\theta(i)$ of species i on the catalyst surface and a specific adsorption equilibrium constant $K^{\mathrm{ads}}(i)$. In the form of Equation (2.13), an underlying assumption is that adsorption and desorption are *quasi*-equilibrated. Furthermore, a uniform surface, no interaction between adsorbed species, monolayer adsorption and non-dissociative adsorption are assumed. In addition to the Langmuir isotherm, other approaches also exist [184].

In the following, typical kinetic expressions are introduced: power law, Langmuir, Langmuir-Hinshelwood (LH), Eley-Rideal (ER) and Hougen-Watson (HW). It should be underlined that for these examples, the surface reaction is assumed to be the slowest step, whereas all sorption processes are treated as *quasi*-equilibrated. Although this is a common scenario, conditions where adsorption or desorption become kinetically relevant are also possible. In the following, non-dissociative and competing adsorption of all species is assumed, thereby deviating from the classical formulations of the kinetic expressions found in the literature. At this point, it is important to mention that there is no unique mechanism for any of the preceding kinetic expressions because the resulting equation always depends on the assumptions. This is why all kinetic equations are denoted as type of a certain mechanism here.

The simplest way to construct a kinetic model is using power law expressions [183, 185]. Equation (2.14) is typical of a monomolecular reaction,

$$r_l = k_l p(i)^{\kappa}. \tag{2.14}$$

Here, the rate constant k_l as well as the reaction order κ are unknown. They can be obtained by fitting the model to experimental data [186]. The reaction order does not need to correspond to the stoichiometric coefficient of species i in step l. Especially in power law models, the former value is often determined as a purely empirical value without any physical meaning.

The level of detail is increased by choosing one of the following basic mechanistic approaches. When such a scheme is applied, the reactions are assumed to be elementary in most cases, meaning that the reaction order equals the stoichiometric coefficient.

For monomolecular reactions, the adsorption of the reactant can be described via an L type of isotherm which leads to the kinetic description in Equation (2.15) [178, 183, 187],

$$r_l = \frac{k_l K^{\mathrm{ads}}(i)\, p(i)}{1 + \sum_j K^{\mathrm{ads}}(j)\, p(j)}. \tag{2.15}$$

A similar description is obtained for bimolecular reactions where both reactants i and v must be adsorbed before the reaction takes place. The approach in Equation (2.16) is often referred to as an LH type of mechanism [179, 183],

$$r_l = \frac{k_l K^{\mathrm{ads}}(i)\, p(i)\, K^{\mathrm{ads}}(v)\, p(v)}{\left(1 + \sum_j K^{\mathrm{ads}}(j)\, p(j)\right)^2}. \tag{2.16}$$

In the classical LH expression, which is frequently shown, only the two reactants are included for the inhibiting adsorption term in the denominator. By contrast, Equation (2.16) considers all adsorbing species in the system which is closer to the HW type of mechanism [179, 180, 187, 188]. The latter usually consists of three parts, describing the reaction kinetics (rate constant), the potential (concentrations as well as difference from the thermodynamic equilibrium, if applicable) and inhibition through competing adsorption. Equation (2.17) describes an example of a monomolecular reversible reaction of reactant i which leads to the two products v and w. The equilibrium constant K can either be calculated from thermodynamics $\left(K^{\mathrm{TD}}\right)$ or estimated as an unknown parameter $\left(K_l\right)$. Because both reactants of the backward step adsorb before reaction, it is a combination of LH and HW types of mechanism,

$$r_l = \frac{k_l K^{\mathrm{ads}}(i)\, p(i) - \frac{k_l}{K_l} K^{\mathrm{ads}}(v)\, p(v)\, K^{\mathrm{ads}}(w)\, p(w)}{1 + \sum_j K^{\mathrm{ads}}(j)\, p(j)}. \tag{2.17}$$

A bimolecular reaction where only one of the reactants i has to be adsorbed while the second compound v reacts directly from the gas phase is known as an ER type of mechanism [180], see Equation (2.18), again with a combination of an HW type of mechanism,

$$r_l = \frac{k_l K^{\mathrm{ads}}(i)\, p(i)\, p(v)}{1 + \sum_j K^{\mathrm{ads}}(j)\, p(j)}. \tag{2.18}$$

Besides the description via relative, i.e., dimensionless, quantities for the coverage, absolute concentration values of adsorbed surface species can be applied by multiplying $\theta(i)$ by the total concentration of acid sites. For the well-defined zeolites, this value is usually known. Consequently, the rate and equilibrium constants remain as unknown parameters.

The temperature dependence of the rate constants is expressed via the Arrhenius approach in Equation (2.19) [180] which introduces the activation energy E_a,

$$k = A \exp\left(-\frac{E_\mathrm{a}}{RT}\right). \tag{2.19}$$

The coherence given by Eyring [189] is shown in modified form [190] in Equation (2.20). The pre-exponential factor A contains the Boltzmann constant k_B, the Planck constant h and the entropy change from reactant to transition state $\Delta_\ddagger S^\circ$. Furthermore, the value $\Delta_\ddagger \nu_\mathrm{g}$ resembles the difference in number of moles in the gas phase between activated complex and reactant state; it is required to correctly relate activation enthalpy and energy,

$$k = \frac{k_\mathrm{B} T}{h} \exp\left(\frac{\Delta_\ddagger S^\circ}{R}\right) \exp\left(1 - \Delta_\ddagger \nu_\mathrm{g}\right) \exp\left(-\frac{E_\mathrm{a}}{RT}\right). \tag{2.20}$$

Usually, both pre-exponential factor and activation energy must be estimated. Reparameterization according to Equation (2.21) is often performed to reduce the correlation between these two values [186, 191],

$$k = k^\mathrm{ref} \exp\left(-\frac{E_\mathrm{a}}{R}\left(\frac{1}{T} - \frac{1}{T^\mathrm{ref}}\right)\right) = A^\mathrm{ref} \exp\left(-\frac{E_\mathrm{a}}{RT^\mathrm{ref}}\right) \exp\left(-\frac{E_\mathrm{a}}{R}\left(\frac{1}{T} - \frac{1}{T^\mathrm{ref}}\right)\right). \tag{2.21}$$

Alternatively, the approach in Equation (2.22) can be used [192],

$$k = \exp\left(\left(\ln\left(A^\mathrm{ref}\right) - \frac{E_\mathrm{a}}{RT^\mathrm{ref}}\right) - \frac{E_\mathrm{a}}{R}\left(\frac{1}{T} - \frac{1}{T^\mathrm{ref}}\right)\right). \tag{2.22}$$

The reference temperature T^ref should be within the investigated range and is often chosen as the average, although detailed guidelines for its proper estimation exist [191, 193].

Another option is to additionally consider the temperature dependence of the pre-exponential factor, see Equation (2.23),

$$k = A^{\mathrm{ref}} \frac{T}{T^{\mathrm{ref}}} \exp\left(-\frac{E_{\mathrm{a}}}{R\,T^{\mathrm{ref}}}\right) \exp\left(-\frac{E_{\mathrm{a}}}{R}\left(\frac{1}{T}-\frac{1}{T^{\mathrm{ref}}}\right)\right). \tag{2.23}$$

The pre-exponential factor of a reaction can also be calculated prior to the fitting process to reduce the number of unknown parameters [18, 22, 194]. For this purpose, reliable assumptions for the entropy change $\Delta_{\ddagger}S^{\circ}$ are required [17].

During estimation of adsorption or reaction equilibrium constants, reparameterization is applicable in analogous manner as shown in Equation (2.24) [186, 188],

$$K = K^{\mathrm{ref}} \exp\left(-\frac{\Delta H^{\circ}}{R}\left(\frac{1}{T}-\frac{1}{T^{\mathrm{ref}}}\right)\right). \tag{2.24}$$

Again, the reference value can be written within the exponential function, as it is done in Equation (2.25) [192],

$$K = \exp\left(\left(\frac{\Delta S^{\circ}}{R}-\frac{\Delta H^{\circ}}{R\,T^{\mathrm{ref}}}\right)-\frac{\Delta H^{\circ}}{R}\left(\frac{1}{T}-\frac{1}{T^{\mathrm{ref}}}\right)\right). \tag{2.25}$$

For kinetic models, it is crucial to differentiate the rate r_l of a reaction step l from the net rate of production $R(i)$ of a certain species i [179]. The latter is obtained by summing up all reaction rates q where the compound i is consumed or produced. Each rate must be multiplied by the stoichiometric coefficient $\nu_q(i)$ of i in step q, as shown in Equation (2.26),

$$R(i) = \sum_q \nu_q(i)\, r_q. \tag{2.26}$$

From these remarks, it follows that stoichiometry should be considered for three points: for the formulation of reaction rates $\left(2\mathrm{C}_4^{=} \text{ to } \mathrm{C}_8^{=} \text{ instead of } \mathrm{C}_4^{=} \text{ to } \mathrm{C}_8^{=}\right)$, for the reaction order as long as elementary reactions are assumed $\left(p\left(\mathrm{C}_4^{=}\right)^2 \text{ instead of } p\left(\mathrm{C}_4^{=}\right)\right)$ and for the net rate of production $\left(-2k_l p\left(\mathrm{C}_4^{=}\right)^2 \text{ instead of } -k_l p\left(\mathrm{C}_4^{=}\right)^2\right)$. However, approaches exist in literature that deviate from this suggestion. This can still yield a model with high agreement, although it is purely empirical.

The net rate of production is required to obtain the molar flow rate $F(i)$ of a certain species i along the reactor. For this, integration over the catalyst mass W is performed. In most of the kinetic studies found in literature, Equation (2.27) for a one-dimensional, *pseudo*-homogeneous, isothermal plug flow reactor applies [180],

$$\frac{\mathrm{d}F(i)}{\mathrm{d}W} = R(i). \tag{2.27}$$

An objective function compares the difference between modeled and measured output [21, 180]. Several values are suitable, for example, molar flow rates, mass flow rates or mole fractions. The latter option is chosen for the example in Equation (2.28) where $y_k(j)$ characterizes the experimental and $\hat{y}_k(j)$ the modeled mole fraction at the experimental data point k, respectively. In this common approach, the objective function OF equals the sum of squared residuals SSQ which should be minimized during parameter estimation [21]; a more generalized least-squares criterion can be found elsewhere [180],

$$OF = SSQ = \sum_{k}^{N_{\mathrm{Exp}}} \sum_{j}^{N_{\mathrm{Res}}} \omega_j \left(y_k(j) - \hat{y}_k(j) \right)^2 . \tag{2.28}$$

Evaluation is performed with all experimental data points N_{Exp} and all fitting responses N_{Res}. The latter value comprises all species j which should be used for parameter estimation; however, this need not match the number of lumps in the event that one or several lumps are to be explicitly excluded during fitting. In combination with the number of estimated parameters N_{Par} of the model, its degree of freedom dof can be calculated according to Equation (2.29),

$$dof = N_{\mathrm{Exp}} N_{\mathrm{Res}} - N_{\mathrm{Par}}. \tag{2.29}$$

Equation (2.28) contains a weighting factor ω_j which is accessible through replicate experiments: these yield the experimental errors whose covariance matrix can be inverted, thereby leading to ω_j which equals the diagonal elements [180]. Without replicate experiments, the necessary values can be obtained via Equation (2.30) [21] using the molar flow rate $F(j)$,

$$\omega_j = \frac{\left(\sum_k^{N_{\mathrm{Exp}}} F_k(j) \right)^{-1}}{\sum_j^{N_{\mathrm{Res}}} \left(\sum_k^{N_{\mathrm{Exp}}} F_k(j) \right)^{-1}}. \tag{2.30}$$

2.5.2 Microkinetics

The difference between a simpler approach and microkinetics is well illustrated using again the example of monomolecular cracking of 2-methyl-2-hexene, see Scheme 2.1. In a simple model considering stoichiometry, the reaction would be formulated as $C_7^= \rightleftharpoons C_3^= + C_4^=$ with the corresponding rate equation $r = k\, p\left(C_7^=\right)$. However, this ignores both the backward reaction and the adsorption of $C_7^=$ prior to the reaction. Due to the latter fact, the estimated rate constant is an apparent value that includes adsorption effects. This could lead to negative activation energies, especially when more than one reactant is required in the adsorbed state [195].

In case adsorption was considered using one of the kinetic expressions introduced in Section 2.5.1, the resulting approach would still not be a microkinetic model. The reason is that

all olefins of the same carbon number are summarized as one lump of common reactivity. A microkinetic model has to consider each compound, each isomer and each transition state [17], cf. the approach in Scheme 2.1. Furthermore, it should contain elementary steps exclusively and has to beware thermodynamic consistency [196]. Due to the complex reaction network, the common assumption of a rate-determining step is not to be used in microkinetics [17]. By contrast, some reactions might be *quasi*-equilibrated as they are significantly faster compared to steps of kinetic relevance. Finally, the *pseudo*-steady-state approximation (PSSA) should be used for reactive intermediates. This concept proposes that the net rate of production of these intermediates is zero [179].

Especially for hydrocarbon conversion over zeolites, microkinetic reaction networks are extremely large. This requires additional modeling techniques to reduce computational effort. Examples such as discrete lumping for Fischer-Tropsch product mixtures or vacuum gas oil [197–202] as well as stochastic methods [203] can be found in literature.

For hydrocracking, the single-event methodology developed by the Ghent group [19–21, 59] is an important concept; several applications can be found in literature [21–24, 60–62, 186, 204–213]. The derivation of the single-event methodology starts with the modified coherence according to Eyring in Equation (2.20). Here, all symmetry-related contributions of the entropy change from reactant to transition state $\Delta_{\ddagger}S^{\circ}$ can be separated [214], see Equation (2.31),

$$\Delta_{\ddagger}S^{\circ} = \Delta_{\ddagger}\tilde{S}^{\circ} - R \ln\left(\frac{\sigma_{\mathrm{gl}}^{\mathrm{reac}}}{\sigma_{\mathrm{gl}}^{\ddagger}}\right). \tag{2.31}$$

The global symmetry numbers for the reactant state $\sigma_{\mathrm{gl}}^{\mathrm{reac}}$ and for the transition state $\sigma_{\mathrm{gl}}^{\ddagger}$, respectively, are calculated according to Equation (2.32) [194],

$$\sigma_{\mathrm{gl}} = \frac{\sigma_{\mathrm{gl,int}}\,\sigma_{\mathrm{gl,ext}}}{2^{n^{\mathrm{ch}}}}. \tag{2.32}$$

Thus, the global symmetry number depends on the number of chiral centers n^{ch} as well as internal and external symmetry contributions. For the determination of the latter, amount and position of side groups are, among others, the parameters that have to be taken into account. Rules to calculate $\sigma_{\mathrm{gl,int}}$ and $\sigma_{\mathrm{gl,ext}}$ and some exemplary values can be found in literature [155, 215, 216].

A combination of Equations (2.20) and (2.31) yields Equation (2.33) [215, 216],

$$k = \frac{k_{\mathrm{B}}\,T}{h} \exp\left(\frac{\Delta_{\ddagger}\tilde{S}^{\circ}}{R}\right) \frac{\sigma_{\mathrm{gl}}^{\mathrm{reac}}}{\sigma_{\mathrm{gl}}^{\ddagger}} \exp\left(1 - \Delta_{\ddagger}\nu_{\mathrm{g}}\right) \exp\left(-\frac{E_{\mathrm{a}}}{RT}\right). \tag{2.33}$$

The ratio of symmetry numbers of reactant and transition state is defined as number of single events n_e. It characterizes the number of similar configurations during an elementary reaction because of intramolecular symmetries [18]. The remaining terms are summarized to the single-event rate constant $\tilde{k}$, see Equation (2.34),

$$k = n_e \tilde{k}. \tag{2.34}$$

The value of n_e is accessible via the symmetry numbers and thus can be calculated. By contrast, the single-event rate constants are the unknown parameters that have to be estimated. Since these are free of all symmetry contributions, they only depend on the reaction family (cracking, dimerization, ...) and on the types of reactant and product intermediate (primary, secondary or tertiary). Here, combination possibilities are limited, thereby leading to an effective parameter reduction. More details can be found in literature [19–21, 214–216].

2.6 Literature Models

In this section, different kinetic models are introduced, both for olefin cracking and for MTO. The latter topic is further separated into MTO kinetics with and without olefin co-feed, respectively. All kinetic approaches for MTO published before 2000 are ignored. Apart from the fact that they have already been discussed in the review by Keil [108], most of these examples focus not on MTO, but on MTG where temperatures are lower to increase the yield of the gasoline fraction. In addition to the first kinetic description by Chen and Reagan [74], this includes the models of Chang [217], Ono and Mori [75], Mihail *et al.* [218, 219], Schipper and Krambeck [220], Sedrán *et al.* [221, 222], Schönfelder *et al.* [223] and Bos *et al.* [224]. Noteworthy are the comparably large reaction network [218, 219] and the elevated temperatures [223, 224] which are within the MTO range. In addition to the mentioned review by Keil [108], some of the models are compared elsewhere [221, 225]. Another review giving an overview of MTO kinetic models is the one by Khadzhiev *et al.* [226].

Because all examples shown here are deterministic kinetic models, first principle and *ab initio* studies are ignored; here, no actual fitting to experimental data is performed. Nevertheless, this theory gives important insight into mechanistic details which is why some examples should be mentioned here. Where zeolite chemistry is concerned, there are many publications by the van Speybroeck group. In addition to reviews about the theory [227] and MTO [110, 111], several aspects of the MTO reactivity are investigated in detail: for example, the influence of adsorption effects [122] and especially of water [122, 228], the methylation of aromatics [119, 122], the methylation of olefins [114, 118] and the formation as well as the reactivity of surface methyl

groups [229] are analyzed. Furthermore, general mechanistic details [228, 230] and the relationship between catalyst properties, the morphology of the catalyst and product compositions can be elucidated [128]. Similar investigations exist for the cracking of paraffins [231, 232] and olefins [233–235] using different zeolites.

2.6.1 Olefin Cracking

The models are grouped according to crucial characteristics. The ones by Epelde *et al.* [236], Ying *et al.* [237] and Huang *et al.* [195] depict manifold olefin interconversion reactions over ZSM-5. All three have comparable numeric approaches and especially the studies by Ying *et al.* [237] and Huang *et al.* [195] are very similar, although the latter includes a mechanistic approach. The next part groups the models by Borges *et al.* [53] and Oliveira *et al.* [238] over ZSM-5. Here, the focus is not on a complete olefin interconversion picture, but on describing the feed consumption rate [53] and on considering the different acid strengths of the sites [238]. The next two parts both contain only one model: there is no other microkinetic study for olefin cracking except for von Aretin *et al.* [26] and the model by Zhou *et al.* [136] is the only example over SAPO-34. An overview of the analyzed models can be found in Tables 2.1 and 2.2. At the end of each part, a short summary paragraph compares the models and shows advantages and disadvantages of the respective methodologies. Table 2.1 contains information about the catalysts used in the studies, whereas Table 2.2 lists the experimental conditions and details about the modeling approach. Here, the maximum experimental contact time is given in the same unit as in the original publication. This value is always based on the inlet molar flow rate which is either expressed as molar flow rate of carbon (subscript C) or of all species (subscript t). For the kinetic parameters, only the subscript C is used when the values are explicitly related to carbon units; otherwise, no subscript is shown.

Table 2.1: Properties of the different catalysts which were used for the kinetic models of olefin cracking; besides the zeolite type, its silicon-to-aluminum ratio, its total number of acid sites plus determination method, its ratio of Brønsted to Lewis acid sites BAS/LAS and its surface area according to the method by Brunauer-Emmett-Teller BET are shown; furthermore, the time-on-stream TOS after which the kinetic data were taken, the particle size d_P and the information whether an extrudate or pure powder was used are presented; the horizontal lines separate the different parts grouping models of similar methodology; a hyphen resembles missing information.

Model	Zeolite type	Si/Al	Total acidity	BAS/LAS	BET	TOS	d_P	Extrudate
Epelde [236]	ZSM-5 (1 %$_{wt}$ K)	280[a]	0.033 mmol g_{cat}^{-1} (t-$C_4H_{11}N$)[b]	-	194 m^2 g_{cat}^{-1}	5 h[c]	150–300 µm	25/30/45 %$_{wt}$ (Zeolite/bentonite/alumina)
Ying [237]	ZSM-5	103	0.21 mmol g_{cat}^{-1} (NH_3)	-	340 m^2 g_{cat}^{-1}	0.03 h	420–841 µm	Yes[d]
Huang [195]	ZSM-5	200[a]	0.012 mmol g_{cat}^{-1} (NH_3)	1.35 at 423 K	301.1 m^2 g_{cat}^{-1}	0–10 h[e]	125–149 µm	70/30 %$_{wt}$ (Zeolite/alumina)
Borges [53]	ZSM-5	30	-	-	416 m^2 g_{cat}^{-1}[f]	0–1.4 h	-	No
Oliveira [238]	ZSM-5 (0, 0.52, 0.65 and 0.80 %$_{wt}$ Na)[g]	30	-	-	416 m^2 g_{cat}^{-1}[h]	0–1.4 h	-	No
von Aretin [26]	ZSM-5	90	0.174 mmol g_{cat}^{-1} (C_5H_5N)	4.27	454 m^2 g_{cat}^{-1}	> 6 h	400–500 µm	No
Zhou [136]	SAPO-34[i]	0.25[j]	1.25 mmol g_{cat}^{-1} (NH_3)	-	550 m^2 g_{cat}^{-1}	0.02 h	3.2 µm[k]	No

[a] Value of the zeolite, i.e., without binder
[b] Calculated under the assumption that the total acidity of the extrudate is equal to one fourth of the pure zeolite's acidity according to the study [236]
[c] Results extrapolated to 0 h TOS
[d] No further information available (commercial catalyst from Süd-Chemie), but the cited patent [237] reveals the use of alumina as binder
[e] Regeneration after 10 h TOS
[f] Extracted from a subsequent publication [238]
[g] Corresponds to a catalyst where 0, 2.4, 3.0 and 3.2%, respectively, of the protons were exchanged with Na
[h] Surface areas of 396, 394 and 386 m^2 g_{cat}^{-1}, respectively, with higher Na amounts
[i] SAPO-34 and SAPO-18 disordered intergrowth structure revealed by X-ray diffraction pattern
[j] Value of the gel
[k] Mean size

Table 2.2: Experimental conditions and modeling details for the kinetic models of olefin cracking; the feed components, the temperature range T, the total pressure p_t, the partial pressure range of the feed olefin $p(O_i)$ and the maximum contact time $(W/F^{in})_{max}$ with resulting conversion X_{max} are listed; concerning the model, the number of fitted responses N_{Res}, the number of estimated parameters N_{Par}, the number of experiments N_{Exp} and the degree of freedom *dof* are shown; finally, it is noted whether the model follows a type of a mechanistical scheme, whether adsorption is considered and which side products are included; the horizontal lines separate the different parts grouping models of similar methodology; a hyphen resembles missing information.

Model	Feed	T	p_t	$p(O_i)$	$(W/F^{in})_{max}$	X_{max}	N_{Res}	N_{Par}	N_{Exp}	*dof*	Mech.	Ads.	Side prod.
Epelde [236]	$C_4^=$, He	673–873 K	1.5 bar	0.375–1.35 bar	1.60 g_{cat} h mol_C^{-1}	0.75	8	23	51	385	No	No	$C_{1\text{-}4}$, $C_{6\text{-}8}^{ar}$
							5	16	51	239			
Ying [237]	$C_3^=$, N_2	673–763 K	1.013 bar	0.131 bar	0.23 h[a]	0.67	7	28	115	777	No	No	$C_{3\text{-}7}$, $C_{6\text{-}7}^{ar}$
	$C_4^=$, N_2				0.16 h[a]	0.65							
	$C_5^=$, N_2				0.07 h[a]	0.57							
	$C_6^=$, N_2				0.10 h[a]	0.94							
	$C_7^=$, N_2				0.04 h[a]	0.98							
Huang [195]	$C_3^=$, N_2, H_2O[b]	673–763 K	1.013 bar	0.0832 bar	1.12 g_{cat} s mol_t^{-1}	0.33	6	44	104	580	LH, HW	$C_{2\text{-}7}^=$, H_2O	No
	$C_4^=$, N_2, H_2O[b]			0.0706 bar	0.73 g_{cat} s mol_t^{-1}	0.40							
	$C_5^=$, N_2, H_2O[b]			0.0601 bar	0.39 g_{cat} s mol_t^{-1}	0.23							
	$C_6^=$, N_2, H_2O[b]			0.0532 bar	0.20 g_{cat} s mol_t^{-1}	0.46							
	$C_7^=$, N_2, H_2O[b]			0.0476 bar	0.03 g_{cat} s mol_t^{-1}	0.46							
Borges [53]	$C_2^=$, N_2	473–723 K	1.013 bar	0.05–0.30 bar	9.33 g_{cat} h mol_C^{-1}	-	3	8	36	100	ER, HW	$C_{2\text{-}4}^=$	No
	$C_3^=$, N_2				1.55 g_{cat} h mol_C^{-1}	-							
	$C_4^=$, N_2				0.27 g_{cat} h mol_C^{-1}	-							
Oliveira [238]	$C_2^=$, N_2	473–723 K	1.013 bar	0.05–0.30 bar	9.33 g_{cat} h mol_C^{-1}	-	17	20	61	1017	L, ER, HW	$C_{2\text{-}8}^=$	$C_{2\text{-}8}$, $C_{6\text{-}8}^{ar}$
	$C_3^=$, N_2				1.55 g_{cat} h mol_C^{-1}	-							
	$C_4^=$, N_2				0.27 g_{cat} h mol_C^{-1}	-							
von Aretin [26]	$C_5^=$, N_2	633–733 K	1.2 bar	0.043–0.070 bar	1.6 g_{cat} s mol_t^{-1}	0.55	5	5	141	700	L, ER, HW	$C_{2\text{-}12}^=$	No
Zhou [136]	$C_2^{=(c)}$	723 K	1.013 bar	1.013 bar[c]	0.22 h[d]	0.78	8	14	16	114	No	No	$C_{1\text{-}4}$
	$C_3^{=(c)}$				0.12 h[d]	0.65							
	$C_4^{=(c)}$				0.12 h[d]	0.82							

[a] Contact time defined with the mass flow rate of the reactant

[b] Respective *n*-alcohol was fed instead of the olefin

[c] Three measurements diluted with N_2 (excluded for parameter estimation)

[d] Inverse value of minimum weight hourly space velocity containing only the mass flow rate of the reactant

Studies focusing on olefin interconversion over ZSM-5

Epelde *et al.* [236]: Eight- and five-lump approach for $C_4^=$ feeds at elevated partial pressures

Catalyst The self-synthesized ZSM-5 zeolite had a comparatively high Si/Al ratio (280). It was used to attenuate hydrogen transfer so that side product formation is hindered and propene yields are increased. In addition to this, $1\%_{wt}$ of K was added to the zeolite which lowers overall acidity and leads to a homogeneous distribution of acid strength. This should reduce side reactions and especially the evolution of coke precursors [239]. The measurements were performed at a time-on-stream (TOS) of 5 h; however, the authors extrapolated the results to 0 h TOS to characterize the reactivity of a fresh catalyst. In a preliminary study [240], the influencing factors of coke evolution were evaluated in detail.

Setup and conditions The experimental setup consisted of an automated reaction equipment where the feed components were provided as gases. The continuous fixed bed reactor was located within a furnace chamber whose temperature could be controlled via three test points, one of them being inside the catalyst bed and the other two in the chamber and in the transfer line to the product analysis, respectively. The stainless steel reactor had an inner diameter of 9 mm. Product analysis was performed using a micro gas chromatograph (GC) equipped with a thermal conductivity detector (TCD) and four columns. Both the feed and the catalyst bed were diluted using helium and SiC, respectively. More details about the setup can be found in the original publications [236, 239, 240]. In this study, 1-butene was the only reactive feed component analyzed; its partial pressure at the reactor inlet was relatively high.

Reaction network The proposed reaction network results from an analysis of kinetic experiments shown elsewhere [240]. The different species are grouped by means of reactivity which yields eight lumps: $C_2^=$, $C_3^=$, $C_4^=$, aliphatics with a carbon number of five or higher (C_{5+}^{al}), methane (C_1), $C_{2\text{-}3}$, C_4 and aromatics with a carbon number from six to eight ($C_{6\text{-}8}^{ar}$). The reaction rates are formulated based on experimental observations of primary and secondary products and evolution of the lump yields with changing conditions; the network with the best fit is chosen. Here, the formation of ethene (k_3 and $k_{8''}$) as well as of the side products (k_4–k_7 and k_{10}) is assumed to be irreversible whereby a minor part of $C_2^=$, $C_{2\text{-}3}$, C_4 and $C_{6\text{-}8}^{ar}$ can still react to methane. The remaining steps comprise the interconversion between $C_3^=$ to C_{5+}^{al} hydrocarbons (k_1, k_2, k_8, $k_{8'}$ and k_9) where the only irreversible step is the production of propene out of C_{5+}^{al}. Besides methane formation, ethene does not act as reactant. As it can be seen in Scheme 2.3, the steps are considered as elementary reactions. Moreover, the stoichiometry is neglected both in the derivation of the rates and in the formulation of the net rates of production. Adsorption effects are not included.

$C_4^= \underset{k_9}{\overset{k_1}{\rightleftharpoons}} C_3^=$	$r_1 = k_1\, p\,(C_4^=)$	$k_1^{\mathrm{ref}} = (1112 \pm 9) \times 10^{-3}\,\mathrm{mol_C\,g_{cat}^{-1}\,h^{-1}\,atm^{-1}}$ $E_{\mathrm{a},1} = 3.3 \pm 0.5\,\mathrm{kJ\,mol^{-1}}$
$C_4^= \underset{k_8'}{\overset{k_2}{\rightleftharpoons}} C_{5+}^{\mathrm{al}}$	$r_2 = k_2\, p\,(C_4^=)$	$k_2^{\mathrm{ref}} = (1391 \pm 6) \times 10^{-3}\,\mathrm{mol_C\,g_{cat}^{-1}\,h^{-1}\,atm^{-1}}$ $E_{\mathrm{a},2} = 3.7 \pm 0.5\,\mathrm{kJ\,mol^{-1}}$
$C_4^= \xrightarrow{k_3} C_2^=$	$r_3 = k_3\, p\,(C_4^=)$	$k_3^{\mathrm{ref}} = (3.9 \pm 1.0) \times 10^{-2}\,\mathrm{mol_C\,g_{cat}^{-1}\,h^{-1}\,atm^{-1}}$ $E_{\mathrm{a},3} = 31.0 \pm 2.1\,\mathrm{kJ\,mol^{-1}}$
$C_4^= \xrightarrow{k_4} C_{2-3}$	$r_4 = k_4\, p\,(C_4^=)$	$k_4^{\mathrm{ref}} = (1.8 \pm 1.2) \times 10^{-2}\,\mathrm{mol_C\,g_{cat}^{-1}\,h^{-1}\,atm^{-1}}$ $E_{\mathrm{a},4} = (3 \pm 1) \times 10^{-2}\,\mathrm{kJ\,mol^{-1}}$
$C_4^= \xrightarrow{k_{4'}} C_4$	$r_{4'} = k_{4'}\, p\,(C_4^=)$	$k_{4'}^{\mathrm{ref}} = (88 \pm 8) \times 10^{-3}\,\mathrm{mol_C\,g_{cat}^{-1}\,h^{-1}\,atm^{-1}}$ $E_{\mathrm{a},4'} = (3 \pm 1) \times 10^{-2}\,\mathrm{kJ\,mol^{-1}}$
$C_4^= \xrightarrow{k_5} C_{6-8}^{\mathrm{ar}}$	$r_5 = k_5\, p\,(C_4^=)$	$k_5^{\mathrm{ref}} = (82.5 \pm 9.5) \times 10^{-4}\,\mathrm{mol_C\,g_{cat}^{-1}\,h^{-1}\,atm^{-1}}$ $E_{\mathrm{a},5} = (3 \pm 1) \times 10^{-2}\,\mathrm{kJ\,mol^{-1}}$
$C_3^= \xrightarrow{k_6} C_{2-3}$	$r_6 = k_6\, p\,(C_3^=)$	$k_6^{\mathrm{ref}} = (73.2 \pm 8.5) \times 10^{-4}\,\mathrm{mol_C\,g_{cat}^{-1}\,h^{-1}\,atm^{-1}}$ $E_{\mathrm{a},6} = 16.6 \pm 1.2\,\mathrm{kJ\,mol^{-1}}$
$C_3^= \xrightarrow{k_7} C_{6-8}^{\mathrm{ar}}$	$r_7 = k_7\, p\,(C_3^=)$	$k_7^{\mathrm{ref}} = (2.4 \pm 1.1) \times 10^{-2}\,\mathrm{mol_C\,g_{cat}^{-1}\,h^{-1}\,atm^{-1}}$ $E_{\mathrm{a},7} = 6.1 \pm 0.7\,\mathrm{kJ\,mol^{-1}}$
$C_{5+}^{\mathrm{al}} \xrightarrow{k_8} C_3^=$	$r_8 = k_8\, p\left(C_{5+}^{\mathrm{al}}\right)$	$k_8^{\mathrm{ref}} = (2.67 \pm 1.10) \times 10^{-1}\,\mathrm{mol_C\,g_{cat}^{-1}\,h^{-1}\,atm^{-1}}$ $E_{\mathrm{a},8} = 55.9 \pm 1.0\,\mathrm{kJ\,mol^{-1}}$
$C_{5+}^{\mathrm{al}} \underset{k_2}{\overset{k_{8'}}{\rightleftharpoons}} C_4^=$	$r_{8'} = k_{8'}\, p\left(C_{5+}^{\mathrm{al}}\right)$	$k_{8'}^{\mathrm{ref}} = (269.9 \pm 5.6) \times 10^{-2}\,\mathrm{mol_C\,g_{cat}^{-1}\,h^{-1}\,atm^{-1}}$ $E_{\mathrm{a},8'} = 55.9 \pm 1.0\,\mathrm{kJ\,mol^{-1}}$
$C_{5+}^{\mathrm{al}} \xrightarrow{k_{8''}} C_2^=$	$r_{8''} = k_{8''}\, p\left(C_{5+}^{\mathrm{al}}\right)$	$k_{8''}^{\mathrm{ref}} = (2.4 \pm 1.7) \times 10^{-2}\,\mathrm{mol_C\,g_{cat}^{-1}\,h^{-1}\,atm^{-1}}$ $E_{\mathrm{a},8''} = 55.9 \pm 1.0\,\mathrm{kJ\,mol^{-1}}$
$C_3^= \underset{k_1}{\overset{k_9}{\rightleftharpoons}} C_4^=$	$r_9 = k_9\, p\,(C_3^=)$	$k_9^{\mathrm{ref}} = (104.1 \pm 4.2) \times 10^{-2}\,\mathrm{mol_C\,g_{cat}^{-1}\,h^{-1}\,atm^{-1}}$ $E_{\mathrm{a},9} = 0.5 \pm 1.0\,\mathrm{kJ\,mol^{-1}}$
$C_i^{\mathrm{HC}} \xrightarrow{k_{10}} C_1$	$r_{10} = k_{10}\, p\left(C_i^{\mathrm{HC}}\right)$	$k_{10}^{\mathrm{ref}} = (71.1 \pm 3.0) \times 10^{-5}\,\mathrm{mol_C\,g_{cat}^{-1}\,h^{-1}\,atm^{-1}}$ $E_{\mathrm{a},10} = 55.7 \pm 1.0\,\mathrm{kJ\,mol^{-1}}$

Scheme 2.3: Reaction network, rate equations and estimated parameters for the model by Epelde *et al.* [236] (eight lumps) with i ranging from 2 to 4 (olefins) or being 2–3, 4 (paraffins), 6–8 (aromatics) or 5+ (aliphatics).

The net rates of production can be obtained by adding all reaction rates where the respective lump is involved (see Scheme 2.4).

$$
\begin{aligned}
R\left(\mathrm{C}_{2}^{=}\right) &= k_3\, p\left(\mathrm{C}_{4}^{=}\right) + k_{8''}\, p\left(\mathrm{C}_{5+}^{\mathrm{al}}\right) - k_{10}\, p\left(\mathrm{C}_{2}^{=}\right) \\
R\left(\mathrm{C}_{3}^{=}\right) &= k_1\, p\left(\mathrm{C}_{4}^{=}\right) + k_8\, p\left(\mathrm{C}_{5+}^{\mathrm{al}}\right) - k_6\, p\left(\mathrm{C}_{3}^{=}\right) - k_7\, p\left(\mathrm{C}_{3}^{=}\right) - k_9\, p\left(\mathrm{C}_{3}^{=}\right) - k_{10}\, p\left(\mathrm{C}_{3}^{=}\right) \\
R\left(\mathrm{C}_{4}^{=}\right) &= k_{8'}\, p\left(\mathrm{C}_{5+}^{\mathrm{al}}\right) + k_9\, p\left(\mathrm{C}_{3}^{=}\right) - k_1\, p\left(\mathrm{C}_{4}^{=}\right) - k_2\, p\left(\mathrm{C}_{4}^{=}\right) - k_3\, p\left(\mathrm{C}_{4}^{=}\right) - k_4\, p\left(\mathrm{C}_{4}^{=}\right) \\
&\quad - k_{4'}\, p\left(\mathrm{C}_{4}^{=}\right) - k_5\, p\left(\mathrm{C}_{4}^{=}\right) - k_{10}\, p\left(\mathrm{C}_{4}^{=}\right) \\
R\left(\mathrm{C}_{5+}^{\mathrm{al}}\right) &= k_2\, p\left(\mathrm{C}_{4}^{=}\right) - k_8\, p\left(\mathrm{C}_{5+}^{\mathrm{al}}\right) - k_{8'}\, p\left(\mathrm{C}_{5+}^{\mathrm{al}}\right) - k_{8''}\, p\left(\mathrm{C}_{5+}^{\mathrm{al}}\right) - k_{10}\, p\left(\mathrm{C}_{5+}^{\mathrm{al}}\right) \\
R\left(\mathrm{C}_{1}\right) &= k_{10}\, p\left(\mathrm{C}_{2}^{=}\right) + k_{10}\, p\left(\mathrm{C}_{3}^{=}\right) + k_{10}\, p\left(\mathrm{C}_{4}^{=}\right) + k_{10}\, p\left(\mathrm{C}_{5+}^{\mathrm{al}}\right) + k_{10}\, p\left(\mathrm{C}_{2-3}\right) + k_{10}\, p\left(\mathrm{C}_{4}\right) \\
&\quad + k_{10}\, p\left(\mathrm{C}_{6-8}^{\mathrm{ar}}\right) \\
R\left(\mathrm{C}_{2-3}\right) &= k_4\, p\left(\mathrm{C}_{4}^{=}\right) + k_6\, p\left(\mathrm{C}_{3}^{=}\right) - k_{10}\, p\left(\mathrm{C}_{2-3}\right) \\
R\left(\mathrm{C}_{4}\right) &= k_{4'}\, p\left(\mathrm{C}_{4}^{=}\right) - k_{10}\, p\left(\mathrm{C}_{4}\right) \\
R\left(\mathrm{C}_{6-8}^{\mathrm{ar}}\right) &= k_5\, p\left(\mathrm{C}_{4}^{=}\right) + k_7\, p\left(\mathrm{C}_{3}^{=}\right) - k_{10}\, p\left(\mathrm{C}_{6-8}^{\mathrm{ar}}\right)
\end{aligned}
$$

Scheme 2.4: Net rates of production of the different lumps for the model by Epelde *et al.* [236] (eight lumps).

The authors observed only a minor side product formation [239], which is why they reduce the original eight-lump model. All paraffins are grouped together now ($\mathrm{C}_{1\text{-}4}$), whereas the aromatics are summarized with the higher aliphatics to the new hydrocarbon (superscript HC) lump $\mathrm{C}_{5+}^{\mathrm{HC}}$. The resulting reaction network can be found in Scheme 2.5.

$C_4^= \underset{k_9}{\overset{k_1}{\rightleftharpoons}} C_3^=$	$r_1 = k_1\, p\,(C_4^=)$	$k_1^{\mathrm{ref}} = (1073 \pm 10) \times 10^{-3}\,\mathrm{mol_C\,g_{cat}^{-1}\,h^{-1}\,atm^{-1}}$
		$E_{a,1} = 3.1 \pm 0.6\,\mathrm{kJ\,mol^{-1}}$
$C_4^= \underset{k_8'}{\overset{k_2}{\rightleftharpoons}} C_{5+}^{HC}$	$r_2 = k_2\, p\,(C_4^=)$	$k_2^{\mathrm{ref}} = (163.1 \pm 1.5) \times 10^{-2}\,\mathrm{mol_C\,g_{cat}^{-1}\,h^{-1}\,atm^{-1}}$
		$E_{a,2} = 3.3 \pm 0.6\,\mathrm{kJ\,mol^{-1}}$
$C_4^= \xrightarrow{k_3} C_2^=$	$r_3 = k_3\, p\,(C_4^=)$	$k_3^{\mathrm{ref}} = (2.2 \pm 1.0) \times 10^{-2}\,\mathrm{mol_C\,g_{cat}^{-1}\,h^{-1}\,atm^{-1}}$
		$E_{a,3} = 35.6 \pm 2.7\,\mathrm{kJ\,mol^{-1}}$
$C_4^= \xrightarrow{k_4} C_{1-4}$	$r_4 = k_4\, p\,(C_4^=)$	$k_4^{\mathrm{ref}} = (95 \pm 8) \times 10^{-3}\,\mathrm{mol_C\,g_{cat}^{-1}\,h^{-1}\,atm^{-1}}$
		$E_{a,4} = (1 \pm 1) \times 10^{-1}\,\mathrm{kJ\,mol^{-1}}$
$C_3^= \xrightarrow{k_6} C_{1-4}$	$r_6 = k_6\, p\,(C_3^=)$	$k_6^{\mathrm{ref}} = (2.6 \pm 1.3) \times 10^{-2}\,\mathrm{mol_C\,g_{cat}^{-1}\,h^{-1}\,atm^{-1}}$
		$E_{a,6} = 1.3 \pm 7.5\,\mathrm{kJ\,mol^{-1}}$
$C_{5+}^{HC} \xrightarrow{k_8} C_3^=$	$r_8 = k_8\, p\left(C_{5+}^{HC}\right)$	$k_8^{\mathrm{ref}} = (24.5 \pm 9.8) \times 10^{-2}\,\mathrm{mol_C\,g_{cat}^{-1}\,h^{-1}\,atm^{-1}}$
		$E_{a,8} = 55.5 \pm 1.0\,\mathrm{kJ\,mol^{-1}}$
$C_{5+}^{HC} \underset{k_2}{\overset{k_{8'}}{\rightleftharpoons}} C_4^=$	$r_{8'} = k_{8'}\, p\left(C_{5+}^{HC}\right)$	$k_{8'}^{\mathrm{ref}} = 2.759 \pm 2.796\,\mathrm{mol_C\,g_{cat}^{-1}\,h^{-1}\,atm^{-1}}$
		$E_{a,8'} = 55.5 \pm 1.0\,\mathrm{kJ\,mol^{-1}}$
$C_{5+}^{HC} \xrightarrow{k_{8''}} C_2^=$	$r_{8''} = k_{8''}\, p\left(C_{5+}^{HC}\right)$	$k_{8''}^{\mathrm{ref}} = 0.75 \pm 1.29\,\mathrm{mol_C\,g_{cat}^{-1}\,h^{-1}\,atm^{-1}}$
		$E_{a,8''} = 55.5 \pm 1.0\,\mathrm{kJ\,mol^{-1}}$
$C_3^= \underset{k_1}{\overset{k_9}{\rightleftharpoons}} C_4^=$	$r_9 = k_9\, p\,(C_3^=)$	$k_9^{\mathrm{ref}} = (102.0 \pm 5.3) \times 10^{-2}\,\mathrm{mol_C\,g_{cat}^{-1}\,h^{-1}\,atm^{-1}}$
		$E_{a,9} = 2.9 \pm 1.2\,\mathrm{kJ\,mol^{-1}}$

Scheme 2.5: Reaction network, rate equations and estimated parameters for the model by Epelde *et al.* [236] (five lumps).

From this, the net rates of production are defined according to Scheme 2.6.

$$
\begin{aligned}
R\,(C_2^=) &= k_3\, p\,(C_4^=) + k_{8''}\, p\left(C_{5+}^{HC}\right)\\
R\,(C_3^=) &= k_1\, p\,(C_4^=) + k_8\, p\left(C_{5+}^{HC}\right) - k_6\, p\,(C_3^=) - k_9\, p\,(C_3^=)\\
R\,(C_4^=) &= k_{8'}\, p\left(C_{5+}^{HC}\right) + k_9\, p\,(C_3^=) - k_1\, p\,(C_4^=) - k_2\, p\,(C_4^=) - k_3\, p\,(C_4^=) - k_4\, p\,(C_4^=)\\
R\left(C_{5+}^{HC}\right) &= k_2\, p\,(C_4^=) - k_8\, p\left(C_{5+}^{HC}\right) - k_{8'}\, p\left(C_{5+}^{HC}\right) - k_{8''}\, p\left(C_{5+}^{HC}\right)\\
R\left(C_{1-4}\right) &= k_4\, p\,(C_4^=) + k_6\, p\,(C_3^=)
\end{aligned}
$$

Scheme 2.6: Net rates of production of the different lumps for the model by Epelde *et al.* [236] (five lumps).

Parameter estimation The mole fractions and molar flow rates in this study are expressed in carbon units, whereas, for the reaction rates in Scheme 2.3, partial pressures are used. Parameter estimation is performed with a multivariable nonlinear regression in MATLAB. The

molar flow rates along the reactor are obtained with a fourth-order finite differences approximation, whereas the actual regression is two-part: a self-written routine using the Levenberg-Marquardt algorithm delivers initial values for the final step, the minimization of the objective function via *fminsearch*. The objective function returns the weighted sum of squared residuals between the experimental and theoretical mole fractions. For replicate measurements, an average value is used for the experimental value. The calculation of the weighting factor is different to Equation (2.30): due to the lacking division by the sum of the weighting factors for all fitting responses, the individual values might exceed one for Epelde *et al.* [239]. With this methodology, 13 reference rate constants and ten activation energies are estimated. This means the reparameterized Arrhenius approach (see Equation (2.21)) is used with the reference temperature being the average value of the investigated range (773 K). Steps (4) and (4') are assumed to have similar activation energies, as well as Steps (8), (8') and (8"), to reduce the number of estimated parameters. For the five lump version, 16 unknown values exist: nine reference rate constants and seven activation energies. The same simplification for the activation energy of Steps (8), (8') and (8") is introduced.

Ying *et al.* [237]: Seven-lump model for arbitrary olefin feeds including side product formation

Catalyst As shown in Table 2.1, not many details about the catalyst are accessible because the authors used a commercial ZSM-5 extrudate sample from Süd-Chemie. The only noteworthy fact is the relatively large particle size (420–841 µm). The measurements were performed with a fresh catalyst.

Setup and conditions In the kinetic measurements, different olefins from propene to heptene were analyzed as feed. Ethene was also fed at the beginning of the study. It showed almost no reactivity and was therefore ignored. Whereas propene and butenes could be fed directly as gases, the higher olefins were provided as liquids and had to be evaporated. The temperature was measured within the catalyst bed diluted with silica. For feed dilution, nitrogen was chosen. The continuous fixed bed reactor had an inner diameter of 10 mm, but high volumetric flow rates were applied to prevent film diffusion. For each feed, different maximum contact times and conversions had to be analyzed. However, the latter value was comparable for propene, butenes and pentenes. Both hexene and heptene are very reactive and, therefore, conversion was almost one despite having short contact times. Samples were evaluated with a GC equipped with one column and a flame ionization detector (FID).

Reaction network The authors conducted a profound analysis of the selectivity results of each olefin feed. This insight is used to create the reaction network which consists of seven lumps: $C_2^=$, $C_3^=$, $C_4^=$, $C_5^=$, $C_6^=$, $C_7^=$ and side products with carbon number i (C_i^{SP}). The whole

network describes olefin interconversion (k_1–k_8) except for one side product formation step (k_9). It is mentioned that the theoretical $C_7^=$ lump is compared with an experimental result of $C_{7\text{-}8}^=$ olefins. The side product lump contains all paraffins and aromatics with arbitrary carbon numbers. As mentioned above, ethene showed negligible reactivity, so the authors assume its formation reactions to be irreversible. The same is applied to the step leading to C_i^{SP} and to the formation of $C_4^=$ and $C_6^=$ out of two pentenes. The latter assumption is justified with the missing improvement when the backward reaction is implemented. Stoichiometry is considered and various olefin interconversion reactions are included: there is a clear separation between monomolecular cracking ($C_5^=$, $C_6^=$ and $C_7^=$) and dimerization-cracking reactions ($C_3^=$–$C_7^=$, but especially important for lower olefins). For the dimerization, the highest intermediate included is $C_{10}^=$. The steps are treated as elementary reactions without any adsorption effects. Scheme 2.7 shows an overview of all reactions covered by Ying *et al.* [237].

$$2C_3^= \underset{k_{-1}}{\overset{k_1}{\rightleftharpoons}} C_6^= \qquad r_1 = k_1\, C\,(C_3^=)^2 - k_{-1}\, C\,(C_6^=)$$
$$k_1^{\text{ref}} = 14.42 \pm 0.98\,\text{m}^6\,\text{mol}^{-1}\,\text{kg}_{\text{cat}}^{-1}\,\text{h}^{-1} \qquad E_{\text{a},1} = -15.65 \pm 5.08\,\text{kJ mol}^{-1}$$
$$k_{-1}^{\text{ref}} = 89.10 \pm 3.49\,\text{m}^3\,\text{kg}_{\text{cat}}^{-1}\,\text{h}^{-1} \qquad E_{\text{a},-1} = 38.68 \pm 2.68\,\text{kJ mol}^{-1}$$
$$C_3^= + C_6^= \underset{k_{-2}}{\overset{k_2}{\rightleftharpoons}} C_4^= + C_5^= \qquad r_2 = k_2\, C\,(C_3^=)\; C\,(C_6^=) - k_{-2}\, C\,(C_4^=)\; C\,(C_5^=)$$
$$k_2^{\text{ref}} = 188.73 \pm 13.90\,\text{m}^6\,\text{mol}^{-1}\,\text{kg}_{\text{cat}}^{-1}\,\text{h}^{-1} \qquad E_{\text{a},2} = -53.04 \pm 5.36\,\text{kJ mol}^{-1}$$
$$k_{-2}^{\text{ref}} = 73.49 \pm 8.94\,\text{m}^6\,\text{mol}^{-1}\,\text{kg}_{\text{cat}}^{-1}\,\text{h}^{-1} \qquad E_{\text{a},-2} = -26.62 \pm 9.40\,\text{kJ mol}^{-1}$$
$$C_3^= + C_5^= \underset{k_{-3}}{\overset{k_3}{\rightleftharpoons}} 2C_4^= \qquad r_3 = k_3\, C\,(C_3^=)\; C\,(C_5^=) - k_{-3}\, C\,(C_4^=)^2$$
$$k_3^{\text{ref}} = 82.50 \pm 8.11\,\text{m}^6\,\text{mol}^{-1}\,\text{kg}_{\text{cat}}^{-1}\,\text{h}^{-1} \qquad E_{\text{a},3} = -28.12 \pm 7.88\,\text{kJ mol}^{-1}$$
$$k_{-3}^{\text{ref}} = 29.70 \pm 1.77\,\text{m}^6\,\text{mol}^{-1}\,\text{kg}_{\text{cat}}^{-1}\,\text{h}^{-1} \qquad E_{\text{a},-3} = -13.59 \pm 4.01\,\text{kJ mol}^{-1}$$
$$2C_5^= \xrightarrow{k_4} C_4^= + C_6^= \qquad r_4 = k_4\, C\,(C_5^=)^2$$
$$k_4^{\text{ref}} = 7.97 \pm 2.34\,\text{m}^6\,\text{mol}^{-1}\,\text{kg}_{\text{cat}}^{-1}\,\text{h}^{-1} \qquad E_{\text{a},4} = -16.26 \pm 25.49\,\text{kJ mol}^{-1}$$
$$C_5^= \xrightarrow{k_5} C_2^= + C_3^= \qquad r_5 = k_5\, C\,(C_5^=)$$
$$k_5^{\text{ref}} = 2.52 \pm 1.27\,\text{m}^3\,\text{kg}_{\text{cat}}^{-1}\,\text{h}^{-1} \qquad E_{\text{a},5} = 96.73 \pm 26.19\,\text{kJ mol}^{-1}$$
$$C_6^= \xrightarrow{k_6} C_2^= + C_4^= \qquad r_6 = k_6\, C\,(C_6^=)$$
$$k_6^{\text{ref}} = 11.32 \pm 2.35\,\text{m}^3\,\text{kg}_{\text{cat}}^{-1}\,\text{h}^{-1} \qquad E_{\text{a},6} = 63.45 \pm 12.05\,\text{kJ mol}^{-1}$$
$$C_7^= \underset{k_{-7}}{\overset{k_7}{\rightleftharpoons}} C_3^= + C_4^= \qquad r_7 = k_7\, C\,(C_7^=) - k_{-7}\, C\,(C_3^=)\; C\,(C_4^=)$$
$$k_7^{\text{ref}} = 474.49 \pm 23.25\,\text{m}^6\,\text{mol}^{-1}\,\text{kg}_{\text{cat}}^{-1}\,\text{h}^{-1} \qquad E_{\text{a},7} = 23.85 \pm 3.44\,\text{kJ mol}^{-1}$$
$$k_{-7}^{\text{ref}} = 61.46 \pm 9.79\,\text{m}^3\,\text{kg}_{\text{cat}}^{-1}\,\text{h}^{-1} \qquad E_{\text{a},-7} = -43.76 \pm 15.60\,\text{kJ mol}^{-1}$$
$$C_3^= + C_7^= \underset{k_{-8}}{\overset{k_8}{\rightleftharpoons}} 2C_5^= \qquad r_8 = k_8\, C\,(C_3^=)\; C\,(C_7^=) - k_{-8}\, C\,(C_5^=)^2$$
$$k_8^{\text{ref}} = 83.26 \pm 11.76\,\text{m}^6\,\text{mol}^{-1}\,\text{kg}_{\text{cat}}^{-1}\,\text{h}^{-1} \qquad E_{\text{a},8} = -61.87 \pm 16.36\,\text{kJ mol}^{-1}$$
$$k_{-8}^{\text{ref}} = 10.38 \pm 1.74\,\text{m}^6\,\text{mol}^{-1}\,\text{kg}_{\text{cat}}^{-1}\,\text{h}^{-1} \qquad E_{\text{a},-8} = -20.34 \pm 15.55\,\text{kJ mol}^{-1}$$
$$C_i^= \xrightarrow{k_9} C_i^{SP} \qquad r_9 = k_9\, C\,(C_i^=)$$
$$k_9^{\text{ref}} = 2.14 \pm 0.47\,\text{m}^3\,\text{kg}_{\text{cat}}^{-1}\,\text{h}^{-1} \qquad E_{\text{a},9} = -25.87 \pm 19.57\,\text{kJ mol}^{-1}$$

Scheme 2.7: Reaction network, rate equations and estimated parameters for the model by Ying *et al.* [237] with i ranging from 3 to 7.

This network leads to the net rates of production listed in Scheme 2.8.

$$
\begin{aligned}
R\left(\mathrm{C}_2^{=}\right) &= k_5\, C\left(\mathrm{C}_5^{=}\right) + k_6\, C\left(\mathrm{C}_6^{=}\right) \\
R\left(\mathrm{C}_3^{=}\right) &= 2\,k_{-1}\, C\left(\mathrm{C}_6^{=}\right) + k_{-2}\, C\left(\mathrm{C}_4^{=}\right)\, C\left(\mathrm{C}_5^{=}\right) + k_{-3}\, C\left(\mathrm{C}_4^{=}\right)^2 + k_5\, C\left(\mathrm{C}_5^{=}\right) + k_7\, C\left(\mathrm{C}_7^{=}\right) \\
&\quad + k_{-8}\, C\left(\mathrm{C}_5^{=}\right)^2 - 2\,k_1\, C\left(\mathrm{C}_3^{=}\right)^2 - k_2\, C\left(\mathrm{C}_3^{=}\right)\, C\left(\mathrm{C}_6^{=}\right) - k_3\, C\left(\mathrm{C}_3^{=}\right)\, C\left(\mathrm{C}_5^{=}\right) \\
&\quad - k_{-7}\, C\left(\mathrm{C}_3^{=}\right)\, C\left(\mathrm{C}_4^{=}\right) - k_8\, C\left(\mathrm{C}_3^{=}\right)\, C\left(\mathrm{C}_7^{=}\right) - k_9\, C\left(\mathrm{C}_3^{=}\right) \\
R\left(\mathrm{C}_4^{=}\right) &= k_2\, C\left(\mathrm{C}_3^{=}\right)\, C\left(\mathrm{C}_6^{=}\right) + 2\,k_3\, C\left(\mathrm{C}_3^{=}\right)\, C\left(\mathrm{C}_5^{=}\right) + k_4\, C\left(\mathrm{C}_5^{=}\right)^2 + k_6\, C\left(\mathrm{C}_6^{=}\right) + k_7\, C\left(\mathrm{C}_7^{=}\right) \\
&\quad - k_{-2}\, C\left(\mathrm{C}_4^{=}\right)\, C\left(\mathrm{C}_5^{=}\right) - 2\,k_{-3}\, C\left(\mathrm{C}_4^{=}\right)^2 - k_{-7}\, C\left(\mathrm{C}_3^{=}\right)\, C\left(\mathrm{C}_4^{=}\right) - k_9\, C\left(\mathrm{C}_4^{=}\right) \\
R\left(\mathrm{C}_5^{=}\right) &= k_2\, C\left(\mathrm{C}_3^{=}\right)\, C\left(\mathrm{C}_6^{=}\right) + k_{-3}\, C\left(\mathrm{C}_4^{=}\right)^2 + 2\,k_8\, C\left(\mathrm{C}_3^{=}\right)\, C\left(\mathrm{C}_7^{=}\right) - k_{-2}\, C\left(\mathrm{C}_4^{=}\right)\, C\left(\mathrm{C}_5^{=}\right) \\
&\quad - k_3\, C\left(\mathrm{C}_3^{=}\right)\, C\left(\mathrm{C}_5^{=}\right) - 2\,k_4\, C\left(\mathrm{C}_5^{=}\right)^2 - k_5\, C\left(\mathrm{C}_5^{=}\right) - 2\,k_{-8}\, C\left(\mathrm{C}_5^{=}\right)^2 - k_9\, C\left(\mathrm{C}_5^{=}\right) \\
R\left(\mathrm{C}_6^{=}\right) &= k_1\, C\left(\mathrm{C}_3^{=}\right)^2 + k_{-2}\, C\left(\mathrm{C}_4^{=}\right)\, C\left(\mathrm{C}_5^{=}\right) + k_4\, C\left(\mathrm{C}_5^{=}\right)^2 - k_{-1}\, C\left(\mathrm{C}_6^{=}\right) - k_2\, C\left(\mathrm{C}_3^{=}\right)\, C\left(\mathrm{C}_6^{=}\right) \\
&\quad - k_6\, C\left(\mathrm{C}_6^{=}\right) - k_9\, C\left(\mathrm{C}_6^{=}\right) \\
R\left(\mathrm{C}_7^{=}\right) &= k_{-7}\, C\left(\mathrm{C}_3^{=}\right)\, C\left(\mathrm{C}_4^{=}\right) + k_{-8}\, C\left(\mathrm{C}_5^{=}\right)^2 - k_7\, C\left(\mathrm{C}_7^{=}\right) - k_8\, C\left(\mathrm{C}_3^{=}\right)\, C\left(\mathrm{C}_7^{=}\right) - k_9\, C\left(\mathrm{C}_7^{=}\right) \\
R\left(\mathrm{C}_{3-7}^{\mathrm{SP}}\right) &= k_9\, C\left(\mathrm{C}_3^{=}\right) + k_9\, C\left(\mathrm{C}_4^{=}\right) + k_9\, C\left(\mathrm{C}_5^{=}\right) + k_9\, C\left(\mathrm{C}_6^{=}\right) + k_9\, C\left(\mathrm{C}_7^{=}\right)
\end{aligned}
$$

Scheme 2.8: Net rates of production of the different lumps for the model by Ying *et al.* [237].

Parameter estimation Both the contact time and the reactor model are calculated with mass flow rates, which means that the net rate of production of each lump (Scheme 2.8) has to be multiplied by its molar mass. The reaction rates (Scheme 2.7) are expressed with molar concentrations per volume. For parameter fitting, the Levenberg-Marquardt algorithm is used to minimize the objective function. The latter is defined as the unweighted sum of squared residuals between the theoretical and experimental mass fractions. The reparameterized Arrhenius approach according to Equation (2.21) is used with a reference temperature of 673 K, which is the lowest examined value. As unknown parameters, 14 reference rate constants and 14 activation energies follow from this model.

Huang *et al.* [195]: Six-lump approach for arbitrary olefin feeds including LH and HW types of mechanism

Catalyst The authors chose a commercial ZSM-5 catalyst by Shanghai Fuyu Company due to its coking resistance and high propene to ethene (P/E) ratio. As shown in Table 2.1, the increased Si/Al ratio (200) caused a low number of acid sites (0.012 mmol g_{cat}^{-1}). A preliminary test revealed that catalyst deactivation was negligible, which is why a broad spectrum of TOS was chosen with a regeneration after each 10 h. With 17 h TOS, the coke selectivity was still below 0.01%.

Setup and conditions A continuous U-shaped fixed bed reactor made of titanium with an inner diameter of 6 mm was used for kinetic studies. Different olefins from propene to heptene were applied as feed, but, in contrast to the study by Ying *et al.* [237], the corresponding linear 1-alcohols were fed as liquids and evaporated in a pre-heater. The authors stated that the dehydration to the corresponding 1-olefin occurred very quickly when the feed mixture reached the catalyst bed. However, this inevitably caused water release, which can be seen as further diluent, but also interacted with the acid sites of the catalyst. Further feed dilution could be achieved by using nitrogen, whereas the catalyst was diluted 1:5 with an inert not further specified. The reactor was surrounded by a molten salt bath which allowed controlling the temperature, although no thermocouple was available within the catalyst bed. A GC equipped with an FID and one column was used for product analysis. Each data point resulted from a twofold GC sampling. The authors performed two additional experimental series at 713 K and 753 K with a mixture of different olefins as feed. These were not included into parameter fitting, but used to prove the validity of the model not only for single olefins as feed, but also for mixtures. Therefore, the detailed molar composition without inerts was 0.07, 0.235, 0.22, 0.235, 0.12 and 0.12 for $C_2^=$, $C_3^=$, $C_4^=$, $C_5^=$, $C_6^=$ and $C_7^=$, respectively.

Reaction network Similar to Ying *et al.* [237], a detailed study for each olefin feed was performed. This could be used to derive the reaction network which consists of the following six lumps: $C_2^=$, $C_3^=$, $C_4^=$, $C_5^=$, $C_6^=$ and $C_{7+}^=$; the experimental data of the latter also contains species higher than heptenes. All steps in the network are related to olefin interconversion. Huang *et al.* [195] allow the highest intermediate to have a carbon number of twelve, so hexene dimerization can occur. Furthermore, they include not only monomolecular cracking and dimerization, but also four trimolecular alkylation reactions, for example, the trimerization of propene to butene and pentene. The network shows no irreversible steps: no evolution of side products is included and, although ethene dimerization is neglected, the ethene formation out of higher olefins is assumed to be reversible. The resulting network contains a huge variety of olefin interconversion reactions and can be found in Scheme 2.9. For the derivation of the reaction rates, Huang *et al.* [195] follow a combination of LH and HW types of mechanism. This means the backward reactions are determined with equilibrium constants and the denominator contains the inhibition through competing adsorption. For the latter, all olefins and water are considered. The different reactions are assumed to be elementary and stoichiometry is retained.

For this model, the expressions for the reaction rates are comparably complex, which is why Scheme 2.10 only shows r_l.

Parameter estimation The mole fractions shown in the figures [195] are based only on hydrocarbons, whereas the rate expressions in Scheme 2.9 are defined with partial pressures. The estimated parameters are obtained via nonlinear regression which is used to minimize the objective function. The latter returns the weighted sum of squared residuals between measured

and predicted mole fractions. The weighting is performed in a relatively simple manner: the respective feed component is multiplied by 0.25 and the remaining components by 1. In a subsequent study [241], the authors gave some explanations on numerics: the integration is performed with a fourth-fifth-order Runge-Kutta method provided by *ode45* in MATLAB, whereas the Levenberg-Marquardt algorithm is used for minimizing the objective function. The olefin adsorption constant is assumed to be independent of chain length, so only one reference constant and one adsorption enthalpy are fitted. The interaction between water and the catalyst is reduced to a competitive adsorption, which also requires the estimation of these two values. Finally, the equilibrium constants of the backward reactions are fitted and not calculated from thermodynamics, because the lumps resemble isomer distributions which are difficult to characterize with single values. This causes 44 estimated parameters: ten reference rate constants, ten activation energies, twelve reference equilibrium constants, ten reaction enthalpies and two adsorption enthalpies. The reparameterized approach according to Equations (2.21) and (2.24) is used both for rate and for equilibrium constants with a reference temperature of 733 K, which is in the upper third of the investigated range.

$$3C_3^= \underset{k_1/K_1}{\overset{k_1}{\rightleftharpoons}} C_4^= + C_5^= \qquad r_1 = \frac{k_1}{Den^3}\left(p\left(C_3^=\right)^3 - \frac{1}{K_1}\, p\left(C_4^=\right)\, p\left(C_5^=\right)\right)$$

$$k_1^{ref} = (4.55 \pm 0.73) \times 10^{-7}\,\mathrm{mol\,kg_{cat}^{-1}\,s^{-1}\,kPa^{-3}} \qquad E_{a,1} = -173.97 \pm 5.02\,\mathrm{kJ\,mol^{-1}}$$

$$K_1^{ref} = (3.72 \pm 0.87) \times 10^{-3}\,\mathrm{kPa^2} \qquad \Delta_r H_1^\circ = -85.93 \pm 11.44\,\mathrm{kJ\,mol^{-1}}$$

$$2C_4^= \underset{k_2/K_2}{\overset{k_2}{\rightleftharpoons}} C_3^= + C_5^= \qquad r_2 = \frac{k_2}{Den^2}\left(p\left(C_4^=\right)^2 - \frac{1}{K_2}\, p\left(C_3^=\right)\, p\left(C_5^=\right)\right)$$

$$k_2^{ref} = (5.35 \pm 0.43) \times 10^{-5}\,\mathrm{mol\,kg_{cat}^{-1}\,s^{-1}\,kPa^{-2}} \qquad E_{a,2} = -77.47 \pm 4.09\,\mathrm{kJ\,mol^{-1}}$$

$$K_2^{ref} = (3.12 \pm 0.44) \times 10^{-1}\,\mathrm{kPa^2} \qquad \Delta_r H_2^\circ = 5.01 \pm 7.46\,\mathrm{kJ\,mol^{-1}}$$

$$C_5^= \underset{k_3/K_3}{\overset{k_3}{\rightleftharpoons}} C_2^= + C_3^= \qquad r_3 = \frac{k_3}{Den}\left(p\left(C_5^=\right) - \frac{1}{K_3}\, p\left(C_2^=\right)\, p\left(C_3^=\right)\right)$$

$$k_3^{ref} = (1.30 \pm 0.20) \times 10^{-3}\,\mathrm{mol\,kg_{cat}^{-1}\,s^{-1}\,kPa^{-1}} \qquad E_{a,3} = 81.24 \pm 7.08\,\mathrm{kJ\,mol^{-1}}$$

$$K_3^{ref} = 6.08 \pm 0.67\,\mathrm{kPa^2} \qquad \Delta_r H_3^\circ = 103.45 \pm 5.77\,\mathrm{kJ\,mol^{-1}}$$

$$2C_5^= \underset{k_4/K_4}{\overset{k_4}{\rightleftharpoons}} 2C_3^= + C_4^= \qquad r_4 = \frac{k_4}{Den^2}\left(p\left(C_5^=\right)^2 - \frac{1}{K_4}\, p\left(C_3^=\right)^2\, p\left(C_4^=\right)\right)$$

$$k_4^{ref} = (1.70 \pm 0.56) \times 10^{-4}\,\mathrm{mol\,kg_{cat}^{-1}\,s^{-1}\,kPa^{-2}} \qquad E_{a,4} = -80.12 \pm 8.72\,\mathrm{kJ\,mol^{-1}}$$

$$K_4^{ref} = 7.10 \pm 0.45\,\mathrm{kPa^3} \qquad \Delta_r H_4^\circ = 83.92 \pm 8.02\,\mathrm{kJ\,mol^{-1}}$$

$$2C_5^= \underset{k_5/K_5}{\overset{k_5}{\rightleftharpoons}} C_4^= + C_6^= \qquad r_5 = \frac{k_5}{Den^2}\left(p\left(C_5^=\right)^2 - \frac{1}{K_5}\, p\left(C_4^=\right)\, p\left(C_6^=\right)\right)$$

$$k_5^{ref} = (2.44 \pm 0.52) \times 10^{-4}\,\mathrm{mol\,kg_{cat}^{-1}\,s^{-1}\,kPa^{-2}} \qquad E_{a,5} = -87.62 \pm 5.68\,\mathrm{kJ\,mol^{-1}}$$

$$K_5^{ref} = (3.25 \pm 0.41) \times 10^{-1}\,\mathrm{kPa^2} \qquad \Delta_r H_5^\circ = 1.38 \pm 3.36\,\mathrm{kJ\,mol^{-1}}$$

$$C_6^= \underset{k_6/K_6}{\overset{k_6}{\rightleftharpoons}} C_2^= + C_4^= \qquad r_6 = \frac{k_6}{Den}\left(p\left(C_6^=\right) - \frac{1}{K_6}\, p\left(C_2^=\right)\, p\left(C_4^=\right)\right)$$

$$k_6^{ref} = (4.47 \pm 0.45) \times 10^{-3}\,\mathrm{mol\,kg_{cat}^{-1}\,s^{-1}\,kPa^{-1}} \qquad E_{a,6} = 42.55 \pm 7.90\,\mathrm{kJ\,mol^{-1}}$$

$$K_6^{ref} = (1.12 \pm 0.09) \times 10^{1}\,\mathrm{kPa^2} \qquad \Delta_r H_6^\circ = 91.61 \pm 7.37\,\mathrm{kJ\,mol^{-1}}$$

$$C_6^= \underset{k_7/K_7}{\overset{k_7}{\rightleftharpoons}} 2C_3^= \qquad r_7 = \frac{k_7}{Den}\left(p\left(C_6^=\right) - \frac{1}{K_7}\, p\left(C_3^=\right)^2\right)$$

$$k_7^{ref} = (1.59 \pm 0.10) \times 10^{-2}\,\mathrm{mol\,kg_{cat}^{-1}\,s^{-1}\,kPa^{-1}} \qquad E_{a,7} = 77.31 \pm 4.87\,\mathrm{kJ\,mol^{-1}}$$

$$K_7^{ref} = (7.24 \pm 0.76) \times 10^{1}\,\mathrm{kPa^2} \qquad \Delta_r H_7^\circ = 57.89 \pm 8.39\,\mathrm{kJ\,mol^{-1}}$$

$$2C_6^= \underset{k_8/K_8}{\overset{k_8}{\rightleftharpoons}} C_3^= + C_4^= + C_5^= \qquad r_8 = \frac{k_8}{Den^2}\left(p\left(C_6^=\right)^2 - \frac{1}{K_8}\, p\left(C_3^=\right)\, p\left(C_4^=\right)\, p\left(C_5^=\right)\right)$$

$$k_8^{ref} = (1.18 \pm 0.38) \times 10^{-3}\,\mathrm{mol\,kg_{cat}^{-1}\,s^{-1}\,kPa^{-2}} \qquad E_{a,8} = -49.23 \pm 8.96\,\mathrm{kJ\,mol^{-1}}$$

$$K_8^{ref} = (2.45 \pm 0.30) \times 10^{1}\,\mathrm{kPa^3} \qquad \Delta_r H_8^\circ = 81.42 \pm 8.83\,\mathrm{kJ\,mol^{-1}}$$

$$2C_6^= \underset{k_9/K_9}{\overset{k_9}{\rightleftharpoons}} 3C_4^= \qquad r_9 = \frac{k_9}{Den^2}\left(p\left(C_6^=\right)^2 - \frac{1}{K_9}\, p\left(C_4^=\right)^3\right)$$

$$k_9^{ref} = (5.14 \pm 0.23) \times 10^{-5}\,\mathrm{mol\,kg_{cat}^{-1}\,s^{-1}\,kPa^{-2}} \qquad E_{a,9} = -48.51 \pm 12.48\,\mathrm{kJ\,mol^{-1}}$$

$$K_9^{ref} = (7.01 \pm 0.44) \times 10^{1}\,\mathrm{kPa^3} \qquad \Delta_r H_9^\circ = 81.17 \pm 8.44\,\mathrm{kJ\,mol^{-1}}$$

$$C_7^= \underset{k_{10}/K_{10}}{\overset{k_{10}}{\rightleftharpoons}} C_3^= + C_4^= \qquad r_{10} = \frac{k_{10}}{Den}\left(p\left(C_7^=\right) - \frac{1}{K_{10}}\, p\left(C_3^=\right)\, p\left(C_4^=\right)\right)$$

$$k_{10}^{ref} = (2.79 \pm 0.09) \times 10^{-1}\,\mathrm{mol\,kg_{cat}^{-1}\,s^{-1}\,kPa^{-1}} \qquad E_{a,10} = 11.73 \pm 2.18\,\mathrm{kJ\,mol^{-1}}$$

$$K_{10}^{ref} = (1.05 \pm 0.21) \times 10^{2}\,\mathrm{kPa^2} \qquad \Delta_r H_{10}^\circ = 61.82 \pm 4.06\,\mathrm{kJ\,mol^{-1}}$$

$$Den = 1 + K^{ads}\left(C_{2-7}^=\right) \sum_j p\left(C_j^=\right) + K^{ads}\left(H_2O\right)\, p\left(H_2O\right)$$

$$K^{ads,ref}\left(C_{2-7}^=\right) = (2.20 \pm 0.59) \times 10^{-2}\,\mathrm{kPa^{-1}} \qquad \Delta_{ads} H_{C_{2-7}^=}^\circ = -65.58 \pm 6.10\,\mathrm{kJ\,mol^{-1}}$$

$$K^{ads,ref}\left(H_2O\right) = (2.21 \pm 0.10) \times 10^{-2}\,\mathrm{kPa^{-1}} \qquad \Delta_{ads} H_{H_2O}^\circ = -11.19 \pm 2.19\,\mathrm{kJ\,mol^{-1}}$$

Scheme 2.9: Reaction network, rate equations and estimated parameters for the model by Huang *et al.* [195] with j ranging from 2 to 7.

$$
\begin{aligned}
R\,(C_2^=) &= r_3 + r_6 \\
R\,(C_3^=) &= r_2 + r_3 + 2\,r_4 + 2\,r_7 + r_8 + r_{10} - 3\,r_1 \\
R\,(C_4^=) &= r_1 + r_4 + r_5 + r_6 + r_8 + 3\,r_9 + r_{10} - 2\,r_2 \\
R\,(C_5^=) &= r_1 + r_2 + r_8 - r_3 - 2\,r_4 - 2\,r_5 \\
R\,(C_6^=) &= r_5 - r_6 - r_7 - 2\,r_8 - 2\,r_9 \\
R\,(C_7^=) &= -\,r_{10}
\end{aligned}
$$

Scheme 2.10: Net rates of production of the different lumps for the model by Huang *et al.* [195].

Summary

All three examples comprise several olefin interconversion reactions. Whereas Huang *et al.*'s model [195] is experimentally covered only for lower conversions where side product formation can be neglected, this aspect is included for Epelde *et al.*'s [236] model as well as Ying *et al.*'s [237] model. The former example differentiates paraffins and aromatics in four lumps (eight-lump version), whereas the latter only has one general side product lump. On the other hand, the HW type of mechanism used by Huang *et al.* [195] yields a comparably robust model, although performance could be further improved by using different adsorption constants for all carbon numbers. Moreover, the high number of estimated parameters can cause numerical difficulties during estimation. For the two other models, both adsorption effects and a mechanistic approach are missing. In addition, feed partial pressures are relatively high for Epelde *et al.* [236]; consequently, extrapolation to lower values might be difficult. This is the reason why the authors could not notice any improvement when using an HW type of mechanism [236]. Furthermore, use of this model is restricted to butenes as feed, whereas the other two examples can be applied to different olefins and also to mixtures as feed. This feature is derived from their reaction networks, which contain a high number of pure olefin interconversion steps. Conclusions concerning the mechanism are difficult for Epelde *et al.* [236] because their network neglects stoichiometry and, in the five lump version, combines final and intermediate products in one lump. However, it is suitable to describe conversion of butenes over ZSM-5 modified with potassium.

Studies focusing on feed olefin consumption over ZSM-5

Borges *et al.* [53]: Three-lump approach for oligomerization of $C_2^=$ to $C_4^=$ feeds

Catalyst A commercial ZSM-5 powder by Zeolyst International with a rather low Si/Al ratio of 30 was used here. As shown in Table 2.1, no further details are available. Measurements

were performed with a TOS between 0 and 1.4 h; no deactivation was observed during this period. Furthermore, no coke could be detected during heating up the catalyst to 973 K under air and analyzing the effluent with a thermogravimetry (TG)/differential scanning calorimetry (DSC) combination. This was attributed to the mild conditions and steric hindrances of coke evolution [238].

Setup and conditions A continuous fixed bed reactor was used; no additional information about the setup is given. Ethene, propene and 1-butene were provided as gases and fed separately, each of them diluted with nitrogen. The products were analyzed via a GC containing a single column and an FID.

Reaction network This work focuses on the consumption of a certain feed olefin through oligomerization. Thus, no interconversion reactions are implemented, the model consists of only one rate equation, which is equal to the net rate of production of either $C_2^=$, $C_3^=$ or $C_4^=$. For the values of $R(i)$, stoichiometry is not retained. Although the actual rate is written as dimerization, the authors account for the oligomerization through allowing also higher intermediates to participate in this reaction step: one reactant is always the feed component (e.g., $C_2^=$), whereas the other reactant is either also the feed molecule or a multiple of it (e.g., $C_2^=$, $C_4^=$, $C_6^=$, ...). In the derivation of Scheme 2.11, it is assumed that the sum of partial pressures equals the inlet partial pressure of the feed component $p^{\text{in}}\left(C_i^=\right)$ throughout the whole reactor. This allows for expressing the partial pressures of all reactants via the conversion X and $p^{\text{in}}\left(C_i^=\right)$. Furthermore, irreversible elementary reactions are underlaid. This work is an example where ethene dimerization is included. Scheme 2.11 is a combination of ER and HW types of mechanism, so adsorption effects are included for one of the reacting olefins (superscript ads), whereas the other olefin reacts directly from the gas phase. In the numerator, adsorption equilibrium and rate constant as well as the total number of acid sites are summarized to a composite value k_{i-1}^{co}. The scope of describing the feed olefin consumption via oligomerization means that no cracking and no side reactions are considered, although the corresponding interconversion and side products are observed.

$$C_i^= + C_{n\cdot i}^{=,\text{ads}} \xrightarrow{k_{i-1}} C_{i+n\cdot i}^=$$

$$r_{i-1} = -R\left(C_i^=\right) = \frac{k_{i-1}^{\text{co}}\, p^{\text{in}}\left(C_i^=\right)^2 (1-X)}{1+K^{\text{ads}}\left(C_{2-4}^=\right) p^{\text{in}}\left(C_i^=\right)}$$

$$k_{i-1}^{\text{co}} = k_{i-1}\, K^{\text{ads}}\left(C_{2-4}^=\right)\, C_{\text{t}}$$

$$k_1^{\text{co,ref}} = (4.2 \pm 0.1) \times 10^{-3}\,\text{mol}\,\text{h}^{-1}\,\text{g}_{\text{cat}}^{-1}\,\text{bar}^{-2} \qquad E_{\text{a},1}^{\text{co}} = -45.0 \pm 1.6\,\text{kJ}\,\text{mol}^{-1}$$

$$k_2^{\text{co,ref}} = (16.7 \pm 0.4) \times 10^{-3}\,\text{mol}\,\text{h}^{-1}\,\text{g}_{\text{cat}}^{-1}\,\text{bar}^{-2} \qquad E_{\text{a},2}^{\text{co}} = -45.4 \pm 1.3\,\text{kJ}\,\text{mol}^{-1}$$

$$k_3^{\text{co,ref}} = (66.7 \pm 2.7) \times 10^{-3}\,\text{mol}\,\text{h}^{-1}\,\text{g}_{\text{cat}}^{-1}\,\text{bar}^{-2} \qquad E_{\text{a},3}^{\text{co}} = -18.2 \pm 2.2\,\text{kJ}\,\text{mol}^{-1}$$

$$K^{\text{ads,ref}}\left(C_{2-4}^=\right) = 1.9 \pm 0.2\,\text{bar}^{-1} \qquad \Delta_{\text{ads}} H_{C_{2-4}^=}^{\circ} = -77.8 \pm 3.0\,\text{kJ}\,\text{mol}^{-1}$$

Scheme 2.11: Reaction network, rate equations, net rate of production of the different lumps and estimated parameters for the model by Borges *et al.* [53] with i ranging from 2 to 4 and n being a positive integer such that $n \cdot i$ is a multiple of i.

Parameter estimation For the three reaction rates in Scheme 2.11, partial pressures are used. The rates are fitted to measured data points using Microsoft Excel. Here, a non-linear least-squares regression is performed to minimize the sum of squared residuals between experiments and model. In contrast to most other studies, the objective function evaluates catalytic activity and not mole fractions or comparable values. The catalytic activity relates the final conversion with the initial molar flow rate of the olefin and the catalyst mass. For the parameter estimation, no weighting factors are included. The adsorption of the different olefins is realized via the same constant. This is justified by a reference to literature studies and by own hybrid Hartree-Fock (HF) and density functional theory (DFT) calculations which show a significant difference only for ethene. Although the model describes not only the dimerization of two feed molecules, but also of multiples of it and a feed molecule, all rate constants for a certain feed are assumed to be the same. These as well as the adsorption equilibrium constant are expressed via values at the reference temperature of 648 K, which is the mean of the experimentally covered range. The kinetic rate constants are composite values which include the rate constant itself, the adsorption constant and the molar concentration of total acid sites per catalyst mass. Finally, eight parameters are estimated with the experimental data: three reference rate constants, three activation energies, one reference equilibrium constant and one adsorption enthalpy.

Oliveira *et al.* [238]: 17-lump model for $C_2^=$ to $C_4^=$ feeds considering heterogeneity in acid sites

Catalyst This model is a subsequent work to Borges *et al.* [53]. Thus, the same ZSM-5 zeolite powder was used (see Table 2.1). However, focus of this study was creating a kinetic model which has the heterogeneity of the acid sites implemented. The authors investigated the coherence between acidity and activity earlier [242] and found a linear relationship between the activation energy of ammonia desorption resembling acid strength and of several surface reactions as well as of the adsorption enthalpy. These results were further confirmed by *ab initio* calculations. This contradicts the approach by Thybaut *et al.* [21], where a difference in acid strength is fully attributed to the adsorption properties, whereas the kinetic descriptors, i.e., pre-exponential factor and activation energy, are independent of the catalyst properties. However, in Thybaut *et al.*'s study [21], an average acidity was assumed for each catalyst, whereas, for Oliveira *et al.* [238], several sites with different strength were defined. Further variety within the catalyst samples was achieved by exchanging 0%, 2.4%, 3.0% and 3.2% of the protons with Na. The number of acid sites as well as their strength decreased with higher Na contents. By contrast, for Thybaut *et al.* [21], the strength of the acid sites increased when their amount was lowered. An explanation could be that the different catalysts were synthesized already with the reduced number of acid sites, whereas, for Oliveira *et al.* [238], some of the protons were exchanged with Na after synthesis which might especially affect the ones with highest strength.

Setup and conditions The same apparatus and similar conditions as for Borges *et al.* [53] were used (see Table 2.2).

Reaction network As stated above, this kinetic model aims at simulating the olefin interconversion over four different ZSM-5 samples where each had a uniform distribution of acid strength additionally. For this, 17 lumps are introduced: $C_2^=$, $C_3^=$, $C_4^=$, $C_5^=$, $C_6^=$, $C_7^=$, $C_8^=$, C_2, C_3, C_4, C_5, C_6, C_7, C_8, C_6^{ar}, C_7^{ar} and C_8^{ar}. In contrast to the previous study, cracking is also considered as a backward reaction to the dimerization. Furthermore, the irreversible evolution of side products is included. The corresponding rate equations can be found in Scheme 2.12 where θ_h represents the fraction of acid sites having the activation energy of ammonia desorption of $E_{a,h}^{NH_3}$. The total number of acid sites is included in the pre-exponential fitting parameter α^l of each reaction type. The linear relationship between $E_{a,h}^{NH_3}$ and activation energy or adsorption enthalpy is expressed via the parameters β^l and δ^l. The carbon number dependence of the non-equilibrated steps is implemented with a hyperbolic tangent function and the additional parameters γ^l, ϕ^l and φ^l. As in the previous study [53], the sum of partial pressures should always be equal to the inlet partial pressure of the feed component $p\left(C_w^=\right)$. In Scheme 2.12, one olefin is always in adsorbed state (superscript ads), whereas, when applicable, the other one is in the gas phase. Consequently, the dimerization and aromatization steps are combined ER and HW types of mechanism. For the monomolecular cracking reactions, the L and HW types of mechanism are coupled. All steps should occur as elementary reactions. Ethene dimerization reactions are covered by this model. Although Scheme 2.12 proposes that three olefins are converted to three paraffins per evolution of one aromatic molecule, stoichiometry is retained neither in the reaction rate nor in the net rate of production.

$$\mathrm{C}_i^{=,\mathrm{ads}} + \mathrm{C}_v^{=} \underset{k_{i+v}^{\mathrm{cr}}}{\overset{k_{i,v}^{\mathrm{dim}}}{\rightleftharpoons}} \mathrm{C}_{i+v}^{=,\mathrm{ads}} \qquad r_l^{\mathrm{dim/cr}} = \frac{k_l^{\mathrm{dim,co}}\, p\left(\mathrm{C}_i^{=}\right) p(\mathrm{C}_v^{=}) - k_l^{\mathrm{cr,co}}\, p\left(\mathrm{C}_{i+v}^{=}\right)}{1+\sum_h K_h^{\mathrm{ads}}\left(\mathrm{C}_{2-8}^{=}\right) p^{\mathrm{in}}(\mathrm{C}_w^{=})}$$

$$\mathrm{C}_i^{=,\mathrm{ads}} + 3\,\mathrm{C}_v^{=} \xrightarrow{k_{i,v}^{\mathrm{ar}}} \mathrm{C}_i^{\mathrm{ar,ads}} + 3\,\mathrm{C}_v \qquad r_l^{\mathrm{ar}} = \frac{k_l^{\mathrm{ar,co}}\, p\left(\mathrm{C}_i^{=}\right) p(\mathrm{C}_v^{=})}{1+\sum_h K_h^{\mathrm{ads}}\left(\mathrm{C}_{2-8}^{=}\right) p^{\mathrm{in}}(\mathrm{C}_w^{=})}$$

$$k^{\mathrm{dim,co}} = \sum_h \theta_h\, \alpha^{\mathrm{dim}}\, \exp\left(\beta^{\mathrm{dim}}\, \left(E_{\mathrm{a}}^{0,\mathrm{dim}} - \delta^{\mathrm{dim}}\, E_{\mathrm{a},h}^{\mathrm{NH_3}}\right)\right)\, K_h^{\mathrm{ads}}\left(\mathrm{C}_{2-8}^{=}\right)\, \exp\left(-\frac{E_{\mathrm{a}}^{0,\mathrm{dim}} - \delta^{\mathrm{dim}}\, E_{\mathrm{a},h}^{\mathrm{NH_3}}}{R\,T}\right)$$

$$k^{\mathrm{cr,co}} = \sum_h \theta_h\, \alpha^{\mathrm{cr}}\, \exp\left(\beta^{\mathrm{cr}}\, \left(E_{\mathrm{a}}^{0,\mathrm{cr}} - \delta^{\mathrm{cr}}\, E_{\mathrm{a},h}^{\mathrm{NH_3}}\right)\right)\, K_h^{\mathrm{ads}}\left(\mathrm{C}_{2-8}^{=}\right)\, \exp\left(-\frac{E_{\mathrm{a}}^{0,\mathrm{cr}} - \delta^{\mathrm{cr}}\, E_{\mathrm{a},h}^{\mathrm{NH_3}}}{R\,T}\right)$$

$$k^{\mathrm{ar,co}} = \sum_h \theta_h\, \alpha^{\mathrm{ar}}\, \exp\left(\beta^{\mathrm{ar}}\, \left(E_{\mathrm{a}}^{0,\mathrm{ar}} - \delta^{\mathrm{ar}}\, E_{\mathrm{a},h}^{\mathrm{NH_3}}\right)\right)\, v^{\varphi^{\mathrm{ar}}}\, K_h^{\mathrm{ads}}\left(\mathrm{C}_{2-8}^{=}\right)\, \exp\left(-\frac{E_{\mathrm{a}}^{0,\mathrm{ar}} - \delta^{\mathrm{ar}}\, E_{\mathrm{a},h}^{\mathrm{NH_3}}}{R\,T}\right)$$

$$E_{\mathrm{a}}^{0,\mathrm{dim}} = \frac{E_{\mathrm{a}}^{\mathrm{dim}}}{\tanh\left(\gamma^{\mathrm{dim}}\, v\right)} \qquad E_{\mathrm{a}}^{0,\mathrm{cr}} = \frac{E_{\mathrm{a}}^{\mathrm{cr}}}{\tanh(\gamma^{\mathrm{cr}}\,(i+v))}\,\left(1+\phi^{\mathrm{cr}}\,|i-v|\right) \qquad E_{\mathrm{a}}^{0,\mathrm{ar}} = \frac{E_{\mathrm{a}}^{\mathrm{ar}}}{\tanh(\gamma^{\mathrm{ar}}\, v)}$$

$$K_h^{\mathrm{ads}}\left(\mathrm{C}_{2-8}^{=}\right) = K^{\mathrm{ads,ref}}\left(\mathrm{C}_{2-8}^{=}\right)\, \exp\left(-\frac{\Delta_{\mathrm{ads}} H_{\mathrm{C}_{2-8}^{=}}^{\circ} - \delta^{\mathrm{ads}}\, E_{\mathrm{a},h}^{\mathrm{NH_3}}}{R\,T}\right)$$

$$\alpha^{\mathrm{dim}} = 1.05\times10^{5}\,\mathrm{mol\,min^{-1}\,atm^{-1}\,g_{cat}^{-1}} \qquad \beta^{\mathrm{dim}} = 1.27\times10^{-5} \qquad \delta^{\mathrm{dim}} = 0.005$$

$$E_{\mathrm{a}}^{\mathrm{dim}} = 103.5\,\mathrm{kJ\,mol^{-1}} \qquad \gamma^{\mathrm{dim}} = 0.523$$

$$\alpha^{\mathrm{cr}} = 8.16\times10^{2}\,\mathrm{mol\,min^{-1}\,g_{cat}^{-1}} \qquad \beta^{\mathrm{cr}} = 7.73\times10^{-5} \qquad \delta^{\mathrm{cr}} = 0.334$$

$$E_{\mathrm{a}}^{\mathrm{cr}} = 126.1\,\mathrm{kJ\,mol^{-1}} \qquad \gamma^{\mathrm{cr}} = 0.168 \qquad \phi^{\mathrm{cr}} = 0.029$$

$$\alpha^{\mathrm{ar}} = 1.81\times10^{5}\,\mathrm{mol\,min^{-1}\,atm^{-1}\,g_{cat}^{-1}} \qquad \beta^{\mathrm{ar}} = 3.72\times10^{-7} \qquad \delta^{\mathrm{ar}} = 0.374$$

$$E_{\mathrm{a}}^{\mathrm{ar}} = 130.9\,\mathrm{kJ\,mol^{-1}} \qquad \gamma^{\mathrm{ar}} = 0.164 \qquad \varphi^{\mathrm{ar}} = 1.909$$

$$K^{\mathrm{ads,ref}}\left(\mathrm{C}_{2-8}^{=}\right) = 4.86\times10^{-17}\,\mathrm{atm^{-1}} \qquad \Delta_{\mathrm{ads}} H_{\mathrm{C}_{2-8}^{=}}^{\circ} = 132.9\,\mathrm{kJ\,mol^{-1}} \qquad \delta^{\mathrm{ads}} = 0.634$$

Scheme 2.12: Reaction network, rate equations and estimated parameters for the model by Oliveira *et al.* [238] with i and v ranging from 2 to 6 and $i+v$ being less than or equal to 8 for the dimerization/cracking reactions; for the aromatization, i is between 6 and 8 and v between 2 and 8; the carbon number of the feed olefin is characterized by w and can be between 2 and 8.

For each of the lumps, the net rate of production is defined. Because of the many combination possibilities, Scheme 2.13 is written in generalized form.

$$\begin{aligned}
R\left(\mathrm{C}_i^{=}\right) = &\sum_q r_q^{\mathrm{dim/cr}}\left(\mathrm{C}_v^{=,\mathrm{ads}}, \mathrm{C}_{i-v}^{=}; \mathrm{C}_i^{=,\mathrm{ads}}\right) + \sum_q r_q^{\mathrm{dim/cr}}\left(\mathrm{C}_{i-v}^{=,\mathrm{ads}}, \mathrm{C}_v^{=}; \mathrm{C}_i^{=,\mathrm{ads}}\right) \\
&- \sum_q r_q^{\mathrm{dim/cr}}\left(\mathrm{C}_i^{=,\mathrm{ads}}, \mathrm{C}_v^{=}; \mathrm{C}_{i+v}^{=,\mathrm{ads}}\right) - \sum_q r_q^{\mathrm{dim/cr}}\left(\mathrm{C}_v^{=,\mathrm{ads}}, \mathrm{C}_i^{=}; \mathrm{C}_{v+i}^{=,\mathrm{ads}}\right) \\
&- \sum_q r_q^{\mathrm{ar}}\left(\mathrm{C}_i^{=,\mathrm{ads}}, 3\,\mathrm{C}_v^{=}; \mathrm{C}_i^{\mathrm{ar,ads}}, 3\,\mathrm{C}_v\right) - \sum_q r_q^{\mathrm{ar}}\left(\mathrm{C}_v^{=,\mathrm{ads}}, 3\,\mathrm{C}_i^{=}; \mathrm{C}_v^{\mathrm{ar,ads}}, 3\,\mathrm{C}_i\right) \\
R\left(\mathrm{C}_i\right) = &\sum_q r_q^{\mathrm{ar}}\left(\mathrm{C}_v^{=,\mathrm{ads}}, 3\,\mathrm{C}_i^{=}; \mathrm{C}_v^{\mathrm{ar,ads}}, 3\,\mathrm{C}_i\right) \\
R\left(\mathrm{C}_i^{\mathrm{ar}}\right) = &\sum_q r_q^{\mathrm{ar}}\left(\mathrm{C}_i^{=,\mathrm{ads}}, 3\,\mathrm{C}_v^{=}; \mathrm{C}_i^{\mathrm{ar,ads}}, 3\,\mathrm{C}_v\right)
\end{aligned}$$

Scheme 2.13: Net rates of production of the different lumps for the model by Oliveira *et al.* [238] with i ranging from 2 to 8 for $R\left(\mathrm{C}_i^{=}\right)$, from 2 to 8 for $R(\mathrm{C}_i)$ and from 6 to 8 for $R\left(\mathrm{C}_i^{\mathrm{ar}}\right)$, respectively; the same rules as in Scheme 2.12 apply for the different indices of the reaction rates.

Parameter estimation The reaction rates in Scheme 2.12 are defined with partial pressures. As in the previous study, the objective function compares catalytic activities between experiment and model. The discrepancy is minimized via a nonlinear least squares regression using MATLAB and without any weighting. The solver *ode15s* is applied to integrate the differential equations. With *ab initio* HF calculations, the authors could show that only the size of the gas phase olefin is crucial for the activation energy, an effect which is included via γ^l, ϕ^l and φ^l. Again, it is assumed that all olefins have the same value for the adsorption constant. Both the latter and the rate constants are expressed via the reference temperature, a value which is not mentioned. Finally, 20 parameters are estimated: three activation energies, three pre-exponential factors, six values to correlate acid strength and activation energies, five factors for the carbon number dependence, one reference equilibrium constant, one adsorption enthalpy and one factor to correlate acid strength and adsorption enthalpy.

Summary

The model by Borges *et al.* [53] is an effective way to describe the consumption of $C_2^=$ to $C_4^=$ feeds. However, due to the negligence of interconversion and side reactions, its application is restricted to low conversion in contrast to the examples describing olefin interconversion. On the other hand, computational effort is less for Borges *et al.* [53]. The limitation of low conversion is improved by the subsequent model by Oliveira *et al.* [238] where more variability in reactivity is given, but where also more parameters are required. Here, the description of side product formation is also possible. For both models, agreement could be increased by considering the carbon number dependence of adsorption constants. Furthermore, the assumption that the sum of all partial pressures is equal to the inlet partial pressure of the feed component might not always be fulfilled. Nevertheless, the approach by Oliveira *et al.* [238] is the only one found in literature which allows for considering the fact that not all sites of a zeolite have the same acid strength.

Microkinetic study over ZSM-5

Von Aretin *et al.* [26]: Model for arbitrary olefin feeds considering all interconversion steps with maximum carbon number of twelve

This model is introduced in Chapter 3.

Study elucidating the peculiarities over SAPO-34

Zhou *et al.* [136]: Eight-lump model for $C_2^=$ to $C_4^=$ feeds considering side product formation

Catalyst A self-synthesized zeolite was used. Although the X-ray diffraction pattern revealed a 50/50 structure of SAPO-18 and SAPO-34 fragments, it is referred to as SAPO-34 because both zeolite types show the same MTO performance according to the authors. The zeolite powder was sieved to a fine fraction with a mean size of 3.2 µm. Because of the small pores within the eight-membered SAPO rings, the formation of olefins higher than $C_4^=$ and even of isobutene was suppressed. During the measurements, the authors observed significant amounts of coke, which is why a closure of the carbon balances was not possible. Consequently, the kinetic measurements were recorded after 1 min TOS. The coke was analyzed by introducing air subsequent to the kinetic measurements and by monitoring the CO and CO_2 evolution with a TCD.

Setup and conditions Ethene, propene, 1-butene and 2-butene were separately investigated and therefore fed as gas. For this, a continuous fixed bed reactor made of quartz glass with an inner diameter of 6 mm was used. Only in three cases, the feed was diluted with nitrogen, but these data points are not considered during parameter estimation. For the remaining measurements, the partial pressure of the feed equaled the total pressure. In contrast to that, the catalyst bed was diluted each time with silica so that the ratio of bed height and bed diameter was approximately two. For product analysis, the authors applied a GC with one column and an FID.

Reaction network The kinetic description is conducted with eight responses during parameter estimation: $C_2^=$, $C_3^=$, $C_4^=$, $C_5^=$, C_1, C_2, C_3 and C_4. An additional lump C_x^+ is introduced which should resemble a higher protonated intermediate with arbitrary carbon number. For this, the PSSA is applied since no experimental data for comparison are available. The authors justify this C_x^+ lump by referring to the measurements which yield an olefin composition close to the calculated thermodynamic equilibrium on this specific catalyst regardless of the feed olefin used; thus, similar intermediates should be present. The experiments with either 1-butene or 2-butene as feed showed that the linear butenes can be summarized to one lump because isomerization is fast. However, isobutene is excluded from the reaction network due to steric hindrance. For the same reason, no higher olefins and no aromatics are included. This strong molecular sieving effect could be seen as a hint that the majority of acid sites is located within the micropores. In the resulting general reaction pathways, the feed olefin is converted to C_x^+ (k_1–k_6) and then further cracked to olefins (k_7–k_{10}), as can be seen in Scheme 2.14. Through side reactions (k_{11}–k_{14}), the olefins can also react to the respective paraffin, whereas the lump C_x^+ is transformed to methane, respectively. This model considers the dimerization of ethene,

both with itself and with propene or butenes. Only the paraffin formation is assumed to be irreversible. From the equations in Scheme 2.14, it can be seen that neither adsorption nor a mechanistic scheme are implemented. Furthermore, stoichiometry is neglected and the reactions are assumed to be of elementary type. Nevertheless, the order of both $C_4^=$ and $C_5^=$ dimerization is set to one.

$C_2^= \underset{k_7}{\overset{k_1+k_2}{\rightleftharpoons}} C_x^+$	$r_1 = k_1\, C\,(C_2^=)^2$	$k_1 = 0.21 \times 10^{-3}\,\mathrm{m^6\,kg_{cat}^{-1}\,s^{-1}\,mol^{-1}}$
	$+k_2\, C\,(C_2^=)\,(C\,(C_3^=) + C\,(C_4^=))$	$k_2 = 0.81 \times 10^{-3}\,\mathrm{m^6\,kg_{cat}^{-1}\,s^{-1}\,mol^{-1}}$
$C_3^= \underset{k_8}{\overset{k_3+k_4}{\rightleftharpoons}} C_x^+$	$r_2 = k_3\, C\,(C_3^=)^2 + k_4\, C\,(C_3^=)\; C\,(C_4^=)$	$k_3 = 3.1 \times 10^{-3}\,\mathrm{m^6\,kg_{cat}^{-1}\,s^{-1}\,mol^{-1}}$
		$k_4 = 2.3 \times 10^{-3}\,\mathrm{m^6\,kg_{cat}^{-1}\,s^{-1}\,mol^{-1}}$
$C_4^= \underset{k_9}{\overset{k_5}{\rightleftharpoons}} C_x^+$	$r_3 = k_5\, C\,(C_4^=)$	$k_5 = 33 \times 10^{-3}\,\mathrm{m^3\,kg_{cat}^{-1}\,s^{-1}}$
$C_5^= \underset{k_{10}}{\overset{k_6}{\rightleftharpoons}} C_x^+$	$r_4 = k_6\, C\,(C_5^=)$	$k_6 = 8.6 \times 10^{-3}\,\mathrm{m^3\,kg_{cat}^{-1}\,s^{-1}}$
$C_x^+ \underset{k_1+k_2}{\overset{k_7}{\rightleftharpoons}} C_2^=$	$r_5 = k_7\, C\,(C_x^+)$	$k_7 = 2.8 \times 10^{-3}\,\mathrm{m^3\,kg_{cat}^{-1}\,s^{-1}}$
$C_x^+ \underset{k_3+k_4}{\overset{k_8}{\rightleftharpoons}} C_3^=$	$r_6 = k_8\, C\,(C_x^+)$	$k_8 = 32 \times 10^{-3}\,\mathrm{m^3\,kg_{cat}^{-1}\,s^{-1}}$
$C_x^+ \underset{k_5}{\overset{k_9}{\rightleftharpoons}} C_4^=$	$r_7 = k_9\, C\,(C_x^+)$	$k_9 = 21 \times 10^{-3}\,\mathrm{m^3\,kg_{cat}^{-1}\,s^{-1}}$
$C_x^+ \underset{k_6}{\overset{k_{10}}{\rightleftharpoons}} C_5^=$	$r_8 = k_{10}\, C\,(C_x^+)$	$k_{10} = 4.9 \times 10^{-3}\,\mathrm{m^3\,kg_{cat}^{-1}\,s^{-1}}$
$C_x^+ \xrightarrow{k_{11}} C_1$	$r_9 = k_{11}\, C\,(C_x^+)$	$k_{11} = 0.042 \times 10^{-3}\,\mathrm{m^3\,kg_{cat}^{-1}\,s^{-1}}$
$C_2^= \xrightarrow{k_{12}} C_2$	$r_{10} = k_{12}\, C\,(C_2^=)\; \sum_j C\left(C_j^=\right)$	$k_{12} = 0.0075 \times 10^{-3}\,\mathrm{m^6\,kg_{cat}^{-1}\,s^{-1}\,mol^{-1}}$
$C_3^= \xrightarrow{k_{13}} C_3$	$r_{11} = k_{13}\, C\,(C_3^=)\; \sum_j C\left(C_j^=\right)$	$k_{13} = 0.27 \times 10^{-3}\,\mathrm{m^6\,kg_{cat}^{-1}\,s^{-1}\,mol^{-1}}$
$C_4^= \xrightarrow{k_{14}} C_4$	$r_{12} = k_{14}\, C\,(C_4^=)\; \sum_j C\left(C_j^=\right)$	$k_{14} = 0.079 \times 10^{-3}\,\mathrm{m^6\,kg_{cat}^{-1}\,s^{-1}\,mol^{-1}}$

Scheme 2.14: Reaction network, rate equations and estimated parameters for the model by Zhou *et al.* [136] with j ranging from 2 to 5.

The resulting net rates of production can be seen in Scheme 2.15. Here, the lump C_x^+ is also shown. In the original publication [136], the concentrations of all olefins are summed up for the side product formation (see Steps (12)–(14)). It is assumed here that the consumption through this summarized value is not included in the net rates of production of the respective olefins.

$$
\begin{aligned}
R\left(\mathrm{C}_2^{=}\right) &= k_7\, C\left(\mathrm{C}_x^{+}\right) - k_1\, C\left(\mathrm{C}_2^{=}\right)^2 - k_2\, C\left(\mathrm{C}_2^{=}\right)\left(C\left(\mathrm{C}_3^{=}\right) + C\left(\mathrm{C}_4^{=}\right)\right) - k_{12}\, C\left(\mathrm{C}_2^{=}\right) \sum_j C\left(\mathrm{C}_j^{=}\right) \\
R\left(\mathrm{C}_3^{=}\right) &= k_8\, C\left(\mathrm{C}_x^{+}\right) - k_2\, C\left(\mathrm{C}_2^{=}\right)\left(C\left(\mathrm{C}_3^{=}\right) + C\left(\mathrm{C}_4^{=}\right)\right) - k_3\, C\left(\mathrm{C}_3^{=}\right)^2 - k_4\, C\left(\mathrm{C}_3^{=}\right) C\left(\mathrm{C}_4^{=}\right) - \\
&\quad - k_{13}\, C\left(\mathrm{C}_3^{=}\right) \sum_j C\left(\mathrm{C}_j^{=}\right) \\
R\left(\mathrm{C}_4^{=}\right) &= k_9\, C\left(\mathrm{C}_x^{+}\right) - k_2\, C\left(\mathrm{C}_2^{=}\right)\left(C\left(\mathrm{C}_3^{=}\right) + C\left(\mathrm{C}_4^{=}\right)\right) - k_4\, C\left(\mathrm{C}_3^{=}\right) C\left(\mathrm{C}_4^{=}\right) - k_5\, C\left(\mathrm{C}_4^{=}\right) \\
&\quad - k_{14}\, C\left(\mathrm{C}_4^{=}\right) \sum_j C\left(\mathrm{C}_j^{=}\right) \\
R\left(\mathrm{C}_5^{=}\right) &= k_{10}\, C\left(\mathrm{C}_x^{+}\right) - k_6\, C\left(\mathrm{C}_5^{=}\right) \\
R\left(\mathrm{C}_1\right) &= k_{11}\, C\left(\mathrm{C}_x^{+}\right) \\
R\left(\mathrm{C}_2\right) &= k_{12}\, C\left(\mathrm{C}_2^{=}\right) \sum_j C\left(\mathrm{C}_j^{=}\right) \\
R\left(\mathrm{C}_3\right) &= k_{13}\, C\left(\mathrm{C}_3^{=}\right) \sum_j C\left(\mathrm{C}_j^{=}\right) \\
R\left(\mathrm{C}_4\right) &= k_{14}\, C\left(\mathrm{C}_4^{=}\right) \sum_j C\left(\mathrm{C}_j^{=}\right) \\
R\left(\mathrm{C}_x^{+}\right) = 0 &= k_1\, C\left(\mathrm{C}_2^{=}\right)^2 + k_2\, C\left(\mathrm{C}_2^{=}\right)\left(C\left(\mathrm{C}_3^{=}\right) + C\left(\mathrm{C}_4^{=}\right)\right) + k_3\, C\left(\mathrm{C}_3^{=}\right)^2 + k_4\, C\left(\mathrm{C}_3^{=}\right) C\left(\mathrm{C}_4^{=}\right) + k_5\, C\left(\mathrm{C}_4^{=}\right) \\
&\quad + k_6\, C\left(\mathrm{C}_5^{=}\right) - k_7\, C\left(\mathrm{C}_x^{+}\right) - k_8\, C\left(\mathrm{C}_x^{+}\right) - k_9\, C\left(\mathrm{C}_x^{+}\right) - k_{10}\, C\left(\mathrm{C}_x^{+}\right) - k_{11}\, C\left(\mathrm{C}_x^{+}\right)
\end{aligned}
$$

Scheme 2.15: Net rates of production of the different lumps for the model by Zhou *et al.* [136] with j ranging from 2 to 5.

Parameter estimation All mass fractions in this study are defined on a carbon basis, whereas, in the rate equations, molar concentrations per volume have to be used. No information about the actual fitting routine can be found. Only rate constants are estimated because all data points were collected at constant temperature. The reaction network is restricted to the most important dimerization reactions in order to have not too many unknown parameters. This is why the dimerization reactions of ethene with propene and with butenes are assumed to have the same rate constant. For butenes and pentenes, only the self-dimerization is considered. Finally, 14 unknown parameters are obtained. Although only the undiluted measurements are used for parameter estimation, extrapolation to lower feed partial pressures is also possible according to the authors.

Summary

Compared to the other examples presented in this section, the maximum carbon number is significantly lower for Zhou *et al.* [136] because of the smaller zeolite pores. This is why a transfer of ZSM-5 models to SAPO-34 or the other way round is difficult. The approach via reactive intermediates chosen here leads to decent agreement with experimental data and covers also side product formation; however, mechanistic insight is difficult because the rate equations

seem to be rather artificial. Furthermore, no adsorption or mechanistic effects are considered. Finally, application of this model is limited to a temperature of 723 K.

Other studies

Chen *et al.* [243] performed cracking experiments over a commercial ZSM-5 zeolite (Si/Al ratio of 42.6) with single butene, pentene and hexene feeds between 773 and 813 K. Short contact times and low conversions were applied, so dimerization could be neglected. The corresponding model focuses on different cracking steps under these differential conditions, which means it does not describe the evolution along the reactor. However, insight into the energetics of the cracking pathways is provided. By making use of group additivity and correction methods, the formation of an alkoxide as intermediate is calculated. Moreover, the theoretical evaluation of the kinetic experiments yields intrinsic activation energies of the different cracking modes. It is shown that tertiary alkoxides have the lowest stability and therefore very small concentrations. Thus, the contribution of highly branched olefins to the overall cracking performance is smaller than expected although the activation energies starting from tertiary intermediates are in a similar range than for a secondary alkoxide reactant. These results are consistent with an earlier dispersion-corrected DFT study [244]. This model allows describing the cracking products of $C_4^=$ to $C_6^=$ olefin feeds with high accuracy. Moreover, it yields detailed insight into preferred reaction pathways; however, application is limited to differential conditions which excludes consecutive and side reactions. Furthermore, model build-up is comparably complex.

In a recent study, Li *et al.* [245] performed experiments over a commercial ZSM-5 zeolite with a Si/Al ratio of 50. After modification, the catalyst contained $4\%_{wt}$ of P and $2\%_{wt}$ of Fe. Measurements were performed at temperatures between 763 and 883 K with butenes and pentenes as co-feed. The kinetic data are described with a six-lump model, which requires 24 parameters. The model does not consider any mechanistic approaches or adsorption effects, but covers a broad picture of olefin interconversion including side product formation.

The model by Meng *et al.* [246] is beyond the focus because of liquid products.

2.6.2 MTO without Olefin Co-Feed

Both catalyst properties and experimental conditions as well as modeling details are presented in Tables 2.3 and 2.4, respectively. This section presents all kinetic models for a feed of pure oxygenates, i.e., methanol or DME, which means that an initiation phase should be visible for short contact times (see Section 2.3). The first part contains the models by Menges and

Kraushaar-Czarnetzki [31] and Jiang *et al.* [247] over ZSM-5 where methanol and DME are summarized to one lump, which means no differentiation of their reactivity is possible. The next part contains the models by Gayubo *et al.* [173], Aguayo *et al.* [248] and Pérez-Uriarte *et al.* [249], which are all created by the same research group. The one by Gayubo *et al.* [173] is the first MTO model published by this group, meaning that many elements from this approach can be found in the subsequent models and also in the one by Epelde *et al.* [236]. Nevertheless, all three models in this part have a different focus. An important similarity of them is the differentiation of methanol and DME. In the following part, the two microkinetic studies over ZSM-5 by Park and Froment [192, 250] and Kumar *et al.* [18] are discussed. Whereas the former evaluates different possible mechanisms for the formation of the first C-C bond, the latter is a subsequent work which uses the same reaction network except for the mentioned C-C bond formation steps. Instead, these are replaced by reactions of the aromatic hydrocarbon pool. The last part involves different zeolites: Gayubo *et al.* [251], Ying *et al.* [252], Chen *et al.* [253] and Alwahabi and Froment [254] describe MTO over SAPO-34, whereas another model by Gayubo *et al.* [255] and another one by Kumar *et al.* [38] are valid over SAPO-18 and over ZSM-23, respectively. On all these zeolite types, deactivation is significant which is why the different approaches accounting for this fact should be compared. Both models by Gayubo *et al.* [251, 255] are comparable to the ZSM-5 case, whereas the microkinetic studies of Alwahabi and Froment [254] and Kumar *et al.* [38] are subsequent models to Park and Froment [192, 250] and Kumar *et al.* [18] over ZSM-5, respectively.

Table 2.3: Properties of the different catalysts which were used for the kinetic models of methanol-to-olefins without olefin co-feed; besides the zeolite type, its silicon-to-aluminum ratio, its total number of acid sites plus determination method, its ratio of Brønsted to Lewis acid sites BAS/LAS and its surface area according to the method by Brunauer-Emmett-Teller BET are shown; furthermore, the time-on-stream TOS after which the kinetic data were taken, the particle size d_P and the information whether an extrudate or pure powder was used are presented; the horizontal lines separate the different parts grouping models of similar methodology; a hyphen resembles missing information.

Model	Zeolite type	Si/Al	Total acidity	BAS/LAS	BET	TOS	d_P	Extrudate
Menges [31]	ZSM-5	250[a]	-	-	-	0–3 h	2 mm[b]	50/50 $\%_{wt}$[c] (Zeolite/$AlPO_4$)
Jiang [247]	ZSM-5	200	-	-	-	2 h[d]	600–900 µm	No
Gayubo [173]	ZSM-5	24[a]	0.51 mmol g_{cat}^{-1} (NH_3)[a]	2.9[a]	124 m^2 g_{cat}^{-1}	6 h[e]	150–300 µm	25/30/45 $\%_{wt}$ (Zeolite/bentonite/alumina)
Aguayo [248]	ZSM-5	30[a]	0.23 mmol g_{cat}^{-1} (NH_3)	1.5	220 m^2 g_{cat}^{-1}	5 h[e]	150–300 µm	25/30/45 $\%_{wt}$ (Zeolite/bentonite/alumina)
Pérez [249]	ZSM-5	280[a]	0.33 mmol g_{cat}^{-1} (t-$C_4H_{11}N$)	-	301 m^2 g_{cat}^{-1}	0.17 h[e]	125–300 µm	50/30/20 $\%_{wt}$ (Zeolite/boehmite/alumina)
Park [192, 250]	ZSM-5	200	-	-	400 m^2 g_{cat}^{-1}	0–5 h	500–1000 µm	No
Kumar [18]	ZSM-5	200	0.083 mmol g_{cat}^{-1}[f]	-	400 m^2 g_{cat}^{-1}	0–5 h	500–1000 µm	No
Gayubo [251]	SAPO-34	0.16	0.135 mmol g_{cat}^{-1} (NH_3)[g]	-	875 m^2 g_{cat}^{-1}[a]	1 h[e]	100–300 µm	25/30/45 $\%_{wt}$ (Zeolite/bentonite/alumina)
Ying [252]	SAPO-34	-	-	-	264 m^2 g_{cat}^{-1}	0 h	250–400 µm	Yes
Chen [253]	SAPO-34	0.16	-	-	-	> 0 h	105–290 µm	No
Alwahabi [254]	SAPO-34	-	-	-	-	0.25 h	1.1 µm	No
Gayubo [255, 256]	SAPO-18	0.3[h]	0.12 mmol g_{cat}^{-1} (NH_3)	-	171 m^2 g_{cat}^{-1}	0–1.5 h	150–250 µm	25/45/30 $\%_{wt}$ (Zeolite/bentonite/alumina)
Kumar [38]	ZSM-23	26	0.62 mmol g_{cat}^{-1}[f]	-	-	0–7 h[i]	250–420 µm	No

[a] Value of the zeolite, i.e., without binder
[b] Diameter of the cylindrical pellets used in this study (length = 5 mm)
[c] Dry basis
[d] Additional TOS of 50 h to reach a plateau with constant propene yields
[e] Results extrapolated to 0 h TOS
[f] Calculated via the Si/Al ratio
[g] Extracted from an earlier publication [257]
[h] Value of the gel according to literature [43]
[i] Converted to an effective contact time to describe a non-deactivated catalyst

Table 2.4: Experimental conditions and modeling details for the kinetic models of methanol-to-olefins without olefin co-feed; the feed components, the temperature range T, the total pressure p_t, the partial pressure range of the feed oxygenates $p(\mathrm{Ox})$ and the maximum contact time $(W/F^{in})_{max}$ with resulting oxygenates conversion X_{max} are listed; concerning the model, the number of fitted responses N_{Res}, the number of estimated parameters N_{Par}, the number of experiments N_{Exp} and the degree of freedom dof are shown; finally, it is noted whether the model follows a type of a mechanistical scheme, whether adsorption is considered and which side products are included; the horizontal lines separate the different parts grouping models of similar methodology; a hyphen resembles missing information.

Model	Feed	T	p_t	$p(\mathrm{Ox})$	$(W/F^{in})_{max}$	X_{max}	N_{Res}	N_{Par}	N_{Exp}	dof	Mech.	Ads.	Side prod.
Menges [31]	MeOH, N_2	673–723 K	1.65 bar	0.170–0.556 bar	280 g_{zeo} s m_t^{-3}[a]	1	6	16	78[b]	452	No	No	No
Jiang [247]	MeOH	673–773 K	-	-	384 g_{cat} min mol_C^{-1}	-	8	20	24	172	No	No	$C_{1\text{-}3}$
Gayubo [173]	MeOH, H_2O[c]	573–723 K	1.013 bar	1.013 bar[d]	0.37 g_{cat} h g_{MeOH}^{-1}	0.8[e]	3[f]	15	-	-	HW	H_2O	(C_{4+}^{HC})
Aguayo [248]	MeOH	673–823 K	1.013 bar	1.013 bar[d]	2.50 g_{cat} h mol_C^{-1}	1	7	26	18	100	No	No	$C_{1\text{-}4}$, $C_{6\text{-}8}^{ar}$
Pérez [249]	DME	598–673 K	1.10 bar	1.10 bar	6 g_{cat} h mol_C^{-1}	1	10	30	39	360	HW	MW[g]	$C_{1\text{-}4}$, $C_{6\text{-}8}^{ar}$
	DME, He	648 K		0.28–1.10 bar	1 g_{cat} h mol_C^{-1}	0.5							
	DME, H_2O	648 K		0.99–1.10 bar	1 g_{cat} h mol_C^{-1}	0.5							
	DME, MeOH	623–673 K		1.10 bar	1 g_{cat} h mol_C^{-1}	0.5							
Park [192, 250]	MNW[g]	633–753 K	1.04 bar	-	2 g_{cat} h mol_C^{-1}	0.7	9	33	31	246	LLEH[h]	28 MD[g]	C_1
Kumar [18]	MNW[g]	633–753 K	1.04 bar	-	6.5 g_{cat} s mol_C^{-1}	0.7	8[i]	29	31	219	LLEH[h]	27 MD[g]	C_1
Gayubo [251]	MeOH, H_2O[c]	623–748 K	-	-	0.44 g_{cat} h g_{MeOH}^{-1}	1	5[j]	17	-	-	HW	H_2O	$C_{1\text{-}4}$
							4[j]	8	-	-	HW	H_2O	$C_{1\text{-}4}$
Ying [252]	MeOH, H_2O[c]	723–763 K	1.013 bar	0.203–1.013 bar	0.03 g_{cat} h g_{MeOH}^{-1}	1	7	13	43	288	HW	H_2O	$C_{1\text{-}6}$
Chen [253]	MeOH, He[k]	673–823 K	-	0.072–0.830 bar	0.02 h[l]	0.95	7	12 (4x)	-	-	No	No	$C_{2\text{-}3}$
Alwahabi [254]	MeOH, H_2O	673–723 K	1.04 bar	0.208 bar	2.95 g_{cat} s mol_t^{-1}	0.88	6	30	9	24	LLEH[h]	25 MD[g]	C_1
Gayubo [255, 256]	MeOH, H_2O[c]	598–748 K	-	-	0.68 g_{cat} h g_{MeOH}^{-1}	0.9[e]	4	11	-	-	HW	H_2O	C_1
							5	15	-	-	HW	H_2O	C_1
Kumar [38]	MeOH, He	673 K	1.013 bar	-	57.7 g_{cat} s mol_C^{-1}	0.95	7[i]	8	12	76	LLEH[h]	27 MD[g]	C_1

[a] Value based on zeolite mass and on outlet volumetric flow rate where volume expansion is considered
[b] Extracted from another publication [258]
[c] Experiments both with and without water dilution in the feed
[d] No feed dilution mentioned
[e] Calculated with the lowest oxygenates fraction shown; conversion might be higher for measurements not presented
[f] Another lump (higher hydrocarbons) calculated via conservation of mass
[g] D = DME, M = MeOH, N = N_2, W = H_2O, 27 = $C_{2\text{-}7}^{=}$, 28 = $C_{2\text{-}8}^{=}$
[h] LLEH = L, LH, ER, HW
[i] Two additional responses (methanol and water) from carbon and hydrogen balance
[j] Another lump (methanol plus DME) calculated via conservation of mass
[k] Extracted from another publication [259]
[l] Inverse value of the minimum weight hourly space velocity

Studies with lumped oxygenates over ZSM-5

Menges and Kraushaar-Czarnetzki [31]: Six-lump approach focusing on lower olefins production

Catalyst A self-extruded catalyst was applied. It consisted of a commercial zeolite from Zeochem and aluminum phosphate from Riedel-de Haen. In earlier studies [260–262], both the high Si/Al ratio of 250 and the binder were shown to be advantageous for high propene yields. With regular binders such as alumina, the Si/Al ratio could decrease during extrusion because of alumination which means the migration of extra aluminum from the binder into the zeolite. Moreover, alumina is known to produce both methane and coke, whereas aluminum phosphate is non-reactive, leading to a catalyst which has the advantageous macropores, but no changed reactivity. For the kinetic experiments, the catalyst was shaped into cylinders. The measurements were performed with fresh catalyst up to a TOS of 3 h [258] to avoid deactivation effects. For the same reason, the combination of the highest reaction temperature with the highest methanol partial pressure was ignored.

Setup and conditions The measurements were performed in an electrically heated continuous stainless steel fixed bed reactor [258] with an inner diameter of 16 mm. The methanol feed was introduced via a saturator configuration with nitrogen as carrier and dilution gas. Isothermality and plug flow conditions were assured by having SiC particles in front of, behind and also within the catalyst bed. At the latter position, the temperature was controlled via a thermocouple. The setup also contained a pre-reactor with the same dimensions as the main reactor, but filled with 10 g of alumina. At a temperature of 573 K, the equilibrated state between methanol, DME and water was reached when leaving the pre-reactor in order to be closer to industrial conditions. The GC for product analysis had an FID and one column, but could not separate side products. An internal standard was used and with the combination of an afterburner and an infrared (IR) spectroscopy, the amount of CO and CO_2 was analyzed to screen the carbon balance. More details about the setup can be found elsewhere [258]. In addition to the experiments with a pure methanol feed, $C_2^=$ to $C_4^=$ olefins were separately co-fed with methanol for mechanistic analyses, but not for extending the model.

Reaction network During preliminary studies, the authors observed individual reactivities of the olefins with different carbon numbers, which is why they divided them into separate lumps. Moreover, the experiments with different methanol partial pressures showed a behavior which was not necessarily first order. Finally, the methylation reactions revealed a dependency on both methanol and olefin partial pressure. This leads to six lumps: Ox (methanol plus DME), $C_2^=$, $C_3^=$, $C_4^=$, $C_5^=$ and $C_{6+}^=$. As it is obvious, no reaction between methanol and DME is considered. Some side products such as aromatics were measured, but could not be separated from the higher olefins and are thus not included in the reaction network. Because of the relatively

high minimum conversion values, no initiation phase can be observed. Scheme 2.16 contains three different types of reactions: conversion of oxygenates to olefins (k_1–k_4), methylation of olefins (k_5–k_7) and cracking of higher olefins to $C_3^=$ (k_8). The latter step is the only one representing olefin interconversion which means no dimerization is implemented. Ethene is a final product arising only from the oxygenates as methylation is restricted to $C_3^=$, $C_4^=$ and $C_5^=$. All steps are assumed to be irreversible. The influence of water is neglected as well as adsorption. The rate equations represent power law kinetics without any mechanistic background. From Scheme 2.17, it can be seen that stoichiometry is neglected for the net rates of production. The reaction orders result from a preliminary fitting, where these were also adjustable parameters, and thus have no physical meaning. In the study [258], an alternate reaction network can be found which includes the dimerization of $C_3^=$, $C_4^=$ and $C_5^=$ to higher olefins, but which has no improvement in describing the experimental data.

$\mathrm{Ox} \xrightarrow{k_1} C_2^=$	$r_1 = k_1\, C\, (\mathrm{Ox})^{1.50}$	$A_1 = 1.00 \pm 0.52\,\mathrm{mol}^{-0.5}\,\mathrm{m}^{4.5}\,\mathrm{kg}^{-1}\,\mathrm{s}^{-1}$ $E_{a,1} = 45.87 \pm 3.03\,\mathrm{kJ\,mol}^{-1}$
$\mathrm{Ox} \xrightarrow{k_2} C_3^=$	$r_2 = k_2\, C\, (\mathrm{Ox})^{0.80}$	$A_2 = 45.14 \pm 19.74\,\mathrm{mol}^{0.2}\,\mathrm{m}^{2.4}\,\mathrm{kg}^{-1}\,\mathrm{s}^{-1}$ $E_{a,2} = 49.49 \pm 2.50\,\mathrm{kJ\,mol}^{-1}$
$\mathrm{Ox} \xrightarrow{k_3} C_4^=$	$r_3 = k_3\, C\, (\mathrm{Ox})^{0.85}$	$A_3 = 35.88 \pm 20.93\,\mathrm{mol}^{0.15}\,\mathrm{m}^{2.55}\,\mathrm{kg}^{-1}\,\mathrm{s}^{-1}$ $E_{a,3} = 68.75 \pm 13.44\,\mathrm{kJ\,mol}^{-1}$
$\mathrm{Ox} \xrightarrow{k_4} C_5^=$	$r_4 = k_4\, C\, (\mathrm{Ox})^{0.95}$	$A_4 = 42.72 \pm 26.16\,\mathrm{mol}^{0.05}\,\mathrm{m}^{2.85}\,\mathrm{kg}^{-1}\,\mathrm{s}^{-1}$ $E_{a,4} = 74.51 \pm 14.05\,\mathrm{kJ\,mol}^{-1}$
$\mathrm{Ox} + C_3^= \xrightarrow{k_5} C_4^=$	$r_5 = k_5\, C\, (\mathrm{Ox})^{0.75}\; C\, (C_3^=)^{0.25}$	$A_5 = 7.29 \pm 3.81\,\mathrm{m}^3\,\mathrm{kg}^{-1}\,\mathrm{s}^{-1}$ $E_{a,5} = 40.02 \pm 2.96\,\mathrm{kJ\,mol}^{-1}$
$\mathrm{Ox} + C_4^= \xrightarrow{k_6} C_5^=$	$r_6 = k_6\, C\, (\mathrm{Ox})^{0.70}\; C\, (C_4^=)^{0.30}$	$A_6 = 4.12 \pm 1.76\,\mathrm{m}^3\,\mathrm{kg}^{-1}\,\mathrm{s}^{-1}$ $E_{a,6} = 37.45 \pm 2.34\,\mathrm{kJ\,mol}^{-1}$
$\mathrm{Ox} + C_5^= \xrightarrow{k_7} C_{6+}^=$	$r_7 = k_7\, C\, (\mathrm{Ox})^{0.65}\; C\, (C_5^=)^{0.35}$	$A_7 = 3.07 \pm 1.62\,\mathrm{m}^3\,\mathrm{kg}^{-1}\,\mathrm{s}^{-1}$ $E_{a,7} = 35.17 \pm 3.03\,\mathrm{kJ\,mol}^{-1}$
$C_{6+}^= \xrightarrow{k_8} C_3^=$	$r_8 = k_8\, C\, \left(C_{6+}^=\right)^{0.70}$	$A_8 = 4000.0 \pm 1877.9\,\mathrm{mol}^{0.25}\,\mathrm{m}^{2.25}\,\mathrm{kg}^{-1}\,\mathrm{s}^{-1}$ $E_{a,8} = 77.5 \pm 2.81\,\mathrm{kJ\,mol}^{-1}$

Scheme 2.16: Reaction network, rate equations and estimated parameters for the model by Menges and Kraushaar-Czarnetzki [31].

The net rates of production are listed in Scheme 2.17; the stoichiometric coefficients are extracted from another publication [258].

$$
\begin{aligned}
R\,(\mathrm{Ox}) = &-k_1\,C\,(\mathrm{Ox})^{1.50} - k_2\,C\,(\mathrm{Ox})^{0.80} - k_3\,C\,(\mathrm{Ox})^{0.85} - k_4\,C\,(\mathrm{Ox})^{0.95} - k_5\,C\,(\mathrm{Ox})^{0.75}\;C\,(\mathrm{C}_3^{=})^{0.25} \\
&- k_6\,C\,(\mathrm{Ox})^{0.70}\;C\,(\mathrm{C}_4^{=})^{0.30} - k_7\,C\,(\mathrm{Ox})^{0.65}\;C\,(\mathrm{C}_5^{=})^{0.35} \\
R\,(\mathrm{C}_2^{=}) = &\,k_1\,C\,(\mathrm{Ox})^{1.50} \\
R\,(\mathrm{C}_3^{=}) = &\,k_2\,C\,(\mathrm{Ox})^{0.80} + k_8\,C\,\left(\mathrm{C}_{6+}^{=}\right)^{0.70} - k_5\,C\,(\mathrm{Ox})^{0.75}\;C\,(\mathrm{C}_3^{=})^{0.25} \\
R\,(\mathrm{C}_4^{=}) = &\,k_3\,C\,(\mathrm{Ox})^{0.85} + k_5\,C\,(\mathrm{Ox})^{0.75}\;C\,(\mathrm{C}_3^{=})^{0.25} - k_6\,C\,(\mathrm{Ox})^{0.70}\;C\,(\mathrm{C}_4^{=})^{0.30} \\
R\,(\mathrm{C}_5^{=}) = &\,k_4\,C\,(\mathrm{Ox})^{0.95} + k_6\,C\,(\mathrm{Ox})^{0.70}\;C\,(\mathrm{C}_4^{=})^{0.30} - k_7\,C\,(\mathrm{Ox})^{0.65}\;C\,(\mathrm{C}_5^{=})^{0.35} \\
R\,\left(\mathrm{C}_{6+}^{=}\right) = &\,k_7\,C\,(\mathrm{Ox})^{0.65}\;C\,(\mathrm{C}_5^{=})^{0.35} - k_8\,C\,\left(\mathrm{C}_{6+}^{=}\right)^{0.70}
\end{aligned}
$$

Scheme 2.17: Net rates of production of the different lumps for the model by Menges and Kraushaar-Czarnetzki [31].

Parameter estimation For the rate equations in Scheme 2.16, molar concentrations per volume are necessary. These are obtained via the molar flow rate of the respective compound and the current total volumetric flow rate. The differential equations are integrated with the solver *ode23s* in MATLAB, whereas *lsqnonlin* minimizes the unweighted sum of squared residuals between the molar concentrations in model and experiment with the trust-region-algorithm. For the objective function, each residual is normalized by dividing it by the respective experimental value. An Arrhenius equation that is not reparameterized is used for the rate constants, which causes 16 unknown parameters: eight pre-exponential factors and eight activation energies.

Jiang *et al.* [247]: Eight-lump model including side product formation

Catalyst A commercial ZSM-5 zeolite by SINOPEC with a high Si/Al ratio of 200 was used. The authors specify a TOS of 2 h, however, another 50 h pre-reaction phase was applied to reach a stable plateau of propene yield. The authors state this should avoid any deactivation effects impeding the kinetic measurements.

Setup and conditions The experiments were performed in an electrically heated continuous fixed bed reactor with an inner diameter of 20 mm. Here, relatively large particles (600–900 µm) could be investigated. Four thermocouples were installed to control the temperature: three outside of the tube at the top, the middle and the bottom, and one within the catalyst bed. The methanol was provided in liquid state and pumped through a vaporizer before entering the reactor. Neither feed nor catalyst dilution is mentioned. A GC equipped with one column and an FID enabled product analysis.

Reaction network The model is composed of eight lumps: Ox, $\mathrm{C}_2^{=}$, $\mathrm{C}_3^{=}$, $\mathrm{C}_4^{=}$, $\mathrm{C}_{5+}^{=}$, C_1, C_2 and C_3. It should characterize the reactivity in a moving bed reactor where the catalyst slowly settles down to be regenerated at the end. Such a setup would allow the use of a methanol feed

of significantly less purity and an adjustment of the catalyst to have optimum performance. The reactions in Scheme 2.18 can be classified into five types: conversion of oxygenates to olefins (k_2 and k_5–k_7) or to paraffins (k_1, k_3 and k_4), methylation of olefins (k_8), cracking (k_{10}) and a simplified hybrid reaction for $C_4^=$ which should resemble both methylation and dimerization (k_9). The two types of oxygenates are not differentiated. Ethene is a final product in the reaction network, thus not acting as reactant and not being methylated. Furthermore, because its formation is mechanistically separated from the other olefins, the authors omitted cracking reactions leading to $C_2^=$. As side products, small paraffins from C_1 to C_3 are included. Because of missing data points for short contact times, no initiation phase is detected. All steps are formulated as irreversible elementary reactions without any stoichiometry or adsorption effects.

$\mathrm{Ox} \xrightarrow{k_1} \mathrm{C_1}$	$r_1 = k_1\, y_\mathrm{C}\,(\mathrm{Ox})$	$k_1^\mathrm{ref} = 0.44 \pm 0.17\,\mathrm{mol_C\,min^{-1}\,kg_{cat}^{-1}}$ $E_{\mathrm{a},1} = 64.01 \pm 38.44\,\mathrm{kJ\,mol^{-1}}$
$\mathrm{Ox} \xrightarrow{k_2} \mathrm{C_2^=}$	$r_2 = k_2\, y_\mathrm{C}\,(\mathrm{Ox})$	$k_2^\mathrm{ref} = 3.89 \pm 0.21\,\mathrm{mol_C\,min^{-1}\,kg_{cat}^{-1}}$ $E_{\mathrm{a},2} = 40.25 \pm 4.03\,\mathrm{kJ\,mol^{-1}}$
$\mathrm{Ox} \xrightarrow{k_3} \mathrm{C_2}$	$r_3 = k_3\, y_\mathrm{C}\,(\mathrm{Ox})$	$k_3^\mathrm{ref} = 0.15 \pm 0.14\,\mathrm{mol_C\,min^{-1}\,kg_{cat}^{-1}}$ $E_{\mathrm{a},3} = 83.03 \pm 37.11\,\mathrm{kJ\,mol^{-1}}$
$\mathrm{Ox} \xrightarrow{k_4} \mathrm{C_3}$	$r_4 = k_4\, y_\mathrm{C}\,(\mathrm{Ox})$	$k_4^\mathrm{ref} = 9.80 \pm 0.73\,\mathrm{mol_C\,min^{-1}\,kg_{cat}^{-1}}$ $E_{\mathrm{a},4} = 52.16 \pm 3.51\,\mathrm{kJ\,mol^{-1}}$
$\mathrm{Ox} \xrightarrow{k_5} \mathrm{C_3^=}$	$r_5 = k_5\, y_\mathrm{C}\,(\mathrm{Ox})$	$k_5^\mathrm{ref} = 1.76 \pm 0.18\,\mathrm{mol_C\,min^{-1}\,kg_{cat}^{-1}}$ $E_{\mathrm{a},5} = 43.86 \pm 7.87\,\mathrm{kJ\,mol^{-1}}$
$\mathrm{Ox} \xrightarrow{k_6} \mathrm{C_4^=}$	$r_6 = k_6\, y_\mathrm{C}\,(\mathrm{Ox})$	$k_6^\mathrm{ref} = 8.91 \pm 0.76\,\mathrm{mol_C\,min^{-1}\,kg_{cat}^{-1}}$ $E_{\mathrm{a},6} = 42.4 \pm 4.82\,\mathrm{kJ\,mol^{-1}}$
$\mathrm{Ox} \xrightarrow{k_7} \mathrm{C_{5+}^=}$	$r_7 = k_7\, y_\mathrm{C}\,(\mathrm{Ox})$	$k_7^\mathrm{ref} = 8.73 \pm 0.76\,\mathrm{mol_C\,min^{-1}\,kg_{cat}^{-1}}$ $E_{\mathrm{a},7} = 39.46 \pm 4.58\,\mathrm{kJ\,mol^{-1}}$
$\mathrm{Ox} + \mathrm{C_3^=} \xrightarrow{k_8} \mathrm{C_4^=}$	$r_8 = k_8\, y_\mathrm{C}\,(\mathrm{Ox})\; y_\mathrm{C}\,(\mathrm{C_3^=})$	$k_8^\mathrm{ref} = 0.05 \pm 0.01\,\mathrm{mol_C\,min^{-1}\,kg_{cat}^{-1}}$ $E_{\mathrm{a},8} = 75.00 \pm 10.27\,\mathrm{kJ\,mol^{-1}}$
$\mathrm{C_4^=} \xrightarrow{k_9} \mathrm{C_{5+}^=}$	$r_9 = k_9\, y_\mathrm{C}\,(\mathrm{C_4^=})$	$k_9^\mathrm{ref} = 0.14 \pm 0.08\,\mathrm{mol_C\,min^{-1}\,kg_{cat}^{-1}}$ $E_{\mathrm{a},9} = 78.36 \pm 32.50\,\mathrm{kJ\,mol^{-1}}$
$\mathrm{C_{5+}^=} \xrightarrow{k_{10}} \mathrm{C_3^=}$	$r_{10} = k_{10}\, y_\mathrm{C}\,(\mathrm{C_{5+}^=})$	$k_{10}^\mathrm{ref} = 0.66 \pm 0.15\,\mathrm{mol_C\,min^{-1}\,kg_{cat}^{-1}}$ $E_{\mathrm{a},10} = 29.67 \pm 21.08\,\mathrm{kJ\,mol^{-1}}$

Scheme 2.18: Reaction network, rate equations and estimated parameters for the model by Jiang *et al.* [247].

This leads to the net rates of production presented in Scheme 2.19.

$$
\begin{aligned}
R\,(\mathrm{Ox}) = &-k_1\,y_\mathrm{C}\,(\mathrm{Ox}) - k_2\,y_\mathrm{C}\,(\mathrm{Ox}) - k_3\,y_\mathrm{C}\,(\mathrm{Ox}) - k_4\,y_\mathrm{C}\,(\mathrm{Ox}) - k_5\,y_\mathrm{C}\,(\mathrm{Ox}) - k_6\,y_\mathrm{C}\,(\mathrm{Ox}) \\
&- k_7\,y_\mathrm{C}\,(\mathrm{Ox}) - k_8\,y_\mathrm{C}\,(\mathrm{Ox})\;y_\mathrm{C}\,(\mathrm{C}_3^=) \\
R\,(\mathrm{C}_2^=) = &\,k_2\,y_\mathrm{C}\,(\mathrm{Ox}) \\
R\,(\mathrm{C}_3^=) = &\,k_5\,y_\mathrm{C}\,(\mathrm{Ox}) + k_{10}\,y_\mathrm{C}\,\left(\mathrm{C}_{5+}^=\right) - k_8\,y_\mathrm{C}\,(\mathrm{Ox})\;y_\mathrm{C}\,(\mathrm{C}_3^=) \\
R\,(\mathrm{C}_4^=) = &\,k_6\,y_\mathrm{C}\,(\mathrm{Ox}) + k_8\,y_\mathrm{C}\,(\mathrm{Ox})\;y_\mathrm{C}\,(\mathrm{C}_3^=) - k_9\,y_\mathrm{C}\,(\mathrm{C}_4^=) \\
R\,\left(\mathrm{C}_{5+}^=\right) = &\,k_7\,y_\mathrm{C}\,(\mathrm{Ox}) + k_9\,y_\mathrm{C}\,(\mathrm{C}_4^=) - k_{10}\,y_\mathrm{C}\,\left(\mathrm{C}_{5+}^=\right) \\
R\,(\mathrm{C}_1) = &\,k_1\,y_\mathrm{C}\,(\mathrm{Ox}) \\
R\,(\mathrm{C}_2) = &\,k_3\,y_\mathrm{C}\,(\mathrm{Ox}) \\
R\,(\mathrm{C}_3) = &\,k_4\,y_\mathrm{C}\,(\mathrm{Ox})
\end{aligned}
$$

Scheme 2.19: Net rates of production of the different lumps for the model by Jiang *et al.* [247].

Parameter estimation The reaction rates in Scheme 2.18 require mole fractions based on carbon. The objective function equals the unweighted sum of squared residuals between calculated and measured mole fractions and is minimized using *lsqnonlin* within MATLAB. The solver *ode45* is applied to the differential equations. For parameter estimation, the reparameterized Arrhenius approach from Equation (2.21) is used with a reference temperature of 733 K, which is the upper limit of the investigated range. Twenty parameters have to be fitted: ten reference rate constants and ten activation energies.

Summary

The underlying reaction networks of both models show several similarities. Manifold pathways converting oxygenates to lower olefins and describing methylation reactions are considered. These models are fast and simple because no oxygenates interconversion is regarded. However, the different reactivity of methanol and DME cannot be expressed. Furthermore, in both studies, olefin interconversion reactions are implemented in a simplified way, meaning that dimerization reactions are missing and cracking is limited to one step. Extrapolation is difficult because of missing adsorption and mechanistic assumptions; furthermore, stoichiometry is not retained throughout the whole models. The model by Jiang *et al.* [247] allows a description of side product formation.

Studies with differentiated reactivity of methanol and DME over ZSM-5

Gayubo *et al.* [173]: Four-lump approach analyzing the inhibiting effect of water adsorption

Catalyst A self-synthesized ZSM-5 zeolite with a low Si/Al ratio of 24 was mixed with bentonite and alumina. The measurements were started after a TOS of 6 h, but, similar to Epelde *et al.* [236], the results are extrapolated to a TOS of 0 h. This routine should yield the performance of a fresh catalyst although deactivation is significant for this system according to the authors. In a subsequent study [263], the deactivation through coke is modeled based on the kinetics presented in this section. Furthermore, in another publication [264], the authors derived a kinetic description of the irreversible deactivation caused by dealumination.

Setup and conditions The automated reaction equipment is described in detail in an earlier contribution [265]. It consisted of a continuous stainless steel fixed bed reactor with an inner diameter of 7 mm. This unit was surrounded by an oven and allowed for measuring the temperature at three locations within the catalyst bed: close to the reactor wall, in the center and at the end of the bed. Methanol was provided in liquid state and evaporated, whereas the setup enabled the feeding of both liquid and gaseous compounds. For product analysis, the authors used a GC which had three columns and both an FID and a TCD. Additionally, the GC was coupled with a Fourier transform infrared (GC-FTIR) and a mass spectrometer (GC-MS). The catalyst bed was diluted with inert alumina. For the kinetics, the authors applied pure methanol without any dilution as feed. However, the influence of water co-feeding could be investigated in parts of the measurements: the water to methanol ratio based on weight was either zero or one.

Reaction network Four lumps are defined: MeOH, DME, $C_{2\text{-}3}^{=}$ and C_{4+}^{HC}. However, the latter is not fitted to experimental data, but calculated with the results of the remaining lumps and the conservation of mass. The assumed network can be divided into four parts (see Scheme 2.20): the reaction between methanol and DME (k_1), oxygenates transformation to olefins (k_2 and k_3), methylation reactions (k_5 and k_6) and olefin interconversion (k_4, k_7 and k_8). The concentrations of oxygenates are not implemented as equilibrated fractions: the authors observed a DME amount that is much lower than the theoretical equilibrium value and attributed this to the higher reactivity of DME. This is why the reaction to DME is implemented as kinetic step with the backward reaction being expressed via a thermodynamic equilibrium constant. For the latter, the empiric correlation by Spivey [176] is used, which itself is a citation from Hayashi and Moffat [169]. However, in Gayubo *et al.*'s publication [173], different numeric values for this correlation are used (see Section 2.4). All other steps in the reaction network are assumed to be irreversible. No initiation phase can be observed during the measurements. The methylation is implemented both via methanol and via DME to account for the different reactivities. In

addition, the conversion to olefins can start from both types of oxygenates according to the model. The olefin interconversion is limited to one cracking step and two reactions to higher compounds. It can be seen in Scheme 2.20 that the reaction rates are expressed as HW type of mechanism. Only the adsorption of water is considered because this step is significantly slower compared to the hydrocarbons adsorption and not *quasi*-equilibrated according to the authors. Side products are not explicitly mentioned, but especially aromatics should be included in the lump C_{4+}^{HC} as it was done in an earlier model [266]. The reactions are defined as elementary steps, but no stoichiometry is considered.

$$
\begin{aligned}
2\mathrm{MeOH} \underset{k_1/K^{TD}}{\overset{k_1}{\rightleftharpoons}} \mathrm{DME} + \mathrm{H_2O} \qquad & r_1 = \frac{k_1\, w_C(\mathrm{MeOH})^2 - k_1/K^{TD}\, w_C(\mathrm{DME})\, w_C(\mathrm{H_2O})}{1 + k(\mathrm{H_2O})\, w_C(\mathrm{H_2O})} \\
k_1^{ref} = 88.73 \pm 7.89\,\mathrm{g\,g_{cat}^{-1}\,h^{-1}} \qquad & E_{a,1} = -53.10 \pm 4.20\,\mathrm{kJ\,mol^{-1}} \\
\mathrm{MeOH} \xrightarrow{k_2} C_{2-3}^{=} \qquad & r_2 = \frac{k_2\, w_C(\mathrm{MeOH})}{1 + k(\mathrm{H_2O})\, w_C(\mathrm{H_2O})} \\
k_2^{ref} = 11.98 \pm 2.16\,\mathrm{g\,g_{cat}^{-1}\,h^{-1}} \qquad & E_{a,2} = -102.40 \pm 7.10\,\mathrm{kJ\,mol^{-1}} \\
\mathrm{DME} \xrightarrow{k_3} C_{2-3}^{=} \qquad & r_3 = \frac{k_3\, w_C(\mathrm{DME})}{1 + k(\mathrm{H_2O})\, w_C(\mathrm{H_2O})} \\
k_3 = 9.95 \pm 3.29\, k_2 \qquad & \\
2\,C_{2-3}^{=} \xrightarrow{k_4} C_{4+}^{HC} \qquad & r_4 = \frac{k_4\, w_C\left(C_{2-3}^{=}\right)^2}{1 + k(\mathrm{H_2O})\, w_C(\mathrm{H_2O})} \\
k_4^{ref} = 9.42 \pm 3.07\,\mathrm{g\,g_{cat}^{-1}\,h^{-1}} \qquad & E_{a,4} = -38.45 \pm 13.80\,\mathrm{kJ\,mol^{-1}} \\
\mathrm{MeOH} + C_{2-3}^{=} \xrightarrow{k_5} C_{4+}^{HC} \qquad & r_5 = \frac{k_5\, w_C(\mathrm{MeOH})\, w_C\left(C_{2-3}^{=}\right)}{1 + k(\mathrm{H_2O})\, w_C(\mathrm{H_2O})} \\
k_5^{ref} = 34.82 \pm 6.80\,\mathrm{g\,g_{cat}^{-1}\,h^{-1}} \qquad & E_{a,5} = -89.45 \pm 6.30\,\mathrm{kJ\,mol^{-1}} \\
\mathrm{DME} + C_{2-3}^{=} \xrightarrow{k_6} C_{4+}^{HC} \qquad & r_6 = \frac{k_6\, w_C(\mathrm{DME})\, w_C\left(C_{2-3}^{=}\right)}{1 + k(\mathrm{H_2O})\, w_C(\mathrm{H_2O})} \\
k_6 = 7.62 \pm 1.90\, k_5 \qquad & \\
C_{2-3}^{=} + C_{4+}^{HC} \xrightarrow{k_7} C_{4+}^{HC} \qquad & r_7 = \frac{k_7\, w_C\left(C_{2-3}^{=}\right) w_C\left(C_{4+}^{HC}\right)}{1 + k(\mathrm{H_2O})\, w_C(\mathrm{H_2O})} \\
k_7^{ref} = 6.89 \pm 4.90\,\mathrm{g\,g_{cat}^{-1}\,h^{-1}} \qquad & E_{a,7} = -27.60 \pm 16.30\,\mathrm{kJ\,mol^{-1}} \\
C_{4+}^{HC} \xrightarrow{k_8} 2C_{2-3}^{=} \qquad & r_8 = \frac{k_8\, w_C\left(C_{4+}^{HC}\right)}{1 + k(\mathrm{H_2O})\, w_C(\mathrm{H_2O})} \\
k_8^{ref} = 0.60 \pm 0.10\,\mathrm{g\,g_{cat}^{-1}\,h^{-1}} \qquad & E_{a,8} = -127.50 \pm 57.25\,\mathrm{kJ\,mol^{-1}} \\
k\,(\mathrm{H_2O}) = 1.0 \pm 0.3 \qquad &
\end{aligned}
$$

Scheme 2.20: Reaction network, rate equations and estimated parameters for the model by Gayubo *et al.* [173] over ZSM-5; K^{TD} is calculated with a modified version of Hayashi and Moffat's correlation [169] (see Section 2.4).

The net rates of production for all four lumps are presented in Scheme 2.21.

$$R\,(\mathrm{MeOH}) = \frac{k_1/K^{\mathrm{TD}}\, w_{\mathrm{C}}\,(\mathrm{DME})\; w_{\mathrm{C}}\,(\mathrm{H_2O}) - k_1\, w_{\mathrm{C}}\,(\mathrm{MeOH})^2 - k_2\, w_{\mathrm{C}}\,(\mathrm{MeOH})}{1 + k\,(\mathrm{H_2O})\; w_{\mathrm{C}}\,(\mathrm{H_2O})}$$
$$\frac{-k_5\, w_{\mathrm{C}}\,(\mathrm{MeOH})\; w_{\mathrm{C}}\left(\mathrm{C}^{=}_{2-3}\right)}{1 + k\,(\mathrm{H_2O})\; w_{\mathrm{C}}\,(\mathrm{H_2O})}$$

$$R\,(\mathrm{DME}) = \frac{k_1\, w_{\mathrm{C}}\,(\mathrm{MeOH})^2 - k_1/K^{\mathrm{TD}}\, w_{\mathrm{C}}\,(\mathrm{DME})\; w_{\mathrm{C}}\,(\mathrm{H_2O}) - k_3\, w_{\mathrm{C}}\,(\mathrm{DME})}{1 + k\,(\mathrm{H_2O})\; w_{\mathrm{C}}\,(\mathrm{H_2O})}$$
$$\frac{-k_6\, w_{\mathrm{C}}\,(\mathrm{DME})\; w_{\mathrm{C}}\left(\mathrm{C}^{=}_{2-3}\right)}{1 + k\,(\mathrm{H_2O})\; w_{\mathrm{C}}\,(\mathrm{H_2O})}$$

$$R\left(\mathrm{C}^{=}_{2-3}\right) = \frac{k_2\, w_{\mathrm{C}}\,(\mathrm{MeOH}) + k_3\, w_{\mathrm{C}}\,(\mathrm{DME}) + k_8\, w_{\mathrm{C}}\left(\mathrm{C}^{\mathrm{HC}}_{4+}\right) - k_4\, w_{\mathrm{C}}\left(\mathrm{C}^{=}_{2-3}\right)^2}{1 + k\,(\mathrm{H_2O})\; w_{\mathrm{C}}\,(\mathrm{H_2O})}$$
$$\frac{-k_5\, w_{\mathrm{C}}\,(\mathrm{MeOH})\; w_{\mathrm{C}}\left(\mathrm{C}^{=}_{2-3}\right) - k_6\, w_{\mathrm{C}}\,(\mathrm{DME})\; w_{\mathrm{C}}\left(\mathrm{C}^{=}_{2-3}\right) - k_7\, w_{\mathrm{C}}\left(\mathrm{C}^{=}_{2-3}\right)\; w_{\mathrm{C}}\left(\mathrm{C}^{\mathrm{HC}}_{4+}\right)}{1 + k\,(\mathrm{H_2O})\; w_{\mathrm{C}}\,(\mathrm{H_2O})}$$

$$R\left(\mathrm{C}^{\mathrm{HC}}_{4+}\right) = \frac{k_4\, w_{\mathrm{C}}\left(\mathrm{C}^{=}_{2-3}\right)^2 + k_5\, w_{\mathrm{C}}\,(\mathrm{MeOH})\; w_{\mathrm{C}}\left(\mathrm{C}^{=}_{2-3}\right) + k_6\, w_{\mathrm{C}}\,(\mathrm{DME})\; w_{\mathrm{C}}\left(\mathrm{C}^{=}_{2-3}\right)}{1 + k\,(\mathrm{H_2O})\; w_{\mathrm{C}}\,(\mathrm{H_2O})}$$
$$\frac{+k_7\, w_{\mathrm{C}}\left(\mathrm{C}^{=}_{2-3}\right)\; w_{\mathrm{C}}\left(\mathrm{C}^{\mathrm{HC}}_{4+}\right) - k_8\, w_{\mathrm{C}}\left(\mathrm{C}^{\mathrm{HC}}_{4+}\right)}{1 + k\,(\mathrm{H_2O})\; w_{\mathrm{C}}\,(\mathrm{H_2O})}$$

Scheme 2.21: Net rates of production of the different lumps for the model by Gayubo *et al.* [173] over ZSM-5; the $\mathrm{C}^{\mathrm{HC}}_{4+}$ lump is calculated via conservation of mass within the model.

Parameter estimation The reaction rates in Scheme 2.20 are defined with mass fractions of organic compounds where water is explicitly excluded. Even the mass fraction of water is related to the water-free composition. Integration of the differential equations is performed with a code written in FORTRAN which makes use of the DGEAR subroutine of the IMSL library. The objective function returns the sum of squared residuals between modeled and experimental organic mass fractions and is additionally divided by the number of lumps and experiments. This average value is then minimized with the Complex algorithm, as explained in earlier work [267]. After obtaining the parameters of best description, another fitting is performed with the Marquardt algorithm. Reparameterization according to Equation (2.21) is applied with a reference temperature of 673 K, which is in the upper third of the investigated range. For the DME transformation to olefins and the methylation via DME, the same activation energies as for the respective methanol-related steps are assumed, which only requires the fitting of a separate pre-exponential factor. In total, 15 parameters are estimated: eight reference rate constants, six activation energies and one rate constant for water adsorption.

Aguayo *et al.* [248]: Seven-lump model for significant side product formation and resulting interconversion reactions

Catalyst The authors used a commercial ZSM-5 zeolite from Zeolyst International with a low Si/Al ratio of 30 which they further processed to an extrudate. The resulting catalyst showed sufficient activity at 0 h TOS during earlier studies [268], combined with high olefin selectivity, low coke amounts and increased hydrothermal stability. It could be shown that up to ten reaction-regeneration cycles without irreversible deactivation were possible with this catalytic system. The measurements were performed at a TOS of 5 h, but, although it is not explicitly mentioned, the results might be extrapolated to 0 h.

Setup and conditions A continuous fixed bed reactor made of stainless steel with an inner diameter of 9 mm and surrounded by a heated steel chamber with a ceramic cover was applied. The temperature was measured inside the catalyst bed and also within the chamber and at the transfer line connecting the GC. The setup allowed for providing methanol in liquid state which was evaporated before being fed to the reactor. More details about the reaction equipment which has many similarities to Epelde *et al.* [236] are shown in earlier work [268]. The catalyst bed was diluted with SiC in a way that the bed height remained almost constant. The authors analyzed the products with a micro GC equipped with three columns and a TCD.

Reaction network Seven lumps are defined: MeOH, DME, $C_{2\text{-}4}^{=}$, C_{5+}^{HC}, C_1, $C_{2\text{-}4}$ and *n*-butane (C_{n4}). The lump C_{5+}^{HC} comprises $C_{6\text{-}8}$ aromatics as well as $C_{5\text{-}10}$ aliphatics. In Scheme 2.22, eight different types of reactions can be identified: the one between methanol and DME (k_1), the conversion of oxygenates to olefins (k_2 and k_3), methylations (k_5 and k_6), olefin interconversion (k_9), olefin-paraffin interconversion (k_7 and k_8), paraffin formation through oxygenates (k_4) or olefins (k_{10} and k_{11}) and aromatization steps (k_{12} and k_{13}). A separate consideration of *n*-butane is performed because it was co-fed with methanol in an earlier study [268]. All reaction steps except the one between methanol and DME are treated as irreversible. Because the authors performed measurements at relatively short contact times, the initiation phase is clearly visible which means that no detectable conversion to hydrocarbons and only oxygenates equilibration takes place. Nevertheless, the methanol dehydration is implemented as step of kinetic relevance. Its backward reaction is expressed via a thermodynamic equilibrium constant which is calculated with an own correlation derived in another publication [168] (see Section 2.4). As in Gayubo *et al.*'s model [173], both methanol and DME can perform methylation reactions, which yields not only higher hydrocarbons, but also lower olefins. Both types of oxygenates can be converted to olefins or to methane; in the latter reaction, no differentiation between the reactivity of methanol and DME is performed. The olefin interconversion is restricted to one cracking step, whereas dimerization is neglected. Instead, several reactions starting with or leading to paraffins are implemented. The interaction between the formed water and the zeolite is not considered. Neither a mechanistic model nor any adsorption effects are included. The

reactions are assumed to be elementary, except for Steps (10) and (11) which are arbitrarily set to second order because of a better agreement with experimental data. Stoichiometry is not considered for the net rates of production; as for the second order reactions in Steps (10) and (11), the reaction rates of Steps (12) and (13) are arbitrarily multiplied by 2.

$2\mathrm{MeOH} \underset{k_1/K^{\mathrm{TD}}}{\overset{k_1}{\rightleftharpoons}} \mathrm{DME} + \mathrm{H_2O}$	$r_1 = k_1\, y\,(\mathrm{MeOH})^2 - k_1/K^{\mathrm{TD}}\, y\,(\mathrm{DME})\; y\,(\mathrm{H_2O})$
$k_1^{\mathrm{ref}} = 24.5 \pm 2.4\,\mathrm{mol_C\,g_{cat}^{-1}\,h^{-1}}$	$E_{\mathrm{a},1} = 54.4 \pm 5.4\,\mathrm{kJ\,mol^{-1}}$
$\mathrm{MeOH} \xrightarrow{k_2} \mathrm{C}_{2-4}^{=}$	$r_2 = k_2\, y\,(\mathrm{MeOH})$
$k_2^{\mathrm{ref}} = (1.2 \pm 0.1) \times 10^{-6}\,\mathrm{mol_C\,g_{cat}^{-1}\,h^{-1}}$	$E_{\mathrm{a},2} = 4.60 \pm 0.41\,\mathrm{kJ\,mol^{-1}}$
$\mathrm{DME} \xrightarrow{k_3} \mathrm{C}_{2-4}^{=}$	$r_3 = k_3\, y\,(\mathrm{DME})$
$k_3^{\mathrm{ref}} = (1.9 \pm 0.2) \times 10^{-6}\,\mathrm{mol_C\,g_{cat}^{-1}\,h^{-1}}$	$E_{\mathrm{a},3} = 186 \pm 22\,\mathrm{kJ\,mol^{-1}}$
$\mathrm{MeOH/DME} \xrightarrow{k_4} \mathrm{C}_1$	$r_4 = k_4\, y\,(\mathrm{MeOH})\;/\; r_4 = k_4\, y\,(\mathrm{DME})$
$k_4^{\mathrm{ref}} = (19.9 \pm 2.6) \times 10^{-2}\,\mathrm{mol_C\,g_{cat}^{-1}\,h^{-1}}$	$E_{\mathrm{a},4} = 111 \pm 14\,\mathrm{kJ\,mol^{-1}}$
$\mathrm{MeOH} + \mathrm{C}_{2-4}^{=} \xrightarrow{k_5} \mathrm{C}_{2-4}^{=}$	$r_5 = k_5\, y\,(\mathrm{MeOH})\; y\left(\mathrm{C}_{2-4}^{=}\right)$
$k_5^{\mathrm{ref}} = 88.3 \pm 8.8\,\mathrm{mol_C\,g_{cat}^{-1}\,h^{-1}}$	$E_{\mathrm{a},5} = 4.44 \pm 0.45\,\mathrm{kJ\,mol^{-1}}$
$\mathrm{DME} + \mathrm{C}_{2-4}^{=} \xrightarrow{k_6} \mathrm{C}_{2-4}^{=}$	$r_6 = k_6\, y\,(\mathrm{DME})\; y\left(\mathrm{C}_{2-4}^{=}\right)$
$k_6^{\mathrm{ref}} = 331 \pm 23\,\mathrm{mol_C\,g_{cat}^{-1}\,h^{-1}}$	$E_{\mathrm{a},6} = 53.6 \pm 3.7\,\mathrm{kJ\,mol^{-1}}$
$\mathrm{C}_{n4} + \mathrm{C}_{2-4}^{=} \xrightarrow{k_7} \mathrm{C}_{2-4}^{=}$	$r_7 = k_7\, y\,(\mathrm{C}_{n4})\; y\left(\mathrm{C}_{2-4}^{=}\right)$
$k_7^{\mathrm{ref}} = 342 \pm 17\,\mathrm{mol_C\,g_{cat}^{-1}\,h^{-1}}$	$E_{\mathrm{a},7} = 14.1 \pm 0.7\,\mathrm{kJ\,mol^{-1}}$
$\mathrm{C}_{2-4} + \mathrm{C}_{2-4}^{=} \xrightarrow{k_8} \mathrm{C}_{2-4}^{=}$	$r_8 = k_8\, y\left(\mathrm{C}_{2-4}\right)\; y\left(\mathrm{C}_{2-4}^{=}\right)$
$k_8^{\mathrm{ref}} = 228 \pm 23\,\mathrm{mol_C\,g_{cat}^{-1}\,h^{-1}}$	$E_{\mathrm{a},8} = 56.5 \pm 5.6\,\mathrm{kJ\,mol^{-1}}$
$\mathrm{C}_{5+}^{\mathrm{HC}} \xrightarrow{k_9} \mathrm{C}_{2-4}^{=}$	$r_9 = k_9\, y\left(\mathrm{C}_{5+}^{\mathrm{HC}}\right)$
$k_9^{\mathrm{ref}} = (7.2 \pm 0.5) \times 10^{-2}\,\mathrm{mol_C\,g_{cat}^{-1}\,h^{-1}}$	$E_{\mathrm{a},9} = 25.0 \pm 2.1\,\mathrm{kJ\,mol^{-1}}$
$\mathrm{C}_{2-4}^{=} \xrightarrow{k_{10}} \mathrm{C}_{n4}$	$r_{10} = k_{10}\, y\left(\mathrm{C}_{2-4}^{=}\right)^2$
$k_{10}^{\mathrm{ref}} = 35.5 \pm 3.6\,\mathrm{mol_C\,g_{cat}^{-1}\,h^{-1}}$	$E_{\mathrm{a},10} = 4.35 \pm 0.43\,\mathrm{kJ\,mol^{-1}}$
$\mathrm{C}_{2-4}^{=} \xrightarrow{k_{11}} \mathrm{C}_{2-4}$	$r_{11} = k_{11}\, y\left(\mathrm{C}_{2-4}^{=}\right)^2$
$k_{11}^{\mathrm{ref}} = 111 \pm 12\,\mathrm{mol_C\,g_{cat}^{-1}\,h^{-1}}$	$E_{\mathrm{a},11} = 5.02 \pm 0.55\,\mathrm{kJ\,mol^{-1}}$
$\mathrm{MeOH} + \mathrm{C}_{2-4}^{=} \xrightarrow{k_{12}} \mathrm{C}_{5+}^{\mathrm{HC}}$	$r_{12} = k_{12}\, y\,(\mathrm{MeOH})\; y\left(\mathrm{C}_{2-4}^{=}\right)$
$k_{12}^{\mathrm{ref}} = 10.8 \pm 1.6\,\mathrm{mol_C\,g_{cat}^{-1}\,h^{-1}}$	$E_{\mathrm{a},12} = 16.2 \pm 2.4\,\mathrm{kJ\,mol^{-1}}$
$\mathrm{DME} + \mathrm{C}_{2-4}^{=} \xrightarrow{k_{13}} \mathrm{C}_{5+}^{\mathrm{HC}}$	$r_{13} = k_{13}\, y\,(\mathrm{DME})\; y\left(\mathrm{C}_{2-4}^{=}\right)$
$k_{13}^{\mathrm{ref}} = 60.2 \pm 8.4\,\mathrm{mol_C\,g_{cat}^{-1}\,h^{-1}}$	$E_{\mathrm{a},13} = 36.4 \pm 5.1\,\mathrm{kJ\,mol^{-1}}$

Scheme 2.22: Reaction network, rate equations and estimated parameters for the model by Aguayo *et al.* [248]; K^{TD} is calculated with an own correlation [168] (see Section 2.4).

Scheme 2.23 contains the net rates of production of the different lumps.

$$
\begin{aligned}
R\,(\mathrm{MeOH}) &= k_1 / K^{\mathrm{TD}}\, y\,(\mathrm{DME})\; y\,(\mathrm{H_2O}) - k_1\, y\,(\mathrm{MeOH})^2 - k_2\, y\,(\mathrm{MeOH}) - k_4\, y\,(\mathrm{MeOH}) \\
&\quad - k_5\, y\,(\mathrm{MeOH})\; y\left(\mathrm{C}_{2-4}^{=}\right) - k_{12}\, y\,(\mathrm{MeOH})\; y\left(\mathrm{C}_{2-4}^{=}\right) \\
R\,(\mathrm{DME}) &= k_1\, y\,(\mathrm{MeOH})^2 - k_1 / K^{\mathrm{TD}}\, y\,(\mathrm{DME})\; y\,(\mathrm{H_2O}) - k_3\, y\,(\mathrm{DME}) - k_4\, y\,(\mathrm{DME}) \\
&\quad - k_6\, y\,(\mathrm{DME})\; y\left(\mathrm{C}_{2-4}^{=}\right) - k_{13}\, y\,(\mathrm{DME})\; y\left(\mathrm{C}_{2-4}^{=}\right) \\
R\left(\mathrm{C}_{2-4}^{=}\right) &= k_2\, y\,(\mathrm{MeOH}) + k_3\, y\,(\mathrm{DME}) + k_5\, y\,(\mathrm{MeOH})\; y\left(\mathrm{C}_{2-4}^{=}\right) + k_6\, y\,(\mathrm{DME})\; y\left(\mathrm{C}_{2-4}^{=}\right) \\
&\quad + k_7\, y\left(\mathrm{C}_{n4}\right)\; y\left(\mathrm{C}_{2-4}^{=}\right) + k_8\, y\left(\mathrm{C}_{2-4}\right)\; y\left(\mathrm{C}_{2-4}^{=}\right) + k_9\, y\left(\mathrm{C}_{5+}^{\mathrm{HC}}\right) - k_{10}\, y\left(\mathrm{C}_{2-4}^{=}\right)^2 \\
&\quad - k_{11}\, y\left(\mathrm{C}_{2-4}^{=}\right)^2 - k_{12}\, y\,(\mathrm{MeOH})\; y\left(\mathrm{C}_{2-4}^{=}\right) - k_{13}\, y\,(\mathrm{DME})\; y\left(\mathrm{C}_{2-4}^{=}\right) \\
R\left(\mathrm{C}_{5+}^{\mathrm{HC}}\right) &= 2\,k_{12}\, y\,(\mathrm{MeOH})\; y\left(\mathrm{C}_{2-4}^{=}\right) + 2\,k_{13}\, y\,(\mathrm{DME})\; y\left(\mathrm{C}_{2-4}^{=}\right) - k_9\, y\left(\mathrm{C}_{5+}^{\mathrm{HC}}\right) \\
R\left(\mathrm{C}_1\right) &= k_4\, y\,(\mathrm{MeOH}) + k_4\, y\,(\mathrm{DME}) \\
R\left(\mathrm{C}_{2-4}\right) &= k_{11}\, y\left(\mathrm{C}_{2-4}^{=}\right)^2 - k_8\, y\left(\mathrm{C}_{2-4}\right)\; y\left(\mathrm{C}_{2-4}^{=}\right) \\
R\left(\mathrm{C}_{n4}\right) &= k_{10}\, y\left(\mathrm{C}_{2-4}^{=}\right)^2 - k_7\, y\left(\mathrm{C}_{n4}\right)\; y\left(\mathrm{C}_{2-4}^{=}\right)
\end{aligned}
$$

Scheme 2.23: Net rates of production of the different lumps for the model by Aguayo *et al.* [248].

Parameter estimation Whereas the mole fractions shown in the figures of Aguayo *et al.* [248] are defined with carbon units, regular mole fractions including water have to be inserted for the rate equations in Scheme 2.22. The kinetic parameters are obtained via multivariable nonlinear regression using MATLAB. The objective function returns the weighted sum of squared residuals between modeled and measured output, see the description for Epelde *et al.* [236] above and an earlier publication [269] for details. Reparameterization according to Equation (2.21) is performed with a reference temperature of 773 K which is in the upper third of the investigated range. Finally, 26 parameters have to be fitted: 13 reference rate constants and 13 activation energies.

Pérez-Uriarte *et al.* [249]: Eleven-lump approach for DME feeds

Catalyst A central difference of this study is the use of DME as feed which changes oxygenates conversion, product selectivities and deactivation rates and therefore requires different conditions and kinetic models [270]. The authors extruded a commercial high-silica (Si/Al = 280) ZSM-5 catalyst from Zeolyst International with boehmite from Sasol as binder and with α-alumina as inert filler. This composition showed a satisfying compromise between activity, stability and mechanical resistance in earlier work [271] through moderate acidity, a mesoporous structure and additional acid sites through γ-alumina, which is a calcination product of boehmite. The measurements were performed at 0.17 h TOS, but extrapolated to 0 h in order to represent the fresh catalyst. Deactivation through coke should be higher compared to methanol feeds according to the authors because of the lower water content. These effects are ignored in this study, but considered in a subsequent kinetic model for deactivation [272].

Setup and conditions The setup was almost identical to the studies by Aguayo *et al.* [248] and Epelde *et al.* [236], see above and the original publication [271] for more details. Additionally, liquid components could be fed by pumping them through an evaporator. Besides the experiments with pure DME as feed, some other combinations with DME/helium, DME/methanol and DME/water mixtures were investigated and are also included in the model. The catalyst bed was diluted with SiC particles to reach a uniform height of 50 mm. A GC with four columns and a TCD enabled product analysis.

Reaction network Eleven lumps are defined: MeOH, DME, $C_2^=$, $C_3^=$, $C_4^=$, $C_{5+}^=$, C_1, $C_{2\text{-}4}$, $C_{6\text{-}8}^{ar}$, CO and H_2O. For parameter estimation, the amount of water is not fitted to the experimental data, thereby reducing the number of responses in Table 2.4 to ten. The steps in Scheme 2.24 can be summarized to nine sections: DME to lower olefins (k_1), the reaction between DME and methanol (k_2), methanol to lower olefins (k_3), reactions of lower olefins with DME (k_4–k_6) or with methanol (k_7–k_9), conversion of lower to higher olefins (k_{10}, $k_{10'}$ and $k_{10''}$), formation of $C_{6\text{-}8}^{ar}$ and lower paraffins out of higher (k_{11}) or lower olefins (k_{12}, $k_{12'}$ and $k_{12''}$) and DME cracking to CO and methane (k_{13}). It follows that the differing reactivity of methanol and DME is considered; both can react either to or with lower olefins. The mechanism of the latter step is not resolved, but it is different to the methylations postulated in other models. For the oxygenates interconversion, no instant equilibrium is assumed, causing a kinetic rate constant; for the backward reaction, the same equilibrium constant as for Aguayo *et al.* [248] is assumed. In the experimental data, no initiation phase can be observed, which might be either due to relatively high minimum contact times or due to the higher reactivity of DME. The olefin interconversion includes only dimerization, no cracking is included. The different reactivity of ethene and butenes compared to propene is accounted for via multiplying the rate constant for propene with a specific factor. The same is done for the side product formation out of these olefins. Besides $C_{2\text{-}4}$ paraffins and $C_{6\text{-}8}^{ar}$, methane and CO are implemented, both being directly produced out of DME. All steps are formulated as elementary reactions, but with partially deviating reaction orders and except for the reaction between the oxygenates, all steps are irreversible. For the HW type of mechanism, the adsorption of methanol and water is considered with a common equilibrium constant K^{ads} (MW). Arbitrary values are used for the stoichiometric coefficients (see Scheme 2.25). The reaction network is compared with two other versions where the steps 4 to 9 are summarized to two reactions or where more olefin interconversion steps are implemented [249]; however, statistical evaluation proves that no improvement is achieved with these two variations.

$$\mathrm{DME} \xrightarrow{k_1} \mathrm{C_2^= + C_3^= + C_4^= + H_2O} \qquad r_1 = \frac{k_1\, p_\mathrm{C}(\mathrm{DME})}{1+K^\mathrm{ads}(\mathrm{MW})\,(p_\mathrm{C}(\mathrm{MeOH})+p_\mathrm{C}(\mathrm{H_2O})}$$

$$k_1^\mathrm{ref} = (4.99 \pm 0.01) \times 10^{-2}\,\mathrm{mol_C\,g_{cat}^{-1}\,h^{-1}\,atm^{-1}} \qquad E_{\mathrm{a},1} = 41.5 \pm 0.3\,\mathrm{kJ\,mol^{-1}}$$

$$\mathrm{DME + H_2O} \underset{k_2/K^\mathrm{TD}}{\overset{k_2}{\rightleftharpoons}} \mathrm{2MeOH} \qquad r_2 = \frac{num}{1+K^\mathrm{ads}(\mathrm{MW})\,(p_\mathrm{C}(\mathrm{MeOH})+p_\mathrm{C}(\mathrm{H_2O})}$$

$$num = k_2\, p_\mathrm{C}\,(\mathrm{DME})\; p_\mathrm{C}\,(\mathrm{H_2O}) - k_2/K^\mathrm{TD}\, p_\mathrm{C}\,(\mathrm{MeOH})^2$$

$$k_2^\mathrm{ref} = (7.88 \pm 0.50) \times 10^{1}\,\mathrm{mol_C\,g_{cat}^{-1}\,h^{-1}\,atm^{-2}} \qquad E_{\mathrm{a},2} = 11.9 \pm 0.7\,\mathrm{kJ\,mol^{-1}}$$

$$\mathrm{MeOH} \xrightarrow{k_3} \mathrm{C_2^= + C_3^= + C_4^= + H_2O} \qquad r_3 = \frac{k_3\, p_\mathrm{C}(\mathrm{MeOH})}{1+K^\mathrm{ads}(\mathrm{MW})\,(p_\mathrm{C}(\mathrm{MeOH})+p_\mathrm{C}(\mathrm{H_2O})}$$

$$k_3^\mathrm{ref} = (2.42 \pm 0.15) \times 10^{-3}\,\mathrm{mol_C\,g_{cat}^{-1}\,h^{-1}\,atm^{-1}} \qquad E_{\mathrm{a},3} = 33.8 \pm 0.2\,\mathrm{kJ\,mol^{-1}}$$

$$\mathrm{C_2^= + DME} \xrightarrow{k_4} \mathrm{2C_2^= + H_2O} \qquad r_4 = \frac{k_4\, p_\mathrm{C}(\mathrm{DME})\, p_\mathrm{C}(\mathrm{C_2^=})}{1+K^\mathrm{ads}(\mathrm{MW})\,(p_\mathrm{C}(\mathrm{MeOH})+p_\mathrm{C}(\mathrm{H_2O})}$$

$$k_4^\mathrm{ref} = (2.48 \pm 0.34) \times 10^{-1}\,\mathrm{mol_C\,g_{cat}^{-1}\,h^{-1}\,atm^{-2}} \qquad E_{\mathrm{a},4} = 17.2 \pm 0.2\,\mathrm{kJ\,mol^{-1}}$$

$$\mathrm{2C_3^= + 3DME} \xrightarrow{k_5} \mathrm{4C_3^= + 3H_2O} \qquad r_5 = \frac{k_5\, p_\mathrm{C}(\mathrm{DME})\, p_\mathrm{C}(\mathrm{C_3^=})}{1+K^\mathrm{ads}(\mathrm{MW})\,(p_\mathrm{C}(\mathrm{MeOH})+p_\mathrm{C}(\mathrm{H_2O})}$$

$$k_5^\mathrm{ref} = 2.54 \pm 0.01\,\mathrm{mol_C\,g_{cat}^{-1}\,h^{-1}\,atm^{-2}} \qquad E_{\mathrm{a},5} = 25.7 \pm 0.3\,\mathrm{kJ\,mol^{-1}}$$

$$\mathrm{C_4^= + 2DME} \xrightarrow{k_6} \mathrm{2C_4^= + 4H_2O} \qquad r_6 = \frac{k_6\, p_\mathrm{C}(\mathrm{DME})\, p_\mathrm{C}(\mathrm{C_4^=})}{1+K^\mathrm{ads}(\mathrm{MW})\,(p_\mathrm{C}(\mathrm{MeOH})+p_\mathrm{C}(\mathrm{H_2O})}$$

$$k_6^\mathrm{ref} = (1.44 \pm 0.88) \times 10^{-1}\,\mathrm{mol_C\,g_{cat}^{-1}\,h^{-1}\,atm^{-2}} \qquad E_{\mathrm{a},6} = 9.8 \pm 0.7\,\mathrm{kJ\,mol^{-1}}$$

$$\mathrm{C_2^= + 2MeOH} \xrightarrow{k_7} \mathrm{2C_2^= + 2H_2O} \qquad r_7 = \frac{k_7\, p_\mathrm{C}(\mathrm{MeOH})\, p_\mathrm{C}(\mathrm{C_2^=})}{1+K^\mathrm{ads}(\mathrm{MW})\,(p_\mathrm{C}(\mathrm{MeOH})+p_\mathrm{C}(\mathrm{H_2O})}$$

$$k_7^\mathrm{ref} = (3.02 \pm 0.05) \times 10^{1}\,\mathrm{mol_C\,g_{cat}^{-1}\,h^{-1}\,atm^{-2}} \qquad E_{\mathrm{a},7} = 16.3 \pm 0.1\,\mathrm{kJ\,mol^{-1}}$$

$$\mathrm{C_3^= + 3MeOH} \xrightarrow{k_8} \mathrm{2C_3^= + 3H_2O} \qquad r_8 = \frac{k_8\, p_\mathrm{C}(\mathrm{MeOH})\, p_\mathrm{C}(\mathrm{C_3^=})}{1+K^\mathrm{ads}(\mathrm{MW})\,(p_\mathrm{C}(\mathrm{MeOH})+p_\mathrm{C}(\mathrm{H_2O})}$$

$$k_8^\mathrm{ref} = 2.63 \pm 0.09\,\mathrm{mol_C\,g_{cat}^{-1}\,h^{-1}\,atm^{-2}} \qquad E_{\mathrm{a},8} = 16.9 \pm 0.3\,\mathrm{kJ\,mol^{-1}}$$

$$\mathrm{C_4^= + 4MeOH} \xrightarrow{k_9} \mathrm{2C_4^= + 4H_2O} \qquad r_9 = \frac{k_9\, p_\mathrm{C}(\mathrm{MeOH})\, p_\mathrm{C}(\mathrm{C_4^=})}{1+K^\mathrm{ads}(\mathrm{MW})\,(p_\mathrm{C}(\mathrm{MeOH})+p_\mathrm{C}(\mathrm{H_2O})}$$

$$k_9^\mathrm{ref} = (4.24 \pm 1.14) \times 10^{-1}\,\mathrm{mol_C\,g_{cat}^{-1}\,h^{-1}\,atm^{-2}} \qquad E_{\mathrm{a},9} = 69.0 \pm 0.3\,\mathrm{kJ\,mol^{-1}}$$

$$\mathrm{C_3^=} \xrightarrow{k_{10}} \mathrm{C_{5+}^=} \qquad r_{10} = \frac{k_{10}\, p_\mathrm{C}(\mathrm{C_3^=})}{1+K^\mathrm{ads}(\mathrm{MW})\,(p_\mathrm{C}(\mathrm{MeOH})+p_\mathrm{C}(\mathrm{H_2O})}$$

$$k_{10}^\mathrm{ref} = 1.03 \pm 0.01\,\mathrm{mol_C\,g_{cat}^{-1}\,h^{-1}\,atm^{-1}} \qquad E_{\mathrm{a},10} = 21.2 \pm 0.1\,\mathrm{kJ\,mol^{-1}}$$

$$\mathrm{C_2^=} \xrightarrow{k_{10'}} \mathrm{C_{5+}^=} \qquad r_{10'} = \frac{k_{10'}\, p_\mathrm{C}(\mathrm{C_2^=})}{1+K^\mathrm{ads}(\mathrm{MW})\,(p_\mathrm{C}(\mathrm{MeOH})+p_\mathrm{C}(\mathrm{H_2O})}$$

$$k_{10'} = 1.78 \pm 0.02\; k_{10}$$

$$\mathrm{C_4^=} \xrightarrow{k_{10''}} \mathrm{C_{5+}^=} \qquad r_{10''} = \frac{k_{10''}\, p_\mathrm{C}(\mathrm{C_4^=})}{1+K^\mathrm{ads}(\mathrm{MW})\,(p_\mathrm{C}(\mathrm{MeOH})+p_\mathrm{C}(\mathrm{H_2O})}$$

$$k_{10''} = (6.92 \pm 0.20) \times 10^{-1}\; k_{10}$$

$$\mathrm{C_{5+}^=} \xrightarrow{k_{11}} \mathrm{C_{2-4} + C_{6-8}^{ar}} \qquad r_{11} = \frac{k_{11}\, p_\mathrm{C}\left(\mathrm{C_{5+}^=}\right)}{1+K^\mathrm{ads}(\mathrm{MW})\,(p_\mathrm{C}(\mathrm{MeOH})+p_\mathrm{C}(\mathrm{H_2O})}$$

$$k_{11}^\mathrm{ref} = (1.16 \pm 2.54) \times 10^{-2}\,\mathrm{mol_C\,g_{cat}^{-1}\,h^{-1}\,atm^{-1}} \qquad E_{\mathrm{a},11} = 0.601 \pm 0.135\,\mathrm{kJ\,mol^{-1}}$$

$$\mathrm{C_3^=} \xrightarrow{k_{12}} \mathrm{C_{2-4} + C_{6-8}^{ar}} \qquad r_{12} = \frac{k_{12}\, p_\mathrm{C}(\mathrm{C_3^=})}{1+K^\mathrm{ads}(\mathrm{MW})\,(p_\mathrm{C}(\mathrm{MeOH})+p_\mathrm{C}(\mathrm{H_2O})}$$

$$k_{12}^\mathrm{ref} = (3.10 \pm 0.02) \times 10^{-1}\,\mathrm{mol_C\,g_{cat}^{-1}\,h^{-1}\,atm^{-1}} \qquad E_{\mathrm{a},12} = 20.5 \pm 0.1\,\mathrm{kJ\,mol^{-1}}$$

$$\mathrm{C_2^=} \xrightarrow{k_{12'}} \mathrm{C_{2-4} + C_{6-8}^{ar}} \qquad r_{12'} = \frac{k_{12'}\, p_\mathrm{C}(\mathrm{C_2^=})}{1+K^\mathrm{ads}(\mathrm{MW})\,(p_\mathrm{C}(\mathrm{MeOH})+p_\mathrm{C}(\mathrm{H_2O})}$$

$$k_{12'} = 1.78 \pm 0.02\; k_{12}$$

$$\mathrm{C_4^=} \xrightarrow{k_{12''}} \mathrm{C_{2-4} + C_{6-8}^{ar}} \qquad r_{12''} = \frac{k_{12''}\, p_\mathrm{C}(\mathrm{C_4^=})}{1+K^\mathrm{ads}(\mathrm{MW})\,(p_\mathrm{C}(\mathrm{MeOH})+p_\mathrm{C}(\mathrm{H_2O})}$$

$$k_{12''} = (6.92 \pm 0.20) \times 10^{-1}\; k_{12}$$

$$\mathrm{DME} \xrightarrow{k_{13}} \mathrm{C_1 + CO} \qquad r_{13} = \frac{k_{13}\, p_\mathrm{C}(\mathrm{DME})}{1+K^\mathrm{ads}(\mathrm{MW})\,(p_\mathrm{C}(\mathrm{MeOH})+p_\mathrm{C}(\mathrm{H_2O})}$$

$$k_{13}^\mathrm{ref} = (5.63 \pm 1.10) \times 10^{-4}\,\mathrm{mol_C\,g_{cat}^{-1}\,h^{-1}\,atm^{-1}} \qquad E_{\mathrm{a},13} = 33.7 \pm 0.4\,\mathrm{kJ\,mol^{-1}}$$

$$K^{\mathrm{ads,ref}}\,(\mathrm{MW}) = (1.27 \pm 0.01) \times 10^{1}\,\mathrm{atm^{-1}} \qquad \Delta_\mathrm{ads}H^\circ_\mathrm{MW} = 0.2 \pm 0.1\,\mathrm{kJ\,mol^{-1}}$$

Scheme 2.24: Reaction network, rate equations and estimated parameters for the model by Pérez-Uriarte *et al.* [249]; K^TD is calculated with an own correlation [168] (see Section 2.4); some values are from another publication [272].

The net rates of production are presented in Scheme 2.25.

$$
\begin{aligned}
R\,(\mathrm{MeOH}) = {} & \frac{2\,k_2\,p_\mathrm{C}\,(\mathrm{DME})\;p_\mathrm{C}\,(\mathrm{H_2O}) - 2\,k_2/K^\mathrm{TD}\,p_\mathrm{C}\,(\mathrm{MeOH})^2 - 3\,k_3\,p_\mathrm{C}\,(\mathrm{MeOH})}{1 + K^\mathrm{ads}\,(\mathrm{MW})\;(p_\mathrm{C}\,(\mathrm{MeOH}) + p_\mathrm{C}\,(\mathrm{H_2O}))} \\
& \frac{-k_7\,p_\mathrm{C}\,(\mathrm{MeOH})\;p_\mathrm{C}\,(\mathrm{C_2^=}) - k_8\,p_\mathrm{C}\,(\mathrm{MeOH})\;p_\mathrm{C}\,(\mathrm{C_3^=}) - k_9\,p_\mathrm{C}\,(\mathrm{MeOH})\;p_\mathrm{C}\,(\mathrm{C_4^=})}{1 + K^\mathrm{ads}\,(\mathrm{MW})\;(p_\mathrm{C}\,(\mathrm{MeOH}) + p_\mathrm{C}\,(\mathrm{H_2O}))} \\
R\,(\mathrm{DME}) = {} & \frac{2\,k_2/K^\mathrm{TD}\,p_\mathrm{C}\,(\mathrm{MeOH})^2 - 6\,k_1\,p_\mathrm{C}\,(\mathrm{DME}) - 2\,k_2\,p_\mathrm{C}\,(\mathrm{DME})\;p_\mathrm{C}\,(\mathrm{H_2O})}{1 + K^\mathrm{ads}\,(\mathrm{MW})\;(p_\mathrm{C}\,(\mathrm{MeOH}) + p_\mathrm{C}\,(\mathrm{H_2O}))} \\
& \frac{-2\,k_4\,p_\mathrm{C}\,(\mathrm{DME})\;p_\mathrm{C}\,(\mathrm{C_2^=}) - 2\,k_5\,p_\mathrm{C}\,(\mathrm{DME})\;p_\mathrm{C}\,(\mathrm{C_3^=}) - 2\,k_6\,p_\mathrm{C}\,(\mathrm{DME})\;p_\mathrm{C}\,(\mathrm{C_4^=})}{1 + K^\mathrm{ads}\,(\mathrm{MW})\;(p_\mathrm{C}\,(\mathrm{MeOH}) + p_\mathrm{C}\,(\mathrm{H_2O}))} \\
& \frac{-6\,k_{13}\,p_\mathrm{C}\,(\mathrm{DME})}{1 + K^\mathrm{ads}\,(\mathrm{MW})\;(p_\mathrm{C}\,(\mathrm{MeOH}) + p_\mathrm{C}\,(\mathrm{H_2O}))} \\
R\,(\mathrm{C_2^=}) = {} & \frac{2\,k_1\,p_\mathrm{C}\,(\mathrm{DME}) + k_3\,p_\mathrm{C}\,(\mathrm{MeOH}) + 2\,k_4\,p_\mathrm{C}\,(\mathrm{DME})\;p_\mathrm{C}\,(\mathrm{C_2^=}) + k_7\,p_\mathrm{C}\,(\mathrm{MeOH})\;p_\mathrm{C}\,(\mathrm{C_2^=})}{1 + K^\mathrm{ads}\,(\mathrm{MW})\;(p_\mathrm{C}\,(\mathrm{MeOH}) + p_\mathrm{C}\,(\mathrm{H_2O}))} \\
& \frac{-k_{10'}\,p_\mathrm{C}\,(\mathrm{C_2^=}) - 2.5\,k_{12'}\,p_\mathrm{C}\,(\mathrm{C_2^=})}{1 + K^\mathrm{ads}\,(\mathrm{MW})\;(p_\mathrm{C}\,(\mathrm{MeOH}) + p_\mathrm{C}\,(\mathrm{H_2O}))} \\
R\,(\mathrm{C_3^=}) = {} & \frac{2\,k_1\,p_\mathrm{C}\,(\mathrm{DME}) + k_3\,p_\mathrm{C}\,(\mathrm{MeOH}) + 2\,k_5\,p_\mathrm{C}\,(\mathrm{DME})\;p_\mathrm{C}\,(\mathrm{C_3^=}) + k_8\,p_\mathrm{C}\,(\mathrm{MeOH})\;p_\mathrm{C}\,(\mathrm{C_3^=})}{1 + K^\mathrm{ads}\,(\mathrm{MW})\;(p_\mathrm{C}\,(\mathrm{MeOH}) + p_\mathrm{C}\,(\mathrm{H_2O}))} \\
& \frac{-k_{10}\,p_\mathrm{C}\,(\mathrm{C_3^=}) - 2.5\,k_{12}\,p_\mathrm{C}\,(\mathrm{C_3^=})}{1 + K^\mathrm{ads}\,(\mathrm{MW})\;(p_\mathrm{C}\,(\mathrm{MeOH}) + p_\mathrm{C}\,(\mathrm{H_2O}))} \\
R\,(\mathrm{C_4^=}) = {} & \frac{2\,k_1\,p_\mathrm{C}\,(\mathrm{DME}) + k_3\,p_\mathrm{C}\,(\mathrm{MeOH}) + 2\,k_6\,p_\mathrm{C}\,(\mathrm{DME})\;p_\mathrm{C}\,(\mathrm{C_4^=}) + k_9\,p_\mathrm{C}\,(\mathrm{MeOH})\;p_\mathrm{C}\,(\mathrm{C_4^=})}{1 + K^\mathrm{ads}\,(\mathrm{MW})\;(p_\mathrm{C}\,(\mathrm{MeOH}) + p_\mathrm{C}\,(\mathrm{H_2O}))} \\
& \frac{-k_{10''}\,p_\mathrm{C}\,(\mathrm{C_4^=}) - 2.5\,k_{12''}\,p_\mathrm{C}\,(\mathrm{C_4^=})}{1 + K^\mathrm{ads}\,(\mathrm{MW})\;(p_\mathrm{C}\,(\mathrm{MeOH}) + p_\mathrm{C}\,(\mathrm{H_2O}))} \\
R\,(\mathrm{C_{5+}^=}) = {} & \frac{k_{10}\,p_\mathrm{C}\,(\mathrm{C_3^=}) + k_{10'}\,p_\mathrm{C}\,(\mathrm{C_2^=}) + k_{10''}\,p_\mathrm{C}\,(\mathrm{C_4^=}) - 2.5\,k_{11}\,p_\mathrm{C}\,(\mathrm{C_{5+}^=})}{1 + K^\mathrm{ads}\,(\mathrm{MW})\;(p_\mathrm{C}\,(\mathrm{MeOH}) + p_\mathrm{C}\,(\mathrm{H_2O}))} \\
R\,(\mathrm{C_1}) = {} & \frac{4\,k_{13}\,p_\mathrm{C}\,(\mathrm{DME})}{1 + K^\mathrm{ads}\,(\mathrm{MW})\;(p_\mathrm{C}\,(\mathrm{MeOH}) + p_\mathrm{C}\,(\mathrm{H_2O}))} \\
R\,(\mathrm{C_{2-4}}) = {} & \frac{k_{11}\,p_\mathrm{C}\,(\mathrm{C_{5+}^=}) + k_{12}\,p_\mathrm{C}\,(\mathrm{C_3^=}) + k_{12'}\,p_\mathrm{C}\,(\mathrm{C_2^=}) + k_{12''}\,p_\mathrm{C}\,(\mathrm{C_4^=})}{1 + K^\mathrm{ads}\,(\mathrm{MW})\;(p_\mathrm{C}\,(\mathrm{MeOH}) + p_\mathrm{C}\,(\mathrm{H_2O}))} \\
R\,(\mathrm{C_{6-8}^{ar}}) = {} & \frac{1.5\,k_{11}\,p_\mathrm{C}\,(\mathrm{C_{5+}^=}) + 1.5\,k_{12}\,p_\mathrm{C}\,(\mathrm{C_3^=}) + 1.5\,k_{12'}\,p_\mathrm{C}\,(\mathrm{C_2^=}) + 1.5\,k_{12''}\,p_\mathrm{C}\,(\mathrm{C_4^=})}{1 + K^\mathrm{ads}\,(\mathrm{MW})\;(p_\mathrm{C}\,(\mathrm{MeOH}) + p_\mathrm{C}\,(\mathrm{H_2O}))} \\
R\,(\mathrm{CO}) = {} & \frac{2\,k_{13}\,p_\mathrm{C}\,(\mathrm{DME})}{1 + K^\mathrm{ads}\,(\mathrm{MW})\;(p_\mathrm{C}\,(\mathrm{MeOH}) + p_\mathrm{C}\,(\mathrm{H_2O}))} \\
R\,(\mathrm{H_2O}) = {} & \frac{k_1\,p_\mathrm{C}\,(\mathrm{DME}) + k_2/K^\mathrm{TD}\,p_\mathrm{C}\,(\mathrm{MeOH})^2 + k_3\,p_\mathrm{C}\,(\mathrm{MeOH}) + k_4\,p_\mathrm{C}\,(\mathrm{DME})\;p_\mathrm{C}\,(\mathrm{C_2^=})}{1 + K^\mathrm{ads}\,(\mathrm{MW})\;(p_\mathrm{C}\,(\mathrm{MeOH}) + p_\mathrm{C}\,(\mathrm{H_2O}))} \\
& \frac{+k_5\,p_\mathrm{C}\,(\mathrm{DME})\;p_\mathrm{C}\,(\mathrm{C_3^=}) + k_6\,p_\mathrm{C}\,(\mathrm{DME})\;p_\mathrm{C}\,(\mathrm{C_4^=}) + k_7\,p_\mathrm{C}\,(\mathrm{MeOH})\;p_\mathrm{C}\,(\mathrm{C_2^=})}{1 + K^\mathrm{ads}\,(\mathrm{MW})\;(p_\mathrm{C}\,(\mathrm{MeOH}) + p_\mathrm{C}\,(\mathrm{H_2O}))} \\
& \frac{+k_8\,p_\mathrm{C}\,(\mathrm{MeOH})\;p_\mathrm{C}\,(\mathrm{C_3^=}) + k_9\,p_\mathrm{C}\,(\mathrm{MeOH})\;p_\mathrm{C}\,(\mathrm{C_4^=}) - k_2\,p_\mathrm{C}\,(\mathrm{DME})\;p_\mathrm{C}\,(\mathrm{H_2O})}{1 + K^\mathrm{ads}\,(\mathrm{MW})\;(p_\mathrm{C}\,(\mathrm{MeOH}) + p_\mathrm{C}\,(\mathrm{H_2O}))}
\end{aligned}
$$

Scheme 2.25: Net rates of production of the different lumps for the model by Pérez-Uriarte *et al.* [249].

Parameter estimation The mole fractions are defined with carbon units and therefore only for carbon containing species which pertains for the partial pressures. The numeric routine is similar to Epelde *et al.* [236] and is therefore described above. As reference temperature, 623 K is chosen, which is within the lower third of the pure DME experiments. Thirty parameters have

to be estimated: 13 reference rate constants, 13 activation energies, one reference equilibrium constant, one adsorption enthalpy and two factors relating the rate constants for ethene and butenes with that of propene.

Summary

All models in this part differentiate the methylation via methanol and via DME. However, this causes several additional parameters, not only for the methylations themselves, but also for the interconversion of the oxygenates. In all three examples, the latter reaction is implemented as step of kinetic relevance with the backward reaction being described by the thermodynamic equilibrium constant. For this value, no reasonable results are obtained with the equation shown [173], whereas the outcome for the other two models is close to thermodynamics. When a detailed description of lower olefins is desired, the combined ethene and propene lump of Gayubo *et al.* [173] might be problematic. In addition, no side products are described here. On the other hand, this model explicitly includes the effect of water adsorption, similar to Pérez-Uriarte *et al.* [249]. Moreover, Gayubo *et al.* [173] described olefin interconversion in a simple, but effective way. By contrast, more reactions were considered by Aguayo *et al.* [248]. Here, the separate description of *n*-butane is noteworthy. In general, this model is useful for significant side product formation: these evolve to such an extent that they interact with olefins. In this model, both adsorption and mechanistic effects are missing. These were considered by Pérez-Uriarte *et al.* [249] who, besides water, implemented methanol adsorption. Further improvement would be possible through extending this with olefin and DME adsorption. Their model is the only one that is explicitly created for DME feeds. Nevertheless, it should be also valid at least for oxygenates mixtures as feed. A vast reactivity including side products is covered by the reaction network by Pérez-Uriarte *et al.* [249]; however, some reactions and especially their stoichiometry seem to be arbitrarily chosen. Furthermore, the number of estimated parameters is comparably high.

Microkinetic studies over ZSM-5

Park and Froment [192, 250]: Analysis of first C-C bond formation mechanisms

Catalyst A self-synthesized ZSM-5 zeolite powder having a high Si/Al ratio of 200 was used without any binder. The particle size of 500–1000 µm was small enough to exclude any effects of heat and mass transfer limitations according to the authors. Until 5 h TOS, no deactivation effects could be observed. Complete catalyst regeneration in air was possible up to 50 times.

Setup and conditions The measurements were performed in a continuous fixed bed stainless steel reactor with an inner diameter of 21.4 mm. A tube made of titanium was chosen for experiments at temperatures higher than 723 K. The reactor could be positioned within a molten salt bath during reaction. For product analysis, a GC with several columns, an FID and a TCD was applied with nitrogen as internal standard. Moreover, the authors evaluated the $C_{6+}^{=}$ fraction with a GC-MS. The catalyst bed was diluted 5:1 in a volumetric ratio using glass beads; these were also stacked in front of the catalyst bed. The latter was located on a stainless steel sieve and both glass wool and beads were placed in between. For dilution of the gaseous methanol feed, both water and nitrogen were used. The temperature within the bed could be controlled with a thermocouple sliding inside a well. More details about the setup can be found elsewhere [273].

Reaction network In the original publications [192, 250], a detailed overview of all included reactions, rate equations and net rates of production can be found. This is why only references and no schemes are shown here. In this microkinetic study, formation of the first C-C bond is modeled with the oxonium ylide mechanism [274]. This route comprises the formation of an oxonium methylide (OM) out of a surface methyl group $\left(R_{Me}^{+}\right)$ and a basic site (Step (iii.a".1) in Table 1 in [250]), the reaction of OM and a protonated DME species $\left(R_{DME}^{+}\right)$ to protonated ethene and methanol (Step (iii.a".2) in Table 1 in [250], LH type of mechanism) as well as to protonated propene and water (Step (iii.a".4) in Table 1 in [250]). Similar to these three steps, the deprotonation of ethene is also considered as reaction of kinetic relevance (Step (iii.a".3) in Table 1 in [250]). Both consumption steps of the R_{DME}^{+} species are assumed to be irreversible. The surface methyl group is formed by methanol protonation (Step (i.1) in Table 1 in [250]) and subsequent water release (Step (i.2) in Table 1 in [250]). This surface group can perform methylation reactions; when methanol is the other reactant, R_{DME}^{+} is the product (Step (i.3) in Table 1 in [250]) whose desorption releases DME (backward reaction of DME protonation, Step (i.4) in Table 1 in [250]). Another pathway starting from these two reactants is the formation of methane and formaldehyde (Step (ii.1) in Table 1 in [250]). Whereas the two protonations are assumed to be *quasi*-equilibrated, the remaining steps are kinetically relevant; except for the methane formation, all reactions are further assumed to be reversible. The surface methyl group can also methylate gas phase olefins (ER type of mechanism); all possible steps for $C_2^{=}$ to $C_7^{=}$ as reactants are included (Table 3 in [250]). In the olefin interconversion network, all cracking (Table 5 in [250]), dimerization (Table 4 in [250]) and isomerization steps are implemented for a maximum carbon number of eight. Only methyl side groups are allowed because of the small ZSM-5 pores. On the other hand, quaternary carbon atoms are considered. All steps starting from or leading to a primary intermediate are excluded except for ethene methylation and ethene self-dimerization to butene. Methylation reactions are assumed to be irreversible in contrast to cracking/dimerization. The isomerization, protonation and deprotonation steps are assumed to be *quasi*-equilibrated. Cracking and dimerization are expressed as L and ER types of mechanism, respectively, where protonation of the gas phase olefins leads to the surface

intermediates. Finally, 172 pathways of kinetic relevance remain in the whole network. No side product formation is covered by this model because only measurements at methanol conversions less than 0.7 are included. In this regime, side product formation is negligible. Only 31 of the original 222 data points are evaluated by the model. For comparison with the experimental results, the isomers of same carbon number are lumped, leading to the following fitting responses: DME, $C_2^=$, $C_3^=$, $C_4^=$, $C_5^=$, $C_6^=$, $C_7^=$, $C_8^=$ and C_1. The corresponding net rates of production, in the same order, are formulated in Equations (8), (9), (11), (31) (exemplary equation for $C_4^=$ to $C_8^=$) and (7) in [250]. The reaction rates for methylation, dimerization and cracking are shown in Equation (24) in [250]. The concentration of reactive intermediates, i.e., surface methyl group and OM, is accessed via the PSSA (Equations (14) and (16) in [250]) and site balances are applied both for acid and for basic centers (Equations (21) and (23) in [250]) according to an HW type of mechanism.

Parameter estimation Results [192] are shown as weight-based yields, whereas the rate equations require partial pressures. The objective function compares the weighted squared differences of measured and modeled yields; the weighting factors are not obtained via replicate experiments, but calculated via Equation (2.30) where –1 as exponent is replaced by 0.3 for $C_7^=$, $C_8^=$ and C_1. Integration of the differential equations of stiff character is performed using Gear's method. The deviation between model and experiment is minimized via a hybrid genetic algorithm (GA) approach [275]. At first, the GA searches for parameters satisfying the constraints and lowering the objective function to a significant extent. When these conditions are fulfilled, two local optimizers use the initial guesses obtained by the GA: a sequential quadratic program called FFSQP, which also considers constraints, and the Levenberg-Marquardt algorithm for an unconstrained final parameter estimation. Even when a suitable solution is found, new initial guesses are tried up to the maximum number of GA iterations. Through this routine, finding of the global minimum should be ensured. For the GA, values of 0.10 and 0.005 are chosen for the crossover and mutation probability, respectively. The mentioned constraints should avoid physically unreasonable values, i.e., negative activation energies or positive reaction enthalpies for methylation and dimerization. Furthermore, the protonation values have to match Boudart's criteria [276]. Finally, the higher the carbon number, the lower the protonation enthalpy should be. All the linearized constraints can be found in Table 2 in [192]. Except for the methylation and dimerization rates, reparameterization is performed according to Equations (2.22) and (2.25). Table 1 in [192] contains all dimensionless fitting parameters. Their number is drastically reduced by using the single-event methodology [19, 20] in combination with the Evans-Polanyi relation [277] and the concept of thermodynamic consistency [196]. The required thermodynamic data are calculated via Benson's group contribution method [155] as well as via quantum chemical approaches. In total, 33 values have to be estimated: eight pre-exponential factors, eight activation energies, nine protonation enthalpies, three protonation entropies, one hydration enthalpy, one hydration entropy and one combination of pre-exponential factor, activation energy and transfer coefficient for the Evans-Polanyi relation (see Table 3 in [192] for the values).

This model is used in a subsequent study to simulate isothermal fixed bed and adiabatic multi-stage reactors [278].

Kumar *et al.* [18]: Implementation of aromatic hydrocarbon pool

Catalyst The authors used the same catalyst as Park and Froment [192, 250], see above.

Setup and conditions The setup is already explained above as it is similar to Park and Froment [192, 250].

Reaction network In contrast to the previous microkinetic implementation [192, 250], the conversion of oxygenates to lower olefins is implemented via the side-chain mechanism of the aromatic hydrocarbon pool according to Arstad *et al.* [87] (see Figure 1 in [18]). The formation of these polymethylated aromatics is not described by the model, but their contribution to the overall MTO reactivity is explicitly considered. Starting from *para*-xylene, a sequence of methylations (Steps (i), (iii) and (vi) in Figure 1 in [18]), deprotonations (Steps (ii), (v) and (viii) in Figure 1 in [18]) and dealkylations (Steps (iv) and (vii) in Figure 1 in [18]) releases ethene and propene. All these steps are assumed to be reversible and of kinetic relevance. The DME and methane formation (Steps (i)–(v) in Table 1 in [18]) is implemented in a similar way to Park and Froment [192, 250]. Finally, olefin interconversion is accounted for up to a maximum carbon number of seven. This excludes all transformations of a tertiary reactant to a tertiary product intermediate. Moreover, the ethene self-dimerization is not considered. The other assumptions of Park and Froment [192, 250] are retained, including the negligence of side products. The protonation is extended with a physisorption step before, the data for which are taken from Denayer *et al.* [279, 280]. The reaction network leads to 64 pathways of kinetic relevance. The experimental data are fitted to eight responses: DME, $C_2^=$, $C_3^=$, $C_4^=$, $C_5^=$, $C_6^=$, $C_7^=$ and C_1. The net rates of production for DME, methane, ethene and propene can be found in Equations (12), (13), (16) and (17) in [18]. For the higher olefins, this coherence is not shown, but it follows from a summation of all methylation (Equation (18) in [18]) and alkylation rates (Equation (19) in [18]) where these species are involved. The amount of methanol and water is calculated using a carbon and hydrogen balance, respectively. The concentrations of surface methyl groups and the seven intermediates in the aromatic hydrocarbon pool follow from applying the PSSA (Equations (15) and (14) in [18]). In addition, the total concentration of all aromatic hydrocarbon pool species is fitted (Equation (26) in [18]); the value is comparable to a concentration of active catalyst sites. The balance for the acid sites is found in Equation (29) in [18].

Parameter estimation All figures [18] use weight-based yields. For the reaction rates, partial pressures have to be used. The objective function evaluates the weighted squared residuals

between calculated and measured molar flow rates and is minimized by a combination of a Rosenbrock and a Levenberg-Marquardt algorithm. For the former, an in-house code is used, whereas the latter is provided by the ordinary least-squares option of *ODRPACK*, version 2.01, from Netlib. Integration of the differential equations is performed by *DDASPK*, which is also part of Netlib. Here, a consistent set of boundary conditions is required, which is accessible for the gas-phase species, but not for the reactive intermediates. The latter is obtained by applying the numerical routine *DNSQE* which solves the PSSA conditions via a hybrid Powell method. The weighting factors are calculated according to Equation (2.30). For parameter reduction, the single-event methodology [19, 20] is applied as well as the principle of thermodynamic consistency [196]. In addition, all protonation entropies and pre-exponential factors are calculated before fitting based on statistical thermodynamics and the principle of microscopic reversibility [17] (see Table 3 in [18]). Here, the necessary values for entropy changes are extracted from databases [139], calculated via group contribution methods [155] or obtained via DFT. The aromatic hydrocarbon pool is characterized by only one average concentration and, finally, two deprotonation, two methylation and two dealkylation steps within this catalytic cycle are assumed to have similar activation energies. During fitting, Boudart's criteria [276] and the ordering according to carbon number are introduced as constraints for the protonation enthalpies. The rate constants are reparameterized according to Equation (2.21). Finally, besides the total concentration of aromatic hydrocarbon pool species, 29 parameters are fitted: 21 activation energies and eight protonation enthalpies.

Summary

Both models show high complexity and cause much computational effort. On the other hand, an almost complete picture of reactivity is obtained here as the reaction network covers oxygenates interaction, olefin production out of oxygenates, methylation and olefin interconversion reactions. Only side product formation is left out because the maximum methanol conversion is limited to 0.7. In contrast to all other models found in literature, the formation of lower olefins out of the oxygenates is not simply characterized by an arbitrary rate equation; the pathways and intermediates are included. Whereas Park and Froment [192, 250] focused on the formation of the first C-C bond on a direct way, Kumar *et al.* [18] considered the indirect formation via the aromatic hydrocarbon pool. In both models, the interaction between water and the zeolite is assumed to be negligible.

Studies with significant deactivation effects over SAPO-34, SAPO-18 and ZSM-23

Gayubo *et al.* [251]: Six- and five-lump approach with and without differentiation in side products over SAPO-34

Catalyst The authors synthesized a SAPO-34 zeolite with moderate acid strength that consisted mainly of Brønsted acid sites [257]. After that, the final catalyst was obtained by mixing the zeolite with bentonite and inert alumina. The deactivation through coke is considerably fast over SAPO-34 systems: it was observed that, under harsh conditions, 3 to 4% of the methanol was deposited on the catalyst even during the first minute TOS. However, this coking rate could be decreased through higher water contents, temperatures or contact times. The maximum coking rate under water co-feeding was 1%. Nevertheless, the measurements were performed at a TOS of 1 h with the results being extrapolated to the fresh catalyst.

Setup and conditions The experimental setup was the same as for Gayubo *et al.*'s model over ZSM-5 [173], cf. the description above and in the publication [265] for more details. For the SAPO-34 experiments, the catalyst was diluted 1:3 on a weight base with alumina. Furthermore, dilution of the methanol feed with water was performed with the following weight ratios: 0, 1 and 3.

Reaction network Six lumps are applied: Ox, $C_2^=$, $C_3^=$, $C_4^=$, $C_5^=$ and $C_{1\text{-}4}$. Consequently, no differentiation and no reactions between the oxygenates are considered. Their amount is not fitted to experimental data, but calculated via conservation of mass. No methylation reactions are included; the network in Scheme 2.26 is restricted to either oxygenates conversion to olefins (k_1–k_4) or olefin interconversion (k_6–k_8). The latter comprises conversion of $C_3^=$ to $C_5^=$ olefins to ethene and propene. In this model, ethene is seen as final product because it cannot act as reactant. Similar to Zhou *et al.* [136], no compounds with more than five carbon atoms are detected because of the shape selectivity. For the same reason, the amount of isobutene is lower than expected. Side product formation is considered as oxygenates conversion to $C_{1\text{-}4}$ paraffins (k_5). All steps are assumed to be irreversible and elementary, whereas stoichiometry is neglected; the consumption of pentenes in Scheme 2.27 is arbitrarily set to two. Water adsorption is taken into account according to the ZSM-5 model by the same group [173], meaning that the reaction rates in Scheme 2.26 are formulated as HW type of mechanism where the adsorption of all hydrocarbons is not considered.

$$\mathrm{Ox} \xrightarrow{k_1} \mathrm{C_2^=} \qquad r_1 = \frac{k_1\, w_\mathrm{C}(\mathrm{Ox})}{1+K^\mathrm{ads}(\mathrm{H_2O})\, w_\mathrm{C}(\mathrm{H_2O})} \qquad k_1^\mathrm{ref} = 9.92 \pm 0.35\,\mathrm{g\,g_{cat}^{-1}\,h^{-1}}, \; E_{\mathrm{a},1} = -11.30 \pm 0.60\,\mathrm{kJ\,mol^{-1}}$$

$$\mathrm{Ox} \xrightarrow{k_2} \mathrm{C_3^=} \qquad r_2 = \frac{k_2\, w_\mathrm{C}(\mathrm{Ox})}{1+K^\mathrm{ads}(\mathrm{H_2O})\, w_\mathrm{C}(\mathrm{H_2O})} \qquad k_2^\mathrm{ref} = 14.2 \pm 0.6\,\mathrm{g\,g_{cat}^{-1}\,h^{-1}}, \; E_{\mathrm{a},2} = -9.70 \pm 0.75\,\mathrm{kJ\,mol^{-1}}$$

$$\mathrm{Ox} \xrightarrow{k_3} \mathrm{C_4^=} \qquad r_3 = \frac{k_3\, w_\mathrm{C}(\mathrm{Ox})}{1+K^\mathrm{ads}(\mathrm{H_2O})\, w_\mathrm{C}(\mathrm{H_2O})} \qquad k_3^\mathrm{ref} = 5.66 \pm 0.43\,\mathrm{g\,g_{cat}^{-1}\,h^{-1}}, \; E_{\mathrm{a},3} = -8.25 \pm 1.15\,\mathrm{kJ\,mol^{-1}}$$

$$\mathrm{Ox} \xrightarrow{k_4} \mathrm{C_5^=} \qquad r_4 = \frac{k_4\, w_\mathrm{C}(\mathrm{Ox})}{1+K^\mathrm{ads}(\mathrm{H_2O})\, w_\mathrm{C}(\mathrm{H_2O})} \qquad k_4^\mathrm{ref} = 0.812 \pm 0.343\,\mathrm{g\,g_{cat}^{-1}\,h^{-1}}, \; E_{\mathrm{a},4} = -6.90 \pm 1.50\,\mathrm{kJ\,mol^{-1}}$$

$$\mathrm{Ox} \xrightarrow{k_5} \mathrm{C_{1-4}} \qquad r_5 = \frac{k_5\, w_\mathrm{C}(\mathrm{Ox})}{1+K^\mathrm{ads}(\mathrm{H_2O})\, w_\mathrm{C}(\mathrm{H_2O})} \qquad k_5^\mathrm{ref} = 0.341 \pm 0.094\,\mathrm{g\,g_{cat}^{-1}\,h^{-1}}, \; E_{\mathrm{a},5} = -11.50 \pm 4.40\,\mathrm{kJ\,mol^{-1}}$$

$$\mathrm{C_3^=} \xrightarrow{k_6} \mathrm{C_2^=} \qquad r_6 = \frac{k_6\, w_\mathrm{C}(\mathrm{C_3^=})}{1+K^\mathrm{ads}(\mathrm{H_2O})\, w_\mathrm{C}(\mathrm{H_2O})} \qquad k_6^\mathrm{ref} = 1.14 \pm 0.36\,\mathrm{g\,g_{cat}^{-1}\,h^{-1}}, \; E_{\mathrm{a},6} = -10.20 \pm 5.20\,\mathrm{kJ\,mol^{-1}}$$

$$\mathrm{C_4^=} \xrightarrow{k_7} \mathrm{C_2^=} \qquad r_7 = \frac{k_7\, w_\mathrm{C}(\mathrm{C_4^=})}{1+K^\mathrm{ads}(\mathrm{H_2O})\, w_\mathrm{C}(\mathrm{H_2O})} \qquad k_7^\mathrm{ref} = 1.19 \pm 0.34\,\mathrm{g\,g_{cat}^{-1}\,h^{-1}}, \; E_{\mathrm{a},7} = -9.70 \pm 3.90\,\mathrm{kJ\,mol^{-1}}$$

$$\mathrm{C_5^=} \xrightarrow{k_8} \mathrm{C_2^=} + \mathrm{C_3^=} \qquad r_8 = \frac{k_8\, w_\mathrm{C}(\mathrm{C_5^=})}{1+K^\mathrm{ads}(\mathrm{H_2O})\, w_\mathrm{C}(\mathrm{H_2O})} \qquad k_8^\mathrm{ref} = 0.916 \pm 3.953\,\mathrm{g\,g_{cat}^{-1}\,h^{-1}}, \; E_{\mathrm{a},8} = -8.20 \pm 34.00\,\mathrm{kJ\,mol^{-1}}$$

$$K^\mathrm{ads}\,(\mathrm{H_2O}) = 1.0 \pm 0.15$$

Scheme 2.26: Reaction network, rate equations and estimated parameters for the model by Gayubo *et al.* [251] over SAPO-34 (six lumps).

The resulting net rates of production can be found in Scheme 2.27.

$$R\,(\mathrm{Ox}) = \frac{-k_1\, w_\mathrm{C}\,(\mathrm{Ox}) - k_2\, w_\mathrm{C}\,(\mathrm{Ox}) - k_3\, w_\mathrm{C}\,(\mathrm{Ox}) - k_4\, w_\mathrm{C}\,(\mathrm{Ox}) - k_5\, w_\mathrm{C}\,(\mathrm{Ox})}{1 + K^\mathrm{ads}\,(\mathrm{H_2O})\; w_\mathrm{C}\,(\mathrm{H_2O})}$$

$$R\,(\mathrm{C_2^=}) = \frac{k_1\, w_\mathrm{C}\,(\mathrm{Ox}) + k_6\, w_\mathrm{C}\,(\mathrm{C_3^=}) + k_7\, w_\mathrm{C}\,(\mathrm{C_4^=}) + k_8\, w_\mathrm{C}\,(\mathrm{C_5^=})}{1 + K^\mathrm{ads}\,(\mathrm{H_2O})\; w_\mathrm{C}\,(\mathrm{H_2O})}$$

$$R\,(\mathrm{C_3^=}) = \frac{k_2\, w_\mathrm{C}\,(\mathrm{Ox}) + k_8\, w_\mathrm{C}\,(\mathrm{C_5^=}) - k_6\, w_\mathrm{C}\,(\mathrm{C_3^=})}{1 + K^\mathrm{ads}\,(\mathrm{H_2O})\; w_\mathrm{C}\,(\mathrm{H_2O})}$$

$$R\,(\mathrm{C_4^=}) = \frac{k_3\, w_\mathrm{C}\,(\mathrm{Ox}) - k_7\, w_\mathrm{C}\,(\mathrm{C_4^=})}{1 + K^\mathrm{ads}\,(\mathrm{H_2O})\; w_\mathrm{C}\,(\mathrm{H_2O})}$$

$$R\,(\mathrm{C_5^=}) = \frac{k_4\, w_\mathrm{C}\,(\mathrm{Ox}) - 2\,k_8\, w_\mathrm{C}\,(\mathrm{C_5^=})}{1 + K^\mathrm{ads}\,(\mathrm{H_2O})\; w_\mathrm{C}\,(\mathrm{H_2O})}$$

$$R\,(\mathrm{C_{1-4}}) = \frac{k_5\, w_\mathrm{C}\,(\mathrm{Ox})}{1 + K^\mathrm{ads}\,(\mathrm{H_2O})\; w_\mathrm{C}\,(\mathrm{H_2O})}$$

Scheme 2.27: Net rates of production of the different lumps for the model by Gayubo *et al.* [251] over SAPO-34 (six lumps); the Ox lump is calculated via conservation of mass within the model.

Compared to the model with six lumps, $C_5^=$ and $C_{1\text{-}4}$ are summarized to the lump Rest. Furthermore, all olefin interconversion reactions are neglected (see Scheme 2.28). The resulting network thus only considers oxygenates conversion to olefins and to the Rest lump.

$$\begin{aligned}
&\mathrm{Ox} \xrightarrow{k_1} \mathrm{C_2^=} && r_1 = \frac{k_1\, w_\mathrm{C}(\mathrm{Ox})}{1+K^\mathrm{ads}(\mathrm{H_2O})\, w_\mathrm{C}(\mathrm{H_2O})} && k_1^\mathrm{ref} = 10.5 \pm 0.4\,\mathrm{g\,g_{cat}^{-1}\,h^{-1}} \\
& && && E_{\mathrm{a},1} = -11.8 \pm 0.6\,\mathrm{kJ\,mol^{-1}} \\
&\mathrm{Ox} \xrightarrow{k_2} \mathrm{C_3^=} && r_2 = \frac{k_2\, w_\mathrm{C}(\mathrm{Ox})}{1+K^\mathrm{ads}(\mathrm{H_2O})\, w_\mathrm{C}(\mathrm{H_2O})} && k_2^\mathrm{ref} = 13.7 \pm 0.5\,\mathrm{g\,g_{cat}^{-1}\,h^{-1}} \\
& && && E_{\mathrm{a},2} = -9.5 \pm 0.6\,\mathrm{kJ\,mol^{-1}} \\
&\mathrm{Ox} \xrightarrow{k_3} \mathrm{C_4^=} && r_3 = \frac{k_3\, w_\mathrm{C}(\mathrm{Ox})}{1+K^\mathrm{ads}(\mathrm{H_2O})\, w_\mathrm{C}(\mathrm{H_2O})} && k_3^\mathrm{ref} = 5.49 \pm 0.37\,\mathrm{g\,g_{cat}^{-1}\,h^{-1}} \\
& && && E_{\mathrm{a},3} = -7.1 \pm 1.0\,\mathrm{kJ\,mol^{-1}} \\
&\mathrm{Ox} \xrightarrow{k_4} \mathrm{Rest} && r_4 = \frac{k_4\, w_\mathrm{C}(\mathrm{Ox})}{1+K^\mathrm{ads}(\mathrm{H_2O})\, w_\mathrm{C}(\mathrm{H_2O})} && k_4^\mathrm{ref} = 1.00 \pm 0.22\,\mathrm{g\,g_{cat}^{-1}\,h^{-1}} \\
& && && E_{\mathrm{a},4} = -9.0 \pm 3.6\,\mathrm{kJ\,mol^{-1}}
\end{aligned}$$

Scheme 2.28: Reaction network, rate equations and estimated parameters for the model by Gayubo *et al.* [251] over SAPO-34 (five lumps).

The network reduces the net rates of production to the ones in Scheme 2.29.

$$\begin{aligned}
R\,(\mathrm{Ox}) &= \frac{-k_1\, w_\mathrm{C}\,(\mathrm{Ox}) - k_2\, w_\mathrm{C}\,(\mathrm{Ox}) - k_3\, w_\mathrm{C}\,(\mathrm{Ox}) - k_4\, w_\mathrm{C}\,(\mathrm{Ox})}{1 + K^\mathrm{ads}\,(\mathrm{H_2O})\; w_\mathrm{C}\,(\mathrm{H_2O})} \\
R\,(\mathrm{C_2^=}) &= \frac{k_1\, w_\mathrm{C}\,(\mathrm{Ox})}{1 + K^\mathrm{ads}\,(\mathrm{H_2O})\; w_\mathrm{C}\,(\mathrm{H_2O})} \\
R\,(\mathrm{C_3^=}) &= \frac{k_2\, w_\mathrm{C}\,(\mathrm{Ox})}{1 + K^\mathrm{ads}\,(\mathrm{H_2O})\; w_\mathrm{C}\,(\mathrm{H_2O})} \\
R\,(\mathrm{C_4^=}) &= \frac{k_3\, w_\mathrm{C}\,(\mathrm{Ox})}{1 + K^\mathrm{ads}\,(\mathrm{H_2O})\; w_\mathrm{C}\,(\mathrm{H_2O})} \\
R\,(\mathrm{Rest}) &= \frac{k_4\, w_\mathrm{C}\,(\mathrm{Ox})}{1 + K^\mathrm{ads}\,(\mathrm{H_2O})\; w_\mathrm{C}\,(\mathrm{H_2O})}
\end{aligned}$$

Scheme 2.29: Net rates of production of the different lumps for the model by Gayubo *et al.* [251] over SAPO-34 (five lumps); the Ox lump is calculated via conservation of mass within the model.

Parameter estimation The numeric routine is similar to the ZSM-5 model by Gayubo *et al.* [173], see above. The reference temperature for reparameterization is set to 698 K which is close to the mean value of the experimentally covered range. The reaction scheme causes 17 unknown parameters: eight reference rate constants, eight activation energies and one equilibrium constant for water adsorption. As for the study over ZSM-5, the latter value is determined to unity, which converts the organic mass fractions to total mass fractions. Because of the poor numeric significance of the estimated parameters in Scheme 2.26, the network is reduced to five lumps in the following. For the version with five lumps, only eight parameters have to

be estimated due to the simplified network: four reference rate constants and four activation energies. The equilibrium constant of water adsorption is kept fixed at a value of one.

Ying *et al.* [252]: Seven-lump model with subsequent fitting of deactivation parameters over SAPO-34

Catalyst The authors used the commercial DMTO catalyst by Chia Tai Energy Materials in order to ensure transferability of their model to an industrial plant. It was based on SAPO-34 crystals. Because of confidentiality, not many details about the final catalyst extrudate are given. Concerning the kinetic model, the measured data were obtained with a fresh catalyst. In addition to this, the authors analyzed deactivation effects using TOS values up to 1.67 h. For this, they applied a fluidized bed reactor because coke evolution in a fixed bed is prone to zoning effects, which cause a non-uniform coke distribution. The authors found that the reactor type has no influence on the final coke content. Furthermore, the coke growth rate was comparably high at the beginning and leveled off towards the maximum. At a certain deactivation level, the catalyst showed a maximum olefin production rate. This is why the authors include a seventh step to their kinetic scheme which accounts for coke formation out of methanol. The other six reaction rates are multiplied by a deactivation value φ_l. This stems from an exponential approach consisting of several constants and a rate-specific value α_l. The deactivation model as well as the resulting reactor model are beyond the scope which is why it is referred to the original contribution [252].

Setup and conditions The experiments were performed in a continuous fixed bed quartz glass reactor with an inner diameter of 4 mm. The liquid feed consisted of either pure methanol or a water-methanol stream with a molar ratio of 2:1 or 4:1; it was vaporized before entering the reactor. A GC with one column and an FID was used for product analysis. For the coking experiments, the authors applied a fluidized bed reactor with an inner diameter of 19 mm where the evolved coke could be evaluated via TG.

Reaction network The reaction network in Scheme 2.30 considers no DME formation; all reactions start from methanol as reactant. These steps are assumed to be irreversible and lead to both olefins (k_2, k_3, k_5 and k_6) and paraffins (k_1, k_4 and k_6). Neither methylations nor olefin interconversion reactions are implemented. The following lumps are defined: MeOH, $C_2^=$, $C_3^=$, C_4^{HC}, C_1, C_3 and $C_{2,5,6}^{HC}$. The latter comprises both olefins and paraffins with five and six carbon atoms as well as ethane. In preliminary experiments, no further side products and no higher compounds could be detected. Water attenuates the overall reaction rates, which is why its adsorption is included via an HW type of mechanism. The interaction of the hydrocarbons with the acid sites is neglected. All reactions are formulated as first-order with respect to methanol,

which is the result of an experimental observation. Stoichiometry is retained for the net rates of production.

$$\mathrm{MeOH} \xrightarrow{k_1} \mathrm{C_1} \qquad r_1 = \frac{k_1\, C(\mathrm{MeOH})\, M_\mathrm{m}(\mathrm{C_1})}{1+K^\mathrm{ads}(\mathrm{H_2O})\, w(\mathrm{H_2O})} \qquad k_1^\mathrm{ref} = 0.10\,\mathrm{L\,g_{cat}^{-1}\,min^{-1}},\ E_{\mathrm{a},1} = 117.7\,\mathrm{kJ\,mol^{-1}}$$

$$\mathrm{MeOH} \xrightarrow{k_2} \mathrm{C_2^=} \qquad r_2 = \frac{k_2\, C(\mathrm{MeOH})\, M_\mathrm{m}(\mathrm{C_2^=})}{1+K^\mathrm{ads}(\mathrm{H_2O})\, w(\mathrm{H_2O})} \qquad k_2^\mathrm{ref} = 4.93\,\mathrm{L\,g_{cat}^{-1}\,min^{-1}},\ E_{\mathrm{a},2} = 56.9\,\mathrm{kJ\,mol^{-1}}$$

$$\mathrm{MeOH} \xrightarrow{k_3} \mathrm{C_3^=} \qquad r_3 = \frac{k_3\, C(\mathrm{MeOH})\, M_\mathrm{m}(\mathrm{C_3^=})}{1+K^\mathrm{ads}(\mathrm{H_2O})\, w(\mathrm{H_2O})} \qquad k_3^\mathrm{ref} = 7.32\,\mathrm{L\,g_{cat}^{-1}\,min^{-1}},\ E_{\mathrm{a},3} = 41.9\,\mathrm{kJ\,mol^{-1}}$$

$$\mathrm{MeOH} \xrightarrow{k_4} \mathrm{C_3} \qquad r_4 = \frac{k_4\, C(\mathrm{MeOH})\, M_\mathrm{m}(\mathrm{C_3})}{1+K^\mathrm{ads}(\mathrm{H_2O})\, w(\mathrm{H_2O})} \qquad k_4^\mathrm{ref} = 0.52\,\mathrm{L\,g_{cat}^{-1}\,min^{-1}},\ E_{\mathrm{a},4} = 13.4\,\mathrm{kJ\,mol^{-1}}$$

$$\mathrm{MeOH} \xrightarrow{k_5} \mathrm{C_4^{HC}} \qquad r_5 = \frac{k_5\, C(\mathrm{MeOH})\, M_\mathrm{m}\left(\mathrm{C_4^{HC}}\right)}{1+K^\mathrm{ads}(\mathrm{H_2O})\, w(\mathrm{H_2O})} \qquad k_5^\mathrm{ref} = 2.60\,\mathrm{L\,g_{cat}^{-1}\,min^{-1}},\ E_{\mathrm{a},5} = 31.2\,\mathrm{kJ\,mol^{-1}}$$

$$\mathrm{MeOH} \xrightarrow{k_6} \mathrm{C_{2,5,6}^{HC}} \qquad r_6 = \frac{k_6\, C(\mathrm{MeOH})\, M_\mathrm{m}\left(\mathrm{C_{2,5,6}^{HC}}\right)}{1+K^\mathrm{ads}(\mathrm{H_2O})\, w(\mathrm{H_2O})} \qquad k_6^\mathrm{ref} = 1.02\,\mathrm{L\,g_{cat}^{-1}\,min^{-1}},\ E_{\mathrm{a},6} = 45.8\,\mathrm{kJ\,mol^{-1}}$$

$$K^\mathrm{ads}\,(\mathrm{H_2O}) = 3.05$$

Scheme 2.30: Reaction network, rate equations and estimated parameters for the model by Ying *et al.* [252].

An overview of the net rates of production can be found in Scheme 2.31.

$$R\,(\mathrm{MeOH}) = \frac{-k_1\, C\,(\mathrm{MeOH})\; M_\mathrm{m}\,(\mathrm{MeOH}) - k_2\, C\,(\mathrm{MeOH})\; M_\mathrm{m}\,(\mathrm{MeOH}) - k_3\, C\,(\mathrm{MeOH})\; M_\mathrm{m}\,(\mathrm{MeOH})}{1 + K^\mathrm{ads}\,(\mathrm{H_2O})\; w\,(\mathrm{H_2O})}$$
$$\frac{-k_4\, C\,(\mathrm{MeOH})\; M_\mathrm{m}\,(\mathrm{MeOH}) - k_5\, C\,(\mathrm{MeOH})\; M_\mathrm{m}\,(\mathrm{MeOH}) - k_6\, C\,(\mathrm{MeOH})\; M_\mathrm{m}\,(\mathrm{MeOH})}{1 + K^\mathrm{ads}\,(\mathrm{H_2O})\; w\,(\mathrm{H_2O})}$$

$$R\,(\mathrm{C_2^=}) = \frac{1}{2}\,\frac{k_2\, C\,(\mathrm{MeOH})\; M_\mathrm{m}\,(\mathrm{C_2^=})}{1 + K^\mathrm{ads}\,(\mathrm{H_2O})\; w\,(\mathrm{H_2O})}$$

$$R\,(\mathrm{C_3^=}) = \frac{1}{3}\,\frac{k_3\, C\,(\mathrm{MeOH})\; M_\mathrm{m}\,(\mathrm{C_3^=})}{1 + K^\mathrm{ads}\,(\mathrm{H_2O})\; w\,(\mathrm{H_2O})}$$

$$R\left(\mathrm{C_4^{HC}}\right) = \frac{1}{4}\,\frac{k_5\, C\,(\mathrm{MeOH})\; M_\mathrm{m}\left(\mathrm{C_4^{HC}}\right)}{1 + K^\mathrm{ads}\,(\mathrm{H_2O})\; w\,(\mathrm{H_2O})}$$

$$R\,(\mathrm{C_1}) = \frac{k_1\, C\,(\mathrm{MeOH})\; M_\mathrm{m}\,(\mathrm{C_1})}{1 + K^\mathrm{ads}\,(\mathrm{H_2O})\; w\,(\mathrm{H_2O})}$$

$$R\,(\mathrm{C_3}) = \frac{1}{3}\,\frac{k_4\, C\,(\mathrm{MeOH})\; M_\mathrm{m}\,(\mathrm{C_3})}{1 + K^\mathrm{ads}\,(\mathrm{H_2O})\; w\,(\mathrm{H_2O})}$$

$$R\left(\mathrm{C_{2,5,6}^{HC}}\right) = \frac{1}{5}\,\frac{k_6\, C\,(\mathrm{MeOH})\; M_\mathrm{m}\left(\mathrm{C_{2,5,6}^{HC}}\right)}{1 + K^\mathrm{ads}\,(\mathrm{H_2O})\; w\,(\mathrm{H_2O})}$$

Scheme 2.31: Net rates of production of the different lumps for the model by Ying *et al.* [252].

Parameter estimation In Scheme 2.30, molar concentrations per volume have to be used for organic compounds while the water content is expressed as mass fraction. Whereas water

is excluded for the figures shown [252], the integrated rate expressions lead to mass fractions where water is included. Parameter estimation is performed via the Levenberg-Marquardt algorithm which minimizes the objective function. The latter returns the weighted sum of squared residuals between the modeled and the experimental mass fractions, but the calculation of the weighting factors is not shown. The adsorption equilibrium constant of water is assumed to be the same for all steps. Reparameterization according to Equation (2.21) is performed with a reference temperature of 723 K, the lowest experimentally investigated value. In total, without the coking values, 13 parameters are obtained: six reference rate constants, six activation energies and one equilibrium constant for water adsorption.

Chen *et al.* [253]: Seven-lump model with simultaneous fitting of deactivation parameters over SAPO-34

Catalyst A commercial SAPO-34 powder from SINTEF was used. As it is known for this zeolite type, the coking rate was high and significant deactivation could be observed from the beginning on. In an earlier contribution [281], a detailed kinetic model for the coke evolution was derived. For the reaction kinetics, a simpler approach via a linear function is chosen: a deactivation constant α_l is multiplied by the weight percent of coke on the catalyst; subtracting the result from one yields the corresponding deactivation function φ_l. It depends on the reaction step l because of a selective deactivation, which means the higher the carbon number, the more selectivity loss through coke deposition can be observed. The authors supposed changes in shape selectivity for this behavior.

Setup and conditions The experiments were performed in a tapered element oscillating microbalance reactor which is described elsewhere [259, 282]. This allowed for measuring mass changes without bypass effects, making it a useful tool to measure product evolution and coke formation, equivalent to main and deactivation kinetics, simultaneously. The setup exhibited fixed-bed characteristics with almost gradientless operation. Temperature control was ensured by two thermocouples, one at the outside and one below the outlet of the reactor. The latter consisted of proprietary glass. Liquid feeds were provided from a storage cylinder and evaporated. The catalyst bed was diluted with quartz particles and the feed stream with helium. Because of the rapid deactivation, methanol was fed in pulses of 3 min at mild and of 1 min at harsh conditions. It could be shown that such a procedure does not affect conversion and selectivity [281]. For the same reason, not all combinations of conditions shown in Table 2.4 were performed (cf. the original study [253]). The products were analyzed via a GC using one column and an FID.

Reaction network The reaction network is derived from preliminary measurements evaluated via yield-conversion plots. For one specific condition, several pulse amounts were applied.

When connecting all data points of the first pulse, an optimum performance envelope is obtained, which gives further insight. The authors concluded that all olefins are stable secondary products forming in parallel out of DME. The effect of side reactions was low because of high values of the weight hourly space velocity; only the stable tertiary products ethane and propane are produced at high oxygenates conversions. Methane was also detected as stable primary and secondary product, but it is excluded from modeling because of very small mole fractions. As coke deposition was significant throughout all experiments, its formation has to be included in the reaction network. It is classified as stable secondary and tertiary product. These observations lead to seven lumps: Ox, $C_2^=$, $C_3^=$, $C_4^=$, $C_5^=$, $C_6^=$ and $C_{2\text{-}3}$. Scheme 2.32 includes two different types of reactions, the conversion of oxygenates to olefins (k_1–k_5) and the subsequent reaction of olefins to paraffins (k_6). Consequently, no methylation reactions are considered and the reactivity of methanol is restricted to the step converting it to DME. Both oxygenates are summarized to one lump because of intracrystalline diffusion effects, which impede the reliable modeling of DME evolution. As mentioned above, although being lumped together with methanol, the olefin formation is assumed to originate only from DME. No olefin interconversion reactions are considered which is justified with their comparably low reactivity. The reaction rates are formulated as irreversible elementary steps without any stoichiometry. Neither the effect of water nor adsorption phenomena are implemented. An initiation phase is not observed, but the autocatalytic effect should be significantly lower over SAPO-34 according to the authors.

$\mathrm{Ox} \xrightarrow{k_1} \mathrm{C_2^=}$	$r_1 = k_1\,\varphi_1\,y_\mathrm{C}\,(\mathrm{Ox})\;p^\mathrm{in}\,(\mathrm{MeOH})$	$A_1 = 7210\,\mathrm{kmol\,g_{cat}^{-1}\,kPa^{-1}\,h^{-1}}$ $E_{\mathrm{a},1} = 38.4\,\mathrm{kJ\,mol^{-1}}$
$\mathrm{Ox} \xrightarrow{k_2} \mathrm{C_3^=}$	$r_2 = k_2\,\varphi_2\,y_\mathrm{C}\,(\mathrm{Ox})\;p^\mathrm{in}\,(\mathrm{MeOH})$	$A_2 = 40\,\mathrm{kmol\,g_{cat}^{-1}\,kPa^{-1}\,h^{-1}}$ $E_{\mathrm{a},2} = 27.0\,\mathrm{kJ\,mol^{-1}}$
$\mathrm{Ox} \xrightarrow{k_3} \mathrm{C_4^=}$	$r_3 = k_3\,\varphi_3\,y_\mathrm{C}\,(\mathrm{Ox})\;p^\mathrm{in}\,(\mathrm{MeOH})$	$A_3 = 15\,\mathrm{kmol\,g_{cat}^{-1}\,kPa^{-1}\,h^{-1}}$ $E_{\mathrm{a},3} = 26.9\,\mathrm{kJ\,mol^{-1}}$
$\mathrm{Ox} \xrightarrow{k_4} \mathrm{C_5^=}$	$r_4 = k_4\,\varphi_4\,y_\mathrm{C}\,(\mathrm{Ox})\;p^\mathrm{in}\,(\mathrm{MeOH})$	$A_4 = 17\,\mathrm{kmol\,g_{cat}^{-1}\,kPa^{-1}\,h^{-1}}$ $E_{\mathrm{a},4} = 49.8\,\mathrm{kJ\,mol^{-1}}$
$\mathrm{Ox} \xrightarrow{k_5} \mathrm{C_6^=}$	$r_5 = k_5\,\varphi_5\,y_\mathrm{C}\,(\mathrm{Ox})\;p^\mathrm{in}\,(\mathrm{MeOH})$	$A_5 = 5\,\mathrm{kmol\,g_{cat}^{-1}\,kPa^{-1}\,h^{-1}}$ $E_{\mathrm{a},5} = 32.4\,\mathrm{kJ\,mol^{-1}}$
$\mathrm{C_i^=} \xrightarrow{k_6} \mathrm{C_{2-3}}$	$r_6 = k_6\,\varphi_6\;(1 - y_\mathrm{C}\,(\mathrm{Ox}))\;p^\mathrm{in}\,(\mathrm{MeOH})$	$A_6 = 181\,\mathrm{kmol\,g_{cat}^{-1}\,kPa^{-1}\,h^{-1}}$ $E_{\mathrm{a},6} = 59.6\,\mathrm{kJ\,mol^{-1}}$

Scheme 2.32: Reaction network, rate equations and estimated parameters for the model by Chen *et al.* [253] with i ranging from 2 to 6; cf. the original study [253] for the deactivation parameters φ_l.

The resulting net rates of production are listed in Scheme 2.33.

$$
\begin{aligned}
R\,(\mathrm{Ox}) = &-k_1\,\varphi_1\,y_\mathrm{C}\,(\mathrm{Ox})\;p^\mathrm{in}\,(\mathrm{MeOH}) - k_2\,\varphi_2\,y_\mathrm{C}\,(\mathrm{Ox})\;p^\mathrm{in}\,(\mathrm{MeOH}) - k_3\,\varphi_3\,y_\mathrm{C}\,(\mathrm{Ox})\;p^\mathrm{in}\,(\mathrm{MeOH}) \\
&- k_4\,\varphi_4\,y_\mathrm{C}\,(\mathrm{Ox})\;p^\mathrm{in}\,(\mathrm{MeOH}) - k_5\,\varphi_5\,y_\mathrm{C}\,(\mathrm{Ox})\;p^\mathrm{in}\,(\mathrm{MeOH}) \\
R\,(\mathrm{C}_2^=) = &\,k_1\,\varphi_1\,y_\mathrm{C}\,(\mathrm{Ox})\;p^\mathrm{in}\,(\mathrm{MeOH}) \\
R\,(\mathrm{C}_3^=) = &\,k_2\,\varphi_2\,y_\mathrm{C}\,(\mathrm{Ox})\;p^\mathrm{in}\,(\mathrm{MeOH}) \\
R\,(\mathrm{C}_4^=) = &\,k_3\,\varphi_3\,y_\mathrm{C}\,(\mathrm{Ox})\;p^\mathrm{in}\,(\mathrm{MeOH}) \\
R\,(\mathrm{C}_5^=) = &\,k_4\,\varphi_4\,y_\mathrm{C}\,(\mathrm{Ox})\;p^\mathrm{in}\,(\mathrm{MeOH}) \\
R\,(\mathrm{C}_6^=) = &\,k_5\,\varphi_5\,y_\mathrm{C}\,(\mathrm{Ox})\;p^\mathrm{in}\,(\mathrm{MeOH}) \\
R\left(\mathrm{C}_{2-3}\right) = &\,k_6\,\varphi_6\;(1 - y_\mathrm{C}\,(\mathrm{Ox}))\;p^\mathrm{in}\,(\mathrm{MeOH})
\end{aligned}
$$

Scheme 2.33: Net rates of production of the different lumps for the model by Chen *et al.* [253].

Parameter estimation Conversions and selectivities are based on carbon units, as is the mole fraction of oxygenates in Scheme 2.32. Here, the inlet partial pressure of methanol is also necessary. The reaction rates depend on the coke content wherefore a uniform distribution is assumed. The objective function which equals the weighted sum of squared residuals between predicted and measured mole fractions is minimized using *lsqnonlin* in MATLAB with the Levenberg-Marquardt algorithm. No information about the calculation of the weighting factors is given. The differential equations are integrated via a fourth-order Runge-Kutta method. The parameters of best description shown in Scheme 2.32 are obtained via isothermal regression at the four different temperatures and a subsequent Arrhenius plot. This causes twelve unknown values during one fitting run: six rate constants and six deactivation constants.

Alwahabi and Froment [254]: Microkinetic implementation over SAPO-34

Catalyst The investigated SAPO-34 zeolite powder had a small particle size of 1.1 µm. Measurements were performed after 0.25 h TOS where neither deactivation effects nor coke could be observed. In the final section of the publication [254], TOS values of up to 3 h were achieved to model deactivation effects.

Setup and conditions For the measurements, a continuous fixed bed reactor was used. The feed consisted of $80\%_\mathrm{mol}$ water to suppress deactivation effects. The catalyst bed was diluted 1:4 on a weight base with α-alumina in three layers. All experimental data points are shown in the publication [283].

Reaction network The same network as for the work by Park and Froment [250] is applied. Thus, 172 pathways of kinetic relevance are included. However, because of the smaller catalyst pores, fitting is only performed for the following responses: DME, $\mathrm{C}_2^=$, $\mathrm{C}_3^=$, $\mathrm{C}_4^=$, $\mathrm{C}_5^=$ and C_1.

Parameter estimation The numerical method is identical to Park and Froment [250]. Due to the lack of higher olefins in the product stream, three parameters are missing here, i.e, protonation enthalpies of $C_6^=$, $C_7^=$ and $C_8^=$.

Gayubo *et al.* [255, 256]: Four- and five-lump approach including deactivation parameters over SAPO-18

Catalyst A self-synthesized SAPO-18 zeolite was further processed to an extrudate. The total number of acid sites was smaller compared to SAPO-34 and the acid strength was lower with a more uniform distribution which caused less deactivation. The measurements were performed up to a TOS of 1.5 h.

Setup and conditions A fluidized bed reactor with an internal diameter of 20 mm was applied. The catalyst bed was placed on a porous plate at a height of 285 mm from the bottom (total height of 465 mm). A ceramic chamber with a heating surrounded the whole reactor where the feed reactants were provided in liquid state. The temperature was measured both within the catalyst bed and in the vaporization chamber. A GC equipped with one column and an FID was used for product analysis. The whole setup is explained in detail in another publication [284]. For the experiments, alumina as diluent was mixed with the catalyst using a ratio of 1:4 on a weight base. Feed compositions with different gravimetric water/methanol ratios from 0 to 3 were analyzed.

Reaction network As it is obvious from Scheme 2.34, this model describes the reaction system with four lumps: Ox, $C_{2\text{-}5}^=$, C_1 and Int. The latter considers the initiation phase during which the oxygenates build up the first compounds of the hydrocarbon pool which themselves react with further oxygenates to higher intermediates (see Section 2.3). This lump is not further classified, but both the formation out of oxygenates (k_2) and the autocatalytic behavior (k_3) are taken into account. The two remaining steps describe the olefin (k_4) and methane (k_5) evolution, the latter being the only side product detected. Because of the small pores, no species with a carbon number higher than five are detected. Although the reaction between methanol and DME is shown with a kinetic rate constant (k_1) in the original publication, which is similar to the ZSM-5 model by the same authors [173], both oxygenates are summarized to one lump in the model [256]. In another study [284], the authors observed that the amount of intermediates is almost independent of contact time. Thus, their evolution is only evaluated as time-dependent variable (see Scheme 2.34). The adsorption of water is assumed to attenuate the other reaction rates which is why the equations are written as HW type of mechanism without the adsorption of all other compounds. The steps are implemented as elementary reactions and no stoichiometry is retained. All steps are defined as irreversible. The model also describes the deactivation through coke deposition. For this, a rate constant for deactivation r^{d} is introduced. Furthermore,

all reaction rates except for methane production are multiplied with the activity a. This value expresses the ratio of the olefin production rate at a certain TOS to the one when activity would be unity, i.e., the fresh catalyst. For the deactivation rate, a different equilibrium constant and a different exponent of water adsorption are assumed.

$$\begin{aligned}
\mathrm{Ox} &\xrightarrow{k_2} \mathrm{Int} & r_2 &= \frac{k_2\, w_\mathrm{C}(\mathrm{Ox})\, a}{1+K^\mathrm{ads}(\mathrm{H_2O})\, w_\mathrm{C}(\mathrm{H_2O})^{n_{\mathrm{H_2O}}}} \\
k_2^\mathrm{ref} &= (2.39 \pm 2.04) \times 10^{-3}\,\mathrm{h}^{-1} & E_{\mathrm{a},2} &= 69.454 \pm 51.128\,\mathrm{kJ\,mol}^{-1} \\
\mathrm{Ox} + \mathrm{Int} &\xrightarrow{k_3} \mathrm{Int} & r_3 &= \frac{k_3\, w_\mathrm{C}(\mathrm{Ox})\, w_\mathrm{cat}(\mathrm{Int})\, a}{1+K^\mathrm{ads}(\mathrm{H_2O})\, w_\mathrm{C}(\mathrm{H_2O})^{n_{\mathrm{H_2O}}}} \\
k_3^\mathrm{ref} &= 171.600 \pm 6.035\,\mathrm{h}^{-1} & E_{\mathrm{a},3} &= 55.354 \pm 2.853\,\mathrm{kJ\,mol}^{-1} \\
\mathrm{Ox} + \mathrm{Int} &\xrightarrow{k_4} \mathrm{C}_{2-5}^{=} & r_4 &= \frac{k_4\, w_\mathrm{C}(\mathrm{Ox})\, w_\mathrm{cat}(\mathrm{Int})\, a}{1+K^\mathrm{ads}(\mathrm{H_2O})\, w_\mathrm{C}(\mathrm{H_2O})^{n_{\mathrm{H_2O}}}} \\
k_4^\mathrm{ref} &= 7.023 \pm 0.297\,\mathrm{h}^{-1} & E_{\mathrm{a},4} &= 57.153 \pm 1.636\,\mathrm{kJ\,mol}^{-1} \\
\mathrm{Ox} + \mathrm{Int} &\xrightarrow{k_5} \mathrm{C}_1 & r_5 &= \frac{k_5\, w_\mathrm{C}(\mathrm{Ox})\, w_\mathrm{cat}(\mathrm{Int})}{1+K^\mathrm{ads}(\mathrm{H_2O})\, w_\mathrm{C}(\mathrm{H_2O})^{n_{\mathrm{H_2O}}}} \\
k_5^\mathrm{ref} &= (5.62 \pm 4.29) \times 10^{-3}\,\mathrm{h}^{-1} & E_{\mathrm{a},5} &= 126.943 \pm 20.083\,\mathrm{kJ\,mol}^{-1} \\
K^\mathrm{ads}(\mathrm{H_2O}) &= 0.634 \pm 0.025 & n_{\mathrm{H_2O}} &= 1 \\
r(\mathrm{Int}) &= \frac{\mathrm{d}w_\mathrm{cat}(\mathrm{Int})}{\mathrm{d}t} = \frac{k_2\, w_\mathrm{C}(\mathrm{Ox})\, a + k_3\, w_\mathrm{C}(\mathrm{Ox})\, w_\mathrm{cat}(\mathrm{Int})\, a}{1+K^\mathrm{ads}(\mathrm{H_2O})\, w_\mathrm{C}(\mathrm{H_2O})^{n_{\mathrm{H_2O}}}} & r^\mathrm{d} &= -\frac{\mathrm{d}a}{\mathrm{d}t} = \frac{k^\mathrm{d}\left(w_\mathrm{C}(\mathrm{Ox}) + w_\mathrm{C}\left(\mathrm{C}_{2-5}^{=}\right)\right) a^{n^\mathrm{d}}}{1+K^{\mathrm{d,ads}}(\mathrm{H_2O})\, w_\mathrm{C}(\mathrm{H_2O})^{n^\mathrm{d}_{\mathrm{H_2O}}}} \\
k^{\mathrm{d,ref}} &= 31.36 \pm 18.36\,\mathrm{h}^{-1} & E_\mathrm{a}^\mathrm{d} &= 26.355 \pm 21.464\,\mathrm{kJ\,mol}^{-1} \\
n^\mathrm{d} &= 1.5 & K^{\mathrm{d,ads}}(\mathrm{H_2O}) &= 1 \\
n^\mathrm{d}_{\mathrm{H_2O}} &= 1.5
\end{aligned}$$

Scheme 2.34: Reaction network, rate equations and estimated parameters for the model by Gayubo *et al.* [255] over SAPO-18 (four lumps).

Scheme 2.35 contains the resulting net rates of production.

$$\begin{aligned}
R(\mathrm{Ox}) &= \frac{-k_4\, w_\mathrm{C}(\mathrm{Ox})\; w_\mathrm{cat}(\mathrm{Int})\; a - k_5\, w_\mathrm{C}(\mathrm{Ox})\; w_\mathrm{cat}(\mathrm{Int})}{1 + K^\mathrm{ads}(\mathrm{H_2O})\; w_\mathrm{C}(\mathrm{H_2O})^{n_{\mathrm{H_2O}}}} \\
R\left(\mathrm{C}_{2-5}^{=}\right) &= \frac{k_4\, w_\mathrm{C}(\mathrm{Ox})\; w_\mathrm{cat}(\mathrm{Int})\; a}{1 + K^\mathrm{ads}(\mathrm{H_2O})\; w_\mathrm{C}(\mathrm{H_2O})^{n_{\mathrm{H_2O}}}} \\
R(\mathrm{C}_1) &= \frac{k_5\, w_\mathrm{C}(\mathrm{Ox})\; w_\mathrm{cat}(\mathrm{Int})}{1 + K^\mathrm{ads}(\mathrm{H_2O})\; w_\mathrm{C}(\mathrm{H_2O})^{n_{\mathrm{H_2O}}}}
\end{aligned}$$

Scheme 2.35: Net rates of production of the different lumps for the model by Gayubo *et al.* [255] over SAPO-18 (four lumps).

The reaction network for the five-lump model [256] is based on the previous one for SAPO-18, but the lump $\mathrm{C}_{2\text{-}5}^{=}$ is replaced by three separate olefin lumps $\mathrm{C}_2^{=}$, $\mathrm{C}_3^{=}$ and $\mathrm{C}_{4+}^{=}$ in order to account for their different reactivities and evolutions depending on the reaction conditions. In the publication, five different networks with varying complexity for olefin interconversion are introduced and the one presented in Scheme 2.36 is chosen after an evaluation with the Fisher test. It should be noted that, except for the replacement of Step (4) with Steps (4a), (4b) and (4c), the same reaction network as in Scheme 2.34 applies. The earlier rate constant k_4 should

yield the sum of k_{4a}, k_{4b} and k_{4c}. The deactivation approach is unselective: the activity a relates the production rate after a certain TOS to the value at $a = 1$ for ethene, propene and higher olefins.

$$
\begin{aligned}
\mathrm{Ox} + \mathrm{Int} &\xrightarrow{k_{4a}} \mathrm{C}_2^{=} & r_{4a} &= \frac{k_{4a}\, w_C(\mathrm{Ox})\, w_{cat}(\mathrm{Int})\, a}{1+K^{ads}(\mathrm{H_2O})\, w_C(\mathrm{H_2O})} \\
k_{4a}^{ref} &= 1.344 \pm 0.092\,\mathrm{h}^{-1} & E_{a,4a} &= -82.216 \pm 2.887\,\mathrm{kJ\,mol}^{-1} \\
\mathrm{Ox} + \mathrm{Int} &\xrightarrow{k_{4b}} \mathrm{C}_3^{=} & r_{4b} &= \frac{k_{4b}\, w_C(\mathrm{Ox})\, w_{cat}(\mathrm{Int})\, a}{1+K^{ads}(\mathrm{H_2O})\, w_C(\mathrm{H_2O})} \\
k_{4b}^{ref} &= 4.037 \pm 0.148\,\mathrm{h}^{-1} & E_{a,4b} &= -55.647 \pm 1.966\,\mathrm{kJ\,mol}^{-1} \\
\mathrm{Ox} + \mathrm{Int} &\xrightarrow{k_{4c}} \mathrm{C}_{4+}^{=} & r_{4c} &= \frac{k_{4c}\, w_C(\mathrm{Ox})\, w_{cat}(\mathrm{Int})\, a}{1+K^{ads}(\mathrm{H_2O})\, w_C(\mathrm{H_2O})} \\
k_{4c}^{ref} &= 2.266 \pm 0.118\,\mathrm{h}^{-1} & E_{a,4c} &= -43.932 \pm 2.720\,\mathrm{kJ\,mol}^{-1} \\
k_2^{ref} &= (2.486 \pm 0.877) \times 10^{-3}\,\mathrm{h}^{-1} & E_{a,2} &= -57.823 \pm 42.677\,\mathrm{kJ\,mol}^{-1} \\
k_3^{ref} &= 181.100 \pm 6.035\,\mathrm{h}^{-1} & E_{a,3} &= -61.379 \pm 4.519\,\mathrm{kJ\,mol}^{-1} \\
k_5^{ref} &= (4.652 \pm 5.210) \times 10^{-3}\,\mathrm{h}^{-1} & E_{a,5} &= -136.566 \pm 36.610\,\mathrm{kJ\,mol}^{-1} \\
k^{d,ref} &= 36.070 \pm 6.105\,\mathrm{h}^{-1} & E_a^{d} &= -23.849 \pm 4.602\,\mathrm{kJ\,mol}^{-1} \\
K^{ads}(\mathrm{H_2O}) &= 0.655 \pm 0.011
\end{aligned}
$$

Scheme 2.36: Reaction network, rate equations and estimated parameters for the model by Gayubo *et al.* [256] over SAPO-18 (five lumps); the corresponding equations for Steps (2), (3), (5) and (d) can be found in Scheme 2.34.

The net rates of production are the same as for the four-lump model except that $R\left(\mathrm{C}_{2-5}^{=}\right)$ has to be replaced by $R\left(\mathrm{C}_2^{=}\right)$, $R\left(\mathrm{C}_3^{=}\right)$ and $R\left(\mathrm{C}_{4+}^{=}\right)$, which correspond to r_{4a}, r_{4b} and r_{4c}.

Parameter estimation The mass fractions in Scheme 2.34 are defined with carbon units except for the intermediates where $y_{cat}(\mathrm{Int})$ is related to the mass of the fresh catalyst. Both the contact time dependent kinetic expressions as well as the TOS dependent equations for deactivation and intermediates have to be solved simultaneously. For this, a MATLAB script based on finite differences in combination with orthogonal collocation [265] is written. Parameter estimation is performed with the Levenberg-Marquardt algorithm where the objective function evaluates the unweighted squared differences between modeled and experimental mass fractions. Reparameterization according to Equation (2.21) is performed with a reference temperature of 623 K which is close to the lowest investigated value. Different values for n^{d}, $n_{\mathrm{H_2O}}$, $n_{\mathrm{H_2O}}^{d}$ and $K^{d,ads}\left(\mathrm{H_2O}\right)$ are tried, the results with the best fit are shown in Scheme 2.34. Without these, eleven unknown parameters remain: five reference rate constants, five activation energies and one equilibrium constant for water adsorption. For the version with five lumps, 15 parameters are estimated: seven reference rate constants, seven activation energies and one equilibrium constant for water adsorption. As it can be seen in Scheme 2.36, the values which were already included in the model with four lumps [255] are fitted another time here.

Kumar *et al.* [38]: Microkinetic implementation over ZSM-23

Catalyst The authors used a commercial ZSM-23 sample without any binder provided by Zeolyst International. The relatively low Si/Al ratio of 26 caused a high number of acid sites ($0.62\,\mathrm{mol\,kg_{cat}^{-1}}$). The zeolite showed significant deactivation effects due to coke formation [39]. However, it was observed that the selectivity at a specific conversion level is independent of the coke amount [131]. Through the linear dependence between TOS and contact time until a certain conversion is achieved, an effective contact time is calculated in this study. This allows describing intrinsic kinetics free of interfering deactivation effects.

Setup and conditions The continuous fixed bed glass reactor had an inner diameter of 10 mm. It was fed by a saturator with helium as carrier and dilution gas. A GC equipped with an FID and one column enabled product analysis. In this study, only one temperature was analyzed; it was controlled by a thermocouple placed in the middle of the catalyst bed [285, 286].

Reaction network The network is almost similar to the ZSM-5 model by the same authors; the only differences are caused by the use of a different catalyst [10]. Over ZSM-23, profound ethene formation out of olefins is observed which is why two additional cracking routes leading to primary intermediates are introduced, starting from either tertiary or from secondary intermediates. Because the backward reaction takes also place, protonation to a primary intermediate has to be included; the stability difference between secondary and primary intermediates is an additional fitting parameter in this model. Physisorption is included with own experimental data of alkanes over ZSM-22 [287] which are applicable to ZSM-23 [288]. As in the ZSM-5 case, the formation of side products and especially of aromatics is negligible. Finally, 142 pathways of kinetic relevance are obtained. The following responses are fitted to the measurements: Ox, $C_2^=$, $C_3^=$, $C_4^=$, $C_5^=$, $C_{6+}^=$ and C_1. The amount of methanol within the Ox lump is calculated from a carbon balance, whereas water is obtained from a hydrogen balance.

Parameter estimation The numerical routine is similar to the ZSM-5 case. The kinetic descriptors determined earlier [18] are held constant, whereas the different catalyst descriptors are estimated. This leads to eight fitted parameters: two activation energies including primary intermediates, five protonation enthalpies and one stability difference between primary and secondary intermediates. In addition, the total concentration of aromatic hydrocarbon pool species is also obtained via regression as this value changes with a different catalyst type.

Summary

Because of the smaller pore size, deactivation is more pronounced over SAPO-34, SAPO-18 and ZSM-23 compared to ZSM-5 and cannot be ignored during kinetic evaluation. The four

models over SAPO-34 show different methodologies to consider this fact. Gayubo *et al.* [251] chose conditions where deactivation effects are minimized and extrapolate their results to a fresh catalyst. This is why they could neglect coking effects in their model. Alwahabi and Froment [254] had a similar approach as they use kinetic measurements of an almost fresh catalyst and simulate deactivation with separate data. Ying *et al.* [252] estimate their parameters according to their kinetic scheme first; in a subsequent step, these are held constant, whereas rate-specific deactivation parameters are fitted. This procedure requires kinetic data free of deactivation effects for the first step. By contrast, Chen *et al.* [253] estimate these rate-specific deactivation values directly with the kinetic parameters. Except for the microkinetic approach by Alwahabi and Froment [254], the different reactivity of DME is ignored through lumping both oxygenates (Gayubo *et al.* [251] and Chen *et al.* [253]) or through considering only reactions starting from methanol (Ying *et al.* [252]). In the latter study, all olefin interconversion steps as well as methylation reactions are neglected. The same holds for the model by Chen *et al.* [253]. On the other hand, both approaches consider side product formation which is also included for Gayubo *et al.* [251]. In the latter, methylation is also missing, whereas some olefin interconversion steps are assumed. In the five-lump version, lumping of final and intermediate products might impede extrapolation; this is also observed for Ying *et al.* [252]. Furthermore, in the approach with five lumps, the olefin interconversion steps are removed. On the other hand, this model as well as Ying *et al.* [252] consider water adsorption in an HW type of mechanism which is ignored for Chen *et al.* [253]. Finally, the approach by Alwahabi and Froment [254] depicts almost complete reactivity, but at cost of complex reaction networks and high computational effort. The SAPO-18 model by Gayubo *et al.* [255] is comparable to the SAPO-34 case. However, this version includes deactivation parameters which are directly fitted to the kinetic data. This model is the only one found in literature that explicitly describes the evolution of the initiation phase via a lump of intermediates. The five-lump version [256] additionally has the advantage that the lower olefins are split up to separate lumps. Finally, Kumar *et al.* [38] take advantage of the effect that selectivity is independent of coking at a certain conversion level. Through a linear approach, they convert data at specific TOS to the performance of a fresh catalyst. Besides this, the model is almost identical to the one over ZSM-5 with the same advantages and disadvantages. The transfer to ZSM-23 shows how a separation of kinetic and catalyst descriptors [21] allows one to move a specific model obtained on a certain catalyst to another one by holding the kinetics constant and by adapting the reaction network and catalyst specific values.

Other studies

Another well-known model is the one by Kaarsholm *et al.* [289]. Here, a commercial ZSM-5 zeolite was further modified. The final catalyst contained 1.5% of P. Experiments were performed at temperatures between 673 and 823 K. The feed consisted either of pure methanol or of

mixtures with water or argon. Deactivation effects can be neglected for the kinetics. A fluidized bed reactor model is combined with a kinetic scheme consisting of eleven lumps. Here, 16 unknown parameters are estimated to experimental data. The model includes water adsorption in an HW type of mechanism. Furthermore, side product formation is covered. Methanol and DME are assumed to be equilibrated throughout the whole reactor. All steps producing hydrocarbons out of the oxygenates have to proceed via a protonated intermediate with ten carbon atoms.

In a recent study by Yuan *et al.* [290], a kinetic model is derived for converting methanol feeds over a commercial SAPO-34 catalyst. The authors conducted experiments in a fluidized bed reactor at temperatures between 698–763 K. The feed was diluted using nitrogen. The kinetic model consists of nine lumps and requires 34 parameters. The dual cycle is implemented via two virtual species, one characterizing the olefin and another one resembling the aromatic hydrocarbon pool. Deactivation is also considered to describe the product evolution as function of TOS. Several reactor modeling studies were already published by this group [291–293].

In the approach by Strizhak *et al.* [294], a 1:1 mixture of commercial ZSM-5 zeolite (Si/Al ratio of 35.4) and alumina was analyzed at temperatures between 513 and 693 K. The methanol feed was diluted with argon, leading to methanol partial pressures between 0.055 and 0.236 bar. Different theoretical reaction mechanisms are compared to the experimental data. Highest agreement is achieved when the DME formation is assumed to occur on Lewis acid sites, whereas the conversion of oxygenates takes place on Brønsted acid sites.

Other studies in this context are the ones by Sedighi *et al.* [295], Fatourehchi *et al.* [296], Taheri Najafabadi *et al.* [297] and Azarhoosh *et al.* [298].

2.6.3 MTO with Olefin Co-Feed

The properties of the catalysts are listed in Table 2.5 and an overview of experimental conditions as well as modeling details are found in Table 2.6. Then, an explanation of the different models follows, focusing on studies where olefins are co-fed with the oxygenates. Consequently, the initiation phase should disappear which leads to a direct increase of oxygenates conversion (see Section 2.3). No division into different parts is performed because there are only two models: the one by Huang *et al.* [241] and the one by Wen *et al.* [299]. The former is a subsequent study to the olefin interconversion work discussed above.

Table 2.5: Properties of the different catalysts which were used for the kinetic models of methanol-to-olefins with olefin co-feed; besides the zeolite type, its silicon-to-aluminum ratio, its total number of acid sites plus determination method, its ratio of Brønsted to Lewis acid sites BAS/LAS and its surface area according to the method by Brunauer-Emmett-Teller BET are shown; furthermore, the time-on-stream TOS after which the kinetic data were taken, the particle size d_P and the information whether an extrudate or pure powder was used are presented; a hyphen resembles missing information.

Model	Zeolite type	Si/Al	Total acidity	BAS/LAS	BET	TOS	d_P	Extrudate
Huang [241]	ZSM-5	200[(a)]	0.012 mmol g_{cat}^{-1} (NH_3)	1.35 at 423 K	301.1 m^2 g_{cat}^{-1}	0–10 h[(b)]	125–149 µm	70/30%$_{wt}$ (Zeolite/alumina)
Wen [299]	ZSM-5 on microfibers	147	-	-	93 m^2 g_{cat}^{-1} [(c)]	-	16.1 mm[(d)]	No, but 19/81%$_{wt}$ (Zeolite/microfiber)
	ZSM-5	155	-	-	-	-	100–300 µm	No

[(a)] Value of the zeolite, i.e., without binder
[(b)] Regeneration after 10 h TOS
[(c)] Extracted from another publication [300]
[(d)] Diameter of the circular sample chips

Table 2.6: Experimental conditions and modeling details for the kinetic models of methanol-to-olefins with olefin co-feed; the feed components, the temperature range T, the total pressure p_t, the partial pressure range of the feed oxygenates as well as the feed olefins $p(i)$ (in that order) and the maximum contact time $(W/F^{in})_{max}$ with resulting oxygenates conversion X_{max} are listed; concerning the model, the number of fitted responses N_{Res}, the number of estimated parameters N_{Par}, the number of experiments N_{Exp} and the degree of freedom *dof* are shown; finally, it is noted whether the model follows a type of a mechanistical scheme, whether adsorption is considered and which side products are included; a hyphen resembles missing information.

Model	Feed	T	p_t	$p(i)$	$(W/F^{in})_{max}$	X_{max}	N_{Res}	N_{Par}	N_{Exp}	*dof*	Mech.	Ads.	Side prod.
Huang [241]	MeOH, $C_3^=$, N_2, H_2O[a]	673–763 K	1.013 bar	0.050 bar, 0.050 bar	4.3 g_{cat} s mol_t^{-1}	0.90	8	20	79	612	LH, HW, ER	$C_{2\text{-}7}^=$, H_2O, MeOH	No[b]
	MeOH, $C_4^=$, N_2, H_2O[a]				2.9 g_{cat} s mol_t^{-1}	0.92							
	MeOH, $C_5^=$, N_2, H_2O[a]				2.5 g_{cat} s mol_t^{-1}	0.92							
	MeOH, $C_6^=$, N_2, H_2O[a]				2.5 g_{cat} s mol_t^{-1}	0.92							
Wen [299][c]	MeOH, N_2[d]	673–753 K	1.013 bar[e]	0.304 bar	32 g_{cat} h mol_C^{-1}	1	10	38	46	422	No	No	$C_{1\text{-}6}$
Wen [299][c]	MeOH, N_2[d]	673–753 K	1.013 bar[e]	0.304 bar	32 g_{cat} h mol_C^{-1}	1	10	38	45	412	No	No	$C_{1\text{-}6}$

[a] Respective *n*-alcohol was fed instead of the olefin
[b] Side product formation included in subsequent publication [301]
[c] Similar kinetic model for microfibered (first line) and powdered (second line) catalyst, but different *dof*
[d] Pure methanol as feed, but model only works when olefins are present (comparable to co-feeding studies)
[e] Extracted from another publication [300]

Co-feed studies introduced in detail

Huang *et al.* [241]: Eight-lump approach extending the olefin cracking model to MTO

Catalyst The authors used the same catalyst as for the olefin cracking study [195], see above.

Setup and conditions The reaction equipment is already described above. However, another GC column was used here for better separating the oxygenates from the olefins. The partial pressure of water was held constant at 0.24 bar for all measurements which includes the amount released during alcohol dehydration.

Reaction network All reactions from the olefin interconversion model by the same authors [195] are also included here. This network is extended with the methanol-related reactions in Scheme 2.37, which include the conversion to DME and water (k_{11}) as well as methylation steps (k_{12}–k_{18}). Consequently, the following lumps are described: MeOH, DME, $C_2^=$, $C_3^=$, $C_4^=$, $C_5^=$, $C_6^=$ and $C_{7+}^=$. Because of the fast reaction progress under co-feeding conditions, no comparably slow conversion steps of oxygenates to hydrocarbons are implemented. For the same reason, the reaction of methanol to DME and water is not treated as equilibrated: based on experiments and calculations, the authors could show that the fast methylation disturbs the equilibration of the oxygenates. Only propene to hexene are considered as possible reactants for methylations as an earlier study proved this reaction to be very slow when having ethene as co-feed [102]. A mechanistic pathway is implemented here: the methanol chemisorption on a Brønsted acid site leads to a surface methyl group, which methylates an olefin reacting out of the gas phase in a subsequent step. Besides the olefin interconversion steps implemented as combination of LH and HW types of mechanism, the network thus comprises irreversible methylation steps expressed as ER type of mechanism. A first regression without Steps (16)–(18) showed significant deviation especially for propene and butenes, indicating the absence of an important pathway for these species. The comparison with experimental results from Svelle *et al.* [101] leads to the formulation of double methylation reactions. Here [101], it was observed that pentenes contain marked ^{13}C methanol in an amount that cannot be explained by simple stepwise methylation reactions of the co-fed ^{12}C propene. Based on these experiments, Huang *et al.* [241] formulate the double methylation of propene and butenes as well as a triple methylation of propene; all these are also assumed as ER type of mechanism, meaning that two or three methanol molecules have to be chemisorbed first. As for the olefin interconversion model by the same authors [195], stoichiometry is retained and adsorption is considered for all hydrocarbons, for methanol and for water (HW type of mechanism), but not for DME. Furthermore, the methylation through DME is not considered. In this work, side products are neglected because of short contact times. The

yield of aromatics and paraffins was below 0.4% in all experiments. However, in a subsequent study [301], their formation is explicitly included.

$$
\begin{aligned}
2\mathrm{MeOH} \underset{k_{11}/K_{11}}{\overset{k_{11}}{\rightleftharpoons}} \mathrm{DME} + \mathrm{H_2O} \qquad & r_{11} = \frac{k_{11}}{Den^2}\left(p\,(\mathrm{MeOH})^2 - \frac{1}{K_{11}}\,p\,(\mathrm{DME})\;p\,(\mathrm{H_2O})\right) \\
k_{11}^{\mathrm{ref}} = (6.78 \pm 0.23) \times 10^{-3}\,\mathrm{mol\,kg_{cat}^{-1}\,s^{-1}\,kPa^{-2}} \qquad & E_{\mathrm{a},11} = 36.29 \pm 6.94\,\mathrm{kJ\,mol^{-1}} \\
K_{11}^{\mathrm{ref}} = 1.19 \pm 0.30\,\mathrm{kPa^{-2}} \qquad & \Delta_{\mathrm{r}}H_{11}^{\circ} = -15.85 \pm 3.35\,\mathrm{kJ\,mol^{-1}} \\
\mathrm{C_3^=} + \mathrm{MeOH} \xrightarrow{k_{12}} \mathrm{C_4^=} + \mathrm{H_2O} \qquad & r_{12} = \frac{k_{12}}{Den^2}\,p\,(\mathrm{C_3^=})\;p\,(\mathrm{MeOH}) \\
k_{12}^{\mathrm{ref}} = (2.11 \pm 0.39) \times 10^{-3}\,\mathrm{mol\,kg_{cat}^{-1}\,s^{-1}\,kPa^{-2}} \qquad & E_{\mathrm{a},12} = 49.68 \pm 6.14\,\mathrm{kJ\,mol^{-1}} \\
\mathrm{C_4^=} + \mathrm{MeOH} \xrightarrow{k_{13}} \mathrm{C_5^=} + \mathrm{H_2O} \qquad & r_{13} = \frac{k_{13}}{Den^2}\,p\,(\mathrm{C_4^=})\;p\,(\mathrm{MeOH}) \\
k_{13}^{\mathrm{ref}} = (5.20 \pm 0.78) \times 10^{-3}\,\mathrm{mol\,kg_{cat}^{-1}\,s^{-1}\,kPa^{-2}} \qquad & E_{\mathrm{a},13} = 69.19 \pm 4.73\,\mathrm{kJ\,mol^{-1}} \\
\mathrm{C_5^=} + \mathrm{MeOH} \xrightarrow{k_{14}} \mathrm{C_6^=} + \mathrm{H_2O} \qquad & r_{14} = \frac{k_{14}}{Den^2}\,p\,(\mathrm{C_5^=})\;p\,(\mathrm{MeOH}) \\
k_{14}^{\mathrm{ref}} = (7.80 \pm 0.98) \times 10^{-3}\,\mathrm{mol\,kg_{cat}^{-1}\,s^{-1}\,kPa^{-2}} \qquad & E_{\mathrm{a},14} = 53.10 \pm 5.69\,\mathrm{kJ\,mol^{-1}} \\
\mathrm{C_6^=} + \mathrm{MeOH} \xrightarrow{k_{15}} \mathrm{C_7^=} + \mathrm{H_2O} \qquad & r_{15} = \frac{k_{15}}{Den^2}\,p\,(\mathrm{C_6^=})\;p\,(\mathrm{MeOH}) \\
k_{15}^{\mathrm{ref}} = (7.50 \pm 1.08) \times 10^{-3}\,\mathrm{mol\,kg_{cat}^{-1}\,s^{-1}\,kPa^{-2}} \qquad & E_{\mathrm{a},15} = 41.99 \pm 5.63\,\mathrm{kJ\,mol^{-1}} \\
\mathrm{C_3^=} + 2\mathrm{MeOH} \xrightarrow{k_{16}} \mathrm{C_5^=} + 2\mathrm{H_2O} \qquad & r_{16} = \frac{k_{16}}{Den^3}\,p\,(\mathrm{C_3^=})\;p\,(\mathrm{MeOH})^2 \\
k_{16}^{\mathrm{ref}} = (7.80 \pm 0.33) \times 10^{-5}\,\mathrm{mol\,kg_{cat}^{-1}\,s^{-1}\,kPa^{-3}} \qquad & E_{\mathrm{a},16} = 25.27 \pm 11.27\,\mathrm{kJ\,mol^{-1}} \\
\mathrm{C_4^=} + 2\mathrm{MeOH} \xrightarrow{k_{17}} \mathrm{C_6^=} + 2\mathrm{H_2O} \qquad & r_{17} = \frac{k_{17}}{Den^3}\,p\,(\mathrm{C_4^=})\;p\,(\mathrm{MeOH})^2 \\
k_{17}^{\mathrm{ref}} = (9.24 \pm 1.52) \times 10^{-4}\,\mathrm{mol\,kg_{cat}^{-1}\,s^{-1}\,kPa^{-3}} \qquad & E_{\mathrm{a},17} = 11.98 \pm 3.66\,\mathrm{kJ\,mol^{-1}} \\
\mathrm{C_3^=} + 3\mathrm{MeOH} \xrightarrow{k_{18}} \mathrm{C_6^=} + 3\mathrm{H_2O} \qquad & r_{18} = \frac{k_{18}}{Den^4}\,p\,(\mathrm{C_3^=})\;p\,(\mathrm{MeOH})^3 \\
k_{18}^{\mathrm{ref}} = (1.83 \pm 0.42) \times 10^{-4}\,\mathrm{mol\,kg_{cat}^{-1}\,s^{-1}\,kPa^{-4}} \qquad & E_{\mathrm{a},18} = 1.10 \pm 2.87\,\mathrm{kJ\,mol^{-1}} \\
Den = 1 + K^{\mathrm{ads}}\left(\mathrm{C_{2-7}^=}\right)\sum_j p\left(\mathrm{C_j^=}\right) + K^{\mathrm{ads}}\,(\mathrm{H_2O})\;p\,(\mathrm{H_2O}) + K^{\mathrm{ads}}\,(\mathrm{MeOH})\;p\,(\mathrm{MeOH}) \qquad & \\
K^{\mathrm{ads,ref}}\,(\mathrm{MeOH}) = (4.36 \pm 0.35) \times 10^{-2}\,\mathrm{kPa^{-1}} \qquad & \Delta_{\mathrm{ads}}H_{\mathrm{MeOH}}^{\circ} = -47.50 \pm 4.59\,\mathrm{kJ\,mol^{-1}}
\end{aligned}
$$

Scheme 2.37: Reaction network, rate equations and estimated parameters for the model by Huang *et al.* [241] with *j* ranging from 2 to 7.

Because the reaction rates are rather complex, only r_l is shown for the net rates of production in Scheme 2.38.

$$
\begin{aligned}
R\,(\mathrm{MeOH}) &= -2\,r_{11} - r_{12} - r_{13} - r_{14} - r_{15} - 2\,r_{16} - 2\,r_{17} - 3\,r_{18} \\
R\,(\mathrm{DME}) &= r_{11} \\
R\,(\mathrm{C_2^=}) &= r_3 + r_6 \\
R\,(\mathrm{C_3^=}) &= r_2 + r_3 + 2\,r_4 + 2\,r_7 + r_8 + r_{10} - 3\,r_1 - r_{12} - r_{16} - r_{18} \\
R\,(\mathrm{C_4^=}) &= r_1 + r_4 + r_5 + r_6 + r_8 + 3\,r_9 + r_{10} + r_{12} - 2\,r_2 - r_{13} - r_{17} \\
R\,(\mathrm{C_5^=}) &= r_1 + r_2 + r_8 + r_{13} + r_{16} - r_3 - 2\,r_4 - 2\,r_5 - r_{14} \\
R\,(\mathrm{C_6^=}) &= r_5 + r_{14} + r_{17} + r_{18} - r_6 - r_7 - 2\,r_8 - 2\,r_9 - r_{15} \\
R\,(\mathrm{C_7^=}) &= r_{15} - r_{10}
\end{aligned}
$$

Scheme 2.38: Net rates of production of the different lumps for the model by Huang *et al.* [241].

Parameter estimation Details about the numerical routine can be found above. All parameters estimated there are kept constant during fitting the MTO model. For the latter, 20 unknown values exist: eight reference rate constants, eight activation energies, two reference equilibrium constants, one reaction enthalpy and one adsorption enthalpy. This includes the equilibrium constant of methanol dehydration because the experimental value deviated from the theoretical one calculated via thermodynamics. The final kinetic description, enriched with the side reactions [301], is used in subsequent studies to create a heterogeneous model for the recycle reactor [99, 302] or of a monolith reactor [303].

Wen *et al.* [299]: Ten-lump model being valid for ZSM-5 powder and for ZSM-5 on stainless steel fibers

Catalyst A regular ZSM-5 zeolite as well as a catalyst consisting of ZSM-5 crystals grown on three-dimensional stainless steel microfibers were analyzed. The latter showed improved stability and propene yields in earlier studies [300, 304]. This is attributed to higher resistances to the aromatic hydrocarbon pool which reduces ethene formation and to a narrow residence distribution being optimal for propene as intermediate. Furthermore, the small zeolite shell being only a few micrometers thick increases mass transfer as well as acid sites efficiency and thus activity compared to regular powder. Both samples were self-synthesized, but Western Metal Material provided the stainless steel fibers with a diameter of 20 µm and a voidage of 85%. Through the dip-coating method [300], a catalyst with 19%$_{wt}$ ZSM-5 and a Si/Al ratio of 147 was obtained. The powder exhibited a comparable Si/Al value of 155.

Setup and conditions Kinetic experiments were performed in a continuous fixed bed reactor made of quartz glass which had an inner diameter of 16 mm. An electrical furnace surrounding the reactor allowed for elevated temperatures. Methanol was fed in liquid state, evaporated and mixed with nitrogen as diluent. The fibered samples, provided as circular chips, were filled in layer by layer. Their diameter was 0.1 mm larger compared to the reactor to avoid bypass effects. By contrast, the application of quartz sand as diluent enabled comparable bed volumes for the powder sample. For product analysis, the authors used a GC having one column and an FID. As shown in Table 2.6, solely methanol was applied as feed. However, the model only works when olefins are present, otherwise, ethene and paraffins are produced exclusively. Therefore, the application range is similar to co-feeding conditions.

Reaction network For both samples, the same model is applied which consists of ten lumps: MeOH, DME, $C_2^=$, $C_3^=$, $C_4^=$, $C_5^=$, $C_6^=$, $C_{7+}^=$, C_1 and $C_{2\text{-}6}$. The reactions outlined in Scheme 2.39 can be divided into six parts: oxygenates interconversion (k_1 and k_2), methylation (k_3–k_6), olefin interconversion (k_7–k_{13} and k_{19}), oxygenates conversion to olefins (k_{14}) and paraffin formation out of olefins (k_{16} and k_{17}) as well as out of DME (k_{15} and k_{18}). The methylation is assumed

to occur exclusively via DME which increases the carbon number of two similar olefins ($C_3^=$ to $C_6^=$) by one each. As mentioned in the previous paragraph, the model does not start at zero contact time, but at a minimum value where the end of the initiation phase is reached which means that the first olefins are produced already. Because of the low reactivity at the beginning, the oxygenates reached an equilibrated state at the first data points. For their model, the authors implemented both the forward reaction and the backward reaction of methanol dehydration as step of kinetic relevance without any equilibrium constants. The contribution of the aromatic hydrocarbon pool is restricted to the conversion of DME to ethene for simplicity. In general, methanol is not considered as reactant except for DME production. The olefin interconversion comprises the cracking of pentenes and hexenes including backward reactions whereby these are separately fitted again. Moreover, the formation of higher olefins as well as the dimerization of butenes is considered, but without backward reaction. Finally, methane formation is limited to pentenes or DME, whereas the latter or propene can also react to lower paraffins. The origin of hydrogen necessary for methane formation is not resolved; water is ignored in the rate equations of Scheme 2.39. Adsorption effects and mechanistic routes are not covered by this model. According to the authors, the reaction orders are adjusted to have highest agreement, but in fact, all are set to one. This means stoichiometry is neglected, as it also has arbitrary values for the net rates of production.

$2\mathrm{MeOH} \xrightarrow{k_1} \mathrm{DME} + \mathrm{H_2O}$	$r_1 = k_1\, y\,(\mathrm{MeOH})$	$k_1^{\mathrm{MF,ref}} = 2.14\,\mathrm{mol_C\,h^{-1}\,g_{cat}^{-1}}$
$E_{\mathrm{a},1}^{\mathrm{MF}} = 13.46\,\mathrm{kJ\,mol^{-1}}$	$E_{\mathrm{a},1}^{\mathrm{PO}} = -1.77\,\mathrm{kJ\,mol^{-1}}$	$k_1^{\mathrm{PO,ref}} = 0.36\,\mathrm{mol_C\,h^{-1}\,g_{cat}^{-1}}$
$\mathrm{DME} + \mathrm{H_2O} \xrightarrow{k_2} 2\mathrm{MeOH}$	$r_2 = k_2\, y\,(\mathrm{DME})$	$k_2^{\mathrm{MF,ref}} = 3.70\,\mathrm{mol_C\,h^{-1}\,g_{cat}^{-1}}$
$E_{\mathrm{a},2}^{\mathrm{MF}} = 13.46\,\mathrm{kJ\,mol^{-1}}$	$E_{\mathrm{a},2}^{\mathrm{PO}} = -1.77\,\mathrm{kJ\,mol^{-1}}$	$k_2^{\mathrm{PO,ref}} = 0.64\,\mathrm{mol_C\,h^{-1}\,g_{cat}^{-1}}$
$2\mathrm{C_3^=} + \mathrm{DME} \xrightarrow{k_3} 2\mathrm{C_4^=} + \mathrm{H_2O}$	$r_3 = k_3\, y\,(\mathrm{C_3^=})\; y\,(\mathrm{DME})$	$k_3^{\mathrm{MF,ref}} = 13.90\,\mathrm{mol_C\,h^{-1}\,g_{cat}^{-1}}$
$E_{\mathrm{a},3}^{\mathrm{MF}} = 34.62\,\mathrm{kJ\,mol^{-1}}$	$E_{\mathrm{a},3}^{\mathrm{PO}} = 9.72\,\mathrm{kJ\,mol^{-1}}$	$k_3^{\mathrm{PO,ref}} = 1.73\,\mathrm{mol_C\,h^{-1}\,g_{cat}^{-1}}$
$2\mathrm{C_4^=} + \mathrm{DME} \xrightarrow{k_4} 2\mathrm{C_5^=} + \mathrm{H_2O}$	$r_4 = k_4\, y\,(\mathrm{C_4^=})\; y\,(\mathrm{DME})$	$k_4^{\mathrm{MF,ref}} = 43.92\,\mathrm{mol_C\,h^{-1}\,g_{cat}^{-1}}$
$E_{\mathrm{a},4}^{\mathrm{MF}} = 44.03\,\mathrm{kJ\,mol^{-1}}$	$E_{\mathrm{a},4}^{\mathrm{PO}} = 30.08\,\mathrm{kJ\,mol^{-1}}$	$k_4^{\mathrm{PO,ref}} = 7.32\,\mathrm{mol_C\,h^{-1}\,g_{cat}^{-1}}$
$2\mathrm{C_5^=} + \mathrm{DME} \xrightarrow{k_5} 2\mathrm{C_6^=} + \mathrm{H_2O}$	$r_5 = k_5\, y\,(\mathrm{C_5^=})\; y\,(\mathrm{DME})$	$k_5^{\mathrm{MF,ref}} = 47.25\,\mathrm{mol_C\,h^{-1}\,g_{cat}^{-1}}$
$E_{\mathrm{a},5}^{\mathrm{MF}} = 16.49\,\mathrm{kJ\,mol^{-1}}$	$E_{\mathrm{a},5}^{\mathrm{PO}} = 3.23\,\mathrm{kJ\,mol^{-1}}$	$k_5^{\mathrm{PO,ref}} = 16.96\,\mathrm{mol_C\,h^{-1}\,g_{cat}^{-1}}$
$2\mathrm{C_6^=} + \mathrm{DME} \xrightarrow{k_6} 2\mathrm{C_{7+}^=} + \mathrm{H_2O}$	$r_6 = k_6\, y\,(\mathrm{C_6^=})\; y\,(\mathrm{DME})$	$k_6^{\mathrm{MF,ref}} = 25.21\,\mathrm{mol_C\,h^{-1}\,g_{cat}^{-1}}$
$E_{\mathrm{a},6}^{\mathrm{MF}} = 125.89\,\mathrm{kJ\,mol^{-1}}$	$E_{\mathrm{a},6}^{\mathrm{PO}} = 151.27\,\mathrm{kJ\,mol^{-1}}$	$k_6^{\mathrm{PO,ref}} = 20.28\,\mathrm{mol_C\,h^{-1}\,g_{cat}^{-1}}$
$\mathrm{C_6^=} \xrightarrow{k_7} 2\mathrm{C_3^=}$	$r_7 = k_7\, y\,(\mathrm{C_6^=})$	$k_7^{\mathrm{MF,ref}} = 123.31\,\mathrm{mol_C\,h^{-1}\,g_{cat}^{-1}}$
$E_{\mathrm{a},7}^{\mathrm{MF}} = 109.08\,\mathrm{kJ\,mol^{-1}}$	$E_{\mathrm{a},7}^{\mathrm{PO}} = 0.22\,\mathrm{kJ\,mol^{-1}}$	$k_7^{\mathrm{PO,ref}} = 82.27\,\mathrm{mol_C\,h^{-1}\,g_{cat}^{-1}}$
$2\mathrm{C_3^=} \xrightarrow{k_8} \mathrm{C_6^=}$	$r_8 = k_8\, y\,(\mathrm{C_3^=})$	$k_8^{\mathrm{MF,ref}} = 4.39\,\mathrm{mol_C\,h^{-1}\,g_{cat}^{-1}}$
$E_{\mathrm{a},8}^{\mathrm{MF}} = 0.63\,\mathrm{kJ\,mol^{-1}}$	$E_{\mathrm{a},8}^{\mathrm{PO}} = -181.54\,\mathrm{kJ\,mol^{-1}}$	$k_8^{\mathrm{PO,ref}} = 1.25\,\mathrm{mol_C\,h^{-1}\,g_{cat}^{-1}}$
$\mathrm{C_6^=} \xrightarrow{k_9} \mathrm{C_2^=} + \mathrm{C_4^=}$	$r_9 = k_9\, y\,(\mathrm{C_6^=})$	$k_9^{\mathrm{MF,ref}} = 0.86\,\mathrm{mol_C\,h^{-1}\,g_{cat}^{-1}}$
$E_{\mathrm{a},9}^{\mathrm{MF}} = 1.15\,\mathrm{kJ\,mol^{-1}}$	$E_{\mathrm{a},9}^{\mathrm{PO}} = 120.32\,\mathrm{kJ\,mol^{-1}}$	$k_9^{\mathrm{PO,ref}} = 13.12\,\mathrm{mol_C\,h^{-1}\,g_{cat}^{-1}}$
$\mathrm{C_2^=} + \mathrm{C_4^=} \xrightarrow{k_{10}} \mathrm{C_6^=}$	$r_{10} = k_{10}\, y\,(\mathrm{C_2^=})\; y\,(\mathrm{C_4^=})$	$k_{10}^{\mathrm{MF,ref}} = 0.27\,\mathrm{mol_C\,h^{-1}\,g_{cat}^{-1}}$
$E_{\mathrm{a},10}^{\mathrm{MF}} = -103.56\,\mathrm{kJ\,mol^{-1}}$	$E_{\mathrm{a},10}^{\mathrm{PO}} = -48.92\,\mathrm{kJ\,mol^{-1}}$	$k_{10}^{\mathrm{PO,ref}} = 1.57\,\mathrm{mol_C\,h^{-1}\,g_{cat}^{-1}}$
$\mathrm{C_5^=} \xrightarrow{k_{11}} \mathrm{C_2^=} + \mathrm{C_3^=}$	$r_{11} = k_{11}\, y\,(\mathrm{C_5^=})$	$k_{11}^{\mathrm{MF,ref}} = 2.64\,\mathrm{mol_C\,h^{-1}\,g_{cat}^{-1}}$
$E_{\mathrm{a},11}^{\mathrm{MF}} = -61.72\,\mathrm{kJ\,mol^{-1}}$	$E_{\mathrm{a},11}^{\mathrm{PO}} = -143.09\,\mathrm{kJ\,mol^{-1}}$	$k_{11}^{\mathrm{PO,ref}} = 0.57\,\mathrm{mol_C\,h^{-1}\,g_{cat}^{-1}}$
$\mathrm{C_2^=} + \mathrm{C_3^=} \xrightarrow{k_{12}} \mathrm{C_5^=}$	$r_{12} = k_{12}\, y\,(\mathrm{C_2^=})\; y\,(\mathrm{C_3^=})$	$k_{12}^{\mathrm{MF,ref}} = 3.05\,\mathrm{mol_C\,h^{-1}\,g_{cat}^{-1}}$
$E_{\mathrm{a},12}^{\mathrm{MF}} = -123.64\,\mathrm{kJ\,mol^{-1}}$	$E_{\mathrm{a},12}^{\mathrm{PO}} = -200.00\,\mathrm{kJ\,mol^{-1}}$	$k_{12}^{\mathrm{PO,ref}} = 0.50\,\mathrm{mol_C\,h^{-1}\,g_{cat}^{-1}}$
$2\mathrm{C_4^=} \xrightarrow{k_{13}} \mathrm{C_3^=} + \mathrm{C_5^=}$	$r_{13} = k_{13}\, y\,(\mathrm{C_4^=})$	$k_{13}^{\mathrm{MF,ref}} = 0.03\,\mathrm{mol_C\,h^{-1}\,g_{cat}^{-1}}$
$E_{\mathrm{a},13}^{\mathrm{MF}} = 235.91\,\mathrm{kJ\,mol^{-1}}$	$E_{\mathrm{a},13}^{\mathrm{PO}} = 283.90\,\mathrm{kJ\,mol^{-1}}$	$k_{13}^{\mathrm{PO,ref}} = 0.01\,\mathrm{mol_C\,h^{-1}\,g_{cat}^{-1}}$
$\mathrm{DME} \xrightarrow{k_{14}} \mathrm{C_2^=} + \mathrm{H_2O}$	$r_{14} = k_{14}\, y\,(\mathrm{DME})$	$k_{14}^{\mathrm{MF,ref}} = 0.33\,\mathrm{mol_C\,h^{-1}\,g_{cat}^{-1}}$
$E_{\mathrm{a},14}^{\mathrm{MF}} = 94.96\,\mathrm{kJ\,mol^{-1}}$	$E_{\mathrm{a},14}^{\mathrm{PO}} = 133.90\,\mathrm{kJ\,mol^{-1}}$	$k_{14}^{\mathrm{PO,ref}} = 0.02\,\mathrm{mol_C\,h^{-1}\,g_{cat}^{-1}}$
$\mathrm{DME} + 2\mathrm{H_2} \xrightarrow{k_{15}} 2\mathrm{C_1} + \mathrm{H_2O}$	$r_{15} = k_{15}\, y\,(\mathrm{DME})$	$k_{15}^{\mathrm{MF,ref}} = 0.10\,\mathrm{mol_C\,h^{-1}\,g_{cat}^{-1}}$
$E_{\mathrm{a},15}^{\mathrm{MF}} = 141.02\,\mathrm{kJ\,mol^{-1}}$	$E_{\mathrm{a},15}^{\mathrm{PO}} = 99.48\,\mathrm{kJ\,mol^{-1}}$	$k_{15}^{\mathrm{PO,ref}} = 0.03\,\mathrm{mol_C\,h^{-1}\,g_{cat}^{-1}}$
$\mathrm{C_5^=} + \mathrm{H_2} \xrightarrow{k_{16}} \mathrm{C_4^=} + \mathrm{C_1}$	$r_{16} = k_{16}\, y\,(\mathrm{C_5^=})$	$k_{16}^{\mathrm{MF,ref}} = 0.01\,\mathrm{mol_C\,h^{-1}\,g_{cat}^{-1}}$
$E_{\mathrm{a},16}^{\mathrm{MF}} = 63.90\,\mathrm{kJ\,mol^{-1}}$	$E_{\mathrm{a},16}^{\mathrm{PO}} = 5.62\,\mathrm{kJ\,mol^{-1}}$	$k_{16}^{\mathrm{PO,ref}} = 0.01\,\mathrm{mol_C\,h^{-1}\,g_{cat}^{-1}}$
$\mathrm{C_3^=} \xrightarrow{k_{17}} \mathrm{C_{2-6}}$	$r_{17} = k_{17}\, y\,(\mathrm{C_3^=})$	$k_{17}^{\mathrm{MF,ref}} = 0.01\,\mathrm{mol_C\,h^{-1}\,g_{cat}^{-1}}$
$E_{\mathrm{a},17}^{\mathrm{MF}} = -46.72\,\mathrm{kJ\,mol^{-1}}$	$E_{\mathrm{a},17}^{\mathrm{PO}} = -43.38\,\mathrm{kJ\,mol^{-1}}$	$k_{17}^{\mathrm{PO,ref}} = 0.01\,\mathrm{mol_C\,h^{-1}\,g_{cat}^{-1}}$
$\mathrm{DME} \xrightarrow{k_{18}} \mathrm{C_{2-6}}$	$r_{18} = k_{18}\, y\,(\mathrm{DME})$	$k_{18}^{\mathrm{MF,ref}} = 1.13\,\mathrm{mol_C\,h^{-1}\,g_{cat}^{-1}}$
$E_{\mathrm{a},18}^{\mathrm{MF}} = 26.24\,\mathrm{kJ\,mol^{-1}}$	$E_{\mathrm{a},18}^{\mathrm{PO}} = 16.58\,\mathrm{kJ\,mol^{-1}}$	$k_{18}^{\mathrm{PO,ref}} = 0.15\,\mathrm{mol_C\,h^{-1}\,g_{cat}^{-1}}$
$\mathrm{C_6^=} \xrightarrow{k_{19}} \mathrm{C_{7+}^=}$	$r_{19} = k_{19}\, y\,(\mathrm{C_6^=})$	$k_{19}^{\mathrm{MF,ref}} = 0.11\,\mathrm{mol_C\,h^{-1}\,g_{cat}^{-1}}$
$E_{\mathrm{a},19}^{\mathrm{MF}} = 73.92\,\mathrm{kJ\,mol^{-1}}$	$E_{\mathrm{a},19}^{\mathrm{PO}} = 127.89\,\mathrm{kJ\,mol^{-1}}$	$k_{19}^{\mathrm{PO,ref}} = 0.13\,\mathrm{mol_C\,h^{-1}\,g_{cat}^{-1}}$

Scheme 2.39: Reaction network, rate equations and estimated parameters for the model by Wen *et al.* [299].

Scheme 2.40 contains the net rates of production of all species.

$$
\begin{aligned}
R\,(\mathrm{MeOH}) &= 2\,k_2\,y\,(\mathrm{DME}) - 2\,k_1\,y\,(\mathrm{MeOH}) \\
R\,(\mathrm{DME}) &= k_1\,y\,(\mathrm{MeOH}) - k_2\,y\,(\mathrm{DME}) - k_3\,y\,(\mathrm{C_3^=})\;y\,(\mathrm{DME}) - k_4\,y\,(\mathrm{C_4^=})\;y\,(\mathrm{DME}) \\
&\quad - k_5\,y\,(\mathrm{C_5^=})\;y\,(\mathrm{DME}) - k_6\,y\,(\mathrm{C_6^=})\;y\,(\mathrm{DME}) - k_{14}\,y\,(\mathrm{DME}) - k_{15}\,y\,(\mathrm{DME}) - k_{18}\,y\,(\mathrm{DME}) \\
R\,(\mathrm{C_2^=}) &= k_9\,y\,(\mathrm{C_6^=}) + k_{11}\,y\,(\mathrm{C_5^=}) + k_{14}\,y\,(\mathrm{DME}) - k_{10}\,y\,(\mathrm{C_2^=})\;y\,(\mathrm{C_4^=}) - k_{12}\,y\,(\mathrm{C_2^=})\;y\,(\mathrm{C_3^=}) \\
R\,(\mathrm{C_3^=}) &= 2\,k_7\,y\,(\mathrm{C_6^=}) + k_{11}\,y\,(\mathrm{C_5^=}) + k_{13}\,y\,(\mathrm{C_4^=}) - 2\,k_3\,y\,(\mathrm{C_3^=})\;y\,(\mathrm{DME}) - 2\,k_8\,y\,(\mathrm{C_3^=}) \\
&\quad - k_{12}\,y\,(\mathrm{C_2^=})\;y\,(\mathrm{C_3^=}) - k_{17}\,y\,(\mathrm{C_3^=}) \\
R\,(\mathrm{C_4^=}) &= 2\,k_3\,y\,(\mathrm{C_3^=})\;y\,(\mathrm{DME}) + k_9\,y\,(\mathrm{C_6^=}) + k_{16}\,y\,(\mathrm{C_5^=}) - 2\,k_4\,y\,(\mathrm{C_4^=})\;y\,(\mathrm{DME}) \\
&\quad - k_{10}\,y\,(\mathrm{C_2^=})\;y\,(\mathrm{C_4^=}) - 2\,k_{13}\,y\,(\mathrm{C_4^=}) \\
R\,(\mathrm{C_5^=}) &= 3\,k_4\,y\,(\mathrm{C_4^=})\;y\,(\mathrm{DME}) + k_{12}\,y\,(\mathrm{C_2^=})\;y\,(\mathrm{C_3^=}) + k_{13}\,y\,(\mathrm{C_4^=}) - 2\,k_5\,y\,(\mathrm{C_5^=})\;y\,(\mathrm{DME}) \\
&\quad - k_{11}\,y\,(\mathrm{C_5^=}) - k_{16}\,y\,(\mathrm{C_5^=}) \\
R\,(\mathrm{C_6^=}) &= 3\,k_5\,y\,(\mathrm{C_5^=})\;y\,(\mathrm{DME}) + k_8\,y\,(\mathrm{C_3^=}) + k_{10}\,y\,(\mathrm{C_2^=})\;y\,(\mathrm{C_4^=}) - 2\,k_6\,y\,(\mathrm{C_6^=})\;y\,(\mathrm{DME}) \\
&\quad - k_7\,y\,(\mathrm{C_6^=}) - k_9\,y\,(\mathrm{C_6^=}) - k_{19}\,y\,(\mathrm{C_6^=}) \\
R\,(\mathrm{C_{7+}^=}) &= 2\,k_6\,y\,(\mathrm{C_6^=})\;y\,(\mathrm{DME}) + 2\,k_{19}\,y\,(\mathrm{C_6^=}) \\
R\,(\mathrm{C_1}) &= 2\,k_{15}\,y\,(\mathrm{DME}) + k_{16}\,y\,(\mathrm{C_5^=}) \\
R\,(\mathrm{C_{2-6}}) &= k_{17}\,y\,(\mathrm{C_3^=}) + k_{18}\,y\,(\mathrm{DME})
\end{aligned}
$$

Scheme 2.40: Net rates of production of the different lumps for the model by Wen *et al.* [299].

Parameter estimation Mole fractions are required for the rate equations in Scheme 2.39. For parameter estimation, *lsqnonlin* provided by MATLAB is used. It minimizes the objective function, i.e., the unweighted sum of squared residuals between modeled and measured mole fractions. The differential equations are integrated via the fourth-fifth-order Runge-Kutta method of *ode45*, also within MATLAB. The reparameterized Arrhenius approach (see Equation (2.21)) is applied using a reference temperature of 723 K, which is 10 K higher than the mean value of the investigated range. With this routine, 38 parameters are estimated: 19 reference rate constants and 19 activation energies, either for the metal fibers (MF) or for the powder (PO).

Summary

Because the methanol co-feed implementation of Huang *et al.* [241] has similar methodology to the pure olefin interconversion case, advantages and disadvantages of the models are comparable. A problem might arise as the olefin interconversion equations are transferred to MTO without adaption of the denominator where the adsorption of methanol is missing. Nevertheless, the retained stoichiometry, the large reaction network and the HW type of mechanism yield a robust model. Further improvement could be achieved by having carbon number dependent adsorption values and by including DME adsorption. Furthermore, the methylation via DME is missing. On

the other hand, several steps for double methylation are considered. The equilibrium constant of the oxygenates interaction is fitted to experimental data. In the approach by Wen *et al.* [299], both the forward and the backward reaction are estimated as rate constants which might impede thermodynamic consistency. This holds not only for oxygenates interaction, but also for olefin interconversion. This model restricts all methylation and olefin production reactions to DME as reactant. The aromatic hydrocarbon pool is indirectly considered via a step converting DME to ethene. Many different reactions including side product formation are depicted here; however, this causes also many fitting parameters. Extrapolation might be additionally difficult because of missing adsorption, mechanistic basics and stoichiometry. On the other hand, a reasonable agreement with experimental data over two different catalyst systems is achieved.

Other studies

Guo *et al.* [104, 305] performed measurements over a ZSM-5 zeolite (Si/Al ratio of 200) at temperatures between 683 and 753 K. The feed consisted of methanol and different *n*-olefins and was diluted with water and nitrogen. The reaction network contains 14 lumps and requires 32 parameters. Besides olefin methylation, this model considers several olefin interconversion and side product formation steps. The rate equations are formulated as HW type of mechanism with the inhibiting water adsorption.

Another recent contribution by Ortega *et al.* [306] uses a recycle reactor and therefore olefin co-feed conditions, but temperatures are more within the MTG range as they are between 598 and 648 K.

3 Single-Event Kinetics for 1-Pentene Cracking over ZSM-5: Model Description and Reactor Design

Parts of this chapter were published and are reprinted with permission from:

T. von Aretin, S. Standl, M. Tonigold, O. Hinrichsen
Optimization of the Product Spectrum for 1-Pentene Cracking on ZSM-5 Using Single-Event Methodology. Part 1: Two-Zone Reactor
Chemical Engineering Journal 309 (2017), 886–897, DOI 10.1016/j.cej.2016.04.089.

T. von Aretin, S. Standl, M. Tonigold, O. Hinrichsen
Optimization of the Product Spectrum for 1-Pentene Cracking on ZSM-5 Using Single-Event Methodology. Part 2: Recycle Reactor
Chemical Engineering Journal 309 (2017), 873–885, DOI 10.1016/j.cej.2016.10.103.

S. Standl, O. Hinrichsen
Kinetic Modeling of Catalytic Olefin Cracking and Methanol-to-Olefins (MTO) over Zeolites: A Review
Catalysts 8 (2018), 626, DOI 10.3390/catal8120626.

T. von Aretin, S. Schallmoser, S. Standl, M. Tonigold, J. A. Lercher, O. Hinrichsen
Single-Event Kinetic Model for 1-Pentene Cracking on ZSM-5
Industrial & Engineering Chemistry Research 54 (2015), 11792–11803,
DOI 10.1021/acs.iecr.5b02629.

Parts were also published as Supporting Information and are reprinted with permission from:

S. Standl, T. Kühlewind, M. Tonigold, O. Hinrichsen
On Reaction Pathways and Intermediates During Catalytic Olefin Cracking over ZSM-5
Industrial & Engineering Chemistry Research 58 (2019), 18107–18124,
DOI 10.1021/acs.iecr.9b02989.

J. Sundberg, S. Standl, T. von Aretin, M. Tonigold, S. Rehfeldt, O. Hinrichsen, H. Klein
Optimal Process for Catalytic Cracking of Higher Olefins on ZSM-5
Chemical Engineering Journal 348 (2018), 84–94, DOI 10.1016/j.cej.2018.04.060.

3.1 Single-Event Kinetic Model for 1-Pentene Cracking over ZSM-5

3.1.1 Catalyst

A commercial ZSM-5 powder provided by Clariant AG was used for the experiments; the most important characterization results are found in Tables 2.1 and 4.1. The applied particle size is in the upper range. Before the first data point was recorded, the catalyst had to be deactivated for six hours. In this period, a significant loss of activity was observed, whereas it reached an almost constant value for the next ten hours [307].

3.1.2 Setup and Conditions

The experiments were performed with 1-pentene as feed using a continuous fixed bed quartz glass reactor with an inner diameter of 6 mm. During the measurements, two different volumetric flow rates were applied (300 and 400 mL min^{-1}), which caused two total pressures (1.16 and 1.23 bar). An overview of experimental parameters is shown in Tables 2.2 and 4.2. Isothermality was guaranteed by using SiC and nitrogen to dilute the catalyst and the feed, respectively. This was monitored by measuring the temperature at the tube wall. The 1-pentene stream had to be evaporated before it was fed into the reactor. The products were analyzed with a GC that had three columns and both an FID and a TCD.

3.1.3 Reaction Network

The following rules are applied to the molecular structure of olefins:

- maximum carbon number of twelve,
- exclusion of quaternary carbon atoms,
- only methyl side groups,
- maximum number of methyl side groups of two per compound,
- exclusion of all 2,3-dimethylbutenes,
- exclusion of further sterically demanding compounds.

These assumptions result from experimental observations [47, 48, 308, 309]. As mentioned, the influence of the shape selectivity of the catalyst is considered by excluding sterically demanding species from the network [26]. With this, an equilibrium distribution of olefins over ZSM-5 can be described [26]. All included species can participate in different types of elementary reactions, again according to several rules [26], which are shown in Scheme 3.1.

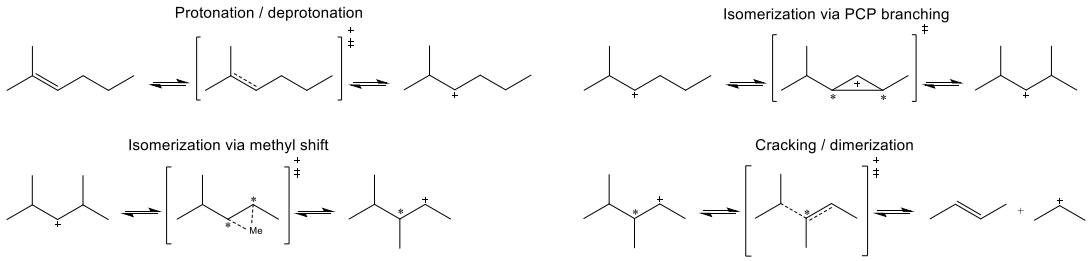

Scheme 3.1: Different types of elementary reactions that are included in the single-event kinetic model for 1-pentence cracking over ZSM-5.

Protonation of the double bond of an olefin leads to a protonated intermediate whereas the backward reaction, the deprotonation, releases the corresponding olefin. The protonated intermediate can undergo isomerization reactions: through a methyl shift, the positive charge and the methyl side group switch position. In another type of isomerization reaction, a PCP evolves as transition state. Then, one of the three bonds breaks and leads to the product. Because of the elevated temperatures during cracking, both (de)protonation and isomerization reactions are assumed as *quasi*-equilibrated [21]; for isomerization, this could be also verified by measurements [26]. By contrast, cracking of a protonated intermediate is a step of kinetic relevance. The same holds for

the backward reaction, the dimerization, where a smaller protonated intermediate and an olefin react to a larger protonated intermediate. Because the single-event methodology is applied, see Section 2.5.2, the kinetic parameters are not assigned to certain carbon numbers, but to types of reactant and product intermediates. The formation of primary intermediates and thus also of ethene is assumed to be irreversible; the reason is that primary intermediates are not considered as reactants due to energetic reasons [215]. In total, the reaction network contains 4379 different elementary reactions. However, as mentioned, all steps where the carbon number is kept constant are assumed as *quasi*-equilibrated, meaning that 601 cracking and 140 dimerization reactions remain. Combined with the different protonation possibilities, 1292 cracking and 293 dimerization pathways of kinetic relevance are considered.

Lumping is still performed during evaluation of the experiments: the model differentiates each isomer, but summarizes them for comparison with the measurements. Here, the responses $C_2^=$, $C_3^=$, $C_4^=$, $C_5^=$ and $C_{6\text{-}12}^=$ are compared during parameter estimation. Although the measurements revealed small amounts of pentane, cyclopentane, cyclopentene, methylcyclopentene and aromatics as side products, their formation is not included in the model because the mole fraction of all side products never exceeded 3%.

3.1.4 Rate Equations

For the single-event kinetic model, chemisorption of the reactant olefin O_i is explicitly included as sequence of π-complex and protonation, meaning that the cracking reactions are formulated with a combination of L (used as subscript in the following) and HW types of mechanism. For the dimerization, the second olefin is assumed to react directly out of the gas phase; this corresponds to coupled ER and HW types of mechanism. For more details about the general definition of kinetic modeling schemes, it is referred to Section 2.5. The equilibrium constants describing the π-complex K^{π} as well as the protonation K^{prot} are extracted from a theoretical study published by Nguyen *et al.* [54, 310] which combines quantum mechanics, interatomic potential functions (QM-Pot) and statistical thermodynamics. As simplification, the π-complex of all olefins is calculated using the equations for 1-olefins. By contrast, a differentiation is performed for protonation, where either the correlations for 1-olefins or for 2-/3-/4-olefins are applied.

In Tables 2.1 and 4.1, the total number of acid sites is shown. However, calculations are performed with the molar concentration of strong Brønsted acid sites per catalyst mass $C_{\mathrm{t}}^{\mathrm{SBAS}}$ which equals 0.135 mmol $\mathrm{g}_{\mathrm{cat}}^{-1}$. For more details about the coherence between regular rate constant, the number of single events n_e as well as the single-event rate constant $\tilde{k}$, see Section 2.5.2.

The final rate expressions to describe cracking r^{cr} and dimerization r^{dim} from protonated intermediate of type m to type n can be found in Equations (3.1) and (3.2), respectively,

$$r^{\mathrm{cr}}(m;n) = n_e \tilde{k}^{\mathrm{cr}}(m;n)\, K^{\mathrm{prot}}\left(\mathrm{O}_i^{\pi};m\right) \frac{C_{\mathrm{t}}^{\mathrm{SBAS}} K_{\mathrm{L}}^{\pi}(\mathrm{O}_i)\, p(\mathrm{O}_i)}{1+\sum_j K_{\mathrm{L}}^{\pi}\left(\mathrm{O}_j\right) p\left(\mathrm{O}_j\right)}, \tag{3.1}$$

$$r^{\mathrm{dim}}(m;n) = n_e \tilde{k}^{\mathrm{dim}}(m;n)\, K^{\mathrm{prot}}\left(\mathrm{O}_i^{\pi};m\right) \frac{C_{\mathrm{t}}^{\mathrm{SBAS}} K_{\mathrm{L}}^{\pi}(\mathrm{O}_i)\, p(\mathrm{O}_i)}{1+\sum_j K_{\mathrm{L}}^{\pi}\left(\mathrm{O}_j\right) p\left(\mathrm{O}_j\right)} p(\mathrm{O}_v). \tag{3.2}$$

The equilibrium constants for olefin protonation can be expressed as product of an equilibrium constant for isomerization to a well-defined reference olefin $\mathrm{O}_{\mathrm{ref}}$ as well as of the protonation equilibrium constant of the latter; more details and derivations are found in literature [19, 21, 26]. The principle of thermodynamic consistency [196] is applied to further reduce the number of estimated parameters. Thus, the rate constant of the backward reaction (dimerization) is expressed as product of the rate constant of the forward reaction (cracking) and an equilibrium constant that contains, among other values, the thermodynamic equilibrium constant between the involved species [26]. The calculation of both equilibrium constants, i.e., the one for isomerization and the one to express the reaction equilibrium, requires thermodynamic data. In the single-event kinetic model, experimental data by Alberty and Gehrig [147] are used for $\mathrm{C}_2^{=}$ to $\mathrm{C}_6^{=}$ olefins. By contrast, Benson's group contribution method [155, 156] is applied to $\mathrm{C}_7^{=}$ to $\mathrm{C}_{12}^{=}$ olefins. Finally, thermodynamic data are also necessary to calculate the isomer composition of each carbon number. The isomerization reactions being *quasi*-equilibrated means that the model for a one-dimensional, *pseudo*-homogeneous, isothermal plug flow reactor in Equation (3.3) has to be solved only for each carbon number and not for each isomer,

$$\frac{\mathrm{d}F(i)}{\mathrm{d}W} = R(i), \tag{3.3}$$

with the molar flow rate of a certain carbon number $F(i)$, the catalyst mass W and the net rate of production of a certain carbon number $R(i)$. The latter is obtained by summing up all reaction rates where a certain carbon number is produced or consumed, see Equations (3.4) and (3.5); the protonated and thus chemisorbed intermediates have to be included,

$$\begin{aligned} R\left(\mathrm{C}_i^{=}\right) = &\sum_q r_q^{\mathrm{cr}}\left(\mathrm{C}_{i+v}^{=,\mathrm{chem}};\mathrm{C}_v^{=,\mathrm{chem}},\mathrm{C}_i^{=}\right) - \sum_q r_q^{\mathrm{dim}}\left(\mathrm{C}_v^{=,\mathrm{chem}},\mathrm{C}_i^{=};\mathrm{C}_{i+v}^{=,\mathrm{chem}}\right) \\ &+ R\left(\mathrm{C}_i^{=,\mathrm{chem}}\right), \end{aligned} \tag{3.4}$$

$$\begin{aligned} R\left(\mathrm{C}_i^{=,\mathrm{chem}}\right) = &\sum_q r_q^{\mathrm{cr}}\left(\mathrm{C}_{i+v}^{=,\mathrm{chem}};\mathrm{C}_i^{=,\mathrm{chem}},\mathrm{C}_v^{=}\right) - \sum_q r_q^{\mathrm{cr}}\left(\mathrm{C}_i^{=,\mathrm{chem}};\mathrm{C}_v^{=,\mathrm{chem}},\mathrm{C}_{i-v}^{=}\right) \\ &+ \sum_q r_q^{\mathrm{dim}}\left(\mathrm{C}_v^{=,\mathrm{chem}},\mathrm{C}_{i-v}^{=};\mathrm{C}_i^{=,\mathrm{chem}}\right) \\ &- \sum_q r_q^{\mathrm{dim}}\left(\mathrm{C}_i^{=,\mathrm{chem}},\mathrm{C}_v^{=};\mathrm{C}_{i+v}^{=,\mathrm{chem}}\right). \end{aligned} \tag{3.5}$$

3.1.5 Parameter Estimation

The definition of reaction rates shown above requires partial pressures. The objective function evaluates the sum of squared residuals between the mole fractions of model and experiment; here, nitrogen as diluent is explicitly included. The sum of squared residuals is minimized with a nonlinear and unweighted regression using the Levenberg-Marquardt algorithm of the solver *lsqnonlin* in MATLAB. The molar flow rates are obtained by applying the solver *ode15s* to the differential equations. Although a broad picture of the olefin interconversion is depicted, only five parameters are necessary. From the explanations of the reaction network given above, it follows that four cracking activation energies are required: secondary (s) to primary (p), secondary to secondary, tertiary (t) to primary and tertiary to secondary. Furthermore, one pre-exponential factor is required; the latter is assumed to be the same for all cracking reactions. During parameter estimation, the reparameterized Arrhenius approach is used, but with the additional temperature dependence of the pre-exponential factor. The reference temperature of 683 K is the mean value of the experimentally investigated range. The estimated parameters are shown in Table 4.3.

3.2 Reactor Design as Tool to Optimize the Product Spectrum

Although the creation of a single-event kinetic model is time-consuming, one of its crucial strengths is the possibility of extrapolating out of the experimentally covered regime [19]. This allows for an analysis of different reactor concepts to maximize the P/E ratio.

3.2.1 Side Products

When dealing with industrial reactor solutions, side product formation has to be considered to depict realistic conditions. For olefin cracking, this means to consider hydrogen transfer products, i.e., paraffins and aromatics. Figure 3.1 shows all side products detected during the experiments for the single-event kinetic model for 1-pentene cracking over ZSM-5 [26].

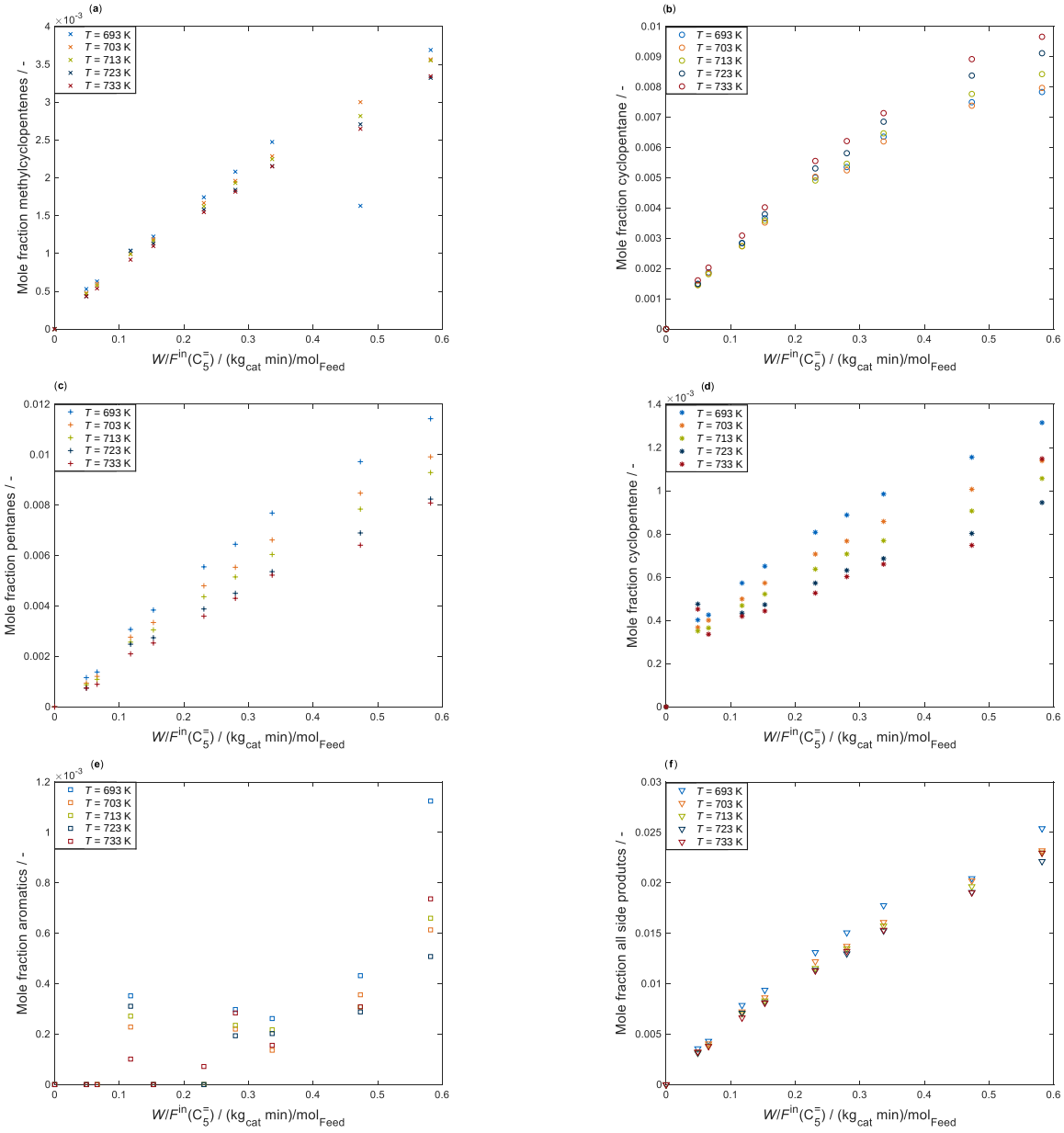

Figure 3.1: Evolution of side products during the experiments for the single-event kinetic model for 1-pentene cracking over ZSM-5; the mole fractions of methylcyclopentenes, (a), cyclopentane, (b), pentanes, (c), cyclopentene, (d), aromatics, (e), and all side products, (f), are shown as function of contact time at different temperatures.

From the results, it follows that all hydrogen transfer products do not contribute significantly to the overall product distribution. This is why their formation is not included in the single-event kinetic model [26]. The amount of these species is added to the respective olefin with the same carbon number to maintain the mass balances. The evolution of methane and hydrogen in the experiments was even less pronounced. It is noteworthy that except for cyclopentane, all compounds showed lower mole fractions at higher temperatures. This trend is expected for the paraffins since increasing temperatures lead to lower rates of the exothermic hydrogen transfer [311]. On the other hand, aromatization reactions are favored by higher temperatures

which is why more aromatics should be detected [52, 240]. Possible explanations for this are the decreasing concentration of higher compounds, which are necessary to form aromatics, through cracking [58] and faster deactivation of the strong acid sites. The total concentration of hydrogen transfer products passes through a catalyst dependent maximum [52]. Apparently, an increment of aromatics and paraffins with higher temperatures is only detectable for temperatures up to 690 K whereas from this point, the decreasing concentration of higher olefins through cracking and also higher deactivation might cause the decline of these products.

There are several reasons for the fact that formation of hydrogen transfer products was very low here in contrast to other literature results [52, 239, 240]. Firstly, the ZSM-5 catalyst had small crystallites [26] and showed high selectivity to olefins therefore. Secondly, the experimental conditions are different to the literature cited. The temperature (633 to 733 K) was lower than for Epelde *et al.* [239, 240] (673 K to 873 K) and Arudra *et al.* [52] (up to 823 K). Both studies obtain less paraffins, but more aromatics with higher temperatures. This fact was already discussed above and shows that it is difficult to compare different catalysts at different temperatures. A better explanation offers the comparison of the residence times which were shorter in most times compared to Epelde *et al.* [240]; higher residence times favor the formation of hydrogen transfer products [58]. In addition, Epelde *et al.* [240] investigated higher conversion values. The most important difference is the TOS after which measurements were performed. Epelde *et al.* [239] extrapolated their results to zero TOS with full catalyst activity; Arudra *et al.* [52] determined their results after one hour TOS. Opposed to this, experiments for the single-event kinetic model were started after six hours TOS [26]. Since an activity loss of 15% was observed during this time and coke preferentially blocks the strong acid sites which show high activity in hydrogen transfer, the negligible amount of paraffins and aromatics can be explained. This trend is also found in literature [52, 239].

In summary, although no side product formation is implemented in the single-event kinetic model, simple reactor concepts optimizing the product distribution can be evaluated as the model represents the actual performance of the catalyst with high accuracy.

3.2.2 Crucial Parameters to Influence the Product Distribution

As described in Section 2.2, two main pathways exist for olefin interconversion [308, 309]: monomolecular cracking and dimerization with subsequent cracking. Scheme 3.2 shows that the former step is only possible for a minimum carbon number of five.

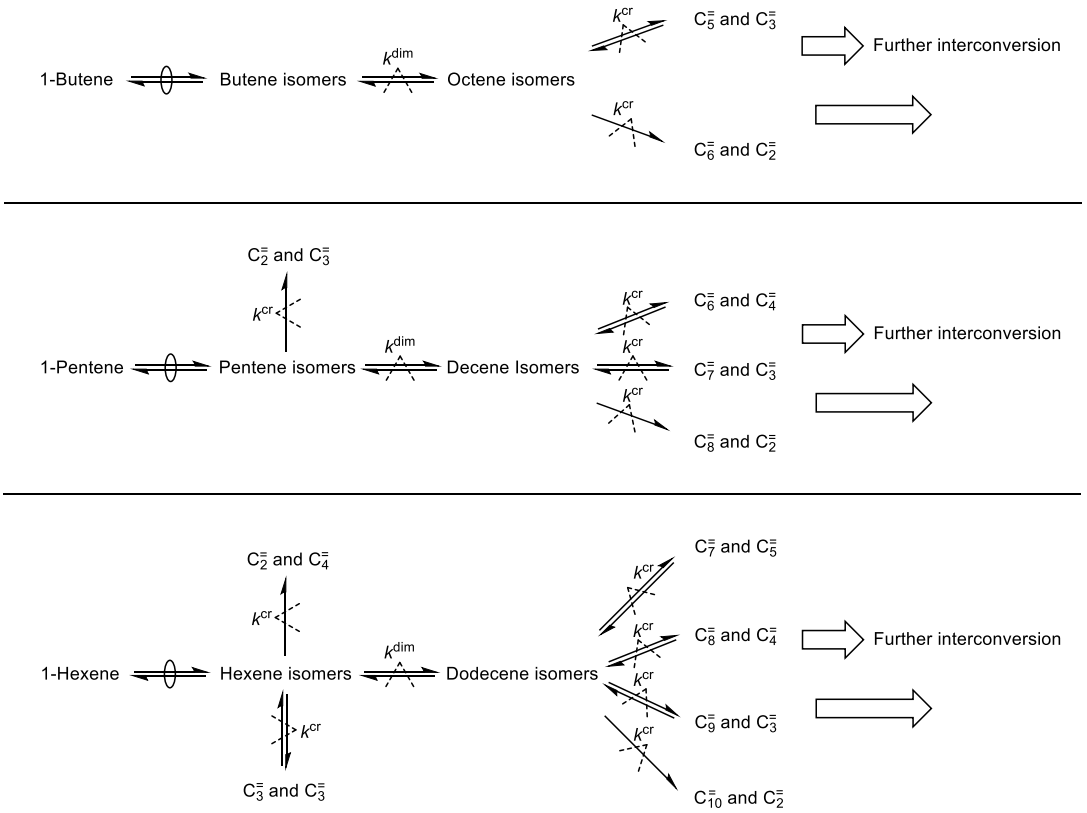

Scheme 3.2: Two main pathways of olefin cracking: dimerization with subsequent cracking and monomolecular cracking; the latter is only possible for a minimum carbon number of five; the pathways are shown for 1-butene, 1-pentene and 1-hexene as exemplary feeds.

For pentenes as feed, monomolecular cracking inevitably leads to the formation of a primary intermediate. This step is energetically demanding [19, 50] and should have a higher activation energy. By contrast, pentene dimerization leads to decenes that have more possibilities of subsequent cracking. Here, the undesired formation of a primary product intermediate can be avoided. Compared to pentenes, hexene has an additional option for monomolecular cracking which should be preferred especially at lower temperatures since it does not lead to the formation of primary product intermediates. Because of the higher carbon number of the dimer, it shows even more options for subsequent cracking. Opposed to that, monomolecular cracking is not possible for butenes since the intermediates and reaction products would be too unstable. Thus, the conversion has to proceed via a dimer first.

Besides these aspects, Figures 2.2 and 2.3 show the influence of temperature and pressure on olefin equilibrium distributions. Due to the exothermicity of dimerization, higher temperatures favor lower olefins. By contrast, elevated pressures increase the amount of higher olefins. Thus, for maximum propene yields, cracking should be performed at ambient pressures; this parameter is not considered for the following optimization.

When having pentenes as feed, low temperatures lead to high conversions, mainly through dimerization. In addition, ethene formation is negligible due to the high activation energy of this step. On the other hand, the product spectrum contains many higher olefins and comparably low amounts of propene. In the intermediate temperature region, none of the two main pathways prevails, which leads to low conversions. High temperatures offer high conversion levels, a low amount of higher olefins and increased propene yields, but also lead to significant ethene formation. Here, a regular reactor setup shows no possibility to decouple propene yields from ethene formation.

3.2.3 Two-Zone Reactor

A reactor having two zones with different temperatures each is proposed to combine the advantages of both main pathways in pentenes conversion. This is analyzed in Figure 3.2 which results from an evaluation of the single-event kinetic model at temperatures between 550 and 850 K. The reactor model for an isothermal fixed bed is solved for both zones, the second one using the product stream of the first one as feed. As contact time, calculated with the inlet molar flow rate of pentenes, $0.48\,\mathrm{kg_{cat}\,min\,mol^{-1}_{Feed}}$ are chosen. The inlet partial pressure of pentene amounts to 73.8 mbar.

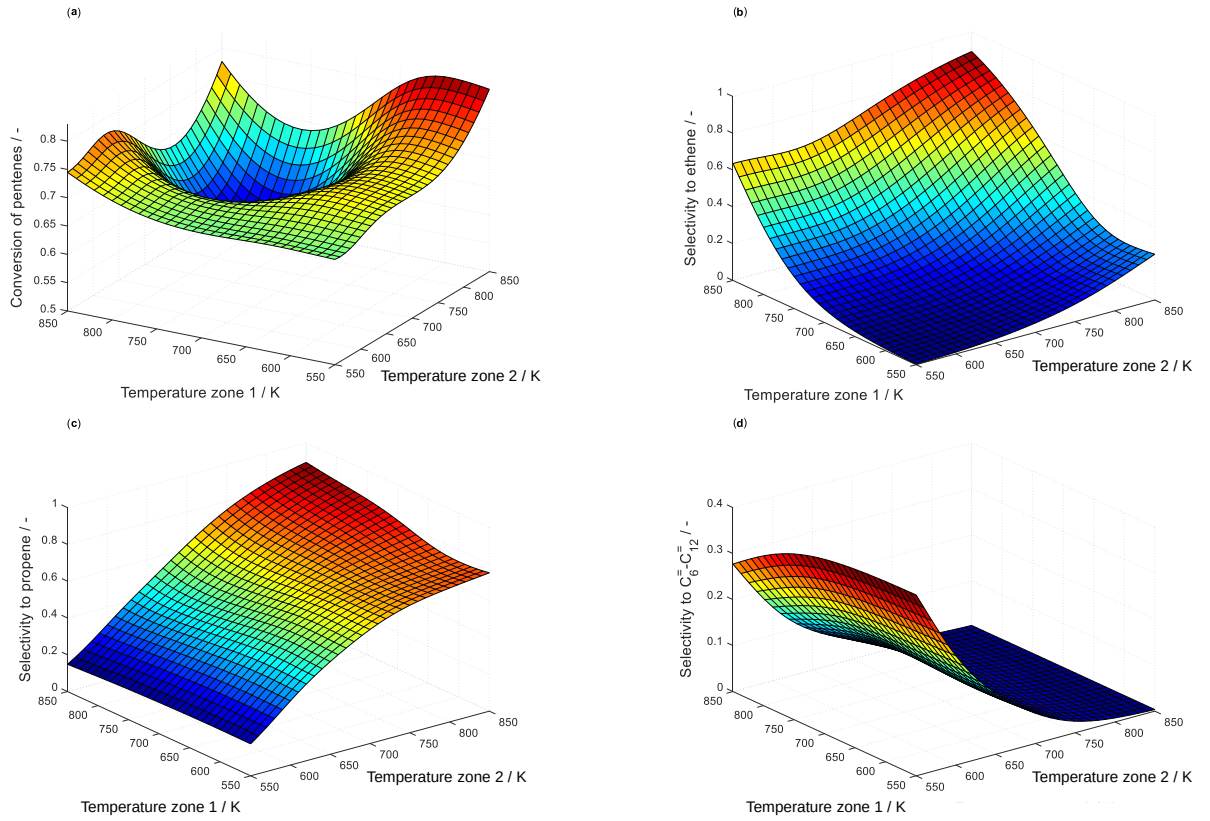

Figure 3.2: Conversion of pentenes, (a), and selectivities to ethene, (b), propene, (c), and $C_6^=$ to $C_{12}^=$ olefins, (d), resulting from an application of the single-event kinetic model to two subsequent fixed beds with varying temperatures; the inlet partial pressure of pentenes is 73.8 mbar whereas the evaluated contact time amounts to 0.48 kg_{cat} min mol_{Feed}^{-1}.

As mentioned above, Figure 3.2 (a) shows that a combination of intermediate temperatures exists where conversions are low. More importantly, decoupling of ethene and propene selectivities is possible now, cf. Figure 3.2 (b) and 3.2 (c): when having high temperatures in the second zone, propene selectivities are almost independent of the temperature in the first zone. By contrast, ethene selectivities decrease with lower temperatures in the first zone. Consequently, a two-zone reactor with maximum P/E ratio should have a first zone at low temperatures to mostly favor dimerization reactions and a second zone with high temperatures, thereby leading to intense cracking of the formerly produced higher olefins. As these have sufficient options to avoid the less favored formation of a primary product intermediate, ethene production is low. It follows that the high ethene selectivities found in Figure 3.2 (b) have to result mainly from the first reactor zone and thus from monomolecular cracking of pentenes. When having low temperatures in this first zone, the reaction rates of these steps producing ethene are small due to the higher activation energies, see also Table 4.3. Some ethene formation in the second high-temperature zone is inevitable, but the key to high P/E ratios is to have a former conversion of pentenes to higher olefins as much as possible.

A combination of 580 K in the first and 760 K in the second zone is seen to be a reasonable compromise between a P/E ratio of 6.4 and a conversion of 0.75. Moreover, as Figure 3.2 (d) shows, selectivities to higher olefins are sufficiently low at these conditions. In Figure 3.2, it can be seen that higher temperatures in the second zone would increase propene yields, but also ethene yields so that the P/E ratio would be lower. By contrast, decreasing the temperature in the second zone lowers cracking of higher olefins and thereby propene selectivities. In the first zone, lower temperatures could increase propene selectivities, but this would be at cost of conversion. Furthermore, it cannot be guaranteed that isomerization reactions are still *quasi*-equilibrated at temperatures significantly lower than 600 K.

Figure 3.3 shows the resulting reactor plot, with the mole fractions given as ratio of molar flow rate to the inlet molar flow rate of pentene.

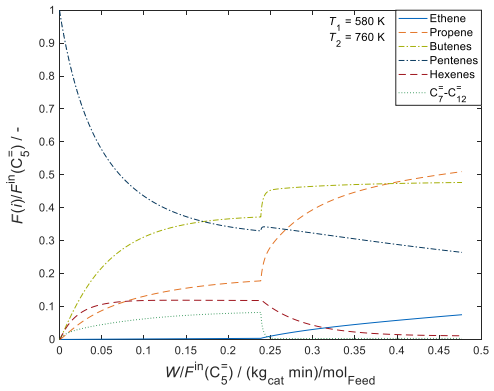

Figure 3.3: Two-zone reactor with 580 K in the first and 760 K in the second zone, respectively; the ratio of molar flow rates to the inlet molar flow rate of pentenes is shown as function of contact time.

This plot summarizes the observations discussed before: in the first zone, significant formation of $C_6^=$ to $C_{12}^=$ olefins is observed whereas ethene evolution is negligible. The higher olefins crack down in the second zone with propene and butenes being the main products. A comparison with the one-zone reactor being operated at the lower temperature shows similar conversion, a slightly higher P/E ratio, but an amount of higher olefins that is ten times higher than in Figure 3.3. On the other hand, the one-zone reactor operated at the higher temperature would lead to high propene yields and low amounts of higher olefins, but also to elevated ethene yields and thus a lower P/E ratio.

3.2.4 Recycle Reactor

Because the product output of the two-zone reactor still contains significant amounts of $C_4^=$, $C_5^=$ and higher olefins, the idea of a recycle reactor suggests that all olefins higher than $C_3^=$ are split off in a separator subsequent to the reactor. This fraction is led back to the reactor inlet whereas $C_2^=$ and $C_3^=$ olefins are selectively obtained. A separation task like this is well-established for steam cracking and described in literature [312, 313]. In this chapter, an ideal separation is assumed which is not realistic for an industrial process; here, traces of ethene and propene might be recycled and higher olefins will contaminate the product stream. However, the study shown in this chapter is about designing a reactor solution for an industrial case using microkinetic parameters obtained in laboratory scale. The applicability of these values for reactor design and product optimization should be shown. Side products are neglected since their amount during the experiments was negligible as shown above.

The kinetic parameters for 1-pentene cracking over ZSM-5, see Table 4.3, are used to solve the reactor model first which is done with the solver *ode15s* in MATLAB and with only 1-pentene as reactive feed. The obtained results for the $C_4^=$ to $C_{12}^=$ olefins are used as start values for the recycle. Thus, the reactor model is solved a second time, this time with the recycle plus 1-pentene as reactive feed. This creates a new output for the $C_4^=$ to $C_{12}^=$ olefins stream, i.e., the recycle. The algorithm should vary the composition of the recycle until it equals the resulting $C_4^=$ to $C_{12}^=$ stream at the reactor outlet. In other words, the solver *lsqnonlin* in MATLAB is used to minimize the difference between the molar flow rates of $C_4^=$ to $C_{12}^=$ olefins obtained at the reactor outlet and inserted at the reactor inlet; both molar flow rates have to be equal. When a solution is found, the reactor model is solved a last time, using the results for the recycle stream plus 1-pentene as reactive feed. This procedure is illustrated in Scheme 3.3.

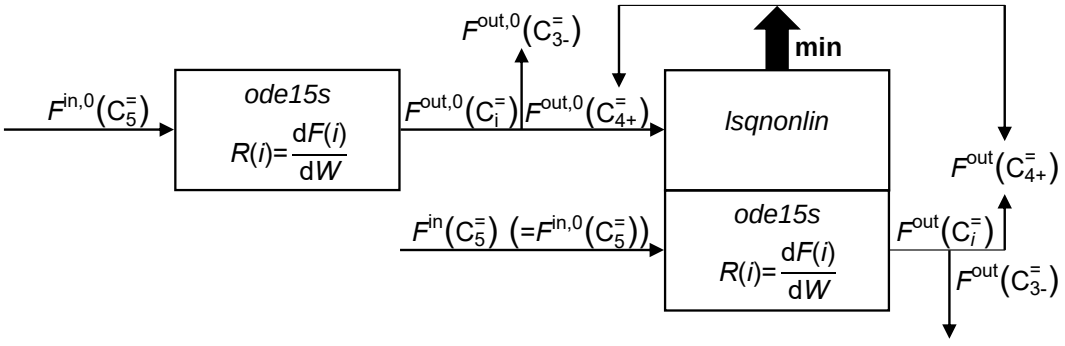

Scheme 3.3: Flow chart of the recycle reactor implementation in MATLAB; the amount of olefins higher than propene predicted by an initial integration (superscript 0) serves as start values for the recycle in a second integration; the final recycle streams are obtained by minimizing the difference between reactor outlet and recycle inlet.

Similar to the two-zone reactor, the temperature is again identified as crucial parameter influencing both product distribution and reactor operation to a significant extent. For this reason, the recycle reactor is evaluated at different temperatures between 600 and 800 K to find an optimal setup that leads to a high P/E ratio. Again, the inlet partial pressure of pentene is set to 73.8 mbar. Figure 3.4 shows temperature-dependent plots for the resulting P/E ratio as well as for the recycle ratio which is defined as the molar flow rates of all recycled olefins divided by the original molar flow rate of pentenes in the feed. The latter value is also used to define the contact time which is held constant at 0.48 kg_{cat} min mol^{-1}_{Feed} for the data in Figure 3.4.

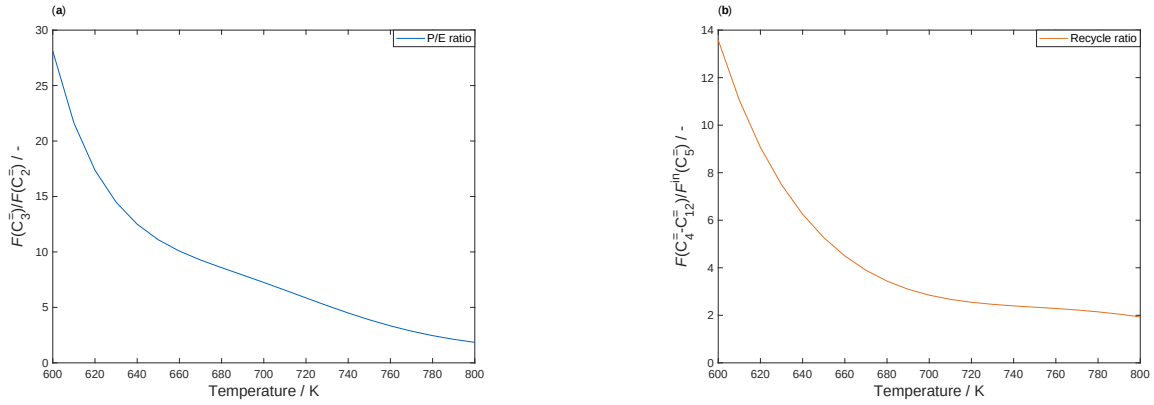

Figure 3.4: Propene to ethene ratio P/E, (a), and recycle ratio, (b), as function of temperature when the single-event kinetic model for 1-pentene cracking over ZSM-5 is applied to a recycle reactor setup.

It can be seen in Figure 3.4 (a) that low temperatures lead to high P/E ratios. As it is described in Section 3.2.2, ethene evolution is negligible at these conditions. Furthermore, propene arises through the subsequent cracking of higher olefins that are products of previous dimerization steps. However, this vast amount of olefins higher than $C_3^=$ is problematic for operating cost as these species have to be separated and recycled. This leads to high values for the the recycle ratio in Figure 3.4 (b). Consequently, the optimum operating point is a compromise between P/E ratio and separation cost. Although the recycle reactor selectively produces ethene and propene out of pentenes as exemplary feed for higher olefins, its overall viability is hard to assess by using only kinetics and reactor modeling. Here, especially the fact that no side product formation is considered might be problematic. These byproducts would leave the separator with the recycle stream since their boiling points are in the range of the higher olefins. This causes a stepwise accumulation of side products in the recycle which is undesired since it means higher operating cost. Consequently, a purge stream is necessary. To account for all these effects, the recycle reactor setup should be further analyzed in Chapter 5.

4 Single-Event Kinetic Modeling of Olefin Cracking over ZSM-5: Proof of Feed Independence

This chapter was published in similar form and is reprinted with permission from:

S. Standl, M. Tonigold, O. Hinrichsen
Single-Event Kinetic Modeling of Olefin Cracking on ZSM-5: Proof of Feed Independence
Industrial & Engineering Chemistry Research 56 (2017), 13096–13108,
DOI 10.1021/acs.iecr.7b01344.

4.1 Abstract

One of the crucial advantages of single-event kinetic models is the possibility of extrapolating them to other reaction conditions, which is highly interesting for catalyst design. However, no study exists that proves the theoretically derived feature of single-event parameters being applicable to different olefins as feed, though derived from kinetic experiments with only one certain feed olefin. Therefore, this chapter provides evidence that a single-event kinetic model for 1-pentene cracking over ZSM-5 is able to reproduce experimental results from literature with $C_3^=$ to $C_7^=$ olefins as feed as long as a consistent set of thermodynamic data is used. The model predicts product distributions from two different kinetic studies of olefin cracking over ZSM-5 with high accuracy at all temperatures (673 to 763 K), all feed partial pressures (47.6 to 131 mbar), for all olefins as reactant ($C_3^=$ to $C_7^=$) and for both water-containing and water-free feeds. The calculations for arbitrary olefin mixtures as feed also show excellent agreement. Consequently, the model describes intrinsic kinetics of olefin interconversion. The underlying kinetic parameters are independent of reaction conditions, feed and composition of ZSM-5 (powder or extrudate) and can be transferred to other systems without adjustment. Limitations in extrapolation emerge when the binder influences the product distribution to a significant

extent, for example, by altering diffusion characteristics. Finally, reproduction of literature results is also performed as function of contact time, which requires an implementation of water adsorption for one of the two literature studies. The analysis of evolutions over contact time reveal both a catalyst and a carbon number dependence of the protonation enthalpy with the latter being independent of investigated ZSM-5 type and thus also transferable.

4.2 Introduction

Ethene and propene are the most important building blocks for the polymer industry [3]. Their main production route is still via steam cracking of naphtha or other hydrocarbon feedstocks [3, 6] which is disadvantageous because of several reasons. Firstly, it requires high temperatures of over 800 °C and therefore is the process with the highest energy demand in chemical industry [3, 7]. Secondly, this energy input causes significant CO_2 emissions [4] which are undesired for environmental issues and governmental regulations. Centi *et al.* [5] report that the production of 1 Mt of ethene releases 1.53 Mt of CO_2 when starting from naphtha. Thirdly, steam cracking offers almost no possibility of influencing the product distribution. This is particularly problematic since its P/E ratio is 0.4–0.6 whereas a significant increase in propene demand is observed [8]. The scenario of an upcoming propene supply gap favors processes with higher P/E values. FCC is not a suitable solution since the focus is on gasoline production with propene as byproduct [7], causing P/E ratios around 1.

Several alternative concepts for the production of light olefins are proposed: catalytic dehydrogenation of lower alkanes [13], oxidative dehydrogenation of small alkanes [15], MTH [10] including MTO, MTP and MTG or modified Fischer-Tropsch [5]. Another promising approach is the cracking of higher hydrocarbons over shape-selective zeolites like ZSM-5 [8]. Here, temperatures are lower, P/E ratios are higher and the catalytic reaction allows more flexibility in feed, which is important in times of fast changing crudes [8]. With the use of higher olefins as reactant, it is possible to exploit these usually undesired byproducts of FCC and steam cracking processes [52]. Since Buchanan *et al.* [50] described the mechanistic background of acid-catalyzed olefin cracking over 20 years ago, several studies in literature have been published, mainly with butenes as feed [52, 240, 311, 314–316].

A kinetic model describes the dependences of a reaction on conditions like temperature, pressure or concentration in a mathematical way [179]. The further advantages depend on the complexity, i.e., whether the model is of lumped or microkinetic character. In lumped models, several compounds are grouped together, for example, according to their carbon number or to other properties like functional groups. Another subdivision is possible here: power law models

fit both the rate constant and mostly the partial reaction order. They are of pure empirical character so the estimated parameters do not have any physical meaning. For instance, the activation energy can be negative because of adsorption effects (apparent activation energy) and the partial reaction orders are not necessarily equivalent to stoichiometry [17]. Nevertheless, such a model might predict reliable results within the experimentally covered range of conditions. The other class of lumped models comprises a differentiation between adsorption and kinetics, so they follow mechanistic schemes. A well-known example is the LH formalism in combination with an HW approach, which contains a reaction term, a term for the driving force and an adsorption term in the denominator. When this methodology is chosen, several assumptions are usually made at the beginning, for example, concerning the rate-determining step. The resulting model is able to depict more physical effects like saturation, but still, the estimated parameters might not have reasonable values [17].

Lumped models can be useful for reactor design whereas process optimization and catalyst design are hardly possible because of the missing ability to extrapolate out of the experimentally covered range [18]. For these purposes, a microkinetic model is the preferred solution. Here, each elementary reaction which is taking place on the catalytic surface is included in the network. No rate-determining step is defined; instead, some elementary reactions might be considered as *quasi*-equilibrated. For the reactive intermediates, the PSSA applies [18]. In a microkinetic model, the estimated parameters have a clear physical background, making them independent of reaction conditions and feed [19]. Furthermore, the rate equations are based on actual elementary reactions which enables insight into mechanisms.

Lumped models are common practice in cracking of hydrocarbons because of the complex reaction networks and the many different isomers. For olefin cracking, an overview of literature studies can be found in Section 2.6.1. When microkinetic modeling is performed, the single-event approach allows for keeping the number of estimated parameters in a reasonable range [18, 20]. Examples in literature exist for hydrocracking [21, 22, 317, 318], for 1-hexene [25] and for 1-pentene cracking [26]. The latter model is described in Chapter 3. Because the single-event parameters only depend on the types of intermediates being involved, i.e., primary, secondary or tertiary, and not on the carbon number, these values should be also valid for other olefin feeds. This feature is a prerequisite to perform reactor optimization and catalyst design since kinetic data are not available for each desired composition. Moreover, the feed independence of such a model would be advantageous for production plants where composition of the supply changes very fast.

However, no publication exists where feed independence of single-event parameters for olefin cracking is actually proven. The objective of this chapter is to show that the values stemming only from 1-pentene cracking data are applicable to other olefin feeds. This is demonstrated by reproducing experimental data from two literature studies [195, 237] without any adjustment

of the kinetics. The data are taken from Huang *et al.* [195] and from Ying *et al.* [237] who used all olefins from $C_3^=$ to $C_7^=$ as feed and subsequently created lumped kinetic models. Further goals of this chapter are an application of the single-event case to arbitrary olefin mixtures as feed and an incorporation of water adsorption. The overall motivation is to increase flexibility; feed independence means kinetic experiments with one key component are sufficient. Moreover, this enhances the single-event kinetic model to a flexible calculation tool on site. The implementation of water adsorption enables the transfer to MTO after accounting also for the methanol-related pathways: water release is inevitable here and olefin interconversion is similar. Finally, a general assessment of the transferability to catalysts with different properties is of interest for further applications which requires a description of the experimental data as function of contact time. In summary, the study in this chapter can be seen as proof of concept whether the theoretically derived features for single-event modeling [19, 59, 179] also pertain for olefin cracking.

4.3 Methods

As mentioned above, the experimental data of two literature studies [195, 237] for olefin cracking over ZSM-5 should be reproduced using the single-event kinetic model for 1-pentene cracking from Chapter 3. This is why the three kinetic studies should be compared first. For more details, see also Section 2.6.1.

4.3.1 Catalyst

Some variety is found when comparing the catalyst properties in Table 4.1. Both literature studies used commercial ZSM-5 samples which means extrudates instead of pure powder as in the single-event case. Furthermore, the total acidity and the ratio of Brønsted acid sites to Lewis acid sites were different for Huang *et al.* [195] which might be due to the higher Si/Al ratio and the use of a water-containing feed. Thus, scope of this chapter is not only to prove feed independence, but also to investigate whether a transfer to catalysts with different composition and properties is possible. Particularly, the influence of acid strength on the protonation properties according to Thybaut *et al.* [21] is analyzed. It should be noted that for the single-event kinetic model, the concentration of strong Brønsted acid sites C_t^{SBAS} is used which was $0.135\,\mathrm{mmol\,g_{cat}^{-1}}$ and not the total acidity shown in Table 4.1. The latter value is shown here to ensure comparability with the literature studies.

Table 4.1: Properties of the catalysts used for olefin cracking experiments in the single-event kinetic model [26] and in the two models from literature [195, 237]; the surface area according to Brunauer-Emmett-Teller is given in $m^2\ g_{cat}^{-1}$, the acidity in $mmol_{NH_3}\ g_{cat}^{-1}$.

Property	Single-event kinetics [26]	Huang [195]	Ying [237]
Si/Al ratio	90	200	103
BET surface area	454	301	340
Total acidity	0.174	0.012	0.21
Brønsted to Lewis acid sites	4.27	1.35	-
Powder or extrudate	Powder	Extrudate	Extrudate

4.3.2 Experimental Setup

All kinetic studies were performed in a plug flow reactor. Table 4.2 compares the experimental parameters. It can be seen that most of them are similar, only three differences are noteworthy: the literature studies used different feeds from $C_3^=$ to $C_7^=$ olefins whereas in the single-event case, only 1-pentene was investigated. In contrast to the other two examples, Huang *et al.* [195] performed experiments with water-containing feeds resulting from dehydration reactions of alcohols to the corresponding olefins. Water is assumed to not only dilute the feed, but also to competitively adsorb on the acid sites, thereby attenuating the overall reaction [173]. Consequently, it has to be considered in the kinetic equations. Finally, Ying *et al.* [237] analyzed higher conversions than the other two studies.

Table 4.2: Experimental parameters for olefin cracking in the single-event kinetic model [26] and in the two models from literature [195, 237]; the temperatures are shown in K, the partial pressures in mbar and the volumetric flow rates in $mL\ min^{-1}$.

Parameter	Single-event kinetics [26]	Huang [195]	Ying [237]
Temperature	633 to 733	673 to 763	673 to 763
Feed olefin	$C_5^=$	$C_3^=$ to $C_7^=$	$C_3^=$ to $C_7^=$
Feed partial pressure	42.7 / 70.3	47.6 ($C_7^=$) to 83.2 ($C_3^=$)	131
Dilution	N_2	N_2 and H_2O	N_2
Total volumetric flow rate	300 / 400	120 to 560	260 to 350
Maximum conversion	0.55	0.46	0.98

4.3.3 Kinetic Modeling

Reaction networks and further modeling background to the two literature studies are found in Section 2.6.1. Similar information about the single-event kinetic model for 1-pentene cracking over ZSM-5 is given in Chapter 3. There, it is also mentioned that in the original model [26], thermodynamic data of two different sources are used. For $C_2^=$ to $C_6^=$ olefins, thermodynamic

equilibria are described by applying experimental data by Alberty and Gehrig [147]. By contrast, no measured data are available for higher species. Therefore, the thermodynamic data for $C_7^=$ to $C_{12}^=$ olefins have to be calculated using Benson's group contribution method [155, 156]. However, this combination of thermodynamic data could become problematic in case of an offset between experiments and calculated data. In the single-event kinetic model, the equilibrium between $2C_3^= \rightleftharpoons C_6^=$ is the only one that is described exclusively with experimental data [147]. All other equilibria, for example, $2C_4^= \rightleftharpoons C_8^=$ or $C_3^= + C_4^= \rightleftharpoons C_7^=$, contain a mixture between experimental [147] and calculated [155, 156] thermodynamic data. This leads to inconsistencies within the overall description of kinetics and, although yielding high accuracy for the 1-pentene cracking case, hampers a broader application. Especially results at lower temperatures are affected: at these conditions, the exothermic dimerization has significant impact. It is described, among others, as function of the thermodynamic equilibrium constant, see Section 3.1.4.

For this reason, the single-event kinetic model is re-fitted to the same experimental data [26], but with a different calculation routine for thermodynamics: in the revised model, Benson's group theory [155, 156] is exclusively used and thus applied to $C_2^=$ to $C_{12}^=$ olefins. Table 4.3 compares the estimated parameters between the original [26] and the revised model; no significant differences within the estimated parameters can be observed.

Table 4.3: Estimated activation energies E_a^{cr} and pre-exponential factors $\tilde{A}^{cr}$, including 95% confidence intervals, and the sum of squared residuals *SSQ*, resulting from an application of the original [26] and of the revised single-event kinetic model to experimental data of 1-pentene cracking; all activation energies are given in kJ mol^{-1}, whereas the pre-exponential factor is shown in s^{-1}.

Parameter	Original [26]	Revised
E_a^{cr}(s;p)	229.6 ± 0.9	229.9 ± 0.9
E_a^{cr}(s;s)	199.7 ± 0.9	200.2 ± 0.9
E_a^{cr}(t;s)	171.2 ± 0.8	171.5 ± 0.8
E_a^{cr}(t;p)	211.8 ± 1.4	211.9 ± 1.5
$\tilde{A}^{cr} \times 10^{-16}$	2.17 ± 0.31	2.73 ± 0.39
SSQ	0.0339	0.0350

Experimental data of the two literature studies are reproduced using the kinetic parameters from the revised model in Table 4.3 exclusively. Thus, if not stated otherwise, no fitting to the literature data is performed. Experimental conditions and the number of acid sites are implemented into the model according to Tables 4.2 and 4.1, respectively. A slight overpressure is assumed for both publications (p_t of 1.1 bar) to account for pressure drops in the catalyst bed. Catalyst masses and volumetric flow rates are adjusted to reach sufficient conversion. Similar to the original model [26], the reactor model is solved by applying *ode15s* from MATLAB.

Ying *et al.* [237] provide a table with all measured data points in their supporting information. For Huang *et al.* [195], no such overview is available; the measurements have to be extracted from the figures. These results are given in mole fractions whereas Ying *et al.* [237] calculate the weight-based yield. In this chapter, the corresponding values from the original publications, either mole fractions or weight-based yields, are used in order to facilitate comparisons. Their calculation is defined in Equations (4.1) and (4.2), respectively; both water (Huang *et al.* [195]) and nitrogen (Huang *et al.* [195] and Ying *et al.* [237]) are explicitly excluded,

$$y(\mathrm{O}_i) = \frac{F(\mathrm{O}_i)}{\sum_j F\left(\mathrm{O}_j\right)}, \tag{4.1}$$

$$Y(\mathrm{O}_i) = \frac{F(\mathrm{O}_i)\, M_\mathrm{m}(\mathrm{O}_i)}{\sum_j F\left(\mathrm{O}_j\right)\, M_\mathrm{m}\left(\mathrm{O}_j\right)}. \tag{4.2}$$

For Ying *et al.* [237], the denominator in Equation (4.2) can be replaced by the molar flow rate of the feed olefin at the reactor inlet multiplied by its molar mass.

At first, the comparison between model predictions and literature results is performed over conversion to suppress the influence of contact time dependent effects like water adsorption or catalyst properties; later on, these are also considered. For Huang *et al.* [195], conversion has to be calculated according to Equation (4.3) with CN_{O_i} being the carbon number of olefin O_i,

$$X(\mathrm{O}_i) = 1 - \frac{CN_{\mathrm{O}_i}\, y(\mathrm{O}_i)}{\sum_j CN_{\mathrm{O}_j}\, y\left(\mathrm{O}_j\right)}. \tag{4.3}$$

4.4 Results and Discussion

4.4.1 Different Individual Olefin Feeds as Function of Conversion

Figure 4.1 shows the results for $\mathrm{C}_3^=$ to $\mathrm{C}_5^=$ olefins as feed when the single-event kinetic model is used to reproduce the experimental data points of Huang *et al.* [195] as function of feed olefin conversion. Only the minimum and maximum temperature are shown as the two extreme cases of high and low influence of the dimerization, respectively. For both literature studies, the results of the intermediate temperatures show comparable trends, being either closer to the one at maximum or to the one at minimum temperature.

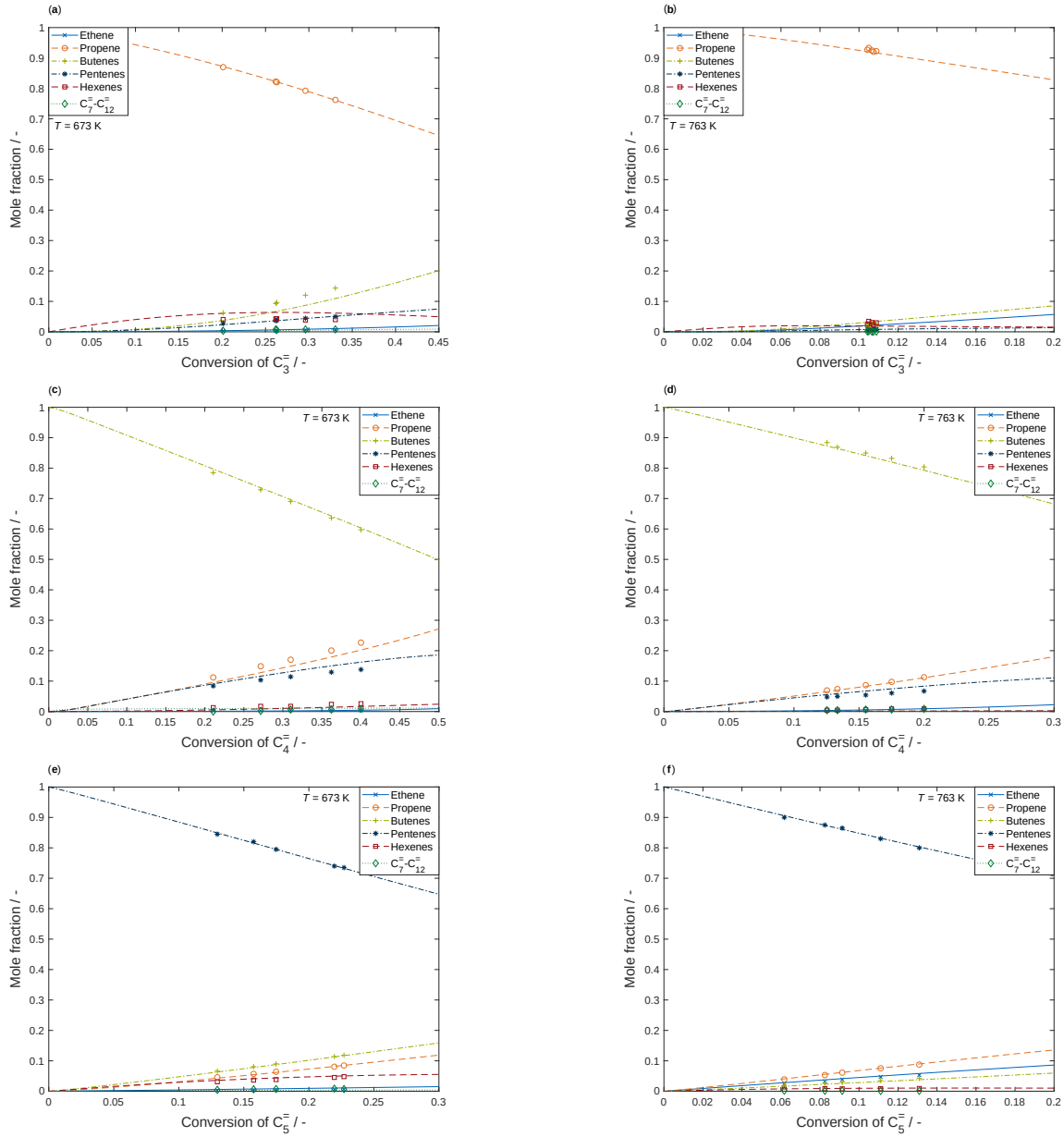

Figure 4.1: Simulation of experimental data points (symbols) from Huang *et al.* [195] using the single-event kinetic model (lines) at the lowest (left) and highest (right) temperature investigated and with olefin feeds ranging from $C_3^=$, (a) and (b), over $C_4^=$, (c) and (d), to $C_5^=$, (e) and (f).

Figure 4.1 (e) and (f) reveals high parity between simulated and measured results for pentenes as feed. Thus, in general, a transfer of the model to other reaction systems and catalysts is possible, a prerequisite for upscaling and reactor design. When analyzing Figure 4.1 (a) to (d), it can be seen that also $C_3^=$ and $C_4^=$ olefins as feed can be modeled with high agreement. In both cases, the description between calculations and experiments is of slightly less accuracy at low temperatures. For butene feeds, significant conversion is achieved faster at these conditions since dimerization is preferred here and monomolecular cracking is not possible. Figure 4.2

shows similar plots for experimental data of Huang *et al.* [195] using $C_6^=$ and $C_7^=$ olefins as feed.

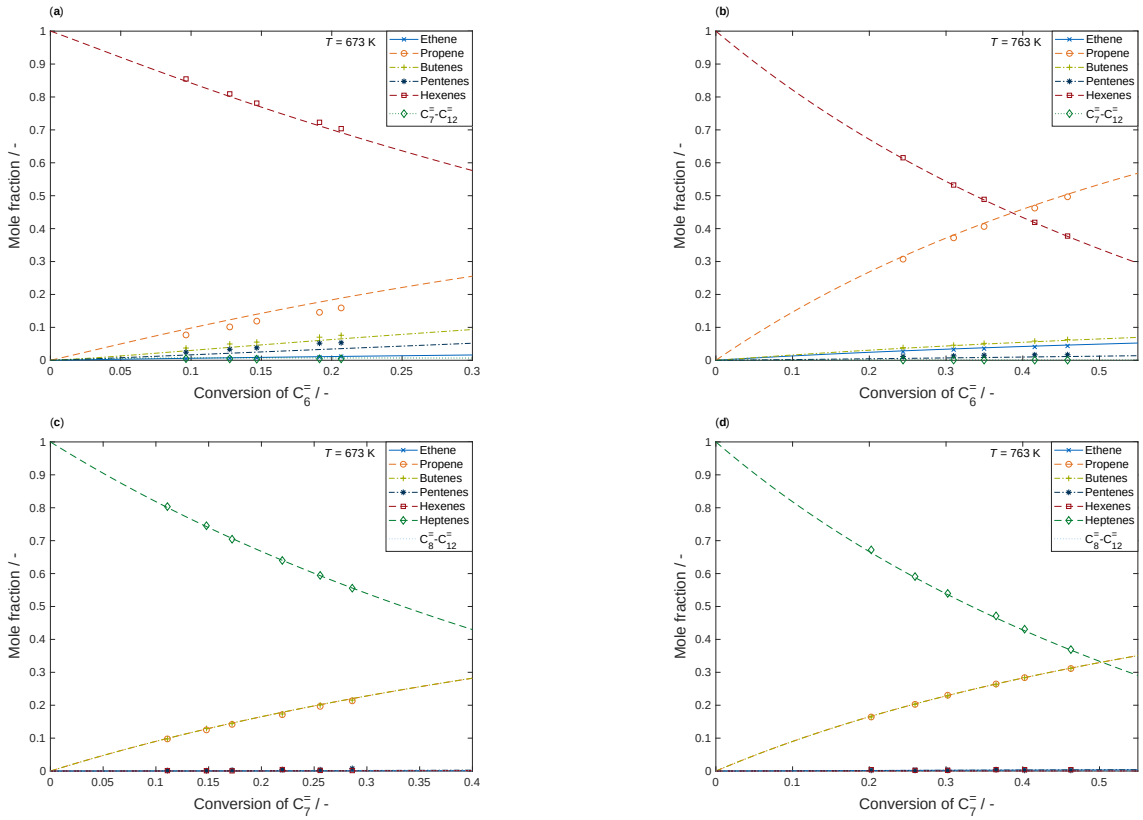

Figure 4.2: Simulation of experimental data points (symbols) from Huang *et al.* [195] using the single-event kinetic model (lines) at the lowest (left) and highest (right) temperature investigated and with olefin feeds consisting of $C_6^=$, (a) and (b), and $C_7^=$, (c) and (d).

High agreement between model and experimental data can be observed. Thus, high parity for all $C_3^=$ to $C_7^=$ feeds, all temperatures and all conversion levels is achieved - although Huang *et al.* [195] studied water-containing feeds in contrast to the single-event case. Because the kinetic model nevertheless predicts right results, it can be stated that water affects not the selectivity, but only the overall reaction rate by competing adsorption [173].

Figure 4.3 gives an overview of the results when the single-event kinetic model is used to reproduce experimental data of Ying *et al.* [237] for $C_3^=$ to $C_5^=$ olefins as feed.

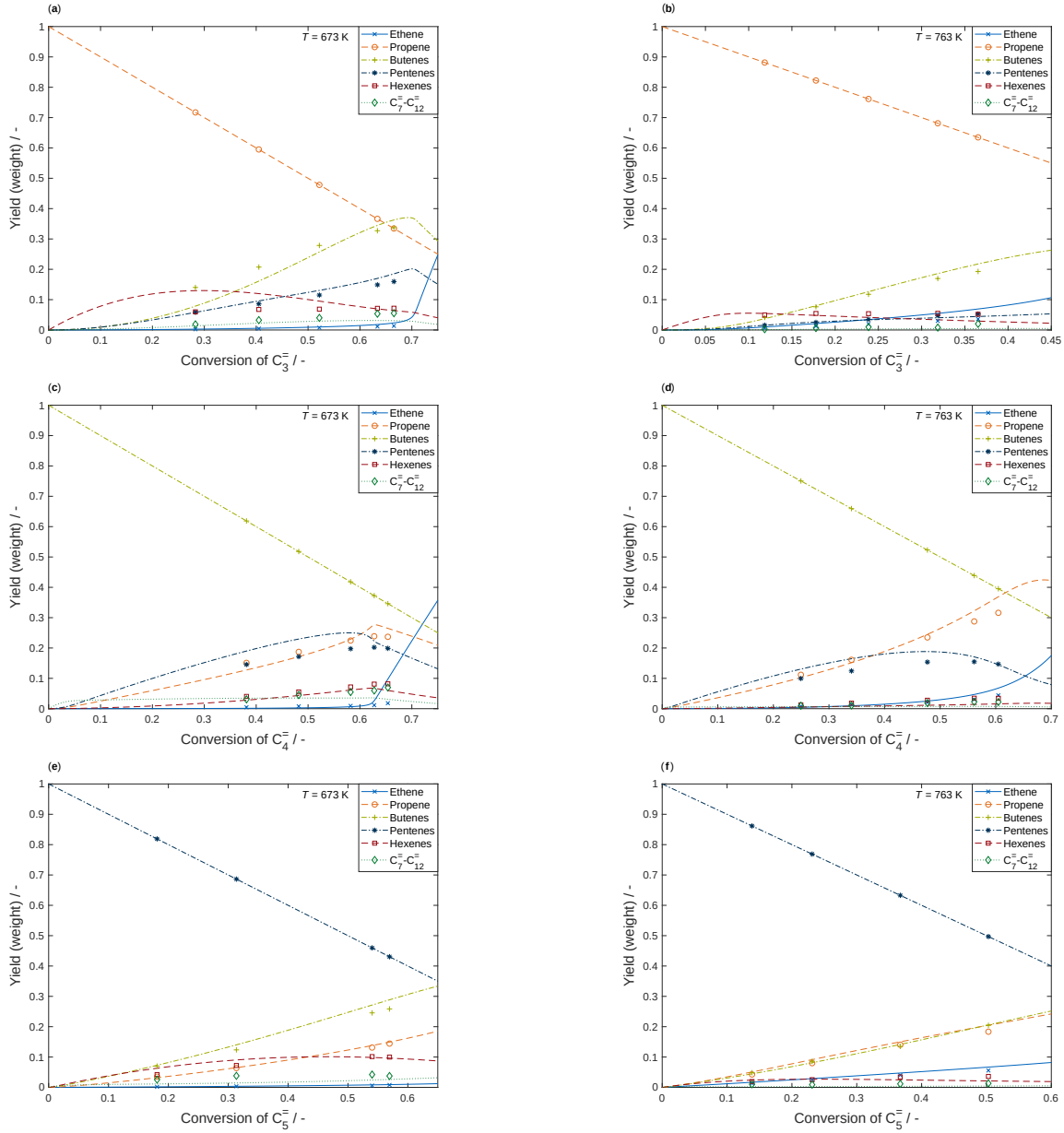

Figure 4.3: Simulation of experimental data points (symbols) from Ying *et al.* [237] using the single-event kinetic model (lines) at the lowest (left) and highest (right) temperature investigated and with olefin feeds ranging from $C_3^=$, (a) and (b), over $C_4^=$, (c) and (d), to $C_5^=$, (e) and (f).

Again, the results at higher temperatures are more accurate. Interestingly, the conversion range of Ying *et al.* [237] is significantly broader compared to Huang *et al.* [195]. Nevertheless, no increasing deviation of the modeled results with higher conversion is observable except for butenes as feed. Here, the kinetic model predicts an intense increase in ethene formation for higher conversions which is not confirmed by experimental data. This can be explained with the measurements for the single-event kinetic model where conversion never exceeded 0.55. This could impair the predictions when the main part of the feed is consumed. On the other hand, it

could also be related to selectivities caused by the catalyst. The reaction network for the single-event kinetic model has to include ethene formation out of all carbon numbers from $C_5^=$ on for maximum accuracy whereas Ying *et al.* [237] reduce its production to $C_5^=$ and $C_6^=$ compounds. Still, the quality of description is sufficient also for high conversions and $C_4^=$ olefins as feed. The agreement for $C_6^=$ and $C_7^=$ feeds can be seen in Figure 4.4.

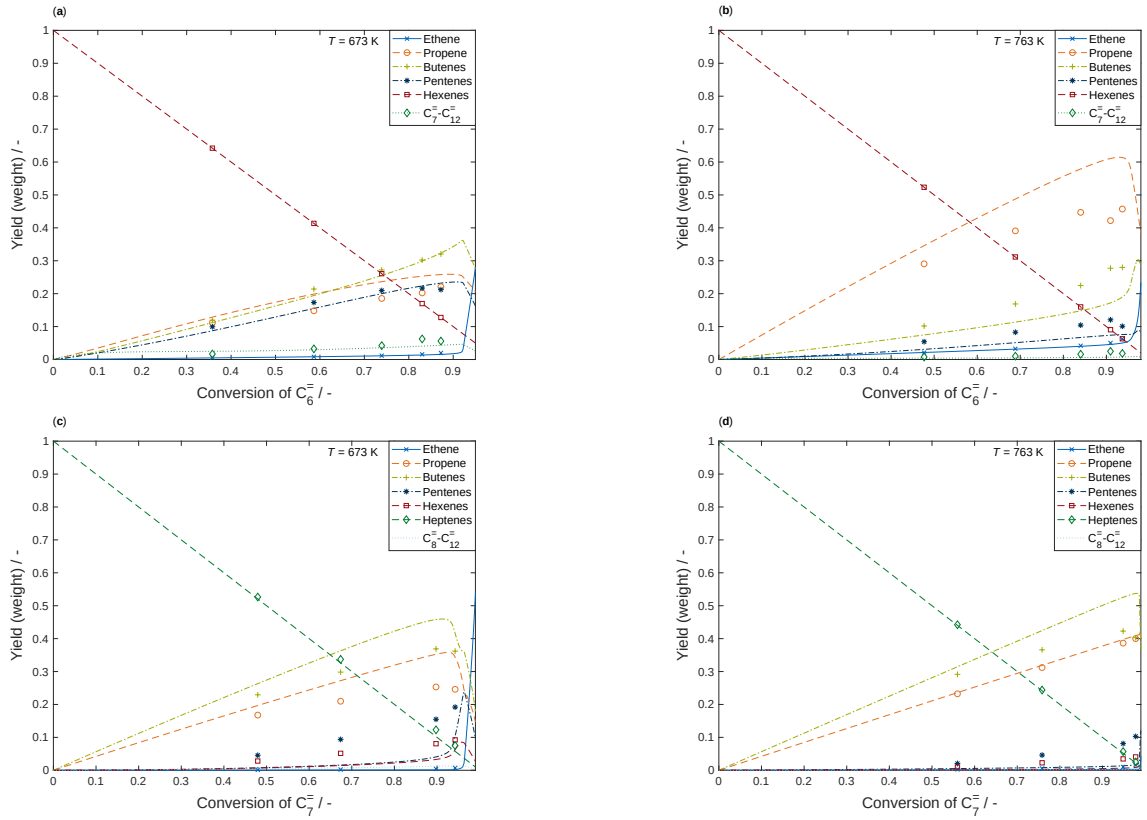

Figure 4.4: Simulation of experimental data points (symbols) from Ying *et al.* [237] using the single-event kinetic model (lines) at the lowest (left) and highest (right) temperature investigated and with olefin feeds consisting of $C_6^=$, (a) and (b), and $C_7^=$, (c) and (d).

Reproduction of experimental data is successful, but the deviation is higher for Ying *et al.* [237] compared to Figure 4.2. This might be caused by several reasons. In contrast to the single-event kinetic model, Ying *et al.* [237] consider paraffins and aromatics as side products both in their measurements and in their model. Whereas any information about this issue is missing in the study by Huang *et al.* [195], a minor fraction of these byproducts was detected during the experiments for the single-event case, see Section 3.2.1. Nevertheless, to reduce calculation effort for the complex reaction network, it was decided to ignore side reaction pathways and to add the amount of byproducts to the olefins with the same carbon number. It follows that the molar flow rate of pentenes and especially of hexenes contains a small additional fraction of side products. This might explain the model's tendency of producing too many hexenes at 673 K for propene as reactant (Figure 4.3 (a)) or the overestimation of pentenes for $C_4^=$ feeds (Figure 4.3 (c)). On the other hand, also the kinetic model by Ying *et al.* [237] overestimates

hexene production and underestimates butene formation for $C_3^=$ feeds which could be a hint for small offsets in the measurements. Moreover, the influence of missing side products should be more significant at higher conversions whereas the differences for 673 K and propene as feed become smaller for increasing contact times. However, since the measured data in Figure 4.4 include conversions of 0.95, an influence of the missing side products cannot be excluded. Another possible reason for deviations might be slightly different partial pressures of the feed olefin during the measurements because this parameter significantly influences the ratio between cracking and dimerization. The fact that simulations are of excellent accuracy for Huang *et al.* [195] suggests an influence of experimental parameters or of catalyst-related properties. Nevertheless, the predictions of the single-event kinetic model are right in their tendencies for all feeds of Ying *et al.* [237] and beyond that very accurate for propene, butenes and pentenes as reactants. Thus, with these two case studies, the feed independence of the single-event parameters derived from 1-pentene can be demonstrated. It proves that the single-event kinetic parameters that are estimated with only 1-pentene as feed are independent of feed olefin, system and reaction conditions.

4.4.2 Olefin Feed Mixture as Function of Conversion

It is still questionable whether the transfer to an arbitrary mixture of olefins is possible. This scenario is of interest because higher olefins are mostly undesired and could be recycled therefore, see Section 3.2.4. The single-event kinetic model is used to simulate the experimental results from Huang *et al.* [195] who analyzed the cracking of an olefin mixture ranging from $C_2^=$ to $C_7^=$ with mole fractions of 0.07/0.235/0.22/0.235/0.12/0.12. Figure 4.5 shows the results when applying the revised single-event kinetic model on this feed mixture and compares it with experimental data.

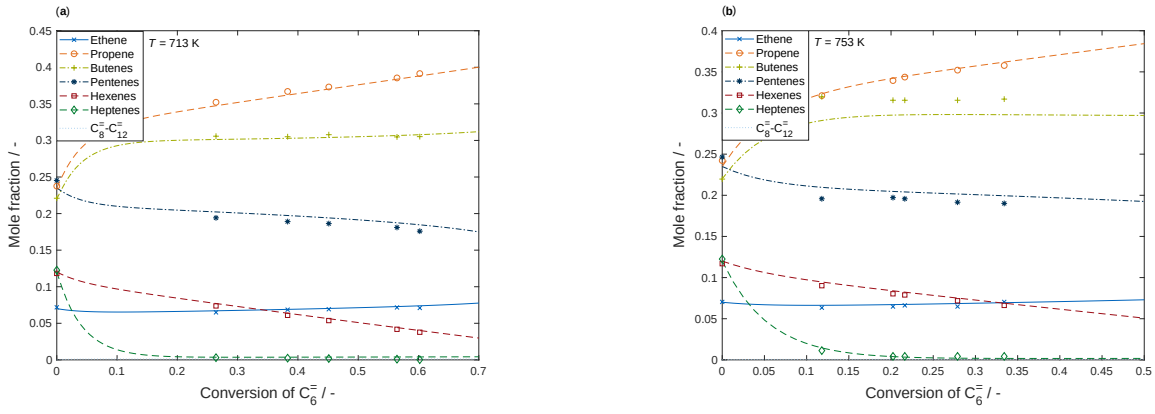

Figure 4.5: Simulation of experimental data points (symbols) from Huang *et al.* [195] for a mixture of olefins as feed using the single-event kinetic model (lines).

The plots show excellent agreement for all olefins and for both temperatures. The slight underprediction of butenes for the higher temperature of 753 K is also observed in the publication by Huang *et al.* [195]. Besides this, no deviation is noticeable. This means although the parameters have been determined with only one key component, the resulting model is able to describe the characteristic reaction pathways for a mixture of different olefins. This clearly underlines the advantages of microkinetic modeling combined with the single-event approach. Instead of performing many experiments with different olefins, one detailed experimental schedule with one component is enough. Of course, the number of experiments has to be comparably high here, which might compensate for the advantage in time. However, since the feeds in industry become more and more complex, the additional flexibility and extrapolation possibility with the single-event kinetic model are crucial advantages.

4.4.3 Different Individual Olefin Feeds as Function of Contact Time

So far, it is shown that a single-event kinetic model derived from 1-pentene cracking experiments yields kinetic parameters that predict the reactivity of different pure or mixed olefins in a right way. This is analyzed as function of conversion over two different catalysts, meaning the model calculates the right selectivities for a certain reaction progress. However, the two catalysts vary from each other and also from the one for which the kinetic model was developed. They differ in number of acid sites and acid strength. This should influence activity whereas selectivity remains unchanged as shown above. The latter fact proves that all steps of kinetic relevance from the reaction network are influenced by the change of acid strength to the same extent [21]. Consequently, both activation energies and pre-exponential factor are independent of this catalyst property. These are the kinetic descriptors of olefin cracking that have to be clearly separated from the catalyst descriptors according to the Ghent group [20, 194, 206, 207]. Whereas kinetic descriptors are constant for each of the three investigated ZSM-5 samples, catalyst descriptors like number of acid sites, adsorption values and shape selectivity have to be adapted individually.

The number of acid sites is adjusted to the corresponding values in Table 4.1 in order to reproduce the literature results as function of contact time; the kinetic descriptors from Table 4.3 remain unchanged. However, neither for Huang *et al.* [195] nor for Ying *et al.* [237], simulations yield satisfying results. This can be attributed to the different acid strength of the sites. For example, the catalyst of Huang *et al.* [195] had only one-tenth of acid sites compared to the single-event case. On the other hand, these remaining sites have higher acid strength, which again increases activity. In the following, the methodology of Thybaut *et al.* [21] is applied to account for this effect. Here, the change in activity between two catalysts because of different acid strength is ascribed to a change in protonation enthalpy $\Delta^{\mathrm{zeo}}_{\mathrm{prot}}H^{\circ}$. Thus, the single-event kinetic model is applied to the experimental results from both author groups [195, 237] with the

kinetic descriptors held constant and with $\Delta^{\mathrm{zeo}}_{\mathrm{prot}}H^{\circ}$ being the only estimated variable. This is performed only for the data with pentenes as feed to avoid any influences of the carbon number. For the data of Huang *et al.* [195], water adsorption has to be taken into account according to Equation (4.4),

$$K^{\mathrm{ads}}\left(\mathrm{H_2O}\right) = K^{\mathrm{ads,ref}}\left(\mathrm{H_2O}\right) \exp\left(-\frac{\Delta_{\mathrm{ads}}H^{\circ}_{\mathrm{H_2O}}}{R}\left(\frac{1}{T}-\frac{1}{T^{\mathrm{ref}}}\right)\right). \tag{4.4}$$

The reference temperature is set to 718 K as medium temperature of the experiments performed by Huang *et al.* [195]. An unconstrained fitting of the adsorption equilibrium constant at reference temperature $K^{\mathrm{ads,ref}}\left(\mathrm{H_2O}\right)$ and of the adsorption enthalpy $\Delta_{\mathrm{ads}}H^{\circ}_{\mathrm{H_2O}}$ leads to values of $2.9 \times 10^4\,\mathrm{bar}^{-1}$ and $-56.1\,\mathrm{kJ\,mol}^{-1}$, respectively. However, this also causes an unrealistic value for $\Delta^{\mathrm{zeo}}_{\mathrm{prot}}H^{\circ}$ of almost $-60\,\mathrm{kJ\,mol}^{-1}$. Thus, adsorption parameters are extracted from literature [319]; with $-55\,\mathrm{kJ\,mol}^{-1}$ and $-128\,\mathrm{J\,mol}^{-1}\,\mathrm{K}^{-1}$, respectively, average values for enthalpy and entropy are chosen. Using these adsorption parameters, a value of $-14.5\,\mathrm{kJ\,mol}^{-1}$ is obtained for $\Delta^{\mathrm{zeo}}_{\mathrm{prot}}H^{\circ}$. Figure 4.6 (a) depicts the results of the single-event kinetic model after including $\Delta^{\mathrm{zeo}}_{\mathrm{prot}}H^{\circ}$ and water adsorption; experimental data of Huang *et al.* [195] for pentene cracking at 763 K is shown as function of contact time.

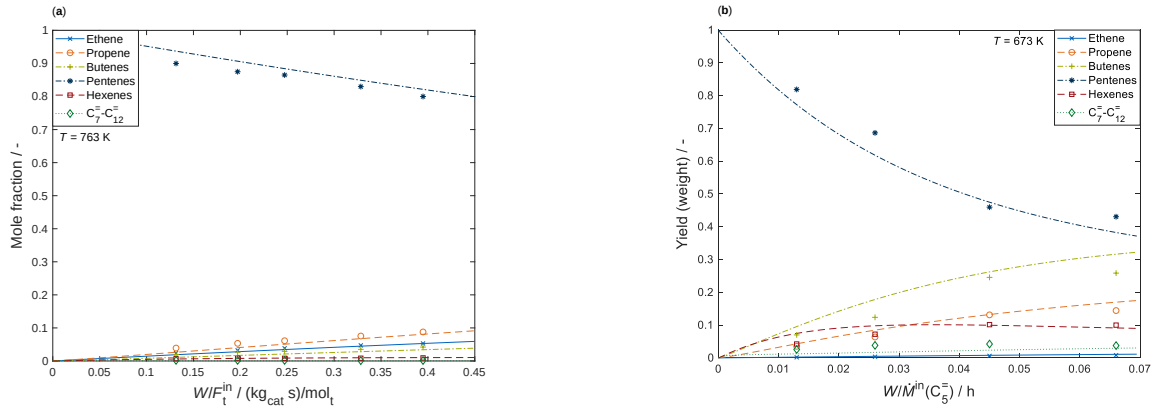

Figure 4.6: Reproduction of literature data (symbols) for pentene cracking as function of contact time with the single-event kinetic model (lines) including water adsorption and the change in protonation enthalpy caused by different acid strength of the catalyst for Huang *et al.* [195], (a), and with the adjusted protonation enthalpy for Ying *et al.* [237], (b).

For the data of Ying *et al.* [237], only $\Delta^{\mathrm{zeo}}_{\mathrm{prot}}H^{\circ}$ has to be estimated since water was absent during their measurements; a value of $6.6\,\mathrm{kJ\,mol}^{-1}$ is obtained. Figure 4.6 (b) underlines that simulations of pentene cracking at 673 K are close to the measurements when accounting for the change in acid strength.

The value of $\Delta^{\mathrm{zeo}}_{\mathrm{prot}}H^{\circ}$ for Huang *et al.* [195] is comparably low. This resembles a significant increase in acid strength which is a common phenomenon for zeolites with high Si/Al values and therefore small number of acid sites [21]. However, since the exact amount of water dilution

in these experiments is not known, a small offset in the estimated parameter is possible. By contrast, the catalyst used by Ying *et al.* [237] is similar to the one in the single-event case leading to a value for $\Delta^{zeo}_{prot}H^{\circ}$ close to zero. Nevertheless, the acid strength of the latter one is slightly higher because of the lower number of sites. Figure 4.7 (a) illustrates these effects; the line is only to guide the eyes.

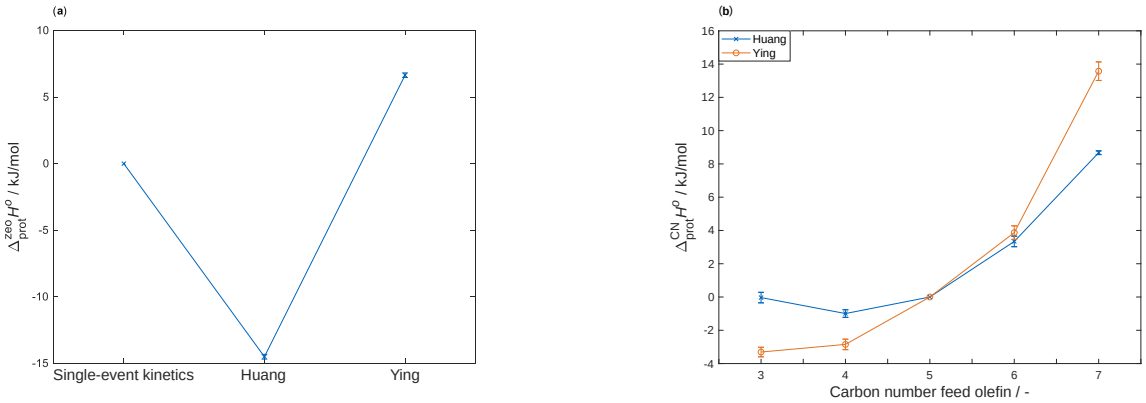

Figure 4.7: Change in protonation enthalpy when switching to experimental data of pentene cracking over different zeolites, (a), and when changing the feed olefin with the zeolite effect already considered, (b); the comparison is performed between the single-event kinetic model [26] as well as the literature studies by Huang *et al.* [195] and Ying *et al.* [237].

Although the different acid strength of the catalysts is considered, simulations for the other feed olefins as function of contact time are not successful. Again, this can be attributed to the protonation enthalpy which shows a carbon number dependence according to Thybaut *et al.* [21]. In the single-event kinetic model, this property is calculated for each olefin. However, the correlations given by Nguyen *et al.* [54, 310] yield constant protonation enthalpy values for each carbon number. Thus, the single-event case is fitted separately for each feed and catalyst to the literature data with constant kinetic descriptors, constant water adsorption (if applicable) and the respective value for $\Delta^{zeo}_{prot}H^{\circ}$ mentioned above. This leads to the change in protonation enthalpy for each carbon number $\Delta^{CN}_{prot}H^{\circ}$ as estimated value. The results can be seen in Figure 4.7 (b).

Thybaut *et al.* [21] investigated different Pt/H-(US)Y-zeolites for hydrocracking and observed that $\Delta^{CN}_{prot}H^{\circ}$ is independent of the zeolite type. Figure 4.7 (b) shows that this can be confirmed for ZSM-5 and olefin cracking. Indeed, results for the two studies show slight discrepancies for $C_3^=$ and $C_4^=$ olefins as feed. On the other hand, this has to be seen with respect to some unknown values when reproducing the literature results, e.g., the exact water amount for Huang *et al.* [195] or the concentration of strong Brønsted acid sites for Ying *et al.* [237].

Consequently, when transferring the single-event kinetic model to another ZSM-5 type, only the catalyst descriptor $\Delta^{zeo}_{prot}H^{\circ}$ has to be determined; $\Delta^{CN}_{prot}H^{\circ}$ can be extracted from Figure 4.7 (b).

The trend of the carbon number dependence is different from Thybaut *et al.* [21] who received the highest increase for the lower olefins whereas the effect was almost zero for carbon numbers higher than eight. However, they analyzed hydrocracking experiments where no dimerization occurs, meaning the reactivity is restricted to the feed olefin. In contrast to this, also olefins with other carbon numbers than the feed component undergo kinetic steps in the single-event case. So $\Delta^{\mathrm{CN}}_{\mathrm{prot}}H^{\circ}$ is more an averaged value that characterizes the change in protonation enthalpy for the whole reactive mixture and not only for the feed olefin.

The results prove that single-event parameters derived from the cracking of one key olefin can be used to describe reactivity of other individual olefins and even of their mixtures with high accuracy. The kinetic descriptors are independent of temperature, partial pressures, feed, system or catalyst.

Figure 4.8 shows parity plots for both studies when analyzed over conversion.

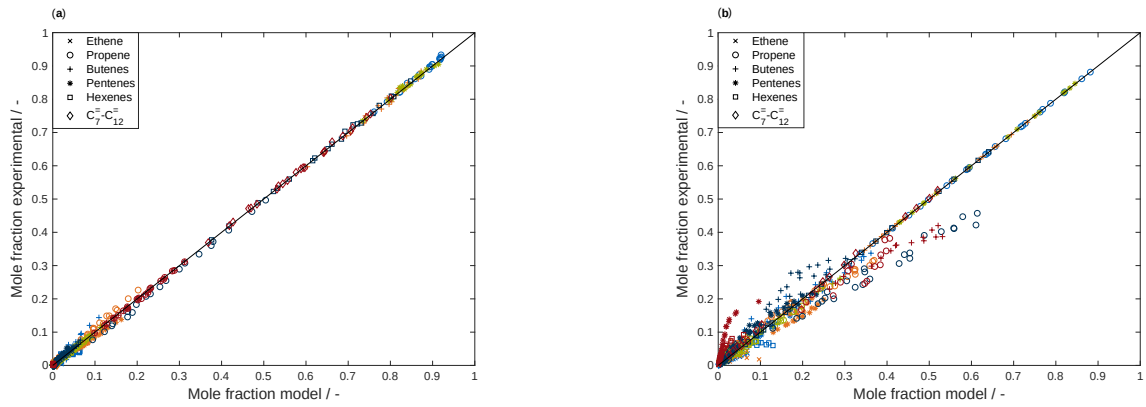

Figure 4.8: Parity plots for the simulation of experimental results from Huang *et al.* [195], (a), and Ying *et al.* [237], (b); the symbols represent the respective compounds whereas the color marks the feed olefin (blue = propene, orange = butenes, green = pentenes, dark blue = hexenes, red = heptenes).

For both cases, the high agreement is obvious. The *SSQ*-values based on mole fractions are 0.0335 in Figure 4.8 (a) and 0.7698 in Figure 4.8 (b), respectively. For Huang *et al.* [195], no systematic deviation is found. On the other hand, Figure 4.8 (b) reveals much more scatter for Ying *et al.* [237]. The most significant differences between predictions and measurements are obtained for hexenes and heptenes as feed. In both cases, monomolecular cracking to propene or propene and butenes, respectively, is overestimated by the kinetic model as it can be seen from Figure 4.8 (b). The consequence is an underestimation of secondary cracking products. Interestingly, this deteriorates at higher temperatures for hexenes as feed, but it improves at 763 K when using heptenes.

The reason for these effects cannot be resolved. The higher conversions during the measurements of $C_6^=$ and $C_7^=$ olefins might be a possible explanation. However, the data points of Huang *et al.* [195] at the highest conversions almost reach the minimum values of Ying *et al.* [237]. When comparing these points, no deviation is found for Huang *et al.* [195]. An abrupt change of the kinetic model to less exact results is not realistic. Other possible reasons like small offsets during the measurements, unknown experimental parameters or slightly different partial pressures are already mentioned. Finally, a different shape selectivity of the catalyst is also possible. In the single-event case, this factor is incorporated by excluding sterically demanding species from the reaction network [26] which is transferred to the two literature studies without adjustments. This matches Huang *et al.* [195] although they used extrudates instead of the pure ZSM-5 powder whereas for Ying *et al.* [237], it is possible that the binder affects diffusion properties and therefore selectivity. As Ying *et al.* [237] detect more side products compared to the other two studies and the selectivity differences deteriorate for higher feed olefins, an influence of this catalyst descriptor cannot be excluded. Nevertheless, the trends of the kinetic model are still right and exact for a broad range of conditions.

It is already mentioned that Thybaut *et al.* [21] come to a similar conclusion, but observe different trends for the change in standard protonation enthalpy through carbon number. Besides the main reason for this which is the different process of paraffin hydrocracking without dimerization reactions, it should be underlined that their adsorption model is different.

The calculation routine for thermodynamic data according to Benson [155] is a comparably old, but reliable method. Several revised versions [158, 160, 161] exist in literature. The results in this chapter underline the importance of thermodynamic data when transferring a kinetic model to other systems. Agreement might be improved by using one of the more recent group additivity methods. Nevertheless, even when the data calculated from Benson's approach [155] cause some uncertainties, this mistake affects all species since the methodology is consistently used for all reactions.

A precondition of the study shown in this chapter is that the underlying elementary reactions between the different studies are the same. An additional reason for the higher deviation of the data of Ying *et al.* [237] might be the side product formation. In the experiments for the single-event kinetic model, formation of byproducts like paraffins and aromatics was small, see Section 3.2.1. This is why their production pathways are not included in the model. Huang *et al.* [195] followed a similar methodology, no side products are reported here. Ying *et al.* [237] observe up to 5% byproducts which are missing in the reproduction of their measurements. Although the mistake is comparably small, further accuracy might be achieved by implementing side product formation in the single-event kinetic model.

4.5 Conclusions

This chapter proves feed independence of kinetic parameters derived from experimental data of 1-pentene cracking. The underlying single-event kinetic model can describe the cracking reactivity of $C_3^=$ to $C_7^=$ olefins and of their mixtures with high accuracy so that its use is not restricted to $C_5^=$ feeds. This makes it highly suitable for extrapolation, reactor design and on site calculations where a maximum of flexibility is required. Furthermore, a transfer to other processes with similar reactivity like MTO or MTP is possible after implementing the methanol-related pathways.

The single-event kinetic model predicts right selectivities during reproduction of experimental data from two literature studies which reveals that the underlying kinetic descriptors, i.e., activation energy and pre-exponential factor, are independent of reaction conditions, feed olefin and catalyst composition. A minor constraint arises through the slightly different product selectivity for the catalyst of one literature study when using higher feed olefins; this could be caused by a different diffusivity of the binder.

In contrast to this, catalyst descriptors have to be adapted for simulations depending on contact time. This chapter shows that adjusting the number of acid sites is not sufficient since the acid strength also changes. The latter effect can be implemented by varying the protonation enthalpy. This value does not depend only on the catalyst, but also on carbon number. Nevertheless, the change in protonation enthalpy through different feed olefins is independent of the ZSM-5 type. In summary, when the product selectivity of a new catalyst is not significantly different, only the change in protonation enthalpy related to the zeolite has to be estimated whereas all other descriptors remain unchanged. This underlines the high flexibility of the single-event kinetic model for olefin cracking.

5 Optimal Process for Catalytic Cracking of Higher Olefins over ZSM-5

This chapter was published in similar form and is reprinted with permission from:

J. Sundberg, S. Standl, T. von Aretin, M. Tonigold, S. Rehfeldt, O. Hinrichsen, H. Klein
Optimal Process for Catalytic Cracking of Higher Olefins on ZSM-5
Chemical Engineering Journal 348 (2018), 84–94, DOI 10.1016/j.cej.2018.04.060.

5.1 Abstract

Microkinetic models allow extrapolation out of the experimentally covered reaction conditions, which makes them suitable for reactor design. However, efficiency of a proposed reactor setup is hard to assess without considering the whole process including cost for utilities. Therefore, an optimal process design for catalytic cracking of higher olefins over ZSM-5 is developed here. The advantages of complex single-event kinetics available in MATLAB and a profound process simulation software (Aspen HYSYS) are combined via a self-developed interface which is then used for optimization. The process based on a recycle reactor concept is shown to be a suitable solution to selectively convert 1-pentene to the lower olefins ethene and propene. Two of the key optimization variables are reaction temperature and pressure; these are varied within a range of 360 and 460 °C and between 2.1 and 18 bar, respectively. Side product formation is explicitly included to represent realistic operating conditions. The objective function aims at maximizing profits from selling ethene and propene at polymer grade. Four different price scenarios for propene are optimized, accounting for the proposed propene supply gap. One main set of optimal process conditions is identified to maximize profits; this optimum is obtained for propene being at least 25% more expensive than ethene. With this fixed process design, the other price scenarios remain viable, even when propene and ethene have equal prices. The practical relevance of the optimal process design is further checked by a basic equipment sizing. The

purpose is to show the order of magnitude for the two main unit operations in the process, i.e., the reactor and the main column.

5.2 Introduction

Traditional production routes of lower olefins like steam cracking or FCC require high process temperatures and suffer from a propene yield that is insufficient for current demand [1, 7, 8, 13]. Propene is only a byproduct in these processes and thus, the P/E ratio based on molar flow rates of propene and ethene, respectively, at the reactor outlet is usually one or even lower [8]. This is disadvantageous because the propene demand is expected to rise faster compared to ethene [320]. The shift from naphtha to ethane as feed for steam crackers might intensify this problem [6]. Therefore, several alternative concepts for selective propene production have been studied. One of them is catalytic cracking of hydrocarbons where feeds consist either of paraffins [8] or higher olefins [50, 52, 314]. In the latter case, it is possible to convert these low-value byproducts of steam cracking into more valuable lower olefins. For this purpose, zeolites like ZSM-5 are highly suitable due to their acid catalytic function and their well-defined structure which causes a shape-selectivity [10, 321].

Propene is an intermediate product in catalytic cracking. Consequently, it is not sufficient to describe its formation only via thermodynamic equilibria. Profound kinetics are necessary which have to be implemented into a suitable reactor model. These two aspects are supplemented with the creation of a complete process model here. As the scope of this chapter is to find an optimal process design, the three parts are evaluated in a self-developed optimization framework.

Different elementary reactions occur during catalytic cracking of higher olefins: protonation, deprotonation, cracking, dimerization, hydride shift and several isomerization reactions like methyl shift and PCP branching [19, 59]. Besides this, hydrogen transfer leads to the formation of side products like paraffins and aromatics [97]. In terms of elementary reactions, this could be expressed as hydride transfer from an olefin to a carbenium ion yielding a paraffin and a carbenium ion with a double bond [57]. The latter can undergo intramolecular cyclization which, after several additional hydride transfer and deprotonation reactions, leads to aromatics. Finally, polyaromatic species cause catalyst deactivation through coke deposition [57].

Reaction networks for olefin interconversion are complex. For this reason, lumping is a common approach when a kinetic model is created; several examples exist in literature [53, 195, 236, 237], see also Section 2.6. These models might be suitable to calculate and assess reaction kinetics within the experimentally covered range. However, extrapolation is hardly possible which impedes catalyst design and usage in process optimization. For these purposes, a microkinetic

model which considers each elementary reaction is more reliable. When performed accurately, the resulting parameters should be transferable to different feeds and reaction conditions [19, 20, 214]. The single-event methodology is an example for a microkinetic concept which needs only a small number of estimated parameters [20, 21]. Such a model is created for the cracking of 1-pentene over ZSM-5 [26], cf. Chapter 3. Its extrapolation possibilities to both different conditions and different feeds are proven in Chapter 4.

In Chapter 3, it is shown how an application of the single-event kinetic model is possible: as solutions with a high P/E ratio, a two-zone reactor and a recycle reactor are suggested. In the first example, it can be seen that lower temperatures and higher pressures favor the dimerization to higher olefins. By contrast, elevated temperatures and lower pressures favor monomolecular cracking reactions to mostly ethene and propene. Consequently, the selectivity to these two desired product olefins cannot be decoupled with a common one-zone reactor. A setup with two reactor zones having different temperatures, however, increases the P/E ratio to 6.4 at 0.75 pentene conversion. In the first zone at 580 K, dimerization is the main pathway whereas the ethene formation is almost negligible. When entering the second zone at 760 K, significant cracking of the higher olefins formed in the first zone occurs. In contrast to pentene, these heavier species have more cracking options which means the energetically unfavored ethene formation can be avoided, leading to much more propene.

A disadvantage of the two-zone reactor is the fact that the product stream still contains a significant amount of compounds higher than butenes. Therefore, a recycle reactor is also proposed in Chapter 3 where all olefins besides ethene and propene are led back to the reactor inlet. The optimum operating point turns out to be a compromise between recycle ratio and P/E ratio and thus is a function of temperature. For example, a P/E ratio of 8.8 is obtained at 680 K and with a recycle ratio of 3.5. However, these results are only based on the reactor model and the kinetics without taking into account utility cost, e.g., for product separation.

Consequently, in this chapter, an optimal cracking process design for four different price scenarios of the desired product propene is presented. Whereas the ethene price is held constant at $1000\,€\,t^{-1}$, the propene price is varied between $1000\,€\,t^{-1}$, $1250\,€\,t^{-1}$, $1500\,€\,t^{-1}$ and $2000\,€\,t^{-1}$ to consider current market fluctuations. All operating cost is explicitly taken into account, for example, for heating of the endothermic cracking reactions and for coolants used in the separation. Optimization is performed with a so called hybrid approach [322]. The process simulator Aspen HYSYS is used to implement the majority of the process, giving access to a broad library of validated thermodynamic property packages and unit operation models. The optimization problem can also be defined there. In contrast to that, the reactor model with the single-event kinetics is solved in MATLAB. The actual optimization program is also implemented here; it accesses the combined optimization problem via a self-developed interface. The

suitability of the resulting optimal process is further demonstrated with basic sizing calculations for the reactor and the main column.

5.3 Methods

5.3.1 Kinetics

For the kinetic model introduced in Chapter 3, over 100 experiments were performed using 1-pentene as feed. Different combinations of temperature, total volumetric flow rate, feed partial pressure and conversion had to be investigated. During the experiments, a commercial ZSM-5 catalyst provided by Clariant AG was used that had a Si/Al ratio of 90 and a total concentration of strong Brønsted acid sites of 0.135 mmol g_{cat}^{-1}. On the resulting experimental data, a rigorous microkinetic model is applied; parameter estimation is performed by the solver *lsqnonlin* in MATLAB in combination with *ode15s* for integration. The single-event methodology that is applied during model development is described in various literature studies [19–21, 59, 214, 215]. Here, the regular rate constant k is divided into the number of single events n_e and the single-event rate constant $\tilde{k}$ as shown in Equation (5.1),

$$k = n_e \tilde{k}. \tag{5.1}$$

By applying this concept, the number of unknown parameters is drastically reduced despite including each reaction of each possible isomer for species up to $C_{12}^{=}$. This causes a reaction network consisting of almost 4400 reactions. However, all adsorption steps are treated as *quasi*-equilibrated; the corresponding equilibrium constants can be calculated making use of correlations by Nguyen *et al.* [54, 310]. Furthermore, experimental data [26] showed that isomerization is fast compared to the reactions that change the carbon number. Thus, also PCP branching and methyl shift reactions are assumed to be *quasi*-equilibrated. This is helpful especially for the methodology shown in this chapter because during integration, the reactor model has to be solved only for each carbon number and not for each isomer. Within a group of the same carbon number, the isomers are calculated with thermodynamic data. Their detailed resolution is necessary for the steps of kinetic relevance, i.e., cracking and dimerization. Here, the model differentiates between each isomer which causes 601 cracking and 140 dimerization reactions. In combination with the different protonation possibilities, almost 1600 microkinetic reaction pathways have to be considered.

The formation of paraffins and aromatics as side products is shown to be negligible for the kinetic experiments in Chapter 3 which is why their formation is not included in the original single-event model [26]. However, this effect is inevitable in an industrial process and therefore

has to be incorporated for this chapter. Even small amounts of side products can influence profits because they accumulate in the recycle and lead to increased cost for thermal separation. Instead of a microkinetic implementation, side product formation is included in a simplified manner here to reduce computational effort.

The feed independence of the underlying kinetic parameters is shown in Chapter 4: although these are derived from experiments using only 1-pentene as reactant, it is possible to describe $C_3^=$ to $C_7^=$ olefins as feed with excellent agreement. Furthermore, the single-event kinetic model predicts an olefin mixture as feed with high accuracy which is a prerequisite of its use in a recycle reactor concept.

5.3.2 Reactor Model

The underlying reactor model is similar to the one introduced in Section 3.2.4 for the recycle reactor. However, the realization of the recycle problem is performed in a different way. The simpler definition in Section 3.2.4 uses a mathematical concept fulfilling material balances in order to show the benefit on overall propene yields. By contrast, in this chapter, a once-through reactor is combined with a process simulator to rigorously model the recycle with the corresponding thermal separation tasks and energy requirements. This so called recycle reactor concept for the process is then analyzed in terms of overall profitability. From the maximum carbon number of twelve and the reaction conditions, it follows that a gas-solid reactor is investigated in the present work in contrast to some hydrocracking studies (see, for example, a recent study [202]).

5.3.3 Process Model

The proposed cracking process is designed in Aspen HYSYS V9; the resulting flow diagram can be found in Scheme 5.1. The reactant 1-pentene is fed to the process at 1 bar and 20 °C. A mass flow rate of $100\,\mathrm{kt\,a^{-1}}$ is chosen based on a typical value of $C_{4+}^=$ product streams from thermal cracking of naphtha [313]. The pump P1 increases the pressure to the desired value between 2.1 and 18 bar (optimization variable OV1). The feed is combined with the recycle stream of unreacted C_{4+}^{HC} components and heated in the feed-effluent heat exchanger Hex1. Here, a minimum temperature difference of 10 K is specified.

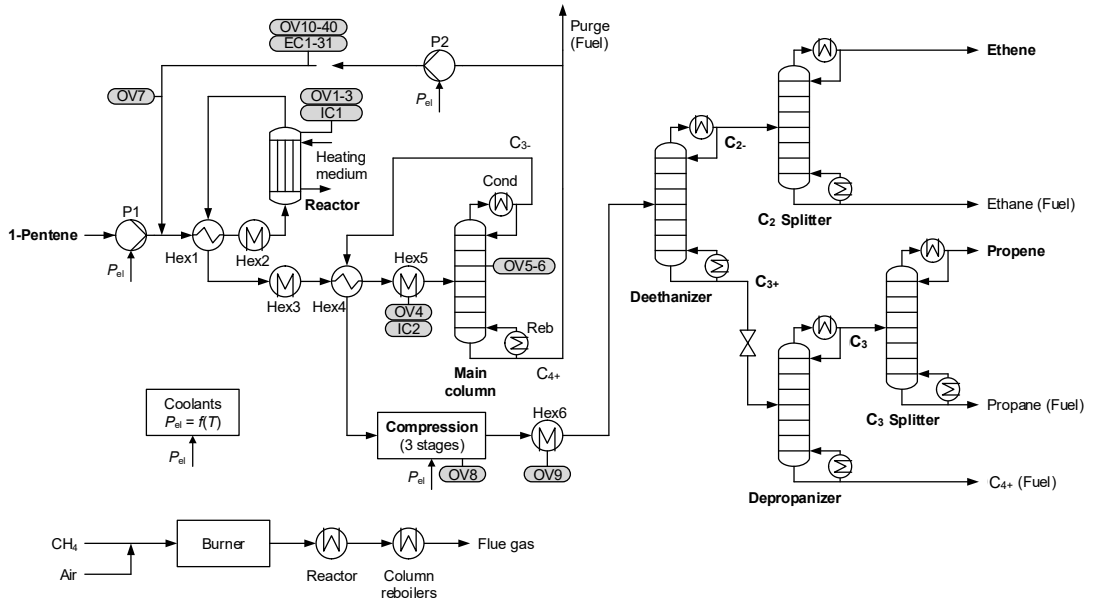

Scheme 5.1: Process flow diagram for the catalytic cracking process.

Before entering the reactor, a second heat exchanger Hex2 increases the temperature of the reactant mixture to the required value between 360 and 460 °C (OV2). The reactor itself is assumed to be isothermal. Furthermore, a linearly decreasing pressure profile is implemented, resulting in a total pressure drop of 1 bar over the whole catalyst bed. The catalyst mass W is chosen in the range between 0.1 and 10 t (OV3). An inequality constraint (IC1) ensures that the gas hourly space velocity (GHSV) with respect to the reactive $C_2^=$ to $C_{12}^=$ olefins remains above $10\,000\,h^{-1}$. The heat for Hex2 and the reactor is supplied by a heating medium which itself is heated by hot flue gases from the burner.

The evolution of side products is accounted for in a simplified way based on their formation rate in the experiments for the kinetic model, see Section 3.2.1. One percent of the $C_2^=$ to $C_{12}^=$ olefins leaving the reactor is hydrogenated to the respective *n*-paraffins. Additionally, one percent of the $C_6^=$ to $C_{10}^=$ olefins from the same stream is converted to aromatics, in detail benzene, toluene, *m*-xylene, 1,3,5-trimethylbenzene and naphthalene. Both irreversible side reaction pathways result in compounds which are inert under the conditions of olefin cracking. Thus, they accumulate in the process; their consideration leads to a more realistic simulation. In a final step the H_2 balance is closed because no H_2 was observed during the kinetic experiments: a proper fraction of $C_2^=$ to $C_{12}^=$ olefins is subjected to coking which releases H_2 and therefore closes the overall H_2 balance to zero.

The product mixture is led through Hex1 and subsequently cooled to 40 °C in the heat exchanger Hex3 using cooling water. Its temperature is further reduced in the heat exchanger Hex4 using the distillate stream from the following main column with a minimum temperature difference of 10 K.

Before entering the main column the stream can be further cooled down in Hex5 with coolants to a temperature between −30 °C and 40 °C (OV4). The removed heat flow is kept greater than or equal to zero by the inequality constraint IC2 to avoid unwanted heating of the stream. The following main column has 32 theoretical stages, including reboiler Reb and condenser Cond. The inlet is positioned on the 22nd theoretical stage from the bottom. A total yield for the C_{3-}^{HC} components between 0.99 and 0.99999 (OV5) is specified for the distillate product, while a total yield for the C_{4+}^{HC} components between 0.99 and 0.99999 (OV6) is set for the bottoms product. The condenser Cond of the main column with a temperature of approximately −25 °C has to be operated with a coolant, the reboiler Reb at approximately 50 °C is heated with steam produced with flue gas from the burner.

The bottoms product of the main column mainly contains unreacted C_{4+}^{HC} components that are recycled to the reactor by pump P2. A small amount has to be purged before in order to remove inerts from the process and to limit the recycle stream. The flow rate of the recycle stream and thus indirectly of the purge is determined via the recycle ratio, which is the molar ratio of recycled to fresh feed and is varied between 0 and 10 (OV7).

The distillate product of the main column contains the main products ethene and propene, small concentrations of ethane and propane and traces of C_{4+}^{HC} components. The separation sequence for this raw product is based on a typical layout described in literature [313]. For all following distillation columns the feed stage has been adjusted manually until no further enhancement on the process performance could be observed.

Before separation, the process stream is usually compressed to an elevated pressure in order to avoid low temperatures in the condensers of the distillation columns. For this reason the heat exchanger Hex4 is followed by a compression unit with three stages. The isentropic efficiency of each stage η_C is assumed to 0.75 with cooling to 40 °C after each stage using cooling water. Here, the raw product is compressed to a pressure between 18 and 27 bar (OV8).

Subsequent to compression, the temperature of the raw product can be further decreased to a temperature between −30 °C and 40 °C (OV9) in Hex6 using coolants. The chosen combination of pressure (OV8) and temperature (OV9) influences the following separation section in terms of energy consumption, for example, through the required condenser temperatures.

The deethanizer column has 22 theoretical stages, including reboiler and condenser. The inlet is positioned on the 17th theoretical stage from the bottom. An ethene yield of 0.9999 is specified for the distillate product and a propene yield of 0.999 for the bottoms product. Due to the elevated pressure, the condenser can be operated at roughly −30 °C using coolants, while the reboiler at 50 °C is heated with steam produced with flue gas from the burner.

The distillate product from the deethanizer column mainly contains ethene and small amounts of ethane. Further separation is carried out in the C_2 splitter column with 52 theoretical stages, including reboiler and condenser. The inlet is positioned on the 27^{th} theoretical stage from the bottom. For the distillate product an ethene mass purity of 0.999 is specified to match polymer grade specifications as well as an ethene yield of 0.99. Also here, the condenser can be operated at roughly −30 °C using coolants, while the reboiler at approximately −10 °C operates below ambient temperature and does not require heating with steam. The main product ethene can be withdrawn from the process as the distillate product, while the bottoms product mainly consists of ethane that is used as fuel for the process burner.

The product stream from the bottom of the deethanizer column mainly consists of the C_{3+}^{HC} fraction that is fed to the depropanizer column with 32 theoretical stages, including reboiler and condenser. As described in literature [313], the column operates at a fixed pressure of 18 bar. The inlet is positioned on the 17^{th} theoretical stage from the bottom. For the distillate product a propene yield of 0.999 is specified, for the bottoms product a butene yield of 0.999. Due to the elevated pressure the condenser can be operated at roughly 45 °C using cooling water, while the reboiler at approximately 60 °C is heated with steam produced with flue gas from the burner. The bottoms product of the depropanizer mainly contains C_{4+}^{HC} components that are used as fuel for the process burner.

The distillate product of the depropanizer contains primarily propene and small amounts of propane. It is fed to the C_3 splitter column with 152 theoretical stages, including reboiler and condenser. The inlet is positioned on the 102^{nd} theoretical stage from the bottom. For the distillate product a propene mass purity of 0.995 is specified to match polymer grade specifications, as well as a propene yield of 0.999. Again, the condenser in the C_3 splitter column can be operated at roughly 45 °C using cooling water, while the reboiler at approximately 50 °C is heated with steam produced with flue gas from the burner. Propane as main fraction of the bottoms product is used as fuel for the process burner whereas the main product propene is withdrawn as distillate from the process.

The process burner is operating with methane as fuel and 10% excess air at an inlet temperature of 20 °C and a pressure of 1.013 bar. The hot flue gas is first used to heat the reactor heating medium. After that, steam for the distillation columns is produced. The total fuel demand is adjusted to match a flue gas exit temperature of 150 °C. A higher temperature would result in heat loss, while a lower temperature causes corrosion by condensation of sulfur trace components stemming from the natural gas [323]. The heating value of purge and distillate streams (except for ethene and propene) is converted into an equivalent methane stream which reduces the imported amount of methane.

For process temperatures down to 40 °C, cooling water is used which is assumed to have negligible cost. In the case of lower temperatures, the coolants propene and ethene are used as a compression based cooling cascade with three pressure levels each. The high pressure (HP) level for both coolants is determined by the heat removal, for propene by condensation at 40 °C with cooling water and for ethene by the coldest propene stage and a minimum temperature difference of 5 K. The low pressure (LP) level for both coolants is set to 1.1 bar to achieve a small positive pressure difference to the atmosphere. The medium pressure (MP) level for each of the coolants is then determined by choosing the same pressure ratio between the HP and MP as well as the MP and LP levels. The resulting mechanical power requirements P_{mech} per heat Q_{cool} removed at a specific process temperature level were calculated in a preliminary study and can be found in Table A.1 in the Appendix. The temperature values include a minimum temperature difference of 5 K between the process and coolants side. The results are used to calculate the mechanical power requirements at a specific process temperature by piecewise linear interpolation. This creates a function with non-differentiable points. However, due to the usage of difference quotients to estimate the gradients, these are averaged over the range of the stepsize, thereby avoiding numerical problems.

5.3.4 Optimization Task

Objective function

The profit per ton of feed is chosen as the objective function for the optimization task. The prices for sales products and utilities are specified as shown in Table 5.1.

Table 5.1: Prices for sales products and utilities; four different scenarios are considered for the propene price; olefin and natural gas prices are given in € t^{-1} whereas the electrical power price is shown in € $kW^{-1}\,h^{-1}$.

Description	Value
Ethene (polymer grade) price $c_{C_2^=}$	1000
Propene (polymer grade) price $c_{C_3^=}$	1000/1250/1500/2000
Natural gas (methane) price c_{NG}	368.3
Electrical power price c_{el}	0.1285

Especially the propene price and its ratio to the ethene price is important for the feasibility of the process. Therefore, four different scenarios are considered for the propene price while the rest of the prices are kept constant.

The specific prices for natural gas and electrical power in Table 5.1 are derived from a publication by the Statistisches Bundesamt (Federal Statistical Office) in Germany [324]. The objective function OF can be expressed as shown in Equation (5.2),

$$OF = \frac{\dot{M}\left(\mathrm{C}_2^{=}\right) c_{\mathrm{C}_2^{=}} + \dot{M}\left(\mathrm{C}_3^{=}\right) c_{\mathrm{C}_3^{=}} - \dot{M}\,(\mathrm{NG})\, c_{\mathrm{NG}} - P_{\mathrm{el}}\, c_{\mathrm{el}}}{\dot{M}\,(\mathrm{Feed})}, \tag{5.2}$$

with the mass flow rates $\dot{M}\left(\mathrm{C}_2^{=}\right)$ of ethene product, $\dot{M}\left(\mathrm{C}_3^{=}\right)$ of propene product and $\dot{M}\,(\mathrm{NG})$ of natural gas import as well as the electrical power import P_{el}. For the generation of mechanical power from electrical power, a conversion efficiency of 0.95 is assumed.

Constraints

The inequality constraint IC1 for the GHSV of the reactor with respect to the reactive $\mathrm{C}_2^{=}$ to $\mathrm{C}_{12}^{=}$ olefins described in Section 5.3.3 is chosen in order to keep the reactor size within a technically feasible range. The inequality constraint IC2 for the cooler in the feed of the main column ensures that heat is removed from the stream.

The equality constraints EC1 to EC31 are required to solve the recycle problem as part of the optimization task. They represent the temperature, pressure and component mass flow rates for the recycle problem.

Optimization variables

The optimization variables and their respective lower and upper bounds are summarized in Table 5.2.

Table 5.2: Tag names and description of the optimization variables as well as their variation range; pressures are given in bar, temperatures in °C and the catalyst mass in t.

Tag	Description	Lower bound	Upper bound
OV1	Reactor pressure	2.1	18
OV2	Reactor temperature	360	460
OV3	Reactor catalyst mass	0.1	10
OV4	Main column feed temperature	-30	40
OV5	Yield of $\mathrm{C}_{3-}^{\mathrm{HC}}$ in main column (top)	0.99	0.99999
OV6	Yield of $\mathrm{C}_{4+}^{\mathrm{HC}}$ in main column (bottom)	0.99	0.99999
OV7	Molar recycle ratio	0	10
OV8	Separation pressure	18	27
OV9	Deethanizer feed temperature	-30	40
OV10 to OV40	Degrees of freedom recycle	0	1

The lower bound of the reactor pressure (OV1) is chosen based on a minimal process pressure of 1.1 bar that is slightly higher than ambient pressure. The value of 2.1 bar results from allowing a pressure drop of 1 bar along the reactor. The upper limit of 18 bar is set to match the lowest pressure in the following separation section.

The bounds for the reactor temperature (OV2) are adapted to the range of the measurements for the kinetic model [26].

For the lower limit of the reactor catalyst mass (OV3), a value that guarantees significant conversion of the reactants is chosen. The upper bound is set large enough to allow operating points with a high yield of the irreversible ethene formation.

The lower temperature limits for the additional cooling (OV4 and OV 9) are given by the typical condenser temperatures in the subsequent columns. The upper values are determined by the temperature that can be achieved through cooling water.

In the main column, the total C_{3-}^{HC} yield in the distillate product (OV5) and the total C_{4+}^{HC} yield in the bottoms product (OV6) have as upper limits a value of practically one, the theoretical maximum. The lower limits are chosen that both a substantial impurity of C_{3-}^{HC} in the bottom product as well as C_{4+}^{HC} in the top product can be allowed if favorable with respect to the objective function.

The lower limit of the recycle ratio (OV7) represents the case that nothing is recycled back to the reactor. The upper limit keeps the recycle stream within a technically relevant order of magnitude.

The lower bound for the initial separation pressure (OV8) is chosen to match the fixed pressure in the final C_3 splitter column in a conventional thermal cracking process [313]. The upper limit is mentioned in the same publication [313] as the maximal pressure for the deethanizer column upstream in the process.

The remaining optimization variables OV10 to OV40 are required as degrees of freedom for the recycle problem. They represent the temperature, pressure and component mass flow rates of the recycle and are treated as normalized values between zero and one relative to reference values.

Optimization approach

As stated before, a hybrid approach developed in previous studies [322] is chosen for optimization. The process from Section 5.3.3 is implemented in Aspen HYSYS where the property method predictive Soave-Redlich-Kwong is used to describe the thermodynamic behavior of the components. The optimization problem is also defined here. A self-developed MATLAB interface then allows the application of kinetics (Section 5.3.1), of the reactor model (Section 5.3.2) and of the gradient-based solver *fmincon* with the *sqp* algorithm for process optimization. Derivatives are determined by numerical differentiation. All values are converted to dimensionless variables between zero and one before optimization. As described in previous work on the optimization interface [322], supplying accurate estimates for the derivatives is crucial for the success of gradient-based optimization algorithms. The accuracy of both reactor and process simulation were increased significantly in order to guarantee this. Thereby, an overall relative numerical error of around 10^{-6} was achieved for the combined simulation. For the numerical differentiation, a general step size of 10^{-2} for the scaled variables was found to be sufficiently large to suppress this numerical error while the systematic error due to nonlinearities is still kept small. Additionally, central differences had to be used instead of forward differences to obtain reliable derivative information for the gradient-based optimization algorithm. Convergence tolerances were set to 10^{-4} in terms of optimality measure *TolFun*, to 10^{-5} in terms of step size *TolX* and to 5×10^{-5} for constraints *TolCon*. In the case that the simulation is unable to obtain a solution for a given set of optimization variables, the objective function and constraints are replaced by predefined values indicating a low performance and unfeasible point. A sign change of the objective function in Equation (5.2) converts the maximization problem into a minimization problem as it is required by *fmincon*.

The MATLAB interface to the external process simulator is extended to incorporate the reactor implemented in MATLAB. After a first process simulation call the temperature, pressure and component molar flow rates at the reactor inlet stream are used as input for the MATLAB reactor model. Its output is then fed back to the outlet stream in the process simulator and used for the second process simulation call. This methodology works as long as no recycle around the reactor is present. However, the recycle problem in this chapter has to be represented by a set of additional optimization variables and equality constraints and is solved as part of the optimization problem. The coupling of MATLAB and Aspen HYSYS is illustrated in Scheme 5.2.

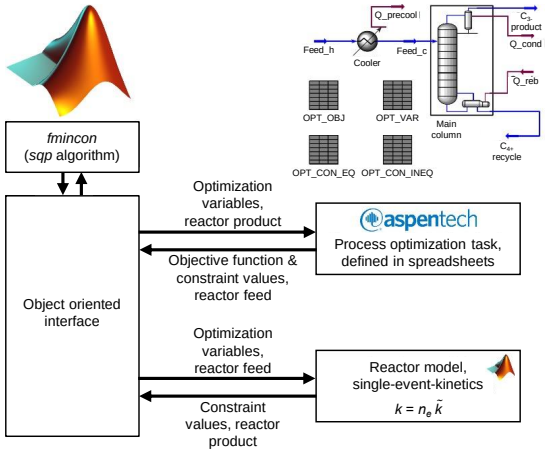

Scheme 5.2: Block flow diagram of the optimization approach.

The reactor model yields the molar flow rates for each group of isomers as output. As isomerization is assumed to be at thermodynamic equilibrium (Section 5.3.1), the specific isomer components for each carbon number are not resolved as separate species during integration, but calculated after each integration step using thermodynamic data, see Section 3.1.4. Therefore, the molar flow rates of the isomer groups can be represented by C_2^{HC}–C_{12}^{HC} (*n*-paraffins and 1-olefins) within the process simulation. For the implementation of the side reactions described in Section 5.3.3, the C_6^{ar}–C_{10}^{ar} aromatics benzene, toluene, *m*-xylene, 1,3,5-trimethylbenzene and naphthalene are added.

The optimization is performed from different starting points for each scenario to check for dependencies on these values. Approximately 15 iterations are made for each run until convergence is reached. This requires roughly 600 function evaluations, including determination of numerical derivatives. One optimization run can be performed in around 5 h (single CPU core with 3.5 GHz).

5.3.5 Basic Equipment Sizing

Reactor

A fixed bed shell-and-tube reactor design is chosen with the ZSM-5 catalyst filled in the tubes and the heating medium on the outside. The dimensions of the reactor are either determined by reaction or heat supply. Additionally, the pressure drop over the catalyst bed has to be considered.

In terms of the reaction, the bulk volume V_{cat} of the catalyst bed restricts the reactor size. It is calculated according to Equation (5.3),

$$V_{cat} = \frac{W}{\rho_{cat}(1-\varepsilon)}, \tag{5.3}$$

with the required catalyst mass W (OV3), the void fraction ε, set to 0.4, and the catalyst density ρ_{cat}. For the latter, a typical value of 1.8 g cm^{-3} is taken [307].

For the heat supply, the required heat transfer area A_{ht} determines the reactor size. It is calculated via Equation (5.4),

$$A_{ht} = \frac{\dot{Q}_r}{U\,\Delta T_m}, \tag{5.4}$$

with the heat of reaction $\dot{Q}_r$, the overall heat transfer coefficient U and the logarithmic mean temperature difference ΔT_m. The value of U is estimated based on typical heat transfer coefficients on the inside and the outside of the tube. On the inside, a heat transfer coefficient α_i of 1000 W m^{-2} K^{-1} for a fixed bed reactor with similar dimensions is derived from literature [325]. The wall is assumed to have no significant impact on the overall heat transfer coefficient. On the outside of the tube, a molten salt mixture of sodium and potassium nitrate can be used as heating medium, which is state of the art for solar power plants and stable for temperatures up to 550 °C according to Tamme *et al.* [326]. A heat transfer coefficient α_o of 1000 W m^{-2} K^{-1} is assumed here. The value would correspond to forced convection of water as described in literature [327]. This results in an estimated overall heat transfer coefficient U of 500 W m^{-2} K^{-1}. The logarithmic mean temperature difference ΔT_m is set to 10 K.

For both size determining quantities, i.e., V_{cat} and A_{ht}, the number of tubes N_T can be calculated for a given tube length using a typical outer tube diameter D_O of 25 mm with a wall thickness of 2 mm [328]. The higher number of tubes N_T of the two approaches determines the design. In the case that the reaction and not the heat transfer is limiting, a sufficiently large heat transfer area is automatically present and the driving temperature difference can be reduced. In the case of limiting heat transfer the area could be enlarged by dilution of the active catalyst mass with inert material.

The tube length L itself is determined by the total pressure drop in the reactor. The specific pressure drop per length is calculated with the Ergun equation given in Equation (5.5) [329],

$$\frac{\Delta p}{\Delta L} = 150\,\frac{(1-\varepsilon)^2}{\varepsilon^3}\,\frac{\eta_{fl}\,v_{fl}}{d_P^2} + 1.75\,\frac{1-\varepsilon}{\varepsilon^3}\,\frac{\rho_{fl}\,v_{fl}^2}{d_P}, \tag{5.5}$$

with the dynamic viscosity of the fluid η_{fl}, the superficial velocity of the fluid v_{fl}, the particle diameter d_P, which is 2 mm, and with ρ_{fl} as the density of the fluid.

Because the superficial velocity v_{fl} in Equation (5.5) depends on the number of tubes, the tube length is determined iteratively such that the total pressure drop of 1 bar is achieved.

With the number of tubes and the tube length fixed, the diameter of the tube bundle D_R in the reactor is calculated according to Wolf and Kirchner [328]. The correlation is adapted to a triangular pitch of the tubes, a tube-tube center distance of 32 mm and one pass within the shell. The diameter of the tube bundle in the reactor is then determined by the coherence shown in Equation (5.6),

$$D_R = \frac{32\sqrt{1.1\,n_T} + D_O}{1000}, \tag{5.6}$$

with D_O in mm and D_R in m.

Main column

The dimensions of the main column are analyzed separately for the tray sections above (top section) and below the feed (bottom section). The gas load is used to determine the column diameter for an optimal process design. According to literature [330], it is characterized by the F-factor in Equation (5.7),

$$F = v_g \sqrt{\rho_g}, \tag{5.7}$$

with the superficial gas velocity v_g referred to the active area A_{ac} of one tray and the density ρ_g of the gas. A typical value for F of 1.5 $Pa^{0.5}$ is chosen [330].

Assuming a reasonable value of 0.7 for the ratio of weir length to total column diameter D_{col} [330], the active area A_{ac} can be related with the total area A_t and defined as shown in Equation (5.8),

$$A_{ac} = 0.825\,A_t = 0.825\,D_{col}^2\,\frac{\pi}{4}. \tag{5.8}$$

Using the coherences in Equations (5.7) and (5.8), the required column diameter can be calculated using the volumetric flow rate $\dot{V}_g$ and the gas density ρ_g from the simulation, see Equation (5.9),

$$D_{col} = \sqrt{\frac{4\,\dot{V}_g\sqrt{\rho_g}}{0.825\,\pi\,F}}. \tag{5.9}$$

For the top and bottom sections of the column, different diameters D_T and D_B, respectively, are calculated. For each result, it is checked whether the resulting liquid load relative to the weir

length is between 2 and 100 $m^3\,m^{-1}\,h^{-1}$ given as limits in literature [330]. In the case that the liquid load exceeds these limits, the column diameter is adjusted accordingly.

The separation section with deethanizer, C_2 splitter, depropanizer and C_3 splitter subsequent to compression is state of the art for thermal cracking plants [313] and thus not considered in terms of equipment design here.

5.4 Results and Discussion

The results stemming from the process optimization calculations with four different propene price scenarios are shown in Table 5.3 where the ethene price is held constant at 1000 € t^{-1}.

Table 5.3: Optimization variable results for different propene price scenarios; pressures are given in bar, temperatures in °C, the catalyst mass in t, propene prices in € t^{-1} and the output of the objective function in € t_{Feed}^{-1}.

Tag	Description	Propene price			
		1000	1250	1500	2000
OV1	Reactor pressure	9.84	4.59	4.14	3.44
OV2	Reactor temperature	460	460	460	460
OV3	Reactor catalyst mass	6.55	1.22	1.20	1.49
OV4	Main column feed temperature	34.2	30.1	28.4	22.6
OV5	Yield of C_{3-}^{HC} in main column (top)	0.99293	0.99403	0.99456	0.99584
OV6	Yield of C_{4+}^{HC} in main column (bottom)	0.99869	0.99986	0.99999	0.99999
OV7	Molar recycle ratio	4.07	10	10	10
OV8	Separation pressure	19.6	20.2	18.9	18.8
OV9	Deethanizer feed temperature	12.2	26.4	30.8	31.1
IC1	Reactor minimum gas hourly space velocity	Active	-	-	-
IC2	Heat removal before main column	-	-	-	-
	Output objective function	899	1056	1267	1693

Generally, a low propene price results in a reduced profit per ton of feed compared to the utilities natural gas and electric power. In this case, the optimal process design favors a lower utility consumption over additional propene yields. By contrast, Table 5.4 shows the rise in propene yields for higher prices. In addition, Table A.2 in the Appendix reveals that for these scenarios, the increased sales profit allows for higher specific energy consumption.

Table 5.4: Product yields for different propene price scenarios with the ethene price held constant at 1000 €t^{-1}; propene prices are shown €t^{-1}.

Description	Propene price			
	1000	1250	1500	2000
Ethene yield	0.748	0.089	0.077	0.074
Propene yield	0.217	0.830	0.843	0.854
Total product yield	0.965	0.918	0.921	0.927

Optimizing the process to the lowest propene price of 1000 €t^{-1} in Table 5.3 leads to a high reactor pressure (OV1). This increases the condensation temperature in the main column and reduces coolant cost. Within the reactor, the high pressure increases the partial pressures and reaction rates, but also creates an undesired driving force to higher olefins. This negative effect is compensated by a high active catalyst mass (OV3) which is only limited by the active inequality constraint for the reactor GHSV (IC1). The resulting high conversion per pass allows a lower recycle ratio (OV7), which reduces the throughput and energy consumption of the main column additionally. A low propene yield is observed, see Table 5.4, because the low GHSV favors the irreversible formation of ethene.

When optimizing the process to higher propene prices from 1250 €t^{-1} onwards, the propene yield becomes more important compared to the utility cost as it can be seen in Tables 5.4 and A.2; the latter is found in the Appendix.

The gradually decreasing pressure (OV1) increases the overall propene yield, thereby causing additional coolant cost in the main column. The selectivity to the intermediate product propene is increased additionally by a lower active catalyst mass (OV3) and higher GHSV. The recycle ratio (OV7) is increased to the upper bound in order to maximize the propene yield.

The reactor temperature (OV2) is kept at the upper limit of 460 °C for all scenarios. Thereby, the driving force for the endothermal cracking reactions is kept as high as possible. Additionally, the rate of reaction stays high and increases the conversion per pass.

The remaining optimization variables OV4, OV5, OV6, OV8 and OV9 have only secondary influence on the objective function and mainly depend on the primary effects discussed before.

The optimal main column feed temperature (OV4) becomes gradually lower as it is a function of the decreasing condenser temperature and thus of the reactor pressure (OV1).

The optimal C_{3-}^{HC} yield (OV5) increases for a rise in propene price. Nevertheless, the feed composition with regard to ethene and propene is different for each optimal design and the trend of the C_{3-}^{HC} yield should not be overinterpreted in terms of the objective function. However, it

can be seen as important finding that the value lies between the bounds and thus is not limiting the design.

The C_{4+}^{HC} yield (OV6) in the main column is high and gradually approaches towards the upper bound for an increasing propene price. As for the C_{3-}^{HC} yield, an interpretation of the trend in terms of the objective function is difficult. However, for all cases, a high C_{4+}^{HC} yield in the recycle stream is worth the additional energy consumption of the column, a trend that is further increasing for higher propene prices.

The trends of the separation pressure (OV8) and the deethanizer feed temperature (OV9) should not be further discussed here, because their influence on the objective function at the optimum is not significant. This effect can be explained with the low directional derivatives when analyzing these variables at the optimum.

The basic equipment design results in Table 5.5 show a reasonable size for the main column diameters in the top and bottom section. The bottom section of the column requires a significantly larger area due to the high liquid recycle flow rate.

For the reactor, the heat transfer determines the size for all price scenarios. The required length of the catalyst tubes in the reactor is significantly higher when optimizing the process to a propene price of $1000\,€\,t^{-1}$ due to the lower recycle stream at a fixed pressure drop of 1 bar. The number of tubes and the tube bundle diameter show reasonable values for the scenarios, although the resulting low length to diameter ratio of the reactor for higher propene prices might be unconventional.

Table 5.5: Basic equipment design results for different propene price scenarios; diameters and lengths are given in m, the gas hourly space velocity GHSV in h^{-1} and propene prices in $€\,t^{-1}$.

Location	Description	Propene price			
		1000	1250	1500	2000
Main column	Top section diameter	1.21	1.84	1.97	2.15
	Bottom section diameter	2.29	4.24	4.10	3.85
Reactor	Number of tubes	6432	10633	10920	11590
	Tube length	2.45	0.69	0.66	0.62
	Tube bundle diameter	2.69	3.46	3.51	3.61
	Limiting criterion	Heat	Heat	Heat	Heat
	GHSV (reactive components)	10000	119233	121143	93253

Overall, the increase of the propene price from $1250\,€\,t^{-1}$ onwards shows a significant change of the objective function which can be seen in Table 5.3. However, this is mainly caused by the direct influence of the price on the objective function, while the optimization variables and

especially the product yields only show minor differences as it is obvious in Table 5.4. It would be uneconomical to adapt the process drastically each time the current propene price changes.

For these reasons, the process design derived from the optimization to a propene price being 25% higher than the ethene price is exemplarily used to further evaluate its economical robustness against volatile propene prices. The resulting objective function values and their relative difference to the respective optimal design are shown in Table 5.6.

Table 5.6: Objective function values with the fixed optimal process design for a propene price of 1250 €t^{-1} subjected to different propene price scenarios; propene prices are shown in €t^{-1}, the output of the objective function in €t^{-1}_{Feed} and the relative change in %.

Description	Propene price			
	1000	1250	1500	2000
Output objective function	848	1056	1263	1678
Relative change to optimal design	-5.6	0	-0.3	-0.9

These results reveal that the process being optimized for a propene price of 1250 €t^{-1} can remain unchanged for different price fluctuations of propene with still a nearly optimal objective function value. Even when ethene and propene prices are equal, the profit is only 6% lower. Nevertheless, even this scenario is seen to be more viable with the proposed setup than with a conventional cracking unit.

The results in Table 5.6 show that one main set of optimal process conditions is enough to cover a broad range of price scenarios for lower olefins. The identified main process design optimized for a propene price of 1250 €t^{-1} can be used for the whole price range, from propene having the same price as ethene up to a scenario where propene is as twice as expensive. For higher propene prices, the additional gain of slightly adapted conditions might not be worth the effort of significantly changing a running process. Nevertheless, an adjustment to the optimum results from Table 5.3 would be possible during annual shutdowns if desired. A change to the optimal process conditions for a propene price of 1000 €t^{-1} is not as easy due to different dimensions of the equipment. Additionally, it might not be reasonable to realize the current process in the case that ethene and propene have an equal price. However, some of the optimization variables like the pressure could be adapted to this scenario also in a unit designed for higher propene prices. This is why the optimal process design is chosen to be the one for a propene price of 1250 €t^{-1} which is an intermediate case and can also cover lower propene prices with still nearly maximized profit. Beyond that, the scenario of increasing propene prices seems to be more realistic due to the predicted supply gap.

In general, the two main pathways leading to lower olefins have to be differentiated: whereas ethene formation is irreversible, propene is both reactant and product of the numerous olefin

interconversion reactions, see also Chapter 3. It follows that for maximized ethene yields, the GHSV has to be very low. Figure 5.1 (a) shows the evolution of the molar flow rates of the different olefins at optimal process conditions for a propene price of $1000\,€\,t^{-1}$. In the case that the propene price is high, the optimum evolves for an intermediate catalyst mass. Here, the optimum is rather flat; for a GHSV which is slightly too low, no severe breakdown of propene yields can be observed. Consequently, the case when having slightly too much catalyst in the reactor is more advantageous compared to the opposite case. This conclusion is further supported with respect to catalyst deactivation which diminishes the active catalyst mass. Figure 5.1 (b) shows typical molar flow rates along the reactor optimized to the scenario with a propene price of $1250\,€\,t^{-1}$. Similar plots for propene prices of $1500\,€\,t^{-1}$ and $2000\,€\,t^{-1}$, respectively, can be found in Figure A.1 in the Appendix.

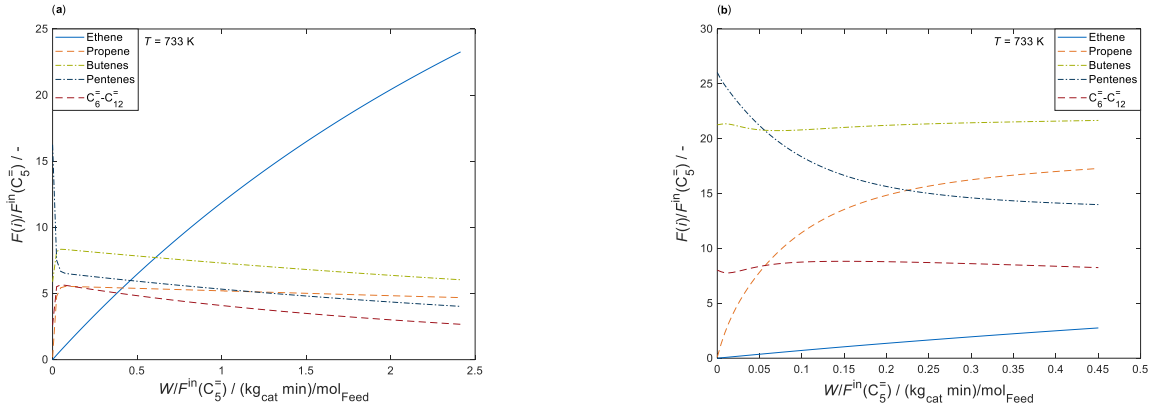

Figure 5.1: Reactor plots showing the evolution of the different olefins at optimized conditions for a propene price of $1000\,€\,t^{-1}$, (a), and $1250\,€\,t^{-1}$, (b).

As described in Section 5.3.3, side product formation is set to 1% relative conversion of the $C_2^=$ to $C_{12}^=$ olefins to paraffins and to 1% relative conversion of the $C_6^=$ to $C_{10}^=$ olefins to aromatics. The influence of this formation rate is investigated by evaluating two additional scenarios where these values are both changed to 0.5% (less side products) or 2% (more side products). Not surprisingly, a higher formation rate of side products decreases profitability. Nevertheless, the selective conversion of higher olefins to ethene and propene with a recycle remains viable: when both formation rates are set to 2%, the objective function value decreases not more than about 5% for all propene price scenarios. For formation rates of 0.5%, the lower side product formation increases the objective function by around 3%. Furthermore, none of the values for the optimization variables changes significantly, indicating that the results shown in this study are still valid even when the formation rate of side products is different. As stated in Section 5.3.3, the assumed amount of side products is defined based on observations during the kinetic measurements, see Section 3.2.1. Here, a catalyst with high selectivity to olefins was used which impedes parameter estimation for side reactions. Additional experimental data with higher yields of side products would be necessary to incorporate these effects into the kinetics. This could possibly lead to a more realistic simulation concerning side products.

The latter paragraph is closely related to the limitations of the approach shown here: if side reactions play a crucial role (mole fraction of side products > 5%), the kinetic description is not accurate anymore. Furthermore, when having a complex feed, this case might not be covered by the single-event model. It should be underlined that although the kinetic parameters were derived with 1-pentene as model component, the results do have validity for $C_3^=$ to $C_7^=$ olefins as feed or even for their mixtures, see Chapter 4. However, in scenarios where the feed consists not only of olefins, but also of paraffins, naphthenes and aromatics as it is the case for a Fischer-Tropsch product distribution, the resulting interconversion reactions during cracking cannot be described. This restricts the transfer to hydrocracking systems, all the more when the feed contains also liquid compounds. For this purpose, the kinetics have to be enriched with additional reactions first as it is described in literature [57, 214]. Another possibility besides the effortful and time-consuming single-event calculations for such complex feedstocks is discrete lumping. Here, in contrast to regular lumped models, several *pseudo*-components are defined which focus on the molecular structure. Pellegrini *et al*. [197] perform this for hydrocracking of C_4 to C_{70} *n*-paraffins. With their model consisting of nine discrete lumps, they are able to describe isomerization and cracking reactions as function of temperature, pressure, H_2 amount and contact time. Browning *et al*. [202] extend this approach to a real feedstock; here, with 217 discrete lumps in total, also naphthenic and aromatic interconversion reactions are included. The model describes experimental data of vacuum gas oil hydrocracking with carbon numbers between 22 and 44 with high accuracy although having only 17 parameters. This shows that the approach of discrete lumping is an effective compromise between the single-event kinetics and regular lumping.

Reaction temperature and pressure are known to have crucial influence on the product distribution which is demonstrated in Section 3.2.2. The high pressure demand in the scenario optimized for a propene price of $1000\,€\,t^{-1}$ might be surprising because formation of lower olefins is favored at low pressures. On the other hand, as ethene production is an irreversible step, it is advantageous to accelerate kinetics by increasing the partial pressures. Thus, the unfavorable driving force of the thermodynamic equilibrium is not dominant for this case. Besides, also process-related variables favor higher pressures for this scenario: the GHSV has to reach a minimum value and the condenser temperature can be higher for higher pressures. It has to be stated that both higher partial pressures and a lower value for the GHSV result in higher side product formation. Therefore, the included amount of 1% paraffins and 1% aromatics might be too low especially for this case. The results from the former paragraph might lead to the assumption that this issue does not lead to results which are significantly different. However, yields of the desired products might be lower, underlining again the fact that the study in this chapter is focused on the case of higher propene prices.

5.5 Conclusions

An optimal process design that maximizes the profit from selling ethene and propene is determined for the catalytic cracking of higher olefins over ZSM-5. This is done by combining complex single-event kinetics in MATLAB with a profound process simulation in Aspen HYSYS, while a self-developed MATLAB interface allows for the optimization of the combined process. A recycle reactor concept is found to be a suitable and profitable solution even when accounting for utility cost and side products. With such a setup, it is possible to convert undesired higher olefins that emerge during thermal cracking into the main products ethene and propene.

The underlying single-event kinetic model allows extrapolation out of the experimentally covered range. Thus, it yields a realistic characterization of olefin interconversion at the conditions investigated here. However, formation of side products (paraffins and aromatics) has not been incorporated in this microkinetic model yet. For this reason, their production is considered via the process simulation software to guarantee a realistic process description; the formation rate is set to a reasonable value observed during kinetic measurements. The main fraction of the resulting side products is purged and used as fuel for the burner that provides heat for the main reactor and the separation section.

Four different propene price scenarios are analyzed. When ethene and propene prices are almost equal, high pressures and large catalyst beds with a low GHSV should be applied to reduce utility cost and to maximize ethene formation. For rising propene prices, higher recycle ratios and lower pressures are proposed to maximize propene yields. Here, a higher GHSV is recommended because propene is an intermediate product in contrast to ethene. The impact of fluctuating propene prices is investigated, showing that the process being optimized for the case when propene is 25% more expensive than ethene offers only slightly reduced profitabilities compared to the respective individual optima. Thus, with this optimal design, the two scenarios of higher propene prices and the case of ethene having the same price as propene still retain an almost maximum profitability.

The validity of the proposed setups is further underlined with sizing calculations of the reactor and the main column. For all sets of process conditions, reasonable values for the equipment dimensions are obtained.

The optimized setup is based on a fixed heat exchanger network and a state-of-the-art separation sequence. It is also possible to investigate the potential when variations within this setup are allowed. This would give more insight into interdependencies. For this, an improvement in numerics would be helpful: the estimation of the derivatives for the reactor model in MATLAB could be done separately in order to decrease the time necessary for optimization. In this

context, automatic differentiation or complex numbers could be used because the code of the reactor model is accessible directly, in contrast to that of the process simulation model.

In summary, this chapter shows how rigorous kinetics can be combined with process optimization to assess the profitability of a whole process and also its dependence on current market situations.

6 On Reaction Pathways and Intermediates During Catalytic Olefin Cracking over ZSM-5

This chapter was published and is reprinted with permission from:

S. Standl, T. Kühlewind, M. Tonigold, O. Hinrichsen
On Reaction Pathways and Intermediates During Catalytic Olefin Cracking over ZSM-5
Industrial & Engineering Chemistry Research 58 (2019), 18107–18124,
DOI 10.1021/acs.iecr.9b02989.

6.1 Abstract

The concept of catalytic olefin cracking is an alternative method to produce ethene and propene. Undesired higher olefins formed on site are converted using acid zeolites at temperatures higher than 600 K. Although the underlying elementary reactions can be explained by interconversion steps of carbenium ions, relatively little is known about the exact procedure of adsorption and the nature of intermediates. However, detailed knowledge about these topics is indispensable for a comprehensive theoretical description. In this chapter, a microkinetic single-event model for olefin cracking over ZSM-5 is analyzed in terms of reaction pathways and intermediates. An evaluation of adsorption states underlines the importance of differentiating between physisorption and π-complex formation because the latter leads to significantly higher accuracy when describing olefin cracking. A further investigation of protonation predicts the resulting intermediates to be of comparably low stability. Therefore, their total concentration is negligible, a conclusion that should nevertheless not be used for all approaches from literature. Finally, protonation enthalpies are estimated; the resulting values suggest carbenium ions as intermediates at least for tertiary species, which is in line with the stability order of the obtained activation energies. These findings can help to understand the interaction between olefins

and acid zeolites, a topic of high importance in constructing exact and physically consistent theoretical descriptions.

6.2 Introduction

The catalytic cracking of higher olefins over acid zeolites is an alternative approach to produce ethene and propene [2], which are important building blocks for the chemical industry [6]. Compared to steam cracking, temperatures and CO_2 emissions are lower [3, 4]. Additionally, the use of a catalyst allows for product adjustment and higher flexibility in feed. FCC, though it is the other established industrial route towards lower olefins, is designed for gasoline production [7]. In times of rising environmental concerns [5], stricter governmental rules and higher demand, especially for propene [9], alternative processes gain in importance [2].

The conversion of higher olefins to ethene and propene is a concept to exploit the undesired byproducts of refining processes directly on site. Although no broad commercialization has been achieved yet, several project and demo plants have been realized [2]. When using a suitable catalyst like ZSM-5, the crucial advantage of this concept is the high P/E ratio that is achieved by adjusting reaction conditions and reactor setups as shown in Chapter 3. As discussed in Chapter 5, the industrial olefin cracking process consisting of a recycle reactor and a complete separation unit is viable, especially at higher propene prices.

However, more flexibility in operational mode and feed will be necessary in the future. Robust and reliable models are thus inevitable in order to have a realistic depiction of the overall reactivity. In literature, several lumped models exist [53, 136, 195, 236–238]; an overview and comparison of these can be found in Section 2.6.1. With these models, a useful description of product distribution is obtained within their respective experimental range, but although some of the approaches underly a mechanistic scheme, their application area is limited because of the missing microkinetic character [18, 19]. As a consequence, the estimated parameters are of artificial character without clear physical background; they might contain, for example, adsorption enthalpies or active site concentrations. This impedes a transfer to different catalysts or reaction setups and therefore optimization of both process and catalyst properties in which an extrapolation out of experimentally covered regimes is required [19, 20].

By contrast to this, a microkinetic model offers vast extrapolation possibilities because each elementary reaction taking place on the catalytic surface is explicitly included [19]. Using such a model, the optimization of both process and catalyst is possible [20]. Additionally, it yields insight into reaction intermediates and preferred pathways [17]. On the other hand, reaction networks are huge and complex when each step is considered, especially for hydrocarbon

conversion over zeolites. Usually, a high number of reactions causes a high number of estimated parameters and therefore much computational effort as well as challenging numerics. For that reason, the single-event theory was developed almost 30 years ago by the Ghent group [19, 59]. It allows for the description of thousands of elementary reactions with only a handful of different parameters; for details, refer to the literature [18, 19, 21].

Von Aretin *et al.* [26] present a microkinetic model based on the single-event concept in order to describe the cracking of 1-pentene over ZSM-5. Here, only five fundamental parameters, i.e., four activation energies and one pre-exponential factor, are sufficient to describe 1585 pathways of kinetic relevance, see Chapter 3. The microkinetic character of this model is proven in Chapter 4: although the parameter estimation relies on only 1-pentene as feed, the model correctly predicts all olefins from propene to heptene as reactants. Furthermore, the microkinetic description can be used to model olefin mixtures as feed and even catalysts with different properties.

In microkinetics, it is extremely important that each implemented step has a reasonable physical background; only then, the transferability to different systems is guaranteed. The single-event model introduced in Chapters 3 and 4 is used here to gain a deeper understanding of the steps ongoing during olefin cracking with special focus on adsorption. In order to elaborate a consistent description that has broad validity, concepts and correlations from literature for the adsorption of hydrocarbons on zeolites are applied. These are combined with own fittings and assessed in terms of both accuracy and significance. From this, general conclusions on the prevailing intermediates are drawn. Thus, for the first time, a deep insight into the interplay of microkinetics and adsorption during olefin cracking is provided, the results of which are compared with previously published work of both experimental [331] and theoretical [234, 235] nature. These coherences are helpful also for other processes such as MTO or hydrocracking.

6.3 Methods

6.3.1 Reaction Network

In the original study [26], the reaction network is mainly derived through observations described in literature [48, 308, 309]; cf. Section 3.1.3 for more details. A summary of the underlying assumptions as well as a short explanation of the different types of elementary reactions can be also found in Section 3.1.3. The same reaction network is used here, but with slight adaptations that improve the fitting procedure. When using the original network, some of the implemented

adsorption models cause insignificant values for one of the estimated cracking activation energies.

For that reason, a refinement of the reaction network was performed in a preliminary study. Indeed, a version showing improved agreement and parameter significance can be found. On the other hand, the differences of the fitting results are too small to be statistically significant. This is why the whole preliminary study analyzing six different reaction networks RN01–RN06 is shown in Section A.2.1 in the Appendix.

Only the differences between RN01 (original study [26]) and RN06 (this chapter) should be mentioned here. An important assumption of the original work [26] is the irreversible formation of primary intermediates. Examples exist in which ethene especially is not a final product, since it can be a reactant in dimerization steps [47, 53, 195, 238]. This is why ethene formation steps are assumed to be reversible in RN06; in addition, the cracking to primary intermediates is only allowed when the step leads to ethene. Scheme 6.1 represents the main characteristics of the two reaction networks.

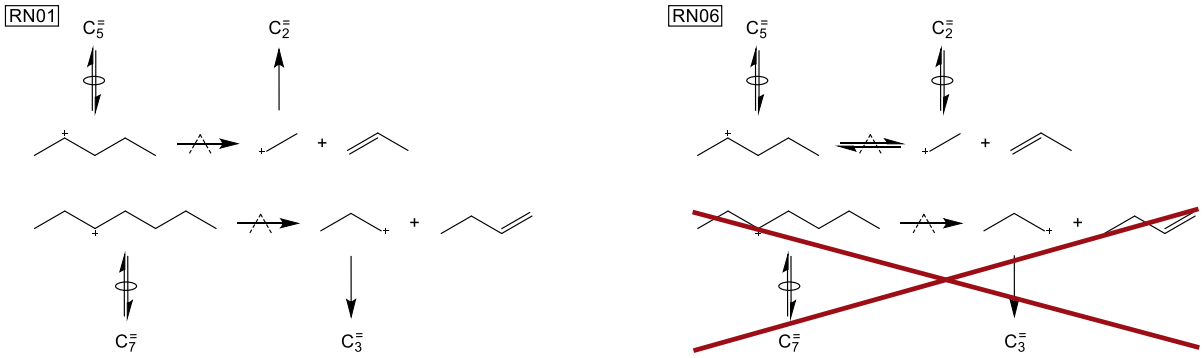

Scheme 6.1: Differences between the two reaction networks RN01 and RN06 with respect to the role of primary intermediates.

Due to the restriction of the formation of primary intermediates, the number of cracking reactions is lower in RN06, see Table 6.1. Furthermore, the reversibility of ethene formation leads to an equal amount of cracking and dimerization reactions.

Table 6.1: Types of elementary reactions being implemented in different reaction networks RN of the single-event kinetic model for olefin cracking, including the number of different reactions and of pathways of kinetic relevance; furthermore, the number of different olefins and protonated intermediates is shown.

Type	RN01	RN06
Olefin protonation	956	957
Cracking	601	238
Pathways cracking	1292	511
Dimerization	140	238
Pathways dimerization	293	511
PCP branching	1530	1530
Methyl shift	148	148
Olefin deprotonation	1004	957
Olefins	591	591
Protonated intermediates	498	451

At this point, it should be underlined that the network in the original work is not wrong and is not corrected here; by contrast, the focus of this chapter is different. Whereas a kinetic model as it is derived in the previous contribution [26] should have broad validity which makes an inclusion of a variety of reactions advantageous, the detailed analysis of intermediates requires that only pathways playing a crucial role at the respective conditions are included. Although the single-event model is of microkinetic character, the reaction network has thus to be adapted before an adsorption study is possible.

6.3.2 Adsorption States

For an analysis of adsorption models, it is important to differentiate between the characteristics of hydrocarbon interaction with zeolites [331]. For the adsorption of alkanes, it is irrelevant whether an acid site is available or not [332]; the contribution of these Brønsted centers is negligible. The interaction is almost completely restricted to non-directed van der Waals [54] or, more precisely, to dispersion forces between the alkane and the pore wall [331]. This physisorption effect can be measured using different methods [280, 333]. By contrast to this, the occurrence of a double bond within olefins increases the complexity of the adsorption process. When no acid site is present, the interaction is again restricted to the zeolite wall and thus to physisorption [331], see Scheme 6.2 on the right side. It should be noted that at regular olefin cracking conditions, temperatures are sufficiently high so that *quasi*-equilibrated adsorption is achieved [60], which is why Scheme 6.2 shows the corresponding equilibrium constants. Quantitatively, the physisorption of olefins is comparable to that of alkanes [23, 60]. However, the left side of Scheme 6.2 shows the crucial difference when a free acid site is available. Here, the directed interaction between the double bond and the acid site leads to the formation of a

π-complex, which causes a higher degree of stabilization compared to pure physisorption [54, 331]. Although the average distance between olefin and zeolite wall might be higher in a π-complex, the dispersion forces still contribute [54].

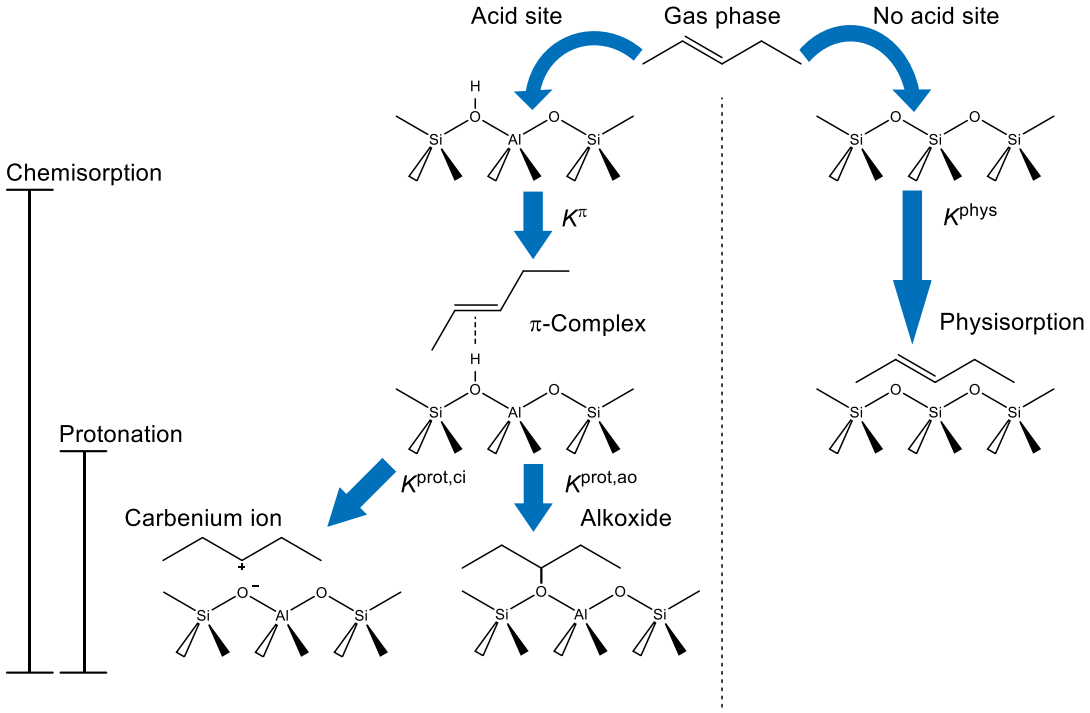

Scheme 6.2: Two different main pathways of olefin adsorption: chemisorption on an acid site (left side, π-complex plus protonation) and physisorption without contribution of an acid site (right side).

In a subsequent step, the proton of the acid site is transferred to the olefin. It is still under debate whether this protonation leads to a carbenium ion [18, 317] or to an alkoxide [54–56] as an intermediate. For a long time, even simple examples of carbenium ions could not be identified via nuclear magnetic resonance spectroscopy [334]; evidence for their existence was only found for cyclic or aromatic species [335, 336]. Quite recently, the identification of the *tert*-butyl carbenium ion on ZSM-5 was successful by combining measurement and theory [337]. This corresponds to earlier theoretical evidence on mordenite (MOR) [338] and ferrierite (FER) [339]. However, this example is seen to be one of the most stable carbenium ions because their stability decreases in the order tertiary > secondary > primary [338]. Theoretical studies suggest that their existence as intermediates is possible, but only favored when the positive charge is delocalized [340] or not easily accessible [341]; otherwise, the corresponding alkoxide should evolve. This is why in most of the calculations, carbenium ions cannot be found as minima in the potential energy surface, thereby excluding them as possible intermediates. Instead, they are assumed as short-living transition states here [55, 341, 342]. On the other hand, carbenium ions might be favored at high temperatures due to the gain of entropy compared to an alkoxide [234, 339]. This matches experimental results with carbenium ions being absent

during isomerization reactions of 1-butene over ZSM-5 at 230 K [343], whereas they can be detected over FER when temperatures are higher than 290 K [344].

Alkoxides lead to typical minima found on potential energy surfaces and are therefore frequently seen as intermediates in theoretical studies [339]. However, steric constraints arise here due to the close distance between the hydrocarbon and zeolite wall. This can lead to a destabilization of especially tertiary alkoxides. Although similar stability for all types of alkoxides is observed in some work [56], most publications suggest an ordering opposite to carbenium ions, i.e., the alkoxide stability decreases in the order primary > secondary > tertiary. This holds for different zeolites like CHA [345–347], FER [339, 348], MOR [338, 347], faujasite [349], Theta-1 [342, 347] or MFI [350]. It has to be underlined that these theoretical results highly depend on the applied methodology, the cluster model and a realistic description of the acid site including its surroundings [235, 342, 351]. For example, all alkoxide types show the same stability when a small and flexible cluster is used, but they reveal significant differences for a more realistic description of the surroundings of the acid site [341]. For the same reason, alkoxides are observed as having a much higher stability than a π-complex in some studies [54, 348, 349], whereas values for the protonation enthalpy, which are close to or even above zero, are found in other work [235, 338, 339, 342, 347, 352]. This contradiction is even seen within the same study when different cluster models are used [342]. Because of this, no conclusions can be drawn from one zeolite to another [342]. Another reason for discrepancies in literature is the use of pure density functionals or free clusters versus hybrid approaches [348].

The adsorption properties of olefins on acid zeolites are not easily accessible through experiments due to their high reactivity [54]. Therefore, the theoretical insights discussed above are required to understand the underlying chemistry. However, the results of quantum chemical calculations depend on several factors and, in most cases, depict one specific case that might not represent a catalyst applied at industrial conditions. Here, microkinetic models can be a step linking realistic conditions with theoretical calculations, which is why the single-event model for 1-pentene cracking [26] should be further evaluated. Besides their potential for selective industrial propene production, pentenes are interesting reactants as they offer two main pathways: monomolecular cracking and dimerization with subsequent cracking; cf. Section 3.2.2 for more details.

In literature, two recent studies tackling pentene adsorption on ZSM-5 are available. Schallmoser *et al.* [331] found experimental evidence for fast π-complex evolution and equilibrated double-bond isomerization at a low temperature of 323 K. Moreover, they observed dimerization steps taking place with a lower rate. They compared the energetics of pentene interaction over silicalite as well as over FER: whereas only physisorption took place in the former example due to the lack of acid sites, evolution of the π-complex could be observed in the latter case without subsequent dimerization reactions, which were suppressed due to steric constraints. By

comparing the resulting enthalpy values as well as the measured overall reaction enthalpy of dimerization, they determined the protonation enthalpy to an alkoxide to be –41 kJ mol^{-1}.

The other recent work is of theoretical nature and authored by Hajek *et al.* [235]. They applied static calculations, molecular dynamics and metadynamic methods to investigate pentene adsorption. Their main finding is that π-complex and alkoxide showed almost equal stability with the exception of 3-pentoxide being the least stable species because of steric repulsions. Positive protonation enthalpies were obtained for all types of alkoxides in the static calculations, but this was rather caused by an overestimation of π-complex stability. The inclusion of finite temperature effects yielded a more realistic description of the adsorption process; here, protonation enthalpies in the range of –20 kJ mol^{-1} to 10 kJ mol^{-1} were found. The application of the metadynamic simulations showed that the formation of an alkoxide out of the π-complex is an activated step with carbenium ions as transition states. However, all these results were restricted to a temperature of 323 K. In a subsequent study [234], the similar methodology was extended to temperatures of 573 K and 773 K. Again, the static approach was found to be inappropriate, as it predicted the π-complex to be the most stable intermediate for all examples by far, although tertiary carbenium ions were found to be favored compared to tertiary alkoxides and might occur as intermediates at high temperatures. Because the mobility of the chemisorbed species and therefore entropy was underestimated with the static approach, molecular dynamics had to be applied. Here, the π-complex was still detected as a stable intermediate, but with increasing temperatures, a higher amount of olefins was stabilized only via van der Waals forces, thus losing the fixation at the double bond. For linear species, both alkoxides and carbenium ions were not stable at typical cracking conditions: the former quickly transformed into the corresponding carbenium ion as a metastable intermediate that underwent rapid deprotonation into the π-complex then. Branched compounds were observed to be much more mobile than their linear counterparts, both in a neutral and in protonated state. Tertiary carbenium ions were found to be a dominating intermediate at high temperatures, whereas alkoxides might only exist in primary form for branched species.

6.3.3 Mathematical Description of Adsorption

A robust mathematical formulation of adsorption phenomena is necessary for implementation into a model. The thermodynamic equilibrium constant for π-complex formation, protonation, physisorption and chemisorption of compound i is defined in Equation (6.1),

$$K^{\mathrm{ads}}(i) = \exp\left(-\frac{\Delta_{\mathrm{ads}}H_i^{\circ} - T\,\Delta_{\mathrm{ads}}S_i^{\circ}}{RT}\right), \tag{6.1}$$

ads = π, prot, phys or chem.

It should be explicitly stated that within this work, physisorption solely means the interaction between an olefin and the zeolite wall without the contribution of an acid site. This is strictly differentiated from the π-complex that can only evolve at Brønsted acid sites, leading to an additional interaction between the double bond of the olefin and the proton. Protonation means the transformation of a π-complex to the protonated intermediate, the latter being either a carbenium ion or an alkoxide. Finally, chemisorption describes the whole step from a gas phase olefin towards the protonated intermediate. For simplicity, the change in enthalpy or entropy due to adsorption is denoted as adsorption enthalpy or adsorption entropy, respectively. As mentioned above, these adsorption steps are usually assumed as *quasi*-equilibrated at typical cracking conditions. A common approach to obtain the concentration of adsorbed intermediates is the use of a Langmuir isotherm according to Equation (6.2) [332],

$$C^{\mathrm{ads}}(i) = \frac{C^{\max} K_{\mathrm{L}}^{\mathrm{ads}}(i)\, p(i)}{1 + K_{\mathrm{L}}^{\mathrm{ads}}(i)\, p(i)}. \tag{6.2}$$

The Langmuir adsorption constant $K_{\mathrm{L}}^{\mathrm{ads}}(i)$ and therefore the concentration depend on the temperature. The relative coverage $\theta(i)$ of species i is obtained by dividing Equation (6.2) by the maximum concentration of adsorption sites $C^{\max}$, see Equation (6.3):

$$\theta(i) = \frac{K_{\mathrm{L}}^{\mathrm{ads}}(i)\, p(i)}{1 + K_{\mathrm{L}}^{\mathrm{ads}}(i)\, p(i)}. \tag{6.3}$$

As shown in Section 3.1.4, $C^{\max}$ equals the total concentration of strong Brønsted acid sites $C_{\mathrm{t}}^{\mathrm{SBAS}}$ for the π-complex; alternatively, the concentration of all Brønsted acid sites $C_{\mathrm{t}}^{\mathrm{BAS}}$ can be used. By contrast, the saturation concentration of compound i on the zeolite surface $C^{\mathrm{sat}}(i)$ has to be used for physisorption. The coherence between the Langmuir adsorption constant and the thermodynamic equilibrium constant of adsorption is shown in Equation (6.4),

$$K^{\mathrm{ads}}(i) = K_{\mathrm{L}}^{\mathrm{ads}}(i)\, p^{\circ}, \tag{6.4}$$

where p° should be chosen as 10^5 Pa according to IUPAC [138]. For the protonation, the thermodynamic equilibrium constant equals the Langmuir constant as the transfer of a proton is part of the whole chemisorption step where the standard pressure is already considered during calculation of the π-complex.

Both for adsorption enthalpy and for entropy, linear correlations with the carbon number CN_i as variable can be found [54, 279, 332], see Equations (6.5) and (6.6),

$$\Delta_{\mathrm{ads}} H_i^{\circ} = \alpha\, CN_i + \beta, \tag{6.5}$$

$$\Delta_{\mathrm{ads}} S_i^{\circ} = \gamma\, CN_i + \delta. \tag{6.6}$$

The values of α to δ are usually fitted to experimental [279, 332] or theoretical [54] adsorption data. Depending on whether olefins or alkanes are investigated, Equations (6.5) and (6.6) describe the formation of a π-complex or the physisorption as adsorption step. The former case is provided by Nguyen *et al.* [54] whereas both the studies by de Moor *et al.* [332] and Denayer *et al.* [279] characterize the physisorption of alkanes. In all three literature concepts, both enthalpy and entropy are assumed to be temperature independent within the respective investigated range. The influence of temperature is nevertheless considered when calculating the thermodynamic equilibrium constant. The contribution of Nguyen *et al.* [54] additionally contains correlations in form of Equations (6.5) and (6.6) to calculate the formation of secondary alkoxides out of a π-complex; these protonation values include a minor thermal correction. From the same authors, a conference paper exists [350] comprising an alternative set of correlations; with these, the formation of not only secondary, but also of tertiary alkoxides can be calculated. Both approaches [54, 350] differentiate between 1-olefins and 2-/3-/4-olefins as well as the special case of isobutene adsorption [310]. More details about all three literature adsorption studies [54, 279, 332] are explained in Section A.2.2 in the Appendix.

6.3.4 Mathematical Formulation of Overall Reactivity

Von Aretin *et al.* [26]: Use of correlations by Nguyen *et al.* [54, 310]

In the original cracking model by von Aretin *et al.* [26], Equation (6.7) is used for describing the cracking reaction rate of olefin O_i from a protonated intermediate R_i^+ of type m to type n,

$$r^{\mathrm{cr}}(m;n) = k^{\mathrm{cr}}(m;n)\, C\left(R_i^+\right) = n_e\, \tilde{k}^{\mathrm{cr}}(m;n)\, K^{\mathrm{prot}}\left(O_i^{\pi};m\right) \frac{C_{\mathrm{t}}^{\mathrm{SBAS}}\, K_{\mathrm{L}}^{\pi}(O_i)\, p(O_i)}{1+\sum_j K_{\mathrm{L}}^{\pi}\left(O_j\right) p\left(O_j\right)}. \qquad (6.7)$$

The coherence between regular rate constant k and the number of single events n_e as well as the single-event rate constant $\tilde{k}$ is not discussed here and can be found in literature [19–21]. The structure of the rate equation for dimerization is found to be similar to Equation (6.7), but multiplied by the partial pressure of the second reactant olefin, see Section 3.1.4. It follows that no adsorption effects are considered to define this second reactant. By contrast, the regular correlations by Nguyen *et al.* [54] are used to describe both π-complex and alkoxide formation of the reactant olefin in Equation (6.7). For the special case of isobutene protonation, the values leading to a tertiary alkoxide are applied [310].

An underlying assumption of Equation (6.7) is the negligible concentration of protonated intermediates on the acid sites. In this chapter, an alternative approach according to Equation (6.8) is tested where this concentration is explicitly included,

$$r^{\mathrm{cr}}(m;n) = n_e\,\tilde{k}^{\mathrm{cr}}(m;n)\,K^{\mathrm{prot}}\left(\mathrm{O}_i^{\pi};m\right)\,\frac{C_{\mathrm{t}}^{\mathrm{SBAS}}\,K_{\mathrm{L}}^{\pi}(\mathrm{O}_i)\,p(\mathrm{O}_i)}{1+\sum_j K_{\mathrm{L}}^{\pi}\left(\mathrm{O}_j\right)\,p\left(\mathrm{O}_j\right)+\sum_j K_{\mathrm{L}}^{\mathrm{chem}}\left(\mathrm{O}_j\right)\,p\left(\mathrm{O}_j\right)}. \quad (6.8)$$

It should be noted that the product of $K_{\mathrm{L}}^{\pi}(\mathrm{O}_i)$ and $K^{\mathrm{prot}}\left(\mathrm{O}_i^{\pi};m\right)$ equals $K_{\mathrm{L}}^{\mathrm{chem}}(\mathrm{O}_i)$. In the model by von Aretin *et al.* [26], the protonation constant $K^{\mathrm{prot}}\left(\mathrm{O}_i^{\pi};m\right)$ consists of symmetry contributions, an isomerization constant to a well-defined reference olefin $\mathrm{O}_{\mathrm{ref}}$ [21] and the actual protonation constant [19]. In the following, reference olefins are applied only in these cases in which a carbon number dependence of protonation is not guaranteed.

Martens *et al.* [22]: Use of correlations by Denayer *et al.* [279, 280]

Whereas both the evolution of the π-complex as well as chemisorption take place on the same acid sites, two different Langmuir approaches are necessary for the equations typically found in hydrocracking [21, 22, 317]: one for the saturation effect on the catalyst surface due to physisorption and another one for the balance of acid sites. The latter, however, is often neglected because of a low concentration of protonated intermediates [21]. Nevertheless, accuracy can be increased by implementing this additional balance [317]. After adapting the equation to olefin cracking by leaving out all hydrogenation/dehydrogenation steps, the approach neglecting the concentration of protonated intermediates can be found in Equation (6.9) [22],

$$r^{\mathrm{cr}}(m;n) = n_e\,\tilde{k}^{\mathrm{cr}}(m;n)\,C_{\mathrm{t}}^{\mathrm{SBAS}}\,K^{\mathrm{prot}}\left(\mathrm{O}_i^{\mathrm{phys}};m\right)\,\frac{C^{\mathrm{sat}}(i)\,K_{\mathrm{L}}^{\mathrm{phys}}(\mathrm{O}_i)\,p(\mathrm{O}_i)}{1+\sum_j K_{\mathrm{L}}^{\mathrm{phys}}\left(\mathrm{O}_j\right)\,p\left(\mathrm{O}_j\right)}. \quad (6.9)$$

It follows that besides proper physisorption values, this approach requires data for $C^{\mathrm{sat}}(i)$, which can be calculated using Equation (6.10) [22],

$$C^{\mathrm{sat}}(i) = \frac{v^{\mathrm{po}}}{V_{\mathrm{m}}^{\mathrm{l}}(i)}, \quad (6.10)$$

with v^{po} as the specific pore volume of the catalyst and $V_{\mathrm{m}}^{\mathrm{l}}(i)$ as the molar volume of compound i in liquid state. In this work, $2\times10^{-4}\,\mathrm{m^3\,kg_{cat}^{-1}}$ is chosen as the specific pore volume of ZSM-5, whereas the molar volumes in liquid state can be calculated [163] using either the Hankinson-Brobst-Thomson (HBT) method [353] or the approach by Elbro *et al.* [354]. The former uses empiric equations to express the coherence between $V_{\mathrm{m}}^{\mathrm{l}}(i)$ and the critical volume, reduced temperature as well as acentric factor; the equations and constants are shown elsewhere [163]. By contrast, the concept by Elbro *et al.* [354] is a group contribution method.

Different organic groups are tabulated [163]; for each group, three values are available that allow for a consideration of temperature effects. For the protonation entropy, Martens *et al.* [22] suggested a calculation routine according to Equation (6.11),

$$\Delta_{\mathrm{prot}} S_i^{\circ} = -S_i^{\circ,\mathrm{trans}} - \Delta_{\mathrm{phys}} S_i^{\circ}. \tag{6.11}$$

The total translational entropy $S_i^{\circ,\mathrm{trans}}$ is accessible via the Sackur-Tetrode equation according to Equation (6.12) [355],

$$S_i^{\circ,\mathrm{trans}} = k_{\mathrm{B}} N_{\mathrm{A}} \left\{ \ln\left(\frac{[2\pi M(i)\, k_{\mathrm{B}} T]^{3/2}}{h^3} \right) + \ln\left(\frac{V_{\mathrm{m}}^{\mathrm{g}}(i)}{N_{\mathrm{A}}} \right) + \frac{5}{2} \right\}, \tag{6.12}$$

with the Boltzmann constant k_{B}, the Planck constant h, the Avogadro constant N_{A}, the molecular mass $M(i)$ of compound i and its molar volume in the gas phase $V_{\mathrm{m}}^{\mathrm{g}}(i)$. When using the adsorption values of Denayer *et al.* [279, 280], no direct correlation for the physisorption entropy exists. The approach in Equation (A.6) in the Appendix, which is applied here, is slightly different from the one originally proposed by Martens *et al.* [22] where no standard pressure is considered. By contrast, a direct possibility to calculate the physisorption entropy exists for the adsorption values by de Moor *et al.* [332] via Equation (6.6).

Toch *et al.* [194]: Simplified protonation approach

Toch *et al.* [194] suggested a simplified concept to calculate the changes in entropy. According to them, physisorption leads to the loss of one degree of freedom of the translational entropy, see Equation (6.13),

$$\Delta_{\mathrm{phys}} S_i^{\circ} = \frac{-S_i^{\circ,\mathrm{trans}}}{3}. \tag{6.13}$$

This should resemble the fixation of the hydrocarbon in z-direction, whereas it is still able to move in x- and y-direction. In this approach, electric contributions to the entropy are negligible whereas rotational and vibrational entropies are assumed to remain constant. After the protonation step, the species is bound to the surface and should therefore lose the remaining two degrees of freedom of translational entropy according to Equation (6.14),

$$\Delta_{\mathrm{prot}} S_i^{\circ} = \frac{-2\, S_i^{\circ,\mathrm{trans}}}{3}. \tag{6.14}$$

This concept allows for the use of physisorption enthalpy values both by de Moor *et al.* [332] and by Denayer *et al.* [279].

6.3.5 Parameter Estimation

All models in this chapter are fitted to the same experimental data set that is shown elsewhere [26]. For this, MATLAB version R2018a is used. The objective function *OF* is defined by Equation (6.15),

$$OF = SSQ = \sum_{k}^{N_{\mathrm{Exp}}} \sum_{j}^{N_{\mathrm{Res}}} \left(y_k(j) - \hat{y}_k(j)\right)^2, \tag{6.15}$$

with $y_k(j)$ being the experimental and $\hat{y}_k(j)$ the modeled mole fraction of each fitting response j and each experimental data point k. Nitrogen as diluent is explicitly considered within the mole fractions. The unweighted sum of squared residuals *SSQ* is minimized by applying *lsqnonlin* with the Levenberg-Marquardt algorithm except for the cases in which constraints are required. For these scenarios, an initial fitting using the trust-region-reflective algorithm is performed, whereas the Levenberg-Marquardt algorithm is applied in a second run using the previous results as initial values. Tolerances are set to $TolFun = 10^{-8}$ in terms of optimality measure and to $TolX = 10^{-8}$ in terms of step size. In order to integrate the differential equations, the solver *ode15s* is used which has proven to be advantageous for partly stiff systems. The integration tolerances are set to $AbsTol = 10^{-11}$ and $RelTol = 10^{-8}$ for absolute and relative tolerances, respectively. The whole set of equations can be found in Section 3.1.4.

6.4 Results and Discussion

6.4.1 Reaction Network

A detailed description of the performance of all reaction networks can be found in Section A.2.1 in the Appendix. Here, only the results of RN06 as reference case for the adsorption analysis should be discussed as well as RN01 for comparison, see Table 6.2.

Table 6.2: Estimated activation energies E_a^{cr} and pre-exponential factors $\tilde{A}^{cr}$, including 95% confidence intervals, and the sum of squared residuals *SSQ* using different reaction networks RN; all activation energies are given in kJ mol^{-1}, whereas the pre-exponential factor is shown in s^{-1}.

Parameter	RN01	RN06
E_a^{cr}(s;p)	229.9 ± 1.0	229.6 ± 1.0
E_a^{cr}(s;s)	200.2 ± 0.9	199.8 ± 0.9
E_a^{cr}(t;s)	171.5 ± 0.9	171.2 ± 0.9
E_a^{cr}(t;p)	211.9 ± 1.5	210.7 ± 1.5
$\tilde{A}^{cr} \times 10^{-16}$	2.73 ± 0.40	2.59 ± 0.38
SSQ	0.0350	0.0345

The slight deviation of the confidence intervals in RN01 compared to Table 4.3 is ascribed to minor changes in the underlying numerics. As stated above, almost no difference can be observed between the results of both reaction networks. Nevertheless, RN06 leads to a higher agreement and, more importantly, to higher parameter significance during fitting of the adsorption models; the inclusion of reversible ethene formation avoids insignificant values for E_a^{cr}(s;p) and E_a^{cr}(t;p). Thus, without overinterpreting the results, it can be stated that the backward reaction of ethene formation has to play a significant role at certain reaction conditions covered by the experiments, although the protonation of ethene should be energetically unfavored [50]. A possible explanation refers to the transition state that is highly ionic [56, 341, 342]. Usually, these ionic transition states impede the formation of primary products, not only in protonation [338], but also in cracking and dimerization steps. For ethene as product, however, the evolving primary intermediate can be easily stabilized by another oxygen in the zeolite lattice assuming a ring-like transition state [56]. This step might be sterically hindered for larger primary product intermediates, whereas it allows the formation of ethene in cracking steps and also the protonation to ethyl intermediates as first step of the backward reaction. Another possibility is the formation of a primary alkoxide out of ethene that might have higher stability compared to a primary carbenium ion. Nevertheless, also in that case, the following transition state is of ionic character.

The agreement with experimental data resulting from an application of RN06 is found in the parity plots of Figure 6.1.

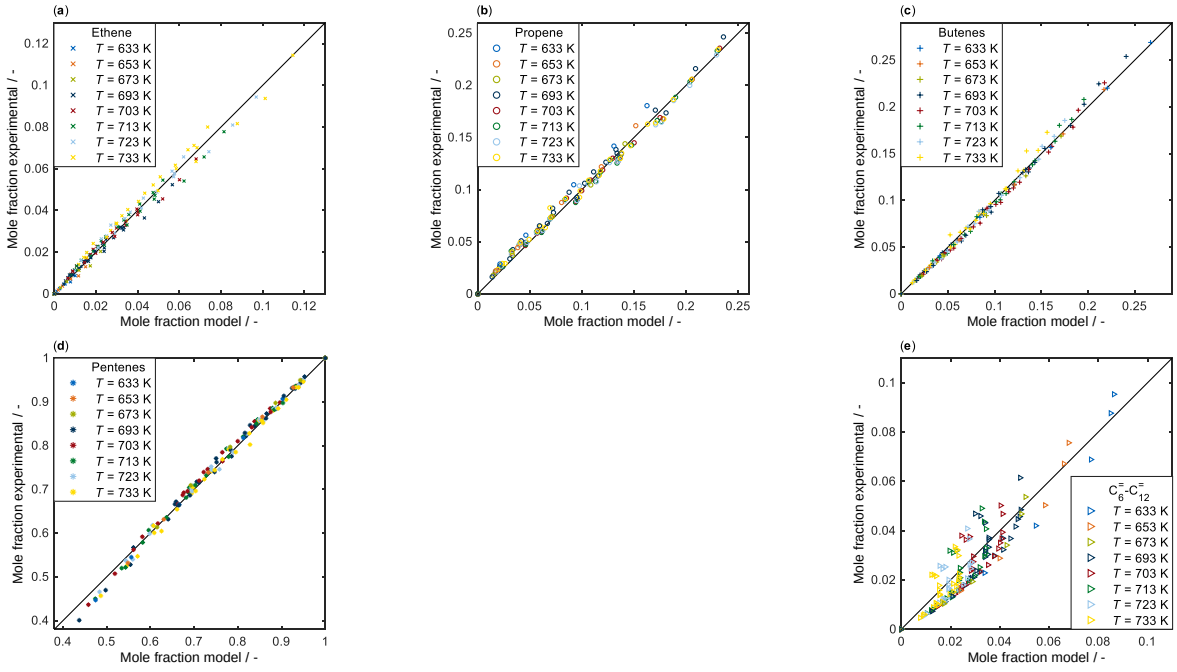

Figure 6.1: Parity plots for ethene, (a), propene, (b), butenes, (c), pentenes, (d), and $C_6^=$ to $C_{12}^=$ olefins, (e), resulting from an application of reaction network RN06.

As preparation for the following adsorption studies, some minor modifications of the microkinetic model are made. At first, the reference olefins [21] are removed. Theoretically, these species are required to avoid a thermodynamic inconsistency in the single-event concept: the protonation should be independent from the carbon number, meaning that it only depends on the type of protonated intermediate [21]. If the same is assumed for the deprotonation, the equilibrium constant of protonation will always be unity [215]. Hence, the reference olefins are introduced to maintain a carbon number dependence, but to avoid a separate fitting of each isomer [318]. However, in the original single-event model, the equilibrium constants for protonation are not estimated, but calculated before fitting; see Section 3.1.4. The underlying correlations [54] ensure a carbon number dependence of the resulting constants. Consequently, the conversion into reference olefins is dropped because it causes additional insecurities through calculating thermodynamic data. Another change is that the earlier simplification of using only the equations for 1-olefins to describe the π-complex of all isomers is removed. Depending on the olefin structure, either the correlation for 1-olefins or for 2/3/4-olefins is used. These adaptations are already considered for the results shown in Table 6.2 and in Figure 6.1.

6.4.2 Adsorption States

As shown in Section 6.3.3, several different approaches exist to describe the adsorption of hydrocarbons on acid zeolites. At first, the resulting values should be analyzed as a function

of the carbon number. This is done in Figure 6.2 for enthalpy and entropy of physisorption or of π-complex formation. An evaluation is performed for linear 1-olefins as well as linear 2-olefins. A differentiation between these can only be made when using the correlations by Nguyen *et al.* [54].

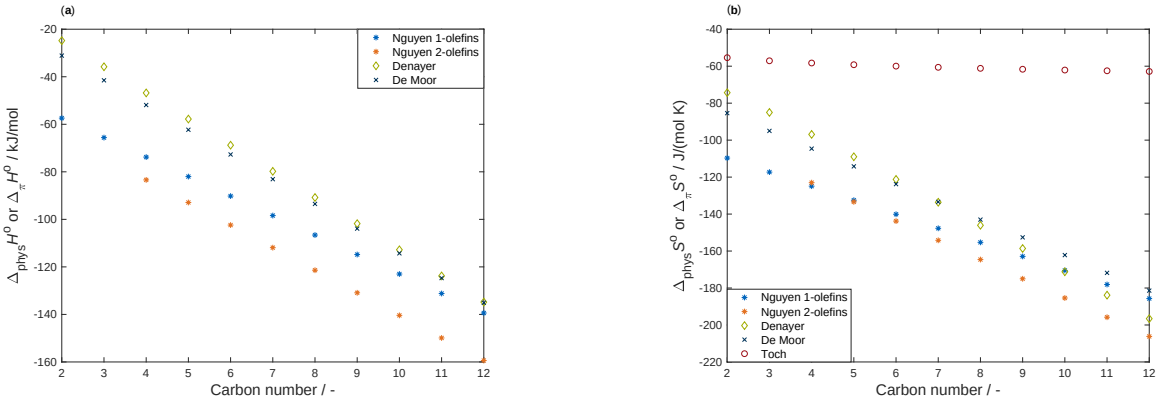

Figure 6.2: Differences in enthalpy, (a), and entropy, (b), caused by π-complex formation or physisorption, calculated for linear 1-olefins and 2-olefins; the different literature concepts cover the regular correlations by Nguyen *et al.* [54, 310], the physisorption data by de Moor *et al.* [332] as well as by Denayer *et al.* [279] and the simplified entropy approach by Toch *et al.* [194].

Figure 6.2 (a) shows increasing enthalpy release for higher carbon numbers, independent of the prevailing adsorption mechanism. This can be attributed to higher van der Waals forces caused by the growing chain length. As expected, the π-complex between olefin and acid site leads to higher stabilities of the adsorbates compared to pure alkane physisorption effects. For the latter, no significant difference between the correlations by de Moor *et al.* [332] and Denayer *et al.* [279] can be observed. Furthermore, as these two concepts rely on the measured data of alkane adsorption, not all isomers can be described and thus, no differentiation between 1-olefins and 2-olefins is possible. By contrast, the theoretically derived correlations by Nguyen *et al.* [54] show that the stabilization through the π-complex is higher for 2-olefins, a fact that is confirmed by other studies [234, 235]. With higher carbon numbers, the difference between physisorption and π-complex diminishes for 1-olefins. Due to the fixation at one end of the chain, more steric hindrance might arise for higher carbon numbers compared to the π-complex of 2-olefins, where at least one methyl group can be positioned towards another direction [235].

In Figure 6.2 (b), similar trends are observed: the loss in entropy is higher for the evolution of the π-complex and again, the 2-olefins are subjected to a higher change. This is not surprising, as the π-complex leads to a stronger fixation, whereas physisorbed hydrocarbons have higher mobility. However, similar to Figure 6.2 (a), the difference between π-complex and physisorption decreases for a longer hydrocarbon chain, where an effective fixation is impeded by steric

constraints. Again, there is no significant deviation between both physisorption models. Finally, Figure 6.2 (b) shows that assuming the physisorption entropy to correspond to one-third of the translational entropy leads to almost carbon number independent values. This is caused by the small variations within molar masses and therefore in translational entropies of the different compounds. Although this concept is an efficient solution that works with networks where the involved species differ significantly in molar masses [194], an application to olefin cracking might be problematic. At least it is expected that the real physisorption entropies show higher variation than the red data points in Figure 6.2 (b).

The chemisorption step is analyzed in Figure 6.3. Here, protonation enthalpies and entropies for linear 1-olefins as well as linear 2-olefins are shown. Figure 6.3 (b) additionally depicts the Boudart criteria for protonation entropies. Whereas the upper limit (black) is universal and thus valid for all species, the lower limit depends on the protonation enthalpy which is why it can be calculated only for the Nguyen correlations (blue and orange).

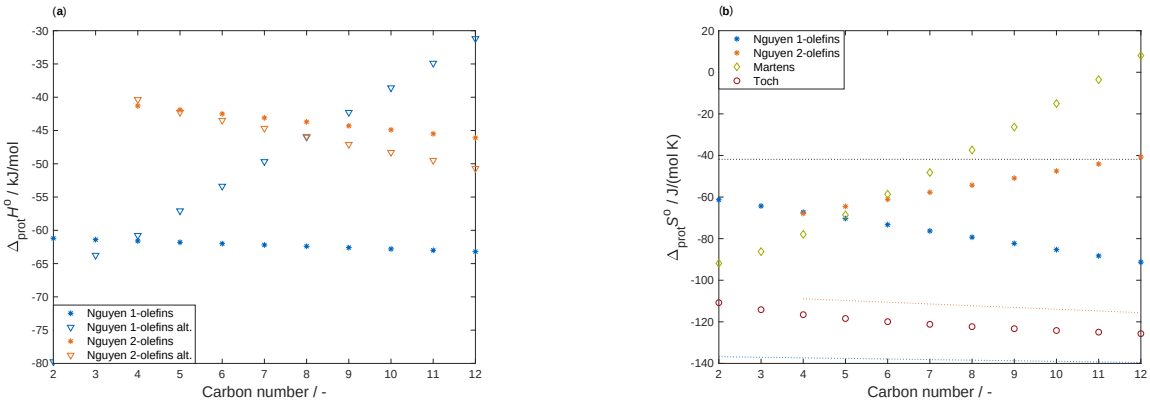

Figure 6.3: Differences in enthalpy, (a), and entropy, (b), caused by protonation, calculated for linear 1-olefins and 2-olefins; the different literature concepts cover the regular correlations by Nguyen *et al.* [54, 310], the alternative correlations by Nguyen *et al.* [350] and the physisorption data by Denayer *et al.* [279] in combination with the protonation approach by Martens *et al.* [22] as well as in combination with the protonation approach by Toch *et al.* [194]; for the protonation entropies, the upper (black) and the lower Boudart criteria (blue and orange) are shown [276].

Figure 6.3 (a) yields insight into the different types of Nguyen correlations. The regular set of equations leads to almost constant protonation enthalpies with the values for 1-olefins being significantly lower. Contrary trends are obtained for the alternative correlations: here, carbon number dependent values are obtained. These slightly decrease for the 2-olefins, whereas a sharp increase is observed for 1-olefins. This increase for linear olefins is not expected from theory and can impair the results when using these equations in a kinetic model. Especially the value of ethene that shows the highest protonation stabilization by far is extremely unrealistic.

The change in entropy due to protonation decreases for higher carbon numbers of 1-olefins according to Figure 6.3 (b). By contrast, the formation of alkoxides out of 2-olefins causes increasing protonation entropies, which again is caused by steric constraints [235]. The same trend results from the approach by Martens *et al.* [22] where carbenium ions are assumed as protonated intermediates. However, an entropy gain is predicted for a carbon number of twelve, which is not reasonable. Furthermore, these values are not in accordance with the upper Boudart criterion [276] from a carbon number of eight on. The approach by Toch *et al.* [194] also leads to results outside the Boudart criteria; here, the values are too low. As the correlations by Nguyen *et al.* [54] were created for maximum carbon numbers of eight, their limited validity for higher compounds can be seen in Figure 6.3 (b): the change in entropy for $C_{12}^{=}$ olefins is slightly above the upper Boudart criterion. Thus, these correlations should not be used for chain lengths higher than $C_{12}^{=}$.

As described in Section 6.3.4, different possibilities exist to describe the saturation concentration $C^{\mathrm{sat}}(i)$ of hydrocarbons on the catalytic surface. For Figures 6.2 and 6.3, the group contribution method by Elbro *et al.* [354] is used, which is also applied for most of the investigations shown here if not stated otherwise. This is done for several reasons. Firstly, this method allows for the calculation of individual values for all species present in the huge reaction network, whereas for the HBT concept, tabulated values are required that cannot be found for hundreds of different compounds. Secondly, the HBT method should be applied below the critical temperature [163], whereas for Elbro *et al.* [354], temperatures not higher than the normal boiling point are required [163]. This is because both concepts were created to calculate molar volumes of the condensed phase; an application to the gas phase can only be a prediction based on similarities. The temperature limits of both methods are not sufficient for typical cracking conditions. However, extrapolation to temperatures around 700 K can be performed for Elbro in contrast to the HBT method, even though the results might not be physically reasonable. Preliminary studies revealed a better agreement for Elbro evaluated at the mean experimental temperature of 683 K compared to the HBT method applied at the respective boiling temperatures. On the other hand, the same studies yielded no significant differences from the results in Figures 6.2 and 6.3 when values stemming from the HBT method were used. For this procedure, it was irrelevant whether the tabulated values of alkanes or of olefins were chosen.

Figure 6.4 shows a plot similar to Figure 6.2 for 1-olefins as well as 2-olefins with a methyl side group at the second carbon atom.

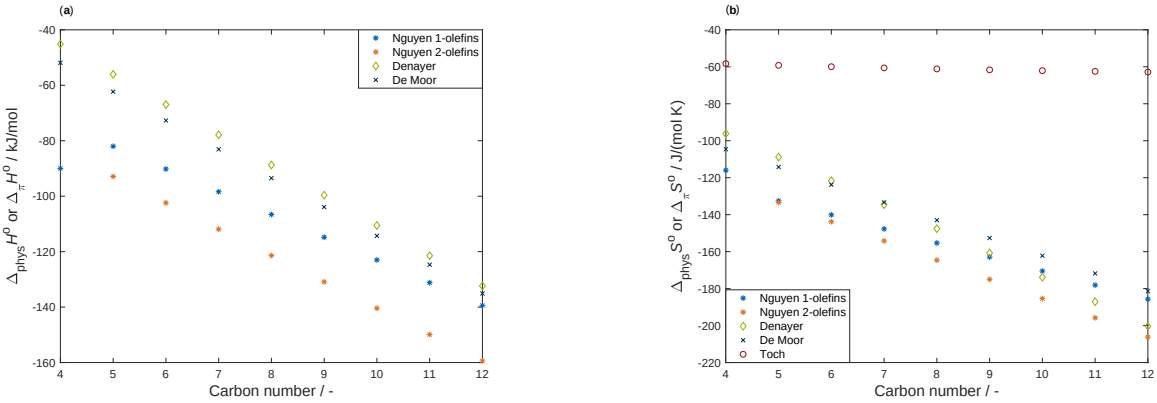

Figure 6.4: Differences in enthalpy, (a), and entropy, (b), caused by π-complex formation or physisorption, calculated for 2-methyl-1-olefins and 2-methyl-2-olefins; the different literature concepts cover the regular correlations by Nguyen *et al.* [54, 310], the physisorption data by Denayer *et al.* [279] as well as by de Moor *et al.* [332] and the simplified entropy approach by Toch *et al.* [194].

In Figure 6.4, the special role of isobutene is obvious because the results deviate in comparison to the other carbon numbers. No branched olefins are covered by the regular Nguyen correlations which is why the results are similar to Figure 6.2; also for the remaining data sets, no significant differences are found. Again, the problematic description of olefin physisorption using the approach by Toch *et al.* [194] can be observed. The protonation step for branched olefins is analyzed in Figure 6.5.

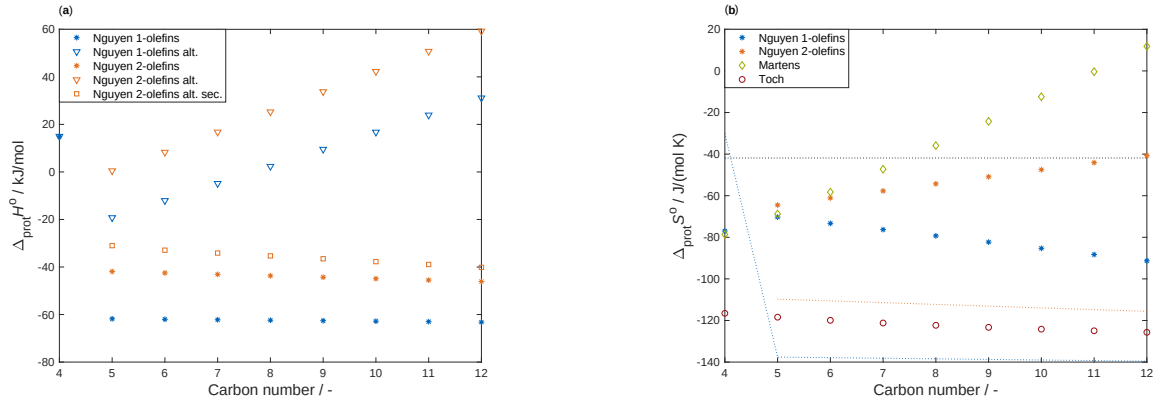

Figure 6.5: Differences in enthalpy, (a), and entropy, (b), caused by protonation, calculated for 2-methyl-1-olefins and 2-methyl-2-olefins; the different literature concepts cover the regular correlations by Nguyen *et al.* [54, 310], the alternative correlations by Nguyen *et al.* [350] and the physisorption data by Denayer *et al.* [279] in combination with the protonation approach by Martens *et al.* [22] as well as in combination with the protonation approach by Toch *et al.* [194]; for the protonation entropies, the upper (black) and the lower Boudart criteria (blue and orange) are shown [276].

Figure 6.5 (a) shows totally different trends for the protonation enthalpies when a tertiary alkoxide is calculated using the alternative set of equations by Nguyen *et al.* [310] (Nguyen 1-olefins

alt. and Nguyen 2-olefins alt.). Here, steric hindrance destabilizes the protonated intermediate, which is even more pronounced for branched 2-olefins. Although a lower stability is expected for tertiary alkoxides, the linear increase of these two data sets is again questionable. The results of the alternative approach describing protonation of branched 2-olefins to secondary alkoxides (Nguyen 2-olefins alt. sec.) are more reasonable as these are comparable to the regular Nguyen correlations. Also here, the special role of isobutene protonation becomes obvious.

No additional equations for the entropy change are available in the alternative Nguyen concept which is why the results in Figure 6.5 (b) are similar to Figure 6.3 (b). As stated above, using the concepts of Martens *et al.* [22] as well as of Toch *et al.* [194] is problematic for this reaction network of olefin cracking as the resulting values for protonation entropy are outside the Boudart criteria. This also holds for the Nguyen values for isobutene, but here, the lower criterion is above the upper one due to the positive protonation enthalpy.

In summary, a variety of concepts and approaches to describe adsorption phenomena of hydrocarbons on acid zeolites exists, all of them leading to different results. Thus, in the following, which adsorption model suits the reactivity of olefin cracking data best will be evaluated.

6.4.3 Mathematical Formulation of Overall Reactivity

In order to have a better overview of the different models and the corresponding results, these are divided into three parts and introduced with Tables 6.3 to 6.5. Here, it is shown whether the first adsorption step consists of physisorption or the formation of a π-complex. Another column reveals the implementation of protonation as second adsorption step, thereby leading to intrinsic parameters. If protonation is not explicitly considered, the estimated activation energies are of composite character and contain the respective protonation enthalpies. For both adsorption steps, the sources for the adsorption data are shown. Furthermore, the tables show the type of saturation value used for the Langmuir approach as well as the intermediate concentrations considered for the denominator. Finally, the underlying rate equation and specific remarks are presented.

The first part comprises the description of overall reactivity according to von Aretin *et al.* [26] combined with different implementations of the Nguyen correlations, see Table 6.3.

Table 6.3: First set of microkinetic models analyzed, specified by type and data source of one or two adsorption steps, by the saturation value and considered concentrations of the Langmuir term and by the implemented rate equations.

No.	Ads. 1	Data 1	Ads. 2	Data 2	Langmuir	Rate	Remarks
1	π	Nguyen [54, 310]	Prot.[a]	Nguyen [54, 310]	C_t^{SBAS}: π & Prot.[a]	Equation (6.8)	-
2	π	Nguyen [54, 310]	-	-	C_t^{SBAS}: π	Equation (6.16)	Comp. values;[b] w/ O_{ref}
3	π	Nguyen [54, 310]	Prot.[a]	Nguyen alt. [350][c]	C_t^{SBAS}: π & Prot.[a]	Equation (6.8)	Alt. approach for s and t[c]

[a] Protonation
[b] Composite values
[c] Alternative approach

Whereas the Nguyen correlations in Table 6.3 describe the evolution of a π-complex as first adsorption step, alkane physisorption approaches are analyzed in the second part. These include the equations for overall reactivity according to Martens *et al.* [22], combined with either the Denayer or the de Moor adsorption correlations, see Table 6.4.

Table 6.4: Second set of microkinetic models analyzed, specified by type and data source of one or two adsorption steps, by the saturation value and considered concentrations of the Langmuir term and by the implemented rate equations.

No.	Ads. 1	Data 1	Ads. 2	Data 2	Langmuir	Rate	Remarks
4	Phys.[a]	Denayer [279]	-	-	$C^{sat}(i)$: Phys.[a]	Equation (6.17)	Comp. values;[b] w/ C_t^{SBAS}; w/ O_{ref}; 2nd dim.: phys.[c]
5	Phys.[a]	De Moor [332]	-	-	$C^{sat}(i)$: Phys.[a]	Equation (6.17)	Comp. values;[b] w/ C_t^{SBAS}; w/ O_{ref}; 2nd dim.: phys.[c]
6	Phys.[a]	De Moor [332]	Prot.[d]	- ($\Delta_{ads}H_i^\circ$); Martens [22] ($\Delta_{ads}S_i^\circ$)	$C^{sat}(i)$: Phys.[a]	Equation (6.17)	Comp. values;[b] w/ C_t^{SBAS}; w/ O_{ref}; 2nd dim.: phys.[c]
7	Phys.[a]	De Moor [332]	-	-	$C^{sat}(i)$: Phys. & π[a]	Equation (6.18)	Comp. values;[b] w/o C_t^{SBAS}; w/ O_{ref}; 2nd dim.: phys.[c]

[a] Physisorption
[b] Composite values
[c] Relates to the second olefin during dimerization = physisorbed
[b] Protonation

Finally, as the Nguyen correlations lead to results of higher accuracy, these are further refined in the third part of the analysis. This includes the estimation of protonation enthalpies, see Table 6.5.

Table 6.5: Third set of microkinetic models analyzed, specified by type and data source of one or two adsorption steps, by the saturation value and considered concentrations of the Langmuir term and by the implemented rate equations.

No.	Ads. 1	Data 1	Ads. 2	Data 2	Langmuir	Rate	Remarks
8	π	Nguyen [54, 310]	Prot.[(a)]	Est. ($\Delta_{ads}H_i^\circ$);[(b)] Nguyen [54, 310] ($\Delta_{ads}S_i^\circ$)	C_t^{SBAS}: π & Prot.[(a)]	Equation (6.8)	Est. of s and t[(b)]
9	π	Nguyen [54, 310]	Prot.[(a)]	Est. ($\Delta_{ads}H_i^\circ$);[(b)] Nguyen [54, 310] ($\Delta_{ads}S_i^\circ$)	C_t^{SBAS}: π & Prot.[(a)]	Equation (6.8)	s = 0 kJ mol^{-1}; Est. of t[(b)]
10	π	Nguyen [54, 310]	Prot.[(a)]	Pre-set ($\Delta_{ads}H_i^\circ$); Nguyen [54, 310] ($\Delta_{ads}S_i^\circ$)	C_t^{SBAS}: π & Prot.[(a)]	Equation (6.8)	s = 0 kJ mol^{-1}; t = −30 kJ mol^{-1}
11	π	Nguyen [54, 310]	Prot.[(a)]	Pre-set ($\Delta_{ads}H_i^\circ$); Nguyen [54, 310] ($\Delta_{ads}S_i^\circ$)	C_t^{SBAS}: π & Prot.[(a)]	Equation (6.19)	s = 0 kJ mol^{-1}; t = −30 kJ mol^{-1}; 2nd Dim.: phys.[(c)]

[(a)] Protonation
[(b)] Estimation
[(c)] Relates to the second olefin during dimerization = physisorbed

Von Aretin *et al.* [26]: Use of correlations by Nguyen *et al.* [54, 310]

Figures 6.3 (a) and 6.5 (a) show high protonation enthalpies when using the regular equations by Nguyen *et al.* [54]. Thus, it is expected that a significant amount of protonated intermediates, i.e., alkoxides according to the Nguyen equations, exists on the acid sites and that the introduction of Equation (6.8) leads to improved results. However, the inclusion of the concentration term of protonation to the Langmuir approach leads to a poorer description of experimental data compared to the original model [26] ignoring the concentration of alkoxides. In Table 6.6, the results including the concentration term of protonated intermediates can be found as model No. 1. In addition, the parity plots are shown in Figure A.2 in the Appendix.

Table 6.6: Estimated activation energies E_a^{cr} and pre-exponential factors $\tilde{A}^{cr}$, including 95% confidence intervals, and the sum of squared residuals *SSQ* for the first set of models using different implementations of the Nguyen correlations; all activation energies are given in kJ mol^{-1}, whereas the pre-exponential factor is shown in s^{-1}.

Parameter	No. 1	No. 2	No. 3
E_a^{cr}(s;p)	209.8 ± 1.2	189.0 ± 1.0[(a)]	202.3 ± 1.4
E_a^{cr}(s;s)	192.2 ± 1.2	158.2 ± 1.0[(a)]	171.3 ± 1.2
E_a^{cr}(t;s)	174.8 ± 1.1	129.0 ± 0.9[(a)]	91.9 ± 1.5
E_a^{cr}(t;p)	210.8 ± 5.6	256.7 ± 2.8 ×10^{6}[(a)]	216.2 ± 6.1 ×10^{5}
$\tilde{A}^{cr} \times 10^{-16}$	0.95 ± 0.18	0.0036 ± 0.0006[(a)]	0.32 ± 0.07
SSQ	0.0480	0.0373	0.0669

[(a)] Composite value

The decline in agreement is surprising with respect to the high alkoxide stability suggested by Figures 6.3 (a) and 6.5 (a). The lower agreement with experimental data speaks for an incorrect description of the protonation, an error which then accumulates in the Langmuir sum.

In the following, the total concentration of adsorbed intermediates at typical reaction conditions is calculated to further analyze the reason for this deviation. Figure 6.6 shows the total concentration of π-complexes and of alkoxides (left) as well as the coverages and the relative amount of free acid sites θ^* (right) as a function of pentenes conversion. Different reaction conditions applied during the kinetic measurements [26] are covered. The results are obtained by evaluating the single-event model according to Equation (6.8) in combination with the regular Nguyen correlations.

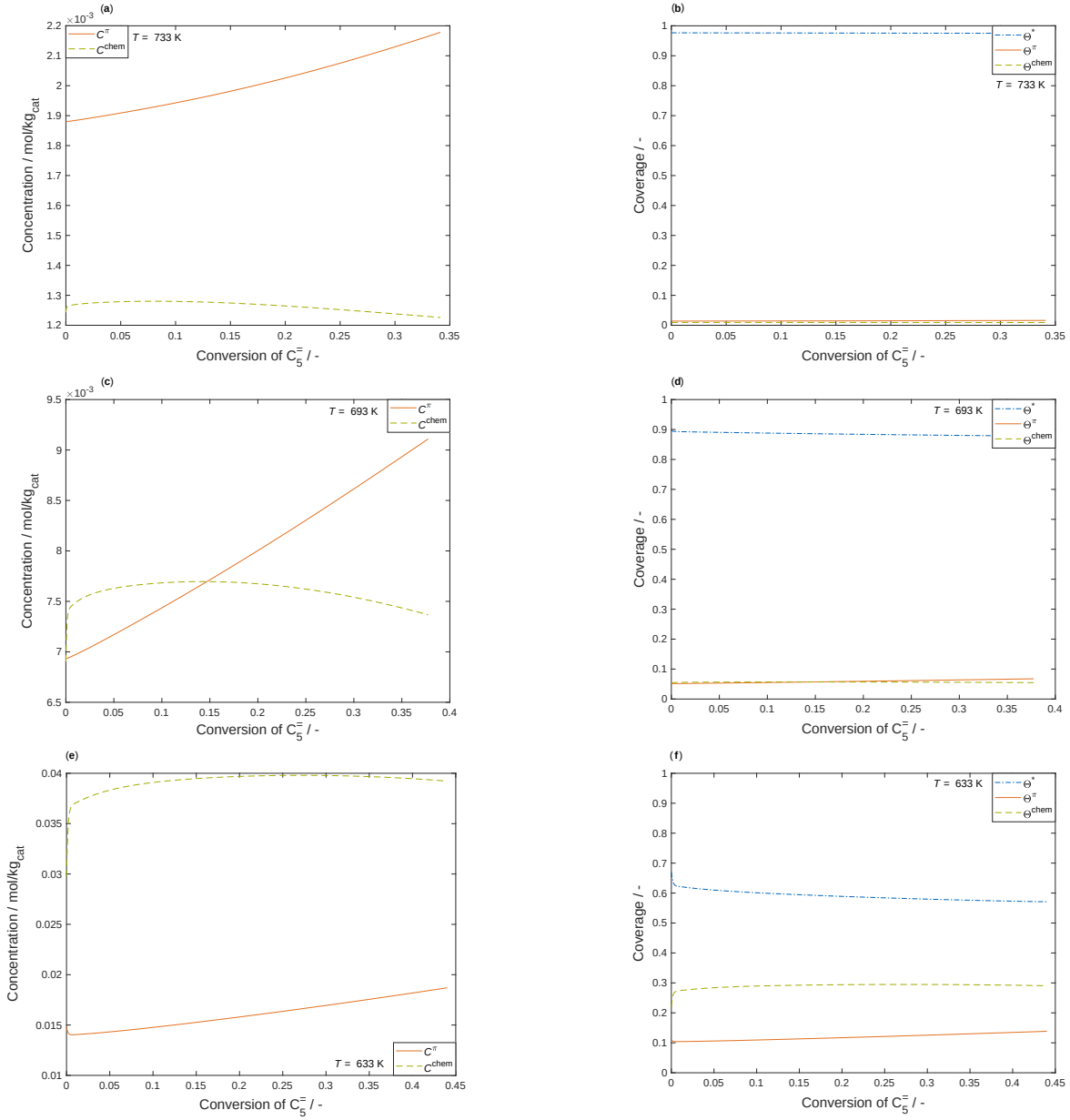

Figure 6.6: Total concentration of adsorbed species, either π-complex or chemisorption, (a), (c) and (e), and relative coverages or amount of free acid sites, (b), (d) and (f), at three different reaction conditions: 733 K and inlet partial pressure of 1-pentene $p^{\mathrm{in}}\left(\mathrm{C}_5^{=}\right)$ = 42.7 mbar, (a) and (b), 693 K and $p^{\mathrm{in}}\left(\mathrm{C}_5^{=}\right)$ = 70.3 mbar, (c) and (d), 633 K and $p^{\mathrm{in}}\left(\mathrm{C}_5^{=}\right)$ = 42.7 mbar, (e) and (f); the total pressure p_{t} is set to 1.23 bar for all subfigures.

As Figure 6.6 (a) reveals, alkoxide concentrations are negligible at high temperatures. In combination with Figure 6.6 (b), it can be seen that under these conditions, even the total concentration of π-complexes is extremely low and only a minor fraction of the acid sites is occupied. However, for intermediate temperatures and increased feed partial pressures, the concentration of alkoxides is higher than the one of π-complexes at the inlet region of the reactor as shown in Figure 6.6 (c). In addition, throughout the whole reactor length, the coverage of π-complexes and alkoxides is almost similar, see Figure 6.6 (d). Thus, it is not reasonable to neglect the chemisorbed species at these conditions. Another decrease in temperature aggravates this situation, which is depicted in Figure 6.6 (e) and (f). Here, the concentration of alkoxides is significantly higher along the whole catalyst bed. Furthermore, the relative concentration of free acid sites is comparably low. It follows that the use of a site balance including both the chemisorbed species and the compounds interacting in a π-complex is inevitable to maintain a broad application range of the model. The dependence of adsorbed intermediates on temperature, reaction progress and feed partial pressure is further analyzed in Figure 6.7.

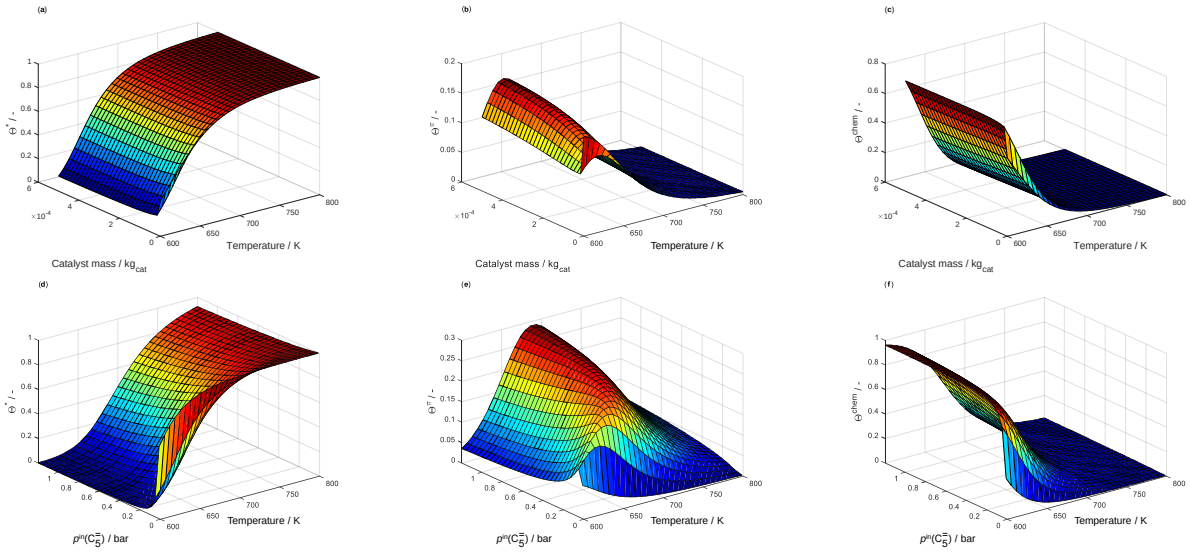

Figure 6.7: Surface plots for the relative amount of free acid sites, (a) and (d), the π-complex coverage, (b) and (e), and the alkoxide coverage, (c) and (f), which are shown as a function of temperature and catalyst mass, (a) to (c), and of temperature and inlet partial pressure of 1-pentene, (d) to (f); p_t is set to 1.195 bar for all subfigures, whereas $p^{in}\left(C_5^=\right) = 56.5\,\text{mbar}$ for (a) to (c) and maximum catalyst mass $W_{max} = 2.5 \times 10^{-4}\,kg_{cat}$ for (d) to (f), respectively.

From Figure 6.7 (a), it is obvious that higher temperatures lead to a less occupied catalyst surface. The site balance is of less importance at temperatures higher than 700 K because here, the relative amount of free acid sites is always above 0.92. Interestingly, the trend for the two types of adsorbates is different, see Figure 6.7 (b) and (c). The lower the temperature, the more alkoxides can be found on the surface whereas less olefins interact in a π-complex at 600 K. When increasing the temperature, the free sites emerging from alkoxide desorption can be effectively used by π-complexes due to the lower entropy loss, which is why a maximum is observed

around 650 K. Above this value, also the π-complex coverage decreases, but to a lower extent compared to alkoxides. A trend already observed in Figure 6.6 is the almost linear increase of π-complexes along the reactor length, whereas the alkoxide concentration shows only minor variation. This can be explained with the changing reactant composition since especially butenes contribute to the π-complex coverage and 1-pentene is converted to mainly $C_2^=$ to $C_4^=$ olefins along the reactor. Similar coherences for the temperature are found in Figure 6.7 (d) to (f), in which the influence of feed partial pressure is additionally shown. Here, higher values lead to higher coverage of both π-complex and alkoxide; again, the latter reveals a sharper increase. Compared to temperature, the influence of the feed partial pressure is less pronounced, but nevertheless, at temperatures lower than 700 K, the concentration of chemisorbed intermediates is not negligible at almost all feed partial pressure values. In summary, the analysis shows that for a physically consistent microkinetic model, the concentration of chemisorbed species cannot be ignored when using the regular correlations by Nguyen *et al.* [54].

Next, it has to be investigated why the agreement is worse when correctly accounting for the concentrations of all adsorbed intermediates. In a first step, an adapted version of Equation (6.9) is used, cf. Equation (6.16),

$$r^{\mathrm{cr}}(m;n) = n_e \tilde{k}^{\mathrm{cr,co}}\left(\mathrm{O}_i^{\pi};n\right) \frac{C_{\mathrm{t}}^{\mathrm{SBAS}} K_{\mathrm{L}}^{\pi}(\mathrm{O}_i)\, p(\mathrm{O}_i)}{1+\sum_j K_{\mathrm{L}}^{\pi}\left(\mathrm{O}_j\right) p\left(\mathrm{O}_j\right)}, \tag{6.16}$$

$$\tilde{k}^{\mathrm{cr,co}}\left(\mathrm{O}_i^{\pi};n\right) = \tilde{k}^{\mathrm{cr}}(m;n)\, K^{\mathrm{prot}}\left(\mathrm{O}_i^{\pi};m\right).$$

This is the typical approach used by the Ghent group [21, 22] when no values for protonation are available. It is adapted to olefin cracking, thus accounting for the π-complex formation whereas the hydrogenation/dehydrogenation expressions are removed. The composite rate constant $\tilde{k}^{\mathrm{cr,co}}\left(\mathrm{O}_i^{\pi};n\right)$ consists of both the intrinsic rate constant and the protonation equilibrium constant. This is why the estimated activation energies contain the protonation enthalpy, whereas the protonation entropy contributes to the composite pre-exponential factor $\tilde{A}^{\mathrm{cr,co}}$. The results of this approach are listed in Table 6.6 where it is denoted as model No. 2; the corresponding parity plot is shown in Figure A.3 in the Appendix. Throughout this part analyzing different application variations of the Nguyen correlations, model No. 2 is the only example where reference olefins are used. As stated above, these are necessary if no carbon number dependence of protonation is implemented which is the case when fitting composite values with one mutual pre-exponential factor. The estimated activation energies of model No. 2 are significantly lower. There are two possible explanations: either the protonation enthalpies have values of around $-50\,\mathrm{kJ\,mol^{-1}}$ and therefore decrease the composite activation energies or the protonation enthalpies calculated via the Nguyen correlations are too low. The latter scenario would decrease the energetic starting level of the model, thereby increasing the estimated intrinsic activation energies. The only exception is the cracking value (t;p), which is higher than before, but also shows poor numeric significance. Model No. 2 leads to lower agreement

with the experimental data. In contrast to model No. 1, the carbon number dependence of the protonation step is lost since no entropies are calculated here. Instead, the protonation entropy is part of the estimated pre-exponential factor, which is indeed three orders of magnitude lower. However, one pre-exponential factor to describe the overall reactivity including protonation and surface reaction is obviously not sufficient. By contrast to that, no dimerization occurs for hydrocracking, which reduces the amount of carbon numbers to be covered, thus enabling an application of Equation (6.9) [21, 22]. The less accurate description of model No. 2 in olefin cracking underlines the importance of correctly describing the protonation step. Although the π-complex is of high stability [54, 234], it is not sufficient to have it as only intermediate described in detail in a microkinetic model for olefin cracking.

Next, an improved protonation model should be found. Therefore, the alternative equations by Nguyen *et al.* [350] are implemented according to Equation (6.8), thus accounting for the concentration of protonated intermediates. The resulting model is denoted as No. 3 in Table 6.6. Apparently, this approach leads to a poor description of the experimental data, see the parity plots in Figure A.4 in the Appendix. Since also the regular Nguyen protonation correlations show inaccurate results when correctly considering the concentration of protonated intermediates, the evolution of alkoxides or at least their high stability has to be challenged; the description both without [54] and with stability difference [350] between secondary and tertiary alkoxides is not satisfying, see models No. 1 and 3 in Table 6.6.

Martens *et al.* [22]: Use of alkane physisorption approaches

Before further refining the description of protonation with the Nguyen correlations, the results of the alkane physisorption approaches should be discussed. For this, a reaction rate formulation similar to Equation (6.16) is proposed which includes the description of physisorption according to Equation (6.9), see Equation (6.17),

$$r^{\mathrm{cr}}(m;n) = n_e \tilde{k}^{\mathrm{cr,co}}\left(\mathrm{O}_i^{\mathrm{phys}};n\right) C_{\mathrm{t}}^{\mathrm{SBAS}} \frac{C^{\mathrm{sat}}(i)\, K_{\mathrm{L}}^{\mathrm{phys}}(\mathrm{O}_i)\, p(\mathrm{O}_i)}{1+\sum_j K_{\mathrm{L}}^{\mathrm{phys}}\left(\mathrm{O}_j\right) p\left(\mathrm{O}_j\right)}, \tag{6.17}$$

$$\tilde{k}^{\mathrm{cr,co}}\left(\mathrm{O}_i^{\mathrm{phys}};n\right) = \tilde{k}^{\mathrm{cr}}(m;n)\, K^{\mathrm{prot}}\left(\mathrm{O}_i^{\mathrm{phys}};m\right).$$

Model No. 4 in Table 6.7 represents an application of this approach when using physisorption data by Denayer *et al.* [279] in combination with the HBT method [353] for the saturation concentrations. Due to the lack of protonation data, all results in Table 6.7 are composite values. Furthermore, all models are evaluated using reference olefins. Finally, they contain the assumption of negligible concentrations of protonated intermediates; no balance for the acid sites is thus contained. For some of these models, no reasonable results were achieved when the ER type of mechanism of the original model [26] was implemented so that the second

reactant olefin in the dimerization is characterized only by its partial pressure. Thus, another physisorption term is introduced for all models in Table 6.7 to account for confinement effects for the second olefin in the dimerization.

Table 6.7: Estimated activation energies E_a^{cr} and pre-exponential factors $\tilde{A}^{cr}$, including 95% confidence intervals, and the sum of squared residuals *SSQ* for the second set of models using different alkane physisorption approaches; all activation energies are given in kJ mol^{-1}, whereas the pre-exponential factor is shown in s^{-1}.

Parameter	No. 4	No. 5	No. 6	No. 7
E_a^{cr}(s;p)	153.2 ± 2.4	167.3 ± 1.0	168.8 ± 0.8	193.8 ± 1.4
E_a^{cr}(s;s)	113.4 ± 2.7	136.2 ± 1.0	149.0 ± 0.6	160.0 ± 1.4
E_a^{cr}(t;s)	96.7 ± 2.0	114.9 ± 0.9	$191.7 \pm 1.2 \times 10^3$	136.9 ± 1.2
E_a^{cr}(t;p)	133.0 ± 5.0	$200.0 \pm 7.9 \times 10^3$	158.3 ± 1.7	200.0 ± 196.2
$\tilde{A}^{cr} \times 10^{-12}$	0.97 ± 0.35	7.66 ± 1.14	$(1.42 \pm 0.14) \times 10^4$	73.28 ± 15.62
SSQ	0.1051	0.0332	0.0971	0.0608

The agreement with experimental data is poor for model No. 4, see also Figure A.5 in the Appendix. The results do not improve when changing the underlying calculation for the saturation concentrations. Consequently, using the Denayer correlations cannot be recommended at olefin cracking conditions. By contrast, reasonable results are achieved for model No. 5 where physisorption data by de Moor *et al.* [332] are used, which is also obvious from Figure A.6 in the Appendix. This observation is surprising regarding Figures 6.2 and 6.4: here, the correlations by de Moor and Denayer show almost similar enthalpy and entropy values. Nevertheless, the small variations lead to significantly different fitting results. In general, the alkane physisorption data by de Moor *et al.* [332] are suitable to describe olefin interaction. However, the accuracy is lower than for the best π-complex model in Table 6.6. Moreover, numerical security is less for the composite values, which is revealed by the high confidence interval of the cracking parameter (t;p). In model No. 5, this value cannot be determined to a reasonable order of magnitude; it always tends towards the maximum constraint, which is 200 kJ mol^{-1} in this case. Consequently, when applied in olefin cracking, the approach via alkane physisorption leads to estimated parameters of artificial character. These values cannot be interpreted in terms of intermediates and thus allow no mechanistic insight.

In a subsequent step, the approaches according to Martens *et al.*[22] and Toch *et al.* [194] are tested. Both make use of Equation (6.17), but the description of physisorption and protonation entropy is different, cf. Equations (A.6) (in the Appendix) and (6.11) with Equations (6.13) and (6.14), respectively. The approach by Martens *et al.* [22] is denoted as model No. 6 in Table 6.7. This implementation leads to poor agreement, see Figure A.7 in the Appendix, and low numerical security. This deteriorates for the approach by Toch *et al.* [194] (not shown). Because of the high agreement achieved with model No. 5, physisorption data by de Moor *et al.* [332] are used, but the findings remain unchanged when switching to Denayer *et al.* [279].

From this, it follows that both concepts expressing the overall reactivity, though successfully applied in other reaction systems, are not suitable to describe the whole bandwidth of olefin interconversion during cracking. This matches the high deviations found for both protonation entropies in Figures 6.3 (b) and 6.5 (b) where Boudart's criteria [276] are violated.

Finally, the combination of physisorption and π-complex formation is tested. This would correspond to an olefin being only physisorbed on the catalytic surface first, so without the contribution of an acid site. Subsequently, this physisorbed compound might migrate to an acid center where the π-complex is formed. For the theoretical description, the correlations by Nguyen *et al.* [54] and de Moor *et al.* [332] are combined. In contrast to the methodology in Table 6.6, saturation effects are correlated to the catalyst surface and not to the acid sites in accordance with Thybaut et al. [317], cf. Equation (6.18),

$$r^{\mathrm{cr}}(m;n) = n_e \tilde{k}^{\mathrm{cr,co}}\left(\mathrm{O}_i^{\pi};n\right) C_{\mathrm{t}}^{\mathrm{SBAS}} \frac{C^{\mathrm{sat}}(i)\, K^{\pi}(\mathrm{O}_i)\, p(\mathrm{O}_i)}{Den}, \qquad (6.18)$$

$$Den = 1 + \sum_j C^{\mathrm{sat}}(j)\, K^{\pi}\left(\mathrm{O}_j\right) p\left(\mathrm{O}_j\right) + \sum_j K_{\mathrm{L}}^{\mathrm{phys}}\left(\mathrm{O}_j\right) p\left(\mathrm{O}_j\right).$$

The resulting description can be found as model No. 7 in Table 6.7 and as Figure A.8 in the Appendix. An acceptable agreement is observed, but the results are less accurate compared to model No. 5. Still, the highest agreement is achieved when assuming a π-complex as crucial intermediate before protonation. Composite models that include only physisorption suffer from the fact that the estimated parameters contain several adsorption steps, which might be difficult to express in a common parameter. Furthermore, only the models based on π-complex formation allow for insight into intermediate stabilities.

Own enthalpy fitting: Use of correlations by Nguyen *et al.* [54, 310]

Since the alkane physisorption approaches lead to results of comparably low accuracy and the description of protonation using the Nguyen correlations as shown above is still not satisfying, the latter should be refined. An application of Equation (6.8) allows for an estimation of the protonation enthalpies to secondary and tertiary intermediates because the protonation equilibrium constant is also part of the denominator and therefore distinguishable from the activation energies [317]. The results can be found as model No. 8 in Table 6.8.

Table 6.8: Estimated activation energies E_a^{cr}, protonation enthalpies $\Delta_{prot}H^\circ$ and pre-exponential factors A^{cr}, including 95% confidence intervals, and the sum of squared residuals *SSQ* for the third set of models where the Nguyen correlations are refined with own fittings; all activation energies and protonation enthalpies are given in kJ mol^{-1}, whereas the pre-exponential factor is shown in s^{-1}.

Parameter	No. 8	No. 9	No. 10	No. 11
E_a^{cr}(s;p)	176.6 ± 1.1	177.2 ± 0.9	177.0 ± 0.9	177.6 ± 0.9
E_a^{cr}(s;s)	157.8 ± 1.1	158.5 ± 0.9	158.3 ± 0.9	158.3 ± 1.0
E_a^{cr}(t;s)	155.4 ± 57.0	152.3 ± 53.2	169.7 ± 0.8	171.7 ± 0.8
E_a^{cr}(t;p)	194.9 ± 57.5	193.3 ± 53.8	210.6 ± 8.0	204.4 ± 2.9
$\tilde{A}^{cr} \times 10^{-16}$	4.58 ± 0.71	5.04 ± 0.67	4.86 ± 0.64	5.18 ± 0.72
$\Delta_{prot}H^\circ(O_i^\pi;s)$	0.03 ± 0.14	-	-	-
$\Delta_{prot}H^\circ(O_i^\pi;t)$	-16.1 ± 57.2	-12.5 ± 53.1	-	-
SSQ	0.0279	0.0278	0.0280	0.0282

The agreement of this model with experimental data is extremely high, which follows from the parity plots in Figure 6.8.

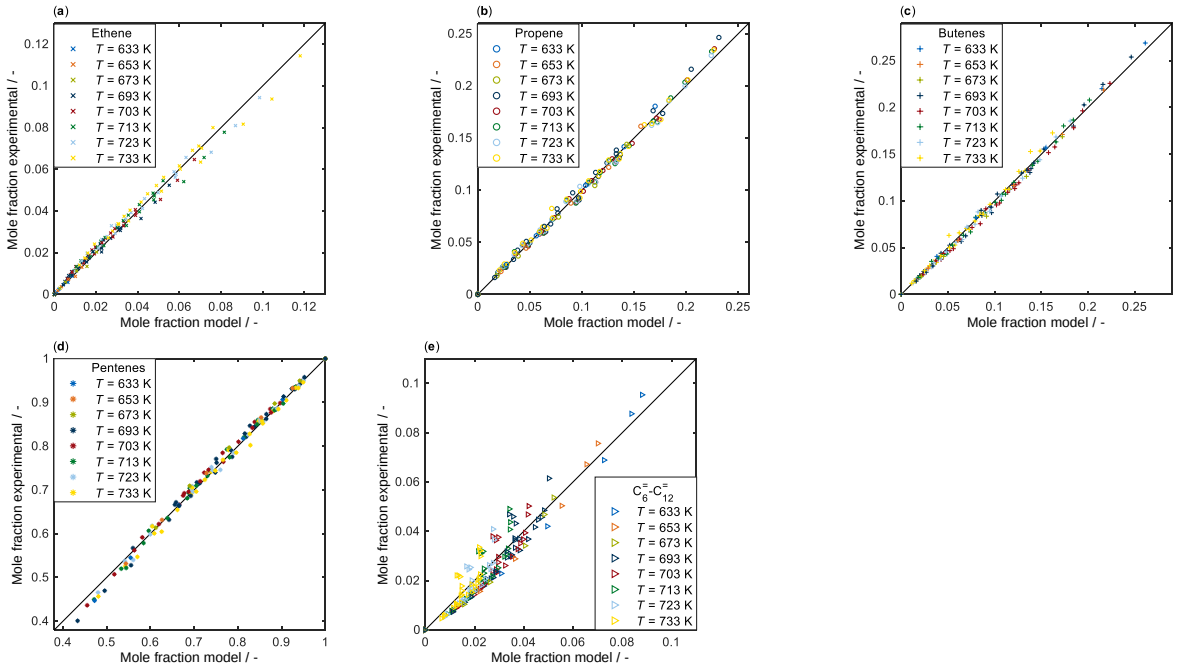

Figure 6.8: Parity plots for ethene, (a), propene, (b), butenes, (c), pentenes, (d), and $C_6^=$ to $C_{12}^=$ olefins, (e), resulting from an application of model No. 8, see Table 6.5.

By comparing Figure 6.8 (e) with Figure 6.1 (e), it follows that the improved description can be ascribed to the higher olefins. The former systematic deviation disappeared, which speaks for a more realistic implementation of their reactivity. For these frequently branched compounds, the parameters starting from a tertiary intermediate are of crucial importance and should thus be discussed here. In contrast to the original single-event model [26], the cracking parameter (t;p)

shows the highest activation energy. This result is only reasonable when assuming carbenium ions as reactive intermediates. In such a case, the cracking step (t;p) converts the most stable intermediate into the least stable one, which requires the highest activation energy. Similarly, the cracking step (t;s) should have a higher activation energy than (s;s), whereas Table 6.8 reveals that these two values are almost equal for model No. 8. However, a high numeric insecurity for all parameters starting from a tertiary intermediate can be observed. Indeed, the results shown in Table 6.8 represent a global optimization minimum, but similar to the recent study by Cnudde *et al.* [234], exact quantitative values are difficult to obtain. Therefore, the results should not be overinterpreted in terms of their numeric value, but they are meaningful in relation to each other and in the right order of magnitude. The fact that the tertiary protonation enthalpy is lower than the secondary one confirms the assumption of carbenium ions being the protonated intermediates for tertiary compounds. As stated above, the exact value is not reliable, but in all simulations, the enthalpy towards secondary intermediates is around zero, whereas the one to tertiary intermediates is lower. These results are completely different from the protonation enthalpies calculated with the Nguyen correlations, see Figures 6.3 (a) and 6.5 (a). In contrast to the latter, see Figures 6.6 and 6.7, the concentration of protonated intermediates is extremely low for the enthalpies obtained by model No. 8, hampering the estimation of exact protonation values. In addition, as shown by DFT studies [234, 235], protonation enthalpies show a variety of values, depending, among others, on molecular structure as well as the surrounding and strength of the acid site, a fact which also aggravates obtaining an average value. In model No. 8, the carbon number dependence of protonation is preserved by calculating the entropy loss with the regular Nguyen correlations. Although these assume alkoxides as intermediates, a suitable approximation for the entropy loss due to protonation is also obtained for carbenium ions. The additional mobility of the latter is then considered by an increased pre-exponential factor.

Due to the fact that all simulations lead to a protonation enthalpy to secondary intermediates of almost zero, model No. 8 is re-evaluated using this value and without estimating this parameter. The resulting model is shown as No. 9 in Table 6.8. Although there is one estimated parameter less, the agreement with experimental data is of similar quality. This is why no additional parity plot is shown as no difference to Figure 6.8 can be observed. Again, the tertiary protonation enthalpy is significantly lower than zero, see Table 6.8. On the other hand, the numeric insecurity for this parameter is still observed. In model No. 10, the protonation enthalpy to tertiary intermediates is set to $-30\,\mathrm{kJ\,mol^{-1}}$ according to the stability difference between secondary and tertiary carbenium ions estimated by Thybaut *et al.* [317]. It can be seen that the model yields maximum agreement (no parity plot shown, results similar to Figure 6.8), although another fitting parameter is removed. This clearly speaks for an optimized depiction of adsorption and therefore overall reactivity: all activation energies are in the right stability order and the numeric significance is very high. The results confirm the ionic character of protonated tertiary intermediates. Because of the crucial improvement in describing the reactivity of especially

higher olefins, it is reasonable to assume that branched olefins contribute to the overall reactivity to a significant extent. Concerning secondary and primary (= ethyl) intermediates, it can be stated that no protonated intermediates of high stability are formed. These might be alkoxides, but of significantly less stability as proposed by Nguyen *et al.* [54]. The idea of a metastable intermediate [235] can be confirmed for these species, where either a deprotonation to the π-complex or a reaction via a stabilized transition state are realistic scenarios. In contrast to earlier proposals, no decision between carbenium ions or alkoxides as protonated intermediates for all species is possible. Their evolution highly depends on the molecular structure and conditions. This explains why a recent experimental investigation [331] mentions only alkoxides as intermediates: linear pentenes were investigated here and lower temperatures as well as small feed partial pressures excluded the contribution of cracking. By contrast, the entropic advantage of carbenium ions should be crucial at industrial reaction conditions.

Finally, the description of dimerization is again extended in model No. 11; a physisorption term for the second olefin in the dimerization is introduced in Equation (6.19),

$$r^{\mathrm{dim}}(m;n) = n_e \tilde{k}^{\mathrm{dim}}(m;n)\, K^{\mathrm{prot}}\left(\mathrm{O}_i^{\pi};m\right) \frac{C_{\mathrm{t}}^{\mathrm{SBAS}} K_{\mathrm{L}}^{\pi}(\mathrm{O}_i)\, p(\mathrm{O}_i)}{1+\sum_j K_{\mathrm{L}}^{\pi}\left(\mathrm{O}_j\right) p\left(\mathrm{O}_j\right)+\sum_j K_{\mathrm{L}}^{\mathrm{chem}}\left(\mathrm{O}_j\right) p\left(\mathrm{O}_j\right)} \times \frac{C^{\mathrm{sat}}(\mathrm{O}_v)\, K_{\mathrm{L}}^{\mathrm{phys}}(\mathrm{O}_v)\, p(\mathrm{O}_v)}{1+\sum_j K_{\mathrm{L}}^{\mathrm{phys}}\left(\mathrm{O}_j\right) p\left(\mathrm{O}_j\right)}. \tag{6.19}$$

For $K_{\mathrm{L}}^{\mathrm{phys}}(\mathrm{O}_v)$, the experimentally derived correlation by de Moor *et al.* [332] is used in combination with the method by Elbro *et al.* [354] to obtain $C^{\mathrm{sat}}(\mathrm{O}_v)$. The values in Table 6.8 show similar results compared to model No. 10 (no parity plot shown, results similar to Figure 6.8). By considering physisorption effects for the second reactant olefin, model No. 11 offers the version of maximum consistency and physical correctness. On the other hand, the implementation of physisorption implies some uncertainty concerning adsorption data so that the more detailed description is not advantageous in terms of model accuracy. However, model No. 11 should be used for extrapolation purposes because its broad validity can only be guaranteed when all underlying steps are described in the physically correct way.

In summary, several conclusions can be drawn from the evaluation with different versions of the Nguyen correlations [54, 310, 350]. Firstly, the predicted high stability of the π-complex is suitable to describe the overall olefin cracking reactivity. Such high stability values are confirmed by both experiment [331] and DFT [234, 235]. Secondly, the protonation enthalpy values predicted by the regular Nguyen correlations [54] are comparably low, which means their application leads to a significant, non-negligible concentration of protonated intermediates. Thirdly, a consideration of this concentration term leads to an incorrect description of overall kinetics. Fourthly, an exact determination of protonation enthalpy values is difficult, however, the results speak for protonated intermediates of comparably low stability, thereby causing their

negligible concentration on the acid sites. Fifthly, a detailed implementation of the protonation step is required nevertheless. Here, the stability order in the simulations suggests carbenium ions to be the reactive intermediates during olefin cracking at high temperatures at least for tertiary species. Sixtly, an implementation of the lower stability of protonated intermediates leads to an optimized cracking model of maximum accuracy, minimum numeric uncertainty and vast extrapolation possibilities. As these results are significantly different from hydrocracking [21, 22], they are also helpful for other processes with olefin interconversion like MTO.

6.5 Conclusions

A microkinetic single-event model is analyzed in terms of detailed adsorption steps. Thereby, broad insight into the reactivity of olefin cracking is obtained. This allows for an assessment of important reaction pathways and intermediates. The resulting optimized model depicts all elementary reactions in a physically consistent way and is therefore highly suitable for calculating industrial applications.

A huge variety of approaches to describe the adsorption of hydrocarbons on zeolites is found in literature, comprising physisorption, π-complex formation and protonation. An analysis of the original single-event model yields considerable amounts of protonated intermediates on the catalytic surface. However, the agreement with experimental data is significantly lower when accounting for the corresponding concentration term. This observation is caused by an overestimation of the stability of the protonated intermediates by the underlying equations. However, the assumption of the π-complex as crucial intermediate is advantageous in these models.

By contrast, less accuracy is obtained when implementing alkane physisorption approaches. At least, this method provides the opportunity to include experimental adsorption data. On the other hand, for complex reaction networks with many isomers, extrapolations and estimations are inevitable for species for which no measured data are available. In addition, the agreement with kinetic data is considerably higher by implementing the π-complex, which implies this approach realistically depicts the ongoing elementary reactions.

An exact calculation of the protonation enthalpies is difficult, especially for the tertiary intermediates. Nevertheless, the results speak for comparably low stability and thus a negligible concentration of the protonated intermediates. The protonation enthalpy to secondary species is close to zero; their distinct nature is thus hard to assess. The value of tertiary species is lower, which speaks for carbenium ions as reaction intermediates for these species. By introducing a realistic stability difference between secondary and tertiary intermediates, which is found in

literature and within the bandwidth of the fitted results, a model of high accuracy and physical consistency is obtained. This can be used to describe the complex olefin interconversion chemistry, even at conditions beyond the experimentally covered regimes.

7 Single-Event Kinetic Model for MTO with Olefin Co-Feed over ZSM-5

This chapter was published and is reprinted with permission from:

S. Standl, F. M. Kirchberger, T. Kühlewind, M. Tonigold, M. Sanchez-Sanchez, J. A. Lercher, O. Hinrichsen
Single-Event Kinetic Model for Methanol-to-Olefins (MTO) over ZSM-5: Fundamental Kinetics for the Olefin Co-Feed Reactivity
Chemical Engineering Journal 402 (2020), 126023, DOI 10.1016/j.cej.2020.126023.

7.1 Abstract

MTO is an alternative pathway to selectively produce lower olefins on demand. Acid zeolites like ZSM-5 convert methanol to DME and water, followed by the formation of olefins as well as of paraffins and aromatics as side products. In this chapter, butene was used as model compound for the recycle in the industrial MTP process and co-fed with methanol. During these kinetic experiments, both methanol and butene inlet partial pressures were varied as well as the total volumetric flow rates. Temperatures between 708 and 788 K were applied as the aim of this chapter is to model the fundamental kinetics of the MTO chemistry at olefin co-feed conditions. For the kinetic model, the single-event methodology is used in order to reduce the number of estimated parameters while depicting each surface reaction. Olefin interconversion as well as olefin methylation and oxygenate interconversion steps are all covered by the model. Only the formation of aromatics is described in a simplified and thus not fundamental way. Over 4000 reaction steps are modeled using only eleven estimated parameters. The resulting high numeric significance of the activation energies allows a mechanistic analysis of the different reaction pathways and an assessment of the most important propene production steps. This shows high temperatures to be advantageous for fast carbon transfer to the olefin hydrocarbon pool and subsequent cracking of mainly hexenes and heptenes to propene.

7.2 Introduction

In times of depleting crude reserves, stricter governmental regulations as well as severe environmental concerns throughout the whole society, alternative approaches to produce ethene and propene are of crucial importance. Both established production routes, steam cracking and FCC, suffer from high energy input, tremendous CO_2 emissions [5] and poor selectivities especially for propene. The latter fact is problematic in the context of propene demands being predicted to further increase in near future, caused by its excessive use in the polymer industry.

One of the alternative concepts is the calatytic conversion of methanol to lower olefins, which requires acid zeolites like ZSM-5 as catalyst. Serendipitously discovered by coincidence [63], MTO has experienced vast research interest over the last years, cf. a literature overview [10]. The high amount of publications covers all kinds of topics like catalyst synthesis [260], structural properties [128], mechanistic studies [73], kinetic evaluation [115], *ab initio* modeling [111], kinetic modeling [18] or catalyst deactivation [132]. Nevertheless, because of the complex reactivity, there are several aspects not fully understood yet.

In that context, theoretical approaches are helpful tools to further investigate experimental findings related to mechanism or reactivity. Whereas DFT studies are important tools to analyze adsorption and reaction pathways [227, 234], deterministic kinetic modeling combines theory with experimental results and thus is able to portray a catalyst applied at industrial conditions. Especially microkinetic models depicting all possible elementary reactions yield insight, provided they are prepared in a detailed and proper way. Besides their higher stability when extrapolating out of the experimentally covered regime [19], they lead to a more realistic description of reactivity in contrast to lumped models [18]. Even for the case of a mechanistic approach being used for the latter, lumping several isomers hinders a detailed analysis of preferred reaction pathways.

A disadvantage of microkinetic models is that they require a large number of estimated parameters. Because of this, the single-event approach was developed by Froment and co-workers almost 30 years ago [19, 59]. Here, all information related to structure and conformity of the species taking part in a certain reaction are summarized in the number of single events n_e. This value can be calculated prior to parameter estimation. The remaining single-event rate constant $\tilde{k}$ only depends on reaction family and types of reactant and product intermediates. This drastically reduces the amount of unknown parameters. More details are found in literature [18–21].

For MTO, many different kinetic models exist, most of them being compared in Sections 2.6.2 and 2.6.3. There, it is concluded that each study has a different focus which means each model

is unique in assumptions and methodology. This can be explained with the high complexity of MTO. Most of the examples found in literature are designed for pure methanol or DME feeds. This is not representative for the industrial MTP process where a significant part of reaction products is recycled. By contrast, Huang *et al.* [241] create a model describing MTO experiments over ZSM-5 with $C_3^=$ to $C_6^=$ olefins as co-feed. The authors apply a mechanistic scheme, thus formulating the reactions as LH, HW and ER type. Although the model is suitable to describe the experimental data, the estimated parameters are not of fundamental nature, which impedes mechanistic insight. Indeed, several microkinetic modeling examples exist for MTO over ZSM-5, cf. the work by Kumar *et al.* [18, 38] as well as by Park and Froment [192, 250, 278], all published by the Ghent group and therefore based on the single-event concept. However, all of them are fitted to kinetic experiments where pure methanol was used as feed. Consequently, a microkinetic model for MTO over ZSM-5 at industrial co-feed conditions is not available so far.

In earlier work [26], the single-event theory is successfully applied to 1-pentene cracking over ZSM-5. Further analysis shows that this model is highly flexible in conditions and catalyst properties; furthermore, it can be used to describe all olefins from $C_3^=$ to $C_7^=$ and even their mixtures as feed, see Chapter 4, thereby proving the fundamental nature of the estimated parameters. Besides the methanol-related reactions, olefin interconversion plays a crucial role for MTO. Therefore, the existing cracking case is used here as starting point for a MTO model. Kinetic experiments without heat and mass transport limitations were performed in order to acquire a set of data adequate for deriving model parameters. In these lab scale catalytic tests, a synthetic recycle was achieved by co-feeding $C_4^=$ olefins with methanol to obtain a model representative of the conditions in an industrial MTP reactor. Subsequently, the whole MTO reactivity including side product formation is modeled making use of the single-event concept. Thus, a fundamental description of methanol conversion at industrial recycle conditions over ZSM-5 is achieved.

7.3 Methods

7.3.1 Catalyst

All measurements were conducted with a commercial ZSM-5 zeolite without binder provided by Clariant (Si/Al = 90). The sample was crushed and sieved to particle diameters between 200 and 280 µm. The resulting pure zeolite powder was diluted with SiC in a weight-based ratio of 1:10. Catalyst masses between 2 and 20 mg_{cat} were analyzed, leading to carbon-based contact times between 0.010 and 0.023 $kg_{cat}\,min\,mol_C^{-1}$. Prior to the filling step, the catalyst was

steamed at 753 K and a steam pressure of 1 bar for 24 h to achieve hydrothermal stability. At the end of this treatment, the concentrations of strong Brønsted acid sites, C_t^{SBAS}, and of Lewis acid sites, C_t^{Le}, amounted to 0.061 mol kg_{cat}^{-1} and 0.039 mol kg_{cat}^{-1}, respectively. Even in long-time tests with a time-on-stream of more than ten hours, the conversion remained almost constant. Thus, it can be excluded that catalyst deactivation effects interfered with reaction kinetics. Nevertheless, a fresh catalyst sample was used when changing the reaction temperature.

7.3.2 Experimental Setup

Kinetic measurements were performed in a continuous quartz glass plug flow reactor [105] having an inner diameter of 6 mm. The feed consisted of methanol and butanol as reactive components and further contained water and nitrogen as diluents. Preliminary tests showed an instant butanol dehydration to butenes without interfering the kinetics. Methanol, water and butanol were provided as liquids and evaporated using saturators. Temperature control of the isothermal zone was performed via a thermocouple situated at the reactor wall.

The partial pressures of the reactive compounds, i.e., p(MeOH) and $p(C_4^=)$, were varied during the experiments. Tables A.5 and A.6 in the Appendix show the respective values. The total pressure was set between 1200 and 1250 mbar and thus slightly above ambient pressure. The exact value depended on the total volumetric flow rate which was also varied. Five different temperatures between 708 and 788 K were applied in steps of 20 K each. In total, 31 different experimental conditions were realized. Product analysis was performed using a *Hewlett Packard 5890 Series 2* GC equipped with a *HP-PLOTQ* column and an FID. More details can be found in Section A.3.1 in the Appendix.

7.3.3 Reaction Network

The MTO reaction network consists of four parts: olefin interconversion, oxygenate (methanol and DME) interconversion, reactions between oxygenates and olefins and side product formation. Table 7.1 lists all types of elementary steps comprised by the single-event model as well as the implemented number of reactions of that type. Different protonation reactions can lead to the same product, for example, protonation of 1-butene and 2-butene, both leading to a 2-butyl intermediate. As both cracking and dimerization start with such a protonated olefin intermediate as reactant, these can be combined with the protonation step to reaction pathways. This is why the number of pathways is higher than the actual number of cracking/dimerization reactions. For the olefin interconversion, all isomerization reactions, i.e., branching via PCP as transition

state and methyl shift, are assumed to be *quasi*-equilibrated [49]. This also holds for the protonation and deprotonation steps. The nine oxygenate interconversion reactions in Table 7.1 contain three adsorption steps that are also treated as *quasi*-equilibrated [356]. Moreover, each methylation step requires a precedent co-adsorption which means that 20 of 40 reactions of that type in Table 7.1 are *quasi*-equilibrated adsorption steps as well. Thus, the single-event model includes 4077 reactions in total; of these, 462 are of kinetic relevance with 866 pathways to be differentiated. The reaction network contains 591 different olefins, two types of oxygenates, water, five paraffins, seven aromatic compounds as well as 481 protonated intermediates.

Table 7.1: Types of elementary reactions being implemented in the single-event kinetic model for MTO, including the number of different reactions and pathways for each step.

Type	Reactions	Pathways
Olefin protonation	957	-
Cracking	211	433
Dimerization	211	433
PCP branching	1530	-
Methyl shift	148	-
Olefin deprotonation	957	-
Oxygenate interconversion	9	-
Methylation	40	-
Double methylation	8	-
Hydrogen transfer	6	-

Olefin interconversion

All assumptions of the olefin cracking model are transferred to MTO without any adaptations, cf. Section 3.1.3. This means a maximum carbon number of twelve, no quarternary carbon atoms, only methyl side groups and a maximum number of side groups of two per compound. Furthermore, all 2,3-dimethylbutenes are excluded from the network. According to Section 6.3.1, ethene formation steps are implemented as reversible reactions. Furthermore, cracking leading to a primary intermediate is only allowed in case of ethene production. The high reactivity of the oxygenate-olefin system diminishes significance of certain olefin interconversion steps as long as oxygenates are present. For this reason, no cracking of tertiary to primary intermediates has to be taken into account. In summary, three possible cracking pathways are implemented: (s;p), (s;s) and (t;s). The rules for isomerization as well as for the olefin protonation and deprotonation reactions are the same that are used in the cracking model in Section 3.1.3.

Oxygenate interconversion

This comprises the conversion of two molecules of methanol to DME and water. In this equilibrium reaction, the forward step is slightly exothermic. Consequently, lower temperatures favor DME formation whereas the equilibrium distribution is independent of pressure because of the unchanged number of moles during reaction, see Section 2.4. It is still under debate whether the formation of DME takes place within a concerted step or via a surface methyl group [66–72, 120]. For the latter, both experimental [75, 357] as well as theoretical [18, 72] evidence exists, especially at typical MTO temperatures around 475 °C. This is why the reaction sequence according to Scheme 7.1 is implemented in the single-event kinetic model.

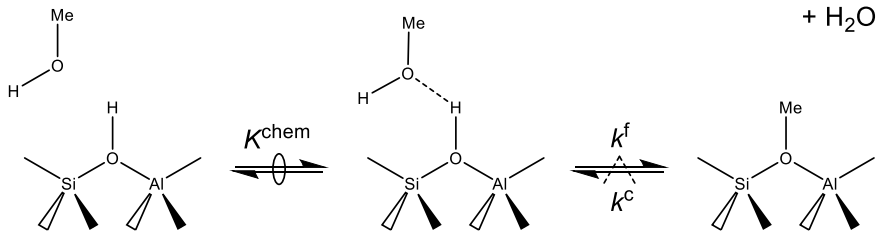

Scheme 7.1: Formation of surface methyl group as sequence of methanol chemisorption and subsequent water release.

At first, methanol is chemisorbed on an acid site as shown in Scheme 7.1. Similar to all adsorption steps in this work, the chemisorption of methanol is treated as *quasi*-equilibrated reaction [67]. This can be explained with the high temperatures applied during MTO [21]. In a second step, the water release leads to the evolution of a surface methyl group R^+_{Me}. This reversible reaction is of kinetic relevance and thus requires two rate constants: one describing the formation, $k^f\left(R^+_{Me}\right)$, and one characterizing the consumption, $k^c\left(R^+_{Me}\right)$, of the surface methyl group, the latter being the backward reaction of the formation step.

Starting from this surface intermediate, DME formation is proposed to follow the mechanism shown in Scheme 7.2 [71]. In the first step, a protonated DME intermediate R^+_{DME} is formed. In the single-event model, this step is considered to be of kinetic relevance; the same holds for the backward reaction. Subsequently, desorption of the protonated DME intermediate releases DME. This can be expressed as backward step to DME chemisorption, which is assumed to be *quasi*-equilibrated as stated above [356].

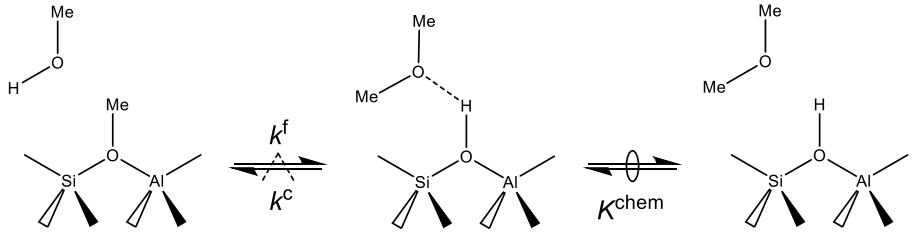

Scheme 7.2: Formation of DME out of a surface methyl group and methanol, leading to a protonated DME species that desorbs in the second step.

Another important aspect in this context is the role of water. During the experiments, it is not only formed in the reaction of methanol to DME and in the methylations, but also used as diluent. The interaction of water and zeolite catalysts is manifold and still topic of scientific debates. A decrease of reactivity due to the presence of water has been widely reported [173, 241, 289, 358]. Besides dilution effects, this can be ascribed to hydrogen bonds evolving between water molecules and the acid sites of the zeolite [359], thereby reducing the amount of active centers available for reaction. It is reported that this adsorption is weaker compared to the one of methanol and DME which is why water can be replaced by these oxygenates [360]. The adsorption of water as *quasi*-equilibrated step is included in this chapter to increase accuracy.

Oxygenate-olefin interconversion

As long as oxygenates are present, olefin methylation reactions are observed. These cause a growth of the olefin chain length due to the addition of carbon stemming from the oxygenates, thereby releasing water [10, 116]. Again, it is subject of debate whether methylation takes place via surface methyl groups [75] or within a concerted step [93]. Similar to the oxygenate interconversion, the methylation is implemented via surface methyl groups in this chapter. It is reported that the overall rate of this reaction depends on the carbon number of the olefin to be methylated [101, 241]. A co-adsorption approach [71, 229, 361–363] is introduced to account for this effect in the single-event kinetic model. Here, the olefin shows a significant interaction with the surface methyl group and, more importantly, with the zeolite surface before being methylated. For the rate equation, this means that the maximum concentration of the Langmuir term is represented by the concentration of surface methyl groups. A schematic representation is shown in Scheme 7.3. In accordance with other studies [18, 241], the reactant olefin for methylation reactions is restricted to a maximum carbon number of six. For higher olefins, the probability of cracking prevails. Furthermore, ethene methylation is neglected [100–102] because it leads to a primary product intermediate of low stability which means this step is comparably slow. Thus, for the methylation, only secondary and tertiary product intermediates are allowed whereas the reactant intermediate is always of primary nature as it is restricted to

the surface methyl group. Because of the high stability of the products compared to the reactant state, all methylation steps are implemented as irreversible reactions.

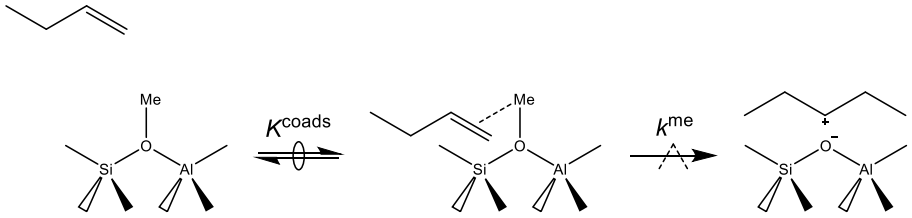

Scheme 7.3: Irreversible methylation reaction between an olefin and a surface methyl group with previous evolution of a co-adsorption complex.

When restricting the oxygenate-olefin interconversion to only single methylations in the model, the resulting transfer of carbon from oxygenates to olefins is not fast enough [241]. From literature, it is known that DME can also methylate olefins, a step showing lower barriers compared to methanol [94, 95]. In the model, this possibility is included implicitly as protonated DME can react to the surface methyl group, see Scheme 7.2. In an experimental study, the Svelle group [101] co-fed propene or butene with ^{13}C-methanol and found an amount of methylation products with two ^{13}C atoms significantly exceeding the value expected from random distributions. By extrapolating the selectivities to infinite feed flow rates (contact time of zero), they could prove that these compounds behave as primary products of the methylation reaction. Thus, a transfer of two carbon atoms within one step is required as two consecutive single methylations are not fast enough to describe the experimentally observed methylation rates [241].

For such double methylation steps, no mechanistic proposal exists. Here, DME is suggested to be the reactant in double methylations to combine these findings with its frequently observed enhanced methylation rate. The first step is the chemisorption of DME, see Scheme 7.4. It is followed by the irreversible transfer of both carbon atoms to the olefin, thereby releasing water. Besides adsorbed methanol, a suggested intermediate of this pathway is the protonated olefin subsequent to the transfer of the first methyl group. Due to their vicinity to each other, deprotonation of the olefin and simultaneous protonation of the methanol occur very fast, leading to the second methylation step and water release. As it can be seen in Scheme 7.4, the rather large DME molecule prevents the olefin of interacting with the zeolite surrounding. Consequently, no olefin adsorption effects are considered for this step. The double methylation is seen to be sterically more demanding compared to the single methylation. This is why only reactions leading to a secondary intermediate as product of the first methylation step are considered. For the same reason, it is assumed that the deprotonation subsequent to the first methylation restores the double bond at its original position. Only when the hydrocarbon is still linear prior to the second methylation, the double bond can also evolve towards the

other adjacent carbon atom. All olefins from $C_3^=$ to $C_5^=$ are allowed as possible reactants in this reaction.

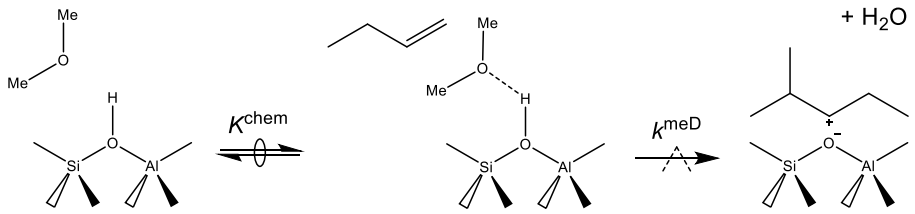

Scheme 7.4: Double methylation of an olefin, starting from a chemisorbed DME and leading to the irreversible transfer of two carbon atoms in the second step.

Side product formation

Two different regimes are observed for MTO side reactions [58]: a high rate regime at conditions where methanol is available in the gas mixture and a low rate regime at conditions of full methanol conversion, thus comparable to the rates observed for the olefin cracking case [58]. The latter scenario is caused by hydride transfer reactions between hydrocarbons [57]. It is regarded as negligible at the reaction conditions used here because oxygenate conversion never exceeded a value of 0.7 and therefore, the high rate regime in presence of methanol dominates. This involves the so called methanol-induced hydrogen transfer pathway, in which formaldehyde plays a crucial role [97]. This mechanism suggests that a fraction of formaldehyde is formed on Brønsted acid sites when methanol irreversibly reacts with a surface methyl group to methane, see Scheme 7.5. It is implemented in the single-event model without considering any adsorption effects.

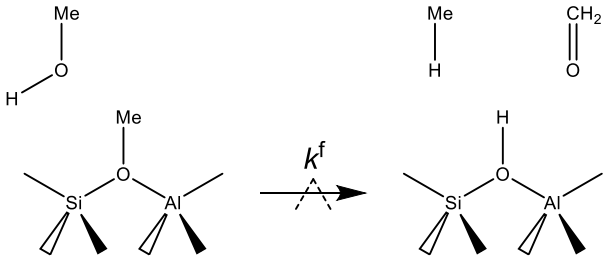

Scheme 7.5: Irreversible methane formation out of a surface methyl group and methanol; formaldehyde is another product of this reaction.

It has been shown that the main part of paraffin formation takes place on Lewis acid sites [97]. Methanol and an olefin react to formaldehyde and the corresponding paraffin as it is shown in Scheme 7.6. In the product streams of the kinetic measurements, the amount of paraffins higher than C_4 was negligible. Consequently, the pathway in Scheme 7.6 is included in the model with

only ethene, propene and butenes as reactants. Due to the high stability of methane and C_2 to C_4 paraffins, the side product formation is assumed to be irreversible in the model.

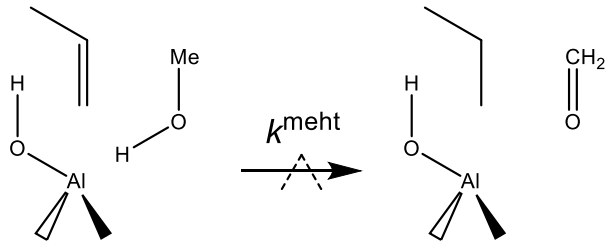

Scheme 7.6: Methanol-induced hydrogen transfer on a Lewis acid site: a lower olefin and methanol irreversibly react to the corresponding paraffin and formaldehyde.

Recently, it has been shown that formaldehyde reacts with olefins in a Prins reaction to dienes and, after several subsequent steps, to aromatics [364]. The microkinetic description of this pathway is however not possible due to the absence of formaldehyde and very low concentrations of aromatics in the product stream. Therefore, this reaction pathway is not included in the model. The formation of aromatics is accounted for by closing the hydrogen balance. The formation of aromatics is accounted for by closing the hydrogen balance. Since no formaldehyde is detected at the reactor outlet, the total molar flow rate of all aromatics has to correspond to one third of the molar flow rates of all paraffins (including methane).

According to the mechanism [97], three molecules of formaldehyde are required to convert an olefin $C_i^=$ to an aromatic species with a carbon number of C_{i+3}^{ar}. An analysis of the experimental output shows toluene, xylenes and trimethylbenzenes as aromatic products, which can be related to the spatial constraints of ZSM-5. Consequently, in the model, butenes, pentenes and hexenes are allowed as reactants for aromatization.

Another mechanistic aspect that has to be mentioned in this context is the aromatic hydrocarbon pool [81]. According to this concept, polymethylated aromatic compounds are built up and trapped within the pores of the zeolite. Through ongoing methylation and dealkylation reactions, they act as a co-catalyst producing lower olefins and especially ethene [91]. In the product streams of this study, ethene yields are comparably low (not higher than 1.5%). In addition, experimental carbon balances could be closed for all data points. Thus, it is reasonable to assume that no significant buildup of the aromatic hydrocarbon pool interfered with the kinetic measurements. The reactions forming aromatics within the pores are comparably slow; the contribution of the aromatic hydrocarbon pool to overall oxygenates conversion can thus be lowered by co-feeding olefins [105]. Because of the use of an olefin co-feed, the high water dilution and the fact that oxygenates conversion never exceeded a value of 0.7, the reactions of the aromatic hydrocarbon pool are neglected for the model.

7.3.4 Adsorption

The adsorption values that are implemented in the model are introduced here, following the structure of Section 7.3.3. An additional overview is given in Table A.7 in the Appendix.

Olefin interconversion

For cracking and dimerization, adsorption is implemented according to Chapter 6. First, a π-complex is formed, that can be described using the theoretical correlations by Nguyen *et al.* [54, 310]. A subsequent protonation step leads to a carbenium ion as intermediate; its evolution is determined using a protonation enthalpy of $0\,\mathrm{kJ\,mol^{-1}}$ for secondary and of $-30\,\mathrm{kJ\,mol^{-1}}$ for tertiary carbenium ions, respectively. The protonation entropy is also derived from the Nguyen correlations [54, 310]. The second olefin during dimerization is assumed to be physisorbed. The required equilibrium constants can be calculated using a correlation provided by de Moor *et al.* [332]; their data is based on physisorption experiments with alkanes on ZSM-5.

Oxygenate interconversion

The chemisorption of methanol is described using the values stemming from a periodic DFT study by Nguyen *et al.* [365]. The results for the most stable configuration, i.e., chemisorption within the zig-zag channels, are used.

For DME, Maihom *et al.* [71] published a chemisorption enthalpy, resulting from their theoretical ONIOM study. For the single-event model, the chemisorption entropy is assumed to correspond to a total loss of translational entropy [18]. The latter can be calculated using the Sackur-Tetrode-Equation [355] that is shown in Equation (7.1),

$$S_i^{\circ,\mathrm{trans}} = k_\mathrm{B} N_\mathrm{A} \left\{ \ln\left(\frac{[2\,\pi M(i)\,k_\mathrm{B}\,T]^{3/2}}{h^3} \right) + \ln\left(\frac{V_\mathrm{m}^\mathrm{g}(i)}{N_\mathrm{A}} \right) + \frac{5}{2} \right\}, \tag{7.1}$$

with the Boltzmann constant k_B, the Avogadro constant N_A, the Planck constant h, the temperature T, the molecular mass $M(i)$ of compound i and its molar volume in the gas phase $V_\mathrm{m}^\mathrm{g}(i)$.

Finally, the adsorption parameters for water are extracted from an experimental study by Pope [319]. Since the author shows results as function of coverage, average values for enthalpy and entropy are chosen.

Oxygenate-olefin interconversion

The group around van Speybroeck [229] published values for the co-adsorption of methanol and DME onto an acid site occupied with either water or methanol. From there, it can be derived that the additional change in enthalpy and entropy through co-adsorption approximately equals three quarters of the direct interaction of the respective species with the acid site. Transferred to olefins, this corresponds to pure physisorption when compared with the evolution of a π-complex. This is reasonable since in a co-adsorption complex, the olefin mainly interacts with the surface methyl group and the zeolite surrounding and not with the acid site itself [363]. Values compilated for the physisorption of olefins on silicalite-1 [366] are in the same range than experimental data of paraffin physisorption on ZSM-5 [332]. Consequently, for the single-event model, the co-adsorption of olefins is described using the correlations by de Moor *et al.* [332]. Following this procedure, the values are comparable to the results of ethene, propene and butene co-adsorption published by the Svelle group [363].

Side product formation

As stated above, no adsorption effects are implemented for the side product formation because there is not any published data for the interaction of methanol and an olefin with a Lewis acid site.

7.3.5 Rate Equations

The reaction rate has to be strictly separated from the net rate of production $R(i)$. The former is assigned to a certain reaction step whereas the latter is formulated for a specific compound i. It can be obtained by summing up all rates of the steps l where this compound is produced or consumed, multiplied by the stoichiometric coefficient, see Equation (7.2),

$$R(i) = \sum_q \nu_q(i)\, r_q. \tag{7.2}$$

Olefin interconversion

The derivation of the rate equations for the olefin cracking and dimerization reactions is presented elsewhere [26]. These are shown in Section 3.1.4 and are slightly adapted in Chapter 6: the concentration of protonated intermediates is explicitly included in the denominator of the

Langmuir term. Moreover, physisorption effects for the second olefin during dimerization are considered. The rate equations for cracking and dimerization are given in Equations (7.3) and (7.4), respectively,

$$r^{\mathrm{cr}}(m;n) = n_e \tilde{k}^{\mathrm{cr}}(m;n)\, K^{\mathrm{prot}}\left(\mathrm{O}_i^{\pi};m\right)\, C_{\mathrm{t}^*}^{\mathrm{SBAS}}\, K_{\mathrm{L}}^{\pi}(\mathrm{O}_i)\, p(\mathrm{O}_i), \tag{7.3}$$

$$r^{\mathrm{dim}}(m;n) = n_e \tilde{k}^{\mathrm{dim}}(m;n)\, K^{\mathrm{prot}}\left(\mathrm{O}_i^{\pi};m\right)\, C_{\mathrm{t}^*}^{\mathrm{SBAS}}\, K_{\mathrm{L}}^{\pi}(\mathrm{O}_i)\, p(\mathrm{O}_i) \times \frac{C^{\mathrm{sat}}(\mathrm{O}_v)\, K_{\mathrm{L}}^{\mathrm{phys}}(\mathrm{O}_v)\, p(\mathrm{O}_v)}{1+\sum_j K_{\mathrm{L}}^{\mathrm{phys}}\left(\mathrm{O}_j\right) p\left(\mathrm{O}_j\right)}. \tag{7.4}$$

The single-event theory is extensively described in literature [19–21, 215]. More information about the division of the regular rate constant k into the number of single events n_e and the single-event rate constant $\tilde{k}$ can be found there. The equilibrium constants for the Langmuir approach K_{L} are calculated using the values in Table A.7 in the Appendix. Due to the fact that adsorption parameters are not estimated, the reference olefins for protonation [21] are omitted. The calculation procedure for the saturation concentration on the catalytic surface $C^{\mathrm{sat}}(\mathrm{O}_v)$ is similar to the one presented in Section 6.4.2.

The olefin interconversion network requires three rate constants: $\tilde{k}^{\mathrm{cr}}$(s;p), $\tilde{k}^{\mathrm{cr}}$(s;s) and $\tilde{k}^{\mathrm{cr}}$(t;s). The dimerization reactions are expressed as backward reaction to the corresponding cracking step by making use of the microscopic reversibility [196], thus causing no additional parameter. This procedure is further explained elsewhere [26].

Oxygenate interconversion

In total, the interconversion of oxygenates causes four unknown rate constants: $k^{\mathrm{f}}\left(\mathrm{R}_{\mathrm{Me}}^{+}\right)$, $k^{\mathrm{c}}\left(\mathrm{R}_{\mathrm{Me}}^{+}\right)$, $k^{\mathrm{f}}\left(\mathrm{R}_{\mathrm{DME}}^{+}\right)$ and $k^{\mathrm{c}}\left(\mathrm{R}_{\mathrm{DME}}^{+}\right)$. In addition, two *quasi*-equilibria have to be described via K^{chem}(MeOH) and K^{chem}(DME). The corresponding rate equations are shown in Equations (7.5) to (7.8),

$$r^{\mathrm{f}}\left(\mathrm{R}_{\mathrm{Me}}^{+}\right) = k^{\mathrm{f}}\left(\mathrm{R}_{\mathrm{Me}}^{+}\right) C\left(\mathrm{MeOH}_2^{+}\right), \tag{7.5}$$

$$r^{\mathrm{c}}\left(\mathrm{R}_{\mathrm{Me}}^{+}\right) = k^{\mathrm{c}}\left(\mathrm{R}_{\mathrm{Me}}^{+}\right) C\left(\mathrm{R}_{\mathrm{Me}}^{+}\right) p\left(\mathrm{H_2O}\right), \tag{7.6}$$

$$r^{\mathrm{f}}\left(\mathrm{R}_{\mathrm{DME}}^{+}\right) = k^{\mathrm{f}}\left(\mathrm{R}_{\mathrm{DME}}^{+}\right) C\left(\mathrm{R}_{\mathrm{Me}}^{+}\right) p(\mathrm{MeOH}), \tag{7.7}$$

$$r^{\mathrm{c}}\left(\mathrm{R}_{\mathrm{DME}}^{+}\right) = k^{\mathrm{c}}\left(\mathrm{R}_{\mathrm{DME}}^{+}\right) C\left(\mathrm{R}_{\mathrm{DME}}^{+}\right). \tag{7.8}$$

The concentrations of protonated methanol, $C\left(\mathrm{MeOH}_2^{+}\right)$, and of protonated DME, $C\left(\mathrm{R}_{\mathrm{DME}}^{+}\right)$, can be replaced by the corresponding chemisorption equilibrium constants, the concentration of

free strong Brønsted acid sites C_{t*}^{SBAS} and the partial pressures, see Equations (7.9) and (7.10), respectively,

$$r^{f}\left(R_{Me}^{+}\right) = k^{f}\left(R_{Me}^{+}\right) K^{chem}(MeOH)\, p(MeOH)\, C_{t*}^{SBAS}, \tag{7.9}$$

$$r^{c}\left(R_{DME}^{+}\right) = k^{c}\left(R_{DME}^{+}\right) K^{chem}(DME)\, p(DME)\, C_{t*}^{SBAS}. \tag{7.10}$$

All these reactions are related via the thermodynamic equilibrium between methanol, DME and water. This coherence is illustrated in Scheme 7.7 in more detail.

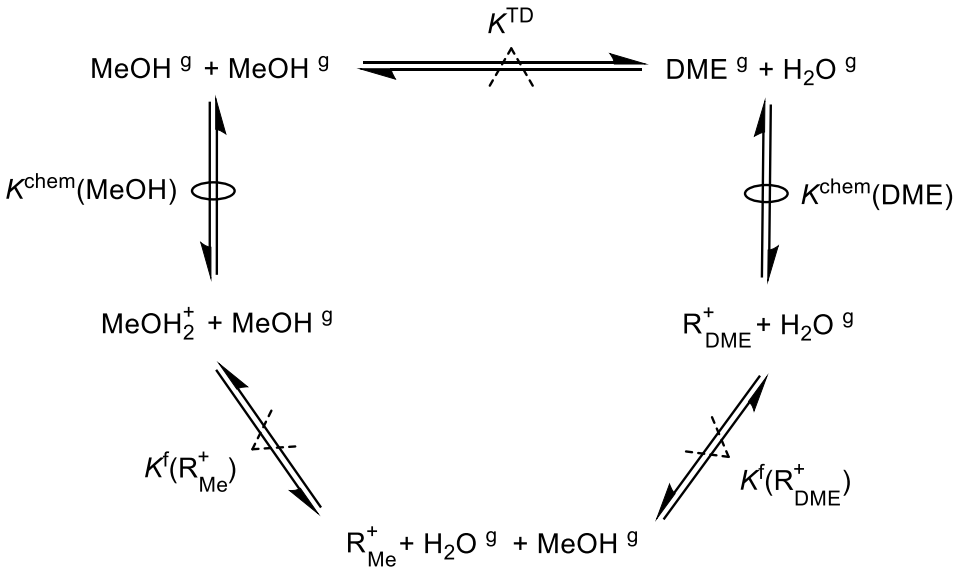

Scheme 7.7: Elementary steps for the reaction of methanol to DME and water as well as their relation via the thermodynamic equilibrium constant K^{TD}.

From there, it follows that one of the unknown rate constants can be replaced by the thermodynamic equilibrium constant in combination with the equilibrium constants of the other steps. This procedure not only reduces the number of unknown parameters, but also ensures thermodynamic consistency, following the principle of microscopic reversibility [196]. Thus, the rate constant for the consumption of protonated DME, $k^{c}\left(R_{DME}^{+}\right)$, is replaced by Equation (7.11),

$$k^{c}\left(R_{DME}^{+}\right) = \frac{k^{f}\left(R_{DME}^{+}\right) K^{f}\left(R_{Me}^{+}\right) K^{chem}(MeOH)}{K^{TD}\, K^{chem}(DME)}. \tag{7.11}$$

The thermodynamic equilibrium constant K^{TD} is calculated using MATLAB, following the methodology explained in Section 2.4.

Oxygenate-olefin interconversion

For the methylation steps, a differentiation of the product stabilities is performed; thus, two different parameters exist: $\tilde{k}^{\mathrm{me}}\,(\mathrm{p;s})$ and $\tilde{k}^{\mathrm{me}}\,(\mathrm{p;t})$. The rate equation is shown in Equation (7.12),

$$r^{\mathrm{me}}\,(\mathrm{p};n) = n_e\,\tilde{k}^{\mathrm{me}}\,(\mathrm{p};n)\;C\left(\mathrm{R}^{+}_{\mathrm{Me}}\right)\;K_{\mathrm{L}}^{\mathrm{coads}}\,(\mathrm{O}_i)\;p\,(\mathrm{O}_i)\,. \tag{7.12}$$

As described in Section 7.3.3, only the formation of secondary intermediates is allowed in the first step of the double methylation. Because the resulting intermediate complex is of high reactivity, it is reasonable to assume that its net concentration remains unchanged over time [18]. Mathematically, this results in a net rate of production of zero [179] according to the PSSA. From this concept, it follows that Equation (7.13) can be used to describe both the consumption of the reactant olefin as well as the production of the evolving olefin. This equation requires the unknown rate constant $\tilde{k}^{\mathrm{meD}}\,(\mathrm{p;s})$,

$$r^{\mathrm{meD}} = n_e\,\tilde{k}^{\mathrm{meD}}\,(\mathrm{p;s})\;C\left(\mathrm{R}^{+}_{\mathrm{DME}}\right)\;p\,(\mathrm{O}_i)\,. \tag{7.13}$$

Side product formation

The methane formation takes place via a surface methyl group; the corresponding rate equation with one unknown rate constant $k^{\mathrm{f}}\left(\mathrm{CH_4}\right)$ can be seen in Equation (7.14),

$$r^{\mathrm{f}}\left(\mathrm{CH_4}\right) = k^{\mathrm{f}}\left(\mathrm{CH_4}\right)\;C\left(\mathrm{R}^{+}_{\mathrm{Me}}\right)\;p\,(\mathrm{MeOH})\,. \tag{7.14}$$

The hydrogen transfer reactions producing paraffins P_i are assumed to proceed at Lewis acid sites [97]. Thus, besides the total concentration of Lewis acid sites $C_{\mathrm{t}}^{\mathrm{Le}}$, an adsorption equilibrium constant $K^{\mathrm{ads,Le}}$ can be found in Equation (7.15),

$$r^{\mathrm{meht}}\,(\mathrm{O}_i;\mathrm{P}_i) = k^{\mathrm{meht}}\,C_{\mathrm{t}}^{\mathrm{Le}}\,K^{\mathrm{ads,Le}}\,p\,(\mathrm{MeOH})\,p\,(\mathrm{O}_i)\,. \tag{7.15}$$

As this value is unknown for all species, it is merged with the rate constant to a composite value $k^{\mathrm{meht,co}}$, see Equation (7.16),

$$r^{\mathrm{meht}}\,(\mathrm{O}_i;\mathrm{P}_i) = k^{\mathrm{meht,co}}\,C_{\mathrm{t}}^{\mathrm{Le}}\,p\,(\mathrm{MeOH})\,p\,(\mathrm{O}_i)\,. \tag{7.16}$$

This combined value is the one to be estimated for the hydrogen transfer reactions. No Langmuir approach is introduced here as the coverage of Lewis acid sites is assumed to be negligibly low.

For the molar flow rates $F(\mathrm{A}_i)$ of all aromatics, the balance according to Equation (7.17) applies,

$$\sum_j F\left(\mathrm{A}_j\right) = \frac{1}{3} F(\mathrm{CHOH}) = \frac{1}{3}\left(F\left(\mathrm{CH_4}\right) + \sum_j F\left(\mathrm{P}_j\right)\right). \tag{7.17}$$

7.3.6 Pre-Exponential Factors

The reparametrized Arrhenius approach in Equation (7.18) is used to include the temperature dependence of the rate constants,

$$k = A^{\mathrm{ref}} \frac{T}{T^{\mathrm{ref}}} \exp\left(-\frac{E_\mathrm{a}}{R\,T^{\mathrm{ref}}}\right) \exp\left(-\frac{E_\mathrm{a}}{R}\left(\frac{1}{T} - \frac{1}{T^{\mathrm{ref}}}\right)\right), \tag{7.18}$$

where T^{ref} is set to 748 K as average temperature of the kinetic measurements. Consequently, each rate constant causes two unknown parameters to be estimated, the pre-exponential factor A^{ref} and the activation energy E_a. However, even in reparametrized form, correlation between these two values is significant which complicates a reasonable fitting. This is why the pre-exponential factors are calculated before parameter estimation [22] by making use of the modified [190] Eyring-approach [189] in Equation (7.19),

$$A^{\mathrm{ref}} = \frac{k_\mathrm{B}\,T^{\mathrm{ref}}}{h} \exp\left(\frac{\Delta_\ddagger S^\circ}{R}\right) \exp\left(1 - \Delta_\ddagger \nu_\mathrm{g}\right). \tag{7.19}$$

For cracking, this value is available from Table 4.3, but adapted to the new reference temperature. The other elementary reactions require assumptions for the change in entropy $\Delta_\ddagger S^\circ$ due to the step from reactant to transition state. Furthermore, the value $\Delta_\ddagger \nu_\mathrm{g}$ resembling the difference in number of moles in the gas phase between these two states has to be considered. Table 7.2 summarizes this information for each pre-exponential factor. It is assumed that the entropy change $\Delta_\ddagger S^\circ$ can be fully attributed to changes in translational entropy [22]. The latter is accessible via Equation (7.1) where the molecular mass $M(i)$ of the respective species has to be used. A maximum value of three is possible for $\Delta_\ddagger n^{\mathrm{trans}}$, resembling a gain or loss of all three translational degrees of freedom.

Table 7.2: Required values to calculate pre-exponential factors at reference temperature A^{ref} via the difference in translational degrees of freedom $\Delta_{\ddagger} n^{\mathrm{trans}}$ as well as in moles in gas phase $\Delta_{\ddagger} \nu_{\mathrm{g}}$ by using Equation (7.19); the molar mass M_{m} is given in kg kmol^{-1}, the entropy change $\Delta_{\ddagger} S^{\circ}$ in J mol^{-1} K^{-1} and the pre-exponential factors in s^{-1}, in s^{-1} bar^{-1} or in s^{-1} bar^{-2}.

Value	$\Delta_{\ddagger} n^{\mathrm{trans}}$	M_{m}	$\Delta_{\ddagger} S^{\circ}$	$\Delta_{\ddagger} \nu_{\mathrm{g}}$	A^{ref}
$\tilde{A}^{\mathrm{me}}$	0	-	0	0	4.24×10^{13}
$\tilde{A}^{\mathrm{meD}}$	1[a]	46.06	58.54	-1	1.04×10^{14}[b]
$A^{\mathrm{f}}\left(\mathrm{R}^{+}_{\mathrm{Me}}\right)$	0	-	0	0	4.24×10^{13}
$A^{\mathrm{c}}\left(\mathrm{R}^{+}_{\mathrm{Me}}\right)$	-	-	-	-	8.34×10^{10}
$A^{\mathrm{f}}\left(\mathrm{R}^{+}_{\mathrm{DME}}\right)$	-1	32.04	-57.04	-1	1.21×10^{11}
$A^{\mathrm{f}}\left(\mathrm{CH}_4\right)$	-2	32.04	-114.07	-1	1.27×10^{8}
$A^{\mathrm{meht,co}}\left(\mathrm{O}_i;\mathrm{P}_i\right)$	-2[c]	$M_{\mathrm{m}}\left(\mathrm{O}_i\right)$	-116.34[d]	-1	1.01×10^{5}[d]

[a] -1/3 $S^{\circ,\mathrm{trans}}_{\mathrm{O}_i}$ has to be included additionally

[b] Calculated for butene

[c] For composite value, -1/3 $S^{\circ,\mathrm{trans}}_{\mathrm{MeOH}}$ has to be included to account for adsorption

[d] Calculated for propene

For the methylation, it was reported [18] that $\Delta_{\ddagger} S^{\circ}$ equals to the loss of one third of the olefin's translational entropy. However, in this chapter, a co-adsorption approach is implemented, meaning that the olefin undergoes physisorption prior to the reaction. As this is accompanied with the loss of one degree of freedom of translational entropy [194], $\Delta_{\ddagger} n^{\mathrm{trans}}$ is set to zero. In contrast to cracking, the transition state is assumed to have the olefin still fixed within the co-adsorption complex which is why $\Delta_{\ddagger} \nu_{\mathrm{g}}$ is zero as well. The double methylation leads to an uncharged oxygenate in the first step. This is why a gain of one third of the total translational entropy of DME is assumed to calculate the pre-exponential factor. In addition, the interaction with the olefin has to be considered. Due to the formation of this complex, the translational entropy of the olefin is reduced by one third and $\Delta_{\ddagger} \nu_{\mathrm{g}}$ equals -1. The assumptions according to Kumar *et al.* [18] are applied to the entropy changes during the formation of the surface methyl group and of protonated DME. Because $A^{\mathrm{c}}\left(\mathrm{R}^{+}_{\mathrm{Me}}\right)$ is the pre-exponential factor of the backward reaction to $A^{\mathrm{f}}\left(\mathrm{R}^{+}_{\mathrm{Me}}\right)$, it is calculated according to Equation (7.20),

$$A^{\mathrm{c}}\left(\mathrm{R}^{+}_{\mathrm{Me}}\right) = A^{\mathrm{f}}\left(\mathrm{R}^{+}_{\mathrm{Me}}\right) \left(\exp\left(\frac{\Delta_{\mathrm{f}} S^{\circ}_{\mathrm{R}^{+}_{\mathrm{Me}}}}{R}\right)\right)^{-1}. \tag{7.20}$$

For both side reactions, a loss of two thirds of translational entropy, either of methanol or of the olefin, is assumed [18]. Because the estimated value is of composite nature for the hydrogen transfer, an additional loss of one degree of freedom of the methanol's translational entropy is implemented to account for adsorption. Except for the formation of the surface methyl group where the transition state shows no change in molarity, a value of -1 for $\Delta_{\ddagger} \nu_{\mathrm{g}}$ is used for all oxygenate interconversion and side reactions because of the addition of another molecule.

7.3.7 Site Balance

The concentration of free strong Brønsted acid sites $C_{t^*}^{SBAS}$ is accessible via a balance over all terms where this value is included, see Equation (7.21),

$$C_{t^*}^{SBAS} = \frac{C_t^{SBAS} - C\left(R_{Me}^+\right)\left(1 + \sum_j K_L^{coads}\left(O_j\right) p\left(O_j\right)\right)}{Den}, \tag{7.21}$$

$$Den = 1 + K^{ads}\left(H_2O\right) p\left(H_2O\right) + K^{chem}\left(MeOH\right) p\left(MeOH\right) + K^{chem}\left(DME\right) p\left(DME\right) + \sum_j K_L^{\pi}\left(O_j\right) p\left(O_j\right) + \sum_j K_L^{chem}\left(O_j\right) p\left(O_j\right).$$

Here, the concentration of surface methyl groups $C\left(R_{Me}^+\right)$ appears. This value is not easily accessible as no direct adsorption equilibrium leads to it. In addition, it is part of several equations of kinetic relevance. However, as its reactivity is high, it is reasonable to assume that whenever a surface methyl group evolves, another one is consumed. It follows that an application of the PSSA is possible, see Equation (7.22),

$$R\left(C\left(R_{Me}^+\right)\right) = 0. \tag{7.22}$$

This enables an analytical solution after introducing reduced reaction rates as it is exemplarily shown in Equations (7.23) and (7.24),

$$r^{f'}\left(R_{Me}^+\right) = \frac{r^f\left(R_{Me}^+\right)}{C_{t^*}^{SBAS}}, \tag{7.23}$$

$$r^{f''}\left(R_{DME}^+\right) = \frac{r^f\left(R_{DME}^+\right)}{C\left(R_{Me}^+\right)}. \tag{7.24}$$

The final expression to calculate $C\left(R_{Me}^+\right)$ is shown in Equation (7.25),

$$C\left(R_{Me}^+\right) = \frac{C_t^{SBAS}\left(r^{f'}\left(R_{Me}^+\right) + r^{c'}\left(R_{DME}^+\right)\right)}{r^{f'}\left(R_{Me}^+\right) + r^{c'}\left(R_{DME}^+\right) + Den\ (Sum)}, \tag{7.25}$$

$$Sum = r^{c''}\left(R_{Me}^+\right) + r^{f''}\left(R_{DME}^+\right) + r^{f''}\left(CH_4\right) + \sum_q r_q^{me''},$$

with *Den* equal to Equation (7.21).

7.3.8 Parameter Estimation

Nine responses N_{Res} are fitted to the experimental data: MeOH, DME, $C_2^=$, $C_3^=$, $C_4^=$, $C_5^=$, $C_6^=$, C_1 and $C_{2\text{-}4}$. Because of their relatively low mole fraction, both $C_{7+}^=$ olefins as well as aromatics

are excluded from the parameter estimation. From the explanations above, it follows that eleven activation energies are fitted. In total, 149 experimental data points N_{Exp} are included. Consequently, the degree of freedom amounts to $dof = 1330$. In the model, the objective function OF returns the sum of squared residuals SSQ of the experimental and modeled mole fractions, $y_k(j)$ and $\hat{y}_k(j)$, respectively, see Equation (7.26) [21],

$$OF = SSQ = \sum_{k}^{N_{\mathrm{Exp}}} \sum_{j}^{N_{\mathrm{Res}}} \omega_j \left(y_k(j) - \hat{y}_k(j)\right)^2. \tag{7.26}$$

The mole fractions include not only the reactive components, but also water and nitrogen. The weighting factor ω_j ensures a significant influence of all responses to the fitting process even when a certain species j has a comparably low molar flow rate $F(j)$. It is calculated according to Equation (7.27) [21],

$$\omega_j = \frac{\left(\sum_{k}^{N_{\mathrm{Exp}}} F_k(j)\right)^{-1}}{\sum_{j}^{N_{\mathrm{Res}}} \left(\sum_{k}^{N_{\mathrm{Exp}}} F_k(j)\right)^{-1}}. \tag{7.27}$$

The molar flow rate $F(i)$ of each species i is obtained by integrating along the catalyst mass W, thereby solving the equation for a one-dimensional, *pseudo*-homogeneous, isothermal plug flow reactor as it is shown in Equation (7.28),

$$\frac{\mathrm{d}F(i)}{\mathrm{d}W} = R(i), \tag{7.28}$$

where $R(i)$ is accessible via Equation (7.2). It should be noted that not only a summation over all steps producing or consuming a certain species i is necessary, but also over steps where the respective protonated intermediates are involved [21].

The result of the objective function is minimized using MATLAB version R2018a. Here, the solver *lsqnonlin* with the Levenberg-Marquardt algorithm is applied. Both optimality measure and step size tolerances, *TolFun* and *TolX*, are set to 10^{-8} each. For the solution of Equation (7.28), the solver *ode15s* is used with absolute and relative tolerances of $AbsTol = 10^{-11}$ and $RelTol = 10^{-8}$, respectively. All estimated parameters are analyzed in terms of numeric significance using confidence intervals and *t*-tests. The validity of the whole model is checked via both *F*-tests [187]. Finally, the validity of the adsorption values is proven by making use of the Boudart criteria [276].

7.4 Results and Discussion

The single-event kinetic model for MTO at co-feeding conditions leads to a final sum of squared residuals of $SSQ = 1.27 \times 10^{-5}$. The model converges within the first 30 iterations. It can be excluded that only a local minimum is found because the same results are achieved even when varying the start values. The estimated kinetic parameters are listed in Table 7.3.

Table 7.3: Estimated kinetic parameters including their 95% confidence intervals; all activation energies E_a are given in kJ mol^{-1}.

Parameter	Value
E_a^{cr}(s;p)	162.8 ± 0.5
E_a^{cr}(s;s)	147.4 ± 0.8
E_a^{cr}(t;s)	157.2 ± 1.9
E_a^{me}(p;s)	112.5 ± 1.4
E_a^{me}(p;t)	122.2 ± 2.9
E_a^{meD}(p;s)	150.6 ± 0.2
$E_a^{f}\left(R^+_{Me}\right)$	124.7 ± 1.5
$E_a^{c}\left(R^+_{Me}\right)$	53.6 ± 1.2
$E_a^{f}\left(R^+_{DME}\right)$	93.6 ± 1.3
$E_a^{f}\left(CH_4\right)$	85.3 ± 1.4
$E_a^{meht,co}$	54.0 ± 0.5

Here, the most important advantage of the single-event methodology becomes obvious. For all values, the 95% confidence intervals are remarkably low. This means all parameters are significant and each of them has a clear physical background. An evaluation of the F-test shows whether the deviation between model and experiment can be mainly attributed to experimental scatter or to an insufficient model. In order to exclude the latter effect, the calculated value representing the model has to be lower than the 95% value of the Fisher-distribution. For the single-event model, the calculated value amounts to 0.69 whereas the tabulated one is 2.58. Consequently, the model significance is ensured. Finally, all adsorption parameters are within the Boudart criteria.

Figure 7.1 shows the parity plots for all nine fitting responses as well as for $C_{7+}^{=}$ olefins and aromatics.

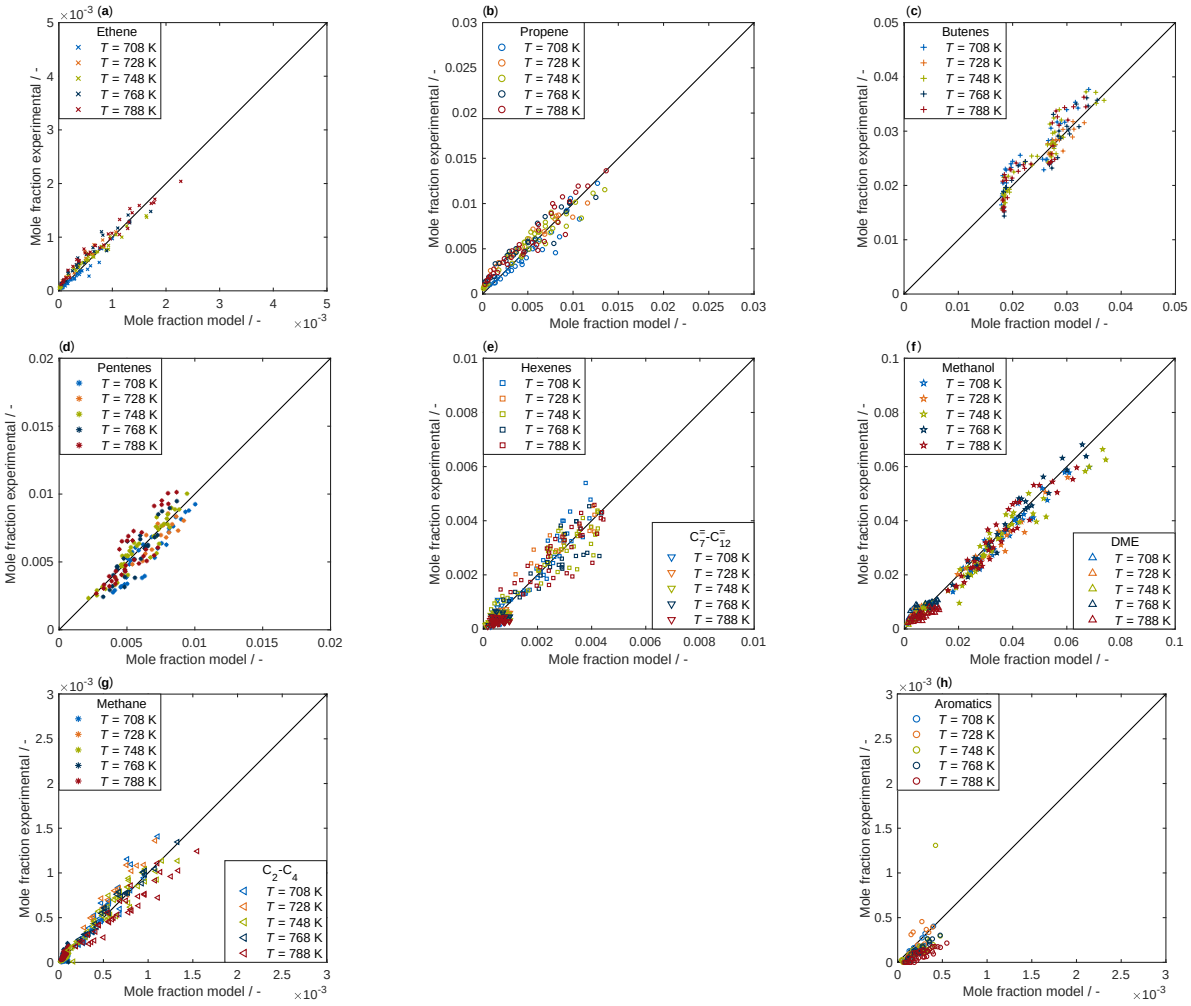

Figure 7.1: Parity plots for ethene, (a), propene, (b), butenes, (c), pentenes, (d), hexenes and $C_7^=$ to $C_{12}^=$ olefins, (e), methanol and DME, (f), methane and C_2 to C_4 paraffins, (g), and aromatics, (h), resulting from an application of the single-event model to experimental data of co-feeding methanol with butenes.

In general, agreement between modeled and measured data is high. Although some scatter is observable, it has to be underlined that a system of high reactivity is investigated where some fluctuations in the experimental data are inevitable. Nevertheless, the model can describe especially the compounds of high interest with sufficient accuracy, i.e., the lower olefins and the oxygenates. More deviation is observed for higher olefins and for the side products, but this has to be seen in the context of their low absolute mole fractions. The description of all species along the reactor length at four different sets of conditions can be found in Figure 7.2.

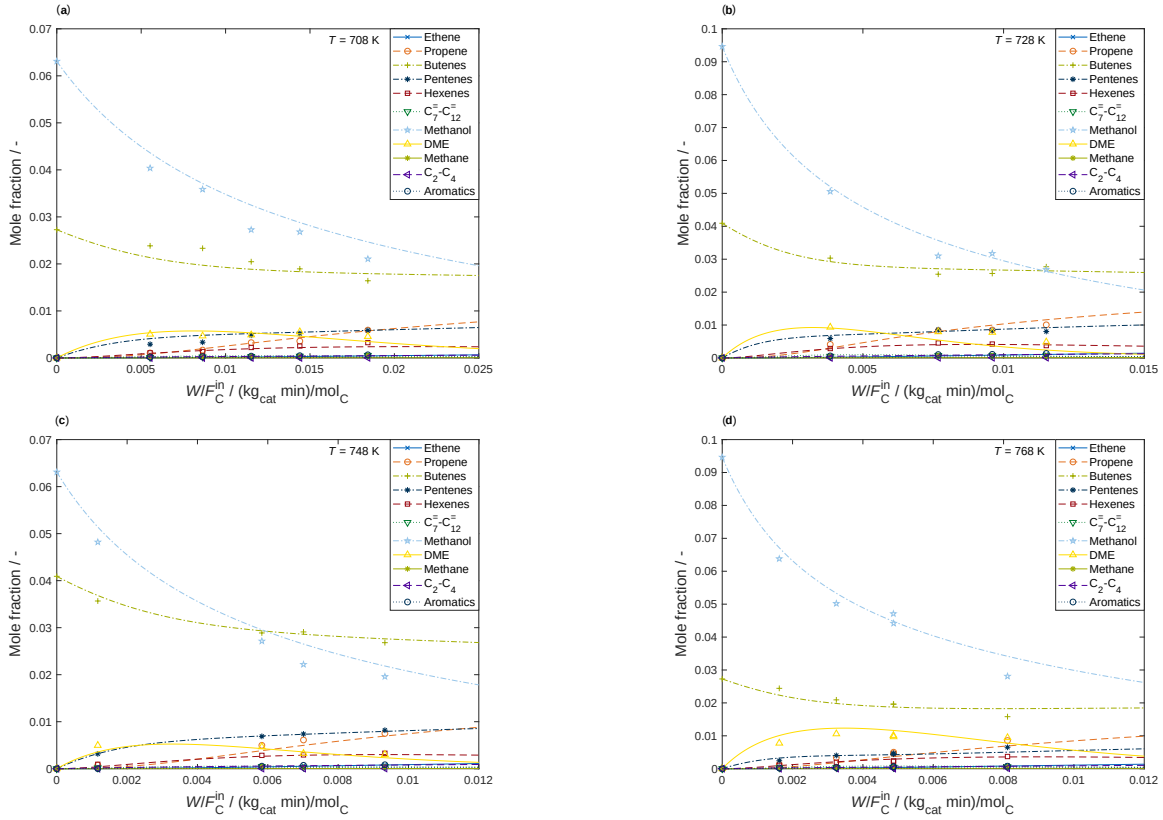

Figure 7.2: Reactor plots comparing the modeled results for each species (lines) with the corresponding measured data (symbols); $p^{\mathrm{in}}(\mathrm{MeOH}) = 76\,\mathrm{mbar}$ and $p^{\mathrm{in}}(\mathrm{C_4^=}) = 33\,\mathrm{mbar}$, (a), $p^{\mathrm{in}}(\mathrm{MeOH}) = 114\,\mathrm{mbar}$ and $p^{\mathrm{in}}(\mathrm{C_4^=}) = 49\,\mathrm{mbar}$, (b), $p^{\mathrm{in}}(\mathrm{MeOH}) = 79\,\mathrm{mbar}$ and $p^{\mathrm{in}}(\mathrm{C_4^=}) = 51\,\mathrm{mbar}$, (c), and $p^{\mathrm{in}}(\mathrm{MeOH}) = 118\,\mathrm{mbar}$ and $p^{\mathrm{in}}(\mathrm{C_4^=}) = 34\,\mathrm{mbar}$, (d).

This depiction excludes any systematic deviation, especially for butenes where two characteristic regimes can be found in Figure 7.1. These are caused by the two different feed partial pressures. The model tends to slightly underpredict the amount of butenes at the inlet region whereas it proposes higher values at the outlet. With the background of Figure 7.2, however, this deviation can be regarded as acceptable. Furthermore, when the single-event model is fitted to the experimental data by Huang *et al.* [241], this effect disappears, see Figure 7.3. Consequently, instead of being a systematic error of the model, it can be ascribed to a slight deviation during feed equilibration.

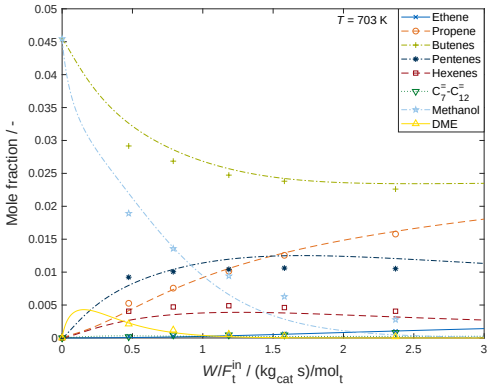

Figure 7.3: Description of experimental data (symbols) provided by Huang *et al.* [241] with the single-event kinetic model (lines); $p^{\mathrm{in}}(\mathrm{MeOH}) = 50\,\mathrm{mbar}$ and $p^{\mathrm{in}}(\mathrm{C_4^=}) = 50\,\mathrm{mbar}$.

From Figure 7.1, it follows that a reasonable description of side products is possible. This confirms the hypothesis of the mechanism explained above [97] having by far the highest contribution to side product formation. Interestingly, even the agreement of aromatics is sufficient for most of the data points despite being implemented only via a balance. This underlines the absence of significant deactivation effects during the measurements. In literature, a positive effect of water on catalyst stability is reported [263, 367], possibly caused by less adsorption and polymerization of aromatics, a reaction sequence leading to coke. Furthermore, the selectivity to lower olefins is increased by the presence of water which is attributed to less olefin dimerization [358]. Consequently, the high water dilution during the kinetic measurements suppressed coke formation. Besides, it should be noted that steaming effects [368], usually known as catalyst pre-treatment method, might also take place during the reaction. This could change the strength and the amount of acid sites. Such an effect however is beyond the focus of an intrinsic kinetic model and therefore neglected here. In addition, the zeolite was extensively steamed before reaction, see Section 7.3.1. As a consequence, severe steaming effects during the reaction are not expected to occur.

On the other hand, it has to be mentioned that a sorting according to temperature can be detected for the aromatics in Figure 7.1. The higher the temperature, the more the model overestimates the amount of aromatics. That speaks for another pathway towards aromatics or other consecutive reactions becoming more important at elevated temperature, i.e., condensation to coke. For the paraffins, such a sorting is not observed, although the highest temperature is also the one with the description of lowest accuracy.

The high accuracy of the model proves that the contribution of the aromatic hydrocarbon pool is negligible when co-feeding olefins. Nevertheless, when analyzing the results for ethene and aromatics in Figure 7.1, it can be seen that the lowest amount of aromatics is detected during the experiments at 788 K. Here, the model predicts ethene amounts that are slightly too low. Thus,

it is possible that more aromatics were trapped within the pores at these conditions, contributing to the performance of the aromatic hydrocarbon pool and therefore producing ethene. Besides, the formation of the first C-C bond out of pure oxygenate feeds has been matter of debate for the last years [64, 73]. During the kinetic measurements, these comparably slow reactions, causing the characteristic autocatalytic S-shaped conversion curve [74], were negligible due to the use of an olefin as co-feed [102, 103]. As a consequence, the olefin-based cycle, consisting of methylations and subsequent cracking of the resulting higher olefin [92] is dominating at all contact times.

From this discussion, the possible application range of the model can be derived. Due to the underlying single-event methodology, it is possible to describe a wide range of experimental conditions [19–21]. Moreover, different olefins as co-feed and also a typical industrial recycle are covered. This feature is shown in Chapter 4 and can be explained by the fact that the actual parameters are based on protonated intermediates instead of carbon numbers [19, 21]. The same can be shown for the MTO model, see Figure A.10 in the Appendix. For this plot, the single-event model is used to reproduce experimental data by Huang *et al.* [241]. In contrast to Figure 7.3, this is done without any additional fitting. Moreover, in Figure A.10 in the Appendix, the temperature of 673 K is substantially below the lowest value of the data range that is included for parameter estimation of the single-event case. Nevertheless, the model is able to predict the different compounds with sufficient accuracy. Consequently, both transfer to a different reaction system and extrapolation to lower temperatures are possible. However, the model accuracy diminishes as soon as the underlying chemistry changes significantly. This is the case for temperatures lower than 673 K. Since the formation of aromatics is pronounced in this range, the model might lead to less exact results due to the simplified implementation of aromatics production. The same holds for conditions where the contribution of the aromatic hydrocarbon pool is dominant. Because of this, the use of the model is not recommended for pure methanol feeds without any co-feed.

One could argue that instead of using the rather complex steps according to Schemes 7.1 and 7.2, the interaction between methanol, DME and water is implemented via a thermodynamic equilibrium calculation more efficiently. There are kinetic models in literature that follow this procedure, cf. Section 2.6.2, as equilibrium between these three oxygen-containing species is achieved fast. However, this cannot be confirmed when having an olefin as co-feed [241]. Figure 7.4 shows the ratio of product (DME and water) and reactant (methanol) partial pressures as function of oxygenate conversion and temperature using own experimental data. Within the whole investigated range, an increase of this characteristic ratio can be observed, speaking clearly against an equilibrated oxygenate system already at the reactor inlet. For each temperature, the colored line marks the respective thermodynamic equilibrium, calculated according to the procedure mentioned in Section 2.4. An approach to these values can be seen at higher conversions. It follows that at olefin co-feed conditions, the oxygenates cannot be treated as

equilibrated as long as their conversion is below 0.7. In the region of low conversions, the amount of DME is too low compared to the equilibrium. This might be caused by a slower equilibration of the oxygenates compared to the case without co-feed because of the high reactivity between oxygenates and olefins. Another possibility is a fast consecutive reaction of the evolving DME in methylation reactions.

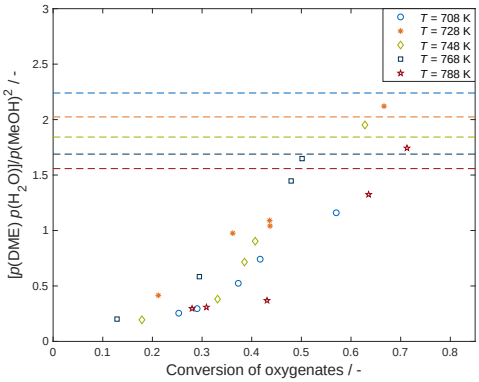

Figure 7.4: Experimental data showing the ratio of product (DME and water) and reactant (methanol) partial pressures of the methanol dehydration reaction as function of oxygenate conversion and temperature (symbols); the respective thermodynamic equilibrium values for each temperature are calculated following the procedure mentioned in Section 2.4 (lines); $p^{\mathrm{in}}(\mathrm{MeOH}) = 118$ mbar and $p^{\mathrm{in}}(\mathrm{C_4^=}) = 51$ mbar.

A point of discussion remains the inclusion of the double methylation via DME. Table A.8 and Figure A.11 in the Appendix show the resulting kinetic parameters and parity plots, respectively, for an identical single-event kinetic model, but without implementing the double methylation. Butenes are underestimated whereas the model leads to pentene amounts higher than the experimental values. This can be explained by the high partial pressures of methanol and butene at the reactor inlet: the model uses the single methylation step to pentenes as the fastest pathway to transfer carbon into the olefin hydrocarbon pool. However, this leads to unrealistic product distributions, cf. Figure A.11. More importantly, as the amount of oxygenates is still overestimated, this carbon transfer with single methylations is not sufficient to model the data. Experimental studies from literature [98, 115] also show an increased amount of hexenes when co-feeding butenes with DME. In combination with the very small confidence intervall of the double methylation in Table 7.3, the necessity of this additional pathway transferring two carbon atoms at once becomes obvious. When using DME as reactant, two carbon atoms can be provided by one molecule; the probability of another reaction subsequent to the first methylation is high. By contrast, the probability of a trimolecular reaction, i.e., the partial pressure of methanol squared multiplied by the partial pressure of the olefin, is seen to be less realistic.

When implementing the single methylation steps without interaction between the surface methyl group and the olefin, i.e., as ER type of reaction, the agreement with experimental

data is significantly lower. Thus, the carbon number dependence provided by the co-adsorption complex is required for a reasonable kinetic description. The implementation of concerted methylation reactions, which means without the formation of a surface methyl group, also leads to results of less accuracy.

The adsorption values for methanol, DME and water are from a different literature source each. An alternative option would be to use the values provided by van der Mynsbrugge *et al.* [229]. In case of an offset, it would be similar for all three species, which is not guaranteed when mixing results from different sources. However, when switching to the mentioned compilation of values [229], the results are not significantly different, neither with regard to accuracy nor to the estimated parameters. This underlines the stability and numerical significance of the proposed model.

In Chapter 4, the transferability of single-event parameters to other catalysts is proven. Thus, one could argue that the cracking parameters do not have to be estimated again as these are available from Table 4.3. However, the differences in catalyst properties like acid strength might play an important role. Additional cracking experiments using the MTO catalyst and pentenes as feed would be required to investigate these changes further. The estimated activation energies in Table 7.3 are approximately $10\,\mathrm{kJ\,mol^{-1}}$ lower compared to the pure olefin interconversion case, see Chapter 6. This relatively small difference could be related to a slight increase of the acid strength in the MTO catalyst as a result of dealumination during steaming. In any case, the values obtained here are overall comparable to the olefin cracking model.

The estimated activation energies for cracking match the stability order when assuming carbenium ions as protonated intermediates at least for tertiary species as discussed in Chapter 6: the value (t;s) is higher than (s;s) because the former step consumes the carbenium ion of highest stability. However, for the methylation, an opposite sorting is observed, i.e., the step towards the tertiary intermediate shows the higher activation energy. Interestingly, increased steric hindrance could be observed for the double methylation which is why no reactions are included that lead to the formation of a tertiary intermediate in the first step. For the same reason, the formation of tertiary intermediates could be hampered in single methylation reactions. This might be explained by the formation of an alkoxide where the stability order is opposite to carbenium ions.

When analyzing the activation energies of the oxygenate interconversion, the value describing the consumption of a surface methyl group is surprisingly low. In this step, water acts as second reactant, thus, co-adsorption effects are expected to play a role here [229]. These are not included within the model, which explains the low activation energy. For the same reason, the value of protonated DME formation is only around $100\,\mathrm{kJ\,mol^{-1}}$ although this step should be energetically demanding. In contrast to the methylation where an inclusion of olefin

co-adsorption is inevitable, the second reactant molecule is always the same species for the oxygenate interconversion (either water or methanol). Therefore, the co-adsorption effects are covered by the activation energy. Finally, both activation energies describing side reactions show small values, especially when considering the low amount of side products. However, these are composite values that additionally contain the adsorption enthalpies.

Similar to this study, the kinetic model by Huang *et al.* [241] considers reactions that change carbon numbers to be rate determining. The olefin interconversion steps are fitted independently before [195]. In addition, the model contains single, double and triple methylations of olefins. The interconversion between methanol, DME and water is also a step of kinetic relevance, but expressed as one overall reaction. The model is also built on the assumption that the contribution of the aromatic hydrocarbon pool is not dominating at these conditions. However, the model by Huang *et al.* [241] does not include side product formation at all; the corresponding pathways are again estimated separately [301]. Contrary to the single-event model, DME is not implemented as possible reactant for methylation reactions. Although there are further differences, especially in methodology, the estimated activation energies for single methylation are comparable. For the single-event case, both values are around 120 kJ mol^{-1}. Huang *et al.* [241] obtain an apparent activation energy of 70 kJ mol^{-1} for the methylation of butenes. As the enthalpy for co-adsorption of $C_4^=$ olefins amounts to −50 kJ mol^{-1}, the intrinsic value is similar to the one obtained via single-event kinetics. Moreover, in both models, the double methylation shows higher activation energies compared to the single methylation. A comparison is more difficult for the models by the Ghent group [18, 192]. Although they are of microkinetic character, the underlying chemistry is different due to the use of a pure methanol feed. This is why their activation energies for the interconversion of methanol, DME and water show higher values; the overall reaction is significantly slower because of the initiation phase. In addition, the authors include the aromatic hydrocarbon pool [18] as it is supposed to play an important role for pure methanol feeds. On the other hand, no paraffin formation is implemented. Besides these major differences, the assumptions for the kinetic relevance of methylation, olefin interconversion and oxygenate interconversion steps are comparable to this chapter, although other types of protonated intermediates are included.

For the industrial MTP process, a maximized propene production is desired. To find a suitable scenario, the contribution of the different reaction pathways along the reactor length is analyzed. The single-event kinetic model is evaluated at 700 and 780 K, respectively. For both temperatures, the contribution of cracking, dimerization, methylation and double methylation is investigated as function of oxygenate conversion. This is performed both for the production and for the consumption of olefins. The respective contribution is obtained by summing up all rates of a certain pathway that either produces or consumes the respective olefin; this value is divided by the sum over all pathways of production or consumption, respectively. For the oxygenates, only the consumption is analyzed. Figure 7.5 shows the results for a temperature of

780 K. According to the model assumptions, ethene is formed and consumed only by cracking and dimerization, respectively, which is why it is not further analyzed here.

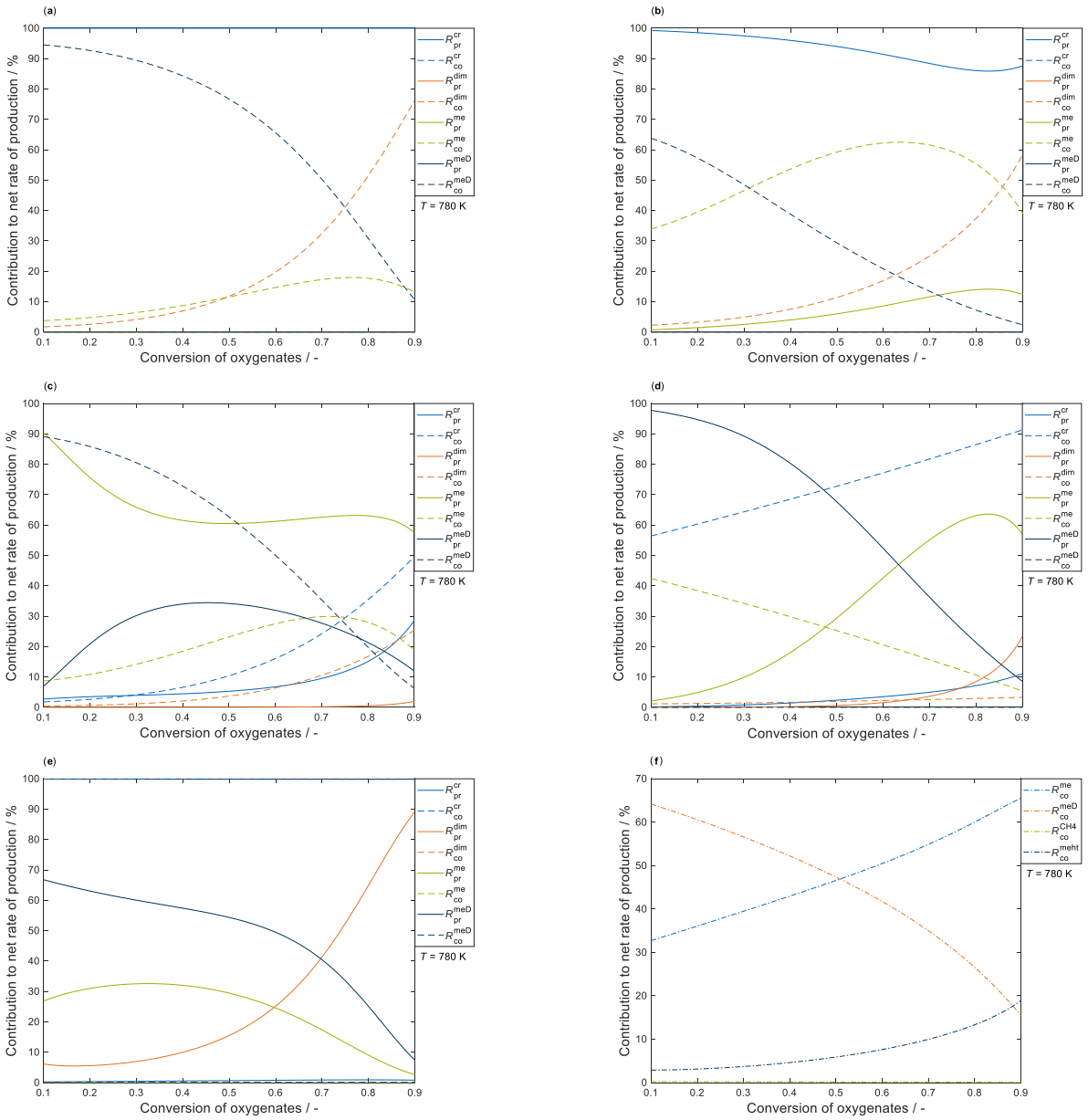

Figure 7.5: Contribution analysis resulting from an application of the single-event kinetic model at 780 K; the fraction of the different pathways to the total production or consumption rate is shown as function of oxygenate conversion for propene, (a), butenes, (b), pentenes, (c), hexenes, (d), $C_7^=$ to $C_{12}^=$ olefins, (e), and methanol plus DME, (f); $W_{max} = 6 \times 10^{-5}$ kg_{cat}, $p^{in}(MeOH) = 76$ mbar and $p^{in}(C_4^=) = 33$ mbar.

Figure 7.5 (a) reveals cracking as sole production pathway for propene. The double methylation is by far the most important reaction pathway consuming propene at the entrance region of the reactor, whereas its contribution is decreasing for higher conversion levels. Single methylation increases with conversion until it reaches a maximum, but still on a lower level than the double methylation. Only at higher oxygenate conversions, the dimerization plays a significant role

in propene consumption, as a result of decreasing concentrations of oxygenates available for methylation reactions.

Cracking is the exclusive production pathway for butenes at the inlet region, see Figure 7.5 (b). For increasing contact times, propene becomes more and more available, yielding butenes through single methylation steps. In contrast to all other carbon numbers, the single methylation step is more important for the consumption of butenes for almost the whole investigated conversion range. Butenes consist of a high fraction of isobutene, which is excluded from the sterically demanding double methylation pathway. Nevertheless, due to the linear butenes, the contribution of the double methylation is still significant up to high conversions. Similar to propene, the dimerization dominates at higher conversion levels, i.e., close to 0.9.

For pentenes, all production and consumption pathways are possible, cf. Figure 7.5 (c). Similar to propene and butenes, the double methylation is the most important consumption pathway at lower conversions and decreases with higher reaction progress, whereas the single methylation reveals a maximum. Due to the high temperatures used in this chapter, cracking is the most important pathway consuming pentenes from conversion levels of 0.75 onwards, showing a contribution twice as high as the one of dimerization. By far the highest fraction of pentenes is produced via single methylation of butenes, which are available from the beginning on. The slope of this curve is almost similar to the development of butenes along the reactor length. By contrast, propene concentration is small at low conversions, which is why the contribution of the double methylation to pentene formation shows a maximum. Finally, cracking as source for pentenes is significant only when no oxygenates are present; here, the contribution of dimerization is still negligible due to the low ethene amounts.

Analysis of hexene formation rates in Figure 7.5 (d) underlines the importance of the double methylation especially at low and intermediate conversion levels. In addition, the low contribution of the single methylation illustrates that the fast formation of hexenes cannot be explained by two consecutive reactions of that type. The single methylation of pentenes becomes more important at higher conversion levels, thereby revealing a maximum in Figure 7.5 (d). Similar to pentenes, cracking and dimerization are important production pathways only at high oxygenate conversion. Despite the high temperatures, the contribution of dimerization to hexene formation is relatively high, because cracking mostly leads to olefins smaller than $C_6^=$. Hexenes are not considered as reactants for the double methylation, their consumption is restricted to single methylation, cracking and dimerization. Whereas the latter is negligible due to the high temperatures, cracking is the most important consumption pathway at all conversion levels. It can be concluded that hexenes are important products of oxygenate-olefin interconversion reactions, but they easily crack yielding small olefins. The same conclusions are reached for the higher olefins, see Figure 7.5 (e).

Finally, Figure 7.5 (f) depicts the consumption rates for oxygenates. The analysis of these data also shows the high importance of the double methylation at lower conversion and the increasing significance of the single methylation with further reaction progress. Whereas methane formation is negligible along the whole reactor length, the contribution of the methanol-induced hydrogen transfer shows a rising trend due to the increasing amount of lower olefins.

Figure 7.6 displays the results for 700 K. As expected, the dimerization shows higher overall contributions compared to cracking due to the lower temperatures. Furthermore, over all carbon numbers, a lower importance of both single and double methylation steps can be observed. Figure 7.6 (b) reveals that the double methylation is even more affected by the decrease of temperature, which is reasonable due to its higher activation energy; the same can be seen in Figure 7.6 (f). As the amount of butenes is relatively constant along the reactor length, the decreasing trend for the pentenes produced by single methylation steps in Figure 7.6 (c) proves a change in reactivity. Particularly due to increased dimerization rates, the olefins replace a part of the oxygenates from the active sites. In other words, the olefin interconversion reactions suppress carbon transfer into the olefin hydrocarbon pool to a certain degree at low temperatures. By contrast, no significant reduction in side product formation can be observed.

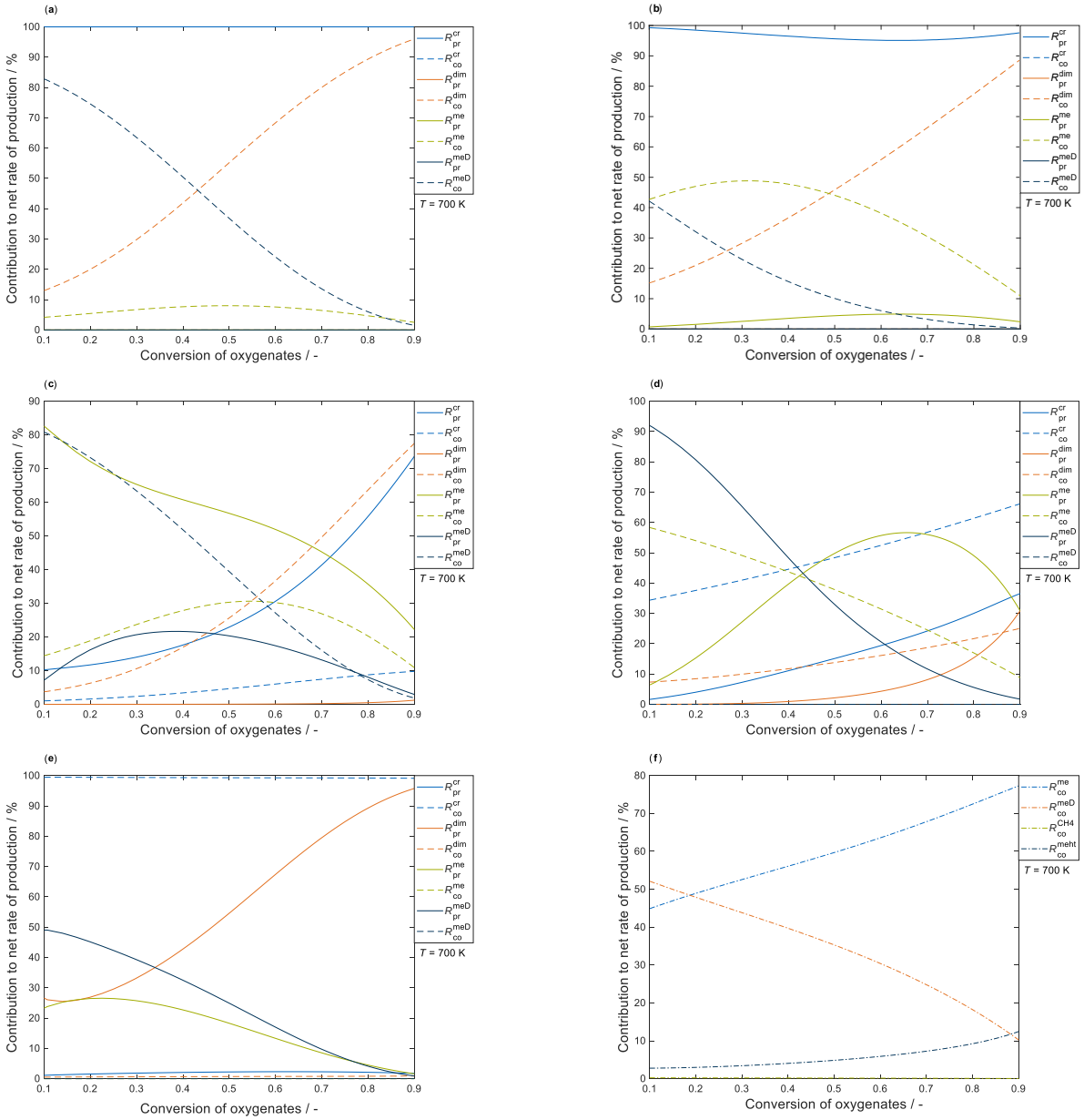

Figure 7.6: Contribution analysis resulting from an application of the single-event kinetic model at 700 K; the fraction of the different pathways to the total production or consumption rate is shown as function of oxygenate conversion for propene, (a), butenes, (b), pentenes, (c), hexenes, (d), $C_7^=$ to $C_{12}^=$ olefins, (e), and methanol plus DME, (f); $W_{max} = 3 \times 10^{-4}\,kg_{cat}$, $p^{in}(MeOH) = 76\,mbar$ and $p^{in}(C_4^=) = 33\,mbar$.

Finally, it should be investigated which carbon numbers preferably crack to propene. Figure 7.7 (a) and (b) show the contribution of the different olefins to propene production as function of oxygenate conversion at 780 and 700 K, respectively.

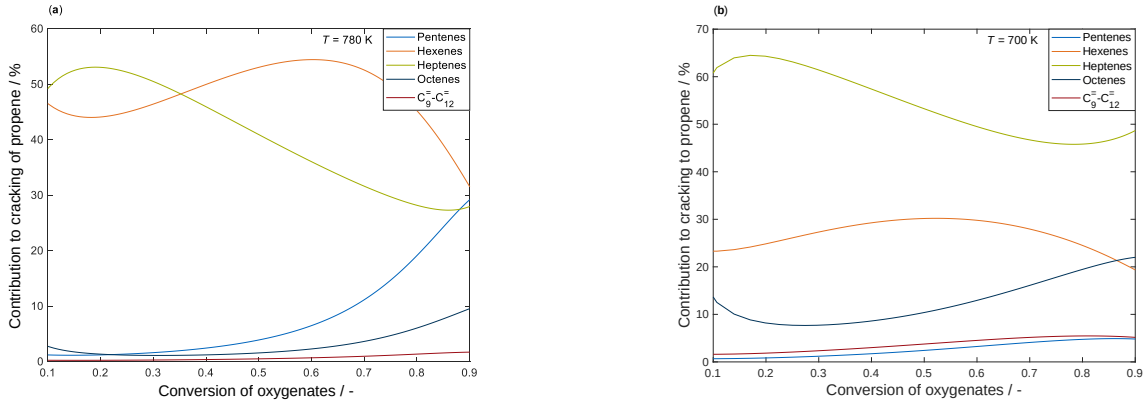

Figure 7.7: Contribution of different olefin carbon numbers to propene production via cracking as function of oxygenate conversion at 780 K, (a), and 700 K, (b); the maximum catalyst mass is $W_{max} = 6 \times 10^{-5}\,kg_{cat}$ and $W_{max} = 3 \times 10^{-4}\,kg_{cat}$, respectively; $p^{in}(MeOH) = 76\,mbar$ and $p^{in}(C_4^=) = 33\,mbar$.

At high temperatures, both hexenes and heptenes are crucial reactants for propene production over the whole conversion range. Whereas heptene cracking is dominant at low conversions, hexenes are the most important reactants at medium and high conversions. This correlates with the double methylation of pentenes and the single methylation of pentenes and hexenes, cf. Figure 7.5. As pentene cracking intensifies at higher conversion, its contribution in propene production increases. By contrast, at 700 K, heptenes are the most important species for cracking to propene, see Figure 7.7 (b). Hexenes again show a maximum, but with lower values compared to Figure 7.7 (a) which can be attributed to the decreased methylation rates. Although octene cracking contributes to propene formation to a comparable degree as for higher temperatures, the subsequent cracking of the evolving pentenes is slow at low temperatures; thus, pentene formation routes translate into a decrease in propene yields.

In summary, an evaluation of the kinetic model underlines the importance of the double methylation especially at low oxygenate conversions. High temperatures favor a fast transfer of carbon to the olefin hydrocarbon pool and lead to elevated amounts of hexenes and heptenes that preferably crack to propene. By contrast, lower temperatures are disadvantageous as they hinder not only an effective oxygenate consumption, but also lead to a variety of higher olefins, thereby reducing cracking to propene.

7.5 Conclusions

A single-event kinetic model for MTO over ZSM-5 at co-feed conditions is presented. All reactions are evaluated with fundamental kinetics except for the aromatics formation because

of their low absolute mole fractions at the investigated conditions. Consequently, it is the first model using complex single-event kinetics for conditions that are relevant for the industrial MTP process.

A comparison of experimental data and thermodynamic calculations proves that methanol and DME are not equilibrated at low conversions under co-feed conditions. The kinetics of methanol conversion to DME and water are best described using a step-wise mechanism via a surface methyl group. The same holds for the olefin methylation reactions. Here, the formation of a co-adsorption complex consisting of the surface methyl group and an olefin is identified. However, these methylations are not sufficient to account for the interconversion between oxygenates and olefins. This is why the double methylation of an olefin with DME is implemented as additional pathway. The olefin interconversion is similar to pure olefin cracking, meaning that a π-complex and a carbenium ion are formed as the first and second adsorption step, respectively. Although the dimerization is of less importance compared to cracking, it is explicitly included here to have maximum agreement also in regimes where the oxygenates are consumed almost completely.

To further increase the applicability of this model, the formation of side products is implemented. A recently proposed pathway for formation of paraffins on Lewis acid sites is used here for the kinetic description and yields high agreement for C_2 to C_4 paraffins. By contrast, a Brønsted assisted sequence is chosen to account for methane production. Finally, the consecutive formation of aromatics via formaldehyde is considered.

The use of only eleven estimated parameters leads to numeric results of high significance. The analysis of the different reaction pathways shows a high contribution of single and double methylation at high temperatures. The latter is especially important at low and medium conversions. The fast transfer of carbon to the olefin hydrocarbon pool in combination with an elevated hexene and heptene formation leads to high propene yields due to subsequent cracking. By contrast, lower temperatures favor olefin interconversion at expenses of methylation, thereby reducing propene yields.

Due to the underlying methodology and the inclusion of side products, the single-event kinetic model can be used to describe the MTO reactivity even beyond the conditions applied during the kinetic experiments. Because extrapolation is explicitly allowed, reactor design becomes possible in a next step. For MTO, this requires a detailed inclusion of transport effects at industrial pellet size. In addition, an implementation of catalyst deactivation via adjusted contact times is required to depict full catalyst operation cycles. With both microkinetics and diffusion being realized, an overall process optimization of the commercial MTP process can be performed.

8 Summary

Parts of this chapter were published and are reprinted with permission from:

S. Standl, O. Hinrichsen
Kinetic Modeling of Catalytic Olefin Cracking and Methanol-to-Olefins (MTO) over Zeolites: A Review
Catalysts 8 (2018), 626, DOI 10.3390/catal8120626.

8.1 Conclusions

In this work, microkinetic modeling studies are shown for catalytic olefin cracking and for MTO as two possible alternative synthesis routes for lower olefins. Both processes are performed over acid zeolites like ZSM-5 and therefore have complex reaction networks. The single-event methodology is used to effectively reduce the number of unknown parameters without loosing accuracy in describing each elementary reaction. In this way, thousands of reactions are modeled with the number of parameters not exceeding a value of eleven. Such a model enables insight into preferred pathways and extrapolation out of the experimentally covered regime. This feature is further used here to optimize model implementation, reaction conditions and reactor setups. For the latter, the maximization of propene yields and P/E ratios are desired.

Chapter 3 introduces the single-event kinetic model for 1-pentene cracking over ZSM-5. The whole olefin interconversion reactivity for carbon numbers up to $C_{12}^{=}$ is described using only five estimated parameters. Due to the low amount of side products, their formation is not included in the model. In addition, Chapter 3 discusses two different reactor setups. A two-zone reactor effectively exploits the two main pathways consuming pentenes, i.e., monomolecular cracking and dimerization with subsequent cracking of the higher intermediate. Propene yields can be increased by having a first reactor zone with a comparably low temperature of 580 K. This favors the exothermic dimerization and thus leads to a significant amount of higher olefins. Their subsequent cracking in the second reaction zone with high temperatures of 760 K enables high propene yields. This concept decouples the production pathways for ethene and propene

in order to increase the P/E ratio. Nevertheless, the product spectrum of the two-zone reactor still contains significant amounts of higher olefins. This is why a recycle reactor is discussed as second solution in Chapter 3. Here, all olefins higher than propene are split off and led back to the reactor inlet. The optimum operating point is a compromise of a high P/E ratio (low temperature) and low separation cost (high temperature).

The reactor solutions explained in Chapter 3 require an application of the single-event model to olefin mixtures as feed. From theory, it is derived that an application to arbitrary olefin feed mixtures is possible although the kinetics are derived with experimental data using solely 1-pentene as feed. This feature is proven in Chapter 4. Experimental data from two different literature studies are extracted where $C_3^=$ to $C_7^=$ olefins were used as feed. The 1-pentene model is able to reproduce all data sets as function of feed olefin conversion without additional fitting. In addition, the conversion of arbitrary feed olefin mixtures can be simulated with high accuracy. The description of literature data as function of contact time requires fitting of the difference in acid strength and of carbon-number effects first. Due to the strict separation of kinetic descriptors and catalyst descriptors, a maximum model flexibility is achieved so that a transfer of the model to different reaction systems, ZSM-5 catalysts and conditions is possible.

In Chapter 5, the recycle reactor introduced in Chapter 3 is further analyzed. By coupling the fundamental single-event kinetics for olefin cracking (MATLAB) with state-of-the-art process simulations including a complete separation unit (Aspen HYSYS), process optimization can be performed. The conditions of maximum specific profit are determined by accounting for energy cost, i.e., electricity and natural gas, and by assuming realistic sales prices for ethene and propene. Side product formation is implemented in a simplified way to resemble realistic industrial conditions. Two different main scenarios are obtained: for similar prices for ethene and propene, the catalyst bed should be as long as possible to have maximum yields of lower olefins and to reduce separation cost. For the same reason, pressures should be high. By contrast, the higher recycling ratio and thus more separation becomes viable when propene has a higher price than ethene. Although an individual optimum can be found for each propene price investigated, the results for propene being 25% more expensive than ethene is suitable for all scenarios of elevated propene prices. For this, basic equipment design values are also given. In summary, Chapter 5 proves the recycle reactor concept for olefin cracking to be viable at realistic industrial conditions as long as propene prices are higher than ethene prices.

The single-event kinetic model for cracking is used for insight into adsorption steps of olefins on ZSM-5 in Chapter 6. Different approaches described in literature are applied and compared. By far the highest agreement is achieved when a π-complex of high stability is assumed as first adsorption intermediate. The use of undirected interaction models, i.e., physisorption due to dispersion forces, leads to significantly lower agreement. No universal statement is possible regarding the product of the subsequent protonation step. However, fitting results speak for

protonated intermediates of comparably low stability. In addition, the estimated protonation enthalpies suggest carbenium ions to be the type of protonated intermediates at least for tertiary species. This is in line with current DFT studies. The refined adsorption model leads to an improved description of cracking data especially for the higher olefins.

The insight gained in the studies mentioned above can be used to develop a single-event kinetic model for the MTO reactivity which is shown in Chapter 7. Thus, a refined reaction network for olefin interconversion including the adsorption model derived in Chapter 6 is extended with the methanol-related reactions. Furthermore, the evolution of C_1 to C_4 paraffins as well as of aromatics as side products is explicitly included. Eleven parameters are estimated using experimental data over ZSM-5 with butenes as co-feed, resembling the industrial recycle. It can be shown that at these conditions, the oxygenates are not equilibrated; thus, the microkinetic steps describing the methanol conversion to DME are required. Moreover, an implementation of carbon transfer from the oxygenates to the olefin hydrocarbon pool via single methylations is not sufficient. A double methylation having DME as reactant is introduced therefore. The resulting model is used to assess the main reaction pathways. Elevated temperatures ensure a fast carbon transfer, significant build-up of hexenes and heptenes and finally improved propene yields due to their subsequent cracking.

Besides the main results of the specific studies that are described above, one of the targets of this work is to define modeling guidelines for future kinetic studies of hydrocarbon conversion over acid zeolites. Although a huge variety of approaches to deal with the complex reaction networks can be seen in Chapter 2, it is tried to sort some of the findings. These are divided into general modeling advices and a reaction-specific part.

General guidelines

- Reparameterization should be performed. The choice of reference temperature is not of highest importance; nevertheless, an optimum value can improve the model performance.

- Forward and backward reactions should be expressed as such and not be fitted independently. The equilibrium constant of the reaction can be extracted from thermodynamics to have less unknown parameters. However, when lumps consisting of several species are involved, the equilibrium constant should be estimated because the lump might deviate from an equilibrium distribution. Thermodynamic consistency has to be retained.

- Expressing the rate equations via partial pressures is advantageous as the influence of pressure changes is directly included. By contrast, when carbon based values are chosen, this effect might be ignored.

- Inclusion of adsorption effects, especially via the HW type of mechanism, should lead to a comparably robust model. The agreement with experimental data can still be satisfying when adsorption is ignored, especially when high partial pressures are applied. However, one should be aware that such a model tends to extrapolation errors when different feed compositions are chosen.

- Negative activation energies might occur when these apparent values contain adsorption effects. Also in empirical models, positive adsorption enthalpies should be avoided because these are physically not reasonable and contradictory to thermodynamics. In such a case, other phenomena seem to impair the underlying model.

- When no microkinetic model is applied, interpretation of preferred reaction pathways should be done with care. The estimated parameters describe the reactivity in an empirical way, but the values are influenced by too many factors to allow for mechanistic analyses. Nevertheless, effects of conditions on product distributions can be elucidated; for example, negative activation energies show that this pathway is less preferred at higher temperatures.

- Although high agreement can be achieved in any way, the stoichiometry within one reaction step should be retained to have a reasonable characterization of the reactivity. Moreover, when the concept of elementary reactions is chosen, this should be applied consistently. It can cause problems when the same lump appears both as reactant and as product within one step.

Olefin cracking and MTO

- For hydrocarbon conversion, a maximum carbon number of seven seems to be sufficient, although the level of detail can be increased by exceeding this value. Nevertheless, some higher intermediates can be included in the network which crack down immediately, thus having no fitting answer. Furthermore, this recommended value also depends on the feed: when pure hexenes are applied, the dimerization to $C_{12}^{=}$ has to be included.

- Lower olefins should not be summarized to one lump as their formation mechanisms and reactivity are different. The same holds for methanol and DME.

- Concerning ethene reactivity, reasonable results are obtained by assuming ethene both as reversibly and as irreversibly formed. However, the latter approach might be advantageous to reduce the number of estimated parameters.

- The complex interaction between zeolite and water is still not fully understood. Nevertheless, a useful approach is the inclusion of water as diluent and as competing adsorptive.

- Especially for MTO, the underlying chemistry is very complex through many different types of reactions. Consequently, it is difficult to describe the whole reactivity with one model. It is recommended to implement the types of reactions stepwise (e.g., first olefin interconversion, then methanol-related reactions and then side reactions) with individual experimental datasets. This reduces the number of unknown parameters in each fitting step and allows focusing on the respective type of reaction.

- Whenever MTO models for pure methanol feeds are created, one has to be aware that the unresolved initiation phase might influence the performance at low contact times which could impede the model. For such cases, it could be reasonable to simulate the product generation not from zero catalyst mass on. By contrast, this effect can be ignored for industrial MTP conditions where hydrocarbons are available from the beginning.

- For pure methanol feeds, an equilibrated state is reached comparably quickly because of the slow formation of the first C-C bond. However, when hydrocarbons are co-fed, this equilibrium among methanol, DME and water might not be reached.

- For MTO, it depends on the catalyst and the reaction conditions whether an implementation of the aromatic hydrocarbon pool is reasonable or not. If so, the underlying reactions have to be simplified to only some characteristic steps that are representative for the whole catalytic cycle.

In the end, it cannot be said which modeling methodology is the best; it always depends on the requirements it should fulfill. However, one always has to be aware of the range within which the model is valid. Simple kinetics might describe the investigated case in a satisfying and comparably fast way. Moreover, conclusions about the influence of reaction conditions on product distributions are possible. However, further application should be performed with caution because extrapolation out of the experimentally covered regime could cause unrealistic results and false trends. Also for microkinetics, one has to be aware that the theoretical description is still a model. Indeed, in the case of satisfying agreement, the probability is high that the chosen approach is a valid way to describe the surface reactions. On the other hand, no reaction mechanism can be proven by solely evaluating a microkinetic model. Thus, in these cases, overinterpretation should also be avoided.

8.2 Outlook

As shown above, microkinetic models exist now for olefin cracking as well as for MTO over ZSM-5. On the other side, even the use of microkinetics is not sufficient to fully decode complexity. For example, during creation of the models shown in Chapters 3 and 7, it is assumed that the active sites all have the same acid strength. Furthermore, no inhomogeneities of the surface are considered. Thus, the resulting models do reproduce the overall reactivity with high accuracy, but they cannot describe local effects. For this, *ab initio* methods are helpful tools. These can be exploited to have a general assessment of possible and favored reaction steps. Microkinetics applied in deterministic models can then be used to evaluate whether the pathways are important at industrially relevant conditions.

Mechanistically, more insight into the double methylation in MTO is desirable. So far, it could be shown both experimentally and via modeling that at olefin co-feed conditions, a transfer of two carbon atoms is too fast to be explained by two consecutive single methylations. However, more experimental studies are needed to unravel reaction pathways and intermediates. Again, microkinetic studies can be used in this context to assess the suggested reactivity.

Similarly, a microkinetic description of aromatics formation would be of high interest for MTO. This would have the potential of combining kinetics, the evolution of the aromatic hydrocarbon pool as well as catalyst deactivation. On the other hand, this requires sophisticated product analysis to have enough fitting responses for the model. Furthermore, the amount and type of aromatics trapped in the pores have to be accessible.

The single-event models shown here represent ideal surface kinetics. In industrial reactors, however, larger pellets are used. Thus, to correctly describe the performance of the industrial process, these surface kinetics have to be coupled with multicomponent transport phenomena. This is interesting especially for MTO when higher amounts of aromatics are formed as these are prone to diffusion limitations. Although this is a task of high complexity and requires vast computational power, the resulting model would be able to describe all relevant aspects of the MTP process. Such multi-scale models offer high potentials to finally optimize both catalyst properties and process conditions.

A Appendix

A.1 Supporting Information to Chapter 5

This section was published as part of the Supporting Information and is reprinted with permission from:

J. Sundberg, S. Standl, T. von Aretin, M. Tonigold, S. Rehfeldt, O. Hinrichsen, H. Klein
Optimal Process for Catalytic Cracking of Higher Olefins on ZSM-5
Chemical Engineering Journal 348 (2018), 84–94, DOI 10.1016/j.cej.2018.04.060.

A.1.1 Preliminary Study

Table A.1: Power requirement P_{mech} per heat removed Q_{cool} at specific values of process temperature T (hot side) and at different pressure levels: high pressure HP, medium pressure MP and low pressure LP; temperatures are given in °C, the ratio P_{mech}/Q_{cool} in s^{-1}.

Type	T	P_{mech}/Q_{cool}
Cooling water	40.0	0
Propene HP	9.5	0.2139
Propene MP	-18.6	0.4188
Propene LP	-41.2	0.6232
Ethene HP	-61.2	0.9342
Ethene MP	-81.2	1.2654
Ethene LP	-97.5	1.6239

A.1.2 Specific Profit and Cost

Table A.2: Operating cost (negative) and sales profit (positive) for different propene price scenarios; both sales and demand as well as equivalents are shown in €t_{Feed}^{-1}.

Type	Description	Propene price			
		1000	1250	1500	2000
Electrical Power	Total demand	-35	-28	-32	-41
Natural gas	Total demand	-43	-67	-67	-69
	Purge stream equivalents	12	25	24	22
Products	Ethene sales	748	89	77	74
	Propene sales	217	1037	1265	1707

A.1.3 Reactor Plots

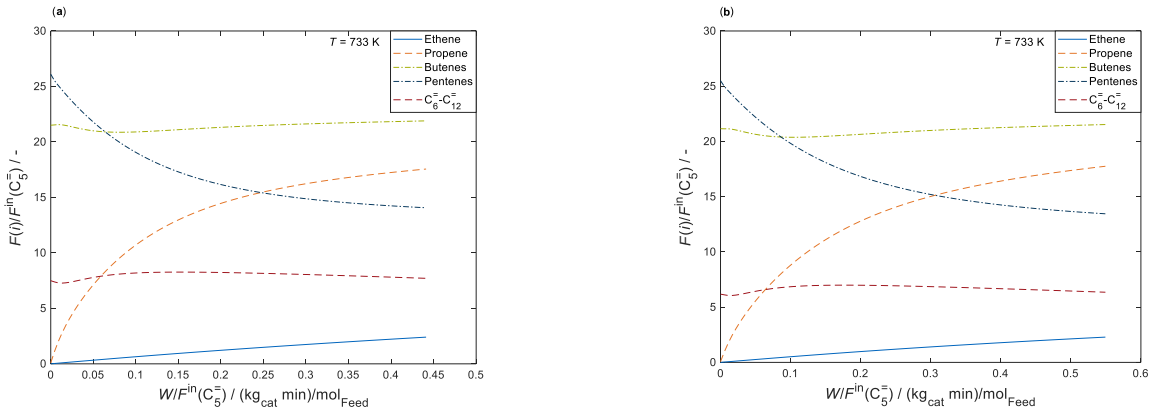

Figure A.1: Reactor plots showing the evolution of the different olefins at optimized conditions for a propene price of 1500 €t^{-1}, (a), and 2000 €t^{-1}, (b).

A.2 Supporting Information to Chapter 6

This section was published as part of the Supporting Information and is reprinted with permission from:

S. Standl, T. Kühlewind, M. Tonigold, O. Hinrichsen
On Reaction Pathways and Intermediates During Catalytic Olefin Cracking over ZSM-5
Industrial & Engineering Chemistry Research 58 (2019), 18107–18124,
DOI 10.1021/acs.iecr.9b02989.

A.2.1 Reaction Network

An overview of the different reaction networks analyzed in the preliminary study can be found in Scheme A.1.

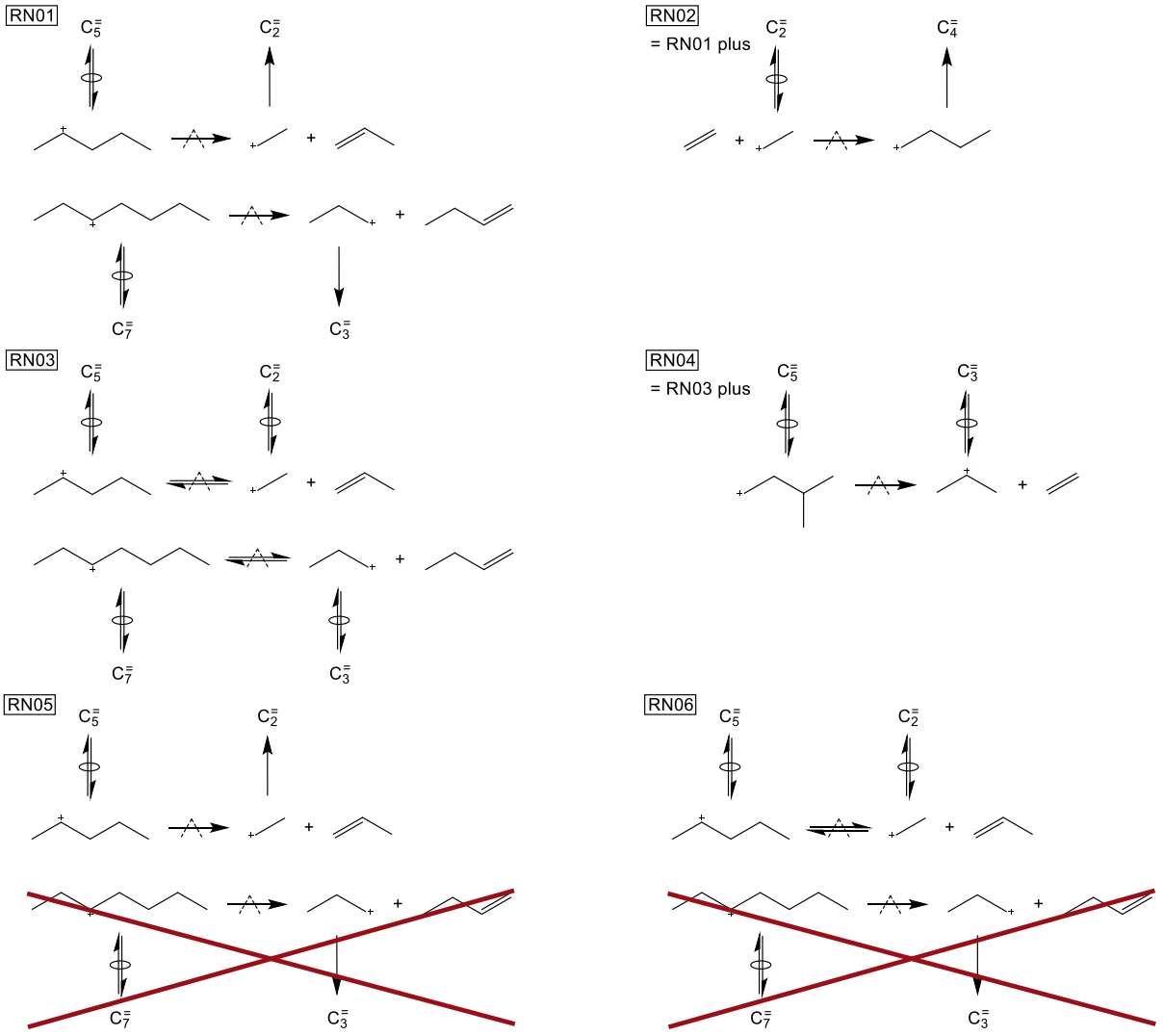

Scheme A.1: Differences between all six reaction networks analyzed in a preliminary study with respect to the role of primary intermediates.

RN01 is the original one [26] where primary intermediates of all carbon lengths between $C_2^=$ and $C_{10}^=$ olefins are formed. RN02 includes the self-dimerization of ethene to $C_4^=$ which causes one additional protonation (ethene to ethyl) and one additional dimerization reaction. In RN03, the protonation to the primary intermediates of each carbon number is required and therefore allowed since the cracking to primary intermediates is assumed to be reversible here. A further extension is made in RN04: because the protonation to primary intermediates is allowed according to RN03, the subsequent cracking of these intermediates might occur and is thus considered. In contrast to that, the original network is reduced in RN05: cracking to primary intermediates is only possible when ethene is formed. Finally, in RN06, the steps leading to ethene are assumed to be reversible. Table A.3 is similar to Table 6.1, but additionally contains the values for RN02–05.

Table A.3: Types of elementary reactions being implemented in different reaction networks RN of the single-event kinetic model for olefin cracking, including the number of different reactions and of pathways of kinetic relevance for all six reaction networks; furthermore, the number of different olefins and protonated intermediates is shown.

Type	RN01	RN02	RN03	RN04	RN05	RN06
Olefin protonation	956	957	1095	1095	956	957
Cracking	601	601	601	636	238	238
Pathways cracking	1292	1292	1292	1327	511	511
Dimerization	140	141	601	601	140	238
Pathways dimerization	293	294	1292	1292	293	511
PCP branching	1530	1530	1530	1530	1530	1530
Methyl shift	148	148	148	148	148	148
Olefin deprotonation	1004	1004	1095	1095	957	957
Olefins	591	591	591	591	591	591
Protonated intermediates	498	498	589	589	451	451

An application of the six different reaction networks to the kinetic model leads to the results in Table A.4.

Table A.4: Estimated activation energies E_a^{cr} and pre-exponential factors $\tilde{A}^{cr}$, including 95% confidence intervals, and the sum of squared residuals *SSQ* for all six reaction networks RN; all activation energies are given in kJ mol^{-1}, whereas the pre-exponential factor is shown in s^{-1}.

Parameter	RN01	RN02	RN03	RN04	RN05	RN06
E_a^{cr}(s;p)	229.9 ± 1.0	229.3 ± 1.1	229.4 ± 1.0	233.1 ± 51.7	229.9 ± 1.0	229.6 ± 1.0
E_a^{cr}(s;s)	200.2 ± 0.9	199.9 ± 1.0	199.7 ± 0.9	199.5 ± 1.0	200.1 ± 0.9	199.8 ± 0.9
E_a^{cr}(t;s)	171.5 ± 0.9	171.1 ± 1.0	171.0 ± 0.9	170.9 ± 1.1	171.5 ± 0.9	171.2 ± 0.9
E_a^{cr}(t;p)	211.9 ± 1.5	211.4 ± 1.6	210.5 ± 1.6	210.5 ± 4.4	212.0 ± 1.6	210.7 ± 1.5
$\tilde{A}^{cr} \times 10^{-16}$	2.73 ± 0.40	2.53 ± 0.41	2.51 ± 0.36	2.45 ± 0.47	2.73 ± 0.41	2.59 ± 0.38
SSQ	0.0350	0.0348	0.0345	0.0341	0.0350	0.0345

RN02 shows a slightly better description of the experiments and thus a lower *SSQ* value, which can be explained by the use of an additional parameter to describe the self-dimerization of ethene. The estimated value of E_a^{cr}(p;p) is 206.0 ± 5.7 kJ mol^{-1}. The almost insignificant improvement means this pathway is irrelevant at cracking conditions due to high temperatures and comparably low ethene fractions. However, the fact that this parameter can be estimated to a reasonable and significant value without changing the results of the other activation energies suggests this pathway to be present. Furthermore, the improvement in describing the experimental data is mainly caused by ethene, which also speaks for the general occurrence of this step. Consequently, the neglection of ethene self-dimerization is an assumption suitable for typical cracking conditions, but care should be taken when extrapolating the model to conditions in which this hypothesis might not be true; in such cases, the parameter E_a^{cr}(p;p) should be included.

An improvement in agreement is found for RN03 where all steps leading to primary intermediates are reversible, increasing the number of (de)protonation and dimerization reactions and therefore the numerical effort to a significant extent.

When the protonation to primary intermediates is allowed, their subsequent cracking might also take place, especially when it offers a transformation to a product intermediate of higher stability. This is why the additional parameter E_a^{cr}(p;s) is introduced for RN04; it can be estimated to a value of $233.3 \pm 56.5\,\mathrm{kJ\,mol^{-1}}$. The high confidence interval, which is also obtained for the cracking step (s;p) in RN04, shows numeric problems when applying this reaction network. For that reason, the underlying pathways are questionable, although the description is the best one found in Table A.4.

The analysis of RN05 shows that an agreement of equal quality compared to RN01 is obtained although cracking to primary product intermediates is only allowed when this step produces ethene. This leads to less cracking and deprotonation reactions and thus to a faster fitting process. It can be stated that except for ethene formation, the cracking to primary intermediates is irrelevant for energetic reasons and should be therefore left out.

Finally, an improved agreement is found for RN06 in which the ethene formation steps from RN05 are assumed to be reversible. The quality of description is similar to RN03, which underlines that in both models, the improvement can be fully ascribed to the reversible ethene formation steps.

A.2.2 Mathematical Description of Adsorption

Nguyen *et al.* [54] provide parameters α to δ for the evolution of a π-complex as well as for the chemisorption of linear olefins on ZSM-5 (Si/Al of 95). The authors investigated chain lengths between $C_2^=$ and $C_8^=$ (1-olefins), between $C_4^=$ and $C_8^=$ (2-olefins) as well as $C_6^=$ and $C_8^=$ (3-olefins) and 4-octene. Two different parameter sets are shown, one for 1-olefins and another one for 2-/3-/4-olefins. In addition, a separate fit of the chemisorption enthalpy of 1-olefins with chain lengths between $C_2^=$ and $C_5^=$ is given. The values resulted from a theoretical DFT study that combined quantum mechanics and molecular mechanics, the latter being considered by interatomic potential functions. This QM-Pot technique originally developed by Sauer and coworkers [349, 369–371] was combined with statistical thermodynamic calculations. Besides the interaction between the double bond and the acid site, these values contain van der Waals contributions resulting from the corrected Lennard-Jones potentials derived earlier [332]. In the regular Nguyen correlations [54], chemisorption leads to secondary alkoxides. In a conference paper authored by the same group [350], a correlation is given that allows for the description of the formation of a tertiary alkoxide. However, a linear coherence was only obtained for the

sum of the chemisorption enthalpy and the standard enthalpy of formation [350]. A similar fit was performed for the chemisorption to secondary alkoxides out of 1-olefins or 2-/3-/4-olefins, respectively. Finally, the special case of isobutene adsorption was treated in a separate publication [310], including formation of π-complex, alkoxide and carbenium ion.

For alkanes, two different main concepts to measure physisorption effects exist in literature. Eder *et al.* [333, 372] determined the physisorption enthalpy using calorimetry, whereas the Langmuir coefficient was fitted to experimental data. From these values, the thermodynamic equilibrium constant is accessible and the physisorption entropy is obtained using Equation (A.1),

$$\Delta_{\mathrm{phys}} S_i^{\circ} = R \ln\left(K^{\mathrm{phys}}(i)\right) + \frac{\Delta_{\mathrm{phys}} H_i^{\circ}}{T}. \tag{A.1}$$

The similar methodology lead to the experimental results of de Moor *et al.* [332]. In this study, other physisorption values from literature are additionally listed and compared. Furthermore, the authors provide both experimental and theoretical physisorption parameters α to δ. For the results shown in Chapter 6, experimentally derived values are used that were obtained with a ZSM-5 catalyst (Si/Al of 35), with *n*-alkanes between C_3 and C_6 as feed and at temperatures between 301 and 400 K.

By contrast, Denayer *et al.* [279, 280] applied a pulse chromatographic technique which is only valid in the linear Henry regime, i.e., when pressures are low. This methodology yielded the Henry constant according to Equation (A.2),

$$K^{\mathrm{H}}(i) = K_0^{\mathrm{H}}(i) \exp\left(-\frac{\Delta_{\mathrm{phys}} H_i^{\circ}}{RT}\right). \tag{A.2}$$

The physisorption enthalpy was derived from the temperature dependence of $K^{\mathrm{H}}(i)$. In addition, the physisorption entropy was related to the pre-exponential Henry factor $K_0^{\mathrm{H}}(i)$, see Equation (A.3),

$$\Delta_{\mathrm{phys}} S_i^{\circ} = R \ln\left(\frac{2p^{\circ} K_0^{\mathrm{H}}(i)}{C_{\mathrm{t}}^{\mathrm{SBAS}}}\right). \tag{A.3}$$

Physisorption parameters α to δ are provided by the authors to calculate enthalpy and the natural logarithm of $K_0^{\mathrm{H}}(i)$. Two data sets are given, accounting for linear and 2-methyl branched alkanes. These were derived from experiments with ZSM-5 (Si/Al of 137) at temperatures between 548 and 648 K using linear and branched C_5 to C_8 alkanes as feed.

Both methodologies can be compared in the low-pressure region which is shown in Equation (A.4),

$$K^{\mathrm{H}}(i) = C^{\mathrm{sat}}(i)\, K_{\mathrm{L}}^{\mathrm{phys}}(i). \tag{A.4}$$

Both sides are converted so that the thermodynamic equilibrium constant is obtained, see Equation (A.5),

$$\frac{C_{\mathrm{t}}^{\mathrm{SBAS}}}{2p^{\circ}} K^{\mathrm{phys}}(i) = \frac{C^{\mathrm{sat}}(i)}{p^{\circ}} K^{\mathrm{phys}}(i). \tag{A.5}$$

Whereas the approach by Eder *et al.* [333, 372] accounts for hydrocarbon-specific saturation effects on the catalytic surface, the carbon number independent value of the acid sites concentration is used for Denayer *et al.* [279, 280]. The deviation is significant especially for ZSM-5, leading in the latter case to physisorption entropies which are increased about 25 J mol^{-1} K^{-1}. Because of this, revised entropy values for Denayer are given by de Moor *et al.* [332] stemming from an application of Equation (A.6),

$$\Delta_{\mathrm{phys}} S_i^{\circ} = R \ln\left(\frac{p^{\circ} K_0^{\mathrm{H}}(i)}{C^{\mathrm{sat}}(i)}\right). \tag{A.6}$$

A.2.3 Additional Parity Plots for Section 6.4.3

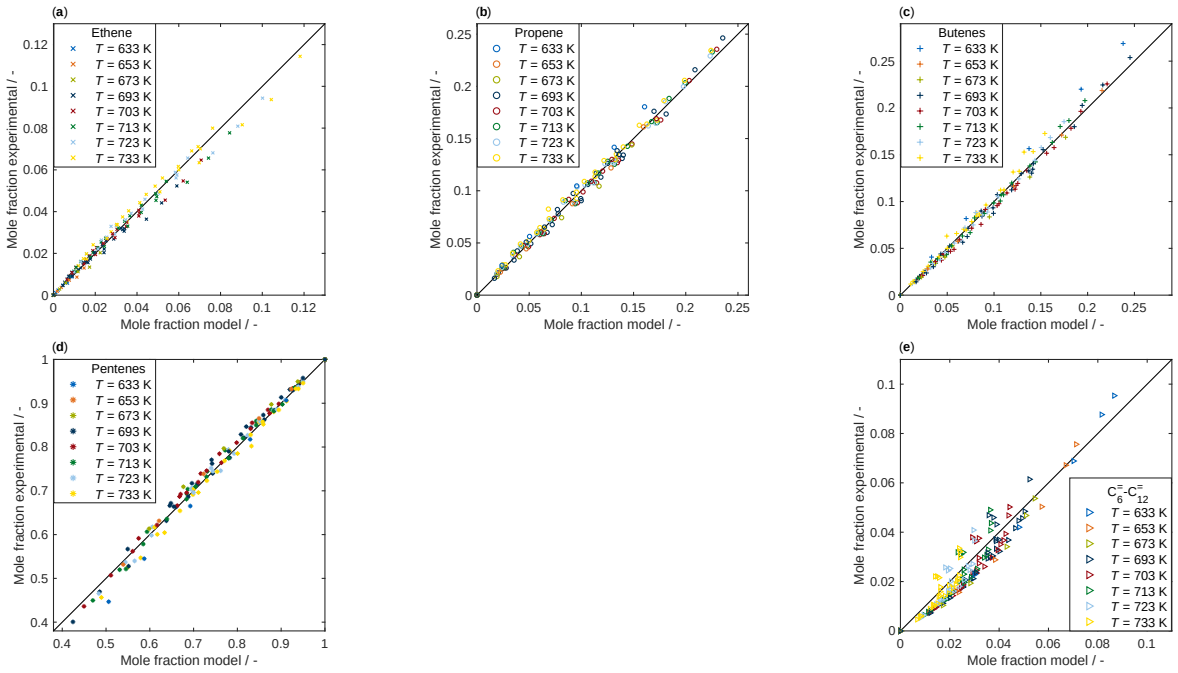

Figure A.2: Parity plots for ethene, (a), propene, (b), butenes, (c), pentenes, (d), and $C_6^=$ to $C_{12}^=$ olefins, (e), resulting from an application of model No. 1, see Table 6.3.

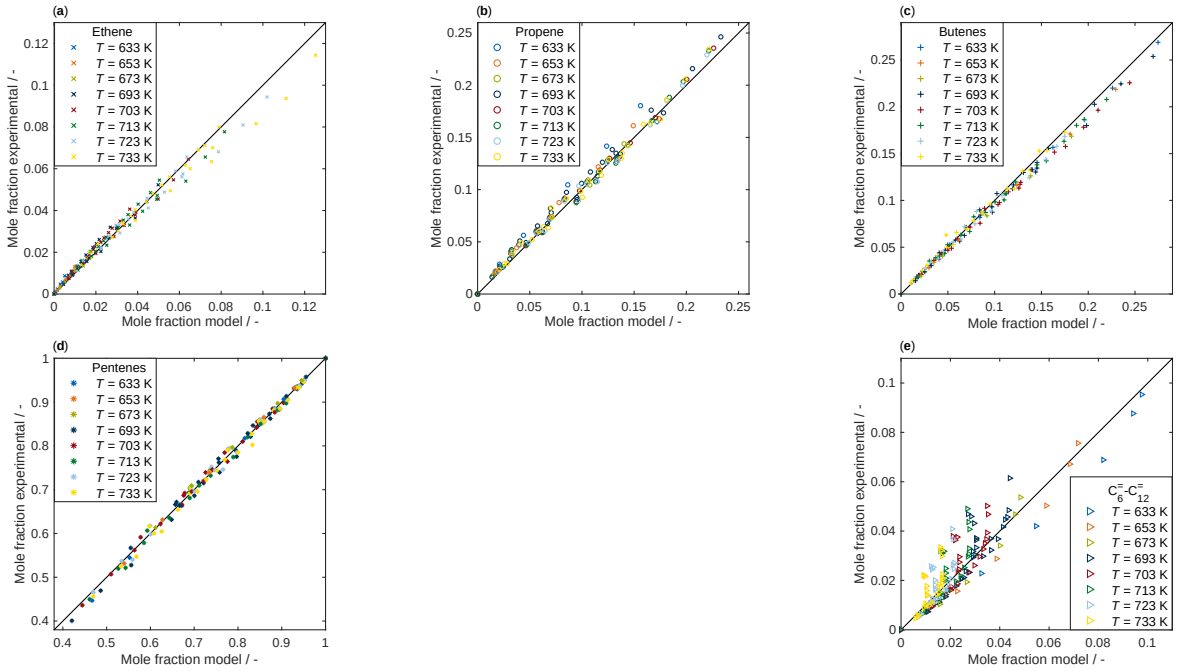

Figure A.3: Parity plots for ethene, (a), propene, (b), butenes, (c), pentenes, (d), and $C_6^=$ to $C_{12}^=$ olefins, (e), resulting from an application of model No. 2, see Table 6.3.

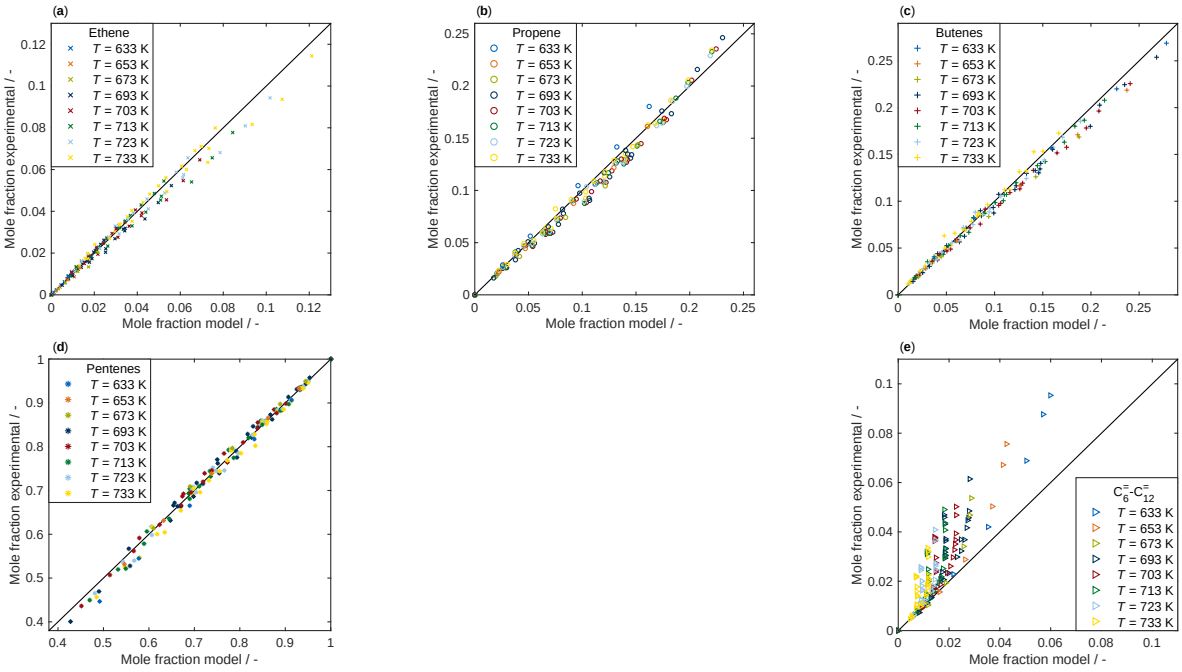

Figure A.4: Parity plots for ethene, (a), propene, (b), butenes, (c), pentenes, (d), and $C_6^=$ to $C_{12}^=$ olefins, (e), resulting from an application of model No. 3, see Table 6.3.

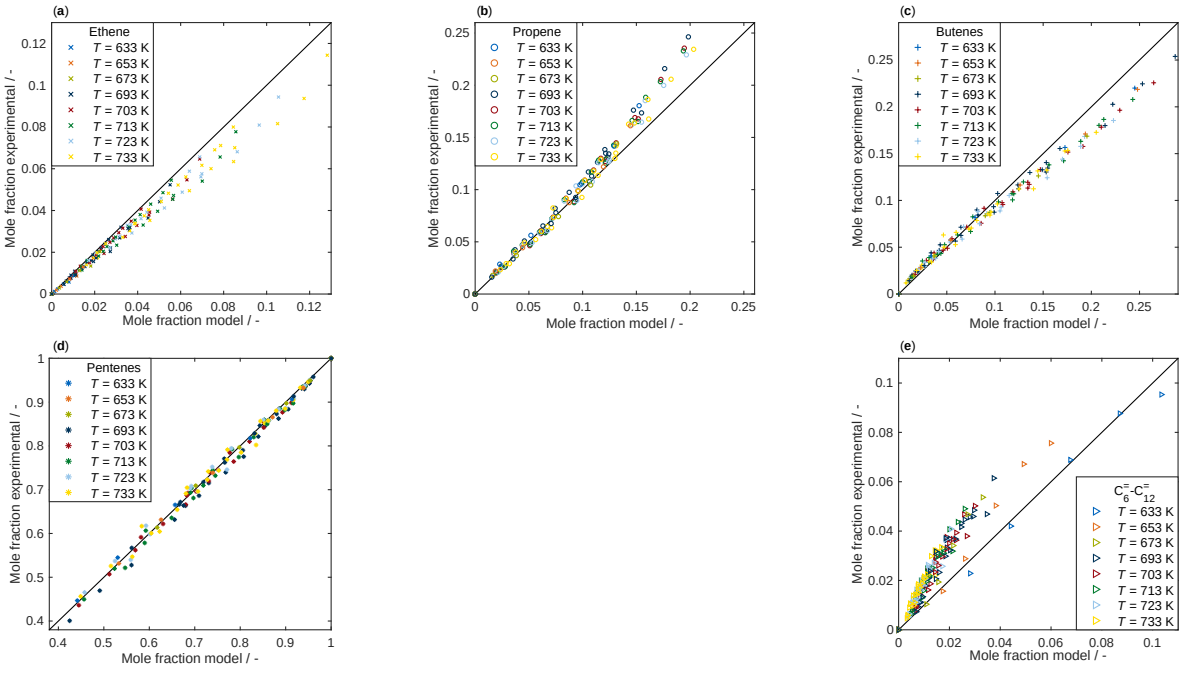

Figure A.5: Parity plots for ethene, (a), propene, (b), butenes, (c), pentenes, (d), and $C_6^=$ to $C_{12}^=$ olefins, (e), resulting from an application of model No. 4, see Table 6.4.

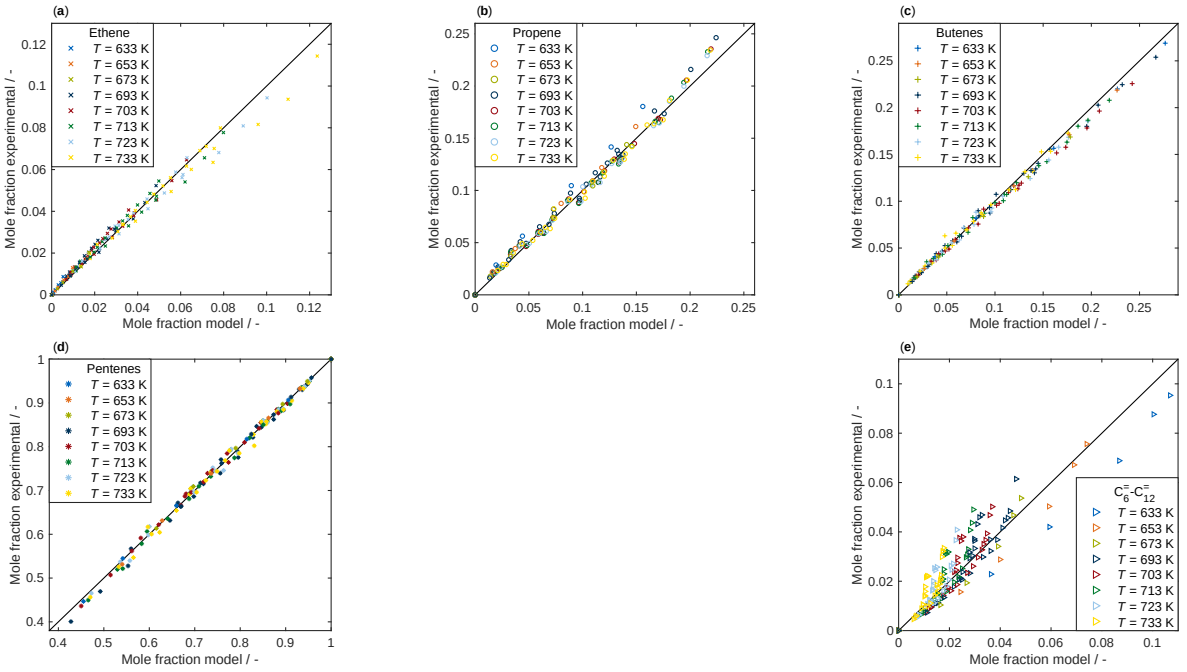

Figure A.6: Parity plots for ethene, (a), propene, (b), butenes, (c), pentenes, (d), and $C_6^=$ to $C_{12}^=$ olefins, (e), resulting from an application of model No. 5, see Table 6.4.

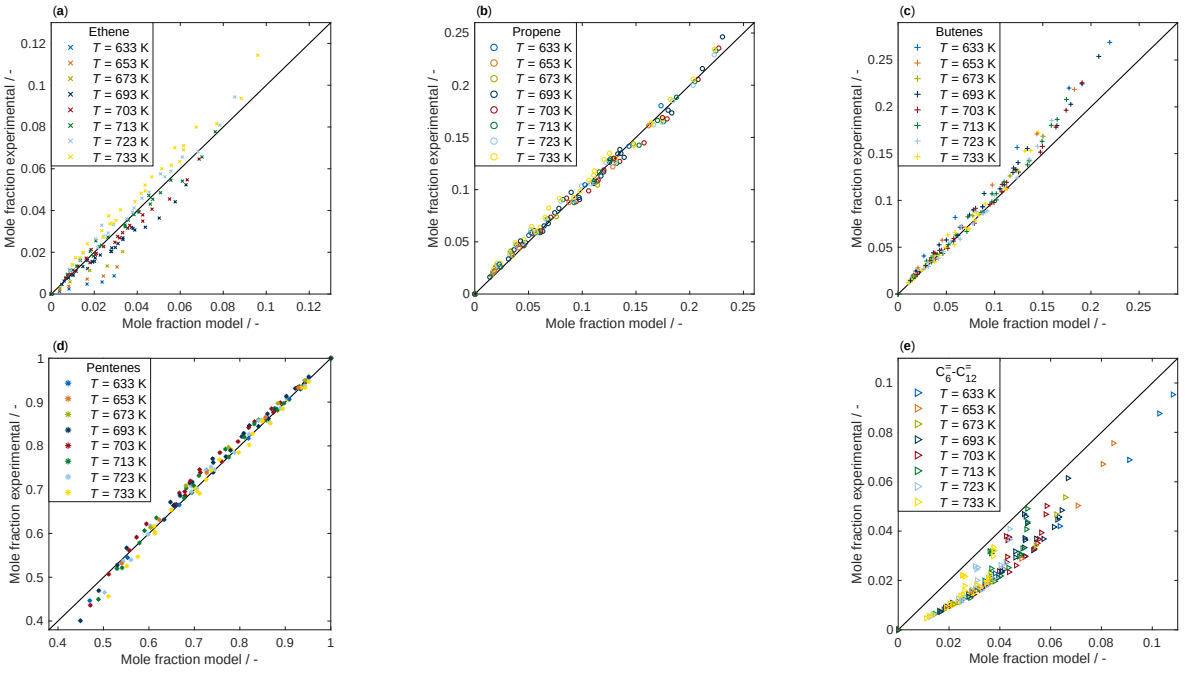

Figure A.7: Parity plots for ethene, (a), propene, (b), butenes, (c), pentenes, (d), and $C_6^=$ to $C_{12}^=$ olefins, (e), resulting from an application of model No. 6, see Table 6.4.

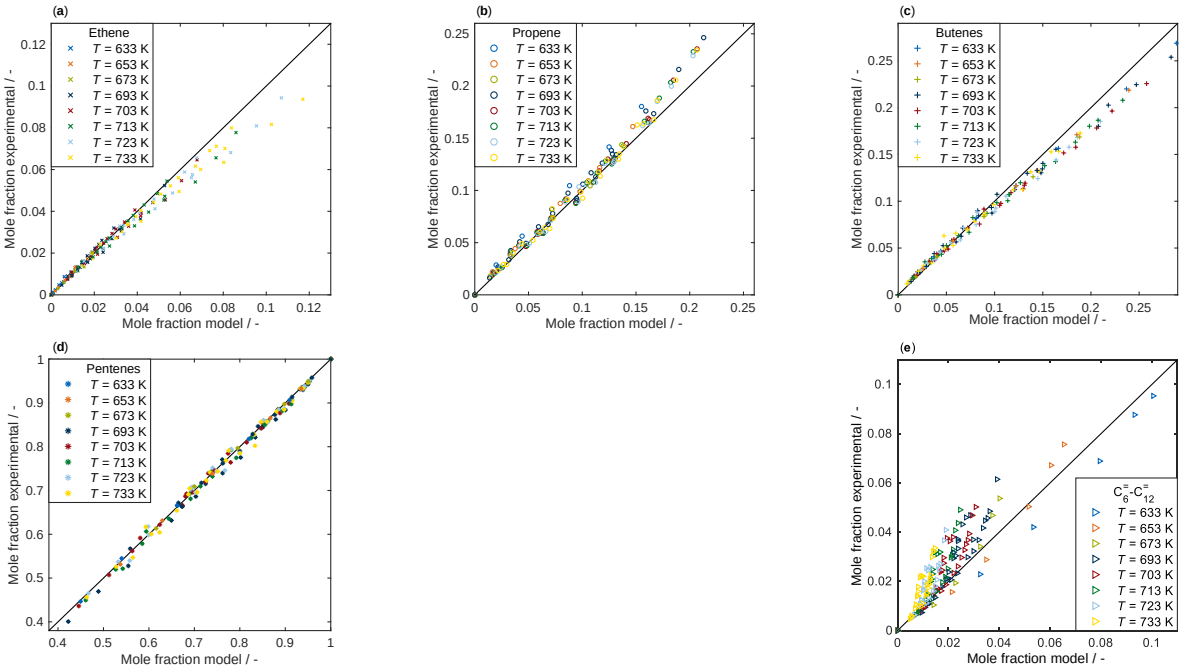

Figure A.8: Parity plots for ethene, (a), propene, (b), butenes, (c), pentenes, (d), and $C_6^=$ to $C_{12}^=$ olefins, (e), resulting from an application of model No. 7, see Table 6.4.

A.3 Supporting Information to Chapter 7

This section was published as Supporting Information and is reprinted with permission from:

S. Standl, F. M. Kirchberger, T. Kühlewind, M. Tonigold, M. Sanchez-Sanchez, J. A. Lercher, O. Hinrichsen
Single-Event Kinetic Model for Methanol-to-Olefins (MTO) over ZSM-5: Fundamental Kinetics for the Olefin Co-Feed Reactivity
Chemical Engineering Journal 402 (2020), 126023, DOI 10.1016/j.cej.2020.126023.

A.3.1 Experimental Setup

During the kinetic measurements, two different volumetric flow rates were applied: 120 and 180 mL min^{-1}. As this caused two different pressure drops, the total pressure was either 1200 or 1250 mbar, respectively. Table A.5 summarizes the different combinations of partial pressures of methanol, p(MeOH), butanol, $p(C_4^=)$, and water, $p(H_2O)$, that were realized at the lower volumetric flow rate.

Table A.5: Experimental conditions for kinetic MTO measurements at the lower volumetric flow rate of 120 mL min^{-1}; all pressure values are given in mbar.

p(MeOH)	$p(C_4^=)$	$p(H_2O)$
76	33	135
114	33	135
76	49	135
114	49	135

At the higher volumetric flow rate, the partial pressures according to Table A.6 were analyzed.

Table A.6: Experimental conditions for kinetic MTO measurements at the higher volumetric flow rate of 180 mL min^{-1}; all pressure values are given in mbar.

p(MeOH)	$p(C_4^=)$	$p(H_2O)$
79	34	141
118	34	141
79	51	141
118	51	141

Volumetric flow rates of the feed were sufficiently high so that any external diffusion limitations can be excluded, see the preliminary tests in Figure A.9. Despite changing the particle size, the product distribution remained constant which means internal diffusion limitations can be neglected. Finally, the high dilution with inert material ensured isothermicity of the catalyst bed. During the reaction, only negligible temperature changes could be observed.

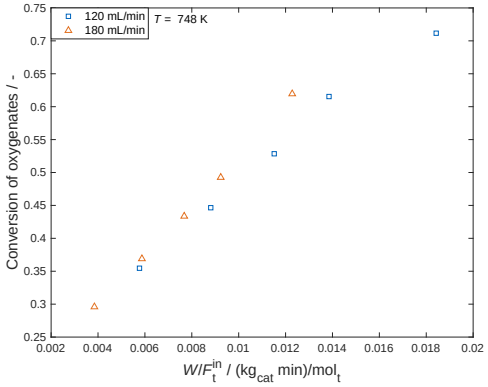

Figure A.9: Preliminary tests to exclude external diffusion limitations: the conversion is independent of the total flow rate.

A.3.2 Adsorption

Table A.7 gives an overview of the adsorption values used in the single-event kinetic model. These are assigned to the different parts of the reaction network, cf. Section 7.3.4.

Table A.7: Overview of adsorption values used within the single-event model; all enthalpies are shown in $\mathrm{kJ\,mol^{-1}}$ whereas entropies are given in $\mathrm{J\,mol^{-1}\,K^{-1}}$; CN_i means the carbon number of olefin i.

Species	Type and part of network	Data source	Values
Olefins	π-Complex: olefin int.[(a)]	Nguyen [54, 310]	$\Delta_\pi H_i^\circ = -8.2\,CN_i - 41$, $\Delta_\pi S_i^\circ = -7.6\,CN_i - 94.5$ (1-Olefins); $\Delta_\pi H_i^\circ = -90$, $\Delta_\pi S_i^\circ = -116$ (isobutene); $\Delta_\pi H_i^\circ = -9.5\,CN_i - 45.4$, $\Delta_\pi S_i^\circ = -10.4\,CN_i - 81.4$ (rest)
Olefins	Protonation: olefin int.[(a)]	Own data (Chapter 6)	$\Delta_{\mathrm{prot}}H^\circ(\mathrm{O}_i^\pi;\mathrm{s}) = 0$; $\Delta_{\mathrm{prot}}H^\circ(\mathrm{O}_i^\pi;\mathrm{t}) = -30$
		Nguyen [54, 310]	$\Delta_{\mathrm{chem}}S_i^\circ = -10.6\,CN_i - 149.8$ (1-Olefins);[(b)] $\Delta_{\mathrm{chem}}S_i^\circ = -193$ (isobutene);[(b)] $\Delta_{\mathrm{chem}}S_i^\circ = -7\,CN_i - 162.9$ (rest)[(b)]
Olefins	Physisorption: olefin int.[(a)]	De Moor [332]	$\Delta_{\mathrm{phys}}H_i^\circ = -10.3\,CN_i - 10.4$, $\Delta_{\mathrm{phys}}S_i^\circ = -9.6\,CN_i - 66.2$
Methanol	Chemisorption: oxygenate int.[(a)]	Nguyen [365]	$\Delta_{\mathrm{chem}}H_i^\circ = -118$, $\Delta_{\mathrm{chem}}S_i^\circ = -161$
DME	Chemisorption: oxygenate int.[(a)]	Maihom [71]	$\Delta_{\mathrm{chem}}H_i^\circ = -123.1$
		Calculated	$\Delta_{\mathrm{chem}}S_i^\circ = -175.7$
Water	Adsorption: oxygenate int.[(a)]	Pope [319]	$\Delta_{\mathrm{ads}}H_i^\circ = -55$, $\Delta_{\mathrm{ads}}S_i^\circ = -128$[(c)]
Olefins	Co-adsorption: oxygenate-olefin int.[(a)]	De Moor [332]	$\Delta_{\mathrm{coads}}H_i^\circ = -10.3\,CN_i - 10.4$, $\Delta_{\mathrm{coads}}S_i^\circ = -9.6\,CN_i - 66.2$

(a) Interconversion
(b) $\Delta_{\mathrm{prot}}S_i^\circ = \Delta_{\mathrm{chem}}S_i^\circ - \Delta_\pi S_i^\circ$
(c) Adsorption type not further specified

A.3.3 Extrapolation of Kinetic Model

Figure A.10 shows the results when the single-event kinetic model is applied to experimental data by Huang *et al.* [241]. It should be considered that for the model predictions in Figure A.10, no fitting to the experimental data is performed. In addition, the temperature of 673 K is almost 40 K below the lowest value of the experiments that were used for parametrization of the single-event model. It follows that because of the fundamental nature of the estimated parameters, the model can predict the product distribution of other reaction systems with reasonable accuracy. For the same reason, an extrapolation to different temperatures and pressures is also possible. The slight overprediction of cracking, i.e., lower amounts of hexene and higher fractions of ethene and propene, can be explained by differences in catalyst properties that are not yet included in the model.

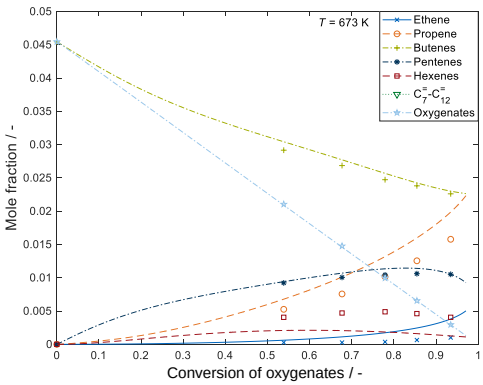

Figure A.10: Reproduction of experimental data (symbols) provided by Huang *et al.* [241] with the single-event kinetic model (lines) without any parameter fitting in advance; $p^{\mathrm{in}}(\mathrm{MeOH}) = 50\,\mathrm{mbar}$ and $p^{\mathrm{in}}(\mathrm{C}_4^{=}) = 50\,\mathrm{mbar}$.

A.3.4 Kinetic Model without Double Methylation

Table A.8 shows the kinetic parameters for the single-event model when no double methylation is included. Besides their poor numeric significance, the single methylation value $E_{\mathrm{a}}^{\mathrm{me}}(\mathrm{p;s})$ is unrealistically low. As mentioned in the main text, carbon transfer from the oxygenates to the olefins is fast, thus forcing the model to provide a pathway with such a high reaction rate.

Table A.8: Estimated kinetic parameters including their 95% confidence intervals for a single-event model without double methylation; all activation energies E_a are given in kJ mol^{-1}.

Parameter	Value
E_a^{cr}(s;p)	161.9 ± 0.8
E_a^{cr}(s;s)	145.6 ± 1.4
E_a^{cr}(t;s)	150.0 ± 1.8
E_a^{me}(p;s)	82.9 ± 809.5
E_a^{me}(p;t)	154.5 ± 3389.9
$E_a^{f}\left(R_{Me}^{+}\right)$	163.5 ± 0.2
$E_a^{c}\left(R_{Me}^{+}\right)$	83.8 ± 809.5
$E_a^{f}\left(R_{DME}^{+}\right)$	62.4 ± 809.7
$E_a^{f}\left(CH_4\right)$	58.7 ± 809.4
$E_a^{meht,co}$	53.1 ± 0.8

However, Figure A.11 reveals that the resulting description is not accurate. The fast single methylation of mainly butenes to pentenes leads to an underestimation of the former and to an overestimation of the latter. The agreement for the remaining compounds is also not sufficient.

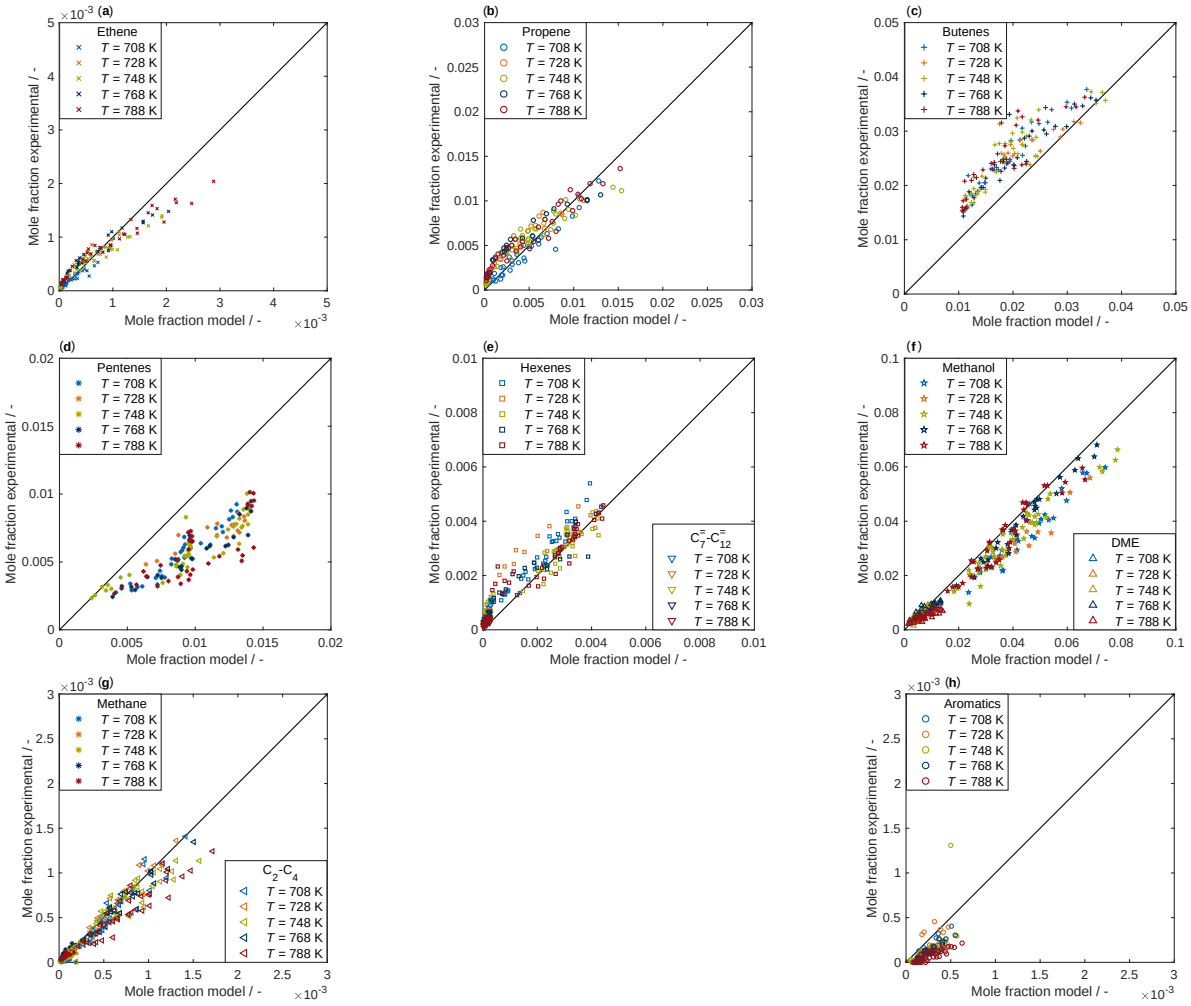

Figure A.11: Parity plots for ethene, (a), propene, (b), butenes, (c), pentenes, (d), hexenes and $C_7^=$ to $C_{12}^=$ olefins, (e), methanol and DME, (f), methane and C_2 to C_4 paraffins, (g), and aromatics, (h), resulting from an application of the single-event model without double methylation to experimental data of co-feeding methanol with butenes.

B Bibliography

[1] T. Ren, M. K. Patel, K. Blok, *Energy* **2008**, *33*, 817–833.

[2] V. Blay, E. Epelde, R. Miravalles, L. A. Perea, *Catal. Rev.: Sci. Eng.* **2018**, *60*, 278–335.

[3] T. Ren, M. K. Patel, K. Blok, *Energy* **2006**, *31*, 425–451.

[4] M. Neelis, M. K. Patel, K. Blok, W. Haije, P. Bach, *Energy* **2007**, *32*, 1104–1123.

[5] G. Centi, G. Iaquaniello, S. Perathoner, *ChemSusChem* **2011**, *4*, 1265–1273.

[6] H. M. Torres Galvis, K. P. de Jong, *ACS Catal.* **2013**, *3*, 2130–2149.

[7] T. Mokrani, M. Scurrell, *Catal. Rev.: Sci. Eng.* **2009**, *51*, 1–145.

[8] N. Rahimi, R. Karimzadeh, *Appl. Catal. A* **2011**, *398*, 1–17.

[9] N. Nesterenko, J. Aguilhon, P. Bodart, D. Minoux, J.-P. Dath in *Zeolites and Zeolite-Like Materials*, (Eds.: B. F. Sels, L. M. Kustov), Elsevier, Amsterdam, NLD, **2016**, pp. 189–263.

[10] U. Olsbye, S. Svelle, M. Bjørgen, P. Beato, T. V. W. Janssens, F. Joensen, S. Bordiga, K. P. Lillerud, *Angew. Chem. Int. Ed.* **2012**, *51*, 5810–5831.

[11] H. Balcar, J. Čejka, *Coord. Chem. Rev.* **2013**, *257*, 3107–3124.

[12] N. Gholampour, M. Yusubov, F. Verpoort, *Catal. Rev.: Sci. Eng.* **2016**, *58*, 113–156.

[13] J. J. H. B. Sattler, J. Ruiz-Martínez, E. Santillan-Jimenez, B. M. Weckhuysen, *Chem. Rev.* **2014**, *114*, 10613–10653.

[14] Z. Nawaz, *Rev. Chem. Eng.* **2015**, *31*, 413–436.

[15] C. A. Carrero, R. Schlögl, I. E. Wachs, R. Schomäcker, *ACS Catal.* **2014**, *4*, 3357–3380.

[16] M. Ghashghaee, *Rev. Chem. Eng.* **2018**, *34*, 595–655.

[17] J. A. Dumesic, D. F. Rudd, L. M. Aparicio, J. E. Rekoske, A. A. Treviño, *The Microkinetics of Heterogeneous Catalysis*, American Chemical Society, Washington, D.C., USA, **1993**.

[18] P. Kumar, J. W. Thybaut, S. Svelle, U. Olsbye, G. B. Marin, *Ind. Eng. Chem. Res.* **2013**, *52*, 1491–1507.

[19] E. Vynckier, G. F. Froment in *Kinetic and Thermodynamic Lumping of Multicomponent Mixtures*, (Eds.: G. Astarita, S. I. Sandler), Elsevier, Amsterdam, NLD, **1991**, pp. 131–161.

[20] J. W. Thybaut, G. B. Marin, *J. Catal.* **2013**, *308*, 352–362.

[21] J. W. Thybaut, G. B. Marin, G. V. Baron, P. A. Jacobs, J. A. Martens, *J. Catal.* **2001**, *202*, 324–339.

[22] G. G. Martens, G. B. Marin, J. A. Martens, P. A. Jacobs, G. V. Baron, *J. Catal.* **2000**, *195*, 253–267.

[23] C. S. L. Narasimhan, J. W. Thybaut, G. B. Marin, P. A. Jacobs, J. A. Martens, J. F. Denayer, G. V. Baron, *J. Catal.* **2003**, *220*, 399–413.

[24] B. D. Vandegehuchte, I. R. Choudhury, J. W. Thybaut, J. A. Martens, G. B. Marin, *J. Phys. Chem. C* **2014**, *118*, 22053–22068.

[25] T. von Aretin, O. Hinrichsen, *Ind. Eng. Chem. Res.* **2014**, *53*, 19460–19470.

[26] T. von Aretin, S. Schallmoser, S. Standl, M. Tonigold, J. A. Lercher, O. Hinrichsen, *Ind. Eng. Chem. Res.* **2015**, *54*, 11792–11803.

[27] P. A. Wright, G. M. Pearce in *Zeolites and Catalysis*, *Vol. 1*, (Eds.: J. Čejka, A. Corma, S. Zones), Wiley-VCH, Weinheim, DEU, **2010**, pp. 171–207.

[28] F. Schmidt, L. Reichelt, C. Pätzold in *Methanol: Asinger's Vision Today*, (Eds.: M. Bertau, H. Offermanns, L. Plass, F. Schmidt, H.-J. Wernicke), Springer, Berlin, DEU, **2014**, pp. 423–440.

[29] P. A. Wright, *Microporous Framework Solids*, The Royal Society of Chemistry, Cambridge, GBR, **2008**.

[30] L. H. Ong, Ph.D. Dissertation, Technical University of Munich, Munich, **2009**.

[31] M. Menges, B. Kraushaar-Czarnetzki, *Microporous Mesoporous Mater.* **2012**, *164*, 172–181.

[32] L. B. McCusker, C. Baerlocher in *Introduction to Zeolite Science and Practice*, (Eds.: H. van Bekkum, E. M. Flanigen, P. A. Jacobs, J. C. Jansen), Studies in Surface Science and Catalysis, Elsevier, Amsterdam, NLD, **2001**, pp. 37–67.

[33] C. Baerlocher, L. B. McCusker, Database of Zeolite Structures. Available online: http://www.iza-structure.org/databases/ (accessed on 6 January 2020).

[34] R. F. Lobo in *Handbook of Zeolite Science and Technology*, (Eds.: S. M. Auerbach, K. A. Carrado, P. K. Dutta), Marcel Dekker, New York, NY, USA, **2003**, pp. 80–112.

[35] G. T. Kokotailo, S. L. Lawton, D. H. Olson, W. M. Meier, *Nature* **1978**, *272*, 437–438.

[36] C. D. Chang, *Catal. Rev.: Sci. Eng.* **1983**, *25*, 1–118.

[37] A. C. Rohrman, R. B. LaPierre, J. L. Schlenker, J. D. Wood, E. W. Valyocsik, M. K. Rubin, J. B. Higgins, W. J. Rohrbaugh, *Zeolites* **1985**, *5*, 352–354.

[38] P. Kumar, J. W. Thybaut, S. Teketel, S. Svelle, P. Beato, U. Olsbye, G. B. Marin, *Catal. Today* **2013**, *215*, 224–232.

[39] S. Teketel, W. Skistad, S. Benard, U. Olsbye, K. P. Lillerud, P. Beato, S. Svelle, *ACS Catal.* **2012**, *2*, 26–37.

[40] B. M. Lok, C. A. Messina, L. Patton, R. T. Gajek, T. R. Cannan, E. M. Flanigen, *J. Am. Chem. Soc.* **1984**, *106*, 6092–6093.

[41] E. Epelde, M. Ibáñez, J. Valecillos, A. T. Aguayo, A. G. Gayubo, J. Bilbao, P. Castaño, *Appl. Catal. A* **2017**, *547*, 176–182.

[42] M. Stöcker in *Zeolites and Catalysis*, *Vol. 2*, (Eds.: J. Čejka, A. Corma, S. Zones), Wiley-VCH, Weinheim, DEU, **2010**, pp. 687–711.

[43] J. Chen, J. M. Thomas, P. A. Wright, R. P. Townsend, *Catal. Lett.* **1994**, *28*, 241–248.

[44] J. Chen, P. A. Wright, J. M. Thomas, S. Natarajan, L. Marchese, S. M. Bradley, G. Sankar, R. A. Catlow, P. Gai-Boyes, R. P. Townsend, M. Lok, *J. Phys. Chem.* **1994**, *98*, 10216–10224.

[45] R. M. Dessau, R. B. LaPierre, *J. Catal.* **1982**, *78*, 136–141.

[46] J. Weitkamp, P. A. Jacobs, J. A. Martens, *Appl. Catal.* **1983**, *8*, 123–141.

[47] W. E. Garwood in *Intrazeolite Chemistry*, (Eds.: G. D. Stucky, F. G. Dwyer), ACS Symposium Series, American Chemical Society, Washington, D.C., USA, **1983**, pp. 383–396.

[48] S. A. Tabak, F. J. Krambeck, W. E. Garwood, *AIChE J.* **1986**, *32*, 1526–1531.

[49] R. J. Quann, L. A. Green, S. A. Tabak, F. J. Krambeck, *Ind. Eng. Chem. Res.* **1988**, *27*, 565–570.

[50] J. S. Buchanan, J. G. Santiesteban, W. O. Haag, *J. Catal.* **1996**, *158*, 279–287.

[51] J. S. Buchanan, *Appl. Catal. A* **1998**, *171*, 57–64.

[52] P. Arudra, T. I. Bhuiyan, M. N. Akhtar, A. M. Aitani, S. S. Al-Khattaf, H. Hattori, *ACS Catal.* **2014**, *4*, 4205–4214.

[53] P. Borges, R. Ramos Pinto, A. Lemos, F. Lemos, J. C. Védrine, E. G. Derouane, F. Ramôa Ribeiro, *Appl. Catal. A* **2007**, *324*, 20–29.

[54] C. M. Nguyen, B. A. de Moor, M.-F. Reyniers, G. B. Marin, *J. Phys. Chem. C* **2011**, *115*, 23831–23847.

[55] V. B. Kazansky, M. V. Frash, R. A. van Santen, *Appl. Catal. A* **1996**, *146*, 225–247.

[56] A. M. Rigby, G. J. Kramer, R. A. van Santen, *J. Catal.* **1997**, *170*, 1–10.

[57] R. Quintana-Solórzano, J. W. Thybaut, G. B. Marin, R. Lødeng, A. Holmen, *Catal. Today* **2005**, *107-108*, 619–629.

[58] X. Sun, S. Müller, Y. Liu, H. Shi, G. L. Haller, M. Sanchez-Sanchez, A. C. van Veen, J. A. Lercher, *J. Catal.* **2014**, *317*, 185–197.

[59] W. Feng, E. Vynckier, G. F. Froment, *Ind. Eng. Chem. Res.* **1993**, *32*, 2997–3005.

[60] G. G. Martens, G. B. Marin, *AIChE J.* **2001**, *47*, 1607–1622.

[61] G. G. Martens, J. W. Thybaut, G. B. Marin, *Ind. Eng. Chem. Res.* **2001**, *40*, 1832–1844.

[62] R. Quintana-Solórzano, J. W. Thybaut, G. B. Marin, *Appl. Catal. A* **2006**, *314*, 184–199.

[63] C. D. Chang, A. J. Silvestri, *J. Catal.* **1977**, *47*, 249–259.

[64] M. Stöcker, *Microporous Mesoporous Mater.* **1999**, *29*, 3–48.

[65] H. Koempel, W. Liebner in *Natural Gas Conversion VIII*, (Eds.: F. Noronha, M. Schmal, E. F. Sousa-Aguiar), Studies in Surface Science and Catalysis, Elsevier, Amsterdam, NLD, **2007**, pp. 261–267.

[66] T. R. Forester, R. F. Howe, *J. Am. Chem. Soc.* **1987**, *109*, 5076–5082.

[67] M. W. Anderson, P. J. Barrie, J. Klinowski, *J. Phys. Chem.* **1991**, *95*, 235–239.

[68] K. A. Martin, R. F. Zabransky, *Appl. Spectrosc.* **1991**, *45*, 68–72.

[69] S. R. Blaszkowski, R. A. van Santen, *J. Am. Chem. Soc.* **1996**, *118*, 5152–5153.

[70] S. R. Blaszkowski, R. A. van Santen, *J. Phys. Chem. B* **1997**, *101*, 2292–2305.

[71] T. Maihom, B. Boekfa, J. Sirijaraensre, T. Nanok, M. Probst, J. Limtrakul, *J. Phys. Chem. C* **2009**, *113*, 6654–6662.

[72] A. J. Jones, E. Iglesia, *Angew. Chem. Int. Ed.* **2014**, *53*, 12177–12181.

[73] Y. Liu, S. Müller, D. Berger, J. Jelic, K. Reuter, M. Tonigold, M. Sanchez-Sanchez, J. A. Lercher, *Angew. Chem. Int. Ed.* **2016**, *55*, 5723–5726.

[74] N. Y. Chen, W. J. Reagan, *J. Catal.* **1979**, *59*, 123–129.

[75] Y. Ono, T. Mori, *J. Chem. Soc. Faraday Trans. 1* **1981**, *77*, 2209–2221.

[76] I. M. Dahl, S. Kolboe, *Catal. Lett.* **1993**, *20*, 329–336.

[77] I. M. Dahl, S. Kolboe, *J. Catal.* **1994**, *149*, 458–464.

[78] I. M. Dahl, S. Kolboe, *J. Catal.* **1996**, *161*, 304–309.

[79] M. Bjørgen, U. Olsbye, D. Petersen, S. Kolboe, *J. Catal.* **2004**, *221*, 1–10.

[80] W. Wang, Y. Jiang, M. Hunger, *Catal. Today* **2006**, *113*, 102–114.

[81] U. Olsbye, M. Bjørgen, S. Svelle, K. P. Lillerud, S. Kolboe, *Catal. Today* **2005**, *106*, 108–111.

[82] U. Olsbye, S. Svelle, K. P. Lillerud, Z. H. Wei, Y. Y. Chen, J. F. Li, J. G. Wang, W. B. Fan, *Chem. Soc. Rev.* **2015**, *44*, 7155–7176.

[83] P. Tian, Y. Wei, M. Ye, Z. Liu, *ACS Catal.* **2015**, *5*, 1922–1938.

[84] T. Mole, J. A. Whiteside, *J. Catal.* **1982**, *75*, 284–290.

[85] A. Sassi, M. A. Wildman, H. J. Ahn, P. Prasad, J. B. Nicholas, J. F. Haw, *J. Phys. Chem. B* **2002**, *106*, 2294–2303.

[86] J. F. Haw, W. Song, D. M. Marcus, J. B. Nicholas, *Acc. Chem. Res.* **2003**, *36*, 317–326.

[87] B. Arstad, J. B. Nicholas, J. F. Haw, *J. Am. Chem. Soc.* **2004**, *126*, 2991–3001.

[88] D. Lesthaeghe, A. Horré, M. Waroquier, G. B. Marin, V. van Speybroeck, *Chem. - Eur. J.* **2009**, *15*, 10803–10808.

[89] R. F. Sullivan, C. J. Egan, G. E. Langlois, R. P. Sieg, *J. Am. Chem. Soc.* **1961**, *83*, 1156–1160.

[90] R. M. Dessau, *J. Catal.* **1986**, *99*, 111–116.

[91] S. Svelle, F. Joensen, J. Nerlov, U. Olsbye, K. P. Lillerud, S. Kolboe, M. Bjørgen, *J. Am. Chem. Soc.* **2006**, *128*, 14770–14771.

[92] M. Bjørgen, S. Svelle, F. Joensen, J. Nerlov, S. Kolboe, F. Bonino, L. Palumbo, S. Bordiga, U. Olsbye, *J. Catal.* **2007**, *249*, 195–207.

[93] S. Svelle, B. Arstad, S. Kolboe, O. Swang, *J. Phys. Chem. B* **2003**, *107*, 9281–9289.

[94] S. Svelle, S. Kolboe, O. Swang, U. Olsbye, *J. Phys. Chem. B* **2005**, *109*, 12874–12878.

[95] J. S. Martínez-Espín, M. Mortén, T. V. W. Janssens, S. Svelle, P. Beato, U. Olsbye, *Catal. Sci. Technol.* **2017**, *7*, 2700–2716.

[96] G. J. Hutchings, R. Hunter, *Catal. Today* **1990**, *6*, 279–306.

[97] S. Müller, Y. Liu, F. M. Kirchberger, M. Tonigold, M. Sanchez-Sanchez, J. A. Lercher, *J. Am. Chem. Soc.* **2016**, *138*, 15994–16003.

[98] J. S. Martínez-Espín, K. de Wispelaere, T. V. W. Janssens, S. Svelle, K. P. Lillerud, P. Beato, V. van Speybroeck, U. Olsbye, *ACS Catal.* **2017**, *7*, 5773–5780.

[99] X. Huang, H. Li, H. Li, W.-D. Xiao, *AIChE J.* **2017**, *63*, 306–313.

[100] S. Svelle, P. O. Rønning, S. Kolboe, *J. Catal.* **2004**, *224*, 115–123.

[101] S. Svelle, P. O. Rønning, U. Olsbye, S. Kolboe, *J. Catal.* **2005**, *234*, 385–400.

[102] W. Wu, W. Guo, W.-D. Xiao, M. Luo, *Chem. Eng. Sci.* **2011**, *66*, 4722–4732.

[103] S. Ilias, A. Bhan, *J. Catal.* **2012**, *290*, 186–192.

[104] W. Guo, W.-D. Xiao, M. Luo, *Chem. Eng. J.* **2012**, *207-208*, 734–745.

[105] X. Sun, S. Müller, H. Shi, G. L. Haller, M. Sanchez-Sanchez, A. C. van Veen, J. A. Lercher, *J. Catal.* **2014**, *314*, 21–31.

[106] C. D. Chang, *Catal. Rev.: Sci. Eng.* **1984**, *26*, 323–345.

[107] G. F. Froment, W. J. H. Dehertog, A. J. Marchi in *Catalysis*, *Vol. 9*, (Ed.: J. J. Spivey), The Royal Society of Chemistry, Cambridge, GBR, **1992**, pp. 1–64.

[108] F. J. Keil, *Microporous Mesoporous Mater.* **1999**, *29*, 49–66.

[109] S. Svelle, M. Visur, U. Olsbye, Saepurahman, M. Bjørgen, *Top. Catal.* **2011**, *54*, 897–906.

[110] K. Hemelsoet, J. van der Mynsbrugge, K. de Wispelaere, M. Waroquier, V. van Speybroeck, *ChemPhysChem* **2013**, *14*, 1526–1545.

[111] V. van Speybroeck, K. de Wispelaere, J. van der Mynsbrugge, M. Vandichel, K. Hemelsoet, M. Waroquier, *Chem. Soc. Rev.* **2014**, *43*, 7326–7357.

[112] S. Ilias, A. Bhan, *ACS Catal.* **2013**, *3*, 18–31.

[113] S. Svelle, M. Bjørgen, *J. Phys. Chem. A* **2010**, *114*, 12548–12554.

[114] V. van Speybroeck, J. van der Mynsbrugge, M. Vandichel, K. Hemelsoet, D. Lesthaeghe, A. Ghysels, G. B. Marin, M. Waroquier, *J. Am. Chem. Soc.* **2011**, *133*, 888–899.

[115] I. M. Hill, Y. S. Ng, A. Bhan, *ACS Catal.* **2012**, *2*, 1742–1748.

[116] I. M. Hill, S. Al Hashimi, A. Bhan, *J. Catal.* **2012**, *285*, 115–123.

[117] I. Hill, A. Malek, A. Bhan, *ACS Catal.* **2013**, *3*, 1992–2001.

[118] J. van der Mynsbrugge, J. de Ridder, K. Hemelsoet, M. Waroquier, V. van Speybroeck, *Chem. - Eur. J.* **2013**, *19*, 11568–11576.

[119] S. L. Moors, K. de Wispelaere, J. van der Mynsbrugge, M. Waroquier, V. van Speybroeck, *ACS Catal.* **2013**, *3*, 2556–2567.

[120] R. Y. Brogaard, C.-M. Wang, F. Studt, *ACS Catal.* **2014**, *4*, 4504–4509.

[121] R. Y. Brogaard, R. Henry, Y. Schuurman, A. J. Medford, P. G. Moses, P. Beato, S. Svelle, J. K. Nørskov, U. Olsbye, *J. Catal.* **2014**, *314*, 159–169.

[122] K. de Wispelaere, B. Ensing, A. Ghysels, E. J. Meijer, V. van Speybroeck, *Chem. - Eur. J.* **2015**, *21*, 9385–9396.

[123] J. S. Martínez-Espín, K. de Wispelaere, M. Westgård Erichsen, S. Svelle, T. V. W. Janssens, V. van Speybroeck, P. Beato, U. Olsbye, *J. Catal.* **2017**, *349*, 136–148.

[124] J. Li, Y. Wei, G. Liu, Y. Qi, P. Tian, B. Li, Y. He, Z. Liu, *Catal. Today* **2011**, *171*, 221–228.

[125] S. M. T. Almutairi, B. Mezari, E. A. Pidko, P. C. M. M. Magusin, E. J. M. Hensen, *J. Catal.* **2013**, *307*, 194–203.

[126] R. Khare, A. Bhan, *J. Catal.* **2015**, *329*, 218–228.

[127] M. Westgård Erichsen, K. de Wispelaere, K. Hemelsoet, S. L. Moors, T. Deconinck, M. Waroquier, S. Svelle, V. van Speybroeck, U. Olsbye, *J. Catal.* **2015**, *328*, 186–196.

[128] I. Yarulina, K. de Wispelaere, S. Bailleul, J. Goetze, M. Radersma, E. Abou-Hamad, I. Vollmer, M. Goesten, B. Mezari, E. J. Hensen, J. S. Martínez-Espín, M. Morten, S. Mitchell, J. Perez-Ramirez, U. Olsbye, B. M. Weckhuysen, V. van Speybroeck, F. Kapteijn, J. Gascon, *Nat. Chem.* **2018**, *10*, 804–812.

[129] W. Wu, W. Guo, W.-D. Xiao, M. Luo, *Fuel Process. Technol.* **2013**, *108*, 19–24.

[130] M. Kaarsholm, F. Joensen, J. Nerlov, R. Cenni, J. Chaouki, G. S. Patience, *Chem. Eng. Sci.* **2007**, *62*, 5527–5532.

[131] T. V. W. Janssens, *J. Catal.* **2009**, *264*, 130–137.

[132] H. Schulz, *Catal. Today* **2010**, *154*, 183–194.

[133] F. L. Bleken, K. Barbera, F. Bonino, U. Olsbye, K. P. Lillerud, S. Bordiga, P. Beato, T. V. W. Janssens, S. Svelle, *J. Catal.* **2013**, *307*, 62–73.

[134] S. Müller, Y. Liu, M. Vishnuvarthan, X. Sun, A. C. van Veen, G. L. Haller, M. Sanchez-Sanchez, J. A. Lercher, *J. Catal.* **2015**, *325*, 48–59.

[135] S. M. Walas, *Phase Equilibria in Chemical Engineering*, Butterworth, Boston, MA, USA, **1985**.

[136] H. Zhou, Y. Wang, F. Wei, D. Wang, Z. Wang, *Appl. Catal. A* **2008**, *348*, 135–141.

[137] R. Zhang, Z. Wang, H. Liu, Z. Liu, G. Liu, X. Meng, *Appl. Catal. A* **2016**, *522*, 165–171.

[138] *Compendium of Chemical Terminology: Gold Book*, 2nd, (Ed.: International Union of Pure and Applied Chemistry), IUPAC, **2014**.

[139] *CRC Handbook of Chemistry and Physics*, 87th, (Ed.: D. R. Lide), Taylor and Francis Group, Boca Raton, FL, USA, **2006**.

[140] R. A. Alberty, *J. Phys. Chem.* **1983**, *87*, 4999–5002.

[141] R. A. Alberty, *Ind. Eng. Chem. Fundam.* **1983**, *22*, 318–321.

[142] R. A. Alberty, I. Oppenheim, *J. Chem. Phys.* **1984**, *81*, 4603–4609.

[143] R. A. Alberty, *J. Phys. Chem.* **1985**, *89*, 880–883.

[144] R. A. Alberty, C. A. Gehrig, *J. Phys. Chem. Ref. Data* **1984**, *13*, 1173–1197.

[145] R. A. Alberty, *J. Phys. Chem. Ref. Data* **1985**, *14*, 177–192.

[146] R. A. Alberty, T. M. Bloomstein, *J. Phys. Chem. Ref. Data* **1985**, *14*, 821–837.

[147] R. A. Alberty, C. A. Gehrig, *J. Phys. Chem. Ref. Data* **1985**, *14*, 803–820.

[148] R. A. Alberty, Y. S. Ha, *J. Phys. Chem. Ref. Data* **1985**, *14*, 1107–1132.

[149] R. A. Alberty, E. Burmenko, *J. Phys. Chem. Ref. Data* **1986**, *15*, 1339–1349.

[150] R. A. Alberty, M. B. Chung, T. M. Flood, *J. Phys. Chem. Ref. Data* **1987**, *16*, 391–417.

[151] R. A. Alberty, A. K. Reif, *J. Phys. Chem. Ref. Data* **1988**, *17*, 241–253.

[152] R. A. Alberty, A. K. Reif, *J. Phys. Chem. Ref. Data* **1989**, *18*, 551–553.

[153] R. A. Alberty, M. B. Chung, A. K. Reif, *J. Phys. Chem. Ref. Data* **1989**, *18*, 77–109.

[154] R. A. Alberty, M. B. Chung, A. K. Reif, *J. Phys. Chem. Ref. Data* **1990**, *19*, 349–370.

[155] S. W. Benson, F. R. Cruickshank, D. M. Golden, G. R. Haugen, H. E. O'Neal, A. S. Rodgers, R. Shaw, R. Walsh, *Chem. Rev.* **1969**, *69*, 279–324.

[156] S. W. Benson, *Thermochemical Kinetics: Methods for the Estimation of Thermochemical Data and Rate Parameters*, 2nd, Wiley, New York, NY, USA, **1976**.

[157] N. Cohen, S. W. Benson, *Chem. Rev.* **1993**, *93*, 2419–2438.

[158] N. Cohen, *J. Phys. Chem. Ref. Data* **1996**, *25*, 1411–1481.

[159] E. S. Domalski, E. D. Hearing, *J. Phys. Chem. Ref. Data* **1988**, *17*, 1637–1678.

[160] E. S. Domalski, E. D. Hearing, *J. Phys. Chem. Ref. Data* **1993**, *22*, 805–1159.

[161] M. K. Sabbe, M. Saeys, M.-F. Reyniers, G. B. Marin, V. van Speybroeck, M. Waroquier, *J. Phys. Chem. A* **2005**, *109*, 7466–7480.

[162] M. K. Sabbe, F. de Vleeschouwer, M.-F. Reyniers, M. Waroquier, G. B. Marin, *J. Phys. Chem. A* **2008**, *112*, 12235–12251.

[163] B. E. Poling, J. M. Prausnitz, J. P. O'Connell, *The Properties of Gases and Liquids*, 5th, McGraw-Hill, New York, NY, USA, **2001**.

[164] D. R. Burgess in *NIST Chemistry WebBook, NIST Standard Reference Database Number 69*, (Eds.: P. J. Linstrom, W. G. Mallard), National Institute of Standards and Technology, Gaithersburg, MD, USA, **2018**.

[165] J. Chao, K. R. Hall, K. N. Marsh, R. C. Wilhoit, *J. Phys. Chem. Ref. Data* **1986**, *15*, 1369–1436.

[166] G. Pilcher, S. Pell, D. J. Coleman, *Trans. Faraday Soc.* **1964**, *60*, 499–505.

[167] R. M. Kennedy, M. Sagenkahn, J. G. Aston, *J. Am. Chem. Soc.* **1941**, *63*, 2267–2272.

[168] A. T. Aguayo, J. Ereña, D. Mier, J. M. Arandes, M. Olazar, J. Bilbao, *Ind. Eng. Chem. Res.* **2007**, *46*, 5522–5530.

[169] H. Hayashi, J. B. Moffat, *J. Catal.* **1982**, *77*, 473–484.

[170] B. T. Diep, M. S. Wainwright, *J. Chem. Eng. Data* **1987**, *32*, 330–333.

[171] P. H. Given, *J. Chem. Soc.* **1943**, 589.

[172] Y. Tavan, R. Hasanvandian, *Fuel* **2015**, *142*, 208–214.

[173] A. G. Gayubo, A. T. Aguayo, M. Castilla, A. L. Morán, J. Bilbao, *Chem. Eng. Commun.* **2004**, *191*, 944–967.

[174] R. S. Schiffino, R. P. Merrill, *J. Phys. Chem.* **1993**, *97*, 6425–6435.

[175] M. H. Khademi, M. Farsi, M. R. Rahimpour, A. Jahanmiri, *Chem. Eng. Process.* **2011**, *50*, 113–123.

[176] J. J. Spivey, *Chem. Eng. Commun.* **1991**, *110*, 123–142.

[177] J. I. Steinfeld, J. S. Francisco, W. L. Hase, *Chemical Kinetics and Dynamics*, Prentice Hall, Englewood Cliffs, NJ, USA, **1989**.

[178] M. E. Davis, R. J. Davis, *Fundamentals of Chemical Reaction Engineering*, McGraw-Hill, New York, NY, USA, **2003**.

[179] G. B. Marin, G. S. Yablonsky, *Kinetics of Chemical Reactions: Decoding Complexity*, Wiley-VCH, Weinheim, DEU, **2011**.

[180] G. F. Froment, K. B. Bischoff, J. de Wilde, *Chemical Reactor Analysis and Design*, 3rd, Wiley, New York, NY, USA, **2011**.

[181] R. Dittmeyer, G. Emig in *Handbook of Heterogeneous Catalysis*, (Eds.: G. Ertl, H. Knözinger, F. Schüth, J. Weitkamp), Wiley-VCH, Weinheim, DEU, **2008**, pp. 1727–1784.

[182] J. A. Dumesic, G. W. Huber, M. Boudart in *Handbook of Heterogeneous Catalysis*, (Eds.: G. Ertl, H. Knözinger, F. Schüth, J. Weitkamp), Wiley-VCH, Weinheim, DEU, **2008**, pp. 1–15.

[183] H. Lynggaard, A. Andreasen, C. Stegelmann, P. Stoltze, *Prog. Surf. Sci.* **2004**, *77*, 71–137.

[184] A. V. Neimark, K. S. W. Sing, M. Thommes in *Handbook of Heterogeneous Catalysis*, (Eds.: G. Ertl, H. Knözinger, F. Schüth, J. Weitkamp), Wiley-VCH, Weinheim, DEU, **2008**, pp. 721–738.

[185] M. Schwaab, J. C. Pinto, *Chem. Eng. Sci.* **2008**, *63*, 4631–4635.

[186] K. Toch, J. W. Thybaut, G. B. Marin, *AIChE J.* **2015**, *61*, 880–892.

[187] F. Kapteijn, R. J. Berger, J. A. Moulijn in *Handbook of Heterogeneous Catalysis*, (Eds.: G. Ertl, H. Knözinger, F. Schüth, J. Weitkamp), Wiley-VCH, Weinheim, DEU, **2008**, pp. 1693–1714.

[188] G. Buzzi-Ferraris, F. Manenti, *Chem. Eng. Sci.* **2009**, *64*, 1061–1074.

[189] H. Eyring, *Chem. Rev.* **1935**, *17*, 65–77.

[190] J. K. Nørskov, F. Studt, F. Abild-Pedersen, T. Bligaard, *Fundamental Concepts in Heterogeneous Catalysis*, John Wiley & Sons, Hoboken, NJ, USA, **2014**.

[191] M. Schwaab, J. C. Pinto, *Chem. Eng. Sci.* **2007**, *62*, 2750–2764.

[192] T.-Y. Park, G. F. Froment, *Ind. Eng. Chem. Res.* **2001**, *40*, 4187–4196.

[193] M. Schwaab, L. P. Lemos, J. C. Pinto, *Chem. Eng. Sci.* **2008**, *63*, 2895–2906.

[194] K. Toch, J. W. Thybaut, B. D. Vandegehuchte, C. S. L. Narasimhan, L. Domokos, G. B. Marin, *Appl. Catal. A* **2012**, *425–426*, 130–144.

[195] X. Huang, D. Aihemaitijiang, W.-D. Xiao, *Chem. Eng. J.* **2015**, *280*, 222–232.

[196] A. B. Mhadeshwar, H. Wang, D. G. Vlachos, *J. Phys. Chem. B* **2003**, *107*, 12721–12733.

[197] L. Pellegrini, S. Locatelli, S. Rasella, S. Bonomi, V. Calemma, *Chem. Eng. Sci.* **2004**, *59*, 4781–4787.

[198] P. J. Becker, B. Celse, D. Guillaume, H. Dulot, P. J. Becker, *Fuel* **2015**, *139*, 133–143.

[199] P. J. Becker, B. Celse, D. Guillaume, V. Costa, L. Bertier, E. Guillon, G. Pirngruber, *Fuel* **2016**, *164*, 73–82.

[200] P. J. Becker, N. Serrand, B. Celse, D. Guillaume, H. Dulot, *Fuel* **2016**, *165*, 306–315.

[201] M. Lopez Abelairas, L. P. de Oliveira, J. J. Verstraete, *Catal. Today* **2016**, *271*, 188–198.

[202] B. Browning, P. Afanasiev, I. Pitault, F. Couenne, M. Tayakout-Fayolle, *Chem. Eng. J.* **2016**, *284*, 270–284.

[203] J. R. Shahrouzi, D. Guillaume, P. Rouchon, P. Da Costa, *Ind. Eng. Chem. Res.* **2008**, *47*, 4308–4316.

[204] J. W. Thybaut, C. S. L. Narasimhan, J. F. Denayer, G. V. Baron, P. A. Jacobs, J. A. Martens, G. B. Marin, *Ind. Eng. Chem. Res.* **2005**, *44*, 5159–5169.

[205] C. S. L. Narasimhan, J. W. Thybaut, J. A. Martens, P. A. Jacobs, J. F. Denayer, G. B. Marin, *J. Phys. Chem. B* **2006**, *110*, 6750–6758.

[206] J. W. Thybaut, I. R. Choudhury, J. F. Denayer, G. V. Baron, P. A. Jacobs, J. A. Martens, G. B. Marin, *Top. Catal.* **2009**, *52*, 1251–1260.

[207] I. R. Choudhury, K. Hayasaka, J. W. Thybaut, C. S. L. Narasimhan, J. F. Denayer, J. A. Martens, G. B. Marin, *J. Catal.* **2012**, *290*, 165–176.

[208] B. D. Vandegehuchte, J. W. Thybaut, G. B. Marin, *Ind. Eng. Chem. Res.* **2014**, *53*, 15333–15347.

[209] J. W. Thybaut, G. B. Marin in *Advances in Catalysis*, (Ed.: C. Song), Advances in Catalysis, Academic Press, Cambridge, MA, USA, **2016**, pp. 109–238.

[210] K. Surla, H. Vleeming, D. Guillaume, P. Galtier, *Chem. Eng. Sci.* **2004**, *59*, 4773–4779.

[211] E. Valéry, D. Guillaume, K. Surla, P. Galtier, J. Verstraete, D. Schweich, *Ind. Eng. Chem. Res.* **2007**, *46*, 4755–4763.

[212] M. Mitsios, D. Guillaume, P. Galtier, D. Schweich, *Ind. Eng. Chem. Res.* **2009**, *48*, 3284–3292.

[213] P. J. Becker, N. Serrand, B. Celse, D. Guillaume, H. Dulot, *Comput. Chem. Eng.* **2017**, *98*, 70–79.

[214] G. F. Froment, *Catal. Rev.: Sci. Eng.* **2005**, *47*, 83–124.

[215] M. A. Baltanas, K. K. van Raemdonck, G. F. Froment, S. R. Mohedas, *Ind. Eng. Chem. Res.* **1989**, *28*, 899–910.

[216] J. M. Martinis, G. F. Froment, *Ind. Eng. Chem. Res.* **2006**, *45*, 954–967.

[217] C. D. Chang, *Chem. Eng. Sci.* **1980**, *35*, 619–622.

[218] R. Mihail, S. Straja, G. Maria, G. Musca, G. Pop, *Ind. Eng. Chem. Process Des. Dev.* **1983**, *22*, 532–538.

[219] R. Mihail, S. Straja, G. Maria, G. Musca, G. Pop, *Chem. Eng. Sci.* **1983**, *38*, 1581–1591.

[220] P. H. Schipper, F. J. Krambeck, *Chem. Eng. Sci.* **1986**, *41*, 1013–1019.

[221] U. A. Sedrán, A. Mahay, H. I. de Lasa, *Chem. Eng. J.* **1990**, *45*, 1161–1165.

[222] U. A. Sedrán, A. Mahay, H. I. de Lasa, *Chem. Eng. J.* **1990**, *45*, 33–42.

[223] H. Schönfelder, J. Hinderer, J. Werther, F. J. Keil, *Chem. Eng. Sci.* **1994**, *49*, 5377–5390.

[224] R. Bos, P. J. Tromp, H. N. Akse, *Ind. Eng. Chem. Res.* **1995**, *34*, 3808–3816.

[225] A. G. Gayubo, P. L. Benito, A. T. Aguayo, I. Aguirre, J. Bilbao, *Chem. Eng. J.* **1996**, *63*, 45–51.

[226] S. N. Khadzhiev, M. V. Magomedova, E. G. Peresypkina, *Pet. Chem.* **2015**, *55*, 503–521.

[227] V. van Speybroeck, K. Hemelsoet, L. Joos, M. Waroquier, R. G. Bell, R. A. Catlow, *Chem. Soc. Rev.* **2015**, *44*, 7044–7111.

[228] K. de Wispelaere, C. S. Wondergem, B. Ensing, K. Hemelsoet, E. J. Meijer, B. M. Weckhuysen, V. van Speybroeck, J. Ruiz-Martínez, *ACS Catal.* **2016**, *6*, 1991–2002.

[229] J. van der Mynsbrugge, S. L. Moors, K. de Wispelaere, V. van Speybroeck, *ChemCatChem* **2014**, *6*, 1906–1918.

[230] D. Lesthaeghe, J. van der Mynsbrugge, M. Vandichel, M. Waroquier, V. van Speybroeck, *ChemCatChem* **2011**, *3*, 208–212.

[231] J. van der Mynsbrugge, A. Janda, L.-C. Lin, V. van Speybroeck, M. Head-Gordon, A. T. Bell, *ChemPhysChem* **2018**, *19*, 341–358.

[232] J. van der Mynsbrugge, A. Janda, S. Mallikarjun Sharada, L.-C. Lin, V. van Speybroeck, M. Head-Gordon, A. T. Bell, *ACS Catal.* **2017**, *7*, 2685–2697.

[233] P. Cnudde, K. de Wispelaere, L. Vanduyfhuys, R. Demuynck, J. van der Mynsbrugge, M. Waroquier, V. van Speybroeck, *ACS Catal.* **2018**, *8*, 9579–9595.

[234] P. Cnudde, K. de Wispelaere, J. van der Mynsbrugge, M. Waroquier, V. van Speybroeck, *J. Catal.* **2017**, *345*, 53–69.

[235] J. Hajek, J. van der Mynsbrugge, K. de Wispelaere, P. Cnudde, L. Vanduyfhuys, M. Waroquier, V. van Speybroeck, *J. Catal.* **2016**, *340*, 227–235.

[236] E. Epelde, A. T. Aguayo, M. Olazar, J. Bilbao, A. G. Gayubo, *Ind. Eng. Chem. Res.* **2014**, *53*, 10599–10607.

[237] L. Ying, J. Zhu, Y. Cheng, L. Wang, X. Li, *J. Ind. Eng. Chem.* **2016**, *33*, 80–90.

[238] P. Oliveira, P. Borges, R. Ramos Pinto, A. Lemos, F. Lemos, J. C. Védrine, F. Ramôa Ribeiro, *Appl. Catal. A* **2010**, *384*, 177–185.

[239] E. Epelde, A. G. Gayubo, M. Olazar, J. Bilbao, A. T. Aguayo, *Chem. Eng. J.* **2014**, *251*, 80–91.

[240] E. Epelde, A. G. Gayubo, M. Olazar, J. Bilbao, A. T. Aguayo, *Ind. Eng. Chem. Res.* **2014**, *53*, 4614–4622.

[241] X. Huang, D. Aihemaitijiang, W.-D. Xiao, *Chem. Eng. J.* **2016**, *286*, 150–164.

[242] P. Borges, R. Ramos Pinto, A. Lemos, F. Lemos, J. C. Védrine, E. G. Derouane, F. Ramôa Ribeiro, *J. Mol. Catal. A: Chem.* **2005**, *229*, 127–135.

[243] C.-J. Chen, S. Rangarajan, I. M. Hill, A. Bhan, *ACS Catal.* **2014**, *4*, 2319–2327.

[244] M. N. Mazar, S. Al-Hashimi, M. Cococcioni, A. Bhan, *J. Phys. Chem. C* **2013**, *117*, 23609–23620.

[245] J. Li, T. Li, H. Ma, Q. Sun, C. Li, W. Ying, D. Fang, *Chem. Eng. J.* **2018**, *346*, 397–405.

[246] X. Meng, C. Xu, L. Li, J. Gao, *Energy Fuels* **2010**, *24*, 6233–6238.

[247] B. Jiang, X. Feng, L. Yan, Y. Jiang, Z. Liao, J. Wang, Y. Yang, *Ind. Eng. Chem. Res.* **2014**, *53*, 4623–4632.

[248] A. T. Aguayo, D. Mier, A. G. Gayubo, M. Gamero, J. Bilbao, *Ind. Eng. Chem. Res.* **2010**, *49*, 12371–12378.

[249] P. Pérez-Uriarte, A. Ateka, A. T. Aguayo, A. G. Gayubo, J. Bilbao, *Chem. Eng. J.* **2016**, *302*, 801–810.

[250] T.-Y. Park, G. F. Froment, *Ind. Eng. Chem. Res.* **2001**, *40*, 4172–4186.

[251] A. G. Gayubo, A. T. Aguayo, A. E. Sánchez del Campo, A. M. Tarrío, J. Bilbao, *Ind. Eng. Chem. Res.* **2000**, *39*, 292–300.

[252] L. Ying, X. Yuan, M. Ye, Y. Cheng, X. Li, Z. Liu, *Chem. Eng. Res. Des.* **2015**, *100*, 179–191.

[253] D. Chen, A. Grønvold, K. Moljord, A. Holmen, *Ind. Eng. Chem. Res.* **2007**, *46*, 4116–4123.

[254] S. M. Alwahabi, G. F. Froment, *Ind. Eng. Chem. Res.* **2004**, *43*, 5098–5111.

[255] A. G. Gayubo, A. T. Aguayo, A. Alonso, A. Atutxa, J. Bilbao, *Catal. Today* **2005**, *106*, 112–117.

[256] A. G. Gayubo, A. T. Aguayo, A. Alonso, J. Bilbao, *Ind. Eng. Chem. Res.* **2007**, *46*, 1981–1989.

[257] A. E. Sánchez del Campo, A. G. Gayubo, A. T. Aguayo, A. Tarrío, J. Bilbao, *Ind. Eng. Chem. Res.* **1998**, *37*, 2336–2340.

[258] M. Menges, Ph.D. Dissertation, Karlsruher Institut für Technologie, Karlsruhe, **2012**.

[259] D. Chen, A. Grønvold, H. P. Rebo, K. Moljord, A. Holmen, *Appl. Catal. A* **1996**, *137*, L1–L8.

[260] J. Freiding, F.-C. Patcas, B. Kraushaar-Czarnetzki, *Appl. Catal. A* **2007**, *328*, 210–218.

[261] J. Freiding, Ph.D. Dissertation, Karlsruher Institut für Technologie, Karlsruhe, **2009**.

[262] J. Freiding, B. Kraushaar-Czarnetzki, *Appl. Catal. A* **2011**, *391*, 254–260.

[263] A. G. Gayubo, A. T. Aguayo, A. L. Morán, M. Olazar, J. Bilbao, *AIChE J.* **2002**, *48*, 1561–1571.

[264] A. G. Gayubo, A. T. Aguayo, M. Olazar, R. Vivanco, J. Bilbao, *Chem. Eng. Sci.* **2003**, *58*, 5239–5249.

[265] A. G. Gayubo, J. M. Arandes, A. T. Aguayo, M. Olazar, J. Bilbao, *Chem. Eng. Sci.* **1993**, *48*, 1077–1087.

[266] A. T. Aguayo, A. G. Gayubo, J. M. Ortega, M. Olazar, J. Bilbao, *Catal. Today* **1997**, *37*, 239–248.

[267] P. L. Benito, A. G. Gayubo, A. T. Aguayo, M. Castilla, J. Bilbao, *Ind. Eng. Chem. Res.* **1996**, *35*, 81–89.

[268] D. Mier, A. T. Aguayo, A. G. Gayubo, M. Olazar, J. Bilbao, *Appl. Catal. A* **2010**, *383*, 202–210.

[269] D. Mier, A. T. Aguayo, M. Gamero, A. G. Gayubo, J. Bilbao, *Ind. Eng. Chem. Res.* **2010**, *49*, 8415–8423.

[270] P. Pérez-Uriarte, A. Ateka, M. Gamero, A. T. Aguayo, J. Bilbao, *Ind. Eng. Chem. Res.* **2016**, *55*, 6569–6578.

[271] P. Pérez-Uriarte, M. Gamero, A. Ateka, M. Díaz, A. T. Aguayo, J. Bilbao, *Ind. Eng. Chem. Res.* **2016**, *55*, 1513–1521.

[272] P. Pérez-Uriarte, A. Ateka, A. G. Gayubo, T. Cordero-Lanzac, A. T. Aguayo, J. Bilbao, *Chem. Eng. J.* **2017**, *311*, 367–377.

[273] E. Lox, F. Coenen, R. Vermeulen, G. F. Froment, *Ind. Eng. Chem. Res.* **1988**, *27*, 576–580.

[274] G. J. Hutchings, F. Gottschalk, M. V. M. Hall, R. Hunter, *J. Chem. Soc. Faraday Trans. 1* **1987**, *83*, 571–583.

[275] T.-Y. Park, G. F. Froment, *Comput. Chem. Eng.* **1998**, *22*, S103–S110.

[276] M. Boudart, D. E. Mears, M. A. Vannice, *Ind. Chim. Belge* **1967**, *32*, 281–284.

[277] M. G. Evans, M. Polanyi, *Trans. Faraday Soc.* **1938**, *34*, 11–24.

[278] T.-Y. Park, G. F. Froment, *Ind. Eng. Chem. Res.* **2004**, *43*, 682–689.

[279] J. F. Denayer, W. Souverijns, P. A. Jacobs, J. A. Martens, G. V. Baron, *J. Phys. Chem. B* **1998**, *102*, 4588–4597.

[280] J. F. Denayer, G. V. Baron, J. A. Martens, P. A. Jacobs, *J. Phys. Chem. B* **1998**, *102*, 3077–3081.

[281] D. Chen, H. P. Rebo, A. Grønvold, K. Moljord, A. Holmen, *Microporous Mesoporous Mater.* **2000**, *35–36*, 121–135.

[282] D. Chen, E. Bjorgum, K. O. Christensen, A. Holmen, R. Lodeng in *Advances in Catalysis*, (Eds.: B. C. Gates, H. Knözinger), Advances in Catalysis, Academic Press, Cambridge, MA, USA, **2007**, pp. 351–382.

[283] S. M. Alwahabi, Ph.D. Dissertation, Texas A&M University, College Station, **2003**.

[284] A. G. Gayubo, R. Vivanco, A. Alonso, B. Valle, A. T. Aguayo, *Ind. Eng. Chem. Res.* **2005**, *44*, 6605–6614.

[285] F. Bleken, M. Bjørgen, L. Palumbo, S. Bordiga, S. Svelle, K. P. Lillerud, U. Olsbye, *Top. Catal.* **2009**, *52*, 218–228.

[286] S. Teketel, U. Olsbye, K. P. Lillerud, P. Beato, S. Svelle, *Microporous Mesoporous Mater.* **2010**, *136*, 33–41.

[287] C. S. L. Narasimhan, J. W. Thybaut, G. B. Marin, J. A. Martens, J. F. Denayer, G. V. Baron, *J. Catal.* **2003**, *218*, 135–147.

[288] J. F. Denayer, R. A. Ocakoglu, W. Huybrechts, J. A. Martens, J. W. Thybaut, G. B. Marin, G. V. Baron, *Chem. Commun.* **2003**, 1880–1881.

[289] M. Kaarsholm, B. Rafii, F. Joensen, R. Cenni, J. Chaouki, G. S. Patience, *Ind. Eng. Chem. Res.* **2010**, *49*, 29–38.

[290] X. Yuan, H. Li, M. Ye, Z. Liu, *AIChE J.* **2019**, *65*, 662–674.

[291] X. Yuan, H. Li, M. Ye, Z. Liu, *Chem. Eng. J.* **2017**, *329*, 35–44.

[292] B. Lu, J. Zhang, H. Luo, W. Wang, H. Li, M. Ye, Z. Liu, J. Li, *Chem. Eng. Sci.* **2017**, *171*, 244–255.

[293] J. Zhang, B. Lu, F. Chen, H. Li, M. Ye, W. Wang, *Chem. Eng. Sci.* **2018**, *189*, 212–220.

[294] P. Strizhak, A. Zhokh, A. Trypolskyi, *React. Kinet. Mech. Catal.* **2018**, *123*, 247–268.

[295] M. Sedighi, H. Bahrami, J. Towfighi, *J. Ind. Eng. Chem.* **2014**, *20*, 3108–3114.

[296] N. Fatourehchi, M. Sohrabi, S. J. Royaee, S. M. Mirarefin, *Chem. Eng. Res. Des.* **2011**, *89*, 811–816.

[297] A. Taheri Najafabadi, S. Fatemi, M. Sohrabi, M. Salmasi, *J. Ind. Eng. Chem.* **2012**, *18*, 29–37.

[298] M. J. Azarhoosh, R. Halladj, S. Askari, *J. Phys.: Condens. Matter* **2017**, *29*, 425202.

[299] M. Wen, J. Ding, C. Wang, Y. Li, G. Zhao, Y. Liu, Y. Lu, *Microporous Mesoporous Mater.* **2016**, *221*, 187–196.

[300] M. Wen, X. Wang, L. Han, J. Ding, Y. Sun, Y. Liu, Y. Lu, *Microporous Mesoporous Mater.* **2015**, *206*, 8–16.

[301] X. Huang, H. Li, W.-D. Xiao, D. Chen, *Chem. Eng. J.* **2016**, *299*, 263–275.

[302] X. Huang, H. Li, H. Li, W.-D. Xiao, *Fuel Process. Technol.* **2016**, *150*, 104–116.

[303] X. Huang, X.-G. Li, H. Li, W.-D. Xiao, *Fuel Process. Technol.* **2017**, *159*, 168–177.

[304] X. Wang, M. Wen, C. Wang, J. Ding, Y. Sun, Y. Liu, Y. Lu, *Chem. Commun.* **2014**, *50*, 6343–6345.

[305] W. Guo, W. Wu, M. Luo, W.-D. Xiao, *Fuel Process. Technol.* **2013**, *108*, 133–138.

[306] C. Ortega, V. Hessel, G. Kolb, *Chem. Eng. J.* **2018**, *354*, 21–34.

[307] S. Schallmoser, Ph.D. Dissertation, Technical University of Munich, Munich, **2014**.

[308] J. Abbot, B. W. Wojciechowski, *Can. J. Chem. Eng.* **1985**, *63*, 451–461.

[309] J. Abbot, B. W. Wojciechowski, *Can. J. Chem. Eng.* **1985**, *63*, 462–469.

[310] C. M. Nguyen, B. A. de Moor, M.-F. Reyniers, G. B. Marin, *J. Phys. Chem. C* **2012**, *116*, 18236–18249.

[311] X. Zhu, S. Liu, Y. Song, L. Xu, *Catal. Lett.* **2005**, *103*, 201–210.

[312] H. Zimmermann in *Ullmann's Encyclopedia of Industrial Chemistry, Electronic Release*, Wiley-VCH, Weinheim, DEU, **2013**, pp. 1–18.

[313] H. Zimmermann, R. Walzl in *Ullmann's Encyclopedia of Industrial Chemistry, Electronic Release*, Wiley-VCH, Weinheim, DEU, **2012**, pp. 465–530.

[314] L. Lin, C. Qiu, Z. Zhuo, D. Zhang, S. Zhao, H. Wu, Y. Liu, M. He, *J. Catal.* **2014**, *309*, 136–145.

[315] G. Zhao, J. Teng, Z. Xie, W. Jin, W. Yang, Q. Chen, Y. Tang, *J. Catal.* **2007**, *248*, 29–37.

[316] P. Sazama, J. Dědeček, V. Gábová, B. Wichterlová, G. Spoto, S. Bordiga, *J. Catal.* **2008**, *254*, 180–189.

[317] J. W. Thybaut, C. S. L. Narasimhan, G. B. Marin, J. F. Denayer, G. V. Baron, P. A. Jacobs, J. A. Martens, *Catal. Lett.* **2004**, *94*, 81–88.

[318] G. D. Svoboda, E. Vynckier, B. Debrabandere, G. F. Froment, *Ind. Eng. Chem. Res.* **1995**, *34*, 3793–3800.

[319] C. G. Pope, *J. Colloid Interface Sci.* **1987**, *116*, 221–223.

[320] N. Rane, M. Kersbulck, R. A. van Santen, E. J. Hensen, *Microporous Mesoporous Mater.* **2008**, *110*, 279–291.

[321] K. M. A. de Meyer, S. Chempath, J. F. M. Denayer, J. A. Martens, R. Q. Snurr, G. V. Baron, *J. Phys. Chem. B* **2003**, *107*, 10760–10766.

[322] J. Sundberg, S. Rehfeldt, A. Peschel, H. Klein, *Chem. Ing. Tech.* **2017**, *89*, 675–685.

[323] H. Effenberger, *Dampferzeugung*, Springer, Berlin, DEU, **2000**.

[324] Federal Statistical Office Germany, Daten zur Energiepreisentwicklung, Wiesbaden, **2017**.

[325] D. Schlereth, P. J. Donaubauer, O. Hinrichsen, *Chem. Eng. Technol.* **2015**, *38*, 1845–1852.

[326] R. Tamme, R. Bauer, E. Hahne in *Ullmann's Encyclopedia of Industrial Chemistry, Electronic Release*, Wiley-VCH, Weinheim, DEU, **2012**, pp. 421–438.

[327] W. Wagner, *Wärme-Austauscher*, 4th ed., Vogel, Würzburg, DEU, **2009**.

[328] P. Wolf, G. Kirchner in *VDI-Wärmeatlas*, (Ed.: VDI-Gesellschaft Verfahrenstechnik und Chemieingenieurwesen), Springer, Berlin, DEU, **2013**, pp. 1695–1722.

[329] K.-E. Wirth in *VDI-Wärmeatlas*, (Ed.: VDI-Gesellschaft Verfahrenstechnik und Chemieingenieurwesen), Springer, Berlin, DEU, **2013**, pp. 1275–1279.

[330] A. Mersmann, M. Kind, J. Stichlmair, *Thermal Separation Technology: Principles, Methods, Process Design*, Springer, Berlin, DEU, **2011**.

[331] S. Schallmoser, G. L. Haller, M. Sanchez-Sanchez, J. A. Lercher, *J. Am. Chem. Soc.* **2017**, *139*, 8646–8652.

[332] B. A. de Moor, M.-F. Reyniers, O. C. Gobin, J. A. Lercher, G. B. Marin, *J. Phys. Chem. C* **2011**, *115*, 1204–1219.

[333] F. Eder, J. A. Lercher, *Zeolites* **1997**, *18*, 75–81.

[334] J. F. Haw, J. B. Nicholas, T. Xu, L. W. Beck, D. B. Ferguson, *Acc. Chem. Res.* **1996**, *29*, 259–267.

[335] M. Bjørgen, F. Bonino, S. Kolboe, K. P. Lillerud, A. Zecchina, S. Bordiga, *J. Am. Chem. Soc.* **2003**, *125*, 15863–15868.

[336] L. A. Clark, M. Sierka, J. Sauer, *J. Am. Chem. Soc.* **2003**, *125*, 2136–2141.

[337] W. Dai, C. Wang, X. Yi, A. Zheng, L. Li, G. Wu, N. Guan, Z. Xie, M. Dyballa, M. Hunger, *Angew. Chem. Int. Ed.* **2015**, *54*, 8783–8786.

[338] M. Boronat, P. Viruela, A. Corma, *J. Am. Chem. Soc.* **2004**, *126*, 3300–3309.

[339] C. Tuma, J. Sauer, *Angew. Chem. Int. Ed.* **2005**, *117*, 4847–4849.

[340] J. F. Haw, **2002**, *4*, 5431–5441.

[341] M. Boronat, A. Corma, *Appl. Catal. A* **2008**, *336*, 2–10.

[342] M. Boronat, C. M. Zicovich-Wilson, P. Viruela, A. Corma, *J. Phys. Chem. B* **2001**, *105*, 11169–11177.

[343] J. N. Kondo, L. Shao, F. Wakabayashi, K. Domen, *J. Phys. Chem. B* **1997**, *101*, 9314–9320.

[344] A. G. Stepanov, S. S. Arzumanov, M. V. Luzgin, H. Ernst, D. Freude, *J. Catal.* **2005**, *229*, 243–251.

[345] P. E. Sinclair, A. de Vries, P. Sherwood, R. A. Catlow, R. A. van Santen, **1998**, *94*, 3401–3408.

[346] X. Rozanska, T. Demuth, F. Hutschka, J. Hafner, R. A. van Santen, *J. Phys. Chem. B* **2002**, *106*, 3248–3254.

[347] X. Rozanska, R. A. van Santen, T. Demuth, F. Hutschka, J. Hafner, *J. Phys. Chem. B* **2003**, *107*, 1309–1315.

[348] V. Nieminen, M. Sierka, D. Y. Murzin, J. Sauer, *J. Catal.* **2005**, *231*, 393–404.

[349] L. A. Clark, M. Sierka, J. Sauer in *Impact of Zeolites and other Porous Materials on the new Technologies at the Beginning of the New Millennium*, (Eds.: R. Aiello, G. Giordano, F. Testa), Studies in Surface Science and Catalysis, Elsevier, Amsterdam, NLD, **2002**, pp. 643–649.

[350] C. M. Nguyen, B. A. de Moor, M.-F. Reyniers, G. B. Marin in 2nd International Workshop NAPEN, Rhodes, Greece, June 09–11, (Ed.: Nanoporous Materials in Energy and Environment), **2011**.

[351] R. J. Correa, C. J. A. Mota, *Phys. Chem. Chem. Phys.* **2002**, *4*, 375–380.

[352] A. Bhan, Y. V. Joshi, W. N. Delgass, K. T. Thomson, *J. Phys. Chem. B* **2003**, *107*, 10476–10487.

[353] R. W. Hankinson, G. H. Thomson, *AIChE J.* **1979**, *25*, 653–663.

[354] H. S. Elbro, A. Fredenslund, P. Rasmussen, *Ind. Eng. Chem. Res.* **1991**, *30*, 2576–2582.

[355] G. Yaluris, J. E. Rekoske, L. M. Aparicio, R. J. Madon, J. A. Dumesic, *J. Catal.* **1995**, *153*, 54–64.

[356] S. R. Blaszkowski, R. A. van Santen, *J. Am. Chem. Soc.* **1997**, *119*, 5020–5027.

[357] T. R. Forester, S.-T. Wong, R. F. Howe, *J. Chem. Soc. Chem. Commun.* **1986**, *21*, 1611–1613.

[358] K. P. Möller, W. Böhringer, A. E. Schnitzler, E. van Steen, C. T. O'Connor, *Microporous Mesoporous Mater.* **1999**, *29*, 127–144.

[359] F. Wakabayashi, J. N. Kondo, K. Domen, C. Hirose, *J. Phys. Chem.* **1996**, *100*, 1442–1444.

[360] A. Ison, R. J. Gorte, *J. Catal.* **1984**, *89*, 150–158.

[361] G. Mirth, J. A. Lercher, *J. Catal.* **1991**, *132*, 244–252.

[362] G. Mirth, J. A. Lercher, *J. Phys. Chem.* **1991**, *95*, 3736–3740.

[363] S. Svelle, C. Tuma, X. Rozanska, T. Kerber, J. Sauer, *J. Am. Chem. Soc.* **2009**, *131*, 816–825.

[364] Y. Liu, F. M. Kirchberger, S. Müller, M. Eder, M. Tonigold, M. Sanchez-Sanchez, J. A. Lercher, *Nat. Commun.* **2019**, *10*, 1462.

[365] C. M. Nguyen, M.-F. Reyniers, G. B. Marin, *J. Catal.* **2015**, *322*, 91–103.

[366] S. Jakobtorweihen, N. Hansen, F. J. Keil, *Mol. Phys.* **2005**, *103*, 471–489.

[367] A. A. Cichowlas, P. T. Wierzchowski, L. W. Zatorski, *React. Kinet. Catal. Lett.* **1986**, *32*, 341–346.

[368] L. R. Aramburo, S. Teketel, S. Svelle, S. R. Bare, B. Arstad, H. W. Zandbergen, U. Olsbye, F. M. de Groot, B. M. Weckhuysen, *J. Catal.* **2013**, *307*, 185–193.

[369] J. Sauer, M. Sierka, *J. Comput. Chem.* **2000**, *21*, 1470–1493.

[370] M. Sierka, J. Sauer, *J. Phys. Chem. B* **2001**, *105*, 1603–1613.

[371] P. Nachtigall, J. Sauer in *Introduction to Zeolite Science and Practice*, (Eds.: J. Čejka, H. van Bekkum, A. Corma, F. Schüth), Studies in Surface Science and Catalysis, Elsevier, Amsterdam, NLD, **2007**, pp. 701–738.

[372] F. Eder, M. Stockenhuber, J. A. Lercher, *J. Phys. Chem. B* **1997**, *101*, 5414–5419.

Publication List

Publications

- S. Standl, F. M. Kirchberger, T. Kühlewind, M. Tonigold, M. Sanchez-Sanchez, J. A. Lercher, O. Hinrichsen
  Single-Event Kinetic Model for Methanol-to-Olefins (MTO) over ZSM-5: Fundamental Kinetics for the Olefin Co-Feed Reactivity
  Chemical Engineering Journal 402 (2020), 126023

- S. Standl, T. Kühlewind, M. Tonigold, O. Hinrichsen
  On Reaction Pathways and Intermediates During Catalytic Olefin Cracking over ZSM-5
  Industrial & Engineering Chemistry Research 58 (2019), 18107–18124

- S. Standl, O. Hinrichsen
  Kinetic Modeling of Catalytic Olefin Cracking and Methanol-to-Olefins (MTO) over Zeolites: A Review
  Catalysts 8 (2018), 626

- J. Sundberg, S. Standl, T. von Aretin, M. Tonigold, S. Rehfeldt, O. Hinrichsen, H. Klein
  Optimal Process for Catalytic Cracking of Higher Olefins on ZSM-5
  Chemical Engineering Journal 348 (2018), 84–94

- S. Ewald, S. Standl, O. Hinrichsen
  Characterization of Nickel Catalysts with Transient Methods
  Applied Catalysis A: General 549 (2018), 93–101

- S. Standl, M. Tonigold, O. Hinrichsen
  Single-Event Kinetic Modeling of Olefin Cracking on ZSM-5: Proof of Feed Independence
  Industrial & Engineering Chemistry Research 56 (2017), 13096–13108

- T. von Aretin, S. Standl, M. Tonigold, O. Hinrichsen
  Optimization of the Product Spectrum for 1-Pentene Cracking on ZSM-5 Using Single-Event Methodology. Part 1: Two-Zone Reactor
  Chemical Engineering Journal 309 (2017), 886–897

- T. von Aretin, S. Standl, M. Tonigold, O. Hinrichsen
  Optimization of the Product Spectrum for 1-Pentene Cracking on ZSM-5 Using Single-Event Methodology. Part 2: Recycle Reactor
  Chemical Engineering Journal 309 (2017), 873–885

- T. von Aretin, S. Schallmoser, S. Standl, M. Tonigold, J. A. Lercher, O. Hinrichsen
  Single-Event Kinetic Model for 1-Pentene Cracking on ZSM-5
  Industrial & Engineering Chemistry Research 54 (2015), 11792–11803

Conference Contributions

Oral Contributions

- S. Standl, T. Kühlewind, F. M. Kirchberger, M. Tonigold, J. A. Lercher, O. Hinrichsen
  Methanol-to-Olefins (MTO) on ZSM-5: Single-Event Kinetic Modeling, Mechanistic Analysis and Reactor Design
  XXIII International Conference on Chemical Reactors 2018, Ghent, Belgium

- S. Standl, T. Kühlewind, F. M. Kirchberger, M. Tonigold, J. A. Lercher, O. Hinrichsen
  Kinetic Modeling of Methanol-to-Olefins on ZSM-5: From Macrokinetics to the Single-Event Approach
  International Symposium on Chemical Reaction Engineering 2018, Florence, Italy

- J. Sundberg, S. Standl, T. von Aretin, M. Tonigold, S. Rehfeldt, O. Hinrichsen, H. Klein
  Optimaler Prozess für das katalytische Cracken höherer Olefine auf ZSM-5
  Jahrestreffen der ProcessNet-Fachgemeinschaft "Prozess-, Apparate- und Anlagentechnik" 2017, Würzburg, Germany

- S. Standl, J. Sundberg, M. Tonigold, H. Klein, O. Hinrichsen
  Combining Single-Event Kinetics with Reactor Design and Process Simulation: Maximizing Propene Yields in Catalytic Cracking of Higher Olefins
  Asian-Pacific Chemical Reaction Engineering Symposium 2017, Shanghai, PRC

- S. Standl, M. Tonigold, O. Hinrichsen
  Single-Event Kinetic Modeling for Olefins Cracking and MTO on ZSM-5
  EUROPACAT 2017, Florence, Italy

- S. Standl, T. von Aretin, M. Tonigold, O. Hinrichsen
  Single-Event Kinetic Modeling for Zeolite-Based Processes
  Chemical Research in Flanders - CRF 2016, Blankenberge, Belgium

- S. Standl, T. von Aretin, M. Tonigold, O. Hinrichsen
  Optimization of the Product Spectrum for 1-Pentene Cracking on ZSM-5 Using Single-Event Methodology: Two-Zone Reactor and Recycle Reactor
  International Symposium on Chemical Reaction Engineering 2016, Minneapolis, USA

- S. Standl, T. von Aretin, M. Tonigold, O. Hinrichsen
  Optimization of the Product Spectrum for 1-Pentene Cracking on ZSM-5 Using Single-Event Methodology: Two-Zone Reactor and Recycle Reactor
  49. Jahrestreffen Deutscher Katalytiker 2016, Weimar, Germany

- T. von Aretin, S. Standl, S. Schallmoser, J. A. Lercher, O. Hinrichsen
  Single-Event Kinetic Model for 1-Pentene Cracking on ZSM-5
  European Symposium on Chemical Reaction Engineering 2015, Fürstenfeldbruck, Germany

- T. von Aretin, S. Standl, O. Hinrichsen
  Reactor Optimization for Maximized Propene Yields in Olefins Cracking on ZSM-5 Using Single-Event Methodology
  International Conference on Chemical Kinetics 2015, Ghent, Belgium

Poster Contributions

- S. Standl, T. Kühlewind, F. M. Kirchberger, M. Tonigold, J. A. Lercher, O. Hinrichsen
  Microkinetic Modeling of Olefin Cracking and Methanol-to-Olefins (MTO) over ZSM-5
  EUROPACAT 2019, Aachen, Germany

- S. Standl, T. Kühlewind, F. M. Kirchberger, M. Tonigold, J. A. Lercher, O. Hinrichsen
  Microkinetic Model for Methanol-to-Olefins (MTO) over ZSM-5
  52. Jahrestreffen Deutscher Katalytiker 2019, Weimar, Germany

- S. Standl, T. Kühlewind, F. M. Kirchberger, M. Tonigold, J. A. Lercher, O. Hinrichsen
  Methanol-to-Olefins (MTO) on ZSM-5: Different Kinetic Modeling Approaches for the Methylation of Butenes
  51. Jahrestreffen Deutscher Katalytiker 2018, Weimar, Germany

- S. Standl, M. Tonigold, O. Hinrichsen
  Single-Event Kinetic Modeling for Processes on Zeolites: From Olefins Cracking to MTP
  50. Jahrestreffen Deutscher Katalytiker 2017, Weimar, Germany

Declaration

The submitted thesis was supervised by Prof. Dr.-Ing. Kai-Olaf Hinrichsen.

Affirmation

Hereby, I affirm that I am the sole author of this thesis. To the best of my knowledge, I affirm that this thesis does not infringe upon anyone's copyright nor violate any proprietary rights. I affirm that any ideas, techniques, quotations or any other material are in accordance with standard referencing practices.

Moreover, I affirm that, so far, the thesis has not been forwarded to a third party nor is it published. I obeyed all study regulations of the Technische Universität München.

Remarks about the internet

Throughout the work, the internet was used for research and verification. Many of the keywords provided herein, references and other information can be verified on the internet. However, no sources are given, because all statements made in this work are fully covered by the cited literature sources.

Garching, January 7, 2020

Sebastian Standl